Ground Vehicle Engineering Series

ROAD VEHICLE DYNAMICS

FUNDAMENTALS AND MODELING

GEORG RILL

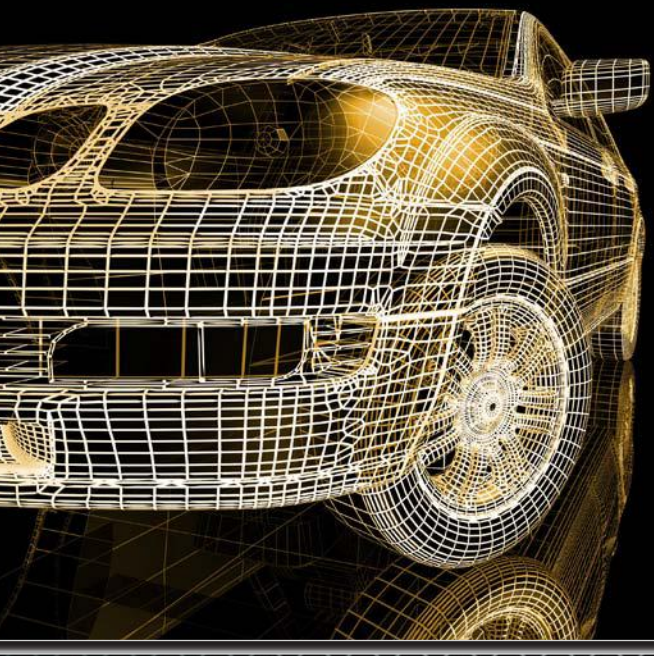

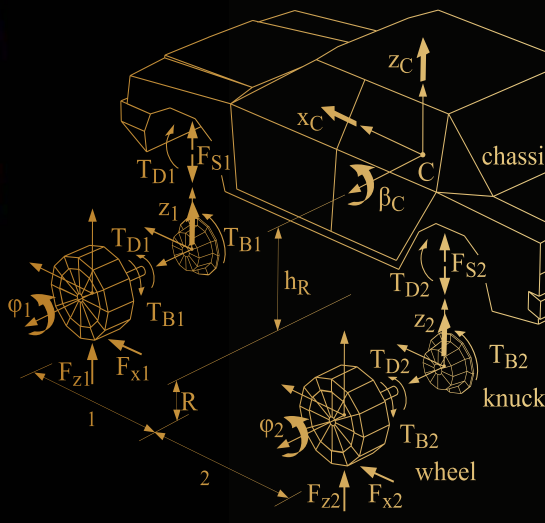

CRC Press
Taylor & Francis Group

ROAD VEHICLE DYNAMICS

FUNDAMENTALS AND MODELING

Ground Vehicle Engineering Series

Series Editor

Dr. Vladimir V. Vantsevich

Professor and Director
Program of Master of Science in Mechatronic Systems Engineering
Lawrence Technological University, Michigan

Driveline Systems of Ground Vehicles: Theory and Design
Alexandr F. Andreev, Viachaslau Kabanau, Vladimir Vantsevich

Road Vehicle Dynamics: Fundamentals and Modeling
Georg Rill

ROAD VEHICLE DYNAMICS

FUNDAMENTALS AND MODELING

GEORG RILL

CRC Press
Taylor & Francis Group
Boca Raton London New York

CRC Press is an imprint of the
Taylor & Francis Group, an **informa** business

CRC Press
Taylor & Francis Group
6000 Broken Sound Parkway NW, Suite 300
Boca Raton, FL 33487-2742

Version Date: 20110823

International Standard Book Number-13: 978-1-4398-9744-7 (eBook - PDF)

Contents

List of Listings

List of Figures

List of Tables

Series Preface

Ground vehicle engineering took shape as an engineering discipline in the 20^{th} century, and became the foundation for significant advancements and achievements, from personal transportation and agriculture machinery to lunar and planetary exploration. As we step into the 21^{st} century with global economic challenges, there is a need for developing fundamentally novel vehicle engineering technologies, and effectively training future generations of engineers. The Ground Vehicle Engineering Series will unite high caliber professionals from the industry and academia to produce top quality professional/reference books and graduate-level textbooks on the engineering of various types of vehicles, including conventional and autonomous mobile machines, terrain and highway vehicles, and ground vehicles with novel concepts of motion.

The Ground Vehicle Engineering Series concentrates on conceptually new methodologies of vehicle dynamics and operation performance analysis and control; advanced vehicle and system design; experimental research and testing; and manufacturing technologies. Applications include, but not limited to, heavy-duty, multi-link, and pickup trucks, farm tractors and agriculture machinery, earth-moving machines, passenger cars, human-assist robotic vehicles, planetary rovers, military conventional and unmanned wheeled and track vehicles, and reconnaissance vehicles.

Dr. Vladimir V. Vantsevich
Series Editor

Preface

The basic objective of this textbook is to provide fundamental knowledge of the dynamics of road vehicles and to impart insight into and details on modeling aspects. Road vehicles have been developed and built for more than 125 years. From the beginning to now, the main goal in vehicle dynamics has been to achieve optimal safety and ride comfort. Today, computer simulations have become an essential tool to develop new and enhance existing concepts for road vehicles. Electronically controlled components provide new options. Usually they are developed and tested in software-in-the-loop (SIL) or hardware-in-the-loop (HIL) environments. Today, an automotive engineer requires a basic knowledge of the fundamentals and the skill to build basic simulation models, to handle sophisticated ones, or to operate simulation tools properly. Yet, only books on the fundamentals of vehicle dynamics or on modeling aspects are available currently. Both subjects are combined for the first time in this textbook. A first course in dynamics and a basic knowledge of a programming language are prerequisites.

Lecture notes for an undergraduate course in vehicle dynamics, form the basis of this textbook. The notes were then extended to serve as the basis for a graduate course, first delivered at the State University in Campinas (UNICAMP) by the author in 1992 and repeated as a short course in vehicle dynamics several times since then. Part of the notes combined with additional material are also used for in-house seminars at different automotive suppliers and in several workshops at conferences on different topics of vehicle dynamics. A truly motivating personal contact with Vladimir V. Vantsevich, the editor of the Ground Vehicle Engineering Series, at the *21st International Symposium on Dynamics of Vehicles on Roads and Tracks* in 2009 resulted in a textbook proposal to Chapman & Hall/CRC. The lecture notes and the material for the seminars were put together and completely revised. Exercises at the end of each chapter serve to repeat the contents and check the knowledge of the reader. Many programming examples, which were used in the seminars and workshops to visualize the results and to deepen insight on vehicle dynamics, are integrated into this textbook. Due to its ease of use and popularity, MATLAB® was used as the programming language. This textbook may be used in a graduate course on vehicle dynamics for classroom teaching and self-study. Skipping the modeling aspects, it will suit an Introduction to Vehicle Dynamics at the senior undergraduate level. The modeling aspects may even be integrated into a course on multibody dynamics. In addition, this textbook will also help practicing engineers and scientists in the field of vehicle

dynamics by providing a full range of vehicle models that may be used for basic studies, for parameter variations, optimization, as well as the simulation of different driving maneuvers.

Modern SI units are used throughout this textbook. The introduction in Chapter 1 provides an overview of units and quantities, discusses the terminology in vehicle dynamics, deals with definitions, gives an overview on multibody dynamics, and derives the equations of motion for a first vehicle model. Chapter 2 is dedicated to the road. At first, a sophisticated road model is discussed, then deterministic and stochastic road models are described in detail. The handling tire model TMeasy is discussed in Chapter 3. It includes a sophisticated contact calculation and provides all forces and torques. The longitudinal and lateral forces as well as the torque about the vertical axis are modeled in a first-order dynamic approach. Besides that, measuring techniques and modeling aspects are also discussed. Chapter 4 focuses on the drive train. Components and concepts of different drive trains are discussed first. Then, the dynamics of wheel and tire are studied in detail. A simple vehicle wheel tire model including a lockable brake torque model is presented and investigated. A short description of the layout and modeling aspects of differentials, standard drive trains, the transmission, the clutch, and different power sources completes this chapter. The purpose and components of suspension systems are discussed in Chapter 5. A dynamic model of rack-and-pinion steering as well as a kinematic model of a double wishbone suspension system are presented and analyzed via the simulation results. Chapter 6 is dedicated to force elements. Besides the standard force elements like springs, anti-roll bars, and dampers, dynamic force elements, including hydro-mounts are discussed in detail. A sophisticated model for a sweep sine excitation, as well as models for different dynamic forces, are provided here. The fundamentals of vehicle dynamics in the vertical, longitudinal, and lateral directions are provided in Chapters 7 to 9. Each chapter starts with a simple model approach. Then, the effects of nonlinear, dynamic, or even active force elements, as well as the influence of suspension kinematics are studied. Practical aspects and applications complete these chapters. Finally, Chapter 10 presents the idea of a full three-dimensional vehicle model and shows and discusses typical results of standard driving maneuvers.

I am very grateful to Vladimir V. Vantsevich, who encouraged me to write this textbook. I am also thankful to the publisher, namely, Senior Editor Jonathan W. Plant, his assistant Arlene Kopeloff, and the Project Coordinator Amber Donley, for all their support, which allowed me to focus on the contents and not to bother with the layout of this textbook.

The results of the exercises as well as all MATLAB®-Examples (M-Files) are available for download on the website[1] of the publisher.

[1] http://www.crcpress.com/product/isbn/9781439838983

About the Author

Georg Rill has been a researcher and a educator for nearly thirty years. He is currently a professor in the faculty of mechanical engineering at the University of Applied Science Regensburg, Germany. For nearly five years he was a technical specialist at the Daimler-Benz Company in Stuttgart, Germany. There, he developed a full vehicle model for trucks that was used in the Daimler-Benz driving simulator for many years. He has been a visiting professor at the State University in Campinas, Brazil. One of his three sabbaticals he spent at Ford Motor Company in Detroit, Michigan. He is the author of numerous journal publications on vehicle dynamics. His first book, entitled *Simulation von Kraftfahrzeugen*, was published in 1994.

1

Introduction

CONTENTS

1.1 Units and Quantities

1.1.1 SI System

The International System of Units[1] is the world's most widely used system of measurement. The International Organization for Standardization (ISO) laid it out in ISO 31 and ISO 1000. The modern SI system will be used through out this textbook. Common quantities, their variations, as well as conversion tables may be found in [11]. The most important physical quantities, their

[1] Abbreviated SI from the French *le Système International d'Unités*.

standardized units, as well as some old but still important units are collected in Table 1.1. The unit *rad* can be replaced by the numeral 1 in calculations.

TABLE 1.1
Physical Quantities, Common Symbols, and Units

Quantity	Name	Unit	SI	Relationship
Length ℓ	meter	m	yes	
	inch	in	no	$1\,in = 0.0254\,m$
Area A	square meter	m^2	yes	
Volume V	cubic meter	m^3	yes	
Angle φ	radian	rad	yes	
	Grad	$^\circ$	no	$1^\circ = 0.01745\,rad$
Mass m	kilogram	kg	yes	
	pound	lb	no	$1\,pd = 0.45359\,kg$
Time t	second	s	yes	
Frequency f	hertz	Hz	no	$1\,Hz = 1/s$
Angular freq. ω		s^{-1}	yes	$\omega = 2\pi f$
Velocity v		m/s	yes	
	kilometers / hour	km/h	no	$1\,km/h = 1/3.6\,m/s$
	miles / hour	mp/h	no	$1\,m/ph = 1.609\,km/h$
Angular velocity v		rad/s	yes	
Rotational speed n	rpm	$1/min$	no	$1\,rpm = (1/60)\,s^{-1}$
Acceleration a		m/s^2	yes	
Angular accel.		rad/s^2	yes	
Force F	newton	N	yes	$1\,N = 1\,kgms^{-2}$
Torque M	newtonmeter	Nm	yes	$1\,Nm = 1\,kgm^2s^{-2}$
pressure p	pascal	Pa	yes	$1\,Pa = 1\,N/m^2$
	bar	bar	no	$1\,bar = 10^5\,Pa$
	pound / square inch	psi	no	$1\,psi = 6\,894.8\,Pa$
Temperature T	kelvin	K	yes	

With the exception of hours ($1\,h = 3,600\,s$) and minutes ($1\,min = 60\,s$), decimal multiples and submultiples will form additional legal units.

1.1.2 Tire Codes

Although the SI unit system has been nearly globally adopted, the alphanumeric code molded into the sidewall of the tire is still a mixture of modern and old units. To take an example, P215/60R16 signifies by the letter P a passenger car tire with a 215-millimeter tire width. The height of the sidewall of the tire is 60% of the width, and the letter R states that the cord threads of the tire casing run in the radial direction. Finally, the tire is designed to fit rims of 16 inches. So, the height of this tire amounts to 215*0.60 = 129 mm, and the conversion from inches to meters and millimeters, given in Table 1.1,

will produce a rim diameter of 16*0.0254 = 0.4064 m = 406.4 mm. Adding twice the tire height to the rim diameter will then result in an overall tire diameter of 2*129 mm + 406.4 mm = 664.4 mm, which is equivalent to a tire radius of 332.2 mm. By adding the load index (a number code, from 0 to 279), along with the speed rating symbol (a letter code, from A to Z), we finally end up in the ISO Metric Sizing System.

Some light truck tires follow the Light Truck High Flotation System, which for example, may read as 37x12.5R17LT. Here, the code starts with a two-digit number separated by the character x from a three- or four-digit number, indicating the diameter of the tire and the section width (cross-section) of the tire. The following letter B for belted bias, D for diagonal bias, or R for radial tire names the construction type. The following two-digit number gives the diameter in inches of the wheel rim that this tire is designed to fit. Finally, the letters LT indicate that this is a Light Truck tire. Load index and speed rating are not required for this type of tire but may be provided by the manufacturer.

1.2 Terminology

1.2.1 Vehicle Dynamics

Vehicle dynamics are a part of engineering primarily based on classical mechanics but may also involve control theory, physics, electrical engineering, chemistry, communications, psychology, etc. Here, the focus is laid on ground vehicles supported by wheels and tires. Vehicle dynamics encompass the interaction of

- Driver
- Vehicle
- Load
- Environment

Vehicle dynamics mainly deals with

- Improvement in active safety and driving comfort
- Reduction in road destruction

Vehicle dynamics employes

- Computer calculations
- Test rig measurements
- Field tests

In the following the interactions between the single systems and the problems with computer calculations and/or measurements are discussed.

1.2.2 Driver

By various means the driver can interfere with the vehicle:

$$\text{Driver} \left\{ \begin{array}{ll} \text{Steering wheel} & \text{Lateral dynamics} \\ \text{Accelerator pedal} & \\ \text{Brake pedal} & \text{Longitudinal dynamics} \\ \text{Clutch} & \\ \text{Gear shift} & \end{array} \right\} \longrightarrow \text{Vehicle}$$

The vehicle provides the driver with the following information:

$$\text{Vehicle} \left\{ \begin{array}{ll} \text{Vibrations:} & \text{longitudinal, lateral, vertical} \\ \text{Sounds:} & \text{motor, aerodynamics, tires} \\ \text{Instruments:} & \text{velocity, external temperature, ...} \end{array} \right\} \longrightarrow \text{Driver}$$

The environment also influences the driver:

$$\text{Environment} \left\{ \begin{array}{l} \text{Climate} \\ \text{Traffic density} \\ \text{Track} \end{array} \right\} \longrightarrow \text{Driver}$$

The driver's reaction is very complex. To achieve objective results, an "ideal" driver is used in computer simulations; and in driving experiments, automated drivers (e.g., steering machines) are employed. Transferring results to normal drivers is often difficult if field tests are made with test drivers. Field tests with normal drivers must be evaluated statistically. Of course, the driver's security must have absolute priority in all tests. Driving simulators provide an excellent means of analyzing the behavior of drivers even in limit situations without danger. Many have tried to analyze the interaction between driver and vehicle with complex driver models for some years.

1.2.3 Vehicle

The following vehicles are listed in the ISO 3833 directive:

- Motorcycles
- Passenger cars
- Buses
- Trucks
- Agricultural tractors
- Passenger cars with trailer
- Truck trailer/Semitrailer
- Road trains

For computer calculations these vehicles must be depicted in mathematically describable substitute systems. The generation of the equations of motion, the numeric solution, as well as the acquisition of data require great expense. In these days of PCs and workstations, computing costs hardly matter anymore. At an early stage of development, often only prototypes are available for field and/or laboratory tests. Results can be falsified by safety devices, e.g., jockey wheels on trucks.

1.2.4 Load

Trucks are conceived for taking up load. Thus, their driving behavior changes.

$$\text{Load} \left\{ \begin{array}{l} \text{Mass, Inertia, Center of gravity} \\ \text{Dynamic behaviour (liquid load)} \end{array} \right\} \longrightarrow \text{Vehicle}$$

In computer calculations, problems occur when determining the inertias and the modeling of liquid loads. Even the loading and unloading process of experimental vehicles takes some effort. When carrying out experiments with tank trucks, flammable liquids must be substituted with water. Thus, the results achieved cannot be simply transferred to real loads.

1.2.5 Environment

The environment influences primarily the vehicle:

$$\text{Environment} \left\{ \begin{array}{ll} \text{Road:} & \text{irregularities, coefficient of friction} \\ \text{Air:} & \text{resistance, cross wind} \end{array} \right\} \longrightarrow \text{Vehicle,}$$

but also affects the driver:

$$\text{Environment} \left\{ \begin{array}{l} \text{Climate} \\ \text{Visibility} \end{array} \right\} \longrightarrow \text{Driver}$$

Through the interactions between vehicle and road, roads can quickly be destroyed. The greatest difficulty with field tests and laboratory experiments is the virtual impossibility of reproducing environmental influences. The main problems with computer simulation are the description of random road irregularities, the interaction of tires and road, as well as the calculation of aerodynamic forces and torques.

1.3 Definitions

1.3.1 Coordinate Systems

If the chassis is supposed to be a rigid body, one coordinate system fixed to the vehicle, which in general is located in the center C, then earth-fixed axis

system 0 will be sufficient to describe the overall motions of the vehicle body, Figure 1.1. The earth-fixed system 0 with the axis x_0, y_0, z_0 serves as inertial

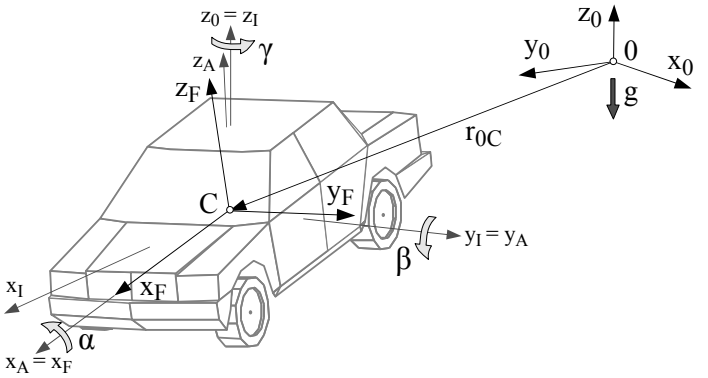

FIGURE 1.1
Position and orientation of the vehicle body.

reference frame. Its origin 0 lies in a reference ground plane. Throughout this textbook the z_0-axis will point in the opposite direction of the gravity vector g. Within the vehicle-fixed system F, the x_F-axis points forward, the y_F-axis to the left, and the z_F-axis upward, which will correspond with the definitions in the ISO 8855 directive.

The orientation of the vehicle-fixed axis system F with respect to the inertial frame 0 may be defined by the Cardan or Bryant angles γ, β, and α, which represent the yaw, the pitch, and the roll motion of the vehicle body. The first rotation about the $z_0{=}z_I$-axis defines the intermediate axis system with x_I and y_I parallel to the horizontal ground.

In complex vehicle models it is often more convenient to attach the vehicle-fixed axis system F to a representative chassis point rather than to the center of gravity of the vehicle, because the latter will change with different loading conditions.

The wheel consists of the tire and the rim. Handling tire models simplify the contact patch by a plane, which is represented by the contact point P and an unit vector e_n perpendicular to this plane. The contact geometry is discussed in detail in Section 3.2. The rim is mounted at the wheel carrier or knuckle. The suspension system, which attaches the wheel carrier to the chassis, is extensively described in Chapter 5. Depending on the type of suspension system, the wheel carrier and the attached wheel can perform a hub motion z and optionally a steering motion δ, Figure 1.2. To describe the position and orientation of the wheel carrier and the wheel, a reference frame with the axes x_C, y_C, z_C is fixed to the wheel carrier. The origin of this axis system is supposed to coincide with the wheel center M. The position and the orientation of the wheel carrier depend on the hub motion z and optionally on the steer

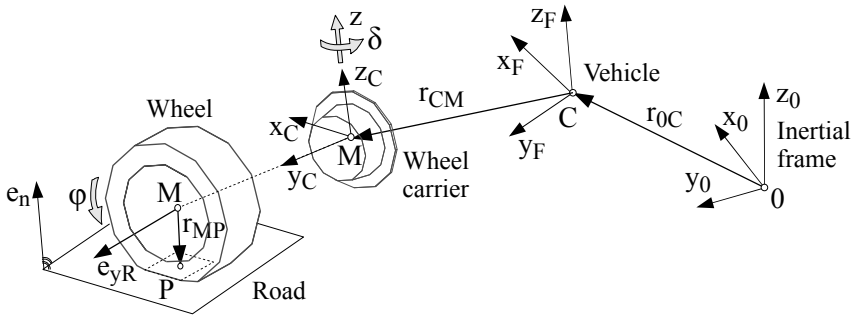

FIGURE 1.2
Wheel position and orientation.

motion δ. In design position, the corresponding axes of the frames C and F are supposed to be parallel. The wheel itself rotates with the angle φ about an axis that is determined by the unit vector e_{yR}, Figure 1.2.

1.3.2 Design Position of Wheel Center

The design position of the wheel center M_0 is roughly[2] determined by the

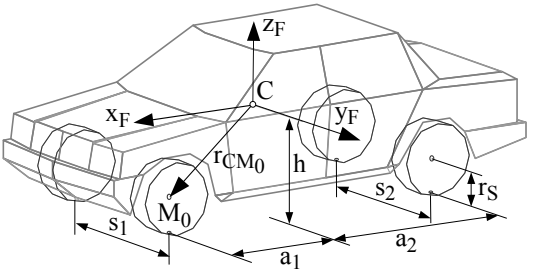

FIGURE 1.3
Design position of wheels.

wheelbase $a = a_1 + a_2$ and the track widths s_1, s_2 at the front and rear axles, Figure 1.3. If left/right symmetry is assumed, then the position vector

$$r_{CM_0,F} = \begin{bmatrix} a_1 \\ s_1/2 \\ -h + r_S \end{bmatrix} \tag{1.1}$$

denoted in the vehicle-fixed reference frame will define the design position of the front left wheel center M_0 relative to the vehicle center C. Here, h denotes

[2]Note: The track width is defined as the distance of the contact points at an axle. On cambered wheels, the distance of the wheel centers is slightly different.

the height of the vehicle center C above the ground and r_S names the static tire radius, which takes the tire deflection caused by the weight of the vehicle into account.

By changing the sign in the second component ($s_1/2 \rightarrow -s_1/2$), Equation }(refEq:introduction:wheel design position relative) applies for the right wheel too. Finally, the design position of rear wheels is obtained by replacing a_1 and s_1 by $-a_2$ and s_2, respectively.

1.3.3 Toe-In, Toe-Out

Wheel toe-in is an angle formed by the center line of the wheel and the longitudinal axis of the vehicle, looking at the vehicle from above, Figure 1.4. When the extensions of the wheel center lines tend to meet in front of the direction of travel of the vehicle, this is known as toe-in. If, however, the lines tend to meet behind the direction of travel of the vehicle, this is known as toe-out. The amount of toe can be expressed in degrees as the angle δ to which the wheels are out of parallel, or, as the difference between the track widths as measured at the leading and trailing edges of the tires or wheels. Note that at the left wheel the sign of toe angle δ does not correspond to a positive rotation around the z-axis. Toe settings affect three major areas of

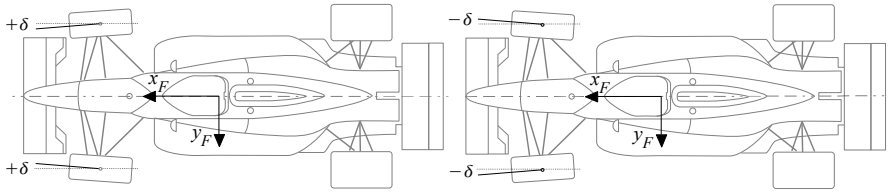

FIGURE 1.4
Toe-in and toe-out.

performance: tire wear, straight-line stability, and corner entry handling characteristics. For minimum tire wear and power loss, the wheels on a given axle of a car should point directly ahead when the car is running in a straight line. Excessive toe-in or toe-out causes the tires to scrub, as they are always turned relative to the direction of travel. Toe-in improves the directional stability of a car and reduces the tendency of the wheels to shimmy.

1.3.4 Wheel Camber

Wheel camber is the angle of the wheel relative to vertical, as viewed from the front or the rear of the car, Figure 1.5. If the wheel leans away from the car, it has positive camber; if it leans in toward the chassis, it has negative camber. Again, at the left wheel, the sign of camber angle γ does not correspond to a positive rotation around the x-axis. The wheel camber angle must not be

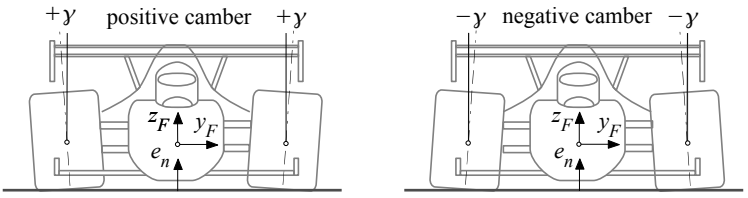

FIGURE 1.5
Positive and negative camber angles.

mixed up with the tire camber angle, which is defined as the angle between the wheel center plane and the local track normal e_n. Excessive camber angles cause nonsymmetric tire wear. A tire can generate maximum lateral force during cornering if it is operated with a slightly negative tire camber angle. As the chassis rolls when cornering, the suspension must be designed such that the wheels perform camber changes as the suspension moves up and down. An ideal suspension will generate an increasingly negative wheel camber as the suspension deflects upward.

1.3.5 Design Position of the Wheel Rotation Axis

Usually, the wheel rotation axis, which is described by the unit vector e_{yR}, will not coincide with the y_C-axis, which is part of the corresponding axis system located in the wheel center and fixed to the wheel carrier, Figure 1.6. The orientation of the unit vector e_{yR} can be defined either by the angles δ_0

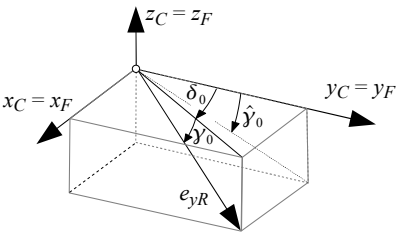

FIGURE 1.6
Design position of wheel rotation axis.

and γ_0, or by δ_0 and $\hat{\gamma}_0$, where δ_0 is the angle between the y_C-axis and the projection line of the wheel rotation axis into the $x_C\, y_C$-plane. The angle $\hat{\gamma}_0$ describes the angle between the y_C-axis and the projection line of the wheel rotation axis into the $y_C\, z_C$-plane, whereas γ_0 is the angle between the wheel rotation axis e_{yR} and its projection into the $x_C\, y_C$-plane. Toe-in and a positive camber angle are indicated by $\delta_0 >$ and $\gamma_0 > 0$ or $\hat{\gamma}_0 > 0$ at the left wheel.

In the design position, where the corresponding axis of the vehicle-fixed axis system F and the wheel carrier-fixed coordinate system C are parallel, one gets by inspecting Figure 1.6,

$$e_{yR,F} \;=\; e_{yR,C} \;=\; \frac{1}{\sqrt{\tan^2\delta_0 + 1 + \tan^2\hat{\gamma}_0}} \begin{bmatrix} \tan\delta_0 \\ 1 \\ -\tan\hat{\gamma}_0 \end{bmatrix}. \qquad (1.2)$$

On the other hand, applying a series of elementary rotations results in

$$e_{yR,F} \;=\; e_{yR,C} \;=\; \begin{bmatrix} \sin\delta_0\,\cos\gamma_0 \\ \cos\delta_0\,\cos\gamma_0 \\ -\sin\gamma_0 \end{bmatrix}. \qquad (1.3)$$

On a flat and horizontal road where the track normal e_n points in the direction of the vertical axis $z_C = z_F$, the angles δ_0 and γ_0 correspond to the toe angle and the camber angle, respectively. To specify the difference between γ_0 and $\hat{\gamma}_0$, the ratio between the third and second component of the unit vector e_{yR} is considered now. Equations (1.2) and (1.3) deliver

$$\frac{-\tan\hat{\gamma}_0}{1} \;=\; \frac{-\sin\gamma_0}{\cos\delta_0\,\cos\gamma_0} \qquad \text{or} \qquad \tan\hat{\gamma}_0 \;=\; \frac{\tan\gamma_0}{\cos\delta_0}\,. \qquad (1.4)$$

Hence, for small angles $\delta_0 \ll 1$, the difference between the angles γ_0 and $\hat{\gamma}_0$ is hardly noticeable. Kinematics and compliance test machines usually measure the angle $\hat{\gamma}_0$. That is why the automotive industry mostly uses this one instead of γ_0 to determine the orientation of the wheel rotation axis in the design position.

1.3.6 Wheel Aligning Point

Often the position of the wheel rotation axis is defined by the wheel center M and an additional point D which is called "wheel alignment point", Figure 1.7. If point D is located inside the wheel center W, then the unit vector pointing

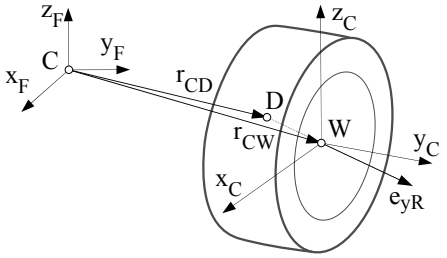

FIGURE 1.7
Wheel alignment point.

in the direction of the wheel rotation axis is given by

$$e_{yR,F} \;=\; \frac{r_{CW,F} - r_{CD,F}}{|r_{CW,F} - r_{CD,F}|}\,, \qquad (1.5)$$

where the vectors $r_{CW,F}$ and $r_{CD,F}$ describe the design position of the wheel center W and the wheel alignment point D relative to the origin C of the vehicle-fixed reference frame F.

1.4 Multibody Dynamics Tailored to Ground Vehicles

1.4.1 Modeling Aspects

For dynamic simulation, the vehicles are usually modeled by multibody systems (MBS), [17]. Typically, the overall vehicle model is separated into different subsystems [30]. Figure 1.8 shows the components of a passenger car model that can be used to investigate handling and ride properties. The ve-

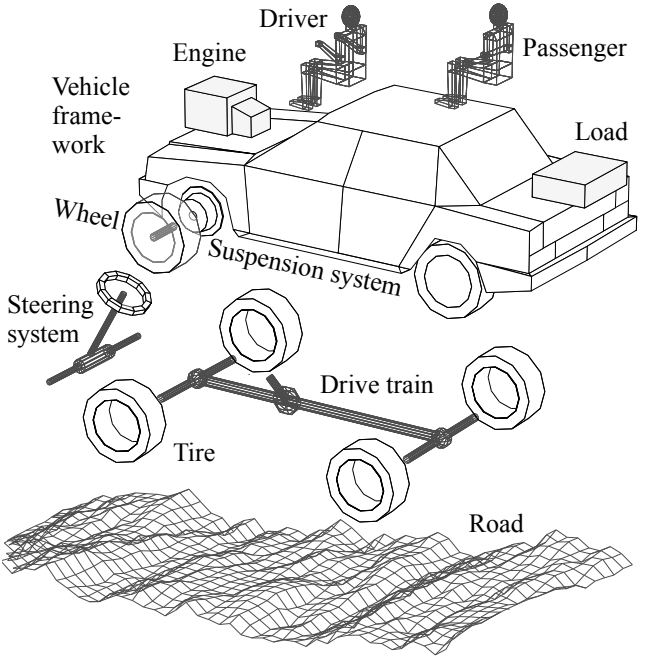

FIGURE 1.8
Vehicle model structure.

hicle model consists of the vehicle framework and subsystems for the steering system and the drive train.

The vehicle framework represents the kernel of the model. It at least includes the module chassis and modules for the wheel/axle suspension systems. The vehicle framework is supplemented by modules for the load, an elas-

tically suspended engine, and passenger/seat models. A simple load module just takes the mass and inertia properties of the load into account. To describe the sloshing effects of liquid loads, dynamic load models are needed [43]. The subsystems, elastically suspended engine, passenger/seat, and in heavy truck models a suspended driver's cabin can all be handled by a generic free-body model [38].

For standard vehicle dynamics analysis, the chassis can be modeled by one rigid body [2]. However, in the case of heavy trucks, the compliance of the frame and the elastically suspended driver's cab will require at least a lumped mass model approach or the embedding of an enhanced finite element structure. Most wheel/axle suspension systems can be described by typical MBS elements such as rigid bodies, links, joints, and force elements [34]. Due to their robustness, leaf springs are still a popular choice for solid axles. They combine guidance and suspension properties, which causes many problems in modeling [9]. A lumped mass approach can overcome these problems [42].

The steering system at least consists of the steering wheel, a flexible steering shaft, and the steering box, which may also be power-assisted. A very sophisticated model of the steering system that includes compliancies, dry friction, and clearance can be found in [24].

Tire forces and torques have a dominant influence on vehicle dynamics. Usually, semi-empirical tire models are used for vehicle handling analysis. They combine a reasonable computer runtime performance with sufficient model accuracy. Complex tire models are valid even for high frequencies and on really rough roads. But, they are computer time consuming and therefore used in special investigations only. The "Tyre Model Performance Test (TMPT)" provides information about the efficiency and problems of tire modeling and parameterization as well as the integration in standard multibody system program codes [21]. In this textbook the tire model "TMeasy" is discussed in detail. This semi-empirical tire model meets the requirements of both user friendliness and sufficient model accuracy [12].

The drive train model in [38] takes lockable differentials into account, and it combines front-wheel, rear-wheel, and all-wheel drive. A simplified model for a rear-wheel drive will be presented in this textbook. The drive train is supplemented by a module describing the engine torque. It may be modeled, as done here, quite simply by a first-order differential equation or by enhanced engine torque modules.

Road irregularities and variations in the coefficient of friction present significant impacts on the vehicle. Simple road models are discussed in Chapter 2. A more enhanced model approach for generating two-dimensional reproducible random profiles is presented in [32].

This textbook restricts itself to the fundamentals of the dynamics of ground vehicles and will therefore focus on simple comfort and handling models for passenger cars. Besides some planar models, a simple three-dimensional model with a rigid chassis and four independently suspended wheels will be provided too.

1.4.2 Kinematics

A simple three-dimensional vehicle model consists of at least five rigid bodies, Figure 1.9. The position and orientation of each model body $i = 1, 2, \ldots$ will

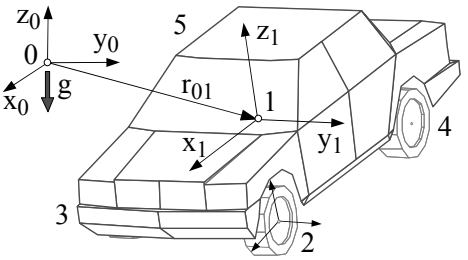

1) Vehicle body (chassis)
2) Wheel and wheel carrier front left
3) Wheel and wheel carrier front right
4) Wheel and wheel carrier rear left
5) Wheel and wheel carrier rear right

FIGURE 1.9
Bodies of a vehicle model.

be described relative to the earth-fixed coordinate system 0 that serves here as an inertial reference frame. Throughout this textbook the z_0-axis of the earth-fixed reference frame will point in the opposite direction of the gravity vector g.

The movements of each wheel and wheel carrier relative to the vehicle body (chassis) are restricted by links, joints, or other guiding elements. The resulting constraint forces and torques may either be eliminated from the equations of motion by appropriate algorithms or taken into account via Lagrange multipliers. The first method is cumbersome but will result in a minimized number of Ordinary Differential Equations (ODEs), whereas the latter will lead to Differential Algebraic Equations (DAEs).

A right-handed Cartesian coordinate system is fixed to each body in its center. Then, the position and the orientation of body i with respect to the inertial reference frame 0 is determined by the position vector

$$r_{0i,0} \;=\; r_{0i,0}(y) \tag{1.6}$$

and the rotation matrix

$$A_{0i} \;=\; A_{0i}(y)\,, \tag{1.7}$$

where the generalized coordinates $y_1, y_2, \ldots y_f$ needed to describe the motions of the multibody system are collected in the vector y and the comma-separated subscript 0 indicates that the coordinates of the position vector r_{0i} are measured in the reference frame 0.

The columns of the rotation matrix A_{0i} are orthogonal unit vectors measured in the inertial frame 0 and pointing in the direction of the axis of the body-fixed coordinate system i. For such kinds of orthonormal matrices

$$A_{0i}^T\, A_{0i} = A_{0i}\, A_{0i}^T = I \quad \text{or} \quad A_{0i}^{-1} = A_{0i}^T \tag{1.8}$$

will hold, where I denotes the corresponding matrix of identity. If the components of the vector r are measured in the body-fixed coordinate system i, multiplication with the rotation matrix A_{0i} transforms this vector via

$$r_{,0} \;=\; A_{0i}\, r_{,i} \tag{1.9}$$

to the earth-fixed axis system 0, and

$$r_{,i} \;=\; A_{0i}^{T}\, r_{,0} \tag{1.10}$$

quite simply defines the inverse transformation.

The velocity with which body i is moving relative to the inertial system 0 is determined by the time derivative of the position vector defined in Equation (1.6)

$$v_{0i,0} \;=\; \frac{d}{dt}\, r_{0i,0}(y) \;=\; \dot{r}_{0i,0}(y) \;=\; \sum_{m=1}^{f} \frac{\partial r_{0i,0}(y)}{\partial y_m}\, \dot{y}_m \;=\; v_{0i,0}(y, \dot{y})\,. \tag{1.11}$$

The time derivative of the rotation matrix multiplied by its transposed results in a skew-symmetric matrix

$$\widetilde{\omega}_{0i,0} \;=\; \frac{d}{dt}\left(A_{0i,0}(y)\right)\, A_{0i,0}^{T}(y) \;=\; \sum_{m=1}^{f} \frac{\partial A_{0i}(y)}{\partial y_m}\, \dot{y}_m\, A_{0i,0}^{T}(y) \;=\; \widetilde{\omega}_{0i,0}(y, \dot{y})\,. \tag{1.12}$$

Its essential components

$$\widetilde{\omega}_{0i,0} \;=\; \begin{bmatrix} 0 & -\omega_{0i,0}(3) & \omega_{0i,0}(2) \\ \omega_{0i,0}(3) & 0 & -\omega_{0i,0}(1) \\ -\omega_{0i,0}(2) & \omega_{0i,0}(1) & 0 \end{bmatrix} \tag{1.13}$$

define the vector of the angular velocity $\omega_{0i,0} = [\omega_{0i,0}(1),\, \omega_{0i,0}(2),\, \omega_{0i,0}(3)]^{T}$ with which the body-fixed axis system i rotates relative to the earth-fixed axis system 0. A direct calculation shows that

$$\widetilde{\omega}_{0i,0}\, r_{,0} \;=\; \omega_{0i,0} \times r_{,0} \tag{1.14}$$

holds for any vector $r_{,0}$, which means that multiplication of the skew-symmetric matrix of the angular velocities can be replaced by the corresponding vector- or cross-product.

Depending on the kind of constraints, the algebraic representation of the velocity vector $v_{0i,0} = v_{0i,0}(y, \dot{y})$ and the vector of the angular velocities $\omega_{0i,0} = \omega_{0i,0}(y, \dot{y})$ may become very complex. However, significant simplifications are possible if the time derivative of the vector of the generalized coordinates $\dot{y}$ is replaced via

$$z \;=\; K(y)\, \dot{y} \tag{1.15}$$

by a corresponding vector of generalized velocities $z = z(y, \dot{y})$. Then, the algebraic representation for the resulting velocities and angular velocities

$$v_{0i,0}(y, \dot{y}) \implies v_{0i,0}(y, z) \quad \text{and} \quad \omega_{0i,0}(y, \dot{y}) \implies \omega_{0i,0}(y, z) \tag{1.16}$$

will be less complicated. In many cases a simple inspection of the resulting velocity terms already leads to appropriate generalized velocities [18]. The trivial choice

$$z \;=\; \dot{y} \tag{1.17}$$

is always possible. Here, the kinematical matrix $K = K(y)$ simplifies to the corresponding matrix of identity.

The time derivatives of the velocities and the angular velocities finally result in the corresponding accelerations

$$\begin{aligned} a_{0i,0} \;&=\; \frac{d}{dt}\, v_{0i,0}(y, z) \;=\; \sum_{m=1}^{f} \frac{\partial v_{0i,0}(y, z)}{\partial y_m}\, \dot{y}_m \;+\; \sum_{m=1}^{f} \frac{\partial v_{0i,0}(y, z)}{\partial z_m}\, \dot{z}_m \,, \\ \alpha_{0i,0} \;&=\; \frac{d}{dt}\, \omega_{0i,0}(y, z) \;=\; \sum_{m=1}^{f} \frac{\partial \omega_{0i,0}(y, z)}{\partial y_m}\, \dot{y}_m \;+\; \sum_{m=1}^{f} \frac{\partial \omega_{0i,0}(y, z)}{\partial z_m}\, \dot{z}_m \,. \end{aligned} \tag{1.18}$$

1.4.3 Equations of Motion

The motions of one rigid body are governed by Newton's law

$$m_i\, a_{0i,0} \;=\; F_{i,0} \tag{1.19}$$

and Euler's equation

$$\Theta_{i,0}\, \alpha_{0i,0} + \omega_{0i,0} \times \Theta_{i,0}\, \omega_{0i,0} \;=\; T_{i,0} \,, \tag{1.20}$$

where m_i is the mass of body i, and $\Theta_{i,0}$ denotes the inertia tensor of body i defined with respect to its center of mass and measured in the inertial frame. If the body is exposed to kinematical constraints, then the forces and torques acting on body i can be split into two parts

$$F_{i,0} \;=\; F^c_{i,0} + F^a_{i,0} \quad \text{and} \quad T_{i,0} \;=\; T^c_{i,0} + T^a_{i,0} \,, \tag{1.21}$$

where $F^c_{i,0}$, $T^c_{i,0}$ represent the forces and torques provided by the constraints and $F^a_{i,0}$, $T^a_{i,0}$ collect all other forces and torques applied to body i.

Similar to D'Alembert's principle of virtual work, Jourdain postulated that the virtual power of all constraint forces and torques must vanish. For a system with k rigid bodies, we get

$$\sum_{i=1}^{k} \left\{ \delta v^T_{0i,0}\, F^c_{i,0} \;+\; \delta \omega^T_{0i,0}\, T^c_{i,0} \right\} \,. \tag{1.22}$$

The virtual velocity and the virtual angular velocity of body i are defined by

$$\delta v_{0i,0} \;=\; \frac{\partial v_{0i,0}}{\partial z}\,\delta z \quad \text{and} \quad \delta\omega_{0i,0} \;=\; \frac{\partial \omega_{0i,0}}{\partial z}\,\delta z\,, \tag{1.23}$$

where the $f\times 1$-vector δz collects the variations of the generalized velocities δz_1, δz_2, $\ldots\,\delta z_f$ and the partial derivatives simply named as partial velocities and partial angular velocities are arranged in the $3\times f$-Jacobian matrices of translation and rotation

$$\frac{\partial v_{0i,0}}{\partial z} \;=\; \left[\,\frac{\partial v_{0i,0}(y,z)}{\partial z_1},\, \frac{\partial v_{0i,0}(y,z)}{\partial z_2}\;\ldots\;\frac{\partial v_{0i,0}(y,z)}{\partial z_f}\,\right], \tag{1.24}$$

$$\frac{\partial \omega_{0i,0}}{\partial z} \;=\; \left[\,\frac{\partial \omega_{0i,0}(y,z)}{\partial z_1},\, \frac{\partial \omega_{0i,0}(y,z)}{\partial z_2}\;\ldots\;\frac{\partial \omega_{0i,0}(y,z)}{\partial z_f}\,\right]. \tag{1.25}$$

Using the Jacobian matrices, the accelerations provided by Equation (1.18) can be written as

$$a_{0i,0} \;=\; \frac{\partial v_{0i,0}}{\partial z}\,\dot z \;+\; a^R_{0i,0} \quad \text{and} \quad \alpha_{0i,0} \;=\; \frac{\partial \omega_{0i,0}}{\partial z}\,\dot z \;+\; \alpha^R_{0i,0}\,, \tag{1.26}$$

where $\dot z$ is the time derivative of the vector of generalized velocities and

$$a^R_{0i,0} \;=\; \sum_{m=1}^{f} \frac{\partial v_{0i,0}(y,z)}{\partial y_m}\,\dot y_m \quad \text{and} \quad \alpha^R_{0i,0} \;=\; \sum_{m=1}^{f} \frac{\partial \omega_{0i,0}(y,z)}{\partial y_m}\,\dot y_m \tag{1.27}$$

abbreviates the remaining terms in the accelerations. By combining Equation (1.21) with Equations (1.19) and (1.20), one is able to put the constraint forces and torques down to dynamic terms and the applied forces and torques. Using the notation in Equations (1.26) and (1.27), Jourdain's principle reads as

$$\begin{aligned}\sum_{i=1}^{k} \Bigg\{ &\frac{\partial v^T_{0i,0}}{\partial z}\left[m_i \frac{\partial v_{0i,0}}{\partial z}\,\dot z + m_i a^R_{0i} - F^a_{i,0}\right] \\ &+\; \frac{\partial \omega^T_{0i,0}}{\partial z}\left[\Theta_{i,0}\frac{\partial \omega^T_{0i,0}}{\partial z}\,\dot z + \Theta_{i,0}\alpha^R_{0i} + \omega_{0i,0}\times\Theta_{i,0}\,\omega_{0i,0} - T^a_{i,0}\right]\Bigg\}\,\delta z = 0\,.\end{aligned} \tag{1.28}$$

The variations of the generalized velocities δz are arbitrary. Hence, the expression in the braces must vanish. The resulting first-order differential equation can be written as

$$M(y)\,\dot z \;=\; q(y,z)\,, \tag{1.29}$$

where the $f\times f$-mass-matrix is defined by

$$M(y) \;=\; \sum_{i=1}^{k}\left[\frac{\partial v^T_{0i,0}}{\partial z}\,m_i\,\frac{\partial v_{0i,0}}{\partial z} \;+\; \frac{\partial \omega^T_{0i,0}}{\partial z}\,\Theta_{i,0}\,\frac{\partial \omega^T_{0i,0}}{\partial z}\right], \tag{1.30}$$

and the $f \times 1$-vector of generalized forces

$$q(y,z) = \sum_{i=1}^{k} \left[\frac{\partial v_{0i,0}^{T}}{\partial z} \left(F_{i,0}^{a} - m_i a_{0i,0}^{R} \right) + \frac{\partial \omega_{0i,0}^{T}}{\partial z} \left(T_{i,0}^{a} - \Theta_{i,0} \alpha_{0i,0}^{R} - \omega_{0i,0} \times \Theta_{i,0}\, \omega_{0i,0} \right) \right] \tag{1.31}$$

combines the inertia and gyroscopic forces and torques with the applied forces and torques. The equations of motion result in a set of two first-order differential equations. The definition of generalized velocities which is done by Equation (1.15) or in the trivial form by Equation (1.17) represent the first set and the dynamic equation defined in Equation (1.29) the second one.

1.5 A Quarter Car Model

1.5.1 Modeling Details

The quarter car model shown in Figure 1.10 consists of the chassis, a trailing arm that is rigidly attached to the knuckle, and the wheel. The model repre-

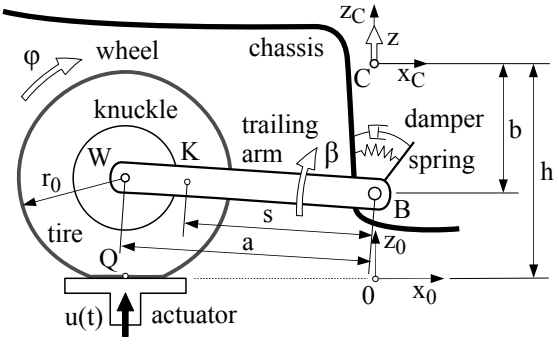

FIGURE 1.10
Quarter car model with trailing arm suspension.

sents a quarter car on a hydropulse test rig. That is why the chassis will here perform vertical motions z only. A revolute joint in B connects the trailing arm with the chassis. The rotation of the trailing arm and the knuckle described by the angle β is affected by a torsional spring damper arrangement. The simple torsional damper will be replaced by a point-to-point damper element with a nonlinear characteristic in Chapter 6. The angle φ characterizes the wheel rotation about the y_0-axis. The position of the actuator that sup-

ports the wheel is controlled to follow a prescribed displacement time history, $u = u(t)$.

A quarter car model is quite a good but surely limited approximation of real vehicle dynamics. So, the simplification that the wheel center W, the center of the knuckle and trailing arm K, and the joint in B are arranged on a straight line will correspond to the overall model quality. In addition, the wheel is supposed to roll, and a simple vertical spring acting between the contact point Q and the wheel center W models the compliance of the tire.

1.5.2 Kinematics

The quarter car model consists of $n = 3$ rigid bodies, Figure 1.11. Their position and orientation are determined by $f = 3$ generalized coordinates $y(1) = z$, $y(2) = \beta$, and $y(3) = \varphi$. Position, velocity, and acceleration of the chassis center C are simply defined by

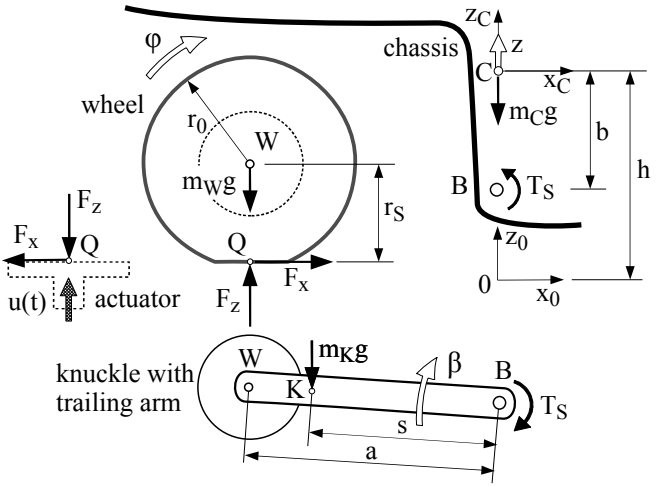

FIGURE 1.11
Quarter car model: Bodies and applied forces and torques.

$$r_{0C,0} = \begin{bmatrix} 0 \\ 0 \\ h+z \end{bmatrix}, \quad v_{0C,0} = \begin{bmatrix} 0 \\ 0 \\ \dot{z} \end{bmatrix}, \quad a_{0C,0} = \begin{bmatrix} 0 \\ 0 \\ \ddot{z} \end{bmatrix}. \tag{1.32}$$

The orientation of the trailing arm and the knuckle with respect to the knuckle fixed axis system C is described by the rotation matrix

$$A_{CK} = \begin{bmatrix} \cos\beta & 0 & \sin\beta \\ 0 & 1 & 0 \\ -\sin\beta & 0 & \cos\beta \end{bmatrix}. \tag{1.33}$$

As the chassis performs no rotation in this particular case, the rotation matrix of the knuckle with respect to the earth-fixed axis system is simply given by

$$A_{0K} \;=\; A_{CK}\,, \tag{1.34}$$

and the angular velocity and the angular acceleration are obtained as

$$\omega_{0K,0} \;=\; \begin{bmatrix} 0 \\ 1 \\ 0 \end{bmatrix} \dot{\beta} \quad \text{and} \quad \alpha_{0K,0} \;=\; \begin{bmatrix} 0 \\ 1 \\ 0 \end{bmatrix} \ddot{\beta}\,. \tag{1.35}$$

The position vector

$$r_{0K,0} \;=\; \begin{bmatrix} 0 \\ 0 \\ h+z \end{bmatrix} + \begin{bmatrix} 0 \\ 0 \\ -b \end{bmatrix} + \begin{bmatrix} -s\,\cos\beta \\ 0 \\ s\,\sin\beta \end{bmatrix} \tag{1.36}$$

describes the momentary position of the center of the knuckle trailing arm combination K, where the first two parts characterize the momentary position of the revolute joint B. The time derivatives yield the velocity

$$v_{0K,0} \;=\; \begin{bmatrix} 0 \\ 0 \\ 1 \end{bmatrix} \dot{z} \;+\; \begin{bmatrix} s\,\sin\beta \\ 0 \\ s\,\cos\beta \end{bmatrix} \dot{\beta} \tag{1.37}$$

and the acceleration

$$a_{0K,0} \;=\; \begin{bmatrix} 0 \\ 0 \\ 1 \end{bmatrix} \ddot{z} \;+\; \begin{bmatrix} s\,\sin\beta \\ 0 \\ s\,\cos\beta \end{bmatrix} \ddot{\beta} \;+\; \begin{bmatrix} s\,\cos\beta \\ 0 \\ -s\,\sin\beta \end{bmatrix} \dot{\beta}^{\,2}\,. \tag{1.38}$$

The orientation of the wheel with respect to the earth-fixed axis system 0 and the momentary position of the wheel center W are determined by

$$A_{0W} \;=\; \begin{bmatrix} \cos\varphi & 0 & \sin\varphi \\ 0 & 1 & 0 \\ -\sin\varphi & 0 & \cos\varphi \end{bmatrix} \tag{1.39}$$

and

$$r_{0W,0} \;=\; \begin{bmatrix} 0 \\ 0 \\ h+z-b \end{bmatrix} + \begin{bmatrix} -a\,\cos\beta \\ 0 \\ a\,\sin\beta \end{bmatrix}\,. \tag{1.40}$$

Then, the velocity and acceleration state are given by

$$\omega_{0W,0} \;=\; \begin{bmatrix} 0 \\ 1 \\ 0 \end{bmatrix} \dot{\varphi}, \quad \alpha_{0K,0} \;=\; \begin{bmatrix} 0 \\ 1 \\ 0 \end{bmatrix} \ddot{\varphi} \tag{1.41}$$

and

$$v_{0W,0} = \begin{bmatrix} 0 \\ 0 \\ 1 \end{bmatrix} \dot{z} + \begin{bmatrix} a \sin\beta \\ 0 \\ a \cos\beta \end{bmatrix} \dot{\beta} \tag{1.42}$$

$$a_{0W,0} = \begin{bmatrix} 0 \\ 0 \\ 1 \end{bmatrix} \ddot{z} + \begin{bmatrix} a \sin\beta \\ 0 \\ a \cos\beta \end{bmatrix} \ddot{\beta} + \begin{bmatrix} a \cos\beta \\ 0 \\ -a \sin\beta \end{bmatrix} \dot{\beta}^2 . \tag{1.43}$$

Using the trivial choice of generalized velocities, the partial velocities which according to Equations (1.26) and (1.27) form the Jacobians of translation and rotation, can easily be depicted from the corresponding velocities. The results are collected in the Tables 1.2 and 1.3.

TABLE 1.2
Partial Velocities, Applied Forces, and Remaining Acceleration Terms

Body name mass	Partial Velocities $\partial v_{0i}/\partial z_j$			Applied Forces	Remaining Terms
	$z_1 = \dot{z}$	$z_2 = \dot{\beta}$	$z_3 = \dot{\varphi}$	$-F_i$	a_{0i}^R
Chassis m_C	0	0	0	0	0
	0	0	0	0	0
	1	0	0	$-m_C g$	0
Knuckle and trailing arm m_K	0	$s \sin\beta$	0	0	$s\dot{\beta}^2 \cos\beta$
	0	0	0	0	0
	1	$s \cos\beta$	0	$-m_K g$	$-s\dot{\beta}^2 \sin\beta$
Wheel m_W	0	$a \sin\beta$	0	F_x	$a\dot{\beta}^2 \cos\beta$
	0	0	0	0	0
	1	$a \cos\beta$	0	$F_z - m_W g$	$-a\dot{\beta}^2 \sin\beta$

TABLE 1.3
Partial Angular Velocities, Applied Torques, and Remaining Terms in the Angular Accelerations

Body name inertia	Partial Angular Velocities $\partial\omega_{0i}/\partial z_j$			Applied Torques	Remaining Terms
	$z_1 = \dot{z}$	$z_2 = \dot{\beta}$	$z_3 = \dot{\varphi}$	T_i	α_{0i}^R
Chassis no rotation	0	0	0	0	0
	0	0	0	$-T_S$	0
	0	0	0	0	0
Knuckle and trailing arm Θ_K	0	0	0	0	0
	0	1	0	T_S	0
	0	0	0	0	0
Wheel Θ_W	0	0	0	0	0
	0	0	1	$-r_S F_x$	0
	0	0	0	0	0

The chassis performs translational motions only. That is why the corresponding rows in Table 1.3 will all vanish. There are also no remaining terms in the angular accelerations within this simple model.

1.5.3 Applied Forces and Torques

Assuming linear characteristics, the torsional spring damper combination acting at the revolute joint in B will generate the torque

$$T_S \;=\; -\left(T_S^0 \;+\; c_S\,\beta \;+\; d_S\,\dot{\beta}\right)\;, \tag{1.44}$$

where T_S^0 describes the preload in the steady design position defined by $\beta = 0$ and $\dot{\beta} = 0$, c_S denotes the torsional spring rate, and d_S denotes the torsional damper constant.

The constants c_x and c_z characterize the compliance of the tire in longitudinal and vertical direction. As long as the tire is in contact with the actuator, the vertical tire force is defined by

$$F_z \;=\; -c_z\,(r_0 - r_S)\;, \tag{1.45}$$

where

$$r_S \;=\; h + z - b \;+\; a\,\sin\beta \;-\; u \tag{1.46}$$

denotes the static tire radius. Assuming adhesion in the contact area,

$$F_x \;=\; -c_x\,(a\,(1-\cos\beta) - r_S\,\varphi) \;-\; d_x\left(a\,\sin\beta\dot{\beta} \;-\; r_S\,\dot{\varphi}\right) \tag{1.47}$$

will model the longitudinal tire force. The constant d_x models the tire damping in the longitudinal direction. The suspension damping here provided by the torque T_s affects the translational motions of the wheel too. However, the wheel rotation is determined by the longitudinal tire force only. That is why damping must be provided via the constant d_x to avoid undamped wheel oscillations.

A detailed model for all tire forces and torques, which also includes nonlinearities and lift-off, is developed in Chapter 3.

1.5.4 Equations of Motion

Jourdain's principle results in a set of two first-order differential equations. As trivial generalized velocities were chosen here, they read as

$$\dot{y} \;=\; z \quad \text{and} \quad M\,\dot{z} \;=\; q\,, \tag{1.48}$$

where y denotes the vector of generalized coordinates, the vector z defines trivial generalized velocities, the mass matrix M is defined by Equation (1.30),

and Equation (1.31) generates the vector q, which contains the generalized forces and torques. Using the notations in Tables 1.2 and 1.3, we get

$$M = \begin{bmatrix} m_C + m_K + m_W & (s\,m_K + a\,m_W)\cos\beta & 0 \\ (s\,m_K + a\,m_W)\cos\beta & \Theta_K + s^2 m_K + a^2 m_W & 0 \\ 0 & 0 & \Theta_W \end{bmatrix} \tag{1.49}$$

and

$$q = \begin{bmatrix} F_z - (m_C + m_K + m_W)\; g + (s\,m_K + a\,m_W)\sin\beta\,\dot\beta^{\,2} \\ T_S - (s\,m_K + a\,m_W)\cos\beta\,g + a\;(F_x\sin\beta + F_z\cos\beta) \\ -r_S\,F_x \end{bmatrix} . \tag{1.50}$$

Inspecting the elements of the mass matrix, we recognize that $m_C+m_K+m_W$ represents the overall mass of the quarter car model and $\Theta_K+s^2m_K+a^2m_W$ denotes the inertia of the wheel mass, the knuckle, and the trailing arm with respect to the revolute joint in B. The inertia of the wheel Θ_W will not show up here because the wheel rotation φ is measured not relative to the knuckle but with respect to the earth-fixed system 0.

In steady state, the time derivatives of the generalized coordinates will vanish. Then, the suspension torque provided by Equation (1.44) simplifies to

$$T_S \longrightarrow T_S^{st} = -\left(T_S^0 + c_S\beta^{st}\right) , \tag{1.51}$$

and the balance of generalized forces expressed by $q=0$ will yield

$$F_z^{st} - (m_C + m_K + m_W)\; g = 0 , \tag{1.52}$$

$$-\left(T_S^0+c_S\beta^{st}\right) - s_S m_S\cos\beta^{st} g + a\left(F_x^{st}\sin\beta^{st}+F_z^{st}\cos\beta^{st}\right) = 0 , \tag{1.53}$$

$$-r_S\,F_x^{st} = 0 , \tag{1.54}$$

where the term sm_K+am_W is replaced by s_Sm_S by introducing the suspension mass $m_S = m_K+m_W$ (knuckle with trailing arm) and s_S as the position of the corresponding mass center. The first an the third equations deliver the steady-state tire forces

$$F_z^{st} = (m_C + m_K + m_W)\; g \quad \text{and} \quad F_x^{st} = 0 , \tag{1.55}$$

where the vertical force F_z^{st} just equals the weight $G=(m_C+m_K+m_W)\,g$ of the quarter car.

1.5.5 Simulation

For any given vehicle data, including the preload of the torsional suspension spring T_S^0, the steady-state rotation angle β^{st} of the trailing arm can be obtained from Equation (1.53). The MATLAB-Script in Listing 1.1 will do the calculation where the MATLAB-Command qcm_data executes the corresponding MATLAB-Script given in Listing 1.2, which provides the data of the quarter car model.

Listing 1.1
Script `qcm_steady_state.m`: Steady-State Position of Quarter Car Model

```
qcm_data

% steady state tire forces
Fx = 0;  Fz = ( mC + mK + mW ) * g ;

% knuckle and trailing arm
mS = mK + mW;  sS = ( s*mK + a*mW ) / mS;

% solve non-linear equation by matlab-function fzero
be0=fzero(@(be) -(Ts0+cs*be)-sS*mS*cos(be)*g+a*(Fx*sin(be)+Fz*cos(be)),0);
disp(['be_st=',num2str(be0*180/pi),' [Grad]'])
```

Listing 1.2
Script `qcm_data.m`: Vehicle Data

```
g = 9.810;  % [m/s^2] gravity [m/s^2]
s = 0.250;  % [m]    distance joint B center of knuckle/trailing arm
a = 0.400;  % [m]    distance joint B center of wheel
b = 0.310;  % [m]    vertical distance chassis center to joint B
h = 0.600;  % [m]    height of chassis center
r0= 0.305;  % [m]    tire radius

mC= 200;   % [kg]    corresponding chassis mass (quarter car)
mK= 35;    % [kg]    mass of knuckle/trailing arm
mW= 15;    % [kg]    mass of wheel (rim and tire)

ThetaK=0.6; % [kgm^2] inertia of knuckle/trailing arm
ThetaW=0.8; % [kgm^2] inertia of wheel

Ts0=1200;  % [Nm]    preload in torsional spring
cs=10000;  % [Nm/rad] torsional spring rate
ds= 800;   % [Nms]   torsional damping
cx=180000; % [N/m]   longitudinal tire stiffness
cz=220000; % [N/m]   vertical tire stiffness
dx=  150;  % [Ns/m]  longitudinal tire damping
```

Finally, the MATLAB-Script given in Listing 1.3 performs a time simulation in the interval from $t_0 = 0\,s$ to $t_E = 1.5\,s$.

Listing 1.3
Script `qcm_main.m`: Quarter Car Model Exposed to Step Input

```
% globals
global g s a b h r0
global mC mK mW ThetaK ThetaW
global Ts0 cs ds cx cz dx
global ustep tstep

% vehicle data
qcm_data

% define step input
ustep=0.05; % [m]    actuator step input
```

```
tstep=0.75; % [s]    @ t=tstep

% initial states
x0 = [ 0; 0; 0; 0; 0; 0];

% time simulation
t0=0; tE=1.5;
[tout,xout] = ode45(@qcm_f,[t0,tE],x0);

% plot results
subplot(3,1,1), plot(tout,xout(:,1)), grid on
               xlabel('t [s]'), ylabel('z [m]')
subplot(3,1,2), plot(tout,xout(:,2)*180/pi), grid on
               xlabel('t [s]'), ylabel('\beta [deg]')
subplot(3,1,3), plot(tout,xout(:,3)*180/pi), grid on
               xlabel('t [s]'), ylabel('\phi [deg]')
```

The MATLAB-Function ode45[3] solves the first-order ordinary differential equations (ODEs) provided by the function given in Listing 1.4 and plots the time histories of the chassis displacement z, the rotation of the knuckle and trailing arm β, as well as the wheel rotation φ versus time t, Figure 1.12.

Listing 1.4
Function `qcm_f.m`: Equations of Motion of the Quarter Car Model

```
function xdot = qcm_f(t,x)
% quarter car model with trailing arm suspension

global g s a b h r0
global mC mK mW ThetaK ThetaW
global Ts0 cs ds cx cz dx
global ustep tstep

% state variables
z  = x(1); beta  = x(2); phi  = x(3);
zd = x(4); betad = x(5); phid = x(6);

% step input to actuator @ t = tstep
if t < tstep, u = 0; else u = ustep; end

% torque in revolute joint
Ts = - ( Ts0 + cs*beta + ds*betad );

% tire deflection (static tire radius)
rS = h + z - b + a*sin(beta) - u ;

% longitudinal tire force (adhesion assumed)
Fx = - cx *( a*(1-cos(beta)) - rS*phi ) ...
     - dx *( a*sin(beta)*betad - rS*phid ) ;

% vertical tire force (contact assumed)
Fz =  cz *( r0 - rS );

% mass matrix
```

[3] ode45 is based on an explicit Runge-Kutta (4,5) formula, the Dormand-Prince pair.

```
30 Massma=[      mC+mK+mW       (s*mK+a*mW)*cos(beta)  0   ; ...
31         (s*mK+a*mW)*cos(beta) ThetaK+s^2*mK+a^2*mW 0   ; ...
32                  0                     0          ThetaW ];
33
34 % vector of generalized forces and torques
35 qgen=[ Fz-(mC+mK+mW)*g+(s*mK+a*mW)*sin(beta)*betad^2 ; ...
36       Ts-(s*mK+a*mW)*cos(beta)*g+a*(Fx*sin(beta)+Fz*cos(beta)); ...
37         -rS*Fx ];
38
39 % state derivatives
40 xdot = [ zd; betad; phid; Massma\qgen ];
41
42 end
```

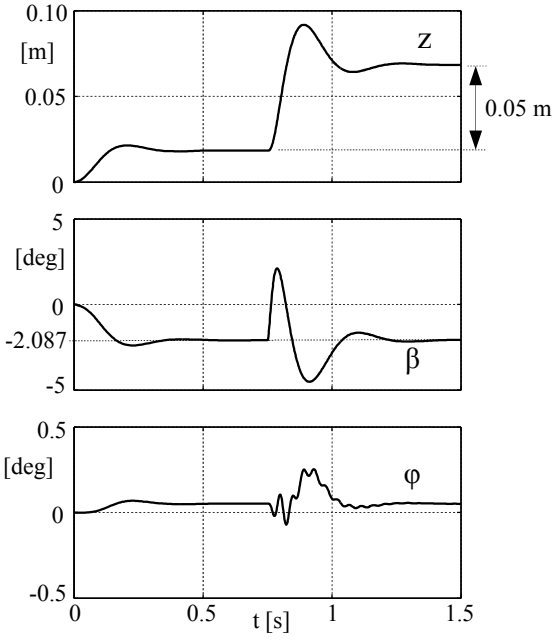

FIGURE 1.12
Simulation results to step input from $u = 0$ to $u = 0.05\,m$ at $t = 0.75\,s$.

During the first time interval $0\,s \leq t \leq 0.75\,s$ where the actuator displacement is kept to $u = 0\,m$ the quarter car model performs the transition from the initial values to steady state. After a short time the rotation angle of knuckle and trailing arm adjusts to the value $\beta = -2.087°$ which is in conformity with the steady state value bK0 calculated and printed by the MATLAB-Script in Listing 1.1. At $t = 0.75\,s$ the actuator is moved in an instant (step input) to the value of $u = 0.05\,m$. The resulting oscillations decay in a short time indicating an appropriate suspension damping. The rotation of the trailing arm $\beta = \beta(t)$ causes the wheel center M to move back and forth. As a conse-

quence, the wheel that is in contact with the strictly vertical moving actuator is forced to rotate too, $\varphi = \varphi(t)$.

Exercises

1.1 Given the tire codes P245/65R17 and 32x10.5R15LT, calculate the radius and width for both tires.

1.2 Measurements on a K&C (Kinematics and Compliance) test rig provide the toe angle $\delta_0 = 0.7°$ and the camber angle $\hat{\gamma}_0 = -1.0°$ in design position. Calculate the components of the unit vector e_{yR} pointing in the direction of the wheel rotation axis.

1.3 Use the unit vector e_{yR} calculated in Exercise 1.2 and generate the coordinates of the wheel alignment point D when its distance to the wheel center W is given by $\overline{DW} = 0.1$ m and the position of the wheel center relative to the origin C of the vehicle-fixed reference frame F is defined by the vector $r_{CW,F} = [\,0.00\ 0.76\ 0.00\,]^T$.

1.4 The steady-state position of the trailing arm depends on the pre-load in the torsional suspension spring. Find the value for T_S^0 which will keep the trailing arm in steady state in a horizontal position, $\beta^{st} = 0°$. Check the result with the MATLAB-Script provided by Listing 1.1. Do not forget to adjust the value for the torsional spring preload Ts0 in Listing 1.2.

1.5 Use the MATLAB-Scripts in Section 1.5.5 and perform simulations with different values of the suspension damping (double or halve the given value).

2

Road

CONTENTS

2.1 Modeling Aspects

Besides single obstacles or track grooves, the irregularities of a road are stochastic in nature. A vehicle driving over a random road profile mainly performs hub, pitch, and roll motions. The local inclination of the road profile also induces longitudinal and lateral motions as well as yaw motions. On normal roads the latter motions will have less influence on ride comfort and ride safety. To limit the effort of the stochastic description, usually simpler road models are used.

Sophisticated three-dimensional road models provide not only the road height $z = z(x, y)$ but also the local friction coefficient $\mu = \mu(x, y)$ at each point x, y, Figure 2.1. In addition, simple road models will often generate the local road normal and the local curvature. Within this general approach the tire model is responsible for calculating the local road inclination and curvature. By separating the horizontal course description from the vertical layout and the surface properties of the roadway almost arbitrary road layouts are possible [4]. Today, high-resolution measurements of road surfaces are performed in moving traffic by measuring vans and generate a huge amount of data. Therefore, a compact but still accurate representation of measured data will be essential for straightforward applications in simulation environments. The recently launched open-source project OpenCRG provides a three-

dimensional road model where a curved regular grid (CRG) is used to achieve a compact and accurate representation of measurements [5].

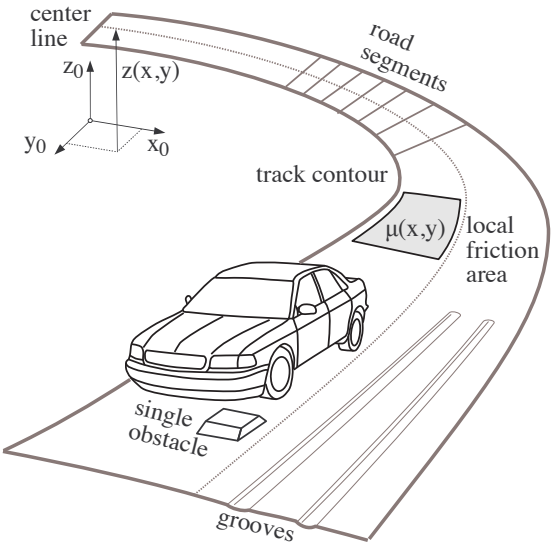

FIGURE 2.1
Sophisticated road model.

If the vehicle drives along a given path, its momentary position can be described by the path variable $s = s(t)$. Hence, a fully three-dimensional road model can be reduced to a parallel track model, Figure 2.2. Now, the

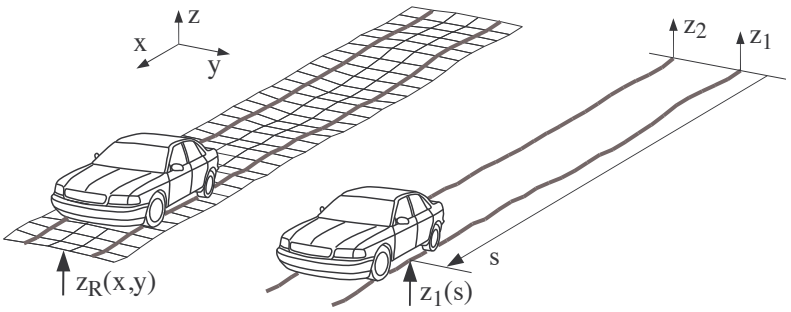

FIGURE 2.2
Parallel track road model.

road heights on the left and right track are provided by two one-dimensional functions $z_1 = z_1(s)$ and $z_2 = z_2(s)$. Within the parallel track model, no information about the local lateral road inclination is available. If this information is not provided by additional functions, the impact of a local lateral road inclination to vehicle motions is not taken into account.

For basic studies the irregularities at the left and the right track can be considered approximately the same, $z_1(s) \approx z_2(s)$. Then, a single track road model with $z_R(s) = z_1(x) = z_2(x)$ can be used. In this case, the roll excitation of the vehicle is neglected too.

2.2 Deterministic Profiles

2.2.1 Bumps and Potholes

Bumps and potholes on the road are single obstacles of nearly arbitrary shape. Already with simple rectangular cleats, the dynamic reaction of a vehicle or a single tire to a sudden impact can be investigated. If the shape of the obstacle is approximated by a smooth function, like a cosine wave, then discontinuities will be avoided. Usually, deterministic obstacles are described in local coordinate systems, Figure 2.3.

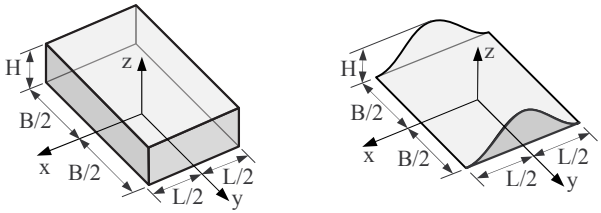

FIGURE 2.3
Rectangular cleat and cosine-shaped bump.

Then, the rectangular cleat is simply defined by

$$z(x,y) = \begin{cases} H & \text{if} \quad -\frac{L}{2} < x < \frac{L}{2} \quad \& \quad -\frac{B}{2} < y < \frac{B}{2} \\ 0 & \text{else} \end{cases} \tag{2.1}$$

and the cosine-shaped bump is given by

$$z(x,y) = \begin{cases} \frac{1}{2}H\left(1+\cos\left(2\pi\frac{x}{L}\right)\right) & \text{if} \quad -\frac{L}{2} < x < \frac{L}{2} \quad \& \quad -\frac{B}{2} < y < \frac{B}{2} \\ 0 & \text{else,} \end{cases} \tag{2.2}$$

where H, B, and L denote the height, width, and length of the obstacle. Potholes are obtained if negative values for the height ($H < 0$) are used.

The function in Listing 2.1 computes the rectangular cleat when the switch parameter OT is set to 1 or with OT=2 the cosine-shaped bump. Case OT=3 generates a rounded bump with a cosine-like transition to the default road

height $z = 0$ in the x-direction and a sharp but still smooth blending in the y-direction.

Listing 2.1
Function `obstacle_f.m`: Deterministic Obstacles

```
function z = obstacle_f(x,y,OT,B,H,L)
% set default road height outside obstacle
  z = 0;
% check if x,y-coordinates are inside obstacle
  if x>-L/2 && x<L/2 && y>-B/2 && y<B/2
    % select type of obstacle
    switch OT
      case 1 % cleat
        z = H;
      case 2 % cosine shaped obstacle
        z = H/2 * ( 1 + cos(2*pi*x/L) );
      case 3 % rounded obstacle
        zx=(1-(x/(L/2))^2)^2; zy=(1-(y/(B/2))^8)^2; z=H*zx*zy;
    end
  end
end
```

In a similar way, track grooves can be modeled too [49]. By appropriate coordinate transformations, the obstacles can then be integrated into the global road description.

2.2.2 Sine Waves

Using the parallel track road model, a periodic excitation can be realized by

$$z_1(s) \;=\; A\,\sin(\Omega\,s) \quad \text{and} \quad z_2(s) \;=\; A\,\sin(\Omega\,s - \Psi)\,, \tag{2.3}$$

where s is the path variable, A denotes the amplitude, Ω the wave number, and the angle Ψ describes a phase lag between the left and right tracks. The special cases $\Psi = 0$ and $\Psi = \pi$ represent in-phase excitation with $z_1 = z_2$ and out-of-phase excitation with $z_1 = -z_2$, respectively.

If the vehicle runs with constant velocity $ds/dt = v_0 = const.$, then the momentary position of the vehicle is simply determined by $s = v_0\,t$, where the initial position $s = 0$ at $t = 0$ was assumed. By introducing the wavelength

$$L \;=\; \frac{2\pi}{\Omega}\,, \tag{2.4}$$

the term $\Omega\,s$ in Equation (2.3) can be written as

$$\Omega\,s = \frac{2\pi}{L}\,s = \frac{2\pi}{L}\,v_0\,t = 2\pi\,\frac{v_0}{L}\,t = \omega\,t\,. \tag{2.5}$$

Hence, in the time domain, the excitation frequency is given by

$$f = \omega/(2\pi) = \frac{2\pi\,\frac{v_0}{L}}{2\pi} = \frac{v_0}{L}\,. \tag{2.6}$$

For most vehicles, the rigid body vibrations are between $0.5\,Hz$ and $15\,Hz$. This range is covered by waves that satisfy the conditions $v_0/L \geq 0.5\,Hz$ and $v_0/L \leq 15\,Hz$.

For a given wavelength, let's say $L = 4\,m$, the rigid body vibrations of a vehicle are excited if the velocity of the vehicle will be varied from $v_0^{min} = 0.5\,Hz * 4\,m = 2\,m/s = 7.2\,km/h$ to $v_0^{max} = 15\,Hz * 4\,m = 60\,m/s = 216\,km/h$. Hence, to achieve an excitation in the whole frequency range with moderate vehicle velocities, road profiles with varying wavelengths are needed.

2.3 Random Profiles

2.3.1 Statistical Properties

Road profiles fit the category of stationary Gaussian random processes [6]. Hence, the irregularities of a road can be described either by the profile itself $z_R = z_R(s)$ or by its statistical properties, Figure 2.4.

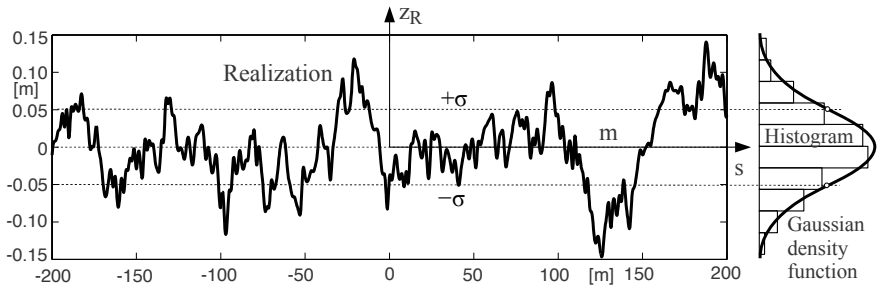

FIGURE 2.4
Road profile and statistical properties.

By choosing an appropriate reference frame, a vanishing mean value

$$m \;=\; E\{z_R(s)\} \;=\; \lim_{X\to\infty} \frac{1}{X} \int_{-X/2}^{X/2} z_R(s)\, ds \;=\; 0 \tag{2.7}$$

can be achieved, where $E\{\}$ denotes the expectation operator. Then, the Gaussian density function that corresponds with the histogram is given by

$$p(z_R) \;=\; \frac{1}{\sigma\sqrt{2\pi}}\, e^{-\dfrac{z_R^2}{2\sigma^2}}\,, \tag{2.8}$$

where the deviation or the effective value σ is obtained from the variance of the process $z_R = z_R(s)$

$$\sigma^2 \;=\; E\left\{z_R^2(s)\right\} \;=\; \lim_{X\to\infty} \frac{1}{X} \int_{-X/2}^{X/2} z_R(s)^2\, ds\,. \tag{2.9}$$

Alteration of σ affects the shape of the density function. In particular, the points of inflection occur at $\pm\sigma$. The probability of a value $|z| < \zeta$ is given by

$$P(\pm\zeta) \;=\; \frac{1}{\sigma\sqrt{2\pi}} \int_{-\zeta}^{+\zeta} e^{-\frac{z^2}{2\sigma^2}}\, dz\,. \tag{2.10}$$

In particular, one gets the values $P(\pm\sigma) = 0.683$, $P(\pm 2\sigma) = 0.955$, and $P(\pm 3\sigma) = 0.997$. Hence, the probability of a value $|z| \geq 3\sigma$ is 0.3%.

As an extension to the variance of a random process, the autocorrelation function is defined by

$$R(\xi) \;=\; E\left\{z_R(s)\, z_R(s{+}\xi)\right\} \;=\; \lim_{X\to\infty} \frac{1}{X} \int_{-X/2}^{X/2} z_R(s)\, z_R(s{+}\xi)\, ds\,. \tag{2.11}$$

The autocorrelation function is symmetric, $R(\xi) = R(-\xi)$, and it plays an important part in the stochastic analysis. In any normal random process, as ξ increases the link between $z_R(s)$ and $z_R(s{+}\xi)$ diminishes. For large values of ξ, the two values are practically unrelated. Hence, $R(\xi \to \infty)$ will tend to 0. In fact, $R(\xi)$ is always less than $R(0)$, which coincides with the variance σ^2 of the process. If a periodic term is present in the process, it will show up in $R(\xi)$.

Usually, road profiles are characterized in the frequency domain. Here, the autocorrelation function $R(\xi)$ is replaced by the power spectral density (psd) $S(\Omega)$. In general, $R(\xi)$ and $S(\Omega)$ are related to each other by the Fourier transformation

$$S(\Omega) \;=\; \frac{1}{2\pi} \int_{-\infty}^{\infty} R(\xi)\, e^{-i\Omega\xi}\, d\xi \quad \text{and} \quad R(\xi) \;=\; \int_{-\infty}^{\infty} S(\Omega)\, e^{i\Omega\xi}\, d\Omega\,, \tag{2.12}$$

where i is the imaginary unit, and Ω in rad/m denotes the wavenumber. To avoid negative wavenumbers, usually a one-sided psd is defined. With

$$\Phi(\Omega) = 2\, S(\Omega)\,, \quad \text{if} \quad \Omega \geq 0 \qquad \text{and} \qquad \Phi(\Omega) = 0\,, \quad \text{if} \quad \Omega < 0\,, \tag{2.13}$$

the relationship $e^{\pm i\Omega\xi} = \cos(\Omega\xi) \pm i\, \sin(\Omega\xi)$, and the symmetry property $R(\xi) = R(-\xi)$ Equation (2.12) results in

$$\Phi(\Omega) \;=\; \frac{2}{\pi} \int_0^{\infty} R(\xi)\, \cos(\Omega\xi)\, d\xi \quad \text{and} \quad R(\xi) \;=\; \int_0^{\infty} \Phi(\Omega)\, \cos(\Omega\xi)\, d\Omega\,. \tag{2.14}$$

Now, the variance is obtained from

$$\sigma^2 \;=\; R(\xi=0) \;=\; \int_0^\infty \Phi(\Omega)\, d\Omega\,. \tag{2.15}$$

In reality, the psd $\Phi(\Omega)$ will be given in a finite interval $\Omega_1 \le \Omega \le \Omega_N$, Figure 2.5. Then, Equation (2.15) can be approximated by a sum, which for

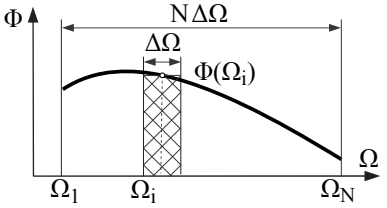

FIGURE 2.5
Power spectral density in a finite interval.

N equal intervals will result in

$$\sigma^2 \;\approx\; \sum_{i=1}^{N} \Phi(\Omega_i)\,\triangle\Omega \quad \text{with} \quad \triangle\Omega = \frac{\Omega_N - \Omega_1}{N}\,. \tag{2.16}$$

2.3.2 Classification of Random Road Profiles

Road elevation profiles can be measured point by point or by high-speed profilometers. The power spectral densities of roads show a characteristic drop in magnitude with the wavenumber, Figure 2.6a. This simply reflects the fact that the irregularities of the road may amount to several meters over the length of hundreds of meters, whereas those measured over the length of 1 meter are normally only some centimeters in amplitude.

Random road profiles can be approximated by a psd in the form of

$$\Phi\,(\Omega) \;=\; \Phi\,(\Omega_0)\,\left(\frac{\Omega}{\Omega_0}\right)^{-w}\,, \tag{2.17}$$

where $\Omega = 2\pi/L$ in rad/m denotes the wavenumber and $\Phi_0 = \Phi\,(\Omega_0)$ in $m^2/(rad/m)$ describes the value of the psd at the reference wavenumber $\Omega_0 = 1\,rad/m$. The drop in magnitude is modeled by the waviness w.

According to the international directive ISO 8608 [16], typical road profiles can be grouped into classes from A to E. By setting the waviness to $w = 2$, each class is simply defined by its reference value Φ_0. Class A with $\Phi_0 = 1 * 10^{-6}\; m^2/(rad/m)$ characterizes very smooth highways, whereas Class E with $\Phi_0 = 256 * 10^{-6}\, m^2/(rad/m)$ represents rather rough roads, Figure 2.6b.

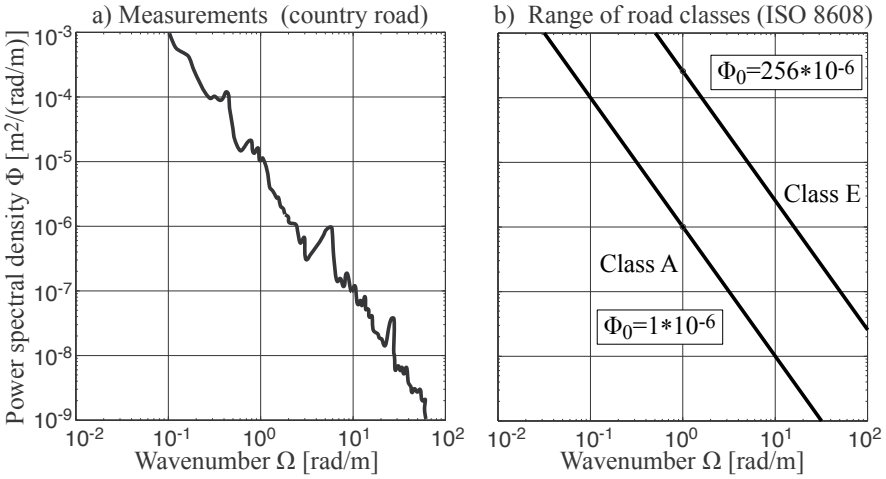

FIGURE 2.6
Road power spectral densities: (a) Measurements [3], (b) classification.

2.3.3 Sinusoidal Approximation

A random profile of a single track can be approximated by a superposition of $N \to \infty$ sine waves

$$z_R(s) \;=\; \sum_{i=1}^{N} A_i \,\sin\left(\Omega_i\, s - \Psi_i\right)\;, \tag{2.18}$$

where each sine wave is determined by its amplitude A_i and its wavenumber Ω_i. By different sets of uniformly distributed phase angles Ψ_i, $i = 1(1)N$ in the range between 0 and 2π different profiles can be generated that are similar in general appearance but different in details.

The variance of the sinusoidal representation is then given by

$$\sigma^2 = \lim_{X\to\infty} \frac{1}{X} \int_{-X/2}^{X/2} \left(\sum_{i=1}^{N} A_i \,\sin\left(\Omega_i\, s - \Psi_i\right) \right) \left(\sum_{j=1}^{N} A_j \,\sin\left(\Omega_j\, s - \Psi_j\right) \right) ds\,. \tag{2.19}$$

For $i = j$ and for $i \neq j$, different types of integrals are obtained. The ones for $i = j$ can be solved immediately:

$$J_{ii} = \int A_i^2 \sin^2\left(\Omega_i s - \Psi_i\right) ds = \frac{A_i^2}{2\Omega_i} \left[\Omega_i s - \Psi_i - \frac{1}{2} \sin\left(2\left(\Omega_i s - \Psi_i\right)\right) \right]. \tag{2.20}$$

Using the trigonometric relationship

$$\sin x \,\sin y \;=\; \frac{1}{2}\cos(x-y) \;-\; \frac{1}{2}\cos(x+y)\,, \tag{2.21}$$

the integrals for $i \neq j$ can be solved also

$$\begin{aligned} J_{ij} &= \int A_i \sin(\Omega_i s - \Psi_i)\, A_j \sin(\Omega_j s - \Psi_j)\; ds \\ &= \frac{1}{2} A_i A_j \int \cos(\Omega_{i-j}\, s - \Psi_{i-j})\, ds \;-\; \frac{1}{2} A_i A_j \int \cos(\Omega_{i+j}\, s - \Psi_{i+j})\, ds \\ &= -\frac{1}{2} \frac{A_i A_j}{\Omega_{i-j}} \sin(\Omega_{i-j}\, s - \Psi_{i-j}) \;+\; \frac{1}{2} \frac{A_i A_j}{\Omega_{i+j}} \sin(\Omega_{i+j}\, s - \Psi_{i+j}) \;, \end{aligned} \tag{2.22}$$

where the abbreviations $\Omega_{i\pm j} = \Omega_i \pm \Omega_j$ and $\Psi_{i\pm j} = \Psi_i \pm \Psi_j$ were used. The sine and cosine terms in Equations (2.20) and (2.22) are limited to values of ± 1. Hence, Equation (2.19) simply results in

$$\sigma^2 = \underbrace{\lim_{X\to\infty} \frac{1}{X} \sum_{i=1}^{N} \left[J_{ii}\right]_{-X/2}^{X/2}}_{\displaystyle\sum_{i=1}^{N} \frac{A_i^2}{2\Omega_i}\,\Omega_i} + \underbrace{\lim_{X\to\infty} \frac{1}{X} \sum_{i,j=1}^{N} \left[J_{ij}\right]_{-X/2}^{X/2}}_{0} = \frac{1}{2} \sum_{i=1}^{N} A_i^2 \,. \tag{2.23}$$

On the other hand, the variance of a sinusoidal approximation to a random road profile is given by Equation (2.16). So, a road profile $z_R = z_R(s)$ described by Equation (2.18) will have a given psd $\Phi(\Omega)$ if the amplitudes are generated according to

$$A_i \;=\; \sqrt{2\,\Phi(\Omega_i)\,\triangle\Omega}\,, \quad i = 1(1)N \tag{2.24}$$

and the wavenumbers Ω_i are chosen to lie at N equal intervals $\triangle\Omega$.

A realization of the country road with a psd of $\Phi_0 = 10 * 10^{-6}\, m^2/(rad/m)$ and a waviness of $w = 2$ is shown in Figure 2.7. The pseudo-random road

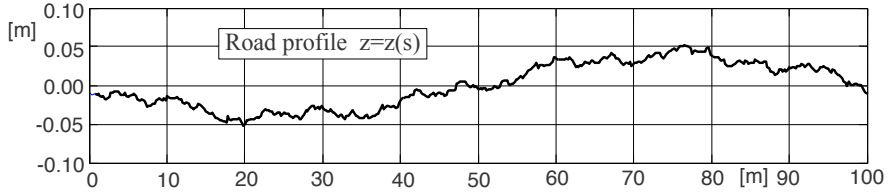

FIGURE 2.7
Realization of a country road.

profile $z = z(s)$ was generated according to Equations (2.18) and (2.24) by $N = 200$ sine waves in the frequency range from $\Omega_1 = 0.0628\, rad/m$ to $\Omega_N = 62.83\, rad/m$.

2.3.4 Example

A slight modification of the function provided in Listing 1.4 makes the pseudo-random road profile available to the quarter car model.

Listing 2.2
Function `qcm_f.m`: Equations of Motion of the Quarter Car Model

```
1  function xdot = qcm_f(t,x)
2  % quarter car model with trailing arm suspension
3
4  global g s a b h r0
5  global mC mK mW ThetaK ThetaW
6  global Ts0 cs ds cx cz dx
7  global v_V Amp Om Psi
8  global z_road fz_wheel
9
10 % state variables
11 z  = x(1); beta = x(2); phi  = x(3);
12 zd = x(4); betad = x(5); phid = x(6);
13
14 % pseudo random road
15 s_V=v_V*t; u = sum( Amp.*sin(Om*s_V+Psi) ); z_road = u;
16
17 % torque in revolute joint
18 Ts = - ( Ts0 + cs*beta + ds*betad );
19
20 % tire deflection (static tire radius)
21 rS = h + z - b + a*sin(beta) - u ;
22
23 % longitudinal tire force (adhesion assumed)
24 Fx = - cx *( a*(1-cos(beta)) - rS*phi ) ...
25      - dx *( a*sin(beta)*betad - rS*phid ) ;
26
27 % vertical tire force (contact assumed) = wheel load
28 Fz =  cz *( r0 - rS ); fz_wheel=Fz;
29
30 % mass matrix
31 Massma=[      mC+mK+mW       (s*mK+a*mW)*cos(beta)  0   ; ...
32         (s*mK+a*mW)*cos(beta) ThetaK+s^2*mK+a^2*mW 0   ; ...
33                  0                     0          ThetaW ];
34
35 % vector of generalized forces and torques
36 qgen=[ Fz-(mC+mK+mW)*g+(s*mK+a*mW)*sin(beta)*betad^2 ; ...
37       Ts-(s*mK+a*mW)*cos(beta)*g+a*(Fx*sin(beta)+Fz*cos(beta)); ...
38         -rS*Fx ];
39
40 % state derivatives
41 xdot = [ zd; betad; phid; Massma\qgen ];
42
43 end
```

The statements in line 15 of the modified function given in Listing 2.2 generate actuator displacements u, which according to Equation (2.18) will approximate a given random road profile. By assuming a constant driving velocity $v_V = const.$, the relationship $s_V = v_V\, t$ will provide the spatial coor-

dinate as a function of time. The additional global variables z_{road} and fz_{wheel} make the road profile and the wheel load also available outside the function. The vectors *Amp*, *Om*, *Psi* stored in global variables define the amplitudes, the spatial frequencies, and the randomly distributed phase angles. They are calculated in the MATLAB-Script given by Listing 2.3.

Listing 2.3
Script `qcm_main.m`: Quarter Car Model Exposed to Pseudo-Random Excitation

```
% globals
global g s a b h r0
global mC mK mW ThetaK ThetaW
global Ts0 cs ds cx cz dx
global v_V Amp Om Psi
global z_road fz_wheel

% vehicle data
qcm_data

% vehicle velocity [km/h --> m/s]
v_V  = 80/3.6;
% spectral density and waviness
Phi0 = 10e-6; w = 2;
% range of frequencies and number of samples
Omin = 0.0628; Omax = 62.83; n = 200;

% calculate amplitudes and random phases
dOm = (Omax-Omin)/(n-1);
Om  = Omin:dOm:Omax;
Om0 = 1;
Phi = Phi0.*(Om./Om0).^(-w); Amp = sqrt(2*Phi*dOm);
Psi = 2*pi*rand(size(Om));

% initial states: x0 = [ zC; betaK; phiW; zCd; betaKd; phiWd ]
x0 = [ 0; 0; 0; 0; 0; 0];

% simulation interval
t0=0; tE=6;
% adjust initial state to road
s_V = v_V*t0; u = sum( Amp.*sin(Om*s_V+Psi) ); x0(1)=u;
% perform time simulation
[tout,xout] = ode45(@qcm_f,[t0,tE],x0);

% get road height, wheel load and chassis acceleration
zr=zeros(size(tout)); fz=zeros(size(tout)); zdd=zeros(size(tout));
for i=1:length(tout)
  xdot = qcm_f(tout(i),xout(i,:)');
  zr(i)= z_road; fz(i)=fz_wheel; zdd(i)=xdot(4);
end

% mean value and standard deviation of wheel load
fz_m = mean(fz); fz_std = std(fz);
disp(['wheel load: mean value =',num2str(fz_m)])
disp(['wheel load: standard deviation =',num2str(fz_std)])

```

```
47 % generate histogram of wheel load
48 nh=20; [nfz,hfz]=hist(fz,nh);
49
50 % generate gaussian density function and adjust to histogramm
51 fzi=linspace(min(fz),max(fz),201);
52 pfz = exp(-(fzi-fz_m).^2./(2*fz_std.^2))./(fz_std*sqrt(2*pi));
53 pfz = pfz * (sum(nfz)*(max(fz)-min(fz))/nh);
54
55 % plot results
56 subplot(3,2,1), plot(tout,zr), grid on
57                 xlabel('time'), legend('road: z_R ')
58 subplot(3,2,2), plot(tout,xout(:,2)*180/pi), grid on
59                 xlabel('time'), legend('\beta [deg]')
60 subplot(3,2,3), plot(tout,xout(:,1)), grid on
61                 xlabel('time'), legend('chassis: z(t)')
62 subplot(3,2,4), plot(tout,xout(:,3)*180/pi), grid on
63                 xlabel('time'), legend('\phi [deg]')
64 subplot(3,2,5), plot(tout,fz/1000), grid on
65                 xlabel('time'), legend('wheel load F_z [kN]')
66 subplot(3,2,6), barh(hfz/1000,nfz), colormap('white'), hold on
67                 plot(pfz,fzi/1000,'k--','Linewidth',2)
68                 legend('Histogram F_z','Gauss')
```

As done in the corresponding script provided by Listing 1.3, the vehicle data are defined in the script qcm_data given in Listing 1.2. The MATLAB-Function rand[1] is used to generate uniformly distributed pseudo-random numbers. To reduce initial disturbances the chassis displacement z represented by the first state variable $x(1)$ is adjusted in line 31 to the initial actuator displacement $u = u(t_0)$.

MATLAB simulations performed by any ode-solver just provide the state variables at different time steps stored in the vector tout and the matrix xout. The loop in lines 37 to 40 calls the MATLAB-Function qcm_f, which while providing the state derivatives xdot as a function of the time t=tout(i) and the state vector x=xout(i,:)', will calculate the corresponding actuator displacement u or respectively the road profile z_road and the wheel load fz_wheel too. The actual values will be stored in the vectors zr and fz, which are pre-allocated in line 36 to speed up the loop.

The MATLAB-Functions mean and std applied to the vector fz provide mean values in the range of 2440N < fz_m < 2460N and standard deviations in the range of 750 N < fz_std < 770 N. As expected, the mean values correspond quite well to the steady-state value $F_z^{st} = 2452.5N$, which results from the first part of Equation 1.55. The MATLAB-Function hist generates a histogram of the wheel load, which is appropriately plotted here via the MATLAB-Function barh next to the time history of the wheel load, Figure 2.8.

The time histories of the chassis and the actuator displacements clearly indicate the filtering effects of the wheel suspension. The quarter car model

[1]Note: Different MATLAB-Version may generate different random numbers. In addition, subsequent calls to rand will produce various results. That is why the pseudo-random road realization will differ from application to application. But, all realizations will have the same statistical properties.

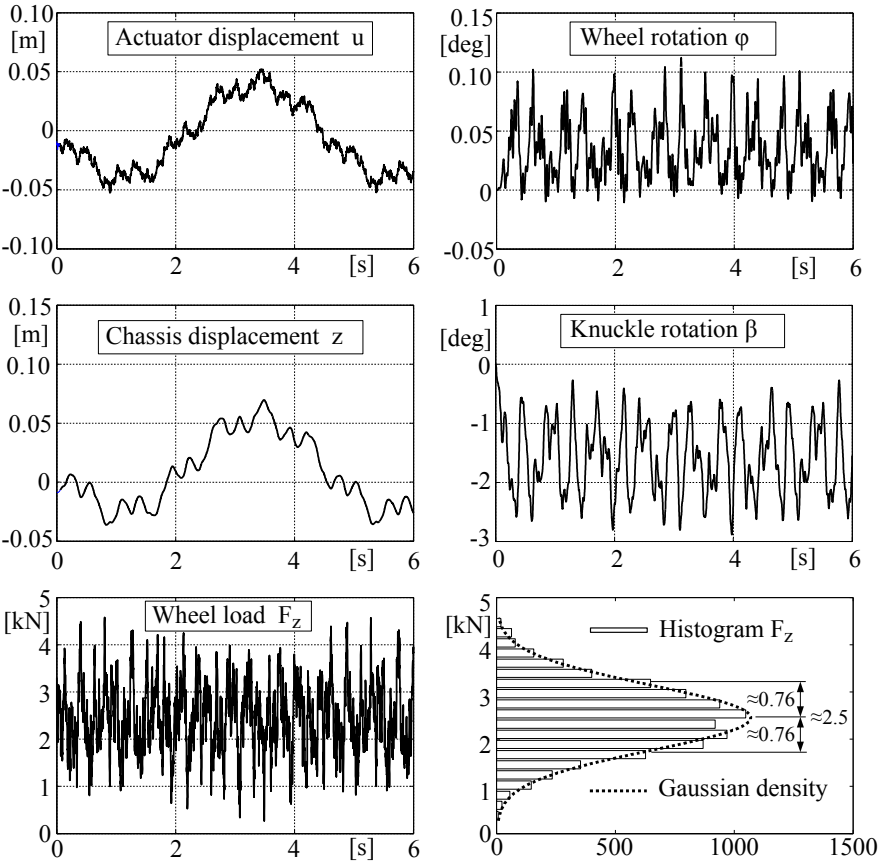

FIGURE 2.8
Simulation results with a pseudo-random excitation.

is here driven with a velocity of $v_V = 80\,km/h$ over a rather rough road that produces large wheel load variations. According to Equation (2.10), the wheel loads will be with a probability of 99.7% in the range of

$$2450 - 3 * 760 < \text{fz} < 2450 - 3 * 760 \quad \text{or} \quad 170 < \text{fz} < 4730\,, \tag{2.25}$$

which takes a Gaussian normal distribution for granted. In fact, the histogram of the wheel load matches the Gaussian density function defined by Equation (2.8) nearly perfectly. As the area below the Gaussian density function equals 1 per definition, the density function pfz must be scaled to equal the area below the histogram. Equation (2.25) indicates by potential wheel loads close to zero $\text{fz} \to 0$ the danger of wheel liftoff. The simple calculations of the longitudinal and vertical tire forces done in lines 24 and 28 of the function qcm_f given in Listing 2.2 are not valid in situations where the wheel is close to

liftoff. Here, a more complex tire model, which will be provided in Chapter 3, is mandatory. In addition, a more sophisticated random road approximation may be applied where the range of the wavenumbers is divided not in equally spaced intervals but in intervals where the bandwidth $b_i = (\Omega_i + \Delta\Omega_i)/\Omega_i$ is kept constant.

2.3.5 Shaping Filter

The white noise process produced by random number generators has a uniform spectral density and is therefore not suitable to describe real road profiles. But, if the white noise process is used as input to a shaping filter, more appropriate spectral densities will be obtained [28]. A simple first-order shaping filter for the road profile z_R reads as

$$\frac{d}{ds}\, z_R(s) \;=\; -\gamma\, z_R(s) + w(s)\,, \tag{2.26}$$

where γ is a constant and $w(s)$ is a white noise process with the spectral density Φ_w. Then, the spectral density of the road profile is obtained from

$$\Phi_R \;=\; H(\Omega)\,\Phi_W\,H^T(-\Omega) \;=\; \frac{1}{\gamma + i\,\Omega}\,\Phi_W\,\frac{1}{\gamma - i\,\Omega} \;=\; \frac{\Phi_W}{\gamma^2 + \Omega^2}\,, \tag{2.27}$$

where Ω is the wavenumber and $H(\Omega)$ is the frequency response function of the shaping filter. By setting $\Phi_W = 10{*}10^{-6} m^2/(rad/m)$ and $\gamma = 0.01 rad/m$, the measured psd of a typical country road can be approximated very well, Figure 2.9. The shape filter approach is also suitable for modeling parallel

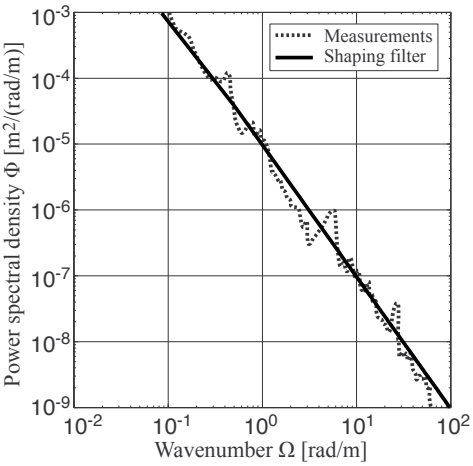

FIGURE 2.9
Shaping filter as approximation to measured psd.

tracks. Here, the crosscorrelation between the irregularities of the left and right track have to be taken into account also [32].

The white noise process $w(s)$ is discontinuous. Hence, the solving shape filter differential equations like Equation (2.26) with standard ode-solvers is extremely time consuming or will cause severe problems. That is why the shape filter approach usually is applied within analytical calculations.

2.3.6 Two-Dimensional Model

The generation of fully two-dimensional road profiles $z_R = z_R(x, y)$ via a sinusoidal approximation is very laborious. Because a shaping filter is a dynamic system, the resulting road profile realizations are not reproducible. By adding band-limited white noise processes and taking the momentary position x, y as seed for the random number generator, a reproducible road profile can be generated [33].

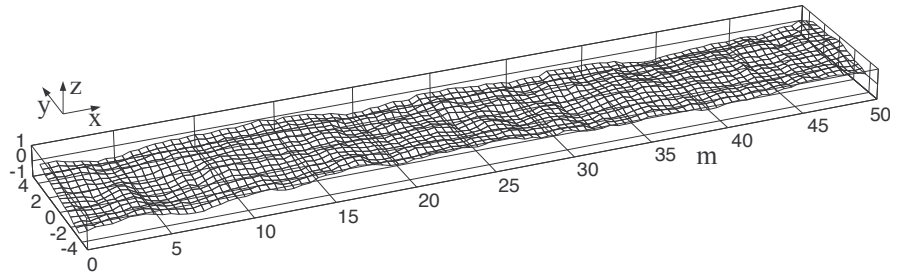

FIGURE 2.10
Two-dimensional road profile.

By assuming the same statistical properties in longitudinal and lateral direction, two-dimensional profiles, like the one in Figure 2.10, can be obtained.

Exercises

2.1 Modify the MATLAB-Script (Listing 2.3) and the corresponding function (Listing 2.2) so that the displacements of the actuator correspond with a cosine-shaped bump. Use the function in Listing 2.1 or the relevant statements in it. Note: The vehicle data are defined in the script qcm_data given in Listing 1.2.

Perform simulations with different heights (including negative values) and lengths of the obstacle. Replace the histogram-plot by the chassis acceleration

which will be provided by the fourth component of the state derivatives xdot. Keep in mind that valid results presume positive wheel loads!

2.2 Use the MATLAB-Script qcm_main (Listing 2.3) together with the MATLAB-Script qcm_data given in Listing 1.2 and the corresponding function (Listing 2.2) to study the influence of the vehicle velocity on the wheel load.

Perform simulations with different values of the road power spectral density. Again, keep in mind that valid results presume positive wheel loads!

3

Tire

CONTENTS

3.1 Introduction

3.1.1 Tire Development

Some important milestones in the development of pneumatic tires are shown in Table 3.1.

TABLE 3.1
Milestones in Tire Development

1839	Charles Goodyear: vulcanization
1845	Robert William Thompson: first pneumatic tire (several thin inflated tubes inside a leather cover)
1888	John Boyd Dunlop: patent for bicycle (pneumatic) tires
1893	The Dunlop Pneumatic and Tyre Co. GmbH, Hanau, Germany
1895	André and Edouard Michelin: pneumatic tires for Peugeot Paris-Bordeaux-Paris (720 mi): 50 tire deflations and 22 complete inner tube changes
1899	Continental: "long-lived" tires (approx. 500 km)
1904	Carbon added: black tires.
1908	Frank Seiberling: grooved tires with improved road traction
1922	Dunlop: steel cord thread in the tire bead
1942	Synthetic rubber: extremely important during World War II
1943	Continental: patent for tubeless tires
1946	Radial tire
1952	High-quality nylon tire
⋮	

Of course tire development did not stop in 1952, but modern tires are still based on these achievements. Today, run-flat tires are under investigation. A run-flat tire enables the vehicle to continue to be driven at reduced speeds (i.e. 80 km/h or 50 mp/h) and for limited distances (80 km or 50 mi). The introduction of run-flat tires makes it mandatory for car manufacturers to fit a system where the drivers are made aware that the run-flat has been damaged.

3.1.2 Tire Composites

Tires are very complex. They combine dozens of components that must be formed, assembled, and cured together. And their ultimate success depends on their ability to blend all of the separate components into a cohesive product that satisfies the driver's needs. A modern tire is a mixture of steel, fabric, and rubber. The main composites[1] of a passenger car tire with an overall mass of 8.5 kg are listed in Table 3.2.

[1]Data taken from `www.felge.de` (last accessed September 2010).

TABLE 3.2
Tire Composites: 195/65 R 15 ContiEcoContact

Reinforcements: steel, rayon, nylon	16%
Rubber: natural/synthetic	38%
Compounds: carbon, silica, chalk, ...	30%
Softener: oil, resin	10%
Vulcanization: sulfur, zinc oxide, ...	4%
Miscellaneous	2%

3.1.3 Tire Forces and Torques

In any point of contact between the tire and the road surface, normal and friction forces are transmitted. According to the tire's profile design, the contact patch forms a not necessarily coherent area, Figure 3.1.

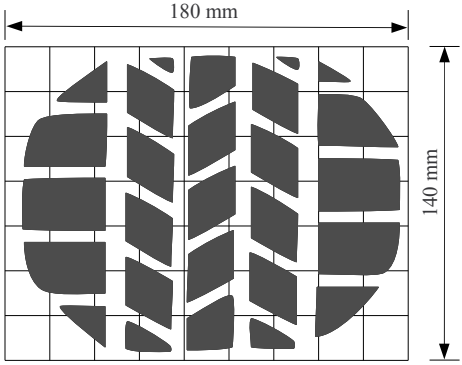

FIGURE 3.1
Footprint of a test tire of size 205/55 R 16 at $F_z = 4700\ N$ and $p = 2.5\ bar$.

The effect of the contact forces can be fully described by a resulting force vector applied at a specific point of the contact patch and a torque vector. The vectors are described in a track-fixed coordinate system. The z-axis is normal to the track, and the x-axis is perpendicular to the z-axis and perpendicular to the wheel rotation axis e_{yR}. Then, the demand for a right-handed coordinate system also fixes the y-axis.

The components of the contact force vector are named according to the direction of the axes, Figure 3.2. A nonsymmetric distribution of the forces in the contact patch causes torques around the x- and y-axes. A cambered tire generates a tilting torque T_x. The torque T_y includes the rolling resistance of the tire. In particular, the torque around the z-axis is important in vehicle dynamics. It consists of two parts,

$$T_z \;=\; T_B + T_S\,. \tag{3.1}$$

F_x	longitudinal force
F_y	lateral force
F_z	vertical force or wheel load
T_x	tilting torque
T_y	rolling resistance torque
T_z	self-aligning and bore torque

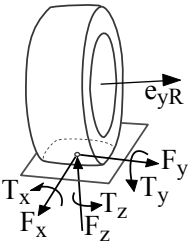

FIGURE 3.2
Contact forces and torques.

The rotation of the tire around the z-axis causes the bore torque T_B. The self-aligning torque T_S takes into account that, in general, the resulting lateral force is not acting in the center of the contact patch.

3.1.4 Measuring Tire Forces and Torques

In general, tire forces and torques are measured under quasi-static operating conditions. Different measurement techniques are available. To measure tire forces and torques on the road, a special test trailer is needed, Figure 3.4. Here,

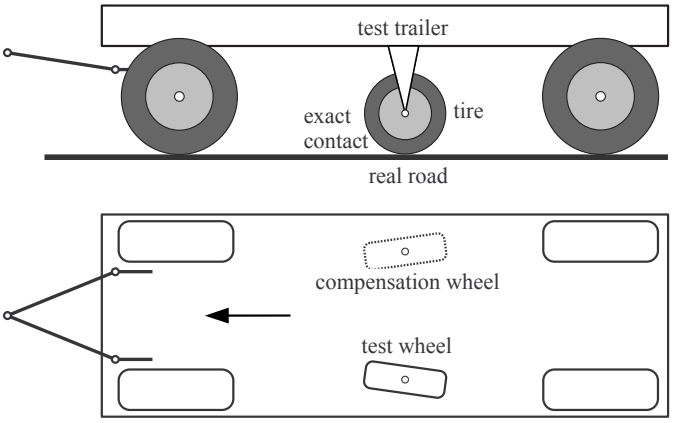

FIGURE 3.3
Layout of a typical tire test trailer.

the measurements are performed under real operating conditions. Arbitrary surfaces like asphalt or concrete and different environmental conditions like dry, wet, or icy are possible. Measurements with test trailers are quite costly and in generalt restricted to passenger car tires.

Indoor measurements of tire forces and torques can be performed on drums or on a flatbed, Figure 3.4. On drum test rigs, the tire is placed either inside

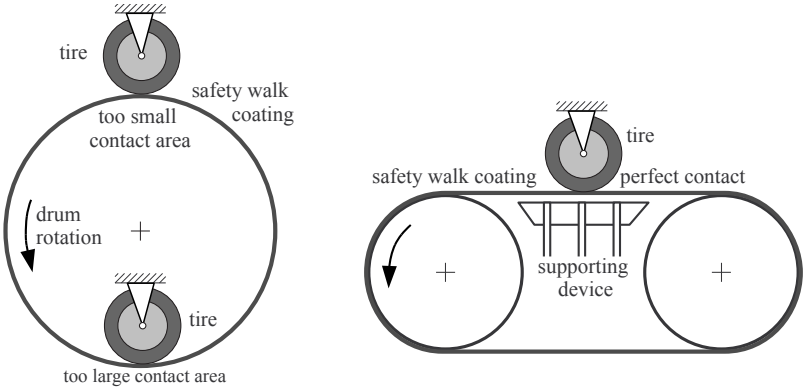

FIGURE 3.4
Tire test rigs: Inner and outer drum as well as flatbed.

or outside the drum. In both cases the shape of the contact area between tire and drum is not correct. That is why one cannot rely on the measured self-aligning torque. Due to its simple and robust design, wide applications including measurements of truck tires are possible. The flatbed tire test rig is more sophisticated. Here, the contact patch is as flat as on the road. But, the safety walk coating that is attached to the steel bed does not generate the same friction conditions as on a real road surface.

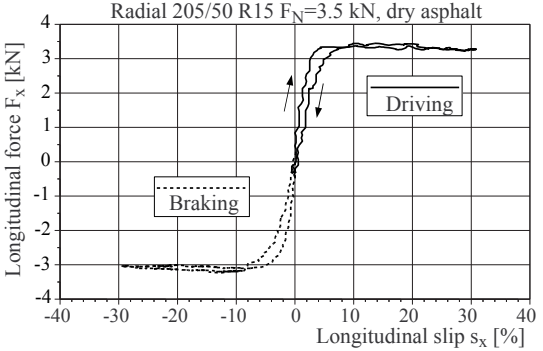

FIGURE 3.5
Typical results of tire measurements.

The slip, a dimensionless quantity that is discussed in Section 3.3.4, is used to quantify the sliding condition in the area where the tire is in contact with the road or the testing device, respectively. Usually, the velocity or angular

velocity of the testing device (trailer, drum, or flatbed) is kept constant. Then, different sliding conditions are generated by slowly increasing or decreasing the angular velocity or slowly varying the alignment of the test wheel. In consequence, the measurements for increasing and decreasing sliding conditions will result in different graphs, Figure 3.5. In general, the mean values are then taken as steady-state results.

3.1.5 Modeling Aspects

For the dynamic simulation of on-road vehicles, the model-element "tire/road" is of special importance, according to its influence on the achievable results. It can be said that the sufficient description of the interactions between tire and road is one of the most important tasks of vehicle modeling, because all the other components of the chassis influence the vehicle dynamic properties via the tire contact forces and torques. Therefore, in the interest of balanced modeling, the precision of the complete vehicle model should stand in reasonable relation to the performance of the applied tire model. At present, two groups of models can be identified: handling models and structural or high-frequency models [21].

Structural tire models are very complex. Within RMOD-K, the tire is modeled by four circular rings with mass points that are also coupled in the lateral direction [26]. Multi-track contact and the pressure distribution across the belt width are taken into account. The tire model FTire consists of an extensible and flexible ring that is mounted to the rim by distributed stiffnesses in the radial, the tangential, and the lateral direction [10]. The ring is approximated by a finite number of belt elements to which a number of mass-less tread blocks are assigned, Figure 3.6.

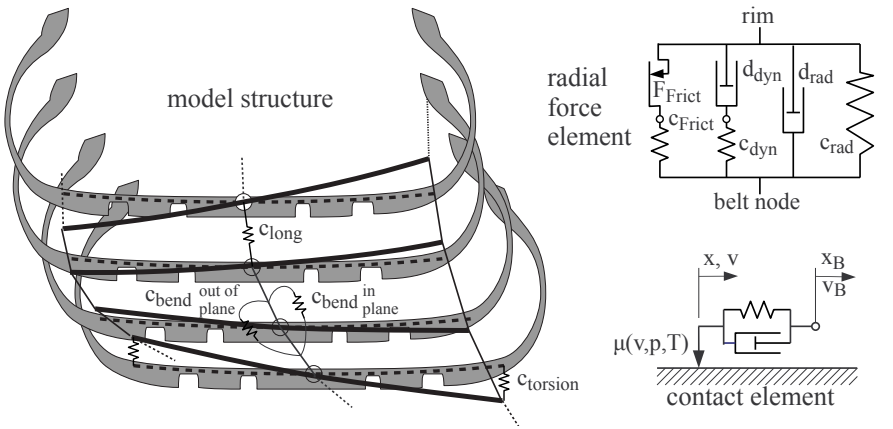

FIGURE 3.6
Complex tire model (FTire).

Complex tire models are computer time consuming and need a lot of data. Usually, they are used for stochastic vehicle vibrations occurring during rough road rides and causing strength-relevant component loads [31].

Comparatively lean tire models are suitable for vehicle dynamics simulations, while, with the exception of some elastic partial structures such as twist-beam axles in cars or the vehicle frame in trucks, the elements of the vehicle structure can be seen as rigid. On the tire's side, "semi-physical" tire models prevail, where the description of forces and torques relies, in contrast to purely physical tire models, also on measured and observed force-slip characteristics. This class of tire models is characterized by useful compromise between user friendliness, model complexity, and efficiency in computation time on the one hand, and precision in representation on the other hand.

In vehicle dynamics practice, often there exists the problem of data provision for a special type of tire for the examined vehicle. Considerable amounts of experimental data for car tires has been published or can be obtained from the tire manufacturers. If one cannot find data for a special tire, its characteristics can be guessed at least by an engineer's interpolation of similar tire types, Figure 3.7. In the field of truck tires, there is still a considerable backlog in data provision. These circumstances must be respected in conceiving a user-friendly tire model.

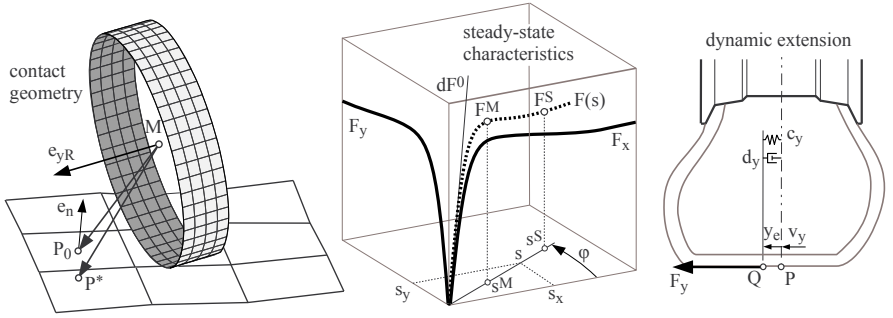

FIGURE 3.7
Handling tire model: TMeasy [12].

For a special type of tire, usually the following sets of experimental data are provided:

- Longitudinal force versus longitudinal slip (mostly just brake-force)
- Lateral force versus slip angle
- Aligning torque versus slip angle
- Radial and axial compliance characteristics

whereas additional measurement data under camber and low road adhesion are favorable special cases.

Any other correlations, especially the combined forces and torques, effective under operating conditions, often must be generated by appropriate assumptions with the model itself, due to the lack of appropriate measurements. Another problem is the evaluation of measurement data from different sources (i.e., measuring techniques) for a special tire [13]. It is a known fact that different measuring techniques result in widely spread results. Here the experience of the user is needed to assemble a "probably best" set of data as a basis for the tire model from these sets of data, and to verify it eventually with his own experimental results.

3.1.6 Typical Tire Characteristics

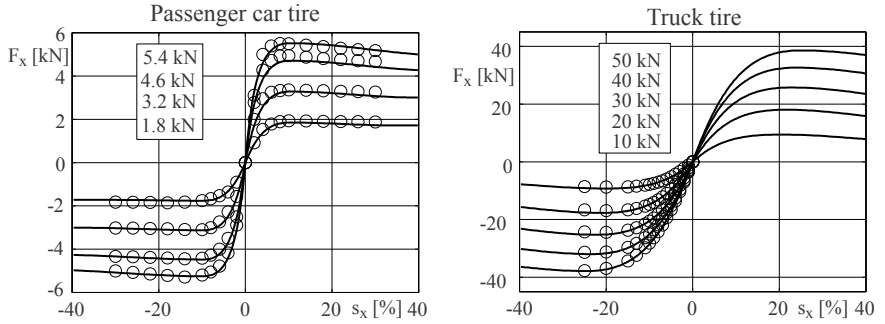

FIGURE 3.8
Longitudinal force: ∘ Measurements, — TMeasy approximation.

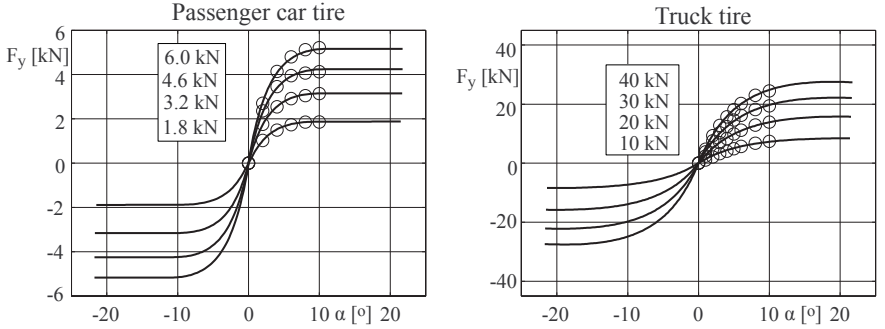

FIGURE 3.9
Lateral force: ∘ Measurements, — TMeasy approximation.

Standard measurements usually performed for different wheel loads F_z provide the longitudinal force F_x as a function of the longitudinal slip s_x and the lateral force F_y and the self-aligning torque T_S as a function of the slip

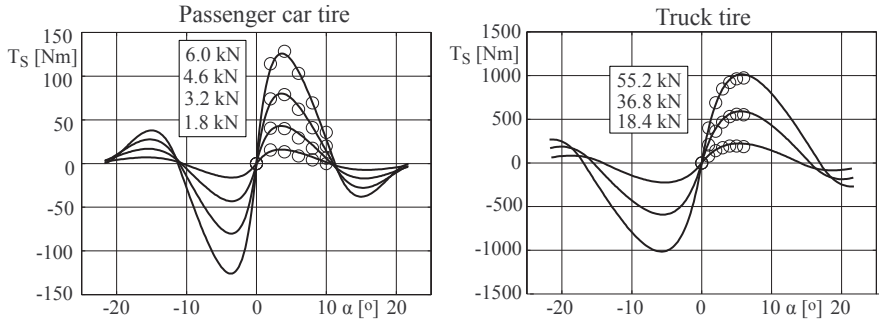

FIGURE 3.10
Self-aligning torque: ∘ Measurements, — TMeasy approximation.

angle α, which is related to the lateral slip by $\tan\alpha = s_y$. Although similar in general, the characteristics of a typical passenger car tire and a typical truck tire differ quite a lot in some details, Figures 3.8 to 3.10. Usually, truck tires

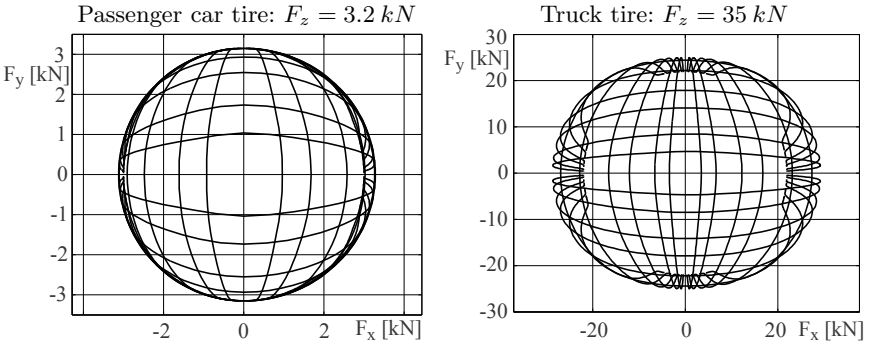

FIGURE 3.11
Combined forces: $|s_x| = 1, 2, 4, 6, 10, 15\,\%$; $|\alpha| = 1, 2, 4, 6, 10, 14°$.

are designed for durability and not for generating large lateral forces. The characteristic curves $F_x = F_x(s_x)$, $F_y = F_y(\alpha)$, and $T_S = T_S(\alpha)$ for the passenger car and truck tire can be approximated quite well by the tire handling model TMeasy [12]. Within the TMeasy model approach, one-dimensional characteristics are automatically converted to two-dimensional combined-slip characteristics, Figure 3.11.

3.2 Contact Geometry

3.2.1 Basic Approach

The current position of a wheel in relation to the earth-fixed x_0-, y_0-, z_0-system is given by the wheel center M and the unit vector e_{yR} in the direction of the wheel rotation axis, Figure 3.12. The irregularities of the track can be

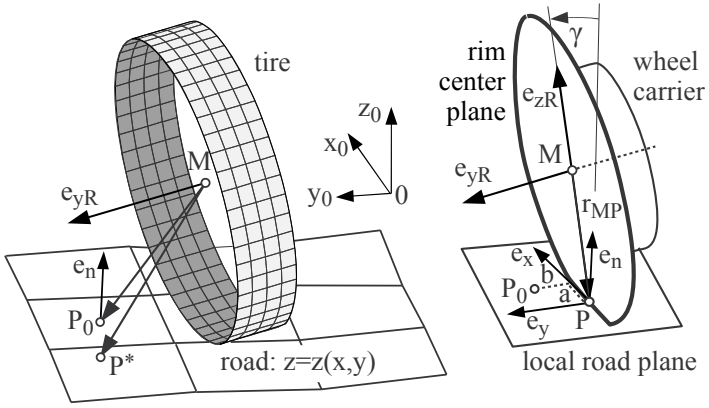

FIGURE 3.12
Contact geometry.

described by an arbitrary function of two spatial coordinates,

$$z \;=\; z(x, y)\,. \tag{3.2}$$

At an uneven track, the contact point P cannot be calculated directly. At first, one can get an estimated value with the vector

$$r_{MP^*} \;=\; -r_0\, e_{zB}\,, \tag{3.3}$$

where r_0 is the undeformed tire radius and e_{zB} is the unit vector in the z-direction of the body-fixed reference frame. The position of this first guess P^* with respect to the earth-fixed reference frame x_0, y_0, z_0 is determined by

$$r_{0P^*,0} \;=\; r_{0M,0} + r_{MP^*,0} \;=\; \begin{bmatrix} x^* \\ y^* \\ z^* \end{bmatrix}\,, \tag{3.4}$$

where the vector r_{0M} describes the position of the rim center M. Usually, the point P^* does not lie on the track because Equation (3.3) generates a vector where neither the deflection of the tire nor its liftoff is taken into account. The

corresponding track point P_0 is determined by

$$r_{0P_0,0} = \begin{bmatrix} x^* \\ y^* \\ z\,(x^*,\, y^*) \end{bmatrix} , \tag{3.5}$$

where Equation (3.2) was used to adjust the z-coordinate to the conforming road height. At the point P_0, the track normal e_n is calculated. Then, the unit vectors in the tire's circumferential direction and lateral direction can be calculated. One gets

$$e_x \;=\; \frac{e_{yR} \times e_n}{|\, e_{yR} \times e_n \,|} \quad \text{and} \quad e_y \;=\; e_n \times e_x \,, \tag{3.6}$$

where e_{yR} denotes the unit vector in the direction of the wheel rotation axis. Calculating e_x demands a normalization, as e_{yR} is not always perpendicular to the track. The tire camber angle γ describes an inclined position of the rim center plane defined by the unit vector e_{yR} against the track normal e_n. By inspecting Figure 3.12 one gets

$$\cos\,(90^\circ - \gamma) \;=\; \sin\gamma \;=\; e_{yR}^T\, e_n \quad \text{or} \quad \gamma \;=\; \arcsin\left(e_{yR}^T\, e_n\right) \,. \tag{3.7}$$

Now, the vector from the rim center M to the track point P_0 is split into three parts,

$$r_{MP_0} \;=\; -r_S\, e_{zR} + a\, e_x + b\, e_y \,, \tag{3.8}$$

where r_S denotes the loaded or static tire radius and a, b are distances measured in the circumferential and lateral direction. The radial direction is defined by the unit vector e_{zR} which is mutually perpendicular to e_x and e_{yR} and hence given by

$$e_{zR} \;=\; e_x \times e_{yR} \,. \tag{3.9}$$

A scalar multiplication of Equation (3.8) with the unit vector e_n results in

$$e_n^T\, r_{MP_0} \;=\; -r_S\, e_n^T\, e_{zR} + a\, e_n^T\, e_x + b\, e_n^T\, e_y \,. \tag{3.10}$$

As the unit vectors e_x and e_y are perpendicular to e_n, Equation (3.10) simplifies to

$$e_n^T\, r_{MP_0} \;=\; -r_S\, e_n^T\, e_{zR} \,. \tag{3.11}$$

Hence, the static tire radius is just given by

$$r_S \;=\; -\,\frac{e_n^T\, r_{MP_0}}{e_n^T\, e_{zR}} \,, \tag{3.12}$$

and

$$r_{MP} \;=\; -r_S\, e_{zR} \tag{3.13}$$

defines the geometric contact point P that lies within the rim center plane. The transition from the point P_0 to the contact point P takes place according

to Equation (3.8) by the terms $a\,e_x$ and $b\,e_y$ perpendicular to the track normal e_n. The track normal, however, was calculated at the point P_0. With an uneven track, the point P shifted perpendicular to the track normal at P_0 may no longer lie on the track and will therefore no longer serve as the contact point. Using P as a new estimation $P^* = P$, Equations (3.5) to (3.13) may be repeated until the shifting distances a and b are sufficiently small.

Tire models that can be simulated within an acceptable time frame, assume that the contact patch is sufficiently flat. At an ordinary passenger car tire, the contact patch has approximately the size of $15 \times 20\ cm$ at normal load. So, it makes no sense to calculate a fictitious contact point to fractions of millimeters, when later on the real track will be approximated by a plane in the range of centimeters. If the track in the contact patch is replaced by a local plane, no further iterative improvements will be necessary for the contact point calculation.

3.2.2 Local Track Plane

Any three points that by chance do not coincide or form a straight line will define a plane. In order to get a good approximation of the local track inclination in the longitudinal and lateral direction not only three but four sample points will be used to determine the local track plane.

The unit vector e_{zB} pointing in the z- or upper direction of the body fixed-reference frame was used in Equation (3.3) to define the initial guess r_{MP^*} for the contact point. As normal roads are sufficiently even, e_{zB} will be close[2] to the local track normal e_n in normal driving situations where all tires are in or at least close to contact with the road. Hence, the unit vector

$$e_x^* = \frac{e_{yR} \times e_{zB}}{|\, e_{yR} \times e_{zB} \,|} \tag{3.14}$$

will provide, on the analogy of Equation (3.6), a first guess of the longitudinal or circumferential direction of the wheel. The points Q_1^*, Q_2^*, Q_3^*, Q_4^* defined by

$$\begin{aligned} r_{MQ_{1,2}^*} &= r_{MP^*} \pm \Delta x\, e_x^* \\ r_{MQ_{3,4}^*} &= r_{MP^*} \pm \Delta y\, e_{yR} \end{aligned} \tag{3.15}$$

will then be located close to the road surface in the front, in the rear, to the left, and to the right of the wheel center M, Figure 3.13. In order to sample the contact patch as well as possible, the distances Δx and Δy in the longitudinal and the lateral direction will be adjusted to the unloaded tire radius r_0 and to the tire width b. By setting $\Delta x = 0.1\, r_0$ and $\Delta y = 0.3\, b$, a quite realistic behavior even on track grooves could be achieved [49]. Similar to Equation (3.5), the corresponding sample points on the road Q_1 to Q_4 can

[2] Using the last value of the unit vector e_{zR} that defines the radial direction of the wheel instead of e_{zB}, a more accurate approach will be possible.

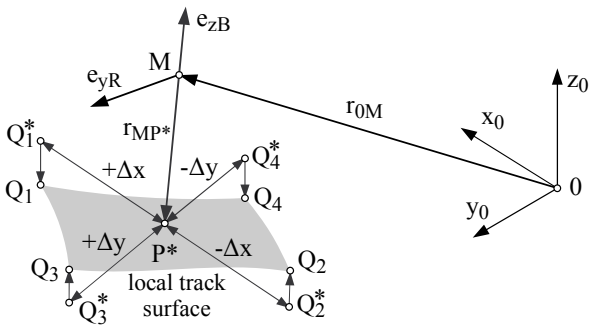

FIGURE 3.13
Sample points on local track surface.

be found from

$$r_{0Q_i,0} = \begin{bmatrix} x_i^* \\ y_i^* \\ z\,(x_i^*,\, y_i^*) \end{bmatrix}, \quad i = 1(1)4\,, \tag{3.16}$$

where x_i^* and y_i^* are the x- and y-components of the vectors

$$r_{0Q_i^*,0} \;=\; r_{0M,0} + r_{MQ_i^*,0} \;=\; \begin{bmatrix} x_i^* \\ y_i^* \\ z_i^* \end{bmatrix}, \quad i = 1(1)4\,, \tag{3.17}$$

describing the absolute position of points Q_1^* to Q_4^*.

The lines fixed by the points Q_1 and Q_2 as well as Q_3 and Q_4, respectively, will now be used to define the inclination of the local track plane in the longitudinal and the lateral direction, Figure 3.14. One gets

$$e_n \;=\; \frac{r_{Q_2Q_1} \times r_{Q_4Q_3}}{|\, r_{Q_2Q_1} \times r_{Q_4Q_3}\,|}\,, \tag{3.18}$$

where $r_{Q_2Q_1} = r_{0Q_1} - r_{0Q_2}$ and $r_{Q_4Q_3} = r_{0Q_3} - r_{0Q_4}$ define vectors pointing from Q_1 to Q_2 and from Q_3 to Q_4. The unit vectors e_x, e_y in the direction of the longitudinal and lateral tire force follow from Equation (3.6). In addition, the mean value of the sample track points

$$r_{0P_0,0} \;=\; \frac{1}{4}\,(r_{0Q_1,0} + r_{0Q_2,0} + r_{0Q_3,0} + r_{0Q_4,0}) \tag{3.19}$$

may serve as a first improvement of the contact point, $P^* \rightarrow P_0$. Finally, the corresponding contact point P in the rim center plane is obtained by Equations (3.12) and (3.13).

As mentioned before, the point P is not always located on the track. But, together with the local track normal e_n, it represents the local track unevenness very well. As in reality, sharp bends or discontinuities, which will occur at very rough roads or step- and ramp-sized obstacles, will be smoothed by this approach.

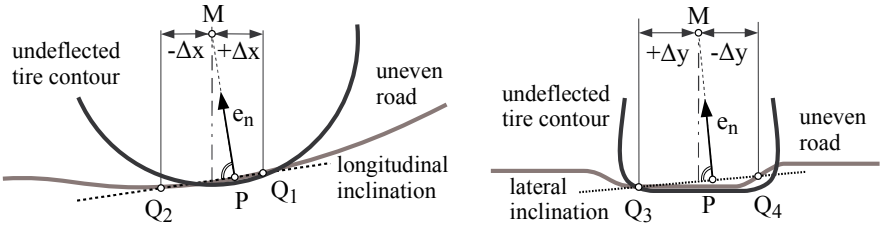

FIGURE 3.14
Inclination of local track plane in longitudinal and lateral directions.

3.2.3 Tire Deflection

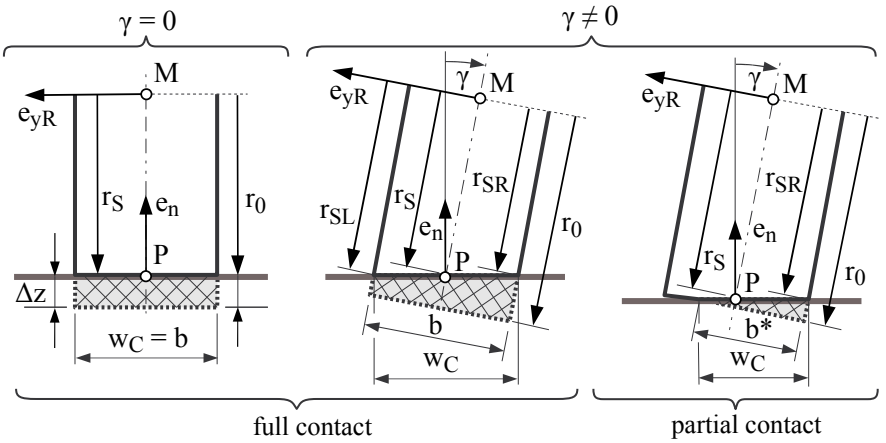

FIGURE 3.15
Deflection of a passenger car or truck tire in different contact situations.

For a vanishing tire camber angle $\gamma = 0$, the deflected zone of a passenger car or truck tire will be close to a rectangle, Figure 3.15. Its area is given by

$$A_0 \;=\; \Delta z\, b\,, \tag{3.20}$$

where b is the width of the tire, and the radial or vertical tire deflection is defined as the difference between the undeflected and the deflected or static tire radius,

$$\Delta z \;=\; r_0 - r_S\,. \tag{3.21}$$

In this case, the width of the contact patch simply equals the tire width, $w_C = b$.

On a cambered tire, the deflected zone of the tire cross-section depends on the contact situation. The magnitude of the tire flank radii

$$r_{SL} \;=\; r_S + \frac{b}{2}\,\tan\gamma \quad \text{and} \quad r_{SR} \;=\; r_S - \frac{b}{2}\,\tan\gamma \tag{3.22}$$

determines the shape of the deflected zone. The tire is in full contact with the road if $r_{SL} \le r_0$ and $r_{SR} \le r_0$ will hold. Then, the deflected zone has a trapezoidal shape with an area of

$$A_\gamma \;=\; \frac{1}{2}\,(r_0 - r_{SR} + r_0 - r_{SL})\;b \;=\; (r_0 - r_S)\;b\,. \tag{3.23}$$

Equalizing the cross-sections $A_\gamma = A_0 = \Delta z\, b$ will again yield the simple vertical tire deflection

$$\Delta z \;=\; r_0 - r_S\,. \tag{3.24}$$

Hence, at full contact, the tire camber angle γ will have no influence on the vertical tire deflection. But, due to

$$w_C \;=\; \frac{b}{\cos\gamma}\,, \tag{3.25}$$

the width of the contact patch increases with the tire camber angle.

The deflected zone will change to a triangular shape if one of the flank radii exceeds the undeflected tire radius. Assuming $r_{SL} > r_0$ and $r_{SR} < r_0$, the area of the deflected zone is obtained by

$$A_\gamma \;=\; \frac{1}{2}\,(r_0 - r_{SR})\;b^*\,, \tag{3.26}$$

where the width of the deflected zone follows from

$$b^* \;=\; \frac{r_0 - r_{SR}}{\tan\gamma}\,. \tag{3.27}$$

Now Equation (3.26) reads as

$$A_\gamma \;=\; \frac{1}{2}\,\frac{(r_0 - r_{SR})^2}{\tan\gamma}\,. \tag{3.28}$$

Equalizing the cross-sections $A_0 = A_\gamma$ finally results in the vertical tire deflection

$$\Delta z \;=\; \frac{1}{2}\,\frac{\left(r_0 - r_S + \frac{b}{2}\,\tan\gamma\right)^2}{b\,\tan\gamma}\,, \tag{3.29}$$

where Equation (3.22) was used to express the flank radius r_{SR} by the static tire radius r_S, the tire width b, and the camber angle γ. Now the width of the contact patch is given by

$$w_C \;=\; \frac{b^*}{\cos\gamma} \;=\; \frac{r_0 - r_{SR}}{\tan\gamma\,\cos\gamma} \;=\; \frac{r_0 - r_S + \frac{b}{2}\,\tan\gamma}{\sin\gamma}\,, \tag{3.30}$$

where Equations (3.27) and (3.22) were used to simplify the expression. If $\tan\gamma$ and $\sin\gamma$ are replaced by $|\tan\gamma|$ and $|\sin\gamma|$, then Equations (3.29) and (3.30) will hold not only for positive but also for negative camber angles.

3.2.4 Static Contact Point

Assuming that the pressure distribution on a cambered passenger car or truck tire corresponds with the shape of the deflected tire area, the acting point of the resulting vertical tire force F_z will be shifted from the geometric contact point P to the static contact point Q, Figure 3.16. The center of the deflected

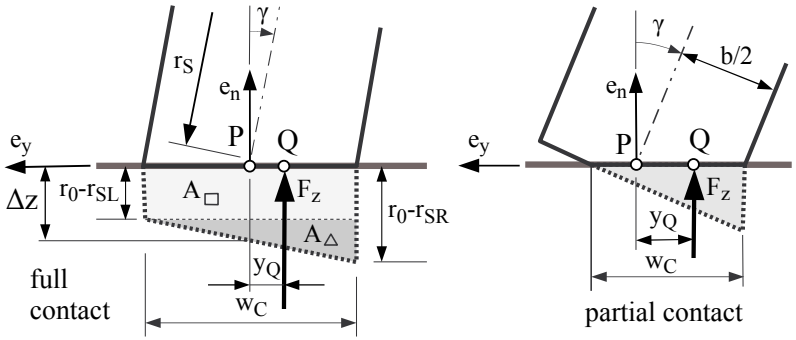

FIGURE 3.16
Lateral deviation of contact point at full and partial contact.

area determines the lateral deviation y_Q of the contact point. By splitting the trapezoidal area into a rectangular and a triangular section, one obtains

$$y_Q \;=\; -\,\frac{y_\square\, A_\square + y_\triangle\, A_\triangle}{A}\,. \tag{3.31}$$

The minus sign takes into account that for positive camber angles, the acting point will move to the right, whereas the unit vector e_y defining the lateral direction will point to the left. The area of the whole cross-section at full contact is given by

$$A \;=\; \tfrac{1}{2}\,(r_0 - r_{SL} + r_0 - r_{SR})\; w_C\,, \tag{3.32}$$

where the width of the contact patch w_C is determined by Equation (3.25). Using Equations (3.22) and (3.24), the expression can be simplified to

$$A \;=\; \Delta z\, w_C\,. \tag{3.33}$$

As the center of the rectangular section is located on the center line that runs through the geometric contact point, $y_\square = 0$ will hold. The distance from the center of the triangular section to the center line is given by

$$y_\triangle \;=\; \tfrac{1}{2} w_C - \tfrac{1}{3} w_C \;=\; \tfrac{1}{6} w_C\,. \tag{3.34}$$

In addition, the area of the triangular section is defined by

$$A_\triangle = \tfrac{1}{2}\,(r_0 - r_{SR} - (r_0 - r_{SL}))\; w_C = \tfrac{1}{2}\,(r_{SL} - r_{SR})\; w_C = \tfrac{1}{2} b\, \tan\gamma\, w_C\,, \tag{3.35}$$

where Equation (3.22) was used to simplify the expression. Now Equation (3.31) can be written as

$$y_Q \;=\; -\,\frac{\frac{1}{6}\,w_C\,\frac{1}{2}\,b\,\tan\gamma\,w_C}{\Delta z\,w_C} \;=\; -\,\frac{b\,\tan\gamma}{12\,\Delta z}\;w_C \;=\; -\,\frac{b^2}{12\,\Delta z}\,\frac{\tan\gamma}{\cos\gamma}\,. \qquad (3.36)$$

If the cambered tire has only partial contact with the road, then according to the deflection area, a triangular pressure distribution will be assumed, Figure 3.16. Now the location of the static contact point Q is given by

$$y_Q \;=\; \pm\left(\frac{1}{3}\,w_C - \frac{b}{2\,\cos\gamma}\right)\,, \qquad (3.37)$$

where the width of the contact patch w_C is determined by Equation (3.30) and the term $b/(2\cos\gamma)$ describes the distance from the geometric contact point P to the outer corner of the contact patch. The plus sign holds for positive and the minus sign for negative camber angles.

The static contact point Q described by the vector

$$r_{0Q} \;=\; r_{0P} \;+\; y_Q\,e_y \qquad (3.38)$$

will represent the contact patch very well in any situation, because it is always placed inside the contact area. Whereas, the geometric contact point P as indicated in Figure 3.16 may even be located outside the contact area in situations where the tire is close to liftoff.

3.2.5 Length of Contact Patch

To approximate the length of the contact patch, the tire deformation is split into two parts, Figure 3.17. By Δz_F and Δz_B, the average tire flank and the belt deformation are measured. Hence, for a tire with full contact to the road,

$$\Delta z \;=\; \Delta z_F + \Delta z_B \;=\; r_0 - r_S \qquad (3.39)$$

will hold. Assuming both deflections being approximately equal will lead to

$$\Delta z_F \;\approx\; \Delta z_B \;\approx\; \frac{1}{2}\,\Delta z\,. \qquad (3.40)$$

Approximating the belt deflection by truncating a circle with the radius of the undeformed tire results in

$$\left(\frac{L}{2}\right)^2 \;+\; (r_0 - \Delta z_B)^2 \;=\; r_0^2\,. \qquad (3.41)$$

Under normal driving conditions, the belt deflections will be small. Taking $\Delta z_B \ll r_0$ for granted, Equation (3.41) simplifies to

$$\frac{L^2}{4} \;=\; 2\,r_0\,\Delta z_B \quad \text{or} \quad L \;=\; \sqrt{8\,r_0\,\Delta z_B} \;=\; \sqrt{8\,r_0\,\frac{1}{2}\,\Delta z} \;=\; 2\,\sqrt{r_0\,\Delta z}\,, \qquad (3.42)$$

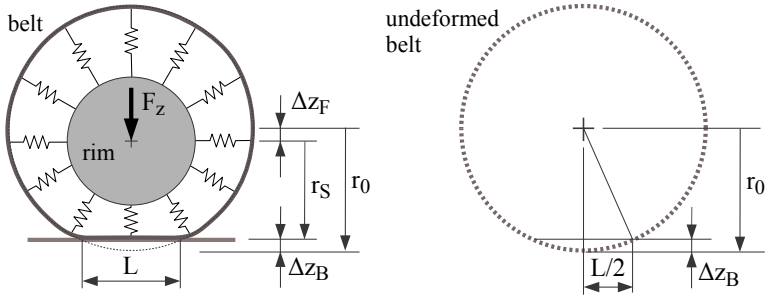

FIGURE 3.17
Length of contact patch.

where Equation (3.40) was used to approximate the belt deflection Δz_B by the overall tire deformation Δz.

Inspecting the passenger car tire footprint in Figure 3.1 leads to a contact patch length of $L \approx 140\,mm$. For this tire, the vertical stiffness and the inflated radius are specified with $c_z = 265\,000\ N/m$ and $r_0 = 316.9\,mm$. The overall tire deflection can be estimated by $\Delta z = F_z/c_z$. At the load of $F_z = 4700\ N$, the deflection amounts to $\Delta z = 4700\ N\,/\,265\,000\ N/m = 0.0177\ m$. Then, Equation (3.42) produces with $L = 2\sqrt{0.3169\,m * 0.0177\,m} = 0.1498\ m \approx 150\,mm$ a contact patch length that will correspond quite well with the length of the tire footprint.

3.2.6 Contact Point Velocity

The velocity of the contact point will be needed to calculate the tire forces and torques that are generated by friction. The momentary position of the static contact point Q defined by Equation (3.38) is given by

$$r_{0Q} \;=\; r_{0M} \;+\; r_{MQ}\,, \tag{3.43}$$

where the vector r_{0M} describes the position of the wheel center M with respect to the origin 0 of an earth-fixed coordinate system, and r_{MQ} denotes the vector from M to the static contact point Q. The absolute velocity of the contact point will be obtained from

$$v_{0Q,0} \;=\; \dot{r}_{0Q,0} \;=\; \dot{r}_{0M,0} \;+\; \dot{r}_{MQ,0}\,, \tag{3.44}$$

where $\dot{r}_{0M,0} = v_{0M,0}$ names the absolute velocity of the wheel center. As the vector r_{MQ} contains the tire deflection Δz normal to the road and it takes part in all those motions of the wheel carrier that do not contain elements of the wheel rotation, its time derivative may be expressed as

$$\dot{r}_{MQ,0} \;=\; \omega^{*}_{0R,0} \times r_{MQ,0} \;+\; \Delta\dot{z}\, e_{n,0}\,, \tag{3.45}$$

where e_n describes the road normal, $\Delta\dot{z}$ denotes the change of the tire deflection, and

$$\omega^*_{0R} \;=\; \omega_{0R} \;-\; e^T_{yR}\,\omega_{0R}\,e_{yR} \tag{3.46}$$

is the angular velocity of the wheel rim without any component in the direction of the wheel rotation axis e_{yR}. Now Equation (3.44) reads as

$$v_{0Q,0} \;=\; v_{0M,0} \;+\; \omega^*_{0R,0}\times r_{MQ,0} \;+\; \Delta\dot{z}\,e_{n,0}\,. \tag{3.47}$$

As the point Q lies on the track, $v_{0Q,0}$ must not contain any component normal to the track,

$$e^T_{n,0}\,v_{0Q,0} \;=\; e^T_{n,0}\,v_{0M,0} + e^T_{n,0}\,\omega^*_{0R,0}\times r_{MQ,0} + \Delta\dot{z}\,e^T_{n,0}\,e_{n,0} = 0\,. \tag{3.48}$$

In addition, $e^T_{n,0}\,e_{n,0} = 1$ will hold because $e_{n,0}$ is a unit vector. Then, the time derivative of the vertical tire deformation is simply given by

$$\Delta\dot{z} \;=\; -\,e^T_{n,0}\,\left(v_{0M,0} + \omega^*_{0R,0}\times r_{MQ,0}\right)\,. \tag{3.49}$$

Finally, the components of the contact point velocity in the longitudinal and the lateral direction are obtained from

$$v_x \;=\; e^T_{x,0}\,v_{0Q,0} \;=\; e^T_{x,0}\,\left(v_{0M,0} + \omega^*_{0R,0}\times r_{MQ,0}\right) \tag{3.50}$$

and

$$v_y \;=\; e^T_{y,0}\,v_{0Q,0} \;=\; e^T_{y,0}\,\left(v_{0M,0} + \omega^*_{0R,0}\times r_{MQ,0}\right)\,, \tag{3.51}$$

where the relationships $e^T_{x,0}e_{n,0} = 0$ and $e^T_{y,0}e_{n,0} = 0$ were used to simplify the expressions. The contact point velocities v_x and v_y will characterize the sliding situation of a nonrotating tire.

3.2.7 Dynamic Rolling Radius

If a rigid disc of radius r_D performs a roll motion on a flat surface, then the constraint equation

$$v \;=\; r_D\,\Omega\,, \tag{3.52}$$

also known as rolling condition, will couple the velocity v of the disc center to the angular velocity Ω of the disc. On a rolling wheel, the tire deflection must be taken into account somehow. To do so, the roll motion of a wheel with r_0 and r_S as unloaded and loaded radius will be compared to a rolling disc of the fictitious or dynamic rolling radius r_D, Figure 3.18.

With $v = dx/dt$ and $\Omega = d\varphi/dt$, the rolling condition (3.52) for the rigid disc results in

$$\frac{dx}{dt} = r_D\,\frac{d\varphi}{dt} \quad \text{or} \quad dx = r_D\,d\varphi \quad \text{or} \quad \Delta x = r_D\,\Delta\varphi\,, \tag{3.53}$$

where Δx denotes the traveling distance if the rolling disc of radius r_D rotates with a specific angle $\Delta\varphi$. Supposing that the rotation angle $\Delta\varphi$ causes the

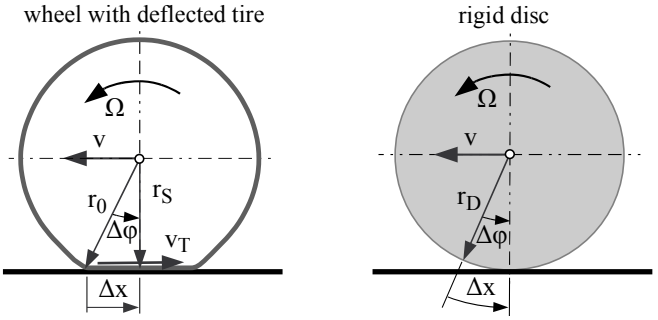

FIGURE 3.18
Dynamic rolling radius.

wheel of the unloaded radius r_0 to perform a rolling motion where a tread particle is transported from the beginning of the contact patch to the center of the contact patch, then the traveling distance of the wheel will be given by

$$\Delta x = r_0 \, \sin \Delta\varphi \, . \tag{3.54}$$

The comparison with a rolling disc on the basis of the same traveling distance will results in

$$r_D \, \Delta\varphi = r_0 \, \sin \Delta\varphi \, . \tag{3.55}$$

Hence, the dynamic tire radius is determined by

$$r_D \; = \; r_0 \, \frac{\sin \Delta\varphi}{\Delta\varphi} \, . \tag{3.56}$$

At small, yet finite angular rotations, the sine function can be approximated by the first terms of its Taylor expansion. Then, Equation (3.56) reads as

$$r_D \; = \; r_0 \, \frac{\Delta\varphi - \frac{1}{6}\Delta\varphi^3}{\Delta\varphi} \; = \; r_0 \, \left(1 - \frac{1}{6} \Delta\varphi^2 \right) \, . \tag{3.57}$$

Using the relationship

$$\cos \Delta\varphi \; = \; \frac{r_S}{r_0} \, , \tag{3.58}$$

which follows by inspecting Figure 3.18 and expanding the cosine function in a Taylor series, one gets

$$\cos \Delta\varphi \; = \; 1 - \frac{1}{2} \Delta\varphi^2 \quad \text{or} \quad \Delta\varphi^2 \; = \; 2 \, (1 - \cos \Delta\varphi) \; = \; 2 \, \left(1 - \frac{r_S}{r_0} \right) \, . \tag{3.59}$$

Then, Equation (3.57) finally reads as

$$r_D \; = \; r_0 \, \left(1 - \frac{1}{3} \left(1 - \frac{r_S}{r_0} \right) \right) \; = \; \frac{2}{3} \, r_0 + \frac{1}{3} \, r_S \, , \tag{3.60}$$

which will represent the dynamic rolling radius r_D as a weighted mean value of the unloaded r_0 and loaded r_S radius of a tire. Note: For a tire close to liftoff $r_S = r_0$ will hold. Then, Equation (3.60) provides a dynamic rolling radius of $r_D = r_0$ that corresponds to the trivial solution of Equation (3.56) when the sine function is approximated by its argument.

By means of the dynamic rolling radius, the roll motion of a wheel can be transferred to the rolling of a rigid disc. But, as a deflected tire is in contact to the road over the whole length of the contact patch, the rolling condition (3.52) must be modified to

$$v_T \;=\; r_D\,\Omega\,, \tag{3.61}$$

where v_T denotes the average velocity at which the tread particles are transported through the contact patch. As the loaded or static tire radius r_S depends on the wheel load F_z, the dynamic rolling radius r_D will automatically be a function of the wheel load too: $r_D = r_D(F_z)$.

3.3 Steady-State Forces and Torques

3.3.1 Wheel Load

The vertical tire force F_z can be calculated as a function of the tire deflection Δz and its time derivative $\Delta\dot{z}$

$$F_z \;=\; F_z(\Delta z,\,\Delta\dot{z})\,. \tag{3.62}$$

Because the tire can only apply pressure forces to the road, the normal force will be restricted to $F_z \geq 0$. In a first approximation, F_z is separated into a static and a dynamic part,

$$F_z \;=\; F_z^{st} + F_z^D\,. \tag{3.63}$$

The static part is described as a nonlinear function of the tire deflection,

$$F_z^{st} \;=\; a_1\,\Delta z \;+\; a_2\,(\Delta z)^2\,. \tag{3.64}$$

The constants a_1 and a_2 may be calculated from the radial stiffness at nominal and double payload,

$$c_{z1} \;=\; \left.\frac{d\,F_z^{st}}{d\,\Delta z}\right|_{F_z^{st}=F_z^N} \quad\text{and}\quad c_{z2} \;=\; \left.\frac{d\,F_z^{st}}{d\,\Delta z}\right|_{F_z^{st}=2F_z^N}\,. \tag{3.65}$$

The derivative of Equation (3.64) results in

$$\frac{d\,F_z^{st}}{d\,\Delta z} \;=\; a_1 \;+\; 2\,a_2\Delta z\,. \tag{3.66}$$

From Equation (3.64) one gets

$$\Delta z \;=\; \frac{-a_1 \pm \sqrt{a_1^2 + 4a_2 F_z^{st}}}{2a_2}\,. \tag{3.67}$$

Because the tire deflection is always positive, the minus sign in front of the square root has no physical meaning and thus can be omitted. Hence, Equation (3.66) can be written as

$$\frac{d\,F_z^{st}}{d\,\Delta z} \;=\; a_1 \;+\; 2\,a_2 \left(\frac{-a_1 + \sqrt{a_1^2 + 4a_2 F_z^{st}}}{2a_2} \right) \;=\; \sqrt{a_1^2 + 4a_2 F_z^{st}}\,. \tag{3.68}$$

Combining Equations (3.65) and (3.68) results in

$$\begin{aligned} c_{z1} \;&=\; \sqrt{a_1^2 + 4a_2 F_z^N} \qquad \text{or} \qquad a_1^2 + 4a_2 F_z^N \;=\; c_{z1}^2\,, \\ c_{z2} \;&=\; \sqrt{a_1^2 + 4a_2 2F_z^N} \qquad \text{or} \qquad a_1^2 + 8a_2 F_z^N \;=\; c_{z2}^2\,, \end{aligned} \tag{3.69}$$

finally leading to

$$a_1 \;=\; \sqrt{2\,c_{z1}^2 - c_{z2}^2} \quad \text{and} \quad a_2 \;=\; \frac{c_{z2}^2 - c_{z1}^2}{4\,F_z^N}\,. \tag{3.70}$$

The parabolic approximation in Equation (3.64) of the static wheel load F_z^{st} as a function of the tire deflection Δz fits very well with measurements, Figure 3.19. The characteristic for the passenger car tire is nearly linear. The

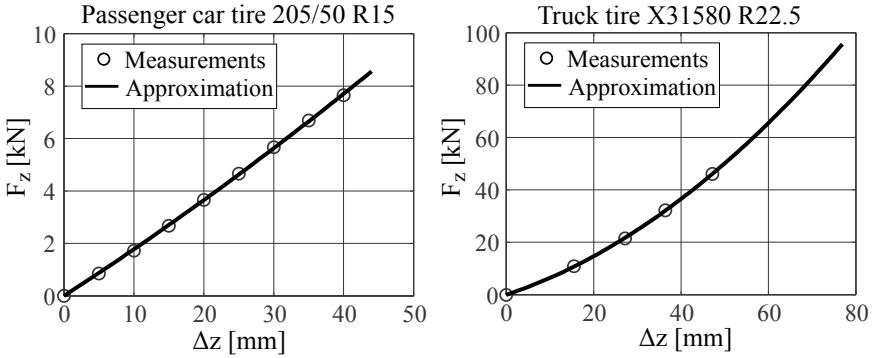

FIGURE 3.19
Static wheel load as a function of the tire deflection.

radial tire stiffness of $c_{z1} = 190\ N/mm$ at the payload of $F_z = 3\,200\ N$ slightly increases to the value of $c_{z2} = 206\,N/mm$ at double the payload. The MATLAB-Script in Listing 3.1 performs a least squares approximation to a measured wheel load characteristic of a truck tire, calculates the stiffness at the given payload and its double, and plots the approximated characteristic as well as the given pairs of measured values.

Listing 3.1
Script `fz_approx.m`: Approximation of a Nonlinear Wheel Load Characteristic

```
% measured wheel load versus tire deflection
Fz = [ 0.0; 10.9; 21.5; 32.2; 46.1 ]; % wheel load [kN]
dz = [ 0.0; 15.5; 27.2; 36.4; 47.2 ]; % tire deflection [mm]
% least square approximation by parabola: Fz = a(1)*dz + a(2)*dz^2
A = [dz, dz.^2]; a = A\Fz;
% get deflections at payload FzN and double the payload 2*FzN
FzN = 35; % tire payload (truck tire)
dz_FzN = ( -a(1) + sqrt(a(1)^2+4*a(2)*FzN) ) / (2*a(2)) ;
dz_2FzN = ( -a(1) + sqrt(a(1)^2+4*a(2)*2*FzN) ) / (2*a(2)) ;
% calculate stiffness at FzN and 2*FzN
c_z1 = ( a(1) + 2*a(2)*dz_FzN );
c_z2 = ( a(1) + 2*a(2)*dz_2FzN );
% plot approximated characteristic and compare to measurements
d_z = linspace(0,2*dz_FzN,201);
F_z = a(1)*d_z + a(2)*d_z.^2;
plot(d_z,F_z,'r','Linewidth',1.5), hold on, plot(dz,Fz,'ok' ), grid on
xlabel('\Delta z [mm]'), ylabel('F_z [kN]')
```

The characteristic of the truck tire shows a significant progressive nonlinearity. Here, the radial stiffness at the payload of $F_z = 35\,kN$ is given by $c_{z1} = 1.25\,kN/mm$ and it rises to $c_{z2} = 1.68\,kN/mm$ at double the payload. If now measurements are available, an appropriate wheel load characteristic can intuitively be modeled by estimating the stiffness c_{z1} at the payload $F_z = F_z^N$ and set the value for the stiffness c_{z2} at double the payload to the same or an increased value depending on the desired or estimated linear or progressive behavior.

The dynamic part of the wheel load is roughly approximated by

$$F_z^D \;=\; d_R\,\Delta\dot{z}\,, \tag{3.71}$$

where d_R is a constant describing the radial tire damping, and the derivative of the tire deformation $\Delta\dot{z}$ is given by Equation (3.49).

3.3.2 Tipping Torque

The lateral shift of the vertical tire force F_z from the geometric contact point P to the static contact point Q is equivalent to a force applied in P and the tipping torque

$$T_x \;=\; F_z\,y_Q \tag{3.72}$$

acting around a longitudinal axis in P. Figure 3.20 shows a negative tipping torque; a positive camber angle moves the contact point in the negative y-direction and hence will generate a negative tipping torque. As long as the cambered tire has full contact with the road, the lateral displacement y_Q is given by Equation (3.36). Then, Equation (3.72) reads as

$$T_x \;=\; -\,F_z\,\frac{b^2}{12\,\Delta z}\,\frac{\tan\gamma}{\cos\gamma}\,. \tag{3.73}$$

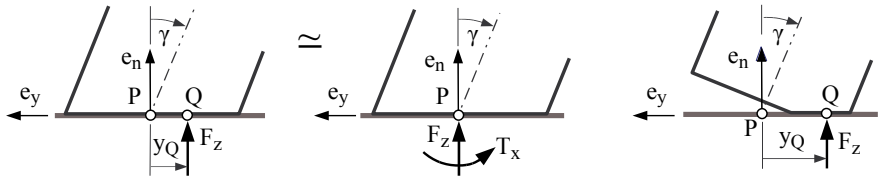

FIGURE 3.20
Tipping torque at full and partial contact.

If the wheel load is approximated by its linearized static part $F_z \approx c_z\,\Delta z$ and small camber angles $|\gamma| \ll 1$ are assumed, then Equation (3.73) simplifies to

$$T_x \;=\; -\,c_z\,\Delta z\,\frac{b^2}{12\,\Delta z}\,\gamma \;=\; -\,\frac{1}{12}\,c_z\,b^2\,\gamma\,, \tag{3.74}$$

where the term $\frac{1}{12}\,c_z b^2$ can be regarded as the tipping stiffness of the tire.

The use of the tipping torque instead of shifting the geometric contact point P to the static static contact point Q is limited to those cases where the tire has full or nearly full contact with the road. If the cambered tire has only partial contact with the road, the geometric contact point P may even be located outside the contact area, whereas the static contact point Q is still a real contact point.

3.3.3 Rolling Resistance

If a nonrotating tire has contact with a flat ground, the pressure distribution in the contact patch will be symmetric from the front to the rear, Figure 3.21. The resulting vertical force F_z is applied in the center of the contact patch that coincides in the xz-plane with the geometric and static contact points P, Q. Hence, it will generate no torque around the y-axis.

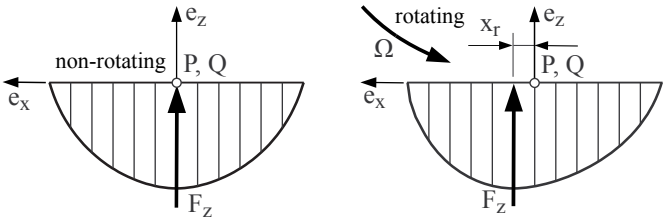

FIGURE 3.21
Pressure distribution at a non-rotation and rotation tire.

If the tire rotates, tread particles will be stuffed into the front of the contact patch, which causes a slight pressure increase, Figure 3.21. Now the resulting vertical force F_z is applied in front of the contact points P and Q

and generates the rolling resistance torque

$$T_y \;=\; -\,|\Omega|\;F_z\,x_R\,, \tag{3.75}$$

where the term $-\,|\Omega|$ ensures that T_y always acts against the sign of the wheel angular velocity Ω. The simple approximation of the sign function

$$|\Omega| \;\approx\; d\,\Omega \quad \text{with} \quad d\;|\Omega\,| \leq 1 \tag{3.76}$$

will avoid discontinuities at $\Omega = 0$. However, the parameter $d > 0$ must be chosen appropriately. The distance x_R from the contact points P, Q to the working point of F_z usually is related to the unloaded tire radius r_0,

$$f_R \;=\; \frac{x_R}{r_0}\,. \tag{3.77}$$

According to [22], the dimensionless rolling resistance coefficient slightly increases with the traveling velocity v of the vehicle

$$f_R \;=\; f_R(v)\,. \tag{3.78}$$

Under normal operating conditions, $20\ km/h < v < 200\ km/h$, the rolling resistance coefficient for typical passenger car tires is in the range of $0.01 < f_R < 0.02$. The rolling resistance hardly influences the handling properties of a vehicle, but it plays a major part in fuel consumption.

3.3.4 Longitudinal Force and Longitudinal Slip

To get a certain insight into the mechanism generating tire forces in the longitudinal direction, we consider a tire on a flatbed test rig. The rim rotates with angular velocity Ω and the flatbed runs with velocity v_x. The distance between the rim center and the flatbed is controlled to the loaded tire radius corresponding to the wheel load F_z, Figure 3.22.

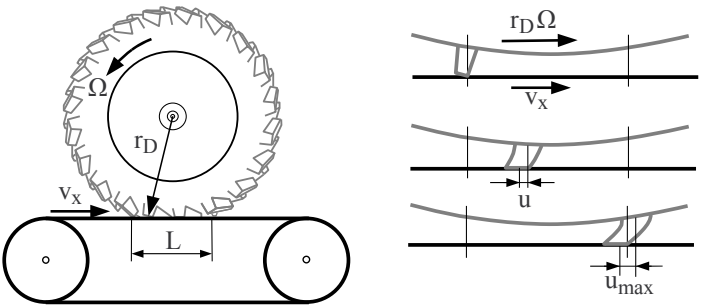

FIGURE 3.22
Tire on flatbed test rig.

A tread particle enters at the time $t = 0$ the contact patch. If we assume adhesion between the particle and the track, then the top of the particle will run with the bed velocity v_x and the bottom with the average transport velocity $v_T = r_D\,\Omega$. Depending on the velocity difference $\Delta v = r_D\,\Omega - v_x$ the tread particle is deflected in longitudinal direction,

$$u \;=\; (r_D\,\Omega - v_x)\,t\,. \tag{3.79}$$

The time a particle spends in the contact patch is given by

$$T \;=\; \frac{L}{r_D\,|\Omega|}\,, \tag{3.80}$$

where L denotes the length of the contact patch and $T > 0$ is assured by $|\Omega|$. Maximum deflection occurs when the tread particle leaves the contact patch at time $t = T$,

$$u_{max} \;=\; u(t = T) \;=\; (r_D\,\Omega - v_x)\,T \;=\; (r_D\,\Omega - v_x)\,\frac{L}{r_D\,|\Omega|}\,. \tag{3.81}$$

The deflected tread particle applies a force to the tire. In a first approximation, we get

$$F_x^t \;=\; c_x^t\,u\,, \tag{3.82}$$

where c_x^t represents the stiffness of one tread particle in the longitudinal direction. On normal wheel loads, more than one tread particle will be in contact with the track, Figure 3.23a. The number p of tread particles can be estimated by

$$p \;=\; \frac{L}{s + a}\,, \tag{3.83}$$

where s is the length of one particle and a denotes the distance between the particles. Particles entering the contact patch are undeformed, whereas the

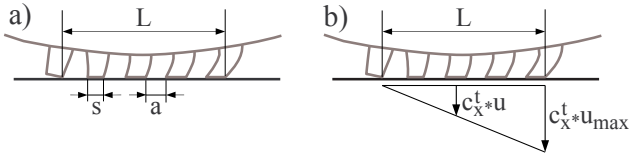

FIGURE 3.23
a) Tread particles, b) force distribution.

ones leaving have the maximum deflection. According to Equation (3.82), this results in a linear force distribution versus the contact length, Figure 3.23b. The resulting force in the longitudinal direction for p particles is then given by

$$F_x \;=\; \frac{1}{2}\,p\,c_x^t\,u_{max}\,. \tag{3.84}$$

Inserting Equations (3.83) and (3.81) results in

$$F_x \;=\; \frac{1}{2}\,\frac{L}{s+a}\,c_x^t\,(r_D\,\Omega - v_x)\,\frac{L}{r_D\,|\Omega|}\;. \tag{3.85}$$

A first approximation of the contact length L was previously calculated in Equation (3.42). Approximating the belt deformation by $\Delta z_B \approx \frac{1}{2}\,F_z/c_z$ results in

$$L^2 \approx 4\,r_0\,\frac{F_z}{c_z}\;, \tag{3.86}$$

where c_z denotes the vertical tire stiffness, and nonlinearities and dynamic parts in the tire deformation were neglected. Now Equation (3.84) can be written as

$$F_x \;=\; 2\,\frac{r_0}{s+a}\,\frac{c_x^t}{c_z}\,F_z\,\frac{r_D\,\Omega - v_x}{r_D\,|\Omega|}\;. \tag{3.87}$$

The nondimensional relation between the sliding velocity of the tread particles in the longitudinal direction $v_x^S = v_x - r_D\,\Omega$ and the average transport velocity $r_D\,|\Omega|$ form the longitudinal slip,

$$s_x \;=\; \frac{-(v_x - r_D\,\Omega)}{r_D\,|\Omega|}\;. \tag{3.88}$$

This slip is not simply defined in order to achieve an appropriate dimensionless quantity, it is, moreover, the plain results from a simple physical approach.

If the tire properties r_0, s, a, c_x^t, and c_z are summarized in the constant k, Equation (3.87) will simplify to

$$F_x \;=\; k\,F_z\,s_x\;. \tag{3.89}$$

Hence, the longitudinal force F_x will be proportional to the wheel load F_z and to the longitudinal slip s_x in this first approximation.

But, Equation (3.89) will hold only as long as all tread particles stick to the track. At moderate slip values, the particles at the end of the contact patch start sliding; and at high slip values, only the parts at the beginning of the contact patch will still stick to the road, Figure 3.24. The resulting

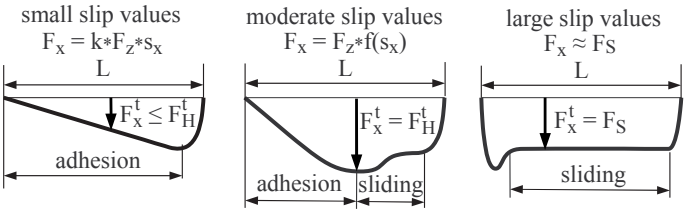

FIGURE 3.24
Longitudinal force distribution for different slip values.

nonlinear function of the longitudinal force F_x versus the longitudinal slip s_x can be defined by the parameters initial inclination (driving stiffness) dF_x^0, location s_x^M, and magnitude of the maximum F_x^M, start of full sliding s_x^S, and the sliding force F_x^S, Figure 3.25.

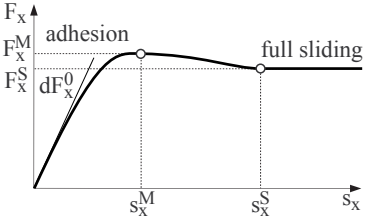

FIGURE 3.25
Typical longitudinal force characteristic.

3.3.5 Lateral Slip, Lateral Force, and Self-Aligning Torque

The wheel rotation with the angular velocity Ω affects the longitudinal slip only. Hence, similar to Equation (3.88), the lateral slip s_y and simultaneously the slip angle α_S will be given by

$$\tan \alpha_S \;=\; s_y \;=\; \frac{-v_y}{r_D\,|\Omega|}\,, \tag{3.90}$$

where the lateral component of the contact point velocity v_y is defined in Equation (3.51). As long as the tread particles stick to the road (small amounts of slip), an almost linear distribution of the forces along the length L of the contact patch will appear. At moderate slip values, the particles at the end of the contact patch start sliding; and at high slip values, only the parts at the beginning of the contact patch stick to the road, Figure 3.26. The nonlinear

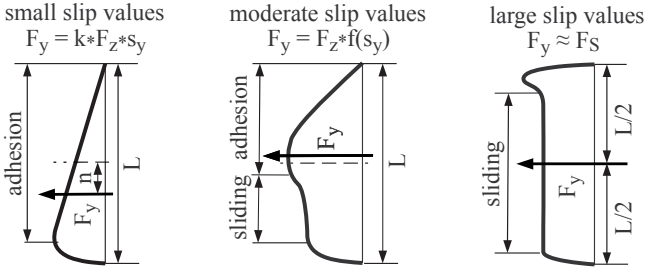

FIGURE 3.26
Lateral force distribution over contact patch.

characteristic of the lateral force versus the lateral slip can be described by the

initial inclination (cornering stiffness) dF_y^0, the location s_y^M and the magnitude F_y^M of the maximum, the beginning of full sliding s_y^S, and the magnitude F_y^S of the sliding force. The distribution of the lateral forces over the contact patch

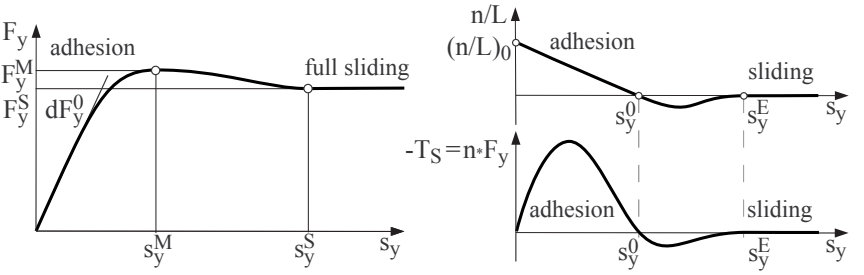

FIGURE 3.27
Typical plot of lateral force, normalized tire offset, and self-aligning torque.

length also defines the point of application of the resulting lateral force. At small slip values, this point lies behind the center of the contact patch (contact points P, Q). With increasing slip values, it moves forward, sometimes even before the center of the contact patch. At extreme slip values, when practically all particles are sliding, the resulting force is applied at the center of the contact patch. The resulting lateral force F_y with the dynamic tire offset or pneumatic trail n as a lever generates the self-aligning torque,

$$T_S \;=\; -n\,F_y\,. \tag{3.91}$$

The lateral force F_y as well as the dynamic tire offset n are functions of the lateral slip s_y. Typical plots of these quantities are shown in Figure 3.27. Characteristic parameters of the lateral force graph are initial inclination (cornering stiffness) dF_y^0, location s_y^M and magnitude of the maximum F_y^M, begin of full sliding s_y^S, and the sliding force F_y^S. The dynamic tire offset n has been normalized by the length of the contact patch L. The normalized dynamic tire offset starts at $s_y = 0$ with an initial value $(n/L)_0 > 0$ and it tends to zero $(n/L \to 0)$ at large slip values $(s_y \geq s_y^E)$. Sometimes the normalized dynamic tire offset overshoots to negative values before it reaches zero again. This behavior can be modeled by introducing the slip values s_y^0 and s_y^E, where the normalized dynamic tire offset passes the s_y-axis and reaches zero again as an additional model parameters, Figure 3.28. In order to achieve a simple and smooth approximation of the normalized tire offset versus the lateral slip, a linear and a cubic function are overlaid in the first section $s_y \leq s_y^0$,

$$\frac{n}{L} = \left(\frac{n}{L}\right)_0 \begin{cases} \left[(1-w)\,(1-s) + w\,\left(1-(3-2s)s^2\right)\right] & |s_y| \leq s_y^0 \\ -\,(1-w)\,\dfrac{|s_y| - s_y^0}{s_y^0}\left(\dfrac{s_y^E - |s_y|}{s_y^E - s_y^0}\right)^2 & s_y^0 < |s_y| \leq s_y^E \\ 0 & |s_y| > s_y^E\,, \end{cases} \tag{3.92}$$

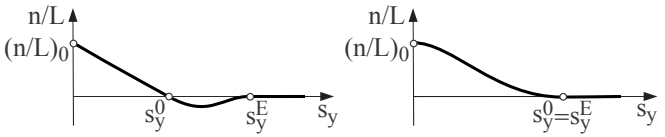

FIGURE 3.28
Normalized tire offset with and without overshoot.

where the abbreviation $s = |s_y|/s_y^0$ was used and the factor $w = s_y^0/s_y^E$ weights the linear and the cubic function according to the values of the parameter s_y^0 and s_y^E. No overshoot will occur for $s_y^0 = s_y^E$. Here, $w = 1$ and $(1 - w) = 0$ will produce a cubic transition from $n/L = (n/L)_0$ to $n/L = 0$ with vanishing inclinations at $s_y = 0$ and $s_y = s_y^0$.

The function provided in Listing 3.2 provides the normalized tire offset as a function of the lateral slip.

Listing 3.2
Function `tmy_tireoff.m`: Normalized Tire Offset

```
function nto=tmy_tireoff( sy ... % lateral slip
                      , nto0 ... % normalized caster offset n/L @ sy=0
                      , synto0 ... % slip where nto passes sy-axis
                      , syntoE ) % slip where sliding starts
% tire offset normalized to contact length

  sy_a = abs(sy); % absolute slip value
  syntoE_loc = max([syntoE,synto0]); % ensure appropriate data

  if sy_a >= syntoE_loc
    nto = 0.d0; %  very high slip values --> pure sliding
  else
    wf = synto0/syntoE_loc; % weighting function for 2 approximations
    if sy_a <= synto0 % low and moderate slip values
      sy_n = sy_a/synto0;
      nto1 = nto0*( 1 - sy_n ); nto2=nto0*(1-(3-2*sy_n)*sy_n^2);
      nto  = (1.d0-wf)*nto1 + wf*nto2 ;
    else % high slip values
      sy_n = ( syntoE_loc - sy_a ) / ( syntoE_loc - synto0 );
      nto = - nto0*(1-wf) * (sy_a-synto0)/synto0 * sy_n^2 ;
    end
  end

end
```

At least the value of $(n/L)_0$ can be estimated very well. At small values of lateral slip $s_y \approx 0$, one gets in a first approximation a triangular, distribution of the lateral forces over the contact patch length (cf. Figure 3.26). The working point of the resulting force is then given by

$$n_0 \;=\; n(F_z \to 0,\; s_y = 0) \;=\; \frac{1}{6}\, L\,. \tag{3.93}$$

Because the triangular force distribution will take for granted a constant pressure in the contact patch, the value $n_0/L = 1/6 = 0.167$ can serve as a first approximation only. In reality, the pressure will drop to zero in the front and in the rear of the contact patch, Figure 3.21. Because low pressure means low friction forces, the triangular force distribution will be rounded to zero in the rear of the contact patch, which will move the working point of the resulting force slightly to the front. If no measurements are available, the slip values s_y^0 and s_y^E where the tire offset passes and finally approaches the x-axis again must be estimated. Usually the value for s_y^0 is somewhat higher than the slip value s_y^M where the lateral force reaches its maximum.

3.4 Combined Forces

3.4.1 Combined Slip

The longitudinal force as a function of the longitudinal slip $F_x = F_x(s_x)$ and the lateral force depending on the lateral slip $F_y = F_y(s_y)$ can be defined by their characteristic parameters initial inclination dF_x^0, dF_y^0, location s_x^M, s_y^M and magnitude of the maximum F_x^M, F_y^M as well as sliding limit s_x^S, s_y^S, and sliding force F_x^S, F_y^S, Figure 3.29. During general driving situations, e.g.,

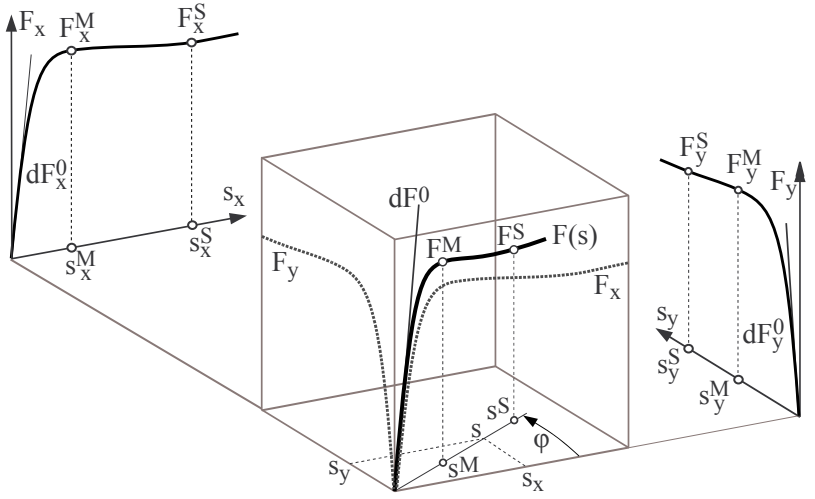

FIGURE 3.29
Combined tire forces.

acceleration or deceleration in curves, longitudinal s_x and lateral slip s_y appear

simultaneously. The combination of the more or less differing longitudinal and lateral tire forces requires a normalization process, cf. [20], [27].

The longitudinal slip s_x and the lateral slip s_y can vectorially be added to the combined slip

$$s = \sqrt{\left(\frac{s_x}{\hat{s}_x}\right)^2 + \left(\frac{s_y}{\hat{s}_y}\right)^2} = \sqrt{\left(s_x^N\right)^2 + \left(s_y^N\right)^2}, \tag{3.94}$$

where the slips were normalized, $s_x \to s_x^N$ and $s_y \to s_y^N$, in order to achieve a nearly equally weighted contribution to the combined slip. The normalizing factors

$$\hat{s}_x = \frac{s_x^M}{s_x^M + s_y^M} + \frac{F_x^M/dF_x^0}{F_x^M/dF_x^0 + F_y^M/dF_y^0} \tag{3.95}$$

and

$$\hat{s}_y = \frac{s_y^M}{s_x^M + s_y^M} + \frac{F_y^M/dF_y^0}{F_x^M/dF_x^0 + F_y^M/dF_y^0} \tag{3.96}$$

take characteristic properties of the longitudinal and lateral tire force characteristics into account. If the longitudinal and lateral tire characteristics do not differ too much, the normalizing factors will be approximately equal to one.

If the wheel locks, the average transport velocity will vanish, $r_D\,|\Omega| = 0$. Hence, longitudinal, lateral, and combined slip will tend to infinity, $s \to \infty$. To avoid this problem, the normalized slips s_x^N and s_y^N are modified to

$$s_x^N = \frac{s_x}{\hat{s}_x} = \frac{-(v_x - r_D\,\Omega)}{r_D\,|\Omega|\,\hat{s}_x} \quad \Rightarrow \quad s_x^N = \frac{-(v_x - r_D\,\Omega)}{r_D\,|\Omega|\,\hat{s}_x + v_N} \tag{3.97}$$

and

$$s_y^N = \frac{s_y}{\hat{s}_y} = \frac{-v_y}{r_D\,|\Omega|\,\hat{s}_y} \quad \Rightarrow \quad s_y^N = \frac{-v_y}{r_D\,|\Omega|\,\hat{s}_y + v_N}\,. \tag{3.98}$$

In normal driving situations, where $r_D\,|\Omega| \gg v_N$ holds, the difference between the original slips and the modified slips are hardly noticeable. However, the fictitious velocity $v_N > 0$ avoids the singularities at $r_D\,|\Omega| = 0$ and will produce in this particular case a combined slip that points exactly in the direction of the sliding velocity of a locked wheel.

Similar to the graphs of the longitudinal and lateral forces, the graph $F = F(s)$ of the combined tire force can be defined by the characteristic parameters dF^0, s^M, F^M, s^S, and F^S. These parameters are calculated from

the corresponding values of the longitudinal and lateral force characteristics

$$dF^0 = \sqrt{\left(dF_x^0\,\hat{s}_x\,\cos\varphi\right)^2 + \left(dF_y^0\,\hat{s}_y\,\sin\varphi\right)^2}\,, \tag{3.99}$$

$$s^M = \sqrt{\left(\frac{s_x^M}{\hat{s}_x}\,\cos\varphi\right)^2 + \left(\frac{s_y^M}{\hat{s}_y}\,\sin\varphi\right)^2}\,, \tag{3.100}$$

$$F^M = \sqrt{\left(F_x^M\,\cos\varphi\right)^2 + \left(F_y^M\,\sin\varphi\right)^2}\,, \tag{3.101}$$

$$s^S = \sqrt{\left(\frac{s_x^S}{\hat{s}_x}\,\cos\varphi\right)^2 + \left(\frac{s_y^S}{\hat{s}_y}\,\sin\varphi\right)^2}\,, \tag{3.102}$$

$$F^S = \sqrt{\left(F_x^S\,\cos\varphi\right)^2 + \left(F_y^S\,\sin\varphi\right)^2}\,, \tag{3.103}$$

where the slip normalization must also be considered at the initial inclination. The angular functions

$$\cos\varphi = \frac{s_x^N}{s} \quad \text{and} \quad \sin\varphi = \frac{s_y^N}{s} \tag{3.104}$$

grant a smooth transition from the characteristic curve of longitudinal to the curve of lateral forces in the range of $\varphi = 0$ to $\varphi = 90°$. The longitudinal and the lateral forces follow then from the according projections in longitudinal

$$F_x = F\,\cos\varphi = F\,\frac{s_x^N}{s} = \frac{F}{s}\,s_x^N = f\,s_x^N \tag{3.105}$$

and lateral direction

$$F_y = F\,\sin\varphi = F\,\frac{s_y^N}{s} = \frac{F}{s}\,s_y^N = f\,s_y^N\,, \tag{3.106}$$

where $f = F/s$ describes the global derivative of the combined tire force characteristic. In addition, the normalized dynamic tire offset $n = n(s_y)$ described by Equation 3.92 and based on a pure lateral slip situation will be extended by

$$n(s) = n(s_y)\,\sin\varphi = n(s_y)\,\frac{s_y^N}{s} \tag{3.107}$$

to a modified normalized tire offset $n = n(s)$, which, similar to the lateral force, is also affected by the combined slip.

3.4.2 Suitable Approximation

The combined tire force characteristic $F = F(s)$ is now approximated in intervals by appropriate functions, Figure 3.30. In the first interval $0 \le s \le s^M$, the rational fraction

$$F(s) = \frac{s}{1 + \frac{s}{s^M}\left(\frac{s}{s^M} + \frac{dF^0\,s^M}{F^M} - 2\right)}\,dF^0 \tag{3.108}$$

is used, which is defined by the initial inclination dF^0 and the location s^M and the magnitude F^M of the maximum tire force. When fixing the parameter

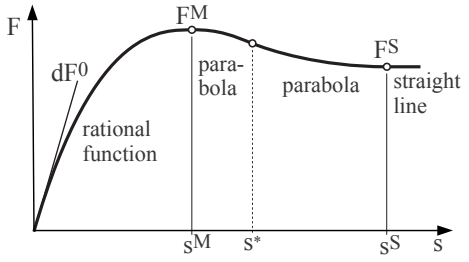

FIGURE 3.30
Approximation of the combined tire force characteristic.

values, one just has to make sure that the condition $dF^0 \geq 2\,F^M/s^M$ is fulfilled, because otherwise the function will have a turning point in the interval of interest. It can be seen that the global derivative of the combined tire force $f = F/s$ is well defined at a vanishing slip and coincides in this particular case with the initial inclination of the combined tire force characteristic $f(s = 0) = dF^0$. In the interval $s^M \leq s \leq s^S$, the combined tire force characteristic is smoothly continued by two parabolas

$$F(s) \;=\; \begin{cases} F^M \;-\; a\,\left(s - s^M\right)^2\;, & s^M \leq s \leq s^* \\ F^S \;+\; b\,\left(s^S - s\right)^2\;, & s^* \leq s \leq s^S \end{cases} \tag{3.109}$$

until it finally reaches the sliding area $s \geq s^S$, where the combined tire force is approximated by a straight line

$$F(s) \;=\; F^S\,. \tag{3.110}$$

The curve parameters a, b, and s^* defining the two parabolas are determined by the demands

$$\left.\frac{d^2\,F}{d\,s^2}\right|_{s \to s^M} \;=\; \left.\frac{d^2\,F}{d\,s^2}\right|_{s^M \leftarrow s}\;, \tag{3.111}$$

$$F(s \to s^*) \;=\; F(s^* \leftarrow s) \quad \text{and} \quad \left.\frac{d\,F}{d\,s}\right|_{s \to s^*} \;=\; \left.\frac{d\,F}{d\,s}\right|_{s^* \leftarrow s}\;. \tag{3.112}$$

To calculate the second derivative of the rational function at $s = s^M$, the first derivative is needed first. Abbreviating the denominator by

$$D \;=\; 1 + \frac{s}{s^M}\left(\frac{s}{s^M} + \frac{dF^0\,s^M}{F^M} - 2\right)\,, \tag{3.113}$$

one gets

$$\frac{d\,F}{d\,s} \;=\; \frac{D - s\left(\dfrac{1}{s^M}\left(\dfrac{s}{s^M} + \dfrac{dF^0\,s^M}{F^M} - 2\right) + \dfrac{s}{s^M}\dfrac{1}{s^M}\right)}{D^2}\,dF^0\,, \tag{3.114}$$

which can be simplified to

$$\frac{d\,F}{d\,s} \;=\; \frac{1-\left(s/s^M\right)^2}{D^2}\,dF^0\,. \tag{3.115}$$

A further derivative yields

$$\frac{d^2\,F}{d\,s^2} = \frac{D^2\left(-2\,s/s^M\,1/s^M\right)-\left(1-\left(s/s^M\right)^2\right)2D\,\dfrac{d\,D}{d\,s}}{D^4}\,dF^0\,. \tag{3.116}$$

At $s = s^M$, the abbreviation D simplifies to

$$D\left(s{=}s^M\right) \;=\; D_M \;=\; 1+\frac{s^M}{s^M}\left(\frac{s^M}{s^M}+\frac{dF^0\,s^M}{F^M}-2\right) \;=\; \frac{dF^0\,s^M}{F^M} \tag{3.117}$$

and Equation (3.116) finally results in

$$\left.\frac{d^2\,F}{d\,s^2}\right|_{s\to s^M} \;=\; dF^0\,\frac{-2/s^M}{D_M^2} \;=\; -2\,\frac{dF^0}{s^M}\,\left(\frac{F^M}{dF^0\,s^M}\right)^2\,. \tag{3.118}$$

The second derivative of the first parabola defined in Equation (3.109) just yields the value $-2\,a$. Hence, the parameter

$$a \;=\; \frac{dF^0}{s^M}\,\left(\frac{F^M}{dF^0\,s^M}\right)^2 \tag{3.119}$$

will grant a smooth transition from the rational function to the first parabola. Now the parameters s^* and b can be calculated. The first demand in Equation (3.112) on the parabolas defined by Equation (3.109) results in

$$F^M - a\left(s^*{-}s^M\right)^2 = F^S + b\left(s^S{-}s^*\right)^2 \tag{3.120}$$

and the second one yields

$$-2\,a\left(s^*{-}s^M\right) = 2\,b\left(s^S{-}s^*\right)(-1) \quad \text{or} \quad a\left(s^*{-}s^M\right) = b\left(s^S{-}s^*\right)\,. \tag{3.121}$$

After multiplication with the term $s^S - s^*$, it can be inserted in Equation (3.120), which then will read

$$F^M - a\left(s^*{-}s^M\right)^2 = F^S + a\left(s^*{-}s^M\right)\left(s^S{-}s^*\right)\,. \tag{3.122}$$

Rearranging some terms, we get

$$F^M - F^S = a\,\left(s^*{-}s^M\right)\left[\left(s^S{-}s^*\right)+\left(s^*{-}s^M\right)\right]\,, \tag{3.123}$$

which finally provides the location of the point where the parabolas are connected to each other

$$s^* \;=\; s^M \;+\; \frac{F^M - F^S}{a\left(s^S{-}s^M\right)}\,, \tag{3.124}$$

and in addition the parameter

$$b = \frac{s^* - s^M}{s^S - s^*}\, a \tag{3.125}$$

as a result from Equation (3.121). Note that for realistic tire characteristics, the connecting point s^* will be located in the transition interval $s^M \le s^* \le s^S$ in general. In the very unrealistic case of $s^* > s^S$, a third-order polynomial instead of the two connected parabolas will realize an "emergency"-transition from the maximum to the sliding force, Listing 3.3.

Listing 3.3
Function `tmy_fcombined.m`: Combined Tire Force

```
function [ f, fos ] = tmy_fcombined( s, df0,fm,sm,fs,ss )
% combined tire force f, global derivative fos and maximum value fmax

% set initial slope to appropriate value if given one is too small
  df0loc = 0;  if sm > 0, df0loc = max(2*fm/sm, df0); end

  if s > 0 &&  df0loc > 0 % normal operating conditions
    if s > ss % full sliding
      f = fs; fos = f/s;
    else
      if  s < sm % adhesion
        p = df0loc*sm/fm - 2 ; sn = s/sm ; dn = 1 + ( sn + p ) * sn ;
        f = df0loc*sm*sn/dn; fos = df0loc/dn;
      else % adhesion --> sliding
        a = (fm/sm)^2/(df0loc*sm); % parameter from 2. deriv. of f @ s=sm
        sstar = sm + (fm-fs)/(a*(ss-sm)); % connecting point
        if sstar <= ss % 2 parabolas (standard approach)
          if s <= sstar % 1. parabola sm < s < sstar
            f = fm - a*(s-sm)^2;
          else          % 2. parabola sstar < s < ss
            b = a*(sstar-sm)/(ss-sstar); f = fs + b*(ss-s)^2;
          end
        else  %  1 cubic function (just in case)
          sn = (s-sm)/(ss-sm) ; f = fm - (fm-fs)*sn^2*(3.d0-2.d0*sn) ;
        end
        fos = f/s ;  % global derivative
      end
    end
  else
    f = 0; fos = df0loc; % defaults (s=0)
  end

end
```

3.4.3 Some Results

Within the TMeasy model approach, the one-dimensional tire characteristics $F_x = F_x(s_x)$ and $F_y = F_y(s_y)$ are automatically converted to two-dimensional characteristics. The combined force characteristic in Figure 3.31 demonstrates

the friction limits of the tire, and Figure 3.32 will show the mutual influence of the longitudinal and lateral slip on the corresponding tire forces.

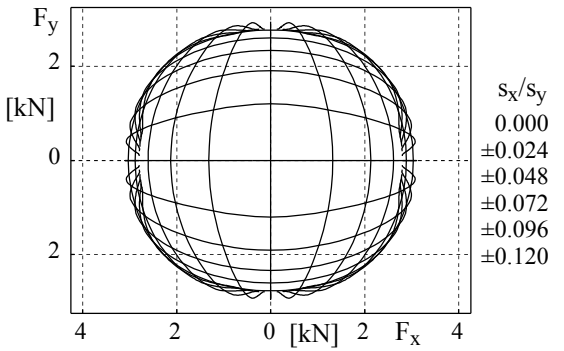

FIGURE 3.31
Combined forces $F_y = F_y(F_x)$ at different slip values.

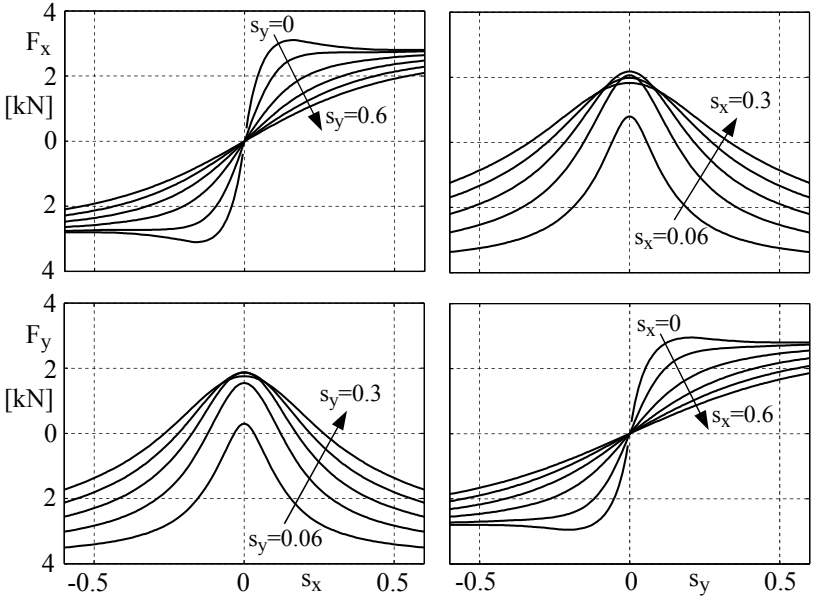

FIGURE 3.32
Two-dimensional tire characteristics.

The MATLAB-Script provided in Listing 3.4 provides the parameters for the longitudinal and lateral tire force characteristic of a typical passenger car tire, calculates the steady-state tire force characteristics for different values of the longitudinal and lateral slip using the function tmy_fcombined given in

Listing 3.3, and finally plots the results. The Listing shows only the plotting commands to create the upper left graph in Figure 3.32, because generating the others will be straightforward.

Listing 3.4
MATLAB-Script `f_steady_state.m`: Steady-State Tire Forces

```
% tire characteristics in longitudinal and lateral direction
dfx0 = 69000;   dfy0 = 66000;  % init slopes dfx/dsx & dfydsy [n/-]
fxm =  3100;   fym =  2950;  % maximum forces [n]
sxm =  0.160;   sym =  0.205;  % s where f(s) = fm [-]
fxs =  2800;   fys =  2800;  % sliding forces [n]
sxs =  0.500;   sys =  0.500;  % s where f(s) = fs [-]

% slip normalizing factors
hsxn = sxm/(sxm+sym) + (fxm/dfx0)/(fxm/dfx0+fym/dfy0);
hsyn = sym/(sxm+sym) + (fym/dfy0)/(fxm/dfx0+fym/dfy0);

% set slip values
nvar = 201; sx = linspace(-1,1,nvar)*1.2*max(sxs); sy = sx;
% pre-allocate fx and fy to speed up loop
fx = zeros(length(sx),length(sy)); fy=zeros(length(sx),length(sy));

for i = 1:length(sx)
  for j = 1:length(sy)
%   combined slip
    sxn = sx(i)/hsxn; syn = sy(j)/hsyn; sc = sqrt ( sxn^2 + syn^2 );
    if sc>0, cphi=sxn/sc;sphi=syn/sc; else cphi=sqrt(2)/2;sphi=sqrt(2)/2; end
%   combined characteristic for normalized slip values
    df0 = sqrt( (dfx0*hsxn*cphi)^2 + (dfy0*hsyn*sphi)^2 );
    fm  = sqrt( (fxm*cphi)^2    + (fym*sphi)^2     );
    sm  = sqrt( (sxm/hsxn*cphi)^2 + (sym/hsyn*sphi)^2 );
    fs  = sqrt( (fxs*cphi)^2    + (fys*sphi)^2     );
    ss  = sqrt( (sxs/hsxn*cphi)^2 + (sys/hsyn*sphi)^2 );
%   combined tire force
    [ f, fos ] = tmy_fcombined( sc, df0,fm,sm,fs,ss );
%   longitudinal and lateral forces
    fx(i,j) = f*cphi; fy(i,j) = f*sphi;
  end
end

subplot(2,2,1), is=101:20:201; % selected lateral slips only
plot(sx,fx(:,is)/1000), axis([-0.6,0.6,-4,4]), grid on
title('f_x=f_x(s_x,s_y)'), xlabel('s_x'), ylabel('kN')
```

The fact that the maximum longitudinal force F_x^M is larger than the maximum lateral force F_y^M is typical for most passenger car and truck tires. The reason is founded in the friction law between tire and road which will react in a degressive manner to the increase of pressure. Longitudinal forces $F_x \neq 0$ cause a circumferential deflection of the tire but they will have nearly no influence on the pressure distribution. The lateral tire deflection caused by lateral forces $F_y \neq 0$, however, will result in a pressure distribution that is downscaled on one side and magnified accordingly on the other, Figure 3.33. The change from the nearly constant pressure distribution to a trapezoidal

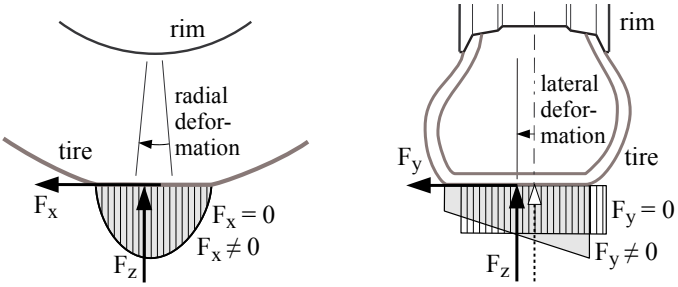

FIGURE 3.33
Effects of F_x and F_y on pressure distribution in the contact patch.

shaped one will then reduce the maximum transmittable friction force in the lateral direction due to the degressive friction law. As there is no similar effect in longitudinal direction, $F_y^M < F_x^M$ will be the consequence.

3.5 Bore Torque

3.5.1 Modeling Aspects

The wheel performs an angular rotation about the axis defined by the unit vector e_{yR} and it is forced to participate on all rotations of the wheel carrier or knuckle that will not coincide with the wheel rotation axis. Hence, the angular velocity of the wheel may be split into two parts,

$$\omega_{0W} \;=\; \omega_{0R}^{*} + \Omega\, e_{yR}\,, \tag{3.126}$$

where the wheel rotation itself is represented by the angular velocity Ω and the vector ω_{0R}^{*} describes the angular velocities of the knuckle without any parts in the direction of the wheel rotation axis. In particular during steering motions, the angular velocity of the wheel has a component in the direction of the track normal e_n

$$\omega_n \;=\; e_n^T\, \omega_{0W} \;\neq\; 0\,, \tag{3.127}$$

which will cause a bore motion of the tire contact patch. If the wheel moves in the longitudinal and lateral direction too, then a very complicated deflection profile of the tread particles in the contact patch will occur. However, by a simple approach, the resulting bore torque can be approximated quite reasonably by the parameter of the combined tire force characteristic.

At first, the complex shape of a tire's contact patch is approximated by a circle, Figure 3.34. By setting

$$R_P \;=\; \frac{1}{2}\left(\frac{L}{2}+\frac{B}{2}\right) \;=\; \frac{1}{4}\,(L+B)\;, \tag{3.128}$$

the radius of the circle can be adjusted to the length L and the width B of the actual contact patch. During pure bore motions, circumferential forces F

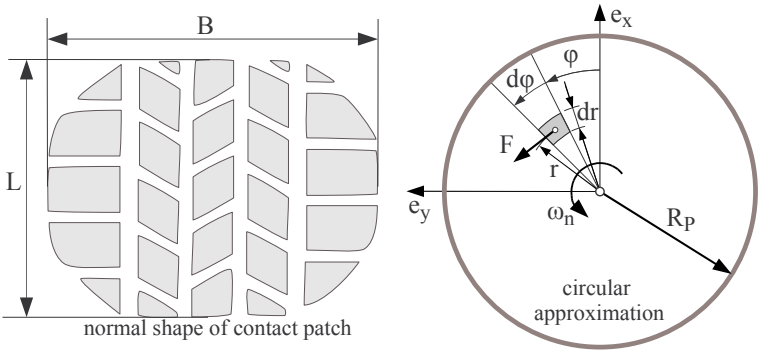

FIGURE 3.34
Bore torque approximation.

are generated at each patch element dA at the radius r. The integration over the contact patch A,

$$T_B \;=\; \frac{1}{A}\int_A F\,r\,dA\,, \tag{3.129}$$

will then produce the resulting bore torque.

3.5.2 Maximum Torque

At large bore motions, all particles in the contact patch are sliding. Then, the circumferential force F will be equal to the sliding force F^S of the combined tire characteristic and will be constant. Then, Equation (3.129) simplifies to

$$T_B^{max} \;=\; \frac{1}{A}\,F^S\int_A r\,dA\,. \tag{3.130}$$

The areas of the circle and the infinitesimal element are given by $A = R_P^2\,\pi$ and $dA = r\,d\varphi\,dr$. Then, Equation (3.130) results in

$$T_B^{max} = \frac{1}{R_P^2\,\pi}\,F^S\int_0^{R_P}\int_0^{2\pi} r\,r d\varphi\,dr \;=\; \frac{2}{R_P^2}\,F^S\int_0^{R_P} r^2\,dr \;=\; \frac{2}{3}\,R_P\,F^S \;=\; R_B\,F^S\,, \tag{3.131}$$

where

$$R_B = \frac{2}{3} R_P \tag{3.132}$$

can be considered the equivalent bore radius of the contact patch.

3.5.3 Simple Approach

Regarding the maximum bore torque, the circular patch can be substituted by a thin ring with the radius r_B. On pure bore motions, the sliding velocity in the ring is given by $R_B \, \omega_n$ and, similar to Equations (3.88) and (3.90), the corresponding bore slip will then be determined by

$$s_B \;=\; \frac{-R_B \, \omega_n}{r_D \, |\Omega|} \, . \tag{3.133}$$

Replacing the sliding force F^S by the slip depending force $F(s_B)$, Equation (3.131) will provide the bore torque as

$$T_B \;=\; R_B \, F(s_B) \, , \tag{3.134}$$

where $F(s_B)$ is determined by the combined force characteristic. On large bore slips, $F(s_B) \to F^S$ holds and will limit the bore torque automatically to the maximum torque defined in Equation (3.131). To avoid numerical problems at a locked wheel, where $\Omega = 0$ will hold, the modified bore slip

$$s_B \;=\; \frac{-R_B \, \omega_n}{r_D \, |\Omega| + v_N} \tag{3.135}$$

can be used for practical applications, where a small fictitious positive velocity $v_N > 0$ is just added in the denominator.

3.5.4 Generalized Slip

Even on steering maneuvers at standstill, a longitudinal, a lateral, and a bore slip will occur simultaneously. By extending the combined slip s defined in Equation (3.94) with the bore slip s_B to the generalized slip

$$s_G \;=\; \sqrt{s^2 + s_B^2} \, , \tag{3.136}$$

the effects of the bore motion on the combined tire forces and vice versa can be taken into account. Similar to the procedure described in Section 3.4, where the combined force was decomposed in the longitudinal and the lateral force, the generalized force characteristic $F_G = F(s_G)$ will now provides, by

$$F \;=\; F_G \, \frac{s}{s_G} \qquad \text{and} \qquad T_B \;=\; R_B \, F_G \, \frac{s_B}{s_G} \, , \tag{3.137}$$

the combined force F and the bore torque T_B in the corresponding parts of the generalized force characteristic.

This simple steady-state bore torque model will serve as a rough approximation only. In particular, it is less accurate at slow bore motions ($s_B \approx 0$) that will occur at parking maneuvers. However, a straightforward extension to a dynamic bore torque model will generate more realistic parking torques later on.

3.6 Different Influences on Tire Forces and Torques

3.6.1 Wheel Load

The resistance of a real tire against deformations has the effect that with increasing wheel load, the distribution of pressure over the contact patch becomes more and more uneven. The tread particles are deflected just as they are transported through the contact patch. The pressure peak in the front of the contact patch cannot be used, for these tread particles are far away from the adhesion limit because of their small deflection. In the rear part of the contact patch, the pressure drop leads to a reduction of the maximally transmittable friction force. With rising imperfection of the pressure distribution over the contact patch, the ability to transmit forces of friction between tire and road lessens. In practice, the tire characteristics are not just scaled by the wheel load as indicated in the simple approach in Sections 3.3.5 and 3.3.4 but they will also depend on it in a much more complicated way. In order to respect this fact in a tire model, the characteristic data for at least two wheel loads must be specified. Within TMeasy the payload F_z^N and its double $2\,F_z^N$ are used for this purpose.

The influence of the wheel load F_z on the tire force characteristics $F_x(s_x)$ and $F_y(s_y)$ is then described by the data set given in Table 3.3.

TABLE 3.3
Tire Data with Degressive Wheel Load Influence

Longitudinal Force F_x		Lateral Force F_y	
$F_z = 4.0\ kN$	$F_z = 8.0\ kN$	$F_z = 4.0\ kN$	$F_z = 8.0\ kN$
$dF_x^0 = 120\ kN$	$dF_x^0 = 200\ kN$	$dF_y^0 = 55\ kN$	$dF_y^0 = 80\ kN$
$s_x^M = 0.110$	$s_x^M = 0.100$	$s_y^M = 0.200$	$s_y^M = 0.220$
$F_x^M = 4.40\ kN$	$F_x^M = 8.70\ kN$	$F_y^M = 4.20\ kN$	$F_y^M = 7.50\ kN$
$s_x^S = 0.500$	$s_x^S = 0.800$	$s_y^S = 0.800$	$s_y^S = 1.000$
$F_x^S = 4.25\ kN$	$F_x^S = 7.60\ kN$	$F_y^S = 4.15\ kN$	$F_y^S = 7.40\ kN$

Assume that at vanishing wheel loads no tire forces can be transmitted,

$$dF_x^0(F_z = 0) = 0, \quad F_x^M(F_z = 0) = 0, \quad F_x^S(F_z = 0) = 0 \tag{3.138}$$

and

$$dF_y^0(F_z{=}0) = 0, \quad F_y^M(F_z{=}0) = 0, \quad F_y^S(F_z{=}0) = 0 \tag{3.139}$$

will hold. As the corresponding values at $F_z = F_z^N$ and $F_z = 2F_z^N$ are provided in Table 3.3, the initial inclinations, the maximal forces, and the sliding forces for arbitrary wheel loads F_z may be inter- or extra-polated by quadratic functions

$$Y(F_z) = \frac{F_z}{F_z^N}\left[\, 2\,Y(F_z^N) - \tfrac{1}{2}Y(2F_z^N) - \left(Y(F_z^N) - \tfrac{1}{2}Y(2F_z^N)\right)\frac{F_z}{F_z^N}\,\right], \tag{3.140}$$

where Y stands for dF_x^0, dF_y^0, F_x^M, F_y^M, F_x^S and F_y^S. However, the location of the maxima s_x^M, s_y^M and the slip values s_x^S, s_y^S at which full sliding will appear cannot be specified at vanishing wheel loads automatically. The corresponding data in Table 3.3 make only a linear inter- or extra-polation possible. Using X as placeholder for s_x^M, s_y^M, s_x^S, and s_y^S, we obtain then

$$X(F_z) = X(F_z^N) + \left(X(2F_z^N) - X(F_z^N)\right)\left(\frac{F_z}{F_z^N} - 1\right). \tag{3.141}$$

The resulting tire characteristics at different wheel loads are plotted in Figure 3.35. As usual, the relationship $\tan\alpha = s_y$, previously provided in Equation (3.90), was used to convert the lateral slip s_y into the slip angle α.

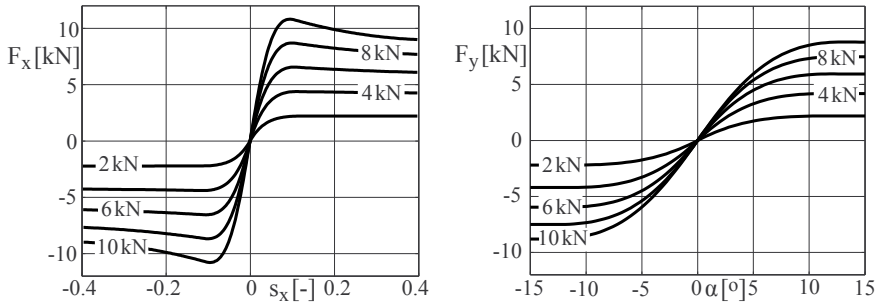

FIGURE 3.35
Tire characteristics at the wheel loads $F_z = [\,2,\,4,\,6,\,8,\,10\,]\,kN$.

According to Equation (3.91), the self-aligning torque is modeled via the lateral force and the dynamic tire offset. The lateral force characteristics are specified in Table 3.3. In addition, the characteristic curve parameters describing the dynamic tire offset will be provided for the single and double payload too. The resulting self-aligning torque as well as typical data are shown in Figure 3.36.

Similar to Equation (3.141), the parameters for arbitrary wheel loads were calculated by linear inter- or extra-polation. The degressive influence of the wheel load on the self-aligning torque can be seen here as well. With the

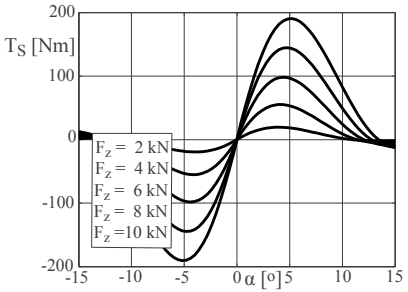

Tire Offset Data

$F_z = 4.0\,kN$	$F_z = 8.0\,kN$
$(n/L)_0 = 0.178$	$(n/L)_0 = 0.190$
$s_y^0 = 0.200$	$s_y^0 = 0.225$
$s_y^E = 0.350$	$s_y^E = 0.375$

FIGURE 3.36
Self-aligning torque at different wheel loads and offset data.

parameters for the description of the tire offset, it has been assumed that at the payload $F_z = F_z^N$, the related tire offset reaches the value of $(n/L)_0 = 1/6 = 0.167$ at vanishing slip values $s_y = 0$. The slip value s_y^0, at which the tire offset passes the x-axis, has been estimated. Usually the value is somewhat higher than the position of the lateral force maximum. With increasing wheel load, it will move to higher values. The values for s_y^S are estimated too.

The dynamic rolling radius r_D is also affected by the wheel load. In extension to Equation (3.60), it will be approximated in the tire model TMeasy by

$$r_D = \lambda\, r_0 + (1-\lambda)\, r_S\,, \tag{3.142}$$

where the weighting factors 2/3 and 1/3 are replaced by the generalized factor λ, which in addition will be modeled as a function of the wheel load F_z. Introducing different weighting factors λ^N and λ^{2N}, which hold for the payload $F_z = F_z^N$ and double the payload $F_z = 2F_z^N$, a linear interpolation results in

$$\lambda = \lambda^N + \left(\lambda^{2N} - \lambda^N\right)\left(F_z/F_z^N - 1\right)\,. \tag{3.143}$$

In addition, the static tire radius is replaced by

$$r_S = r_0 - \Delta r \approx r_0 - F_z^S/c_z\,, \tag{3.144}$$

where the radial tire deformation Δr is approximated by the quotient of the static wheel load F_z^{st} and the vertical tire stiffness c_z. Then, the dynamic rolling radius can be modeled as a pure function of the static wheel load

$$r_D = \lambda(F_z^{st})\, r_0 + \left(1 - \lambda(F_z^{st})\right)\left(r_0 - F_z^{st}/c_z\right)\,, \tag{3.145}$$

where for the sake of simplicity the weighting factor λ determined in Equation (3.143) as a function of wheel load F_z is evaluated for the static wheel load F_z^{st} too. Depending on the values for λ^N and λ^{2N}, which according to Equation (3.143) will provide the load-dependent weighting factor λ, Equation (3.145) may produce a dynamic tire radius r_D that starts to decrease

while the static wheel load F_z^{st} is further increasing. This nonphysical behavior can be avoided by keeping r_D constant when F_z^{st} will start to produce decreasing values for r_D.

TABLE 3.4
TMeasy Model Data for the Dynamic Rolling Radius

$\lambda^N = 0.375$	Weighting factor at payload, $F_z = F_z^N$
$\lambda^{2N} = 0.750$	Weighting factor at double payload, $F_z = 2F_z^N$

The corresponding TMeasy tire model data for a typical passenger car tire at a payload of $F_z^N = 3.2\,kN$ with an undeformed tire radius of $r_0 = 0.315\,m$, and a vertical tire stiffness of $c_z = 190kN/m$ are printed in Table 3.4. This simple but effective model approach fits very well to measurements, Figure 3.37, where the deviation of the dynamic rolling radius r_D from the unloaded tire radius r_0 is plotted versus the wheel load F_z. In this particular case, the dynamic

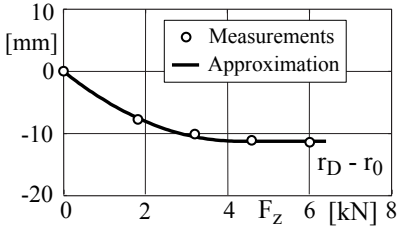

FIGURE 3.37
Wheel load influence on the dynamic rolling radius.

tire radius is kept constant at the value of $r_D(F_z^{st} = 4.2667\,kN) = 0.304\,m$ even on larger static wheel loads. Note that the average of the weighting factors at $F_z = F_z^N$ and $F_z = 2F_z^N$ $\overline{\lambda} = (0.375 + 0.750)/2 = 0.5625$ is rather close to the value of $\lambda = 2/3 = 0.6667$, which was the result of the simple model approach in Section 3.2.7.

3.6.2 Friction

The tire characteristics are valid for one specific tire road combination only. Hence, different tire road combinations will demand different sets of model parameters. A reduced or changed friction coefficient mainly influences the maximum force and the sliding force, whereas the initial inclination will remain unchanged. So, by setting

$$s^M \rightarrow \frac{\mu_L}{\mu_0}\, s^M,\ F^M \rightarrow \frac{\mu_L}{\mu_0}\, F^M,\quad s^S \rightarrow \frac{\mu_L}{\mu_0}\, s^S,\ F^S \rightarrow \frac{\mu_L}{\mu_0}\, F^S, \quad (3.146)$$

the essential tire model parameter, primarily dependent on the friction coefficient μ_0, are adjusted to the new or a local friction coefficient μ_L. The result of this simple approach is shown in Figure 3.38.

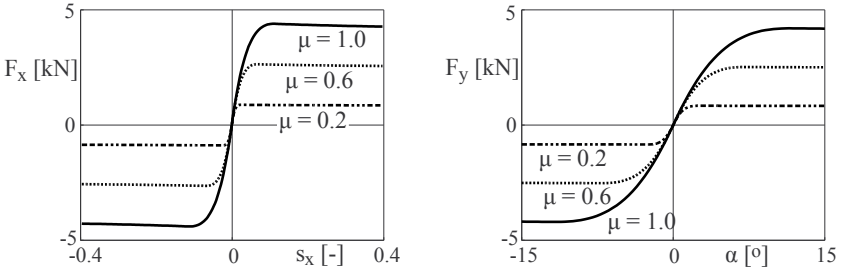

FIGURE 3.38
Force characteristics at different friction coefficients, $\mu = \mu_L/\mu_0$.

If the road model will not only provide the road height z as a function of the coordinates x and y but also the local friction coefficient μ_L, then braking on μ-split maneuvers can easily be simulated [41].

3.6.3 Camber

At a cambered tire, Figure 3.39, the angular velocity of the wheel Ω has a component normal to the road,

$$\Omega_n \;=\; \Omega \sin\gamma\,, \tag{3.147}$$

where γ denotes the camber angle. Now the tread particles in the contact

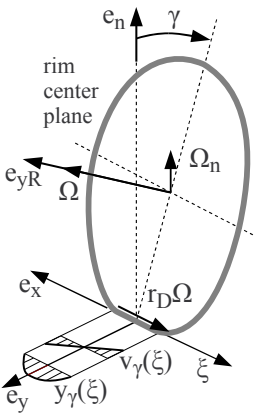

FIGURE 3.39
Velocity state of tread particles at cambered tire.

patch have a lateral velocity that depends on their longitudinal position ξ within the contact patch and is provided by

$$v_\gamma(\xi) \;=\; -\Omega_n \,\frac{L}{2}\,\frac{\xi}{L/2} \;=\; -\Omega\,\sin\gamma\,\xi\,, \qquad -L/2 \le \xi \le L/2\,. \tag{3.148}$$

At the contact point ($\xi = 0$) it vanishes, whereas at the end of the contact patch ($\xi = \frac{L}{2}$) it takes on the same value as at the beginning ($\xi = -\frac{L}{2}$), but pointing in the opposite direction. Assuming that the tread particles stick to the track, the deflection profile will then be defined by

$$\dot{y}_\gamma(\xi) \;=\; v_\gamma(\xi)\,. \tag{3.149}$$

The time derivative of the lateral deflection y can be transformed to a space derivative

$$\dot{y}_\gamma(\xi) \;=\; \frac{d\,y_\gamma(\xi)}{d\,\xi}\,\frac{d\,\xi}{d\,t} \;=\; \frac{d\,y_\gamma(\xi)}{d\,\xi}\;|r_D\,\Omega|\;, \tag{3.150}$$

where the absolute value of the average transport velocity $r_D\,\Omega$ was used to make the result independent of the sign of the wheel rotation. Now Equation (3.149) can be written as

$$\frac{d\,y_\gamma(\xi)}{d\,\xi}\,r_D\,|\Omega| \;=\; -\Omega\,\sin\gamma\,\xi \quad \text{or} \quad \frac{d\,y_\gamma(\xi)}{d\,\xi} \;=\; -\frac{\Omega\,\sin\gamma}{r_D\,|\Omega|}\,\frac{L}{2}\,\frac{\xi}{L/2}\,, \tag{3.151}$$

where the term $L/2$ was used to achieve dimensionless terms. Similar to the lateral slip s_y, which is defined by Equation (3.90), we can introduce a camber slip now

$$s_\gamma \;=\; \frac{-\Omega\,\sin\gamma}{r_D\,|\Omega|}\,\frac{L}{2}\,. \tag{3.152}$$

Then, Equation (3.151) reads as

$$\frac{d\,y_\gamma(\xi)}{d\,\xi} \;=\; s_\gamma\,\frac{\xi}{L/2}\,. \tag{3.153}$$

The shape of the lateral displacement profile is obtained by integration over the contact length

$$y_\gamma \;=\; s_\gamma\,\frac{1}{2}\,\frac{L}{2}\,\left(\frac{\xi}{L/2}\right)^2 \;+\; C\,. \tag{3.154}$$

The boundary condition $y\left(\xi = \frac{1}{2}L\right) = 0$ can be used to determine the integration constant C. One gets

$$C \;=\; -s_\gamma\,\frac{1}{2}\,\frac{L}{2}\,. \tag{3.155}$$

Then, Equation (3.154) finally results in

$$y_\gamma(\xi) \;=\; -s_\gamma\,\frac{1}{2}\,\frac{L}{2}\,\left[1 - \left(\frac{\xi}{L/2}\right)^2\right]\,. \tag{3.156}$$

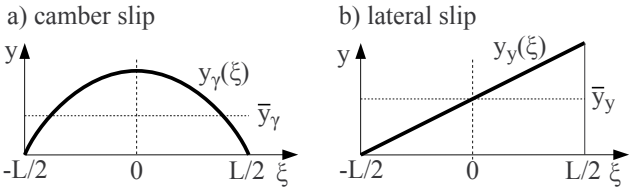

FIGURE 3.40
Displacement profiles of tread particles.

The lateral displacements of the tread particles caused by a camber slip are compared now with the ones caused by pure lateral slip, Figure 3.40. At a tire with pure lateral slip, each tread particle in the contact patch possesses the same lateral velocity, which results in

$$dy_y/d\xi \, r_D \, |\Omega| \; = \; v_y \, , \tag{3.157}$$

where according to Equation (3.150) the time derivative $\dot{y}_y$ was transformed to the space derivative $dy_y/d\xi$. Hence, the deflection profile is linear and reads as

$$y_y \; = \; v_y/(r_D \, |\Omega|) \, \xi \; = \; -s_y \, \xi \, , \tag{3.158}$$

where the definition in Equation (3.90) was used to introduce the lateral slip s_y . Then, the average deflection of the tread particles under pure lateral slip will be given by

$$\bar{y}_y \; = \; -s_y \, \frac{L}{2} \, . \tag{3.159}$$

The average deflection of the tread particles under pure camber slip is obtained from

$$\bar{y}_\gamma \; = \; -s_\gamma \, \frac{1}{2} \, \frac{L}{2} \, \frac{1}{L} \int_{-L/2}^{L/2} \left[1 - \left(\frac{x}{L/2} \right)^2 \right] d\xi \; = \; -\frac{1}{3} \, s_\gamma \, \frac{L}{2} \, . \tag{3.160}$$

Assuming that the hereby-generated lateral forces are proportional to the average deflections of the tread particles,

$$-s_y \, \frac{L}{2} \; \equiv \; -\frac{1}{3} \, s_\gamma \, \frac{L}{2} \quad \text{or} \quad s_y \; \equiv \; \frac{1}{3} \, s_\gamma \tag{3.161}$$

will be the consequence. In normal driving conditions, the camber angle and thus the lateral camber slip are limited to small values, $s_y^\gamma \ll 1$. So, the lateral camber force may be modeled by

$$F_y^\gamma \; = \; dF_y^0 \, \frac{1}{3} \, s_\gamma \, . \tag{3.162}$$

By replacing the initial inclination of the lateral tire force characteristic with the global derivative of the combined tire force characteristic,

$$dF_y^0 \; \longrightarrow \; \frac{F}{s} \; = \; f(s) \, , \tag{3.163}$$

the camber force F_y^γ will then be automatically reduced when the combined slip s is approaching the sliding area.

The angular velocity Ω_n defined in Equation (3.147) generates a bore slip and as a consequence a bore torque T_B. The resulting tire torque around an axis normal to the local road plane is then generated by the self-aligning and the bore torques, $T_z = T_S + T_B$. The resulting torque as well as the lateral force characteristic calculated by the MATLAB-Commands given in Listing 3.5 are plotted in Figure 3.41.

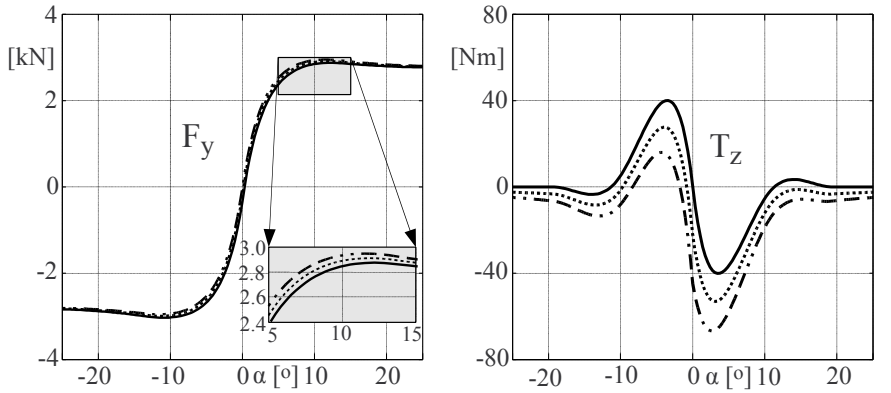

FIGURE 3.41
Camber influence on lateral force and torque around vertical axis: $\gamma = 0,\ 2,\ 4°$.

Listing 3.5
MATLAB-Script `f_steady_state.m` Extended to Camber Influence

```
41 camber = [ 0, 2, 4]*pi/180; % different camber angles [deg -> rad]
42 vt=20; rd=0.310; omega = vt/rd; % set angular velocity (omega=vt/rd)
43
44 % tire offset data
45 nto0=0.178;  % tire offset @ sy = 0
46 synto0=0.20; % sy where nto passes sy-axis
47 syntos=0.35; % sy where nto approaches sy-axis again
48
49 % tire bore radius (estimated from length l and width b of contact patch)
50 l=0.14; b=0.2; rb = 2/3 * 0.5*((l/2)+(b/2));
51
52 % resize fy and allocate tz to speed up loop
53 fy=zeros(length(sy),length(camber)); tz=fy;
54
55 for i = 1:length(sy)
56   for j = 1:length(camber)
57 %   bore slip
58     sb = -rb*omega*sin(camber(j))/abs(vt);
59 %   generalized slip (no longitudinal slip here)
60     sg = sqrt( sy(i)^2 + sb^2 );
61 %   generalized tire force
```

```
62      [f, fos] = tmy_fcombined(sg, dfy0,fym,sym,fys,sys);
63  %   lateral force (no longitudinal force here)
64      if sg>0, fy(i,j) = f*sy(i)/sg; else fy(i,j)=0; end
65  %   tire offset normalized to contact length l and self aligning torque
66      nto = tmy_tireoff(sy(i), nto0,synto0,syntos); ts = -fy(i,j)*nto*l;
67  %   bore torque + resulting torque
68      if sg>0, tb = rb*f*sb/sg; else tb=0; end, tz(i,j) = ts + tb;
69  %   camber slip and force
70      sy_c=-omega*sin(camber(j))/abs(vt)*l/2; fy_c = fos/3*sy_c;
71  %   add camber force
72      fy(i,j) = fy(i,j) + fy_c;
73    end
74  end
75  figure % open new figure
76  subplot(2,2,1), plot(atan(sy)*180/pi,fy'/1000),axis([-25,25,-4,4]), grid on
77  subplot(2,2,2), plot(atan(sy)*180/pi,tz'), axis([-25,25,-80,80]), grid on
```

The MATLAB-Script provided by Listing 3.3 must be executed first, because the above commands will require the data for the lateral tire characteristic and the values for the lateral slip. Listings 3.2 and 3.3 provide the functions tmy_tireoff and tmy_fcombined, which generate the normalized tire offset and the tire force characteristic, respectively.

As the camber angle affects the pressure distribution in the contact patch and it changes the shape of the contact patch from rectangular to trapezoidal, it is extremely difficult, if not impossible, to quantify the camber influence with the aid of such a simple model approach. But, it turns out that the results are very realistic. By introducing a load-dependent weighting factor in Equation (3.162), the camber force can be adjusted to measurements.

3.7 First-Order Tire Dynamics

3.7.1 Simple Dynamic Extension

Measurements show that the dynamic reaction of tire forces and torques to disturbances can be approximated quite well by first-order systems [17]. Then, the dynamic tire forces F_x^D, F_y^D and the dynamic tire torque T_z^D are given by first-order differential equations

$$\tau_x \dot{F}_x^D + F_x^D = F_x^{st}, \tag{3.164}$$

$$\tau_y \dot{F}_y^D + F_y^D = F_y^{st}, \tag{3.165}$$

$$\tau_\psi \dot{T}_z^D + T_z^D = T_z^{st}, \tag{3.166}$$

which are driven by the steady values F_x^{st}, F_y^{st} and T_z^{st}. The time constants τ_x, τ_y, τ_ψ can be derived from corresponding relaxation lengths r_x, r_y, r_ψ. Because the tread particles of a rolling tire move with transport velocity $r_D|\Omega|$ through

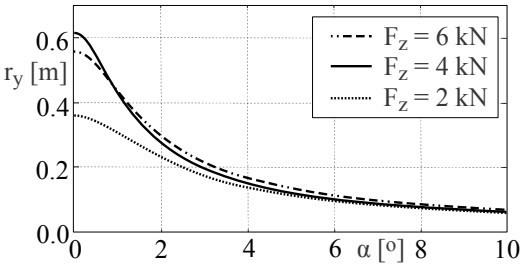

FIGURE 3.42
Measured lateral force relaxation length for a typical passenger car tire, [17].

the contact patch,

$$\tau_i = \frac{r_i}{r_D|\Omega|} \quad i = x, y, \psi \tag{3.167}$$

will hold. But, it turned out that these relaxation lengths are functions of the longitudinal and lateral slip s_x, s_y and the wheel load F_z, Figure 3.42. Therefore, constant relaxation lengths will approximate the real tire behavior in zero-order approximation only. An appropriate model for the dynamic tire performance would be of great advantage because then the cumbersome task of deriving the relaxation lengths from measurements can be avoided.

3.7.2 Enhanced Force Dynamics

The tire forces F_x and F_y acting in the contact patch deflect the tire in the longitudinal and lateral direction, Figure 3.43. In a first-order approximation, the dynamic tire forces in the longitudinal and lateral direction follow from

$$\underbrace{F_x\left(v_x + \dot{x}_e\right)}_{F_x^D} \approx \underbrace{F_x\left(v_x\right)}_{F_x^{st}} + \frac{\partial F_x}{\partial v_x}\,\dot{x}_e\,, \tag{3.168}$$

$$\underbrace{F_y\left(v_y + \dot{y}_e\right)}_{F_y^D} \approx \underbrace{F_y\left(v_y\right)}_{F_y^{st}} + \frac{\partial F_y}{\partial v_y}\,\dot{y}_e\,, \tag{3.169}$$

where x_e and y_e name the longitudinal and the lateral tire deflection, respectively. In the steady state the longitudinal tire forces F_x^{st} and F_y^{st} will be provided as functions of the normalized slips s_x^N and s_y^N. Combining the first relation in Equation (3.137) with Equations (3.105) and (3.106) finally results in

$$F_x^{st} = F\,\frac{s_x^N}{s} = F_G\,\frac{s}{s_G}\,\frac{s_x^N}{s} = \frac{F_G}{s_G}\,s_x^N = f_G\,s_x^N = F_x^{st}(s_x^N)\,, \tag{3.170}$$

$$F_y^{st} = F\,\frac{s_y^N}{s} = F_G\,\frac{s}{s_G}\,\frac{s_y^N}{s} = \frac{F_G}{s_G}\,s_y^N = f_G\,s_y^N = F_y^{st}(s_y^N)\,, \tag{3.171}$$

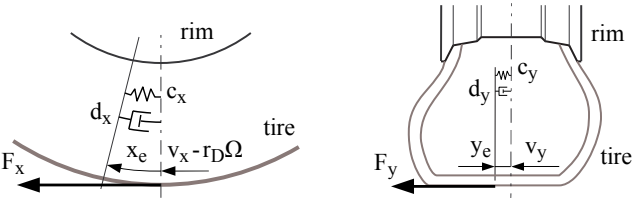

FIGURE 3.43
Tire deflection in the longitudinal and lateral direction.

where s_x^N, s_y^N label the normalized slips in the longitudinal and lateral direction, $F_G = F_G(s_G)$ names the generalized tire force characteristic, and f_G is its global derivative. The derivatives of the steady-state forces with respect to the components of the contact point velocity are then given by

$$\frac{\partial F_x^{st}}{\partial v_x} = \frac{\partial F_x^{st}}{\partial s_x^N}\frac{\partial s_x^N}{\partial v_x} = \frac{\partial F_x^{st}}{\partial s_x^N}\frac{-1}{r_D|\Omega|\hat{s}_x + v_N}, \tag{3.172}$$

$$\frac{\partial F_y^{st}}{\partial v_y} = \frac{\partial F_y^{st}}{\partial s_y^N}\frac{\partial s_y^N}{\partial v_y} = \frac{\partial F_y^{st}}{\partial s_y^N}\frac{-1}{r_D|\Omega|\hat{s}_y + v_N}, \tag{3.173}$$

where the definition of the normalized slips in Equations (3.97) and (3.98) were used to generate its derivatives with respect to the components of the contact point velocity. Corresponding to the first-order approximations in Equations (3.168) and (3.169), the partial derivatives of the steady-state tire forces with respect to the normalized slips will be approximated by their global derivatives

$$\frac{\partial F_x^{st}}{\partial s_x^N} \approx \frac{F_x^{st}}{s_x^N} = \frac{f_G\, s_x^N}{s_x^N} = f_G, \tag{3.174}$$

$$\frac{\partial F_y^{st}}{\partial s_y^N} \approx \frac{F_y^{st}}{s_y^N} = \frac{f_G\, s_y^N}{s_y^N} = f_G. \tag{3.175}$$

Then, Equations (3.168) and (3.169) will read as

$$F_x^D \approx f_G\, s_x^N + f_G \frac{-1}{r_D|\Omega|\hat{s}_x + v_N}\,\dot{x}_e, \tag{3.176}$$

$$F_y^D \approx f_G\, s_y^N + f_G \frac{-1}{r_D|\Omega|\hat{s}_y + v_N}\,\dot{y}_e, \tag{3.177}$$

where according to Equations (3.170) and (3.171), the steady-state tire forces F_x^{st} and F_y^{st} were replaced by the terms $f_G\, s_x^N$ and $f_G\, s_y^N$. On the other hand, the dynamic tire forces can be derived from

$$F_x^D = c_x\, x_e + d_x\, \dot{x}_e, \tag{3.178}$$

$$F_y^D = c_y\, y_e + d_y\, \dot{y}_e, \tag{3.179}$$

where c_x, c_y and d_x, d_y denote stiffness and damping properties of the tire in the longitudinal and lateral direction. Inserting the normalized slips defined by Equations (3.97) and (3.98) into Equations (3.176) and (3.177) and combining them with Equations (3.178) and (3.179) yields first-order differential equations for the longitudinal and lateral tire deflection,

$$\left(d_x + f_G \frac{1}{r_D|\Omega|\hat{s}_x + v_N}\right) \dot{x}_e \;=\; f_G \frac{-(v_x - r_D\,\Omega)}{r_D|\Omega|\hat{s}_x + v_N} \;-\; c_x\, x_e\,, \tag{3.180}$$

$$\left(d_y + f_G \frac{1}{r_D|\Omega|\hat{s}_y + v_N}\right) \dot{y}_e \;=\; f_G \frac{-v_y}{r_D|\Omega|\hat{s}_y + v_N} \;-\; c_y\, y_e\,. \tag{3.181}$$

Multiplying these differential equations with the modified transport velocities

$$v^*_{Tx} \;=\; r_D\,|\Omega|\,\hat{s}_x + v_N \quad \text{and} \quad v^*_{Ty} \;=\; r_D\,|\Omega|\,\hat{s}_y + v_N \tag{3.182}$$

finally results in

$$(v^*_{Tx}\, d_x \;+\; f_G\,)\;\dot{x}_e \;=\; -\,v^*_{Tx}\, c_x\, x_e \;-\; f_G\;(v_x - r_D\,\Omega)\;, \tag{3.183}$$

$$\left(v^*_{Ty}\, d_y \;+\; f_G\,\right)\;\dot{y}_e \;=\; -\,v^*_{Ty}\, c_y\, y_e \;-\; f_G\, v_y\,. \tag{3.184}$$

This first-order dynamic tire force model is completely characterized by the generalized steady-state tire characteristics f_G, and the stiffness c_x, c_y and damping d_x, d_y properties of the tire. Via the steady-state tire characteristics, the dynamics of the tire deflections and hence the dynamics of the tire forces will automatically depend on the wheel load F_z and the longitudinal and lateral slip.

According to Equation (3.167), the relaxation length for the tire deflections and hence for the tire force is now given by

$$r_x \;=\; r_D|\Omega|\,\tau_x \quad \text{and} \quad r_y \;=\; r_D|\Omega|\,\tau_y\,, \tag{3.185}$$

where the corresponding time constants

$$\tau_{x,y} \;=\; \frac{v^*_{Tx,y}\, d_{x,y} \;+\; f_G}{v^*_{Tx,y}\, c_{x,y}} \;=\; \frac{d_{x,y}}{c_{x,y}} \;+\; \frac{f_G}{v^*_{Tx,y}\, c_{x,y}} \tag{3.186}$$

can easily be derived from Equations (3.183) and (3.184).

This simple model approach needs steady-state tire characteristics only. It leads to a relaxation length that is automatically adapted to the tire parameters, Figure 3.44. The relaxation length r_y depends on the wheel load F_z and on the lateral slip s_y or the slip angle $\alpha = \arctan(s_y)$, respectively. A comparison with Figure 3.42 shows that magnitude and the overall behavior of the lateral relaxation length are reproduced quite well. But of course a perfect matching cannot be expected. However, by introducing nonlinear characteristics for the longitudinal and lateral tire stiffness, $c_x \to c_x(x_e)$ and $c_y \to c_y(y_e)$, or an appropriate weighting function, a better fitting to measured relaxation lengths would be possible.

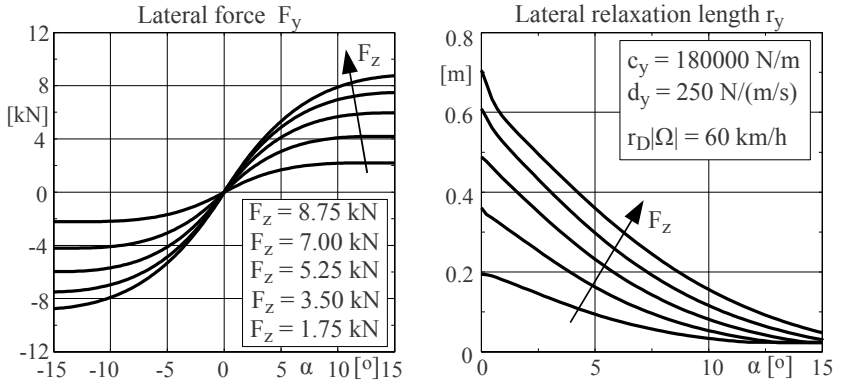

FIGURE 3.44
Lateral force characteristic and relaxation length at different wheel loads.

3.7.3 Enhanced Torque Dynamics

3.7.3.1 Self-Aligning Torque

As described in Section 3.3.5, the self-aligning torque is generated by the tire offset and the lateral force. By neglecting possible dynamics of the tire offset, the dynamic self-aligning torque can be approximated by

$$T_S^D \;=\; -n\, F_y^D\,, \tag{3.187}$$

where n denotes the steady-state tire offset and F_y^D names the dynamic tire force. In this approach the dynamics of the self-aligning torque is controlled by the dynamics of the lateral tire force only.

3.7.3.2 Bore Torque

Following the calculation of the steady-state bore torque in Section 3.5, the contact patch can be approximated by an equivalent contact ring, Figure 3.45. During bore motions, the wheel rim rotates with angle ψ_W around an axis

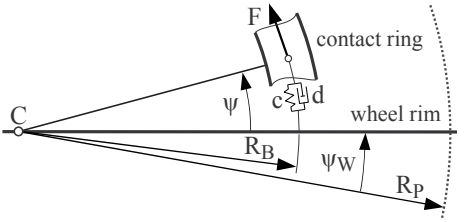

FIGURE 3.45
Simple bore torque model.

normal to the contact patch. The position of the contact ring relative to the wheel is described by the twist angle ψ. The contact ring with a radius that is equal to the bore radius R_B is attached to the rim by a spring damper element, where the constants c and d represent the stiffness and damping properties of the tire in the circumferential direction. Then, the force

$$F \;=\; c\,R_B\,\psi \;+\; d\,R_B\,\dot{\psi} \tag{3.188}$$

applied to the ring generates the dynamic bore torque

$$T_B^D \;=\; R_B\,F \;=\; c\,R_B^2\,\psi + d\,R_B^2\,\dot{\psi}\,. \tag{3.189}$$

The angular velocity of the ring around an axis perpendicular to the local road plane is simply determined by

$$\omega_n \;=\; \dot{\psi}_W + \dot{\psi}\,, \tag{3.190}$$

which according to Equation (3.135) and the second part of Equation (3.137) will result in the the bore torque

$$T_B^* \;=\; R_B\,\frac{F_G}{s_G}\,\underbrace{\frac{-R_B\left(\dot{\psi}_W + \dot{\psi}\right)}{r_D\,|\Omega| + v_N}}_{s_B}\,, \tag{3.191}$$

where s_B names the bore slip. As no mass or inertia effects of the ring will be taken into account, the dynamic torque T_B^D generated between rim and tire ring must equal the torque T_B^* acting between tire ring and road. Putting Equation (3.189) on a level with Equation (3.191) yields

$$c\,R_B^2\,\psi + d\,R_B^2\,\dot{\psi} \;=\; R_B\,\frac{F_G}{s_G}\,\frac{-R_B\left(\dot{\psi}_W + \dot{\psi}\right)}{r_D\,|\Omega| + v_N}\,, \tag{3.192}$$

where

$$c_\psi = c\,R_B^2 \quad \text{and} \quad d_\psi = d\,R_B^2 \tag{3.193}$$

represent the twist stiffness and twist damping of the tire. By neglecting the influence of the time derivative of the twist angle $\dot{\psi}$ on the generalized slip s_G, one gets the first-order differential equation

$$\left(d\,R_B^2 + \frac{F_G}{s_G}\,\frac{R_B^2}{r_D\,|\Omega| + v_N}\right)\dot{\psi} \;=\; -\,c\,R_B^2\,\psi \;+\; R_B\,\frac{F_G}{s_G}\,\frac{-R_B\,\dot{\psi}_W}{r_D\,|\Omega| + v_N}\,. \tag{3.194}$$

where

$$T_B^{st} \;=\; c\,R_B^2\,\psi^{st} \;=\; R_B\,\frac{F_G}{s_G}\,\frac{-R_B\,\dot{\psi}_W}{r_D\,|\Omega| + v_N} \;=\; R_B\,\frac{F_G}{s_G}\,s_B \tag{3.195}$$

represents the steady-state bore torque, which implies a corresponding steady-state torsional tire deflection described by the twist angle ψ^{st}. Multiplying the differential equation with the modified transport velocity $r_D|\Omega|+v_N$, abbreviating the global derivative of the generalized tire force characteristic F_G/s_G by f_G, and finally dividing by R_B^2 results in

$$(d\,(r_D|\Omega|+v_N)+f_G)\,\dot{\psi} \;=\; -\,c\,\psi\,(r_D|\Omega|+v_N) \;-\; f_G\,\dot{\psi}_W\,. \tag{3.196}$$

The time constant

$$\tau_\psi \;=\; \frac{d}{c} \;+\; \frac{f_G}{c\,(r_D|\Omega|+v_N)} \tag{3.197}$$

or the relaxation length

$$r_\psi \;=\; r_D|\Omega|\,\tau_\psi \;=\; r_D|\Omega|\,\frac{d}{c} \;+\; \frac{f_G}{c}\,\frac{r_D|\Omega|}{(r_D|\Omega|+v_N)}\,, \tag{3.198}$$

which for $v_N \ll r_D|\Omega|$ simplifies to

$$r_\psi \;=\; r_D|\Omega|\,\frac{d}{c} \;+\; \frac{f_G}{c}\,, \tag{3.199}$$

characterize the dynamics of the torsional tire deflection ψ and, hence, of the bore torque T_B^D defined in Equation (3.188). The results of this simple approach are rather close to measurements, Figure 3.46. As no further data

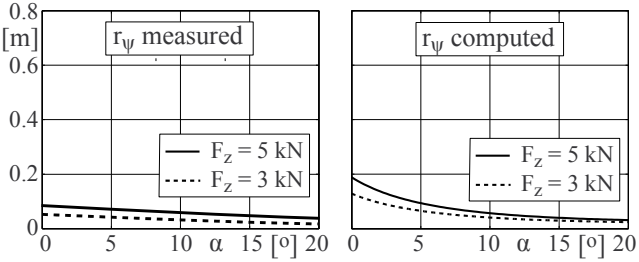

FIGURE 3.46
Measured [17] and computed relaxation length of the dynamic bore torque.

are given in [17], estimated model data that represent typical passenger car tires were used to calculate the relaxation length via Equation (3.199). The corresponding tire data that hold for a payload of $F_z^N = 4000\,N$ are given in Table 3.5. In addition a transport velocity of $r_D|\Omega| = 40\,km/h$ was assumed hereby.

3.7.3.3 Parking Torque

Parking maneuvers are often performed close to or in standstill situations. At standstill, the angular velocity of the wheel Ω is zero. Then, Equation (3.196) will simplify to

$$(d\,v_N + f_G)\,\dot{\psi} \;=\; -\,c\,\psi\,v_N \;-\; f_G\,\dot{\psi}_W\,. \tag{3.200}$$

The fictitious velocity v_N was just introduced to avoid singularities in the slips at standstill. A sufficiently small value will certainly imply,

$$d\,v_N \ll f_G\,. \tag{3.201}$$

If the bore motion performed with a certain amount of the angular rotation of the wheel carrier $\dot{\psi}_W \neq 0$ starts at a vanishing twist angle $\psi = 0$, then the differential equation (3.200) will merge into

$$f_G\,\dot{\psi} = -f_G\,\dot{\psi}_W\,. \quad \text{or} \quad \dot{\psi} = -\dot{\psi}_W \tag{3.202}$$

Hence, at the beginning of the bore motion, the torsional tire deflection represented by the twist angle ψ is just increased or decreased, depending on the magnitude and sign of the steering motion $\dot{\psi}_W$, which corresponds to a simple spring model.

TABLE 3.5
Dynamic Bore Torque Model Data

$dF^0 = 90\,000$	Initial inclination	$v_N = 0.010$	Fictitious velocity
$F^M = 4,250$	Maximum force	$r_D = 0.310$	Dynamic tire radius
$s^M = 0.18$	Slip where $F{=}F^M$	$R_B = 0.060$	Bore radius
$F^S = 4100$	Sliding force	$c_\psi = 2700$	Torsional stiffness
$s^S = 0.50$	Slip where $F{=}F^S$	$d_\psi = 1.8$	Torsional damping

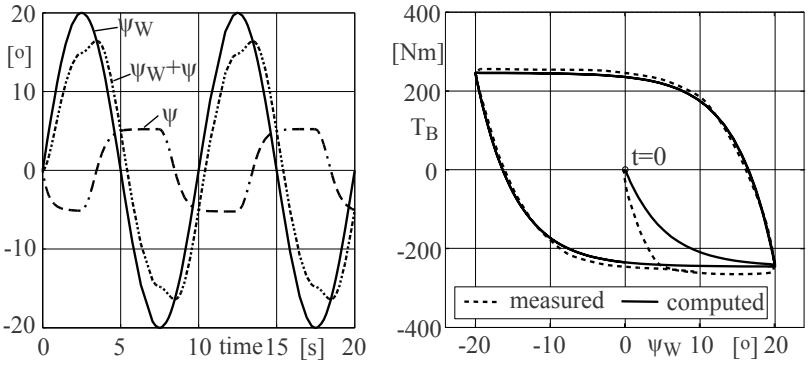

FIGURE 3.47
Measured [17] and computed parking torque at standstill.

The simple dynamic torque model operates with parameter, mostly derived from the steady-state tire properties. In particular, the data given in Table 3.5 are needed. To measure the parking effort, the wheel is rotated at standstill ($\Omega = 0$) with a low frequent sine input $\psi_W = \psi_W^0 \sin 2\pi f_E t$ around an axis perpendicular to the contact patch. The left plot in Figure 3.47 indicates an

amplitude of $\psi_W^0 = 20°$ and an excitation frequency of $f_E = 0.1\,Hz$. The torsional stiffness of the tire $c_\psi = 2700\,Nm/rad$ and the maximum achievable bore torque, which according to Equation (3.131) is given by $T_B^{max} = R_B F^S = 0.06 * 4100 = 246\,Nm$ limits the twist angle to a value of $|\psi| \leq 246/2700 = 0.091\,rad = 5.2°$. The simple dynamic torque model is able to generate periodic cycles that are quite similar to measurements. Only in the beginning the curves will differ because the simple bore torque model approximates the contact patch by one rigid ring that is coupled to the rim by a spring damper combination and while rotating is exposed to a generalized friction force. In reality, all tread particles will stick to the road at first and then pass over to a sliding motion from the outer parts of the contact patch to the inner.

Exercises

3.1 The position of the wheel rotation axis with respect to the earth-fixed system is defined by the unit vector $e_{yR,0} = [0.097;\ 0.995;\ -0.024]^T$ in a particular driving situation. Calculate the unit vectors $e_{x,0}$ and $e_{y,0}$ pointing in the direction of the longitudinal and the lateral tire force as well as the tire camber angle γ when $e_{n,0} = [0;\ 0;\ 1]^T$ defines the track normal.

3.2 A tire with an unloaded radius of $r_0 = 0.546\,m$ is exposed to a vertical force of $F_z = 35\,kN$. Calculate the vertical tire stiffness c_z and the contact length L if a loaded or static tire radius of $r_S = 0.510\,m$ is measured.

3.3 The following table lists the vertical tire deflection of a passenger car at different loads.

$\Delta z\ mm$	0	5	10	15	20	25	30	35	40
$F_z\ kN$	0	0.85	1.75	2.60	3.60	4.60	5.60	6.55	7.55

Plot the tire deflection versus the wheel load. Calculate the tire stiffness at the payload $F_z^N = 3.2\,kN$ and its double. Estimate the length of the contact patch at $F_z = F_z^N$ and the equivalent bore radius when the unloaded tire radius and the width of the tire are given by $r_0 = 293\,mm$ and $b = 205\,mm$, respectively.

3.4 Measurements at a payload of $F_z^N = 3.2\,kN$ result in

$s_x\ [\%]$	0	2	4	6	8	10	14	18	22	26	30
$F_x\ [kN]$	0	2.00	2.95	3.25	3.30	3.35	3.35	3.32	3.30	3.28	3.26
$\alpha\ [deg]$	0	2	4	6	8	10					
$F_y\ [kN]$	0	1.75	2.55	2.92	3.05	3.14					

Plot the tire characteristics $F_x(s_x)$ and $F_y(s_y)$ by converting the slip angle α into the corresponding lateral slip s_y. Deduce by simple inspection the characteristic data tire model data dF_x^0, F_x^M, s_x^M, F_x^S, s_x^S and dF_y^0, F_y^M, s_y^M, F_y^S, s_y^S. Generate the combined force characteristics using the MATLAB-Script given in Listing 3.4.

4

Drive Train

CONTENTS

4.1 Components and Concepts

4.1.1 Conventional Drive Train

The drive train serves two functions: it transmits power from the engine to the drive wheels, and it varies the amount of torque. The main parts of a drive train for conventional ground vehicles are engine, clutch, transmission, differentials, shafts, brakes, and wheels, Figure 4.1.

On heavy trucks, planetary gears are imbedded into the wheels in order to reduce the amount of torque transmitted by the drive- and half-shafts. Most passenger cars have rear- or front-wheel drive. All-wheel drive is often used on upper-class cars and sport utility vehicles. Front-wheel drive is very common on light trucks. Advanced drive trains make use of electronically controlled

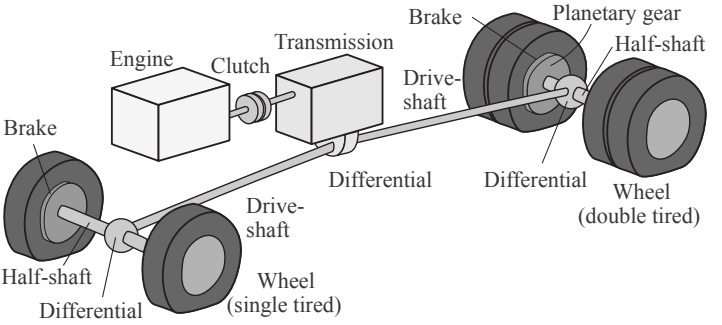

FIGURE 4.1
Components of a conventional drive train.

differentials in order to transfer the driving torque properly to the axles and wheels.

Different kinds of driving concepts can be found on heavy trucks. Here, the notation $w \times d$, where d names the number of wheels in total and d the number of driven wheels, is usually used to specify the driving concept. Hence, 4×4 stands for all-wheel drive on a truck with two axles, and 8×4 names a truck with four axles (= eight wheels) in total, where two axles (= four wheels) are driven. Note that the number of tires and the number of wheels may be different because on solid axles usually on one wheel, two tires (double tires) are mounted.

4.1.2 Hybrid Drive

Nowadays hybrid driven cars have become very popular. At present, many hybrid models are already available and most automobile manufacturers have announced plans to put their own versions on the market. A hybrid drive train combines two or more power sources in general. Only the gasoline-electric hybrid is currently commercially available. Both, at present, available drive sources may operate in series or parallel, Figure 4.2.

In the serial arrangement, the vehicle is driven by the electric motor, which provides an adequate torque over a wide speed range and does not necessarily require a bulky transmission. As the combustion engine will drive the electric generator only, it can be run at a constant and efficient rate even as the vehicle changes speed. Series-hybrids can be also fitted with a capacitor or a flywheel to store regenerative braking energy.

In the parallel layout, both drive sources can be used jointly or separately to accelerate the vehicle. The possibility for power addition permits relatively small dimensioning of the machines, without having to accept disadvantages in the driving performance. As only one electric motor is integrated, it can only be either generative or motive.

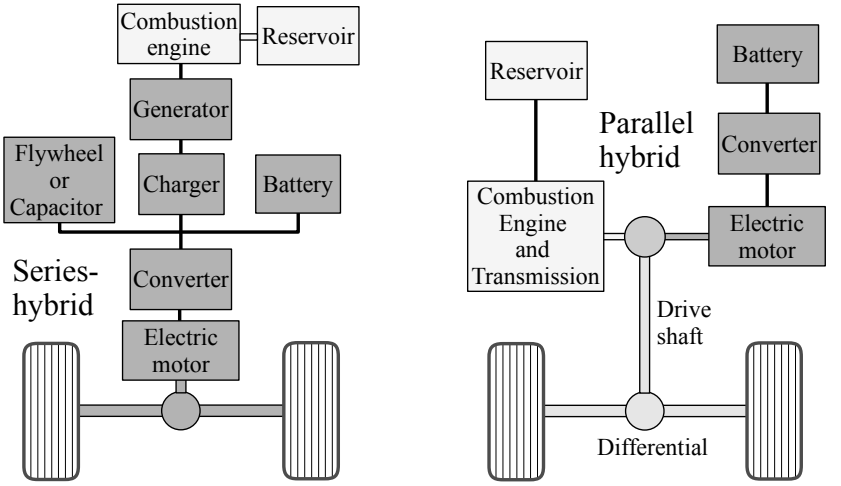

FIGURE 4.2
Typical layout of serial and parallel hybrid drives.

The powersplit hydro drive combines the serial and parallel hybrid to a strong hybrid drive. A transmission (planetary gear) splits the power of the internal combustion engine in one portion that is transmitted directly (mechanically) to the drive shaft, while the other portion is converted into electrical energy and optionally stored in the battery or consumed by the electric motor. Both the combustion engine and the electric motor can be used to drive the vehicle. Even a purely electric drive will be possible.

The hybrid is a compromise. It attempts to significantly increase the mileage and reduce the emissions of a gasoline-powered car while overcoming the shortcomings of an electric car.

4.1.3 Electric Drive

In an electric drive vehicle, the torque is supplied to the wheels by one or more electric motors. Attaching electric motors to each driven wheel will require no drive line at all but will increase the unsprung mass of the wheel significantly. The possibility to provide individual and easily controllable driving torques at the wheels offers a lot options to improve the traction and the handling of a vehicle.

If the electric motor is powered solely by a battery, the vehicle will create less pollution than a gasoline-powered one. A large array of batteries is needed in order to achieve a reasonable range of miles per charge. In addition, recharging the batteries will take a long time. Purely electric driven cars usually are restricted to specific operating conditions. That is why "extended range" electric vehicles as one variant of hydro drive are at present available

on the market only. Here, the batteries are charged from the grid and by a small internal combustion engine that powers a generator which powers the batteries.

4.2 Wheel and Tire

4.2.1 Wheel Dynamics

Besides the longitudinal tire force F_x that generates a torque around the wheel rotation axis e_{yR} via the static tire radius r_S and the rolling resistance torque T_y, the rotation of a wheel is influenced by the driving torque T_D and the braking torque T_B, Figure 4.3. The driving torque may either applied directly

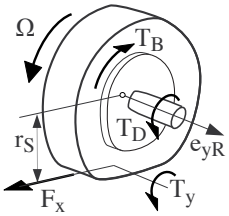

FIGURE 4.3
Wheel and tire.

to the wheel by an electric motor $T_D = T_E$ or transmitted to the wheel by the half-shaft, $T_D = T_S$. The dynamics of the wheel rotation is governed by the angular momentum around the wheel rotation axis

$$\Theta\,\dot{\Omega} \;=\; T_D - T_B - r_S\,F_x + T_y\,, \tag{4.1}$$

where Θ and Ω denote the inertia and the angular velocity of the wheel.

4.2.2 Eigen-Dynamics

4.2.2.1 Steady-State Tire Forces

The dynamics of a wheel that is neither driven ($T_D = 0$) nor braked ($T_B = 0$) may be simplified to

$$\Theta\,\dot{\Omega} \;=\; -r_S\,F_x\,, \tag{4.2}$$

where torque T_y which represents the rolling resistance and usually is very small, was neglected in comparison to the term $r_S\,F_x$. Within handling tire models like TMeasy, the longitudinal tire force F_x is described as a function of the longitudinal slip s_x. For vanishing lateral slips, the normalization factor

$\hat{s}_x$ in Equation (3.97) can be set to one. Then, the longitudinal slip is given by

$$s_x \;=\; \frac{-(v_x - r_D\,\Omega)}{r_D\,|\Omega| + v_N}\,, \tag{4.3}$$

where v_x denotes the longitudinal component of the contact point velocity and the small but positive fictitious velocity $v_N > 0$ avoids numerical problems when the wheel will be locked, $\Omega = 0$. Now, the angular velocity of the wheel is approximated by

$$\Omega \;=\; \frac{v_x}{r_D} + \Delta\Omega \quad \text{or} \quad r_D\,\Omega \;=\; v_x + r_D\,\Delta\Omega\,, \tag{4.4}$$

where in addition

$$|r_D \Delta\Omega| \ll |v_x| \tag{4.5}$$

is assumed, which means that the angular velocity $\Delta\Omega$ describes small deviations from the rolling condition $r_D\Omega = v_x$. Then, the longitudinal slip defined by Equation (4.3) simplifies to

$$s_x \;=\; \frac{-\,(v_x - (v_x + r_D\,\Delta\Omega))}{|v_x + r_D\,\Delta\Omega| + v_N} \;\approx\; \frac{-r_D\,\Delta\Omega}{|v_x| + v_N}\,. \tag{4.6}$$

According to Equation (4.5), the longitudinal slip will be small too, $s_x \ll 1$, and the steady-state longitudinal tire force can be approximated by

$$F_x \;=\; F_x^{st} \;\approx\; dF_x^0\,s_x \;=\; dF_x^0\,\frac{r_D\,\Delta\Omega}{|v_x| + v_N}\,, \tag{4.7}$$

where dF_x^0 describes the initial inclination of the longitudinal tire characteristic $F_x = F_x(s_x)$. Now the angular momentum of the wheel defined in Equation (4.2), simplifies to a linear first-order differential equation,

$$\Theta\,\Delta\dot{\Omega} \;=\; -r_S\,dF_x^0\,\frac{r_D\,\Delta\Omega}{|v_x| + v_N}\,. \tag{4.8}$$

The dynamics of this simple wheel tire model is then characterized by the eigenvalue

$$\lambda = -\,\frac{dF_x^0}{|v_x| + v_N}\,\frac{r_S^2}{\Theta}\,, \tag{4.9}$$

where $r_S \approx r_D$ was assumed in addition. In drive away or braking to standstill maneuvers where $v_x = 0$ will hold, the eigenvalue is proportional to $1/v_N$. This strong dependency on the fictitious velocity causes problems because small values for v_N will result in a very large eigenvalue, which indicates a stiff differential equation for the wheel rotation. On the other hand, too large values for v_N will produce results with poor accuracy [39].

4.2.2.2 Dynamic Tire Forces

However, a simple but effective extension to first-order dynamic tire forces gets rid of the strong influence of the fictitious velocity v_N and produces good results in any driving situation [36]. As shown in Section 3.7, the dynamic longitudinal tire force can be modeled by

$$F_x \;=\; F_x^D \;=\; c_x\, x_e \;+\; d_x\, \dot{x}_e\,, \tag{4.10}$$

where x_e describes the longitudinal tire deflection, and c_x and d_x denote the corresponding stiffness and damping properties. Then, the angular momentum of the wheel provided in Equation (4.2) reads as

$$\Theta\, \Delta\dot{\Omega} \;=\; -r_S\, \left(c_x\, x_e \;+\; d_x\, \dot{x}_e\right)\,. \tag{4.11}$$

The tire deflection x_e is defined by the first-order differential equation (3.183), which in the case of pure longitudinal slip will read as

$$\left(v_{Tx}^*\, d_x \;+\; dF_x^0\right)\, \dot{x}_e \;=\; -\,v_{Tx}^*\, c_x\, x_e \;-\; dF_x^0\, \left(v_x - r_D\, \Omega\right)\,, \tag{4.12}$$

where the global derivative f_G of the generalized tire force characteristic was approximated by the initial inclination of the longitudinal tire force characteristic dF_x^0. As no lateral slip is considered here, a slip normalization is obsolete ($\hat{s}_x = 1$) and Equation (3.182) will deliver by

$$v_{Tx}^* \;=\; r_D\, |\Omega| + v_N \tag{4.13}$$

the modified transport velocity slightly simplified. Then, Equation (4.12) can be written as

$$\begin{aligned}\left(\left(|v_x + r_D\, \Delta\Omega| + v_N\right)\, d_x \;+\; dF_x^0\right)\, \dot{x}_e \;=\;\\ -\;\left(|v_x + r_D\, \Delta\Omega| + v_N\right)\, c_x\, x_e \;-\; dF_x^0\, \left(v_x - \left(v_x + r_D\, \Delta\Omega\right)\right)\,.\end{aligned} \tag{4.14}$$

where Equation 4.4 was used in addition to introduce the small angular velocity $\Delta\Omega$ describing the deviation from the rolling condition. In normal driving situations, the longitudinal tire deflection x_e and its time derivative $\dot{x}_e$ will remain small too. Then, Equation (4.14) simplifies further to

$$\left(|v_x{+}v_N|\, d_x + dF_x^0\right)\, \dot{x}_e \;=\; r_D\, dF_x^0\, \Delta\Omega \;-\; |v_x{+}v_N|\, c_x\, x_e\,. \tag{4.15}$$

Now the time derivative of Equation (4.15) can be combined with Equation (4.11) to one differential equation,

$$\left(|v|\, d_x + dF_x^0\right)\, \ddot{x}_e \;=\; \frac{r_D\, dF_x^0}{\Theta}\, \left(-r_S\, c_x\, x_e - r_S\, d_x\, \dot{x}_e\right) \;-\; |v|\, c_x\, \dot{x}_e\,, \tag{4.16}$$

where the abbreviation $v = v_x{+}v_N$ was introduced in addition. Collecting the terms with $\dot{x}_e$ and isolating the steady-state longitudinal tire force $c_x x_e$, the

second-order differential equation defined in Equation (4.16) can be written as

$$\underbrace{\left(\frac{|v|\,d_x}{dF_x^0}+1\right)\frac{\Theta}{r_S r_D}}_{m}\underbrace{\ddot{x}_e}_{\ddot{x}}+\underbrace{\left(d_x+\frac{|v|\,c_x\,\Theta}{dF_x^0\,r_S r_D}\right)}_{d}\underbrace{\dot{x}_e}_{\dot{x}}+\underbrace{c_x}_{c}\underbrace{x_e}_{x}=0\,, \tag{4.17}$$

which corresponds with a single mass oscillator. As a consequence, the eigenvalues given by

$$\lambda_{1,2}\;=\;-\frac{d}{2m}\;\pm\;i\sqrt{\frac{c}{m}-\left(\frac{d}{2m}\right)^2} \tag{4.18}$$

will characterize the dynamics of the wheel and the longitudinal tire force. The MATLAB-Script in Listing 4.1 calculates the eigenvalues, the eigenfrequencies, and the damping ratios[1] for different driving velocities. The results are plotted in Figure 4.4.

Listing 4.1
Script `eigenvalues_wheel_dynamics.m`: Wheel Tire Dynamics

```
Theta = 1.2;     % [kgm^2] inertia of wheel
r = 0.3;         % [m] wheel radius (dynamic = static)
dfx0 = 100000;   % [N/-] initial incl. force char.
cx = 160000;     % [N/m] longitudinal tire stiffness
dx = 500;        % [N/(m/s)] longitudinal tire damping
vN = 0.01;       % [m/s] fictitious velocity

% set velocity range and allocate space to speed up loop
vi=linspace(0,210/3.6,101); la1=zeros(size(vi));la2=la1; freq=la1;dratio=la1;

for i=1:length(vi)
% corresponding mass oscillator
  v = vi(i) + vN;
  m = Theta/r^2*(1+v*dx/dfx0); d = dx + v*cx*Theta/(r^2*dfx0); c = cx;
% eigenvalues
  la1(i) = -d/(2*m) + sqrt( (d/(2*m))^2 - c/m );
  la2(i) = -d/(2*m) - sqrt( (d/(2*m))^2 - c/m );
% frequency [Hz] and damping ratio [-]
  freq(i)  = imag(la1(i))/(2*pi);
  dratio(i) = d / ( 2*sqrt(c*m) );
end

% plots
subplot(1,3,1), hold on, grid on, title('Eigenvalues'),axis equal
plot(real(la1),imag(la1)), plot(real(la2),imag(la2))
subplot(1,3,2), hold on, grid on, title('Eigenfrequencies [Hz]')
plot(vi,freq)
subplot(1,3,3), hold on, grid on, title('Damping ratio [-]')
plot(vi,dratio)
```

[1] The damping parameter $d = d_C = 2\sqrt{c\,m}$, which happens to satisfy the condition $(d/(2m))^2 = c/m$, is called critical damping because Equation (4.18) will deliver only one real double eigenvalue $\lambda_1 = \lambda_2$ then.

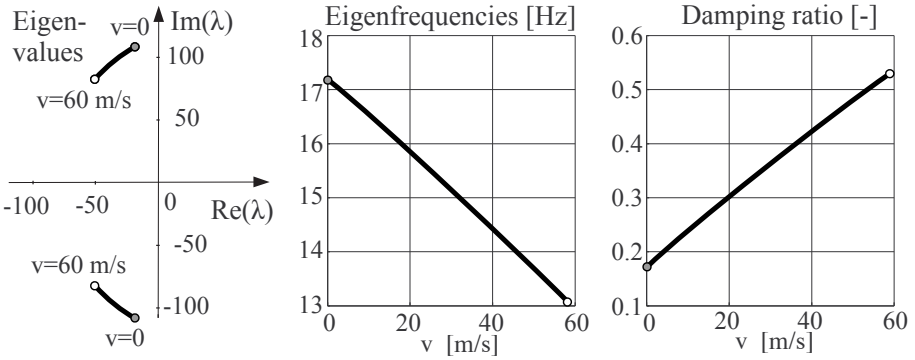

FIGURE 4.4
Wheel tire dynamics for different driving velocities.

The wheel tire dynamics are not sensitive to the fictitious velocity v_N as long as

$$\frac{v_N d_x}{dF_0} \ll 1 \quad \text{or} \quad v_N \ll \frac{dF_0}{d_x} \tag{4.19}$$

and

$$\frac{v_N c_x \Theta}{dF_0 r_S r_D} \ll d_x \quad \text{or} \quad v_N \ll \frac{d_x dF_0 r_S r_D}{c_x \Theta} \tag{4.20}$$

will be granted. In this case the demands will deliver

$$v_N \ll 100\,000\,[N/-]/500\,N/(m/s) = 200\,m/s \quad \text{and}$$
$$v_N \ll \frac{500\,Ns/m * 100\,[kN/-] * 0.3\,m * 0.3\,m}{160\,[kN/m] * 1.2\,[kgm^2]} = 23.4\,m/s$$

in particular. Note that for standard wheel tire data, any value of $v_N < 1\,m/s$ will be appropriate; $v_N = 0.01\,m/s$ was chosen here.

4.2.3 Simple Vehicle Wheel Tire Model

4.2.3.1 Equations of Motion

The wheel tire model in Section 4.2.2.2 is now supplemented by a chassis mass and will be put on a grade, Figure 4.5. The mass m includes the mass of the wheel suspension system and represents the part of the overall vehicle mass that is related to one wheel. The inertia of the wheel is denoted by Θ, the grade angle is named by α, and r serves as simple approximation for the static ($r_S \approx r$) as well as the dynamic tire radius ($r_D \approx r$). The vehicle is supposed to move along the grade only. Its actual position is determined by the coordinate x, and

$$F_z = m\,g\,\cos\alpha \tag{4.21}$$

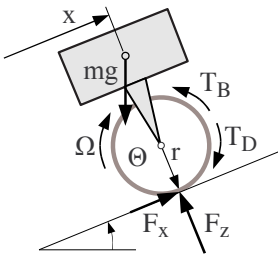

FIGURE 4.5
Simple vehicle model

will provide a constant wheel load here. Then, the equations of motion consisting of the linear momentum for the vehicle, the angular momentum for the wheel, and the dynamics of the longitudinal tire deflection read as

$$m\,\ddot{x} \;=\; \overbrace{c_x x_e + d_x \dot{x}_e}^{F_x^D} - mg\sin\alpha\,, \tag{4.22}$$

$$\Theta\,\dot{\Omega} \;=\; T_D - T_B - r\,\underbrace{(c_x x_e + d_x \dot{x}_e)}_{F_x^D}\,, \tag{4.23}$$

$$(v_{Tx}^*\,d_x \;+\; f_G\,)\;\dot{x}_e \;=\; -\,v_{Tx}^*\,c_x\,x_e \;-\; f_G\;(v_x - r_D\,\Omega)\;, \tag{4.24}$$

where c_x and d_x describe the stiffness and damping properties of the tire in the longitudinal direction, and all forces and torques of resistance were neglected. In addition, the special case of pure longitudinal slip was assumed, which according to Equation (4.13) will simplify the modified transport velocity to $v_{Tx}^* = r_D|\Omega| + v_N$ and reduce the global derivative of the generalized force characteristic to the corresponding derivative of the longitudinal force characteristic. For given driving and braking torques, the equation of motion can be solved numerically.

4.2.3.2 Driving Torque

Usually, the driving torque T_D is transmitted by the half-shaft. By modeling the torsional flexibility of the drive-shaft by a linear spring damper model, one gets

$$T_D \;=\; T_S \;=\; -c_S\,\Delta\varphi_S \;-\; d_S\;(\Omega - \omega_S)\;, \tag{4.25}$$

where c_S and d_S describe the torsional stiffness and damping properties of the half-shaft, Ω denotes the angular velocity of the wheel, and ω_S is the angular velocity of the half-shaft. Finally, the twist angle $\Delta\varphi_S$ of the half-shaft is defined by the differential equation

$$\frac{d}{dt}\;(\Delta\varphi_S) \;=\; \Omega - \omega_S\,. \tag{4.26}$$

If, however, a wheel hub motor is used as the driving source instead, the engine torque T_E will be applied directly to the wheel. Then

$$T_D \;=\; T_E \tag{4.27}$$

simply holds.

4.2.3.3 Braking Torque

The braking torque applied to the wheel usually is generated by friction, Figure 4.6. However, a simple dry friction model will cause severe numerical

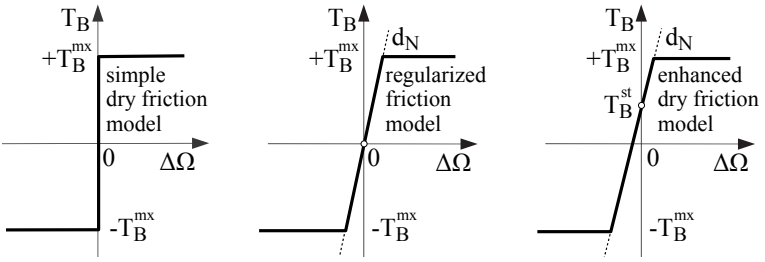

FIGURE 4.6
Coulomb dry friction model and enhanced brake torque model.

problems because it is not defined in a locking situation ($\Delta\Omega = 0$). The regularized model that is mostly used in commercial software packages avoids this problem but becomes less accurate when approaching the locking situation. The enhanced dry friction model avoids the jump at $\Delta\Omega = 0$ and provides an appropriate locking torque [37]. So, the braking torque will here be modeled by

$$T_B \;=\; T_B^{st} + d_N\,\Delta\Omega \quad \text{and} \quad |\,T_B\,| \;\le\; T_B^{mx}\,, \tag{4.28}$$

where T_B^{st} names the static or locking torque, $d_N > 0$ is a constant with the dimension of Nm/(rad/s), T_B^{mx} denotes the maximum braking torque, and

$$\Delta\Omega = \Omega - \omega_K \tag{4.29}$$

describes the relative angular velocity between the wheel and the body where the brake caliper is mounted. Usually this will be the knuckle.

The static part provides a steady-state locking torque when the relative angular velocity is vanishing, $T_B^{st}(\Delta\Omega = 0) = T_B^{st}$. In the steady state when $\dot{\Omega} = 0$ holds in addition, Equation (4.23) delivers

$$0 \;=\; T_D - T_B^{st} - r\,F_x^D\,. \tag{4.30}$$

Hence, the static braking torque

$$T_B^{st} \;=\; T_D - r\,F_x^D \tag{4.31}$$

will counteract appropriately the resulting torque applied to the wheel, namely consisting of the driving torque T_D and the torque $r\,F_x^D$ generated by the longitudinal tire force. Just like the overall braking torque T_B, the steady-state part is bounded to the maximum braking torque

$$\left| T_B^{st} \right| \;\leq\; T_B^{mx} \,. \tag{4.32}$$

The numeric constant d_N is chosen such that the dynamics of a fully braked and freely rolling wheel will be similar. According to Equation (4.23), the dynamics of a fully braked wheel will be approximately described by

$$\Theta\,\dot{\Omega} \;=\; -\left(T_B^{st} + d_N\,\Omega\right) \;-\; r\,F_x^S \,, \tag{4.33}$$

where in a fully braking maneuver the dynamic longitudinal force F_x^D can be replaced by the steady-state sliding force F_x^S and a vanishing driving torque ($T_D = 0$) was stated in addition. Within this simple vehicle model, the knuckle rotation is not taken into account. That is why the relative angular velocity $\Delta\Omega$ required in the braking torque model in Equation (4.28) may be substituted by the absolute angular wheel velocity Ω here. The eigenvalue of the first-order differential equation provided by Equation (4.33), is simply given by

$$\lambda \;=\; d_N/\Theta \,. \tag{4.34}$$

The eigenvalues of a freely rolling wheel are provided in Equation (4.18). Their absolute value is given by

$$|\lambda_{1,2}| = \sqrt{(Re(\lambda))^2 + (Im(\lambda))^2} = \sqrt{\left(-\frac{d}{2m}\right)^2 + \frac{c}{m} - \left(\frac{d}{2m}\right)^2} = \sqrt{\frac{c}{m}} \,, \tag{4.35}$$

where the generalized mass m and the stiffness $c = c_x$ are related to the wheel tire data by Equation (4.17). Hence, by setting

$$d_N \;=\; \Theta\,\sqrt{c/m} \,, \tag{4.36}$$

the dynamics of the braking torque model can be adjusted to the freely rolling wheel that features the highest eigenfrequencies at vanishing driving velocities. At $v = 0$, the generalized mass simplifies to $m = \Theta/(r_s r_D)$ or to $m = \Theta/r^2$ within this simple model approach. Then

$$d_N \;=\; \Theta\sqrt{\frac{c_x}{\Theta/r^2}} \;=\; r\,\sqrt{c_x\,\Theta} \tag{4.37}$$

will provide an appropriate value for the "damping" constant required in the enhanced braking torque model.

4.2.3.4 Simulation Results

The equations of motion for the simple vehicle wheel tire model including the enhanced braking torque model are provided by the function in Listing 4.2 as a set of first-order differential equations.

Listing 4.2
Function `Chassis_Wheel_Tire_f.m`: Vehicle Wheel Tire Model Dynamics

```
function xp=Chassis_Wheel_Tire_f(t,x)
% simple vehicle model including wheel and tire dynamics

global gravity al mass Theta r dfx0 fxm sxm fxs sxs vN cx dx
global t_Drive Drive_Torque t_Brake Brake_Torque dN
global sx fxd tq_B tq_D

% get states
v = x(1); o = x(2); % vehicle velocity and angular velocity of wheel
xe= x(3); xv= x(4); % longitudinal tire deflection and vehicle position

% actual driving and maximum braking torque via linear interpolation
tq_D = interp1(t_Drive,Drive_Torque,t);
tq_Bmx = interp1(t_Brake,Brake_Torque,t);
% modified transport velocity and long. slip without normalization
vt = abs(r*o) + vN; vs = v-r*o; sx = -vs/vt;
% generalized tire characteristics (sx only)
[ f, fos ] = tmy_fcombined( abs(sx), dfx0,fxm,sxm,fxs,sxs ) ;
% time derivative of long. tire deflection and long. dynamic tire force
xedot = -(cx*xe*vt+fos*(v-r*o))/(dx*vt+fos); fxd = cx*xe+dx*xedot;
% applied braking torque (enhanced dry friction model)
tq_B = tq_D-r*fxd + dN*o ; tq_B = sign(tq_B) * min( abs(tq_B), tq_Bmx );
% derivatives
odot = ( tq_D - tq_B - r*fxd ) / Theta; % angular momentum wheel
vdot = ( fxd - mass*gravity*sin(al) ) / mass; % linear momentum chassis
xp = [ vdot; odot; xedot; v ]; % state derivatives

end
```

The function tmy_fcombined.m that generates the combined force characteristic is given in Listing 3.3. The time history of the driving and the maximum braking torques is stored as lookup tables in the vectors t_Drive and Drive_Torque and t_Brake and Brake_Torque, respectively. The MATLAB-Function interp1 calculates the actual values via a linear interpolation. The MATLAB-Script in Listing 4.3 performs a simulation with the simple vehicle model. The results are plotted in Figure 4.7.

Listing 4.3
Script `Chassis_Wheel_Tire_main.m`: Vehicle Wheel Tire Model

```
global gravity al mass Theta r dfx0 fxm sxm fxs sxs vN cx dx
global t_Drive Drive_Torque t_Brake Brake_Torque dN
global sx fxd tq_B tq_D

% chassis and wheel data
gravity = 9.81;   % [m/s^2] constant of gravity
al = 20/180*pi;   % [degree-->rad] grade angle
mass = 400;       % [kg] chassis mass
Theta = 1.2;      % [kgm^2] inertia of wheel
r = 0.3;          % [m] wheel radius

% long. tire characteristic with linear wheel load influence
fzN  = 3100; fz = mass*gravity*cos(al);
```

```
dfx0 = 100000*fz/fzN; % [N/-] initial incl. long. force char.
fxm  = 3200*fz/fzN;  % [N] maximum long. force
sxm  = 0.1;          % [-] sx where fx=fxm
fxs  = 3000*fz/fzN;  % [N] long. sliding force
sxs  = 0.8;          % [-] sx where fx=fxs
cx = 160000;         % [N/m] longitudinal tire stiffness
dx =  500;           % [N/(m/s)] longitudinal tire damping
vN=0.01;             % [m/s] fictitious velocity

% adjust "damping" constant in enhanced braking torque model to wheel/tire
dN = r * sqrt(cx*Theta);
% set driving torque (time [s], torque [Nm])
t_Drive     = [ 0.0  0.9   1.1   3.9  4.1  20.0 ];
Drive_Torque = [ 0.0 0.0   1.0   1.0  0.0   0.0 ]*fxm*r;
% set braking torque (time [s], torque [Nm])
t_Brake     = [ 0.0 5.95  6.05  17.95  18.05  20.0 ];
Brake_Torque = [ 0.0 0.00 1.50  1.50   0.00   0.0 ]*fxm*r;
% perform simulation
tE = min(max(t_Drive),max(t_Brake)); % duration
x0=[ 0; 0; 0; 0]; % simple initial states
tic; [t,xout] = ode23(@Chassis_Wheel_Tire_f,[0,tE],x0); toc
% get additional output quantities
sxi=t; fxi=t; tqb=t; tqd=t;
for i=1:length(t)
  xp = Chassis_Wheel_Tire_f(t(i),xout(i,:)');
  sxi(i)=sx; fxi(i)=fxd; tqb(i)=tq_B; tqd(i)=tq_D;
end
% plot results
subplot(2,2,1); hold on, grid on
 plot(t,xout(:,1),'k','Linewidth',1), plot(t,r*xout(:,2),'--r','Linewidth',1)
 title('Velocities: v and r*Omega')
subplot(2,2,2); hold on, grid on
 plot(t,xout(:,4),'k','Linewidth',1)
 title('vehicle position')
subplot(2,2,3); hold on, grid on
 plot(t,tqd,'k','Linewidth',1), plot(t,tqb,'--r','Linewidth',1)
 title('Driving and braking torque [Nm]')
subplot(2,2,4); hold on, grid on
 plot(t,fxi,'k','Linewidth',1)
 title('Longitudinal force [N]')
```

The vehicle starts from standstill on a grade. At first it rolls backward, $v = r\,\Omega < 0$; then the vehicle is accelerated by the driving torque T_D that causes the wheel to spin, $r\,\Omega > v$. After a short period a braking torque T_B is applied that forces the wheel to lock in an instant, $r\,\Omega = 0$. When the vehicle comes to a standstill $r\,\Omega = 0$, $v = 0$ at $t \approx 6\ s$, the enhanced braking torque model automatically changes the sign in order to prevent the vehicle from moving downhill again. As the brake is not released yet, the vehicle oscillates some time in the longitudinal direction. During this period where the wheel is locked, the system vehicle and tire represent a damped oscillator. The stiffness and damping properties of the tire in the longitudinal direction $c_x = 160\,000\,N/m$ and $d_x = 500\,N/(m/s)$, together with the corresponding vehicle mass of $m = 400\,kg$, result in a frequency $f = \sqrt{c/m - (d/(2m)^2}/(2pi) =$

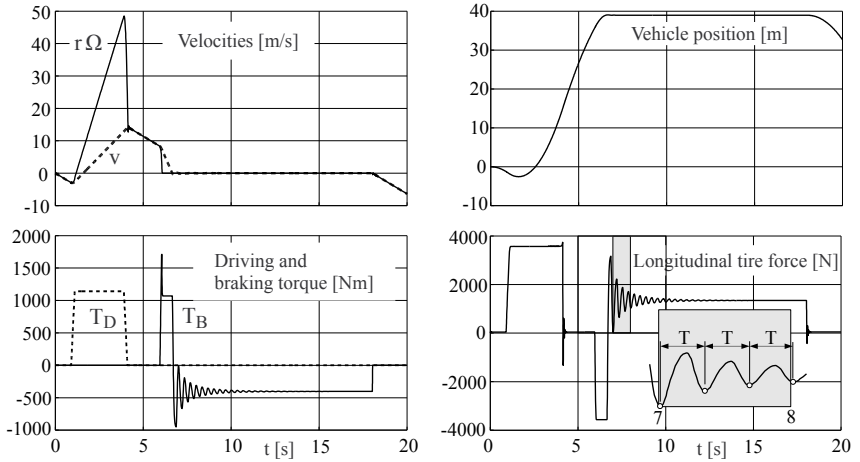

FIGURE 4.7
Driving and braking on a grade.

$3.2Hz$. Inspecting the time history of the longitudinal force $F_x(t)$ in Figure 4.7, one counts approximately three cycles in the interval $7s \leq t \leq 8s$, which is enlarged in the lower right corner of the graph. This results in a vibration period of $T = 1/3\,s$ or a frequency of $f = 1/T = 3\,Hz$, which corresponds quite well with the predicted result. Finally, the vehicle comes to a complete standstill, $v = 0$, $\Omega = 0$. The tire force of $F_x \approx 1340\,N$ that is needed to compensate the downhill force $mg \sin\alpha = 1342\,N$ is maintained as long as the brake is applied. At $t = 18\,s$, the brake is released and the vehicle starts to roll downhill again.

The MATLAB-Solver ode23, which is an implementation of an explicit low-order (2,3) Runge-Kutta algorithm, was used for the simulation because the brake torque model features sharp bends when reaching the maximum. The MATLAB-Script in Listing 4.3 calls ode23 at line 34 by specifying the starting time $t_0 = 0$ and the final time t_E only. Then, the ode solver will adjust the integration step size appropriately in order to match the default relative error tolerance 1e-3 and the default absolute tolerance of 1e-6 for each component of the state vector. Supplementing the MATLAB-Script in Listing 4.3 by the lines

```
figure
semilogy(0.5*(t(1:length(t)-1)+t(2:length(t))),diff(t),'ok','MarkerSize',3)
```

will open a new figure and plot the time history of the integration step size calculated via the MATLAB-Function diff(t) in a semi-logarithmic graph versus the intermediate value of each integration step, Figure 4.8

The maneuver includes all driving situations, which encompasses standstill, a rolling, a spinning, a braked, and a locked wheel. Despite all that, the time history of integration step size h that is automatically adjusted by the

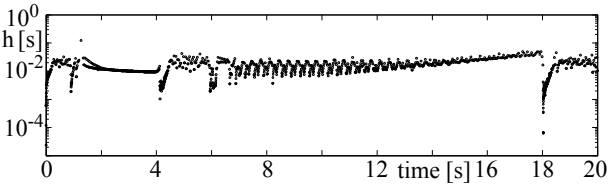

FIGURE 4.8
Integration step size h versus time t.

ode23 solver to the dynamics of the system is quite smooth. Only at the beginning ($t = 0$) when the solver is in the start-up phase and at $t = 18\,s$ when the brake is released again and the wheel changes all of a sudden from locking to rolling, few smaller step sizes will be needed to maintain the required accuracy.

4.3 Differentials

4.3.1 Classic Design

If a vehicle is driven by a single engine, the drive torque must be transmitted to the wheels by allowing them to rotate at different speeds. This is achieved through differentials. Whereas front- or rear-wheel driven cars are equipped with one differential only, all-wheel driven vehicles usually have three differentials. The differentials at the front and the rear axle split the torque equally to the left and to the right. The center differential, however, usually transmits more driving torque to the rear than to the front. This can be achieved by implementing different sized sun gears, Figure 4.9.

Taking no account of the mass and inertia properties of the planetary gears, the differential can be modeled by four rigid bodies that perform rotations only. They are listed in Table 4.1.

TABLE 4.1
Bodies of a Differential (Inertia of Planetary Gears Neglected)

#	Body	Angular Velocity	Inertia	Applied Torques
1	Output shaft and pinion 1	Ω_1	Θ_1	T_1
2	Output shaft and pinion 2	Ω_2	Θ_2	$T_2 - T_L$
3	Crown wheel and housing	Ω_C	Θ_C	T_L
4	Input shaft and pinion	Ω_0	Θ_0	T_0

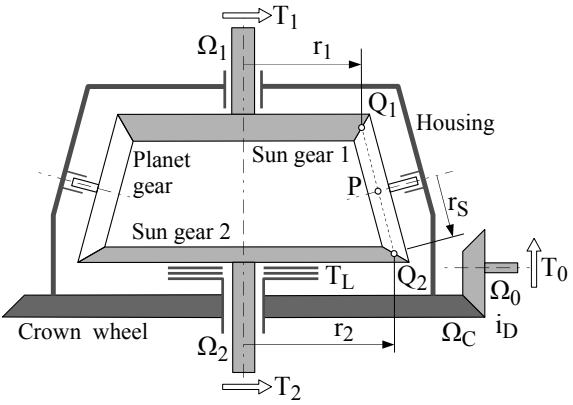

FIGURE 4.9
Differential with different sun gears.

The torque T_0 is applied to the input and the torques T_1, T_2 are applied to the output shafts. The torque T_L is generated by friction plates between the output shaft 2 and the housing, and it will model the effects of a locking device. The gear ratio between the input pinion and the crown wheel is given by i_D. Then,

$$\Omega_0 = i_D \, \Omega_C \tag{4.38}$$

represents a first constraint equation. In addition, the rotation of the input shafts are coupled by the planet gears. The velocities in the contact points Q_1 and Q_2 are simply given by

$$v_{Q1} = r_1 \, \Omega_1 \quad \text{and} \quad v_{Q2} = r_2 \, \Omega_2 \, , \tag{4.39}$$

and its the mean value

$$v_P = \frac{1}{2} \, (v_{Q1} + v_{Q2}) = \frac{1}{2} \, (r_1 \, \Omega_1 + r_2 \, \Omega_2) \tag{4.40}$$

determines the velocity of its center point P. As P is located on the rotation axis of a planet gear that is fixed to the housing,

$$v_P = \frac{r_1 + r_2}{2} \, \Omega_C \tag{4.41}$$

will hold in addition. Combining both relations finally results in a second constraint equation,

$$\Omega_C = \frac{r_1}{r_1 + r_2} \, \Omega_1 + \frac{r_2}{r_1 + r_2} \, \Omega_2 \, , \tag{4.42}$$

which couples the angular velocity of the housing to the angular velocities of the output shafts. Introducing the internal ratio

$$\varrho = \frac{r_1}{r_1 + r_2} \, , \tag{4.43}$$

the two constraint equations (4.42) and (4.38) will finally result in

$$\Omega_C = \varrho\,\Omega_1 + (1-\varrho)\,\Omega_2\,, \tag{4.44}$$

$$\Omega_0 = i_D\,(\varrho\,\Omega_1 + (1-\varrho)\,\Omega_2)\ . \tag{4.45}$$

The equation of motion will be generated via Jordain's Principle of virtual power. Taking only the angular momentum of the bodies into account, it will read as

$$\begin{aligned} &\delta\Omega_1\left(\Theta_1\,\dot\Omega_1 - T_1\right) \ + \ \delta\Omega_2\left(\Theta_2\,\dot\Omega_2 - (T_2 - T_L)\right) \\ +\ &\delta\Omega_C\left(\Theta_C\,\dot\Omega_C - T_L\right) \ + \ \delta\Omega_0\left(\Theta_0\,\dot\Omega_0 - T_0\right)\ .\ = \ 0 \end{aligned} \tag{4.46}$$

Considering the constraint equations yields

$$\begin{aligned} &\delta\Omega_1\left(\Theta_1\,\dot\Omega_1 - T_1\right) \ + \ \delta\Omega_2\left(\Theta_2\,\dot\Omega_2 - (T_2 - T_L)\right) \\ +\ &(\varrho\,\delta\Omega_1 + (1-\varrho)\,\delta\Omega_2)\left(\Theta_C\ \left(\varrho\,\dot\Omega_1 + (1-\varrho)\,\dot\Omega_2\right) - T_L\right) \\ +\ &i_D\,(\varrho\,\delta\Omega_1 + (1-\varrho)\,\delta\Omega_2)\left(\Theta_0\,i_D\,\left(\varrho\,\dot\Omega_1 + (1-\varrho)\,\dot\Omega_2\right) - T_0\right) \ = \ 0\ . \end{aligned} \tag{4.47}$$

Collecting all terms with $\delta\Omega_1$ and $\delta\Omega_2$ results in two coupled differential equations that in matrix form read as

$$\begin{bmatrix} \Theta_1 + \varrho^2\Theta^* & \varrho\,(1-\varrho)\Theta^* \\ \varrho\,(1-\varrho)\Theta^* & \Theta_2 + (1-\varrho)^2\Theta^* \end{bmatrix} \begin{bmatrix} \dot\Omega_1 \\ \dot\Omega_2 \end{bmatrix} = \begin{bmatrix} T_1 + \varrho\,T_L + \varrho\,i_D\,T_0 \\ T_2 - \varrho\,T_L + (1-\varrho)\,i_D\,T_0 \end{bmatrix}, \tag{4.48}$$

where the abbreviation $\Theta^* = \Theta_C + i_D^2\Theta_0$ was used to shorten the elements of the mass matrix.

The locking torque T_L is generated by friction plates between the sun gear 2 and the crown wheel. Corresponding to the braking torque specified in Equation (4.28), it will be modeled by

$$T_L \ = \ T_L^{st} + d_N\ (\Omega_2 - \Omega_C) \quad \text{and} \quad |\,T_L\,| \ \le \ T_L^{mx}\,, \tag{4.49}$$

where T_L^{mx} denotes the maximum torque that can be transmitted by the friction plates between the sun gear 2 and the crown wheel, and $d_N > 0$ is a fictitious damping parameter that generates an appropriate torque when the angular velocities of the sun gear 2 and the crown wheel differ. Finally, a steady-state locking torque is provided by T_L^{st} even if $\Omega_2 = \Omega_C$ holds. In this particular case, the equations of motion for the differential given in Equation (4.48) deliver two demands on the steady-state locking torque,

$$0 = T_1 + \varrho\,T_L^{st} + \varrho\,i_D\,T_0 \quad \text{and} \quad 0 = T_2 - \varrho\,T_L^{st} + (1-\varrho)\,i_D\,T_0\,. \tag{4.50}$$

These two equations $f_1(x) = 0$ and $f_2(x) = 0$ for one unknown $x = T_L^{st}$ can be solved by a least squares approach as best as possible,

$$\tfrac{1}{2}\,f_1^2(x) + \tfrac{1}{2}\,f_2^2(x) \longrightarrow \text{Min} \quad \text{or} \quad \frac{d\,f_1}{dx}\,f_1(x) + \frac{d\,f_2}{dx}\,f_2(x) = 0\,. \tag{4.51}$$

Here, it yields at first

$$\varrho\left(T_1 + \varrho\, T_L^{st} + \varrho\, i_D\, T_0\right) + (-\varrho)\left(T_2 - \varrho\, T_L^{st} + (1-\varrho)\, i_D\, T_0\right) = 0 \qquad (4.52)$$

and will deliver the steady-state locking torque

$$T_L^{st} = \frac{1}{2\varrho}\,(T_2 - T_1) + \left(\frac{1}{2\varrho} - 1\right) T_0\,, \qquad (4.53)$$

which depends on the internal ratio ϱ of the differential and is adjusted to the torque difference $T_2 - T_1$ at the output shafts associated with the torque T_0 applied to the input shaft.

4.3.2 Active Differentials

Today, advanced drive trains include an electronically active center differential and an active yaw control rear differential unit. The active center differential (ACD) is an electronically controlled hydraulic multi-plate clutch that distributes torque between the front and rear to improve traction under acceleration out of a corner. It works in conjunction with active yaw control (AYC), which can actively split torque based on input from various sensors in the vehicle measuring longitudinal and lateral acceleration, steering, brakes, and throttle position.

The recently developed sport differential supplements the classic differential at the rear axle with gearboxes on the left and right whose drive superposition stages are rotating 10% faster than the half-shafts, $\Omega_{S1} = 1.1\,\Omega_1$ and $\Omega_{S2} = 1.1\,\Omega_2$. The two components can be coupled by a multi-plate clutch running in an oil bath, Figure 4.10.

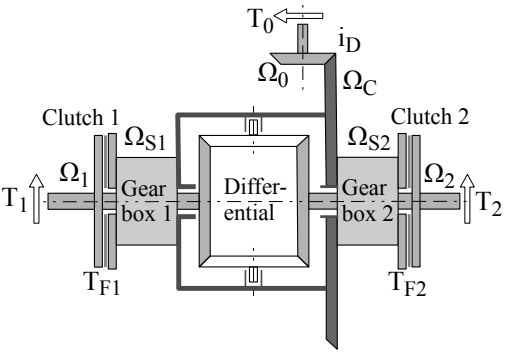

FIGURE 4.10
Enhanced rear axle differential.

When the car is accelerated in a left corner for example, the clutch on the outer side (clutch 2) is engaged, which by friction will generate a torque (T_{F2})

and speed up the corresponding half-shaft ($\Omega_2 \uparrow$) and finally the attached wheel too. As a result, the longitudinal slip at the outer tire is increased, which induces an additional driving force and reduces or completely eliminates the understeer tendency of the car. As the friction torque reacts on the gearbox too, the drive torque transferred to the opposite wheel is decreased accordingly. Thus, this active differential is able to torque the drive torque (torque vectoring) to the left and to the right wheel as needed in specific driving situations. Usually, almost the complete input torque can be diverted to one rear wheel in this way.

4.4 Generic Drive Train

The subsystem consisting of the drive shafts, the differentials, and the half-shafts interacts on one side with the engine and on the other side with the wheels, Fig. 4.11. Engine, clutch, transmission, wheels, and tires are described separately. Hence, the angular velocities of the wheels $\omega_1, \ldots, \omega_4$, and the engine or respectively the transmission output angular velocity ω_T, serve as inputs for this subsystem. The angular velocities of the drive shafts ω_{S1}: front left, ω_{S2}: front right, ω_{SF}: front, ω_{SR}: rear, ω_{S3}: rear left, ω_{S4}: rear right specify the generalized coordinates within this generic 4×4 all-wheel drive model. Via the tire forces and torques, the whole drive train is coupled with the steering system and the vehicle framework.

The generic drive train includes three differentials that may include locking or active parts. Their dynamic behavior can be described by adjusting the equations of motion deduced in Section 4.3 appropriately. The internal ratios of the front and rear differential defined in Equation (4.43) amount to $\varrho_F = \varrho_R = \frac{1}{2}$, which means that the driving torque will be distributed equally[2] to the left and right wheels. Via the internal ratio ϱ_C of the center differential, different drive types can be distinguished. A value of $\varrho_C = 1$ means front-wheel drive, $0 < \varrho_C < 1$ stands for all-wheel drive, and $\varrho_C = 0$ will model a rear-wheel drive. The equation of motion for the generic drive train including the modeling of torques and hints for real-time applications can be found in [38].

[2]Note: The effect of active differentials will be modeled by additional torques generated by friction or electric motors.

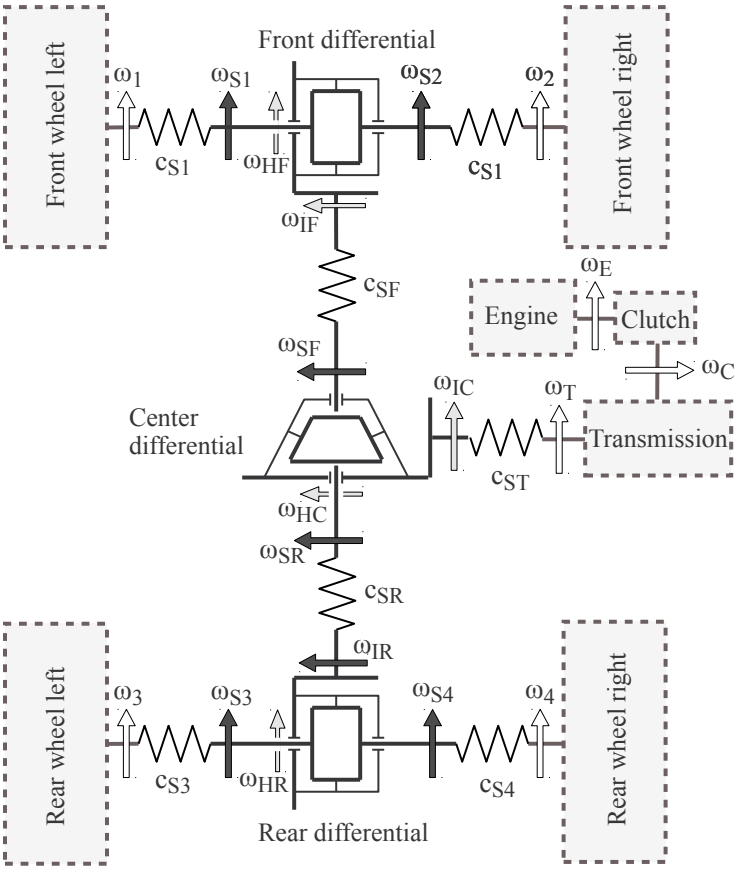

FIGURE 4.11
Drive train model.

4.5 Transmission

The transmission or gearbox allows the gear ratio to be adjusted. This is necessary because combustion engines work best if they run at a limited rate of revolutions. By shifting the gears, which can be done manually or automatically, the engine is kept at its most efficient rate while allowing the vehicle to run at a large range of speed. Operating the gear lever of a manual transmission brings a different train of gear wheels into play, Figure 4.12.

The different ratios of teeth on the gear wheels involved produce different speeds. If a gear is selected, the dog teeth lock the required upper gear wheel to the transmission shaft. Then, the transmission goes from the clutch shaft via the counter shaft and the lower gear wheels to the upper gear wheels and

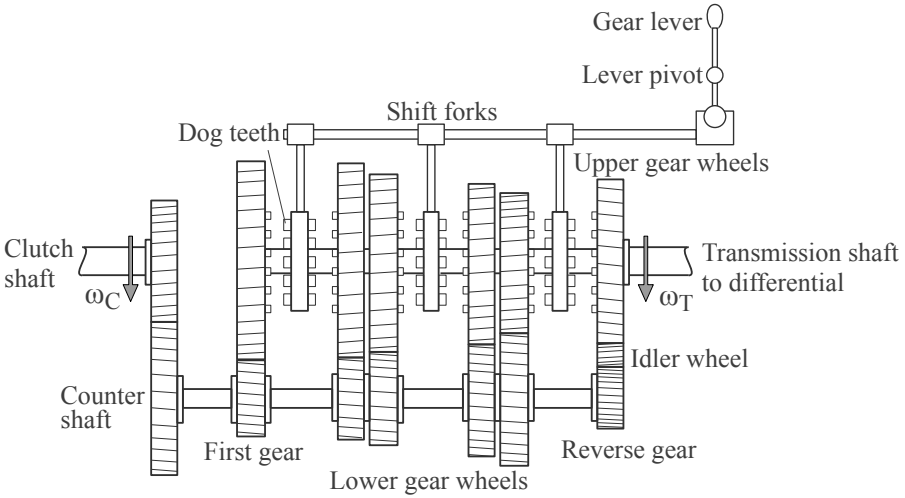

FIGURE 4.12
Manual transmission.

finally to the transmission shaft. Selecting reverse gear introduces the idler wheel, which reverses the rotation of the transmission shaft. Usually the gear ratio is defined as

$$r_G \;=\; \frac{\omega_T}{\omega_C}\,, \tag{4.54}$$

where ω_T and ω_C denote the angular velocities of the transmission and the clutch shaft. Typical gear ratios are given in Table 4.2. The angular momentum

TABLE 4.2
Typical Gear Ratios for a Passenger Car

gear	reverse	neutral	first	second	third	fourth	fifth
ratio	−4.181	0	3.818	2.294	1.500	1.133	0.911

for the transmission shaft results in

$$\Theta_T\,\dot{\omega}_T \;=\; r_G\,T_C - T_T^{FR} - T_T\,, \tag{4.55}$$

where Θ_T is a generalized inertia that includes all rotating parts of the transmission. That is why it will depend on the gear ratio $\Theta_T = \Theta_T(r_G)$. The friction in the transmission is described by T_T^{FR}, and the torque T_T represents the external load that can be modeled by a torsional spring damper

model

$$T_T \;=\; -c_T\,\Delta\varphi_{T0} - d_T\;(\omega_T - \omega_C)\;, \tag{4.56}$$

where c_T, d_T describe the stiffness and damping properties of the shaft connecting the transmission with the differential, and ω_T, ω_C name the angular velocities of the flexible shaft at the transmission output and the input from the clutch. Finally, the differential equation

$$\frac{d}{dt}\,\Delta\varphi_{T0} \;=\; \omega_T - \omega_C \tag{4.57}$$

defines the torsional angle between the input and the output shaft.

For a gear to be engaged, the different speeds of the rotating parts need to be matched and locked together. The synchromesh uses friction to do this smoothly and quietly. Pushed by the selector fork, the collar slides along the transmission shaft, rotating with it. The collar fits over a cone on the upper gear wheel, making the wheel speed up or slow down until both are moving with the same speed. Then, the dog teeth are engaged, locking the upper gear wheel to the collar and, hence, to the transmission shaft.

The synchromesh mode of action can be approximated by a first-order differential equation

$$H_{syn}\,\dot{r}_G^D \;=\; -r_G^D \;+\; r_{G}\;, \tag{4.58}$$

where r_G^D denotes the dynamic gear ratio, H_{syn} is the time constant of the synchromesh process, and r_{G} denotes the static gear ratio. By this differential equation the jump from one static gear ratio to another will be dynamically smoothed, which comes very close to the real synchromesh process. This dynamic gear ratio will then be used instead of the static one.

4.6 Clutch

The clutch makes use of friction to transmit the rotation of the engine crankshaft to the transmission. When the clutch pedal is released ($p_G = 0$), the clutch spring forces the clutch plate and the flywheel, which is turned by the crankshaft, together, Fig. 4.13. Then, the angular momentum for the clutch plate read as

$$\Theta_P\,\dot{\omega}_P \;=\; T_C - T_D \tag{4.59}$$

where Θ_P, ω_P describe the inertia and the angular velocity of the clutch plate. According to the principle "actio" equals "reactio," the torque T_C represents the load applied to the engine. The torque in the drive disk can be modeled by a torsional spring damper combination. Assuming linear characteristics, one gets

$$T_D \;=\; -c_D\,\Delta\varphi_{PC} - d_D\;(\omega_P - \omega_C)\;, \tag{4.60}$$

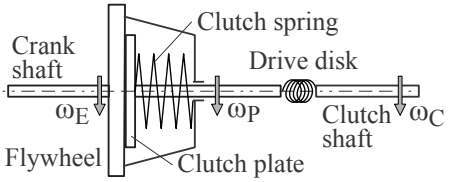

FIGURE 4.13
Clutch model without clutch pedal mechanism.

where ω_C names the angular velocity of the clutch shaft and c_D, d_D describe the stiffness and damping properties of the drive disk. The differential equation

$$\frac{d}{dt}\,\Delta\varphi_{PC} \;=\; \omega_P - \omega_C \tag{4.61}$$

defines the torsional angle φ_{PC} in the drive disk. Similar to the brake torque defined in Equation (4.28), the friction based clutch torque is described by

$$T_C \;=\; T_C^{st} + d_N\;(\omega_E - \omega_P) \quad \text{with} \quad |\,T_C\,| \;\leq\; T_C^{mx}\,, \tag{4.62}$$

where ω_E denotes the angular velocity of the engine and $d_N > 0$ is a constant. The static part T_C^{st} provides a steady-state locking torque when the angular velocities of the engine ω_E and the clutch plate ω_P are equal. In steady state, and when $\omega_E = \omega_P$ will hold in addition, Equations (4.66) to (4.62) simply yield

$$0 \;=\; T_E - T_{FR} - T_C^{st} \quad \text{and} \quad 0 \;=\; T_C^{st} - T_D\,. \tag{4.63}$$

These two equations for one unknown are again solved by a least squares approach that here will result in

$$\frac{\partial}{\partial T_C^{st}}\;\left(\epsilon_1^2 + \epsilon_2^2\right) \;=\; 2\;\left(T_E - T_{FR} - T_C^{st}\right)(-1) + 2\;\left(T_C^{st} - T_D\right)^2 = 0\,. \tag{4.64}$$

Thus, the steady-state locking torque

$$T_C^{st} \;=\; \frac{1}{2}\,(T_E - T_{FR} + T_D) \tag{4.65}$$

will be adjusted to the torques $T_E - T_{FR}$ applied at the engine and to the torque in the drive disk T_{DD} as best as possible.

The maximum friction torque T_C^{mx} transmitted by the clutch depends on the position of the clutch pedal p_C, Figure 4.14. Pressing the clutch pedal reduces the normal force between the clutch plate and the flywheel and hence reduces the maximum friction torque.

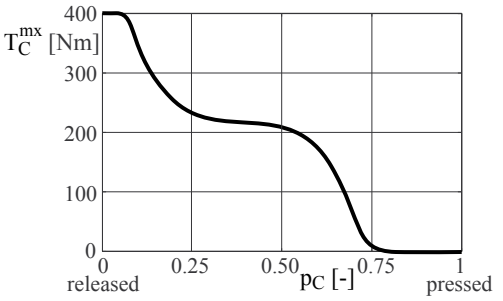

FIGURE 4.14
Example of the maximum friction torque transmitted by a clutch.

4.7 Power Sources

4.7.1 Combustion Engine

Combustion engines are very common in ground vehicles. In a first approximation, the torque T_E of a combustion engine can be characterized as a function of its angular velocity ω_E and the gas pedal p_G, Fig. 4.15. Then, the dynamics

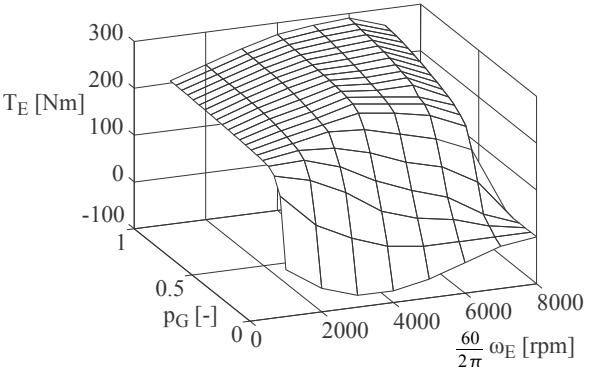

FIGURE 4.15
Example of a combustion engine torque: $T_E = T_E(\omega_E, p_G)$.

of the engine can be described by the angular momentum

$$\Theta_E \dot{\omega}_E = T_E - T_{FR} - T_C \,, \tag{4.66}$$

where Θ_E labels the inertia of the engine, T_{FR} names the friction torque, and T_C is the external load from the clutch.

This simple approach usually is sufficient for vehicle handling and ride analysis. It is even used to design automotive control systems [19]. A sophisticated combustion engine model en-DYNA®, where the air flow, the fuel supply, the torque calculation, and the exhaust system are modeled in detail, will be provided by TESIS[3].

4.7.2 Hybrid Drive

The power sources of a hybrid vehicle can be combined in two different ways. In a series hybrid, the combustion engine turns a generator, and the generator can either charge the batteries or power an electric motor that drives the transmission. Thus, the gasoline engine never directly powers the vehicle. A parallel hybrid has a fuel tank that supplies gasoline to the combustion engine and a set of batteries that supplies power to the electric motor. The batteries store energy recovered from braking or generated by the engine. Both the engine and the electric motor can turn the transmission at the same time. Hence, a significant increase in the drive torque is possible, Figure 4.16.

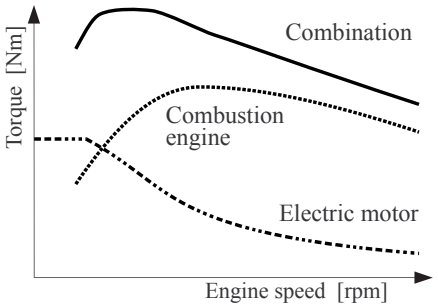

FIGURE 4.16
Hybrid drive torque characteristics.

Usually the combustion engine in a conventional car will be sized for the peak power requirement. Whereas, the hybrid car may use a much smaller engine, one that is sized closer to the average power requirement than to the peak power. Hence, fuel consumption and pollution may be reduced significantly.

Exercises

4.1 Estimate the inertia of a wheel of radius $r = 0.3\,m$ and mass $m = 15\,kg$ by approximating it as a homogenous cylinder.

[3] www.tesis.de.

4.2 A wheel tire combination is characterized by the data $\Theta = 7.5\,kgm^2$, $r_S \approx r_D = 0.54\,m$, $dF_x^0 = 360\,000\,N/m$, $c_x = 680\,000\,N/m$, $d_x = 1000\,N/(m/s)$, and $v_N = 0.02\,m/s$.

Calculate and plot the eigenvalues, the eigenfrequencies and the damping ratio for different driving velocities $0 \leq v \leq 25\,m/s$ by using the MATLAB-Script in Listing 4.1.

Check the influence of the fictitious velocity v_N on the results.

4.3 Use the MATLAB-Script in Listing 4.3 in combination with the functions in Listing 4.2 and 3.3 to perform simulations with the grade angles $\alpha = 0$, $\alpha = 30°$, and $\alpha = 45°$.

Analyze and discuss the simulation results.

Change the lookup tables defined by the vectors t_Drive and Drive_Torque as well as t_Brake and Brake_Torque, which determine the time histories of the drive and brake torque appropriately so that various driving and braking maneuvers can be simulated.

4.4 Extend the MATLAB-Script in Listing 4.3 in such a way that the vehicle wheel tire model can run on surfaces with different friction coefficients.

5

Suspension System

CONTENTS

5.1 Purpose and Components

The automotive industry uses different kinds of wheel/axle suspension systems. Important criteria are costs, space requirements, kinematic properties, and compliance attributes. The main purposes of a vehicle suspension system are

- Carry the car and its weight,
- Maintain correct wheel alignment,
- Control the vehicle's direction of travel,
- Keep the tires in contact with the road,

- Reduce the effect of shock forces.

Vehicle suspension systems consist of

- Guiding elements:
  - Control arms, links
  - Struts
  - Leaf springs
- Force elements:
  - Coil spring, torsion bar, air spring, leaf spring
  - Anti-roll bar, anti-sway bar or stabilizer
  - Damper
  - Bushings, hydro-mounts
- Tires

From a modeling point of view, force elements may be separated into static and dynamic systems. Examples and modeling aspects will be discussed in Chapter 6. Tires are some kind of air springs that support the total weight of the vehicle. The spring action of the tire is very important to the ride quality and safe handling of the vehicle. In addition, the tire must provide the forces and torque that keep the vehicle on track. The tire was already discussed in detail in Chapter 3.

5.2 Some Examples

5.2.1 Multipurpose Systems

The double wishbone suspension, the McPherson suspension, and the multi-link suspension are multipurpose wheel suspension systems, Figure 5.1. They are used as steered front or nonsteered rear axle suspension systems. These suspension systems are also suitable for driven axles. Usually, the damper is attached to the knuckle, whereas the coil spring is connected to one control arm of the double wishbone or the multi-link suspension. In a McPherson suspension however, the spring is attached to the knuckle and will have a well-defined inclination to the strut axis. Thus, bending torques at the strut, which cause high friction forces between the damper piston and the housing, can be reduced.

On pickups, trucks, and buses, solid axles are used often. They are guided either by leaf springs or by rigid links, Figure 5.2. Solid axles tend to tramp on rough roads. Leaf-spring-guided solid axle suspension systems are very robust. Dry friction between the leafs leads to locking effects in the suspension. Although the leaf springs provide axle guidance on some solid axle suspension systems, additional links in longitudinal and lateral direction are used. Thus,

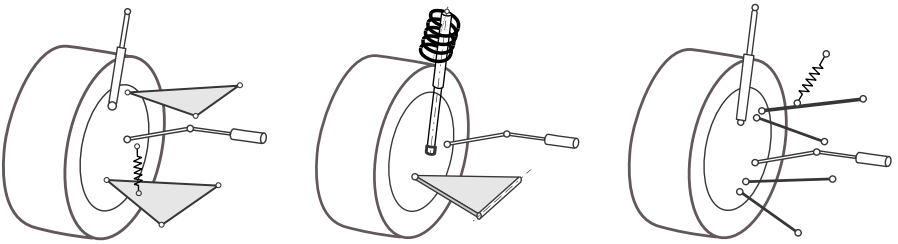

FIGURE 5.1
Double wishbone, McPherson, and multi-link suspensions.

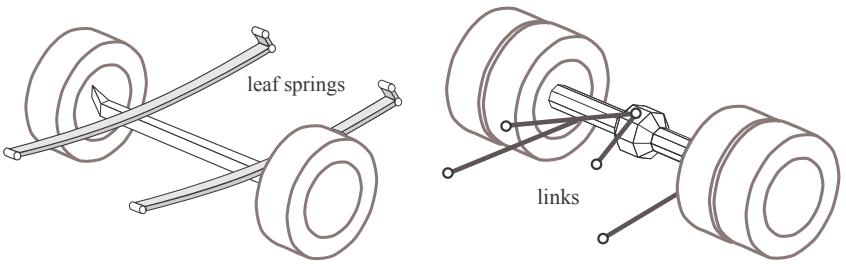

FIGURE 5.2
Solid axles guided by leaf springs and links.

the typical wind-up effect on braking can be avoided. Solid axles suspended by air springs need at least four links for guidance. In addition to good driving comfort, air springs allow level control too.

5.2.2 Specific Systems

The semi-trailing arm, the short-long arm axle (SLA), and the twist beam axle suspension are suitable only for non-steered axles, Figure 5.3. The semi-

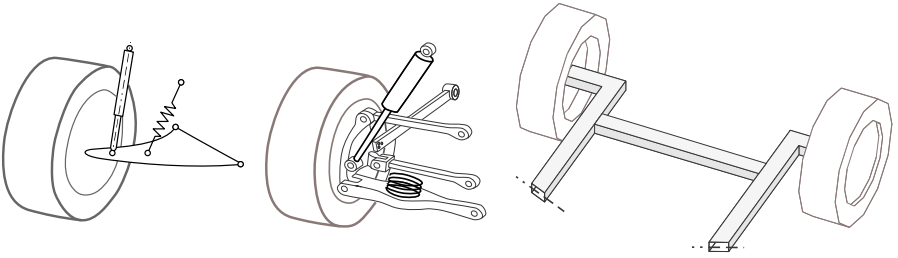

FIGURE 5.3
Semi-trailing arm, short-long arm, and twist beam suspension.

trailing arm is a simple and cheap design that requires only a small space. It is mostly used for driven rear axles. The short-long arm axle design allows a nearly independent layout of longitudinal and lateral axle motions. It is similar to the central control arm axle suspension, where the trailing arm is completely rigid and, hence, only two lateral links are needed. The twist beam axle suspension exhibits either a trailing arm or a semi-trailing arm characteristic. It is used for nondriven rear axles only. The twist beam axle provides enough space for spare tire and fuel tank.

5.2.3 Steering Geometry

On steered front axles, the McPherson-damper strut axis, the double wishbone axis, and the multi-link wheel suspension or the enhanced double wishbone axle are mostly used in passenger cars, Figures 5.4 and 5.5. The wheel body

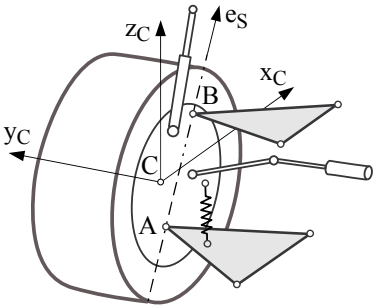

FIGURE 5.4
Double wishbone wheel suspension.

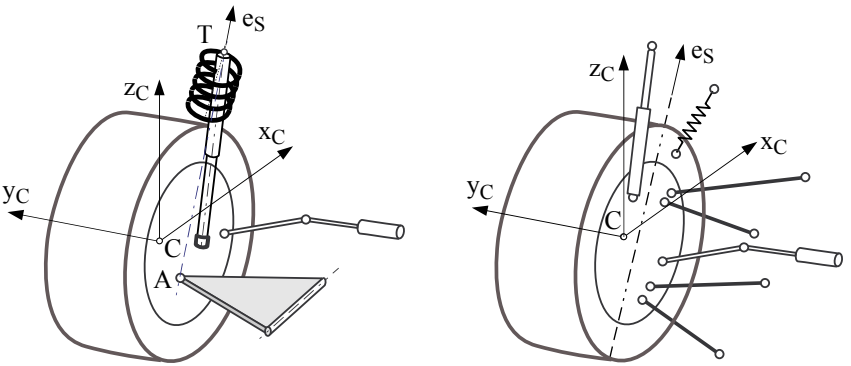

FIGURE 5.5
McPherson and multi-link wheel suspensions.

rotates around the kingpin line at steering motions. For the double wishbone

axle, the ball joints A and B, which determine the kingpin line, are both fixed to the wheel body. Whereas the ball joint A is still fixed to the wheel body at the standard McPherson wheel suspension, the top mount T is now fixed to the vehicle body. On a multi-link axle the kingpin line is no longer defined by real joints. Here, as well as with an enhanced McPherson wheel suspension, where the A-arm is resolved into two links, the momentary rotation axis serves as the kingpin line. In general, the momentary rotation axis is neither fixed to the wheel body nor to the chassis, and it will change its position during wheel travel and steering motions.

The unit vector e_S describes the direction of the kingpin line. Within the vehicle-fixed reference frame F, it can be fixed by two angles. The caster angle ν denotes the angle between the z_F-axis and the projection line of e_S into the $x_F\, z_F$-plane. In a similar way, the projection of e_S into the $y_F\, z_F$-plane results in the kingpin inclination angle σ, Figure 5.6. On many axles the kingpin and

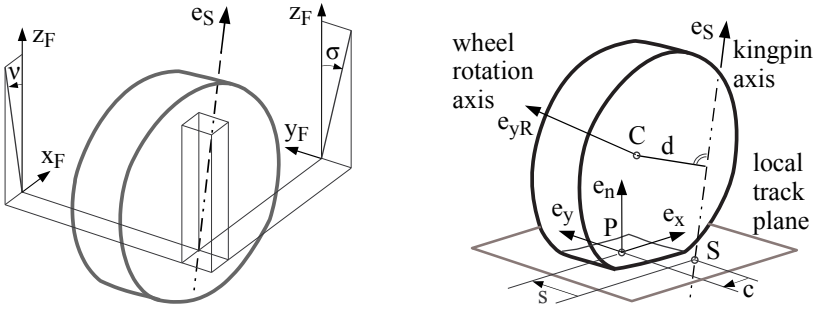

FIGURE 5.6
Kingpin inclination as well as caster and steering offset.

caster angle can no longer be determined directly. Here, the current rotation axis at steering motions, which can be taken from kinematic calculations, will yield a virtual kingpin line. The current values of the caster angle ν and the kingpin inclination angle σ can be calculated from the components of the unit vector e_S in the direction of the kingpin axis,

$$\tan\nu \;=\; \frac{-e^{(1)}_{S,F}}{e^{(3)}_{S,F}} \quad \text{and} \quad \tan\sigma \;=\; \frac{-e^{(2)}_{S,F}}{e^{(3)}_{S,F}}\,, \tag{5.1}$$

where $e^{(1)}_{S,F}$, $e^{(2)}_{S,F}$, $e^{(3)}_{S,F}$ are the components of the unit vector $e_{S,F}$ expressed in the vehicle-fixed axis system F.

The contact point P, the local track normal e_n, and the unit vectors e_x and e_y, which point in the direction of the longitudinal and the lateral tire force, result from the contact geometry. The axle kinematics define the kingpin axis. In general, the point S where an extension of the kingpin axis meets the road surface does not coincide with the contact point P, Figure 5.6. As both points

are located on the local track plane, for the left wheel the vector from S to P can be written as

$$r_{SP} = -c\,e_x + s\,e_y\,, \tag{5.2}$$

where s names the steering offset or scrub radius, and c is the caster offset. Caster and steering offset will be positive if S is located in front of and inwards of P. The kingpin offset d describes the distance between the wheel center C and the king pin axis. It is an important quantity in evaluating the overall steering behavior [24].

5.3 Steering Systems

5.3.1 Components and Requirements

The steering system is a very important interface between driver and vehicle. Via the steering wheel the driver controls the vehicle and gets feedback by the steering torque. The traditional steering system of high-speed vehicles is a mechanical system consisting of the steering wheel, the steering shaft, the steering box, and the steering linkage. Usually the steering torque produced by the driver is amplified by hydraulic or nowadays by electric systems. Modern steering systems use an overriding gear to amplify or change the steering wheel angle. Recently some companies have started investigations on "steer-by-wire" techniques. In the future, steer-by-wire systems will probably be used as standard. Here, an electronically controlled actuator is used to convert the rotation of the steering wheel into steering movements of the wheels. Steer-by-wire systems are based on mechanics, micro-controllers, electro-motors, power electronics, and digital sensors. At present, fail-safe systems with a mechanical backup system are under investigation. Modeling concepts for modern steering systems are discussed in [41].

The steering system must guarantee easy and safe steering of the vehicle. The entirety of the mechanical transmission devices must be able to cope with all loads and stresses occurring in operation. In order to achieve good maneuverability, a maximum steering angle of approx. 40° must be provided at the front wheels of passenger cars. Depending on the wheel base, buses and trucks need maximum steering angles up to 55° at the front wheels.

5.3.2 Rack-and-Pinion Steering

Rack-and-pinion is the most common steering system of passenger cars, Figure 5.7. The rack may be located either in front of or behind the axle. First, the rotations of the steering wheel δ_S are transformed by the steering box to the rack travel $u_R = u_R(\delta_S)$ and then via the drag links transmitted to the wheel rotations $\delta_1 = \delta_1(u_R)$, $\delta_2 = \delta_2(u_R)$. Hence, the overall steering ratio

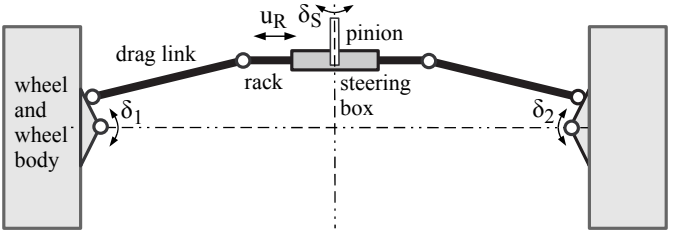

FIGURE 5.7
Rack-and-pinion steering.

depends on the ratio of the steering box and on the kinematics of the steering linkage.

5.3.3 Lever Arm Steering System

Using a lever arm steering system, Figure 5.8, large steering angles at the wheels are possible. This steering system is used on trucks with large wheel

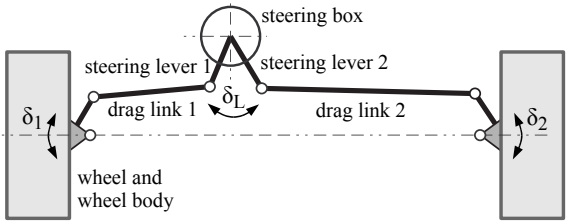

FIGURE 5.8
Lever arm steering system.

bases and independent wheel suspension at the front axle. Here, the steering box can be placed outside the axle center. At first, the rotations of the steering wheel δ_S are transformed by the steering box to the rotation of the steer levers $\delta_L = \delta_L(\delta_S)$. The drag links transmit this rotation to the wheel $\delta_1 = \delta_1(\delta_L)$, $\delta_2 = \delta_2(\delta_L)$. Hence, the overall steering ratio again depends on the ratio of the steering box and on the kinematics of the steering linkage.

5.3.4 Toe Bar Steering System

On solid axles the toe bar steering system is used, Figure 5.9. The rotations of the steering wheel δ_S are transformed by the steering box to the rotation of the steering lever arm $\delta_L = \delta_L(\delta_S)$ and further on to the rotation of the left wheel, $\delta_1 = \delta_1(\delta_L)$. The toe bar transmits the rotation of the left wheel to the right wheel, $\delta_2 = \delta_2(\delta_1)$. The steering ratio is defined by the ratio of the

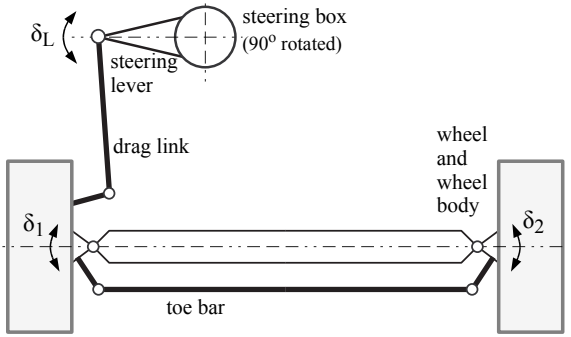

FIGURE 5.9
Toe bar steering system.

steering box and the kinematics of the steering link. Here, the ratio $\delta_2 = \delta_2(\delta_1)$ given by the kinematics of the toe bar can be changed separately.

5.3.5 Bus Steering System

In buses the driver sits more than $2\,m$ in front of the front axle. In addition, large steering angles at the front wheels are needed to achieve good maneuverability. That is why more sophisticated steering systems are needed, Figure 5.10. The rotations of the steering wheel δ_S are transformed by the

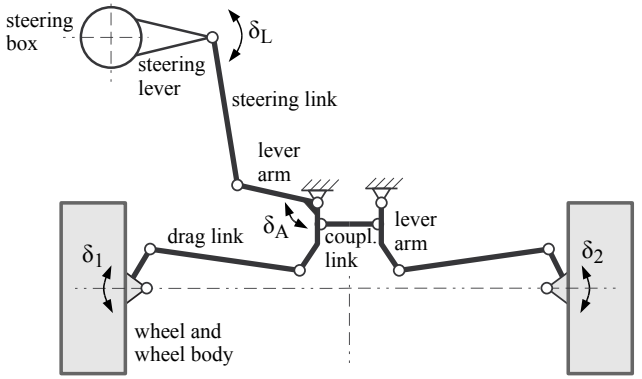

FIGURE 5.10
Typical bus steering system.

steering box to the rotation of the steering lever arm $\delta_L = \delta_L(\delta_S)$. The left lever arm is moved via the steering link $\delta_A = \delta_A(\delta_L)$. This motion is transferred by a coupling link to the right lever arm. Finally, the left and right wheels are rotated via the drag links, $\delta_1 = \delta_1(\delta_A)$ and $\delta_2 = \delta_2(\delta_A)$.

5.3.6 Dynamics of a Rack-and-Pinion Steering System

5.3.6.1 Equation of Motion

Modern steering systems include power assistance, some also overriding gears or even steer-by-wire facilities [41]. The essential parts of a pure mechanical rack-and-pinion steering system are shown in Figure 5.11. The tire forces ap-

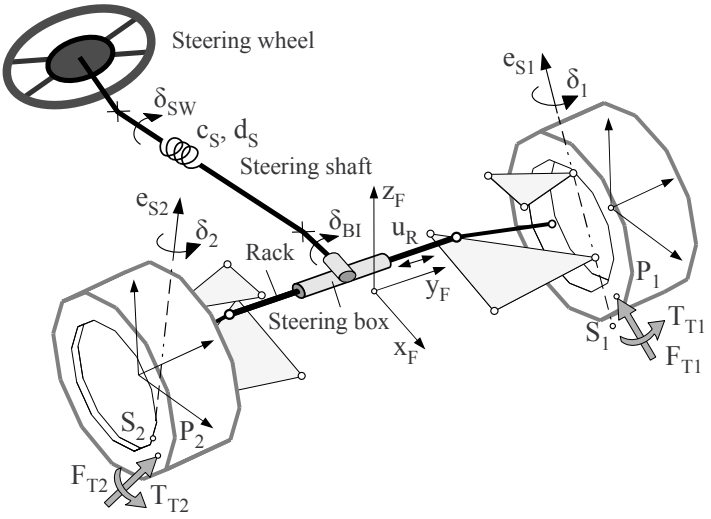

FIGURE 5.11
Rack-and-pinion steering system.

plied at the contact points P_1, P_2 are denoted by F_{T1}, F_{T2}, and the vectors T_{T1}, T_{T2} summarize torques acting on the tire contact patches. The torsional compliance of the steering shaft, modeled by the stiffness c_S and the damping parameter d_S, generates the torque

$$T_S \;=\; c_S\,(\delta_{SW} - \delta_{BI}) + d_S\left(\dot{\delta}_{SW} - \dot{\delta}_{BI}\right)\,, \tag{5.3}$$

where δ_{SW} denotes the steering angle provided by the rotation of the steering wheel. The maximum steering wheel angle δ_{SW}^{mx} and the maximum rack displacement u_R^{mx} define the ratio of the steering box[1]

$$i_{SB} \;=\; \frac{\delta_{SW}^{mx}}{u_R^{mx}}\,. \tag{5.4}$$

Then, the rotation angle of the steering shaft at the steering box input is simply provided by

$$\delta_{BI} \;=\; i_{SB}\,u_R\,. \tag{5.5}$$

[1]Note: Some steering boxes will generate a nonlinear ratio that depends on the rack displacement, $i_{SB} = i_{SB}(u_R)$.

The steering linkage is considered a pure massless kinematical constraint here. It transmits the rack displacements u_R to the wheels and forces them to rotate with the angles δ_1 and δ_2 around the kingpin axes, marked in Figure 5.11 by the unit vectors e_{S1}, e_{S2}.

Applying Jordain's principle of virtual power, the equation of motion for the rack and the wheels including the wheel bodies will result in

$$m_{RG}\,\ddot{u}_R \;=\; F_{TG} + F_{SM} - F_{SF}\,. \tag{5.6}$$

The generalized mass

$$m_{RG} \;=\; m_R \;+\; \sum_{i=1}^{2} \left\{ \left(\frac{\partial v_{Ci}}{\partial \dot{u}_R} \right)^T m_i \, \frac{\partial v_{Ci}}{\partial \dot{u}_R} \;+\; \left(\frac{\partial \omega_{0i}}{\partial \dot{u}_R} \right)^T \Theta_i \, \frac{\partial \omega_{0i}}{\partial \dot{u}_R} \right\} \tag{5.7}$$

adds to the rack mass m_R essential parts of the mass m_1, m_2 and the inertias Θ_1, Θ_2 of the wheel bodies and the wheels. The partial derivatives of the wheel center velocities v_{C1}, v_{C2} and the partial derivatives of the angular velocities ω_{01}, ω_{02} of the wheel bodies with respect to the time derivative of the rack displacement $\dot{u}_R$ will result from a kinematic analysis of the specific steering linkage, which will be done in Section 5.4 elaborately. Furthermore, the principle of virtual power transforms the tire forces F_{T1}, F_{T2} applied at the contact points P_1, P_2 and the tire torques T_{T1}, T_{T2} to a generalized force acting at the rack:

$$F_{TG} = \left(\frac{\partial v_{P1}}{\partial \dot{u}_R} \right)^T F_{T1} + \left(\frac{\partial \omega_{01}}{\partial \dot{u}_R} \right)^T T_{T1} \;+\; \left(\frac{\partial v_{P2}}{\partial \dot{u}_R} \right)^T F_{T2} + \left(\frac{\partial \omega_{02}}{\partial \dot{u}_R} \right)^T T_{T2}\,. \tag{5.8}$$

Here, the partial derivatives of the contact point velocities v_{P1}, v_{P2} with respect to the rack displacement u_R will also be required.

The torque T_S acting in the steering shaft provides the steering force

$$F_{SM} \;=\; i_{SB}\, T_{SS}\,. \tag{5.9}$$

Finally, the friction force is approximated similar to the braking torque defined in Equation (4.28) by an enhanced dry friction model. It provides the friction force as

$$F_{SF} \;=\; F_{SF}^{st} + d_N\, \dot{u}_R \quad \text{and} \quad |\, F_{SF}\,| \;\le\; F_{SF}^{mx}\,, \tag{5.10}$$

where F_{SF}^{mx} denotes the maximum friction force. In steady state when $\dot{u}_R = 0$ and $\ddot{u}_R = 0$ will hold, the static or locking force

$$F_{SF}^{st} = F_{TG} + F_{SM} \tag{5.11}$$

counteracts all other forces applied to the rack and will prevent movements as long as $|\, F_{SF}^{st}\,| \;\le\; F_{SF}^{mx}$ is assured. If the rack is exposed to the steering force F_{SM} only (steering motions in a liftoff situation), the critical damping of free rack oscillations will be given by

$$d_{CR} = 2\sqrt{i_{SB}^2\, c_{TB}\, m_{RG}} = 2\, i_{SB}\, \sqrt{c_{TB}\, m_{RG}}\,. \tag{5.12}$$

By setting

$$d_N = \tfrac{1}{2} d_{CR} = i_{SB} \sqrt{c_{TB}\, m_{RG}}\,, \tag{5.13}$$

the numerical damping in the friction model can be adjusted to the specific steering system.

5.3.6.2 Steering Forces and Torques

According to Equation (5.6), the force balance

$$0 \;=\; F_{TG} + F_{SM} - F_{SF} \tag{5.14}$$

characterizes the steering system at steady-state. Neglecting the friction force $F_{SF} \approx 0$, the steering force F_{SM} that in compliance with Equation (5.9) is generated by the steering torque T_{SS} must counteract the the generalized tire force F_{TG}. Hence, at steady-state, the generalized tire force provides, by

$$T_{SS}^{st} \;=\; -\frac{1}{i_{SB}}\, F_{TG}\,, \tag{5.15}$$

the most part of the steering torque.

In general, the partial angular velocities of the wheel bodies, which according to Equation (5.8) are required to calculate the generalized tire force can be written as

$$\frac{\partial \omega_{0i}}{\partial \dot{u}_R} \;=\; e_{Si}\, \frac{\partial \dot{\delta}_i}{\partial \dot{u}_R} \;=\; e_{Si}\, i_{SLi}\,, \quad i = 1, 2\,, \tag{5.16}$$

where e_{S1}, e_{S2} denote the unit vectors in the direction of the king pin axes and i_{SL1}, i_{SL2} characterize the ratios of the left and the right steering linkage, which in general are not constant but will depend on the rack displacement. The king pin axis will not change its position and orientation during steer motions on standard double wishbone and McPherson suspension systems. Then, the points S_1, S_2 where the king pin axis intersects the local road plane stay where they are and the velocity of the contact points P_1 and P_2 induced by steering motions is just given by

$$v_{Pi} \;=\; \omega_{0i} \times r_{SiPi} \;=\; e_{Si}\, \dot{\delta}_i \times r_{SiPi} \;=\; e_{Si} \times r_{SiPi}\, \dot{\delta}_i\,, \quad i = 1, 2\,. \tag{5.17}$$

As a consequence, the corresponding partial velocities read as

$$\frac{\partial v_{P1}}{\partial \dot{u}_R} \;=\; e_{Si} \times r_{SiPi}\, i_{SLi}\,, \quad i = 1, 2\,, \tag{5.18}$$

where according to Equation (5.16) i_{SL1}, i_{SL2} denote the ratios of the steering linkage. Inserting Equations (5.16) and (5.18) into Equation (5.8) results in

$$F_{TG} = i_{SL1}\Big[(e_{S1} \times r_{S1P1})^T F_{T1} + e_{S1}^T T_{T1}\Big] + i_{SL2}\Big[(e_{S2} \times r_{S2P2})^T F_{T2} + e_{S2}^T T_{T2}\Big]\,. \tag{5.19}$$

Taking into account that

$$(a\times b)^T c = (-b\times a)^T c = \left(-\tilde{b}\, a\right)^T c = \left(\tilde{b}^T a\right)^T c = a^T\, \tilde{b}\, c = a^T (b\times c) \qquad (5.20)$$

holds for arbitrary vectors a, b, c, Equation (5.19) can be rearranged to

$$F_{TG} = i_{SL1}\, e_{S1}^T\, (r_{S1P1}\times F_{T1} + T_{T1}) + i_{SL2}\, e_{S2}^T\, (r_{S2P2}\times F_{T2} + T_{T2})\ . \qquad (5.21)$$

Referring to Figure 5.6, the orientation of the king pin axis can be described by the kingpin and caster angle. According to Equation (5.1),

$$e_{S1,F} \;=\; \frac{1}{\sqrt{\tan^2\nu + \tan^2\sigma + 1}} \begin{bmatrix} -\tan\nu \\ -\tan\sigma \\ 1 \end{bmatrix} \qquad (5.22)$$

holds for the left wheel and

$$e_{S2,F} \;=\; \frac{1}{\sqrt{\tan^2\nu + \tan^2\sigma + 1}} \begin{bmatrix} -\tan\nu \\ +\tan\sigma \\ 1 \end{bmatrix} \qquad (5.23)$$

for the right wheel, where the left/right symmetry of a standard suspension system was taken into account. In addition, the vectors from S_1 to P_1 and from S_2 to P_2 can be expressed by the caster offset c and steering offset s. According to Equation (5.2),

$$r_{S1P1} = \begin{bmatrix} -c \\ s \\ 0 \end{bmatrix} \quad \text{and} \quad r_{S2P2} = \begin{bmatrix} -c \\ -s \\ 0 \end{bmatrix} \qquad (5.24)$$

will hold at the left and the right wheel in design position when symmetry is taken into account again. Combining Equations (5.22), (5.23), (5.24) with Equations (5.21) and (5.15) finally provides the steady-state steering torque in design position as

$$\begin{aligned} T_{SS}^{st} \;=\; & -i_{S1} \begin{bmatrix} -\tan\nu \\ -\tan\sigma \\ 1 \end{bmatrix}^T \left(\begin{bmatrix} -c \\ +s \\ 0 \end{bmatrix} \times \begin{bmatrix} F_{x1} \\ F_{y1} \\ F_{z1} \end{bmatrix} + \begin{bmatrix} T_{x1} \\ T_{y1} \\ T_{z1} \end{bmatrix} \right) \\ & -i_{S2} \begin{bmatrix} -\tan\nu \\ +\tan\sigma \\ 1 \end{bmatrix}^T \left(\begin{bmatrix} -c \\ -s \\ 0 \end{bmatrix} \times \begin{bmatrix} F_{x2} \\ F_{y2} \\ F_{z2} \end{bmatrix} + \begin{bmatrix} T_{x2} \\ T_{y2} \\ T_{z2} \end{bmatrix} \right), \end{aligned} \qquad (5.25)$$

where F_{xi}, F_{yi}, F_{zi}, $i = 1, 2$, are the components of the tire force vectors F_{T1}, F_{T2} expressing the longitudinal, the lateral, and the vertical tire forces or wheel loads, and T_{xi}, T_{yi}, T_{zi}, $i = 1, 2$, name the components of the tire torque vectors T_{T1}, T_{T2} representing the tipping torque, the rolling resistance torque, and the sum of the bore and the self-aligning torque. Furthermore, the abbreviations

$$i_{Si} \;=\; \frac{i_{SLi}}{i_{SB}\sqrt{\tan^2\nu + \tan^2\sigma + 1}}\,, \quad i = 1, 2 \qquad (5.26)$$

define generalized ratios of the steering system. They will be equal or at least approximately equal to or close to the design position. Taking $i_{S1} = i_{S2} = i_S$ for granted, Equation (5.25) simplifies to

$$\begin{aligned} T_{SS}^{st} &= i_S \left[s\,(F_{x1} - F_{x2}) + c\,(F_{y1} + F_{y2}) + (s\tan\nu + c\tan\sigma)\,(F_{z1} - F_{z2}) \right. \\ &= \left. \tan\nu\,(T_{x1} + T_{x2}) - \tan\sigma\,(T_{y1} - T_{y2}) + T_{z1} + T_{z2} \right]. \end{aligned} \tag{5.27}$$

In normal driving situations, $F_{x1} \approx F_{x2}$, $F_{z1} \approx F_{z2}$, $T_{x1} \approx -T_{x2}$, and $T_{y1} \approx T_{y2}$ will hold. Then, the steering torque

$$T_{SS}^{st} \approx c\,(F_{y1} + F_{y2}) + T_{z1} + T_{z2} \tag{5.28}$$

is dominated by the lateral forces and the bore and the self-aligning torques. However, during cornering, the term

$$(s\tan\nu + c\tan\sigma)\,(F_{z1} - F_{z2}) \tag{5.29}$$

will provide an additional steering torque due to the load transfer from the inner to the outer wheel, which will increase according to the lateral acceleration. Modern vehicles are often equipped with an Electronic Stability Program (ESP) that may activate the brake at a single wheel. Then, $F_{x1} \neq F_{x2}$ will be the case and the term

$$s\,(F_{x1} - F_{x2}) \tag{5.30}$$

will contribute to the steering torque unless the suspension system exhibits a vanishing or at least a sufficient small steering offset, $s \approx 0$. In parking maneuvers, the steering torque is dominated by the tire bore torques.

5.3.6.3 Parking Effort

One major design task of a steering system is the investigation of the parking effort. During a static parking maneuver, the steering wheel is turned while the vehicle is still at full stop. In this case, the forces and torques applied to the wheels are dominated by the tire bore torque. The motions of the vehicle can be neglected for a basic study. In addition, we assume here that the steering motion of the wheels is a simple rotation around a vertical axis running through the wheel centers C_1, C_2 and the contact points P_1, P_2. Then, the partial velocities needed in Equations (5.7) and (5.8) will simplify to

$$\frac{\partial v_{Ci}}{\partial \dot{u}_R} = \frac{\partial v_{Pi}}{\partial \dot{u}_R} = \begin{bmatrix} 0 \\ 0 \\ 0 \end{bmatrix} \quad \text{and} \quad \frac{\partial \omega_{0i}}{\partial \dot{u}_R} = \begin{bmatrix} 0 \\ 0 \\ 1 \end{bmatrix} i_{SLi}\,, \quad i = 1, 2\,, \tag{5.31}$$

where according to Equation (5.16), i_{SL1}, i_{SL2} abbreviate the partial derivatives of the time derivatives of the wheel steering angles δ_1, δ_2 with respect to the time derivative of the rack displacement u_R. Then, the generalized mass and the generalized rack force simplify to

$$m_{RG} = m_R + i_{SL1}^2\,\Theta_{z1} + i_{SL2}^2\,\Theta_{z2}\,, \tag{5.32}$$

$$F_{TG} \;=\; i_{SL1}\,(T_{S1}+T_{B1}) \;+\; i_{SL1}\,(T_{S2}+T_{B2}) \;, \tag{5.33}$$

where Θ_{z1}, Θ_{z2} denote the inertias of the left and the right wheel and wheel body around the vertical z-axis. According to Equation (3.1), the tire torques around the z-axis consist of the self-aligning torques T_{S1}, T_{S2} and the bore torques T_{B1}, T_{B2}.

If the steering linkage is designed to satisfy the Ackermann geometry, the steering angles of the left and the right wheel will be provided by

$$\tan\delta_{1,2} = \frac{a\,\tan\left(i_{SL}\,u_R\right)}{a \mp \frac{1}{2}s\,\tan\left(i_{SL}\,u_R\right)} \;, \tag{5.34}$$

where i_{SL} denotes the ratio of the steering linkage at $u_R = 0$, s describes the track width, and a the wheel base of the vehicle. The time derivative of Equation (5.34) results in

$$\frac{1}{\cos^2\delta_{1,2}}\,\dot{\delta}_{1,2} = \frac{a^2}{\left(a \mp \frac{1}{2}s\,\tan\left(i_{SL}\,u_R\right)\right)^2}\;\frac{1}{\cos^2\left(i_{SL}\,u_R\right)}\;i_{SL}\,\dot{u}_R \tag{5.35}$$

and provides the ratios of the steering linkage defined by the partial derivatives

$$i_{SL1,2} = \frac{\partial\dot{\delta}_{1,2}}{\partial\dot{u}_R} = i_{SL}\;\frac{a^2}{\left(a \mp \frac{1}{2}s\,\tan\left(u_R\right)\right)^2}\;\frac{\cos^2\delta_{1,2}}{\cos^2\left(i_{SL}\,u_R\right)} \tag{5.36}$$

as functions of the rack displacement u_R because the corresponding steering angles $\delta_{1,2} = \delta_{1,2}(u_R)$ will be delivered by Equation (5.34).

The performance of the simple steering system model can be studied in a stand-alone simulation, now. The MATLAB-function provided in Listing 5.1 describes the dynamics of the simple steering system model during a parking maneuver by a set of first-order differential equations.

Listing 5.1
Dynamics of a Simple Steering System Model

```
function xdot = steering_system_f(t,x)

% data + output quantities
global A_SW f_SW
global a s  m_R  Thetaz i_SB  i_SL  c_S d_S fr_mx
global df_0 f_m s_m f_s s_s vt_n c_bo d_bo r_b
global dsw d1 d2 ftg fsf tss

% states (standalone model without steering wheel)
ur    = x(1); urdot = x(2); % rack displacement and velocity
ga1   = x(3); ga2   = x(4); % left and right tire torsional deflection

% soft periodic steering wheel input
dsw = A_SW*sin(2*pi*f_SW*t)^2; dswdot=2*A_SW*sin(4*pi*f_SW*t)*pi*f_SW;
if t > 0.5/f_SW, dsw=-dsw; dswdot = -dswdot; end
d   = i_SL*ur; tand = tan(d); % average wheel steering angle

```

```
% kinematics of steering linkage (ackermann geometry)
d1   = atan2( a*tand , a-0.5*s*tand );
dd1  = i_SL * a^2/(a-0.5*s*tand)^2 * cos(d1)^2/cos(d)^2 ; d1dot= dd1*urdot;
d2   = atan2( a*tand , a+0.5*s*tand );
dd2  = i_SL * a^2/(a+0.5*s*tand)^2 * cos(d2)^2/cos(d)^2 ; d2dot= dd2*urdot;

mrg = m_R+(dd1^2+dd2^2)*Thetaz; % general. rack mass, thetaz1=thetaz2=thetaz
tss = c_S*(dsw-i_SB*ur)+d_S*(dswdot-i_SB*urdot); % torque in steering column
fsm = i_SB*tss; % steering torque converted to rack force

% left bore torque (enhanced model @ stand still, vt=vt_n)
sb = -r_b*d1dot/vt_n; sg = abs(sb); % bore slip and generalized slip
[f,fos] = tmy_fcombined(sg,df_0,f_m,s_m,f_s,s_s); % combined tire force
ga1dot=-(c_bo*ga1*vt_n+fos*d1dot*r_b^2)/(d_bo*vt_n+fos*r_b^2); % twist dyn.
tbo1 = c_bo*ga1 + d_bo*ga1dot ; % bore torque

% right bore torque (enhanced model @ stand still, vt=vt_n)
sb = -r_b*d2dot/vt_n; sg = abs(sb); % bore slip and generalized slip
[f,fos] = tmy_fcombined(sg,df_0,f_m,s_m,f_s,s_s); % combined tire force
ga2dot=-(c_bo*ga2*vt_n+fos*d2dot*r_b^2)/(d_bo*vt_n+fos*r_b^2); % twist dyn.
tbo2 = c_bo*ga2 + d_bo*ga2dot ; % bore torque

ftg = dd1*tbo1 + dd2*tbo2 ; % generalized tire torques applied to rack

% enhanced dry friction model
fsfst = ftg + fsm ; % static part
dN = i_SB * sqrt( c_S * mrg ) ; % numerical damping adjusted to data
fsf = fsfst + dN*urdot; fsf = sign(fsf)*min(abs(fsf),fr_mx); % friction force

urdotdot = ( ftg+fsm-fsf ) / mrg ; % rack acceleration (equations of motion)
xdot = [ urdot; urdotdot; ga1dot; ga2dot ]; % state derivatives

end
```

The function assumes a periodic steering input with a soft transition from positive to negative angles achieved by a squared sine function, and it includes a small part of the TMeasy tire model that automatically generates the dynamic bore torques. The MATLAB-Script provided in Listing 5.2 sets the required data, performs a time simulation, and finally plots some results.

Listing 5.2
Simulation of the Parking Effort

```
% data + output quantities
global A_SW  f_SW
global a  s  m_R  Thetaz i_SB  i_SL  c_S d_S fr_mx
global df_0 f_m s_m f_s s_s vt_n c_bo d_bo r_b
global dsw d1 d2 ftg fsf tss

A_SW = 540/180*pi; % steering wheel amplitude [rad]
f_SW    = 0.2;   % steering frequency [Hz]
a       = 2.7;   % wheel_base [m]
s       = 1.5;   % track_width [m]
m_R     = 2.5;   % mass of rack [kg]
Thetaz  = 1.3;   % inertia of wheel body and wheel around z-axis [kgm^2]
i_SB    = 125;   % ratio steering wheel angle / rack displacement [rad/m]
```

```
i_SL    = 9.3;   % ratio wheel steering angle / rack displacement [rad/m]
c_S     = 573;   % stiffness of steering shaft [Nm/rad]
d_S     = 5;     % damping of steering shaft [Nm/(rad/s)]
fr_mx   = 120;   % maximum friction force in steering box [N]
df_0    = 90000; % tire force initial inclination [N/-]
f_m     = 4250;  % maximum tire force [N]
s_m     = 0.18;  % slip where f=f_m [-]
f_s     = 4100;  % sliding force [N]
s_s     = 0.5;   % slip where f=f_s [-]
vt_n    = 0.01;  % fictitious velocity [m/s]
c_bo    = 2400;  % torsional tire stiffness [Nm/rad]
d_bo    = 2;     % torsional tire damping [Nm/(rad/s)]
r_b     = 0.065; % equivalent bore radius [m]

% perorm simulation over one period of a sinusoidal steer input
t0=0; tE=1/f_SW; x0 = [0; 0; 0; 0 ];
tic; [tout,xout]=ode23(@steering_system_f,[t0,tE],x0); toc

% pre-allocate output-quantities to speed up loop and plot some results
io=length(tout); z=zeros(io,1); dswi=z;d1i=z;d2i=z; ftgi=z;fsfi=z; tssi=z;
for i=1:io
  xp=feval(@steering_system_f,tout(i),xout(i,:));
  dswi(i)=dsw; d1i(i)=d1; d2i(i)=d2; ftgi(i)=ftg; fsfi(i)=fsf; tssi(i)=tss;
end
subplot(2,2,1)
  plot(dswi*180/pi,-tssi), grid on
  title('steering torque [Nm] / steering wheel angle [Grad]')
  xy=axis; axis([[-1,1]*A_SW*180/pi,xy(3),xy(4)])
subplot(2,2,2)
  plot(tout,(xout(:,1)*i_SB-dswi)*180/pi), grid on,
  title('twist angle of steering shaft [Grad]')
  xy=axis; axis([0,tE,xy(3),xy(4)])
subplot(2,2,3)
  plot(tout,[d1i,d2i,-xout(:,3:4)]*180/pi), grid on
  legend('wheel left','wheel right','tire twist left','tire twist right')
  xy=axis; axis([0,tE,xy(3),xy(4)])
subplot(2,2,4)
  [AX,H1,H2]=plotyy(tout,ftgi/1000,tout,fsfi); grid on
  legend('generalized tire force [kN]','friction force [N]')
  set(AX(1),'XLim',[0 tE]); set(AX(2),'XLim',[0 tE])
```

The chosen wheelbase of $a = 2.7\,m$ and the track width of $s = 1.5\,m$ match typical mid-sized passenger cars. The rack mass $m_R = 2.5\,kg$ is roughly estimated. The inertia of wheel and wheel body are calculated on the basis of a cylindrical body of mass $m = 50\,kg$, radius $r = 0.3\,m$, and width $b = 0.2\,m$, where a homogeneous mass distribution was also assumed. Then, the inertia is given by $\Theta = \frac{1}{12} m \left(b^2 + 3r^2\right) = 1.3\,kgm^2$. The ratios of the steering system are sized up by specifying the maximum steering wheel amplitude with $\delta_{SW}^{mx} = 540°$ and estimating the maximum rack displacement with $u_R^{mx} = 0.075\,m$. Then, the ratio of the steering wheel angle to rack displacement results in $i_{SB} = 540\,\pi/180/0.075 \approx 125\,rad/m$. Assuming an average wheel steering angle of $\delta = 40°$ the ratio of the wheel steering angle to the rack displacement will be obtained as $i_{SL} = 40\,\pi/180/0.075/ = 9.3\,rad/m$. So, the overall ratio

of steering wheel angle to wheel steering angle is given by $i_S = 125/9.3 = 13.44\,rad/rad$, which corresponds quite well with mechanical rack-and-pinion steering systems. The torsional stiffness $c_S = 10/(1\,\pi/180) = 573\,Nm/rad$ would allow the steering shaft to twist up to 1° when the rack is locked and a torque of 10 Nm is applied at the steering wheel. The damping value $d_S = 5\,Nm/(rad/s)$ is roughly estimated. The tire data represent a typical passenger car tire.

The MATLAB solver ode23, an explicit Runge-Kutta (2,3) pair of Bogacki and Shampine, is slightly more efficient here than the MATLAB standard solver ode45 because the enhanced friction model is based on a simple function with sharp bends. The results of the plot commands[2] are shown in Figure 5.12.

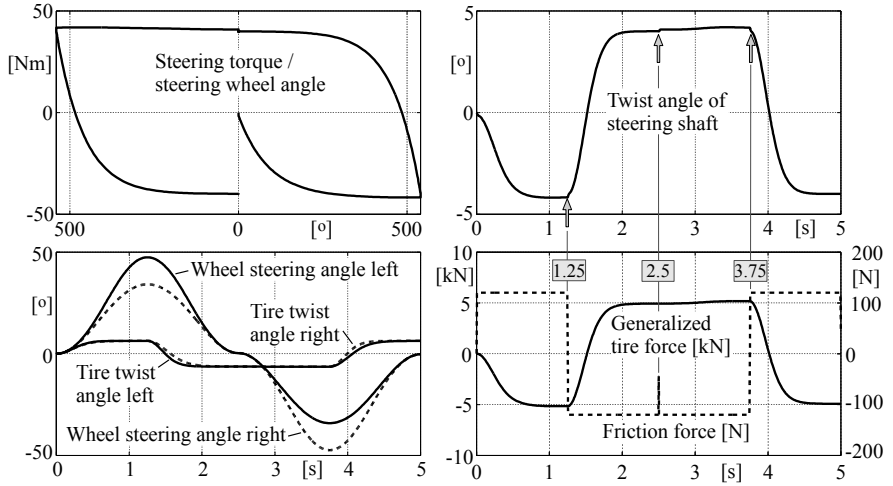

FIGURE 5.12
Stand-alone simulation results for periodic steer input.

Here, the maximum bore torque is obtained by $T_B^{mx} = r_B F^M = 0.065 * 4250 = 276.25\,Nm$ at each tire. Then, in a first approximation, the maximum steering torque is given by $T_S^{mx} = 2\,T_B^{mx}/i_S = 2 * 276.25/13.44 = 41\,Nm$, where i_S names the overall ratio of the steering system. This corresponds quite well with the first graph in Figure 5.12, where the steering wheel torque is plotted versus the steering wheel angle. The lower left graph shows the time histories of the tire twist angles and the wheel steering angles. As long as the tire patch sticks to the road, the tire twist angles will follow the wheel steering angles. When the tire patches start to slide, the maximum tire twist angles are limited to ±6.4°, which corresponds to the value $0.065 * 4100/2400 * 180/\pi = 6.4°$, which is calculated with the actual bore radius $r_B = 0.065\,m$, the sliding force

[2]Note: plotyy generates graphs with y tick labels on the left and right.

$F^S = 4100\,N$, and the torsional tire stiffness $c_{BO} = 2400\,Nm/rad$. The steering motions of the wheels are point-symmetric, ranging from $+47.4°$ to $-34.1°$ or $+34.1°$ to $-47.4°$, respectively. Amplifying the average value by the overall ratio of steering system results in $\delta_M^{mx} = 0.5(\pm 47.4 \pm 34.1) i_S = \pm 40.75 * 13.44 = \pm 547.7°$, which is slightly larger than the amplitude of the periodic steering wheel angle input $\delta_S^{mx} = \pm 540°$.

The friction in the steering box, which is approximated by an enhanced dry friction model where the maximum friction force is limited to $F_F^{mx} = 120\,N$, causes the steering shaft to twist, which reduces the effective steering angle at the steering box input. At times $1.25\,s$ and $3.75\,s$, the friction force, which is plotted in the lower right graph of Figure 5.12, jumps from $+120\,N$ to $-120\,N$ and back again. At the time $2.5\,s$ the steering wheel input, provided by a series of two squared sine functions with opposite signs, shows a point of inflection that causes the friction force to drop to zero at this very moment. On closer inspection of the upper right graph in Figure 5.12 discontinuities are noticeable in the time history of the steering shaft twist angle at these particular times.

5.4 Kinematics of a Double Wishbone Suspension

5.4.1 Modeling Aspects

A classical double wishbone suspension consists of two control arms, the wheel carrier, and the wheel, Figure 5.13. An additional subframe, which will often

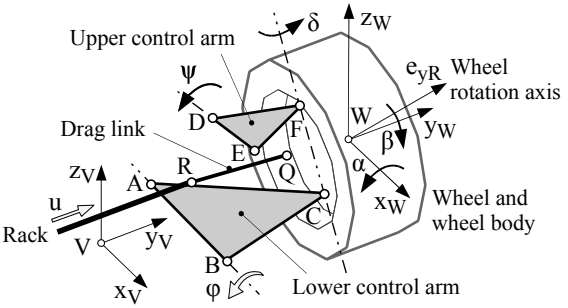

FIGURE 5.13
Double wishbone kinematic model.

be present in sophisticated suspension systems is not considered here. Then, the lower and upper control arms will be attached directly to the chassis. In addition, the compliance of the corresponding bushings in A, B and D, E will be neglected. Ball joints in C and F connect the control arms with the wheel

body. The rotation with the angle δ around the kingpin axis defined by C and D is controlled by the drag link. Via appropriate joints it is attached at point R to the rack and at point Q to the wheel body. The double wishbone suspension has two degrees of freedom. The hub motion is mainly controlled by the rotation of the lower control arm around the axis A-B and the steer motion is mainly induced by the rack movements. Hence, the angle φ and the displacement u are taken as generalized coordinates.

5.4.2 Position and Orientation

The momentary position and orientation of the wheel body is described with respect to the vehicle-fixed axis system with origin V located in the midst of the axle and where the axes x_V, y_V, and z_V point to the front to the left and upward. The axes x_W, y_W, and z_W are fixed to the wheel body. They will be parallel to the corresponding axes of the vehicle-fixed system in the design position. The vector

$$r_{VW,V} \;=\; r_{VA,V} + A_\varphi \, r_{AC,\varphi} + A_{VW} \, r_{CW,W} \tag{5.37}$$

specifies the momentary position of the wheel center W, where the vectors $r_{VA,V}$, $r_{AC,\varphi}$, $r_{CW,W}$ are fixed by the topology of the suspension and A_φ, A_{VW} are matrices describing the rotation of the lower wishbone and the wheel body with respect to the vehicle-fixed axis system. The lower control arm rotates with the angle φ around an axis that is determined by the location of the bushings A and B. Then, the relation

$$A_\varphi = e_{AB,V} \, e_{AB,V}^T + \left(I_{3\times3} - e_{AB,V} \, e_{AB,V}^T\right) \cos\varphi + \tilde{e}_{AB,V} \sin\varphi \tag{5.38}$$

defines the corresponding rotation matrix [25], where $e_{AB,V}$ is a unit vector pointing into the direction A→B, $I_{3\times3}$ is the 3×3 matrix of identity, and $\tilde{e}_{AB,V}$ denotes the skew-symmetric matrix defined by the components of the vector $e_{AB,V}$. The rotation matrix of the wheel body is composed of three rotations,

$$A_{VW} = A_\alpha \, A_\beta \, A_\delta \, , \tag{5.39}$$

where

$$A_\alpha = \begin{bmatrix} 1 & 0 & 0 \\ 0 & \cos\alpha & -\sin\alpha \\ 0 & \sin\alpha & \cos\alpha \end{bmatrix}, \quad A_\beta = \begin{bmatrix} \cos\beta & 0 & \sin\beta \\ 0 & 1 & 0 \\ -\sin\beta & 0 & \cos\beta \end{bmatrix} \tag{5.40}$$

are elementary rotations around the corresponding x- and y-axis and

$$A_\delta = e_{CF,W} \, e_{CF,W}^T + \left(I_{3\times3} - e_{CF,W} \, e_{CF,W}^T\right) \cos\delta + \tilde{e}_{CF,W} \sin\delta \tag{5.41}$$

defines similar to Equation 5.38 the rotation of the wheel body around the kingpin axis defined by the balljoints C and F.

5.4.3 Constraint Equations

5.4.3.1 Control Arms and Wheel Body

The ball joint F connects the upper control arm to the wheel body. Similar to Equation (5.37), the momentary position of F attached to the wheel body is defined by the vector

$$r_{VF,V} \;=\; r_{VA,V} + A_{\varphi}\, r_{AC,\varphi} + A_{VW}\, r_{CF,W}\;, \tag{5.42}$$

where the vector $r_{CF,W}$, measured in the wheel body-fixed axis system, is given by data and describes the position of the upper ball joint F relative to the lower ball joint C. As F is located on the upper control arm too, the vector

$$r_{VF,V} \;=\; r_{VD,V} + A_{\psi}\, r_{DF,\psi} \tag{5.43}$$

will represent another way to determine the momentary position of the upper ball joint. The vector $r_{VD,V}$ describes the location of bushing D with respect to the vehicle-fixed axis system, and the vector $r_{DF,\psi}$ defines the location of the ball joint F relative to D. Both vectors are defined by the topology of the suspension. Similar to Equation (5.38), the matrix

$$A_{\psi} = e_{DE,V}\, e_{DE,V}^{T} + \left(I_{3\times 3} - e_{DE,V}\, e_{DE,V}^{T}\right)\cos\psi + \tilde{e}_{DE,V}\sin\psi \tag{5.44}$$

describes the rotation of the upper control arm with the angle ψ around an axis determined by the location of the bushings D and E. Equation (5.42) with Equation (5.43) results in a first constraint equation

$$r_{VA,V} + A_{\varphi}\, r_{AC,\varphi} + A_{VW}\, r_{CF,W} \;=\; r_{VD,V} + A_{\psi}\, r_{DF,\psi}\;. \tag{5.45}$$

Using Equation (5.39) and rearranging some terms results in

$$\underbrace{A_{\alpha}\, A_{\beta}\, A_{\delta}}_{A_{VW}}\, r_{CF,W} = \underbrace{r_{VD,V} - (r_{VA,V} + A_{\varphi}\, r_{AC,\varphi})}_{r_{CD,V}(\varphi)} + A_{\psi}\, r_{DF,\psi}\;. \tag{5.46}$$

The rotation matrix A_{δ} given by Equation (5.41) describes the rotation around the kingpin axis defined by the unit vector $e_{CF,W}$. As the vector $r_{CF,W}$ coincides with the rotation axis $e_{CF,W}$, it will be not affected by this rotation,

$$A_{\delta}\, r_{CF,W} \;=\; r_{CF,W}\;. \tag{5.47}$$

Then, Equation (5.46) simplifies to

$$A_{\alpha}\, A_{\beta}\, r_{CF,W} \;=\; r_{CD,V}(\varphi) + A_{\psi}\, r_{DF,\psi}\;, \tag{5.48}$$

which makes it possible to calculate the angles α, β, and ψ as a function of the rotation angle φ, which was chosen as a generalized coordinate. Although Equation (5.48) results in three nonlinear trigonometric relations, an algebraic solution is possible here.

Squaring[3] both sides of Equation (5.48) results in

$$(A_\alpha A_\beta r_{CF,W})^T (A_\alpha A_\beta r_{CF,W}) = (r_{CD,V} + A_\psi r_{DF,\psi})^T (r_{CD,V} + A_\psi r_{DF,\psi}) \;, \tag{5.49}$$

where $r_{CD,V}(\varphi)$ was shortened by $r_{CD,V}$. Taking the orthogonality, which is defined in Equation (1.8), for the rotation matrices A_α, A_β, and A_ψ into account, one gets

$$\underbrace{r_{CF,W}^T r_{CF,W}}_{CF^2} = \underbrace{r_{CD,V}^T r_{CD,V}}_{CD^2} + 2\, r_{CD,V}^T\, A_\psi r_{DF,\psi} + \underbrace{r_{DF,\psi}^T r_{DF,\psi}}_{DF^2} \;. \tag{5.50}$$

Making use of Equation (5.44) and rearranging some terms yields

$$r_{CD,V}^T \left\{ ee^T + \left(I - ee^T\right) \cos\psi + \tilde{e} \sin\psi \right\} r_{DF,\psi} + \tfrac{1}{2}\left(CD^2 + DF^2 - CF^2\right) = 0 \,, \tag{5.51}$$

where subscripts of $e_{DE,V}$ and $I_{3\times 3}$ were just omitted. By using the abbreviations

$$a \;=\; r_{CD,V}^T \left(I - ee^T\right) r_{DF,\psi} \,, \quad b \;=\; r_{CD,V}^T\, \tilde{e}\, r_{DF,\psi} \;=\; r_{CD,V}^T\, e \times r_{DF,\psi} \tag{5.52}$$

and

$$c \;=\; -\left[r_{CD,V}^T\, ee^T\, r_{DF,\psi} \;+\; \tfrac{1}{2}\left(CD^2 + DF^2 - CF^2\right) \right] \;, \tag{5.53}$$

Equation (5.51) can be written as

$$a\, \cos\psi + b\, \sin\psi = c \,. \tag{5.54}$$

Interpreting the terms $a/\sqrt{a^2+b^2}$ and $b/\sqrt{a^2+b^2}$ as the sine and cosine of a fictitious angle ϑ, Equation (5.54) will read as

$$\sin\vartheta\, \cos\psi + \cos\vartheta\, \sin\psi = \frac{c}{\sqrt{a^2+b^2}} \,. \tag{5.55}$$

Using the addition theorem $\sin\vartheta\, \cos\psi + \cos\vartheta\, \sin\psi = \sin\left(\vartheta + \psi\right)$ and taking into account that the fictitious angle is defined by the relationship $\tan\vartheta = a/b$, one finally gets

$$\sin\left(\vartheta + \psi\right) = \frac{c}{\sqrt{a^2+b^2}} \quad \text{or} \quad \psi \;=\; \arcsin\frac{c}{\sqrt{a^2+b^2}} \;-\; \arctan\frac{a}{b} \,. \tag{5.56}$$

Note that practical results will be achieved only if the parameter b is not negative. In this case, multiplication of Equation (5.54) with -1 will change the sign appropriately. Equation (5.56) provides the rotation angle of the upper control arm as a function of the lower one, $\psi = \psi(\varphi)$. Then, the corresponding rotation matrix is determined via Equation (5.44) and the right-hand side of Equation (5.48) can be summarized in the vector

$$r_{CF,V}(\varphi) = r_{CD,V}(\varphi) + A_\psi\left(\psi(\varphi)\right)\, r_{DF,\psi} \,. \tag{5.57}$$

[3]Note: Squaring a vector is equivalent to its scalar product, $r^2 = r^T r$.

Multiplying the constraint equation (5.48) by A_α^T and taking Equations (5.57) and (5.40) into consideration results in

$$\begin{bmatrix} \cos\beta & 0 & \sin\beta \\ 0 & 1 & 0 \\ -\sin\beta & 0 & \cos\beta \end{bmatrix} \begin{bmatrix} r_{CF,W}^{(1)} \\ r_{CF,W}^{(2)} \\ r_{CF,W}^{(3)} \end{bmatrix} = \begin{bmatrix} 1 & 0 & 0 \\ 0 & \cos\alpha & \sin\alpha \\ 0 & -\sin\alpha & \cos\alpha \end{bmatrix} \begin{bmatrix} r_{CF,V}^{(1)} \\ r_{CF,V}^{(2)} \\ r_{CF,V}^{(3)} \end{bmatrix}, \tag{5.58}$$

which immediately will deliver two[4] equations,

$$r_{CF,W}^{(1)} \cos\beta + r_{CF,W}^{(3)} \sin\beta = r_{CF,V}^{(1)} , \tag{5.59}$$

$$r_{CF,V}^{(2)} \cos\alpha + r_{CF,V}^{(3)} \sin\alpha = r_{CF,W}^{(2)} . \tag{5.60}$$

These equations of the type of Equation (5.54) are solved similar to Equation (5.56) and will provide the angles $\alpha = \alpha(\varphi)$, $\beta = \beta(\varphi)$ needed to compose the elementary rotation matrices A_α and A_β.

5.4.3.2 Steering Motion

The drag link is attached in R to the rack and in Q to the wheel body. The momentary positions of these points are determined by

$$r_{VR,V} = r_{VR,V}^K + \begin{bmatrix} 0 \\ u \\ 0 \end{bmatrix} \tag{5.61}$$

and

$$r_{VQ,V} = r_{VA,V} + A_\varphi\, r_{AC,\varphi} + A_\alpha\, A_\beta\, A_\delta\, r_{CQ,W} , \tag{5.62}$$

where the vectors $r_{VR,V}^K$, $r_{VA,V}$, $r_{AC,\varphi}$, $r_{CQ,W}$ are determined by the topology of the suspension and a pure lateral movement of the rack was assumed. The drag link is supposed to be rigid, which results in a second constraint equation

$$(r_{VQ,V} - r_{VR,V})^T (r_{VQ,V} - r_{VR,V}) = \ell_{RQ}^2 , \tag{5.63}$$

where ℓ_{RQ} denotes the length of the drag link. Introducing the abbreviation

$$r_{RC,V} = r_{VA,V} + A_\varphi\, r_{AC,\varphi} - r_{VR,V} , \tag{5.64}$$

the constraint equation will read as

$$(r_{RC,V} + A_\alpha\, A_\beta\, A_\delta\, r_{CQ,W})^T (r_{RC,V} + A_\alpha\, A_\beta\, A_\delta\, r_{CQ,W}) = \ell_{RQ}^2 , \tag{5.65}$$

which results in

$$\underbrace{r_{RC,V}^T r_{RC,V}}_{RC^2} + 2\, \underbrace{r_{RC,V}^T\, A_\alpha\, A_\beta}_{r_{RC,H}^T}\, A_\delta\, r_{CQ,W} + \underbrace{r_{CQ,W}^T r_{CQ,W}}_{CQ^2} = \ell_{RQ}^2 . \tag{5.66}$$

[4]Note: The third equation corresponds with Equation (5.49) and thus can provide no additional information.

Inserting the rotation matrix A_δ defined in Equation (5.41) finally yields

$$\begin{aligned} r_{RC,H}^T \left(I - ee^T\right) r_{CQ,W} \cos\delta + r_{RC,H}^T \tilde{e}\, r_{CQ,W} \sin\delta \; = \\ -\left[r_{RC,H}^T ee^T r_{CQ,W} + \tfrac{1}{2}\left(RC^2 + CQ^2 - \ell_{RQ}^2\right)\right] . \end{aligned} \tag{5.67}$$

where the subscripts of the identity matrix $I_{3\times3}$ and the unit vector $e_{CF,W}$ were omitted. Equation (5.67) is again of the type of Equation (5.54) and can be solved accordingly. As the movements of points R and Q depend on the rack displacement and on the rotation of the lower control arm, the steering angle δ will be a function of u and φ. The corresponding rotation matrix A_δ is defined by Equation (5.41).

Now, the momentary position of the wheel center W relative to the vehicle-fixed axis system can be computed. According to Equation (5.37), one gets

$$r_{VW,V}(\varphi, u) \;=\; r_{VA,V} + A_\varphi(\varphi)\, r_{AC,\varphi} + A_{VW}(\varphi, u)\, r_{CW,W} \;, \tag{5.68}$$

where the rotation matrix

$$A_{VW}(\varphi, u) \;=\; A_\alpha(\varphi)\, A_\beta(\varphi)\, A_\delta(\varphi, u) \tag{5.69}$$

describes the orientation of the wheel body-fixed axis system relative to the vehicle-fixed axis system. Within the wheel body-fixed axis system, the unit vector in the direction of the wheel rotation axis may be determined by the toe angle δ_0 and the camber angle $\hat{\gamma}_0$. According to Equation (1.2), one gets

$$e_{yR,V} \;=\; \frac{1}{\sqrt{\tan^2\delta_0 + 1 + \tan^2\hat{\gamma}_0}} \begin{bmatrix} \tan\delta_0 \\ 1 \\ -\tan\hat{\gamma}_0 \end{bmatrix} . \tag{5.70}$$

Then, the orientation of the wheel rotation axis with respect to the vehicle-fixed axis system is simply given by

$$e_{yR,V} = A_{VW}\, e_{yR,V} \;. \tag{5.71}$$

A standard McPherson suspension is modeled in [44]. Besides an analytical solution, the multibody approach with commercial software packages is presented.

5.4.4 Velocities

The time derivative of Equation (5.68) provides the velocity of the wheel center with respect to the vehicle-fixed axis system V,

$$\dot{r}_{VW,V} \;=\; \omega_{\varphi,V} \times \underbrace{A_\varphi(\varphi)\, r_{AC,\varphi}}_{r_{AC,V}} + \omega_{VW,V} \times \underbrace{A_{VW}(\varphi, u)\, r_{CW,W}}_{r_{CW,V}} \;, \tag{5.72}$$

where $r_{VA,V} = \text{const.}$ was already taken into account. The rotation matrix A_φ defined in Equation (5.38) describes the orientation of the lower control arm

around an axis that is defined by the unit vector $e_{AB,V}$. Then, the angular velocity of the lower control arm is simply given by

$$\omega_{\varphi,V} \;=\; e_{AB,V}\,\dot{\varphi}\,. \tag{5.73}$$

According to Equation (5.39), the rotation matrix A_{VW} describing the orientation of the wheel body W relative to the vehicle-fixed axis system V is composed of a series of rotations which are defined in Equations (5.40) and (5.41). Then, the corresponding angular velocity is given by

$$\omega_{VW,V} \;= e_{x_V,V}\,\dot{\alpha} \;+\; \underbrace{A_\alpha\, e_{y_\alpha,\alpha}}_{e_{y_\alpha,V}}\,\dot{\beta} \;+\; \underbrace{A_\alpha\, A_\beta\, e_{CF,W}}_{e_{CF,V}}\,\dot{\delta}\,, \tag{5.74}$$

where

$$e_{x_V,V} = \begin{bmatrix} 1 \\ 0 \\ 0 \end{bmatrix} \quad \text{and} \quad e_{y_\alpha,\alpha} = \begin{bmatrix} 0 \\ 1 \\ 0 \end{bmatrix} \tag{5.75}$$

denote unit vectors in the direction of the corresponding rotation axis. The time derivative of the first constraint equation (5.45) yields

$$\omega_{\varphi,V} \times r_{AC,V} + \omega_{VW,V} \times r_{CF,V} \;=\; \omega_{\psi,V} \times \underbrace{A_\psi\, r_{DF,\psi}}_{r_{DF,V}}\,, \tag{5.76}$$

where the position vectors $r_{AC,V}$, $r_{CW,V}$ are defined in Equation (5.72). Inserting the angular velocities provided by Equations (5.73) and (5.74) results in

$$e_{AB,V}\times r_{AC,V}\dot{\varphi} + \left(e_{x_V,V}\dot{\alpha} + e_{y_\alpha,V}\dot{\beta} + e_{CF,V}\dot{\delta}\right)\times r_{CF,V} = e_{DE,V}\times r_{DF,V}\dot{\psi}\,, \tag{5.77}$$

where the angular velocity of the upper control arm is given by

$$\omega_{\psi,V} \;=\; e_{DE,V}\,\dot{\psi} \tag{5.78}$$

and $e_{DE,V}$ denotes the unit vector in the direction of the rotation axis. The unit vector $e_{CF,V}$ points in the direction of the vector $r_{CF,V}$. Then, the corresponding cross-product vanishes, $e_{CF,V} \times r_{CF,V} = 0$, and Equation (5.77) simplifies to

$$e_{AB,V}\times r_{AC,V}\dot{\varphi} + e_{x_V,V}\times r_{CF,V}\dot{\alpha} + e_{y_\alpha,V}\times r_{CF,V}\dot{\beta} = e_{DE,V}\times r_{DF,V}\dot{\psi}\,. \tag{5.79}$$

The kinematics of the double wishbone suspension is fully determined by the generalized coordinates φ and u, which represent the rotation of the lower control arm and the rack displacement. The constraint equation (5.48) provides the angles α and β as well as the rotation angle of the upper control arm ψ as functions of φ,

$$\psi = \psi(\varphi), \quad \alpha = \alpha(\varphi), \quad \beta = \beta(\varphi)\,. \tag{5.80}$$

Whereas according to the constraint equation (5.67), the angle δ depends on φ and u,

$$\delta = \delta(\varphi,\, u)\,, \tag{5.81}$$

then the time derivatives of the corresponding angles are obtained as

$$\dot{\alpha} = \frac{\partial \alpha}{\partial \varphi}\dot{\varphi}, \quad \dot{\beta} = \frac{\partial \beta}{\partial \varphi}\dot{\varphi}, \quad \dot{\psi} = \frac{\partial \psi}{\partial \varphi}\dot{\varphi}, \quad \dot{\delta} = \frac{\partial \delta}{\partial \varphi}\dot{\varphi} + \frac{\partial \delta}{\partial u}\dot{u}\,. \tag{5.82}$$

Although only the angle δ depends on both generalized coordinates, the partial derivatives were used here for all angles in order to keep the calculations more general.

Inserting Equation (5.82) into Equation (5.79), rearranging some terms, and canceling the angular velocity of the lower control arm $\dot{\varphi}$ finally results in

$$e_{DE,V} \times r_{DF,V} \frac{\partial \psi}{\partial \varphi} \;-\; e_{x_V,V} \times r_{CF,V} \frac{\partial \alpha}{\partial \varphi} \;-\; e_{y_\alpha,V} \times r_{CF,V} \frac{\partial \beta}{\partial \varphi} = e_{AB,V} \times r_{AC,V}\,, \tag{5.83}$$

which represents three scalar equations for the three unknown partial derivatives, $\partial\psi/\partial\varphi$, $\partial\alpha/\partial\varphi$, $\partial\beta/\partial\varphi$.

The time derivative of the second constraint equation (5.63) results in

$$2 \Big(\underbrace{r_{VQ,V} - r_{VR,V}}_{r_{RQ,V}} \Big)^T \Big(\underbrace{\dot{r}_{VQ,V} - \dot{r}_{VR,V}}_{\dot{r}_{RQ,V}} \Big) = 0\,, \tag{5.84}$$

where the position vectors $r_{VR,V}$, $r_{VQ,V}$ are defined in Equations (5.61), (5.62), and their time derivatives are given by

$$\dot{r}_{VR,V} \;=\; \begin{bmatrix} 0 \\ \dot{u} \\ 0 \end{bmatrix} \;=\; \begin{bmatrix} 0 \\ 1 \\ 0 \end{bmatrix} \dot{u} \;=\; e_{y_V,V}\, \dot{u}\,, \tag{5.85}$$

$$\dot{r}_{VQ,V} \;=\; \omega_{\varphi,V} \times r_{AC,V} + \omega_{VW,V} \times r_{CQ,V}\,. \tag{5.86}$$

The angular velocities $\omega_{\varphi,V}$ and $\omega_{VW,V}$ are defined in Equations (5.73) and (5.74). Taking, in addition, Equation (5.82) into account provides the time derivative of the vector $r_{VQ,V}$ as a function of the angular velocity of the lower control arm $\dot{\varphi}$ and the rack velocity $\dot{u}$,

$$\dot{r}_{VQ,V} \;=\; \frac{\partial \dot{r}_{VQ,V}}{\partial \dot{\varphi}}\, \dot{\varphi} \;+\; \frac{\partial \dot{r}_{VQ,V}}{\partial \dot{u}}\, \dot{u}\,, \tag{5.87}$$

where the corresponding partial derivatives are given by

$$\frac{\partial \dot{r}_{VQ,V}}{\partial \dot{\varphi}} \;=\; e_{AB,V} \times r_{AC,V} + \left(e_{x_V,V} \frac{\partial \alpha}{\partial \varphi} + e_{y_\alpha,V} \frac{\partial \beta}{\partial \varphi} + e_{CF,V} \frac{\partial \delta}{\partial \varphi} \right) \times r_{CQ,V}\,, \tag{5.88}$$

$$\frac{\partial \dot{r}_{VQ,V}}{\partial \dot{u}} \;=\; e_{CF,V} \frac{\partial \delta}{\partial u} \times r_{CQ,V}\,. \tag{5.89}$$

Now, Equation (5.84) reads as

$$r_{RQ,V}^T \left(\frac{\partial \dot{r}_{VQ,V}}{\partial \dot{\varphi}} \, \dot{\varphi} + \frac{\partial \dot{r}_{VQ,V}}{\partial \dot{u}} \, \dot{u} - e_{y_V,V} \, \dot{u} \right) = 0 \,, \tag{5.90}$$

where the factor 2 was simply canceled. The time derivatives of the generalized coordinates $\dot{\varphi}$ and $\dot{u}$ are completely independent. Then, Equation (5.90) requires that

$$r_{RQ,V}^T \frac{\partial \dot{r}_{VQ,V}}{\partial \dot{\varphi}} = 0 \quad \text{and} \quad r_{RQ,V}^T \left(\frac{\partial \dot{r}_{VQ,V}}{\partial \dot{u}} - e_{y_V,V} \right) = 0 \tag{5.91}$$

holds separately. By using Equations (5.88) and (5.89), the demands result in

$$r_{RQ,V}^T \left(e_{AB,V} \times r_{AC,V} + \left[e_{x_V,V} \frac{\partial \alpha}{\partial \varphi} + e_{y_\alpha,V} \frac{\partial \beta}{\partial \varphi} \right] \times r_{CQ,V} + e_{CF,V} \times r_{CQ,V} \frac{\partial \delta}{\partial \varphi} \right) = 0 \,, \tag{5.92}$$

$$r_{RQ,V}^T \left(e_{CF,V} \times r_{CQ,V} \frac{\partial \delta}{\partial u} - e_{y_V,V} \right) = 0 \,, \tag{5.93}$$

which will deliver the partial derivatives $\partial\delta/\partial\varphi$ and $\partial\delta/\partial u$ in a few steps.

Now, the angular velocity of the wheel body-fixed axis system W with respect to the vehicle-fixed axis system V defined by Equation (5.74) can be written as

$$\omega_{VW,V} \;=\; \frac{\partial \omega_{VW,V}}{\partial \dot{\varphi}} \, \dot{\varphi} \;+\; \frac{\partial \omega_{VW,V}}{\partial \dot{u}} \, \dot{u} \,, \tag{5.94}$$

where the corresponding partial derivatives are given by

$$\frac{\partial \omega_{VW,V}}{\partial \dot{\varphi}} = e_{x_V,V} \, \frac{\partial \alpha}{\partial \varphi} + e_{y_\alpha,V} \, \frac{\partial \beta}{\partial \varphi} + e_{CF,V} \, \frac{\partial \delta}{\partial \varphi} \quad \text{and} \quad \frac{\partial \omega_{VW,V}}{\partial \dot{u}} = e_{CF,V} \, \frac{\partial \delta}{\partial u} \,. \tag{5.95}$$

Finally, the velocity of the wheel center with respect to the vehicle-fixed axis system V defined by Equation (5.72) is just obtained as

$$\dot{r}_{VW,V} \;=\; \frac{\partial \dot{r}_{VW,V}}{\partial \dot{\varphi}} \, \dot{\varphi} \;+\; \frac{\partial \dot{r}_{VW,V}}{\partial \dot{u}} \, \dot{u} \,, \tag{5.96}$$

where the corresponding partial derivatives are provided by

$$\frac{\partial \dot{r}_{VW,V}}{\partial \dot{\varphi}} = e_{AB,V} \times r_{AC,V} + \frac{\partial \omega_{VW,V}}{\partial \dot{\varphi}} \times r_{CW,V} \quad \text{and} \quad \frac{\partial \dot{r}_{VW,V}}{\partial \dot{u}} = \frac{\partial \omega_{VW,V}}{\partial \dot{u}} \times r_{CW,V} \,. \tag{5.97}$$

The partial derivatives of the angular velocity and the velocity with respect to the generalized velocities, which here equals the time derivatives of the generalized coordinates, form the basis of Jourdain's principle. They are simply called partial velocities in Section 1.4.

5.4.5 Acceleration

The time derivatives of Equations (5.94) and (5.96) provide the angular acceleration of the wheel body-fixed axis system W and the acceleration of the

wheel center with respect to the vehicle-fixed axis system V. Although the kinematics of nearly all suspension systems is nonlinear, the partial derivatives of the angular velocity and the velocity of the wheel center defined by Equations (5.95) and (5.97) do not change very much in the normal range of motion. Then, the accelerations can be approximated by

$$\dot{\omega}_{VW,V} \approx \frac{\partial \omega_{VW,V}}{\partial \dot{\varphi}} \ddot{\varphi} + \frac{\partial \omega_{VW,V}}{\partial \dot{u}} \ddot{u} \,, \tag{5.98}$$

$$\ddot{r}_{VW,V} \approx \frac{\partial \dot{r}_{VW,V}}{\partial \dot{\varphi}} \ddot{\varphi} + \frac{\partial \dot{r}_{VW,V}}{\partial \dot{u}} \ddot{u} \,. \tag{5.99}$$

Neglecting the time derivatives of the partial derivatives saves a lot of computing time and still generates very accurate results [35].

5.4.6 Kinematic Analysis

The function dblwb_kin.m provided by Listing 5.3 calculates the kinematics of a double wishbone suspension system by computing the corresponding equations in the previous subsections. It uses the functions skewsym.m and trigon.m, which are given in Listings 5.4 and 5.5, to generate a skew-symmetric matrix according to Equation (1.13) and to solve trigonometric equations of the type of Equation (5.54).

Listing 5.3
Function `dblwb_kin.m`: Kinematics of a Double Wishbone Axle

```
function [ avw ...  % rotation matrix wheel rim / ref-sys
         , rvwv ...  % actual position of wheel center
         , del ...   % rotation angle arround king pin
         , pv ...    % partial velocities
         ] = ...
 dblwb_kin( phi ... % rotation angle of lower control arm
          , u ...    % rack displacement
          , dt ...   % model data
         )
% kinematics of a double whisbone axle with rack and pinion steering

% lower wishbone
  rab = dt.rvbk-dt.rvak; eab = rab / norm(rab); eabs = skewsym(eab);
  eabeab = eab*eab'; eyeab = eye(3,3)-eabeab;
  aphi = eabeab + eyeab*cos(phi) + eabs*sin(phi);

% upper wishbone
  rcfk = dt.rvfk-dt.rvck; rdfk = dt.rvfk-dt.rvdk;
  racv=aphi*(dt.rvck-dt.rvak); rcdv=dt.rvdk-(dt.rvak+racv);
  rde=dt.rvek-dt.rvdk; ede=rde/norm(rde); edeede=ede*ede'; edes=skewsym(ede);
  a = rcdv'*(eye(3,3)-edeede)*rdfk; b = rcdv'*cross(ede,rdfk);
  c = -rcdv'*edeede*rdfk-0.5*(rdfk'*rdfk+rcdv'*rcdv-rcfk'*rcfk);
  psi = trigon(a,b,c);
  apsi = edeede + (eye(3,3)-edeede)*cos(psi) + edes*sin(psi);

% orientation of wheel body due to control arm motion
```

```
  rvcv = dt.rvak + racv;
  rdfv = apsi*(dt.rvfk-dt.rvdk); rvfv = dt.rvdk + rdfv; rcfv = rvfv - rvcv;
  be = trigon(rcfk(1),rcfk(3),rcfv(1));
  abe = [ cos(be) 0 sin(be) ; ...
            0    1    0    ; ...
         -sin(be) 0  cos(be) ];
  al = trigon(rcfv(2),rcfv(3),rcfk(2));
  aal = [ 1    0      0    ; ...
          0  cos(al) -sin(al) ; ...
          0  sin(al) cos(al) ] ;

% rotation arround king pin
  rvrv = dt.rvrk + [ 0; u; 0 ]; rrcv = rvcv - rvrv; rrcht=rrcv'*aal*abe;
  rrqk = dt.rvqk-dt.rvrk; rcqk = dt.rvqk-dt.rvck; rcfk = dt.rvfk-dt.rvck;
  ecf = rcfk / norm(rcfk); ecfecf = ecf*ecf'; ecfs = skewsym(ecf);
  a = rrcht*(eye(3,3)-ecfecf)*rcqk; b = rrcht*cross(ecf,rcqk);
  c = -( rrcht*ecfecf*rcqk + 0.5*(rrcv'*rrcv + rcqk'*rcqk - rrqk'*rrqk) );
  del=trigon(a,b,c); adel=ecfecf+(eye(3,3)-ecfecf)*cos(del)+ecfs*sin(del);

% wheel body orientation and position
  avw = aal*abe*adel; rcwv = avw*(dt.rvwk-dt.rvck); rvwv = rvcv + rcwv;

% partial derivatives: dpsi/dphi, dal/dphi, dbe/dphi
  exvv=[1;0;0]; eyalv=aal*[0;1;0];
  a = [ cross(ede,rdfv) -cross(exvv,rcfv) -cross(eyalv,rcfv) ];
  c = a \ cross(eab,racv); dpsidphi=c(1); daldphi=c(2); dbedphi=c(3);

% partial derivatives: ddel/dphi, ddel/du
  eyvv=[0;1;0]; ecfv=rcfv/norm(rcfv);
  rcqv=avw*rcqk; rvqv=rvcv+rcqv; rrqv=rvqv-rvrv;
  a = exvv*daldphi + eyalv*dbedphi; b = cross(eab,racv) + cross(a,rcqv);
  c = rrqv'*cross(ecfv,rcqv); ddeldphi = -rrqv'*b/c; ddeldu = rrqv'*eyvv/c;

% partial angular and partial velocities of wheel carrier
  dodphi=exvv*daldphi+eyalv*dbedphi+ecfv*ddeldphi; dodu=ecfv*ddeldu;
  dvdphi=cross(eab,racv)+cross(dodphi,rcwv); dvdu = cross(dodu,rcwv);
  pv = [ dodphi dodu dvdphi dvdu ];

end
```

Listing 5.4
Function `skewsym.m`: Generate Skew-Symmetric Matrix

```
function matrix = skewsym( vector ) % create skew-symmetric matrix from vector
  matrix = [   0     -vector(3) vector(2) ; ...
             vector(3)     0     -vector(1) ; ...
            -vector(2) vector(1)     0     ];
end
```

Listing 5.5
Function `trigon.m`: Solve Trigonometric Equation

```
function psi = trigon( a, b, c ) % solve a*cos(psi) + b*sin(psi) = c
  if b<0
    psi = asin(-c/sqrt(a^2+b^2)) - atan2(-a,-b);
```

```
4     else
5       psi = asin( c/sqrt(a^2+b^2)) - atan2( a, b);
6     end
7   end
```

The MATLAB-Script in Listing 5.6 provides the data for a typical passenger car front suspension and performs a kinematic analysis of the double wishbone suspension. At first, some relevant properties are computed in the design position and displayed via the MATLAB-Function disp. The calculation of kingpin and caster angle is straightforward because its orientation is determined by the ball joints C and F which are defined by the substructures dt.rvck and dt.rvfk in the design position. The caster offset c and the scrub radius s are visualized in Figure 5.6 and defined by Equation 5.2. Here, the vector from the point S where an extension of the kingpin axis intersects the road surface to the contact point P is given by

$$\underbrace{-c\,e_x + s\,e_y}_{r_{SP}} \;=\; \underbrace{\lambda\,e_{CF}}_{r_{SC}} \;+\; \underbrace{r_{CW} + r_{WP}}_{r_{CP}}\,, \tag{5.100}$$

where the caster offset c, the scrub radius s, and the parameter λ are yet unknown. The unit vector e_{CF} in the direction of the kingpin axis is defined by the ball joints C and F, and the vectors r_{CW}, r_{WP} are given by data in the design position. The unit vectors e_x, e_y in the longitudinal and the lateral direction are perpendicular to each other and both perpendicular to the road normal, which is defined by the unit vector e_n. Then, scalar multiplication of Equation 5.100 results in

$$0 \;=\; \lambda\,e_n^T\,e_{CF} + e_n^T\,r_{CP}\,, \tag{5.101}$$

which immediately delivers the parameter λ or the vector

$$r_{SC} \;=\; \lambda\,e_{CF} \;=\; -\,\frac{e_n^T\,r_{CP}}{e_n^T\,e_{CF}}\;e_{CF}\,. \tag{5.102}$$

Finally, the caster offset and the scrub radius,

$$c \;=\; -e_x^T\;(r_{SC} + r_{CP}) \quad \text{and} \quad s \;=\; e_y^T\;(r_{SC} + r_{CP})\;, \tag{5.103}$$

are obtained by scalar multiplication of Equation 5.100 with e_x and e_y, respectively. Running the MATLAB-Script will provide the following results: kingpin angle = 10.5182, caster angle = 7.0561, caster offset = 0.030326, and scrub radius = 0.0010327, which are typical values for modern passenger car front suspension systems. In addition, the script generates some plots, which are shown in Figure 5.14 and Figure 5.15.

Listing 5.6
MATLAB-Script `dblwb_kin_test.m`: Double Wishbone Kinematic Analysis

```
1   % suspension kinematics (typical passenger car front left)
```

```
dt.umx = 0.0745; % max. rack displacement
dt.phimx= 10/180*pi; % max rotation of lower control arm
dt.rvwk= [ 0.0000; 0.7680; 0.0000]; % W: wheel rim center
dt.rvak= [-0.2510; 0.3200; -0.0800]; % A: lower control arm @ chassis rear
dt.rvbk= [ 0.1480; 0.3200; -0.0940]; % B: lower control arm @ chassis front
dt.rvck= [ 0.0130; 0.7370; -0.1450]; % C: lower control arm @ wheel body
dt.rvdk= [-0.1050; 0.4350; 0.1960]; % D: upper control arm @ body rear
dt.rvek= [ 0.1220; 0.4350; 0.2300]; % E: upper control arm @ body front
dt.rvfk= [-0.0250; 0.6800; 0.1620]; % F: upper control arm @ wheel body
dt.rvrk= [-0.1500; 0.3800; -0.0380]; % R: drag link @ rack
dt.rvqk= [-0.1370; 0.6900; -0.0880]; % Q: drag link @ wheel body
% additional data
toe0 = 0.0000/180*pi; % initial toe angle (sign according to ISO def)
camb0= 0.8000/180*pi; % initial camber angle (sign accord. to ISO def)
rs   = 0.2850; % steady state tire radius
en0  = [ 0; 0; 1 ]; % road normal (flat horizontal road)

% wheel/tire orientation in design position
eyrk = [toe0; 1; -camb0]; eyrk = eyrk/norm(eyrk); % wheel rot. axis
exk = cross(eyrk,en0); exk=exk/norm(exk); % longitudinal direction
eyk = cross(en0,exk); % lateral direction
ezk = cross(exk,eyrk); % radial direction
rwpk= -rs*ezk; % wheel center W --> reference point P (contact in design pos.)

% kingpin and caster angle in design position
rcfk = dt.rvfk-dt.rvck; ecfk=rcfk/norm(rcfk); % kingpin orientation
si = atan2(-ecfk(2),ecfk(3)); disp(['kingpin angle = ',num2str(si*180/pi)])
nu = atan2(-ecfk(1),ecfk(3)); disp(['caster angle = ',num2str(nu*180/pi)])

% caster offset and scrub radius in design position
rcpk = dt.rvwk + rwpk - dt.rvck ; rsck = -(en0'*rcpk)/(en0'*ecfk)*ecfk ;
co = -exk'*(rsck+rcpk); disp(['caster offset = ',num2str(co)])
sr =  eyk'*(rsck+rcpk); disp(['scrub radius = ',num2str(sr)])

% range of motion (rotation of lower control arm and rack displacement)
n=11; phi=linspace(-1,1,n)*dt.phimx; m=15; u=linspace(-1,1,m)*dt.umx;

% pre-allocate vars to speed up loops
xw=zeros(n,m);yw=xw;zw=xw; xp=xw;yp=xw;zp=xw; del=xw; toe=xw; camb=xw; ddel=xw;
for i=1:n
  for j=1:m
    [avw,rvwv,del(i,j),pd] = dblwb_kin(phi(i),u(j),dt); % suspension kinematics
    eyrv = avw*eyrk; % actual orientation of wheel rotation axis
    rvpv = rvwv + avw*rwpk; % actual position of reference point P
    xw(i,j)=rvwv(1);yw(i,j)=rvwv(2);zw(i,j)=rvwv(3); % wheel center coord.
    xp(i,j)=rvpv(1);yp(i,j)=rvpv(2);zp(i,j)=rvpv(3); % ref. point coord.
    toe(i,j) = atan2(-eyrv(1), eyrv(2)); % toe angle (+ rot. z-axis)
    camb(i,j)= atan2( eyrv(3), eyrv(2)); % camber angle (+ rot. x-axis)
    ddel(i,j)=norm(pd(:,2)); % partial derivative ddel/du
  end
end

n0=round(n/2); m0=round(m/2); rvpk = dt.rvwk + rwpk ;
axes('position',[0.05,0.05,0.20,0.90]),hold on,axis equal,grid on,title('xz')
plot(xw(:,m0),zw(:,m0)),plot(xp(:,m0),zp(:,m0),'--')
plot(dt.rvwk(1),dt.rvwk(3),'ok'), plot(rvpk(1),rvpk(3),'ok')
axes('position',[0.30,0.05,0.20,0.90]),hold on,axis equal,grid on,title('yz')
```

```
59  plot(yw(:,m0),zw(:,m0)), plot(yp(:,m0),zp(:,m0),'--')
60  plot(dt.rvwk(2),dt.rvwk(3),'ok'),plot(rvpk(2),rvpk(3),'ok')
61  axes('position',[0.60,0.05,0.35,0.40]), colormap('white')
62  surf(u,phi*180/pi,toe*180/pi), grid on, view(-40,10), title('toe')
63  axes('position',[0.60,0.55,0.35,0.40]), colormap('white')
64  surf(u,phi*180/pi,camb*180/pi), grid on, view(-40,10), title('camber')
65  figure % open new figure
66  d1 = del(n0,:); d2 = -d1(m:-1:1); % wheel steering angles in design position
67  a=2.7; s=2*dt.rvwk(2); d2a = atan2(a*tan(d1),a+s*tan(d1)); % ackermann angle
68  axes('position',[0.05,0.55,0.40,0.30]), title('\delta_1(u), \delta_2(u)')
69  plot(u,[d1;d2]*180/pi), grid on, legend('left','right')
70  axes('position',[0.05,0.15,0.40,0.30]), title('d\delta/du')
71  plot(u,ddel(n0,:)), grid on
72  axes('position',[0.55,0.30,0.40,0.40]), axis equal, title('\delta_2(\delta_1)')
73  plot(d1*180/pi,[d2;d2a]*180/pi),grid on, legend('kinematics','ackermann')
```

At first, the motion of the wheel center W and the wheel body-fixed reference point P, which in design position coincides with the contact point, are plotted in the xz- and the yz-plane. By fixing the second index in the corresponding matrices xw, yw, zw, and xp, yp, zp to m0, the motions induced by varying the rotation angle φ are considered only. As typical for most passenger car front axle suspension systems, the reference point moves slightly forward when the wheel goes upward. At the same time, the wheel center travels backward here. This is achieved by a different inclined rotation axis of the lower and the upper control arm. The MATLAB-Function surf is used to plot the toe

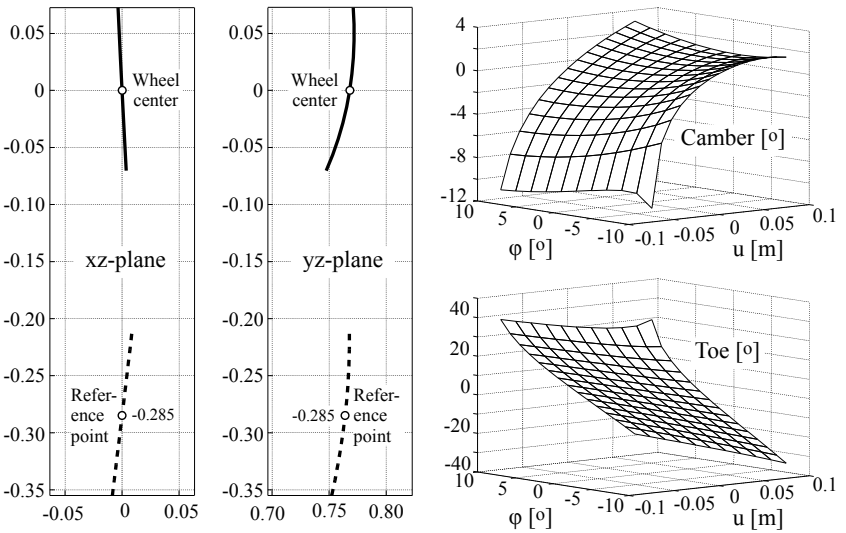

FIGURE 5.14
Double wishbone kinematics.

and the camber angle which define the momentary orientation of the wheel rotation axis as two-dimensional functions of the rack displacement u and the

rotation angle φ of the lower control arm. Positive signs in the toe and camber angle indicate here positive rotations of the left wheel body about the z- and x-axis, which does not match the definitions in Sections 1.3.3 and 1.3.4 but corresponds with the multibody system approach. Due to different-sized control arms, the wheel body rotates around the x-axis when the wheel is moved up and down. As the kingpin is fixed to the wheel body, it will change its orientation at the same time. Thus the camber angle depends on the generalized coordinates u and φ. The toe angle, however, is mainly influenced by the rack displacement u. A potential dependency on the hub motion (rotation angle φ), which becomes visible here on extreme hub and steer motions, will influence the driving behavior of the vehicle and should therefore be designed properly.

The function dblwb_kin provides the rotation angle δ around the kingpin too. The MATLAB command d1 = del(n0,:) extracts the angle of the left wheel in design position as a function of the rack displacement u only. Taking a left/right symmetry for granted, the MATLAB command d2 = -d1(m:-1:1) generates the corresponding angle at the right wheel. Both angles are plotted versus the rack displacement u in the upper left graph of Figure 5.15. The

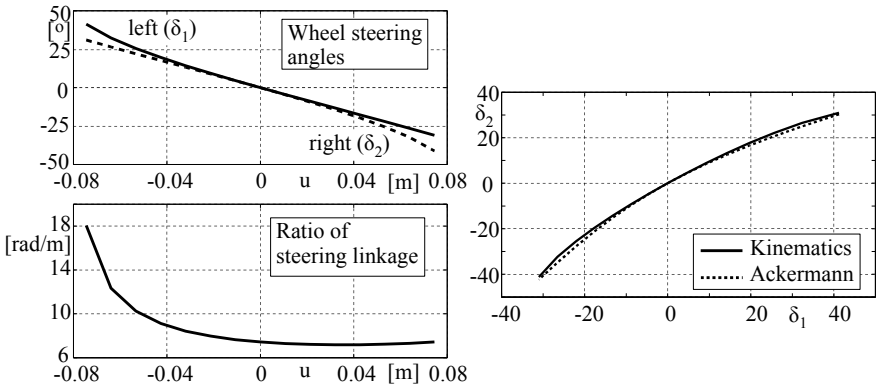

FIGURE 5.15
Double wishbone steering kinematics.

MATLAB-Script given in Listing 5.2 is based on a simple steering system model. A constant ratio of the steering linkage of $i_{SL} = 9.3$ was assumed. As can be seen in the lower left graph of Figure 5.15, the ratio is quite nonlinear here. In a wide range it is close to the mean value of 8.8 rad/m. If the rack displacement approaches its left maximum at $u = -u_{max} = -0.0745\ m$ the ratio goes up rather rapidly to 18.1 rad/m which indicates that the steering linkage comes close to a kinematical singularity. Assuming a wheel base of $a = 2.7m$ and assigning s = 2*dt.rvwk(2), the track width via the y-coordinate of the wheel center, the suspension kinematics can be compared with the

Ackermann steering geometry. Similar to Equation (5.34), the relation

$$\tan \delta_2^A = \frac{a \, \tan \delta_1}{a + s \, \tan \delta_1} \tag{5.104}$$

provides the Ackermann wheel steering angle at the second wheel δ_2^A as a function of the steering angle at the first wheel δ_1. As can be seen from the graph on the right of Figure 5.15 this double wishbone suspension system is designed to match the Ackermann steering geometry quite closely.

Note that the kinematics of a double wishbone suspension combined with a rack-and-pinion steering system are sensitive to the geometric data and may come to singular positions where the kinematics is not defined any more. That is why the maximum rotation angle of the lower control arm and the maximum rack displacement are specified here via the parameter dt.umx and dt.phimx. Increasing these values or changing the geometric data too much or improperly may cause MATLAB to generate warnings or error messages.

Exercises

5.1 Use part of the MATLAB-Script in Listing 5.6 to study the influence of the initial toe and camber angle set by the variables toe0 and camb0 on the caster offset and scrub radius.

5.2 The figure where the underlaying grid is based on a distance of 0.05 m shows the layout of a simple double wishbone suspension for the left rear wheel of a passenger car.

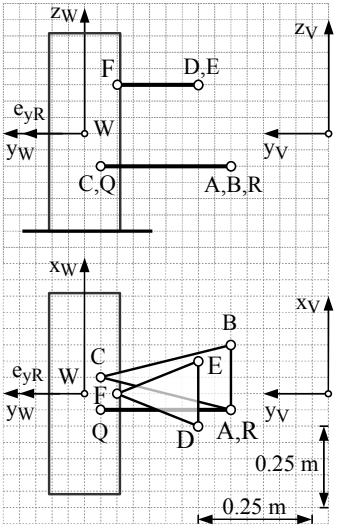

The absence of a steering system is taken into account by a vanishing maximum rack displacement, dt.umx=0. In addition, the wheel is mounted on the wheel body without an initial toe and camber angle, toe0=0 and camb0=0. Furthermore, a flat horizontal road can be assumed, en0 = [0; 0; 1].

Complete the data set needed to analyze the double wishbone suspension by inspecting the sketch. Estimate the maximum possible rotation angle of the lower control arm.

Modify the MATLAB-Script given in Listing 5.6 appropriately to restrict the kinematic analysis to the hub motion of the wheel induced by the rotation of the lower control arm.

5.3 A passenger car is equipped with double wishbone suspension systems at both axles. The specific data for the front and rear axle are given by

```
% suspension kinematics (front left)
dt.umx  = 0.0745;  % max. rack displacement
dt.phimx= 10/180*pi; % max rotation of lower control arm
dt.rvwk= [ 0.0000;  0.7680;  0.0000]; % W: wheel rim center
dt.rvak= [-0.2510;  0.3200; -0.0800]; % A: lower control arm @ chassis rear
dt.rvbk= [ 0.1480;  0.3200; -0.0940]; % B: lower control arm @ chassis front
dt.rvck= [ 0.0130;  0.7370; -0.1450]; % C: lower control arm @ wheel body
dt.rvdk= [-0.1050;  0.4350;  0.1960]; % D: upper control arm @ body rear
dt.rvek= [ 0.1220;  0.4350;  0.2300]; % E: upper control arm @ body front
dt.rvfk= [-0.0250;  0.6800;  0.1620]; % F: upper control arm @ wheel body
dt.rvrk= [-0.1500;  0.3800; -0.0381]; % R: drag link @ rack
dt.rvqk= [-0.1370;  0.6900; -0.0879]; % Q: drag link @ wheel body

% suspension kinematics (rear left)
dt.umx  = 0.0;  % max. rack displacement
dt.phimx= 12/180*pi; % max rotation of lower control arm
dt.rvwk= [ 0.0000;  0.7675;  0.0000]; % W: wheel rim center
dt.rvak= [-0.2900;  0.3200; -0.0890]; % A: lower control arm @ chassis rear
dt.rvbk= [ 0.0500;  0.3200; -0.0725]; % B: lower control arm @ chassis front
dt.rvck= [-0.0260;  0.7370; -0.1435]; % C: lower control arm @ wheel body
dt.rvdk= [-0.2220;  0.4530;  0.2245]; % D: upper control arm @ body rear
dt.rvek= [ 0.0370;  0.4530;  0.2020]; % E: upper control arm @ body front
dt.rvfk= [ 0.0200;  0.6800;  0.1630]; % F: upper control arm @ wheel body
dt.rvrk= [-0.1540;  0.3160;  0.0120]; % R: drag link @ rack
dt.rvqk= [-0.1550;  0.6900; -0.0470]; % Q: drag link @ wheel body
```

The data are based on local vehicle-fixed coordinate systems that are located in the corresponding axle center. Both axles are characterized by the additional data

```
toe0 = 0.00/180*pi; % initial toe angle (sign accord. rot. around z-axis)
camb0=-0.50/180*pi; % initial camber angle (sign accord. rot. around x-axis)
rs   = 0.3450;      % steady-state tire radius
en0  = [ 0; 0; 1 ]; % road normal (flat horizontal road)
```

Modify the MATLAB-Script given in Listing 5.6 appropriately so that the kinematics of both axles can be analyzed. Note that the rear axle is not steered, but is simply realized by setting the maximum rack displacement to zero. Compare the results of the movements of the wheel center W and the reference point P in particular. Adjust the inner loop and the plotting commands appropriately.

6

Force Elements

CONTENTS

6.1 Standard Force Elements

6.1.1 Springs

Springs support the weight of the vehicle. In vehicle suspensions, coil springs, air springs, torsion bars, and leaf springs are used, Figure 6.1.

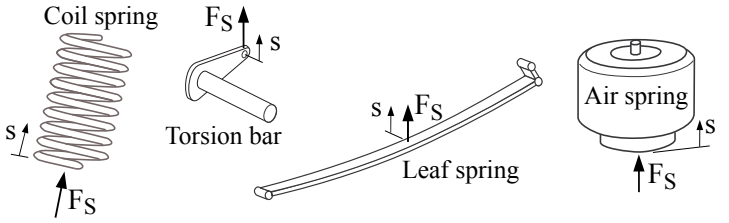

FIGURE 6.1
Vehicle suspension springs.

Coil springs, torsion bars, and leaf springs absorb additional load by compressing. Thus, the ride height depends on the loading condition. Air springs are rubber cylinders filled with compressed air. They are becoming more popular on passenger cars, light trucks, and heavy trucks because here the correct vehicle ride height can be maintained regardless of the loading condition by adjusting the air pressure. A linear coil spring may be characterized by its

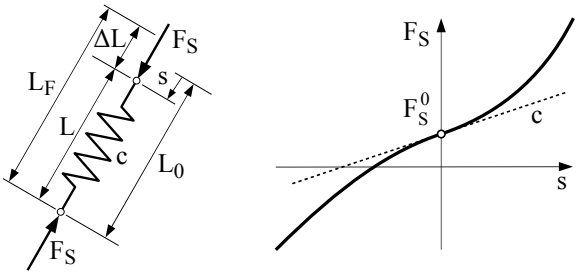

FIGURE 6.2
Linear coil spring and general spring characteristics.

free length L_F and the spring stiffness c, Figure 6.2. The force acting on the spring is then given by

$$F_S \;=\; c\,\big(L_F - L\big) \;=\; c\,\Delta L\,, \tag{6.1}$$

where L denotes the actual length and ΔL the overall deflection of the spring. Mounted in a vehicle suspension, the spring has to support the corresponding chassis weight. Hence, the spring will be compressed to the configuration length $L_0 < L_F$. Now, Equation (6.1) can be written as

$$F_S \;=\; c\,\big(L_F - (L_0 - s)\big) \;=\; c\,\big(L_F - L_0\big) + c\,s \;=\; F_S^0 + c\,s\,, \tag{6.2}$$

where F_S^0 denotes the spring preload and $s = L_0 - L$ describes the spring displacement measured from the spring's configuration length. Note, $s > 0$ indicates compression. In general, the spring force F_S can be defined by a nonlinear function of the spring displacement s,

$$F_S \;=\; F_S(s) \;=\; F_S(L_0 - L)\,. \tag{6.3}$$

Now, arbitrary spring characteristics can be approximated by elementary functions, like polynomials, or by tables that are then inter- and extrapolated by linear functions or cubic splines. The complex behavior of leaf springs and air springs can only be approximated by simple nonlinear spring characteristics, $F_S = F_S(s)$. For detailed investigations, sophisticated [42] or even dynamic spring models [8] must be used.

6.1.2 Anti-Roll Bar

The anti-roll or anti-sway bar or stabilizer is used to reduce the roll angle during cornering and to provide additional stability. Usually, it is simply a U-shaped metal rod connected to both of the lower control arms, Figure 6.3. Thus, the two wheels of an axle are interconnected by a torsion bar spring. This affects each one-sided bouncing. The axle with the stronger stabilizer is rather inclined to breaking out, in order to reduce the roll angle.

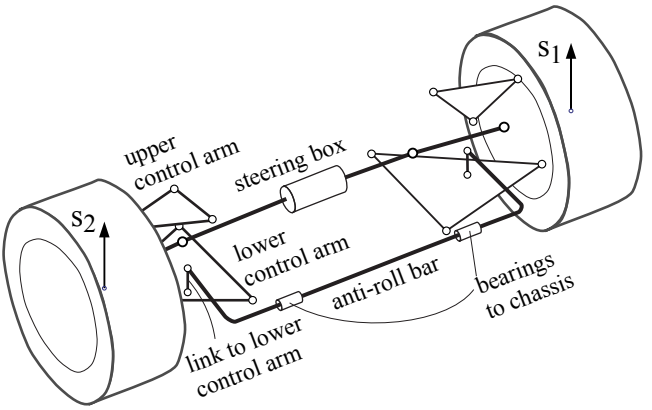

FIGURE 6.3
Axle with anti-roll bar attached to lower control arms.

When the suspension at one wheel moves up and on the other down, the anti-roll bar generates a force acting in the opposite direction at each wheel. In a good approximation, this force is given by

$$F_{arb} \;=\; \pm\, c_{arb}\;(s_1 - s_2)\;, \tag{6.4}$$

where s_1, s_2 denote the vertical suspension motions of the left and the right wheel center, and c^W_{arb} in $[N/m]$ names the stiffness of the anti-roll bar with respect to the vertical suspension motions of the wheel centers.

Assuming a simple U-shaped anti-roll bar, the stiffness of the anti-roll bar is defined by the geometry and material properties. Vertical forces with the magnitude F applied in the opposite direction at both ends of the the anti-roll bar, result in the vertical displacement $\triangle z$ measured between both ends of the anti-roll bar, Figure 6.4. The stiffness of the anti-roll bar itself is then defined by

$$c \;=\; \frac{F}{\triangle z}\;. \tag{6.5}$$

Neglecting all bending effects and taking small deflections for granted, one gets

$$\triangle z \;=\; a\,\triangle\varphi \;=\; a\,\frac{F\,a\,b}{G\,\dfrac{\pi}{32}\,D^4}\;, \tag{6.6}$$

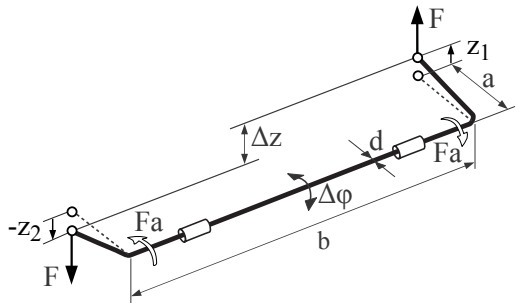

FIGURE 6.4
Anti-roll bar loaded by vertical forces.

where G denotes the modulus of shear and the distances a, b are defined in Figure 6.4. Hence, the stiffness of the anti-roll bar is given by

$$c \;=\; \frac{\pi}{32}\,\frac{G\;D^4}{a^2\,b}\,. \tag{6.7}$$

Depending on the axle design, the ends of the ant-roll bar are attached via links to the knuckle or, as shown in Figure 6.3, to the lower control arm. In both cases, the displacement of the anti-roll bar end is given as a function of the vertical suspension motion of the wheel center. For small displacements, one gets

$$z_1 \;=\; i_{arb}\,s_1 \quad \text{and} \quad z_2 \;=\; i_{arb}\,s_2\,, \tag{6.8}$$

where i_{arb} denotes the ratio of the vertical motions of the wheel centers s_1, s_2 and the anti-roll bar ends z_1, z_2. Now, the stiffness of the anti-roll bar with respect to the vertical suspension motions of the wheel centers is given by

$$c_{arb} \;=\; i_{arb}^2\,\frac{\pi}{32}\,\frac{G\;D^4}{a^2\,b}\,. \tag{6.9}$$

The stiffness strongly depends (fourth power) on the diameter of the anti-roll bar.

For a typical passenger car, the following data will hold: $a = 230\;mm$, $b = 725\;mm$, $D = 20\;mm$ and $i_{arb} = 2/3$. The shear modulus of steel is given by $G = 85\,000\;N/mm^2$. Then, one gets

$$c_{arb} \;=\; \left(\frac{2}{3}\right)^2\,\frac{\pi}{32}\,\frac{85\,000\;N/mm^2\,(20\;mm)^4}{(230\;mm)^2\;725\;mm} \;=\; 15.5\;N/mm = 15\,500\;N/m \tag{6.10}$$

This simple calculation will not produce the real stiffness exactly, because bending effects and compliancies in the anti-roll bar bearings will reduce the stiffness of the anti-roll bar.

6.1.3 Damper

Dampers are basically oil pumps. As the suspension travels up and down, the hydraulic fluid is forced by a piston through tiny holes, called orifices. This slows down the suspension motion. Today, twin-tube and mono-tube dampers are used in vehicle suspension systems, Figure 6.5. Whereas the twin-tube layout stores the oil that is displaced by the piston rod when entering the cylinder in a remote oil chamber, the mono-tube type uses a floating piston that operates against a gas chamber and makes the capacity of the cylinder adaptable.

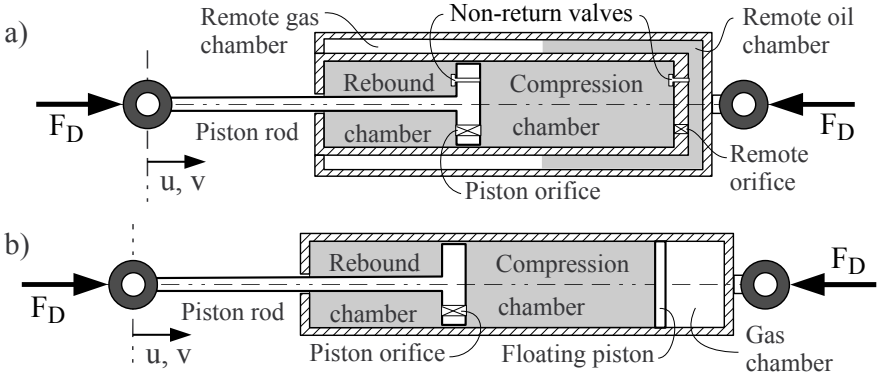

FIGURE 6.5
Types of suspension dampers: (a) twin-tube and (b) mono-tube.

In standard vehicle dynamics applications, simple characteristics

$$F_D \;=\; F_D(v)\,, \tag{6.11}$$

are used to describe the damper force F_D as a function of the damper velocity $v = \dot{u}$. To obtain this characteristics, the damper is excited with a sinusoidal displacement signal $u = u_0 \sin 2\pi f t$. By varying the frequency in several steps from $f = f_0$ to $f = f_E$, different force displacement curves $F_D = F_D(u)$ are obtained, Figure 6.6. By taking the peak values of the damper force at the displacement $u = 0$, which corresponds with the velocity $v(u = 0) = \pm 2\pi f u_0$, the characteristics $F_D = F_D(v)$ is generated now. Here, the compression cycle is associated with positive and the rebound cycle with negative damper velocities. Typical passenger car or truck dampers will have more resistance during the rebound cycle than the compression cycle.

Usually, nonlinear damper characteristics are simply provided by lookup tables. A simple linear or a smoother spline inter- or extrapolation will provide the damping forces. The MATLAB-Script provided in Listing 6.1 provides the lookup table for the damper characteristic $F_D = F_D(v)$, computes the

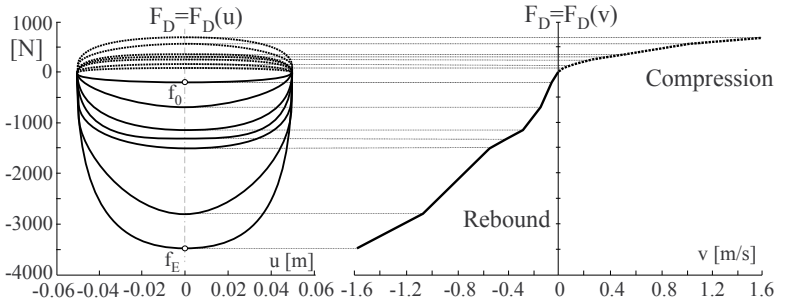

FIGURE 6.6
Damper characteristics generated from measurements [17].

damping force generated by a sine excitation with different frequencies, and plots the damping characteristic as well as the force displacement curves.

Listing 6.1
MATLAB-Script `damper_char.m`: Nonlinear Damper Characteristic

```
% nonlinear damper characteristics F=F(v) provided by lookup table [ v F ]
damper_table = ...
[ -1.5080 -3500; ...
  -1.1310 -2800; ...
  -0.5655 -1500; ...
  -0.4524 -1250; ...
  -0.3016 -1000; ...
  -0.1508  -650; ...
  -0.0377  -200; ...
   0.0000     0; ...
   0.0377   100; ...
   0.1508   150; ...
   0.3016   200; ...
   0.4524   250; ...
   0.5655   300; ...
   1.1310   500; ...
   1.5080   600 ];

subplot(1,2,1), hold on % generate F=F(u) via sine excitation
u0=0.06; freq=[0.1 0.4 0.8 1.2 1.5 3.0 4.0]; % amplitude [m] & frequencies [Hz]
for i=1:length(freq)
  t=linspace(0,1/freq(i),101); % time intervals
  u=zeros(size(t)); F=u; % pre-allocate vars to speed up inner loop
  for j=1:length(t)
    u(j)=u0*sin(2*pi*freq(i)*t(j)); vij=2*pi*freq(i)*u0*cos(2*pi*freq(i)*t(j));
    F(j)=interp1q(damper_table(:,1),damper_table(:,2),vij);
  end
  plot(u,F), grid on % force displacement curve at freq(i)
end

subplot(1,2,2) % plot characteristics F=F(v) and mark given points
plot(damper_table(:,1),damper_table(:,2),'-ok','MarkerSize',5), grid on
```

The lookup table was generated by simply inspecting the damper characteristics $F_D = F_D(v)$ provided in Figure 6.6. According to [17], the damper was excited with a sinusoidal displacement signal at different frequencies and an amplitude of approximately half the maximum stroke of the damper. Estimating the amplitude with $u = 0.06\,m$ and detecting the velocity values in the damper characteristics with $v \approx [0.04\,0.15\,0.30\,0.45\,0.57\,1.13\,1.51]\ m/s$ results via the relationship $v = 2\pi\,f\,u$ in the excitation frequencies defined in Listing 6.1. The MATLAB-Function interp1q provides the actual force for each velocity in between the range defined by the lookup table by a simple linear interpolation. Note that this function is fast, but does not extrapolate.

The results generated by the script just copy the force velocity characteristic and generate force displacement characteristics that are quite similar to the ones in Figure 6.6. However, the specific shape of the curves cannot be reproduced exactly by this simple model approach.

Dynamic damper models, like the one presented in [1], calculate the damper force via the fluid pressure applied to each side of the piston. The dynamic changes of the fluid and gas pressures in the compression and rebound chambers as well as in the gas chamber are calculated by applying physical principles.

6.1.4 Point-to-Point Force Elements

6.1.4.1 Generalized Forces

Usually, the mounts that connect springs, dampers, and actuators to different bodies can be regarded as ball joints, Figure 6.7. Then, the action line of the

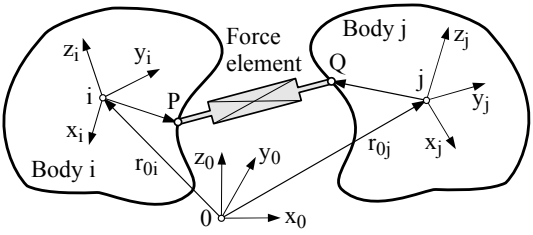

FIGURE 6.7
Point-to-point force element
A point-to-point force element attached between two bodies.

force generated by the element that is mounted between the points P and Q is defined by the unit vector

$$e_{PQ,0} \;=\; \frac{r_{PQ,0}}{|r_{PQ,0}|} \;=\; \frac{r_{0Q,0} - r_{0P,0}}{|r_{0Q,0} - r_{0P,0}|}\,, \tag{6.12}$$

where

$$L \;=\; |r_{PQ,0}| = \sqrt{r_{PQ,0}^T r_{PQ,0}} \tag{6.13}$$

defines the actual length of the force element in addition. The point P is attached to body i and point Q to body j. The vectors $r_{0i,0}$, $r_{0j,0}$ and the rotation matrices A_{0i}, A_{0j} describe the momentary position and orientation of axis systems fixed in the center of each body with respect to the earth-fixed reference frame 0. Then, the position of the attachment points is defined by

$$r_{0P,0} = r_{0i,0} + \underbrace{A_{0i}\, r_{iP,i}}_{r_{iP,0}} \quad \text{and} \quad r_{0Q,0} = r_{0j,0} + \underbrace{A_{0j}\, r_{jQ,j}}_{r_{jQ,0}}\,, \tag{6.14}$$

where the vectors $r_{iP,i}$, $r_{jQ,j}$ characterize the position of P and Q with respect to the corresponding body-fixed axis systems. The deflection of the force element is just given by

$$s = L_0 - L\,, \tag{6.15}$$

where L_0 denotes the length of the force element in the design position and the actual length L is defined by Equation (6.13).

According to Equation (6.3), spring forces can be described by appropriate force displacement characteristics, $F_S = F_S(s)$. In the approach of Equation (6.11), the force provided by a hydraulic damper can be described as a function of the damper velocity $F_D = F_D(v)$. Corresponding to the nonlinear characteristic plotted in Figure 6.6, $v > 0$ will indicate compression, which is in conformity with the sign definition of the spring deflection s too. The time derivative of the force element deflection s given in Equation (6.15) delivers the damper velocity at first as

$$v = \dot{s} = \frac{d}{dt}\,(L_0 - L) = -\dot{L}\,. \tag{6.16}$$

By using Equation (6.13) it results in

$$v = -\frac{2\, r_{PQ,0}^T \dot{r}_{PQ,0}}{2\,\sqrt{r_{PQ,0}^T r_{PQ,0}}} = -\frac{r_{PQ,0}^T}{|r_{PQ,0}|}\,\dot{r}_{PQ,0} = -e_{PQ,0}^T\,(\dot{r}_{0Q,0} - \dot{r}_{0P,0})\,, \tag{6.17}$$

where Equation (6.12) was used to reinsert the unit vector e_{PQ} and to put the time derivative of the vector r_{PQ} down to the time derivatives of the position vectors r_{0Q} and r_{0P}. According to Equation (6.14), the time derivatives of the position vectors are given by

$$\dot{r}_{0P,0} = v_{0i,0} + \omega_{0i,0} \times r_{iP,0} \quad \text{and} \quad \dot{r}_{0Q,0} = v_{0j,0} + \omega_{0j,0} \times r_{jQ,0}\,, \tag{6.18}$$

where $v_{0i,0} = \dot{r}_{0i,0}$, $v_{0j,0} = \dot{r}_{0j,0}$ name the absolute velocities of the body centers and $\omega_{0i,0}$, $\omega_{0j,0}$ denote the absolute angular velocities of the bodies. Finally, the force acting in an arbitrary point-to-point force element can be described by

$$F = F\,(s,\, v,\, u,\, x)\,, \tag{6.19}$$

where the dependency on a control signal u will include actuators and the vector x collects the internal states that are needed to model dynamic force elements too.

The equations of motion for different vehicle models are generated by applying Jourdain's principle of virtual power throughout this textbook. The forces and torques applied to the bodies are converted via partial velocities to generalized forces hereby. Similar to the appropriate terms in Equation (1.28), the force F acting in a point-to-point element is transformed by

$$q_F = \left(\frac{\partial v}{\partial z}\right)^T F\,(s,\, v,\, u,\, x) \tag{6.20}$$

to the corresponding parts of the generalized force vector q. According to Equation (6.17), the partial derivatives of the force element deflection velocity v with respect to the vector of the generalized velocities z are given by

$$\frac{\partial v}{\partial z} = -e_{PQ,0}^T \left(\frac{\partial \dot{r}_{0Q,0}}{\partial z} - \frac{\partial \dot{r}_{0P,0}}{\partial z}\right) = e_{PQ,0}^T \frac{\partial \dot{r}_{0P,0}}{\partial z} - e_{PQ,0}^T \frac{\partial \dot{r}_{0Q,0}}{\partial z}\,, \tag{6.21}$$

which, by using Equation (6.18), results in

$$\frac{\partial v}{\partial z} = e_{PQ}^T \left(\frac{\partial v_{0i}}{\partial z} + \frac{\partial \omega_{0i}}{\partial z} \times r_{iP}\right) - e_{PQ}^T \left(\frac{\partial v_{0j}}{\partial z} + \frac{\partial \omega_{0j}}{\partial z} \times r_{jQ}\right)\,, \tag{6.22}$$

where the comma-separated subscript 0, which indicates that all vectors are expressed in the earth-fixed axis system, was omitted. Then, the part q_F of the generalized force vector q related to the force F that acts in a point-to-point force element is given by

$$q_F = \left(\frac{\partial v_{0i}}{\partial z} + \tilde{r}_{iP}^T \frac{\partial \omega_{0i}}{\partial z}\right)^T e_{PQ} F - \left(\frac{\partial v_{0j}}{\partial z} + \tilde{r}_{jQ}^T \frac{\partial \omega_{0j}}{\partial z}\right)^T e_{PQ} F\,, \tag{6.23}$$

where the cross-products in the partial velocities were replaced by the corresponding skew-symmetric matrix vector multiplications via the relationship $\omega \times r = -r \times \omega = -\tilde{r}\,\omega = \tilde{r}^T \omega$. Rearranging some terms and reintroducing the cross-product notation finally results in

$$q_F = \frac{\partial v_{0i}^T}{\partial z} F_{PQ} + \frac{\partial \omega_{0i}^T}{\partial z} r_{iP} \times F_{PQ} - \frac{\partial v_{0j}^T}{\partial z} F_{PQ} - \frac{\partial \omega_{0j}^T}{\partial z} r_{jQ} \times F_{PQ}\,, \tag{6.24}$$

where $F_{PQ} = e_{PQ}\, F$ simply defines the vector that vectorially describes the magnitude and the orientation of the force acting in the point-to-point element. If body i and j are moving without kinematical constraints, the components of the vectors v_{0i}, v_{0j}, ω_{0i}, ω_{0j} can be used as generalized velocities. Then, the partial derivatives are trivial and Equation (6.24) simply yields

$$q_F = \begin{bmatrix} F_{PQ} \\ r_{iP} \times F_{PQ} \\ -F_{PQ} \\ -r_{jQ} \times F_{PQ} \end{bmatrix} \begin{array}{l} \leftarrow \text{force applied to body } i \\ \leftarrow \text{torque applied to body } i \\ \leftarrow \text{force applied to body } j \\ \leftarrow \text{torque applied to body } j \end{array} \tag{6.25}$$

which satisfies the "actio=reactio" principle and produces via appropriate cross-products the torques applied to body i and j automatically.

6.1.4.2 Example

For the sake of simplicity, the quarter car model in Section 1.5 was equipped just with a torsional spring damper combination in a first model approach. Now, the torsional damper will be replaced by a point-to-point damper element that is attached to the knuckle in point D and to the chassis in point E, Figure 6.8. Similar to Equation (6.12), the action line of the damper force

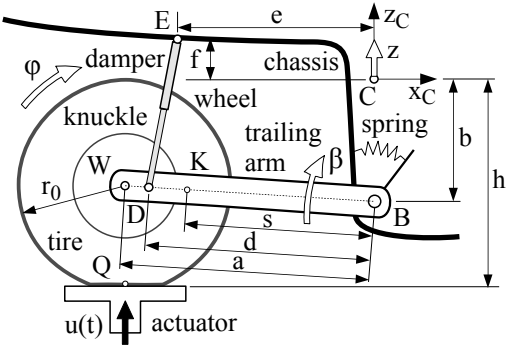

FIGURE 6.8
Quarter car model with a point-to-point damper element.

is defined in the chassis-fixed axis system C by the unit vector

$$e_{DE,C} = \frac{r_{DE,C}}{|r_{DE,C}|} = \frac{r_{CE,C} - r_{CD,C}}{|r_{CE,C} - r_{CD,C}|}, \tag{6.26}$$

where C denotes the center of the chassis mass and

$$L_{DE} = |r_{DE,C}| = \sqrt{r_{DE,C}^T r_{DE,C}} \tag{6.27}$$

defines the actual length of the damper element according to Equation (6.13). Here, the attachment point E is fixed to the chassis, which is common for most suspension systems. Its position relative to the chassis is simply defined by data and is given here by

$$r_{CE,C} = \begin{bmatrix} -e & 0 & f \end{bmatrix}^T. \tag{6.28}$$

The attachment point D is fixed to the knuckle. In general, its momentary position may be described via the knuckle center, which here results in

$$r_{CD,C} = r_{CK,C} + A_{CK}\, r_{KD,K}, \tag{6.29}$$

where $r_{CK,C}$ describes the momentary position of the knuckle center K and A_{CK} the rotation matrix of the knuckle that is defined by Equation (1.33). The vector $r_{KD,K}$ defines the position of D relative to K. It is expressed in the

knuckle-fixed axis system and simply given by data. In this particular case, where it was assumed that the attachment point D is located on a line with the knuckle center K and the revolute joint in B, one gets

$$r_{CD,C} = \begin{bmatrix} -s\cos\beta \\ 0 \\ -b + s\sin\beta \end{bmatrix} + \begin{bmatrix} -(d-s)\cos\beta \\ 0 \\ (d-s)\sin\beta \end{bmatrix} = \begin{bmatrix} -d\cos\beta \\ 0 \\ -b + d\sin\beta \end{bmatrix}. \tag{6.30}$$

The damper force F_D depends on the damper velocity v, which is defined as the time derivative of the element deflection s. According to Equation (6.17), one gets

$$v = \dot{s} = -\dot{L}_{DE} = -e_{DE,C}^T \left(\dot{r}_{CE,C} - \dot{r}_{CD,C}\right) . \tag{6.31}$$

Here, the time derivative of the vector $r_{CE,C}$ will vanish because the attachment point E is fixed to the chassis. Then, Equation (6.31) simplifies to

$$v = e_{DE,C}^T \dot{r}_{CD,C} . \tag{6.32}$$

The unit vector $e_{DE,C}$ is defined by Equation (6.26) and the time derivative of Equation (6.30) results in

$$\dot{r}_{CD,C} = \underbrace{\begin{bmatrix} s\sin\beta \\ 0 \\ s\cos\beta \end{bmatrix}\dot{\beta}}_{\dot{r}_{CK,C}} + \underbrace{\begin{bmatrix} 0 \\ 1 \\ 0 \end{bmatrix}\dot{\beta}}_{\omega_{CK,C}} \times \underbrace{\begin{bmatrix} -(d-s)\cos\beta \\ 0 \\ (d-s)\sin\beta \end{bmatrix}}_{r_{KD,C}} . \tag{6.33}$$

In this particular case, Equation (6.33) simplifies to

$$\dot{r}_{CD,C} = \frac{\partial r_{CD,C}}{\partial \beta}\dot{\beta} = \begin{bmatrix} d\sin\beta \\ 0 \\ d\cos\beta \end{bmatrix}\dot{\beta} . \tag{6.34}$$

The use of the partial derivative should indicate that in general the momentary position of the point D, where the damper is attached to the knuckle, may depend on more than one generalized coordinate. Hence, the damper velocity is given by

$$v = e_{DE,C}^T \frac{\partial r_{CD,C}}{\partial \beta}\dot{\beta} = \frac{\partial v}{\partial \dot{\beta}}\dot{\beta} = \dot{s} = \frac{\partial s}{\partial \beta}\dot{\beta} , \tag{6.35}$$

where $\dot{\beta}$, the time derivative of the generalized coordinate β, serves as the trivial generalized velocity. Then, the relationship

$$\frac{\partial v}{\partial \dot{\beta}} = \frac{\partial s}{\partial \beta} , \tag{6.36}$$

which can be deduced from Equation (6.35) by simply inspecting the corresponding terms, will hold in general. As mentioned in Section 6.1.3 the damper

force F_D is provided as a function of the damper velocity v in standard applications. According to Equation (6.20), the contribution to the generalized force related to the knuckle motion β is obtained finally as

$$q_{F_D}^{\beta} = \left(\frac{\partial v}{\partial \dot{\beta}}\right)^T F_D(v) \ , \tag{6.37}$$

where the partial derivative of the damper velocity v with respect to the angular velocity of the knuckle $\dot{\beta}$ is provided in Equation (6.35).

A simple quarter car model with a trailing arm suspension and a linear torsional spring damper combination acting in the revolute joint was presented in Section 1.5. Replacing the torsional damper by a nonlinear point-to-point damper model requires just a few changes in the corresponding MATLAB programs. At first, the function given in Listing 1.4 is extended and slightly modified to the function provided by Listing 6.2

Listing 6.2
Function `qcm_nl_f.m`: Quarter Car Model with Point-to-Point Damper Element

```
function xdot = qcm_nl_f(t,x)
% quarter car model with trailing arm suspension and nonlinear damper

global g s a b d e f h r0
global mC mK mW ThetaK ThetaW
global Ts0 cs cx cz dx damper_table
global ustep tstep

% state variables
z = x(1); beta = x(2); phi = x(3); zd = x(4); betad = x(5); phid = x(6);

% step input to actuator @ t = tstep
if t < tstep, u = 0; else u = ustep; end

% torque in revolute joint (preloaded linear torsional spring only)
Ts = - ( Ts0 + cs*beta );

% point to point damper element with non linear characteristic
rCDC=[-d*cos(beta);0;-b+d*sin(beta)]; rCEC=[-e;0;f]; % attachment points
rDEC = rCEC-rCDC; LDE=norm(rDEC); eDEC = rDEC/LDE; % action line
dvdbed=eDEC'*[d*sin(beta);0;d*cos(beta)]; v = dvdbed*betad; % velocity
FD=-interp1l(damper_table,v); qFDbe = dvdbed*FD; % element and general. force

% tire deflection (static tire radius)
rS = h + z - b + a*sin(beta) - u ;

% longitudinal tire force (adhesion assumed)
Fx = - cx*(a*(1-cos(beta))-rS*phi) - dx*(a*sin(beta)*betad-rS*phid);

% vertical tire force (contact assumed)
Fz =  cz *( r0 - rS );

% mass matrix
Massma=[      mC+mK+mW       (s*mK+a*mW)*cos(beta)  0   ; ...
```

```
35        (s*mK+a*mW)*cos(beta) ThetaK+s^2*mK+a^2*mW 0   ; ...
36                 0                    0          ThetaW ];
37
38  % vector of generalized forces and torques
39  qgen=[ Fz-(mC+mK+mW)*g+(s*mK+a*mW)*sin(beta)*betad^2 ; ...
40        Ts-(s*mK+a*mW)*cos(beta)*g+a*(Fx*sin(beta)+Fz*cos(beta))+qFDbe; ...
41          -rS*Fx ];
42
43  % state derivatives
44  xdot = [ zd; betad; phid; Massma\qgen ];
45
46  end
```

The global variables d, e, f describe the damper attachment points according to Figure 6.8 and the nonlinear damper characteristic, defined by a look-up table, is stored in the global variable damper_table. Extending the Listing 1.2 by the lines

```
d = 0.425; % [m] distance joint B damper attachment at knuckle
e = 0.420; % [m] damper attachment at chassis (horizontal position C-E)
f = 0.020; % [m] damper attachment at chassis (vertical position C-E)
```

and adding the look-up table given in Listing 6.1 will provide the complete model data. The torque Ts in the revolute joint, calculated in line 17, is reduced to a preloaded linear torsional spring. The calculations for the point-to-point damper element are done in lines 20 to 23. The function interp1l, provided in Listing 6.3, calls the MATLAB-Function interp1q for a fast linear interpolation in the look-up table and performs a linear extrapolation for values of xi that exceed the range of the x-values defined in the first column of the table.

Listing 6.3
Function `interp1l.m`: Evaluation of a Look-Up Table

```
1   function fi = interp1l( table, xi )
2   % linear inter- and extrapolation in lookup table: table = [x, f]
3
4   [n,m] = size(table); % size of table
5
6   if xi >= table(1,1) && xi <= table(n,1) % intermediate points
7     fi = interp1q(table(:,1),table(:,2),xi);
8     return
9   end
10  if xi < table(1,1) % linear extrapolation to the left
11    dfdx = ( table(2,2) - table(1,2) ) / ( table(2,1) - table(1,1) );
12    fi = table(1,2) + dfdx * ( xi - table(1,1) );
13    return
14  end
15  if xi > table(n,1) % linear extrapolation to the right
16    dfdx = ( table(n,2) - table(n-1,2) ) / ( table(n,1) - table(n-1,1) );
17    fi = table(n,2) + dfdx * ( xi - table(n,1) );
18    return
19  end
20
21  end
```

In addition, the generalized damper force assigned to the variable qFDbe is appropriately added in line 42 to the generalized force vector. The simulation

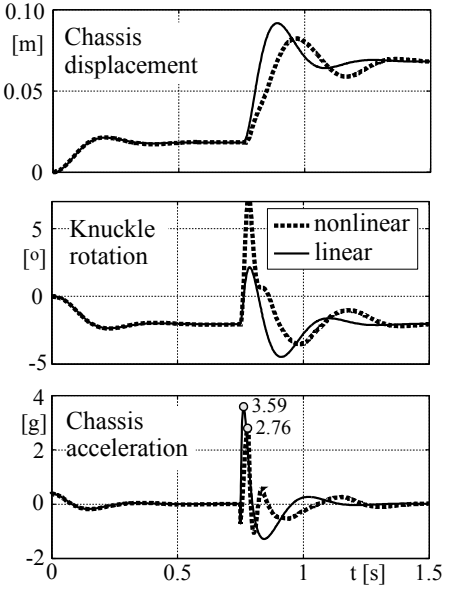

FIGURE 6.9
Simulation results with linear and nonlinear damper.

results of a step input are shown in Figure 6.9. As done in Section 1.5.5, the quarter car model is exposed at $t = 0.75\ s$ to a step input. The simulation results of the model extended to a point-to-point damper element with a nonlinear characteristic are compared to those generated with the model equipped with a simple linear torsional damper. The time histories of the chassis displacements z and the knuckle rotation β, as well as the vertical chassis acceleration $\ddot{z}$, are quite different although the overall damping behavior is rather the same. Due to the fact that the nonlinear damper has less resistance during compression than rebound, the knuckle rotation induced by the step input is faster and much larger in the nonlinear case. As a consequence, the impact to the chassis mass is reduced, which results in a significantly less maximum acceleration ($2.76\,g$ instead of $3.59\,g$). Thus, the ride comfort can be improved using appropriate nonlinear damper characteristics.

6.1.5 Rubber Elements

Force elements made of natural rubber or urethane compounds are used in many locations on the vehicle suspension system, Figure 6.10. Those elements require no lubrication, isolate minor vibration, reduce transmitted road shock, operate noise-free, offer high load carrying capabilities, and are very durable.

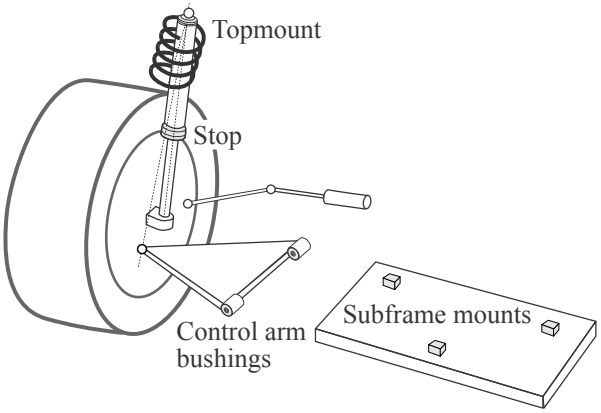

FIGURE 6.10
Rubber elements in vehicle suspension.

During suspension travel, the control arm bushings provide a pivot point for the control arm. They also maintain the exact wheel alignment by fixing the lateral and vertical location of the control arm pivot points. During suspension travel, the rubber portion of the bushing must twist to allow control arm motion. Thus, an additional resistance to suspension motion is generated.

Bump and rebound stops limit the suspension travel. The compliance of the topmount avoids the transfer of large shock forces to the chassis. The subframe mounts isolate the suspension system from the chassis and allow elasto-kinematic steering effects of the whole axle.

It turns out that those elastic elements can hardly be described by simple spring and damper characteristics, $F_S = F_S(u)$ and $F_D = F_D(v)$, because their stiffness and damping properties change with the frequency of the motion. Here, more sophisticated dynamic models are needed.

6.2 Dynamic Force Elements

6.2.1 Testing and Evaluating Procedures

6.2.1.1 Simple Approach

The effect of dynamic force elements is usually evaluated in the frequency domain. For this, on test rigs or in a simulation, the force element is excited by sine waves

$$x_e(t) \;=\; A\,\sin(2\pi\, f\, t) \;=\; A\,\sin\left(\tfrac{2\pi}{T}\, t\right) \tag{6.38}$$

with different frequencies $f_0 \le f \le f_E$ and amplitudes $A_{min} \le A \le A_{max}$, where $T = 1/f$ denotes the time period of the excitation. Starting at $t = 0$, the force element will be in steady state after several periods $t \ge nT$ where the number of cycles $n = 2, 3, \ldots$ must be chosen appropriately. The system response is periodic $F(t + T) = F(T)$ due to nonlinearities, it will be not harmonic, however. That is why the measured or calculated force signal $F = F(t)$ will be approximated by harmonic functions as much as possible. The first harmonic approximation is defined by

$$\underbrace{F(t)}_{\substack{\text{measured/}\\ \text{calculated}}} \approx \underbrace{F_0 + \alpha \sin(\tfrac{2\pi}{T}\, t) + \beta \cos(\tfrac{2\pi}{T}\, t)}_{\text{first harmonic approximation}} . \tag{6.39}$$

A least squares approach over one period from $n\,T$ to $(n+1)T$

$$\frac{1}{2} \int_{nT}^{(n+1)T} \left\{ F_0 + \alpha \sin\left(\tfrac{2\pi}{T}\, t\right) + \beta \cos\left(\tfrac{2\pi}{T}\, t\right) - F(t) \right\}^2 dt \longrightarrow \text{Minimum} \tag{6.40}$$

grants an approximation that fits the original at best. The differentiation of Equation (6.40) with respect to the coefficients F_0, α, and β provides the necessary conditions for a minimum. It results in a system of linear equations

$$\begin{aligned} \int \Big(F_0 + \alpha \sin\left(\tfrac{2\pi}{T}\, t\right) + \beta \cos\left(\tfrac{2\pi}{T}\, t\right) - F(t) \Big)\, dt &= 0\,, \\ \int \Big(F_0 + \alpha \sin\left(\tfrac{2\pi}{T}\, t\right) + \beta \cos\left(\tfrac{2\pi}{T}\, t\right) - F(t) \Big) \sin\left(\tfrac{2\pi}{T}\, t\right)\, dt &= 0\,, \\ \int \Big(F_0 + \alpha \sin\left(\tfrac{2\pi}{T}\, t\right) + \beta \cos\left(\tfrac{2\pi}{T}\, t\right) - F(t) \Big) \cos\left(\tfrac{2\pi}{T}\, t\right)\, dt &= 0\,, \end{aligned} \tag{6.41}$$

where the integral limits from nT to $(n+1)T$ were just omitted. As the integration is performed here exactly over one period from nT to $(n+1)T$, the integrals in Equation (6.41) will simplify to

$$\int dt = T, \quad \int \sin dt = \int \cos dt = \int \sin\cos dt = 0\,, \quad \int \sin^2 dt = \int \cos^2 dt = \tfrac{1}{2} T\,, \tag{6.42}$$

which immediately deliver the coefficients as

$$F_0 = \tfrac{1}{T} \int F\, dt\,, \quad \alpha = \tfrac{2}{T} \int F \sin\, dt\,, \quad \beta = \tfrac{2}{T} \int F \cos\, dt\,. \tag{6.43}$$

However, these are exactly the first coefficients of a Fourier approximation. The first-order harmonic approximation in Equation (6.39) can now be written as

$$F(t) = F_0 + \hat{F} \sin\left(\tfrac{2\pi}{T}\, t + \Psi\right) = F_0 + \hat{F} \sin\left(2\pi\, f\, t + \Psi\right)\,, \tag{6.44}$$

where the amplitude and the phase angle of the sine function are defined by

$$\hat{F} = \sqrt{\alpha^2 + \beta^2} \qquad \text{and} \qquad \tan\Psi = \frac{\beta}{\alpha}\,. \tag{6.45}$$

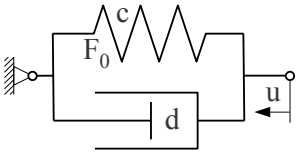

FIGURE 6.11
Linear preloaded spring and linear damper in parallel.

Figure 6.11 shows a simple nondynamic force element consisting of a linear spring with the stiffness c that is preloaded by the force F_0 and a linear damper with the constant d in parallel. It responds to the periodic excitation $u = A\,\sin(2\pi f t) = A\,\sin\left(\frac{2\pi}{T}t\right)$ with the force

$$F(t) \;=\; F_0 + c\,u + d\,\dot{u} \;=\; F_0 + \underbrace{c\,A}_{\alpha}\,\sin\left(2\pi f t\right) + \underbrace{d\,2\pi f}_{\beta}\,A\,\cos\left(2\pi f t\right)\,, \quad (6.46)$$

which represents exactly the first harmonic signal defined in Equation (6.39). Using Equation (6.45), it can be written in the form of Equation (6.44) where the amplitude and the phase angle are simply given by

$$\hat{F} \;=\; A\,\sqrt{c^2 + (2\pi f d)^2} \quad \text{and} \quad \tan\Psi = \frac{d\,2\pi f\,A}{c\,A} = 2\pi f\,\frac{d}{c}\,. \quad (6.47)$$

Hence, the response of a pure spring element ($c \neq 0$ and $d = 0$) is characterized by a force signal with the amplitude $\hat{F} = A\,c$ and a vanishing phase angle $\Psi = 0$, or respectively, $\tan\Psi = 0$. Whereas, a pure damper element ($c = 0$ and $d \neq 0$) will respond with a force signal of the amplitude $\hat{F} = 2\pi f d A$ and a maximum phase angle of $\Psi = 90°$, which corresponds to $\tan\Psi \rightarrow \infty$. As a consequence, the stiffness and damping properties of general force elements (nonlinear and/or dynamic) will be characterized in the sense of a first harmonic approximation by the dynamic stiffness, defined by

$$c_{dyn} \;=\; \frac{\hat{F}}{A}\,, \quad (6.48)$$

and the phase angle Ψ, which is also called the dissipation angle.

6.2.1.2 Sweep Sine Excitation

In practice, the frequency response of a system is not determined punctually, but continuously. For this, the system is excited by a sweep sine. In analogy to the simple sine function

$$x_e(t) \;=\; A\,\sin(2\pi\,f\,t)\,, \quad (6.49)$$

where the period $T = 1/f$ appears as prefactor at differentiation

$$\dot{x}_e(t) \;=\; A\,2\pi\,f\,\cos(2\pi\,f\,t) \;=\; \frac{2\pi}{T}\,A\,\cos(2\pi\,f\,t)\,. \quad (6.50)$$

A generalized sine function can be constructed now. Starting with

$$x_e(t) \;=\; A\,\sin(2\pi\,h(t))\,, \tag{6.51}$$

the time derivative results in

$$\dot{x}_e(t) \;=\; A\,2\pi\,\dot{h}(t)\,\cos(2\pi\,h(t))\,. \tag{6.52}$$

In the following we demand that the function $h(t)$ generates periods fading linearly in time;

$$\dot{h}(t) \;=\; \frac{1}{T(t)} \;=\; \frac{1}{p-q\,t}\,, \tag{6.53}$$

where $p>0$ and $q>0$ are constants yet to determine. Equation (6.53) yields

$$h(t) \;=\; -\,\frac{1}{q}\ln(p-q\,t)\;+\;C\,. \tag{6.54}$$

The initial condition $h(t=0)=0$ fixes the integration constant to

$$C \;=\; \frac{1}{q}\ln p\,. \tag{6.55}$$

With Equations (6.55) and (6.54), Equation (6.51) results in a sine-like function

$$x_e(t) \;=\; A\,\sin\Big(\frac{2\pi}{q}\,\ln\frac{p}{p-q\,t}\Big)\,, \tag{6.56}$$

which is characterized by linear fading periods. The important zero values for determining the period duration lie at

$$\frac{1}{q}\,\ln\frac{p}{p-q\,t_n}=0,1,2,\cdots \quad\text{or}\quad \frac{p}{p-q\,t_n}=e^{n\,q}\,,\ \text{with } n=0,1,2,\cdots \tag{6.57}$$

and

$$t_n=\frac{p}{q}\big(1-e^{-n\,q}\big)\,,\ n=0,1,2,\cdots \tag{6.58}$$

The time difference between two zero values yields the period

$$\begin{aligned} T_n \;&=\; t_{n+1}-t_n \;=\; \tfrac{p}{q}\big(1-e^{-(n+1)q}-1+e^{-nq}\big) \\ &=\; \tfrac{p}{q}\big(-e^{-nq}\,e^{-q}+e^{-nq}\big) \;=\; \tfrac{p}{q}\,e^{-nq}\,\big(1-e^{-q}\big) \end{aligned}\quad,\ n=0,\,1,\,2,\cdots \tag{6.59}$$

For the first ($n=0$) and last ($n=N$) period, one finds

$$\begin{aligned} T_0=\tfrac{1}{f_0} \;&=\; \tfrac{p}{q}\,\big(1-e^{-q}\big)\,, \\ T_N=\tfrac{1}{f_e} \;&=\; \tfrac{p}{q}\,\big(1-e^{-q}\big)\,e^{-N\,q} \;=\; T_0\,e^{-N\,q} \;=\; \tfrac{1}{f_0}\,e^{-N\,q}\,. \end{aligned} \tag{6.60}$$

With the frequency range to investigate, given by the initial f_0 and final frequency f_E, the parameter q and the ratio q/p can be calculated from Equation (6.60),

$$q \;=\; \frac{1}{N}\,\ln\frac{f_E}{f_0} \quad\text{and}\quad \frac{q}{p} \;=\; f_0\left\{1-\left[\frac{f_E}{f_0}\right]^{\frac{1}{N}}\right\}, \tag{6.61}$$

with $N+1$ fixing the number of cycles. The passing of the whole frequency range will then take the time

$$t_{N+1} \;=\; \frac{p}{q}\left(1 - e^{-(N+1)\,q}\right) \;. \tag{6.62}$$

Even if the period of the cycles is changed rather rapidly, the sweep sine generated by Equation (6.56) is close to pure sine functions calculated with the periods of the corresponding cycles, Figure 6.12. In this simple example the

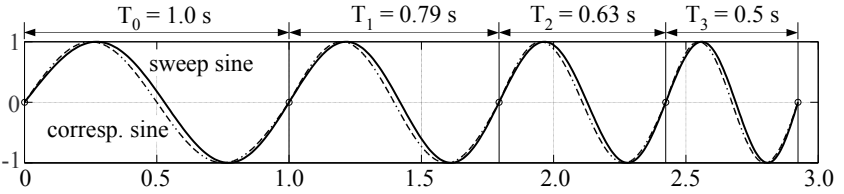

FIGURE 6.12
Sweep sine example.

sine-like function sweeps from $f_0 = 1\ Hz$ to $f_e = 2\ Hz$ in $N+1 = 4$ cycles. The parameter $q = 0.2310$ and the ratio $q/p = 0.2063$ are determined by Equation (6.61) and the duration $t_{N+1} = 2.9237\ s$ is provided by Equation (6.62). This method is very efficient in practical applications because it allows sweeping through large frequency ranges in a rather short time.

6.2.2 Spring Damper in Series

6.2.2.1 Modeling Aspects

Usually, suspension dampers are attached at the chassis via rubber topmounts. This combination represents a dynamic force element where a spring is arranged in series to a damper, Figure 6.13. The coordinate s describes the

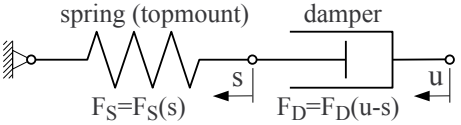

FIGURE 6.13
Spring and damper in series.

displacements of the force element and u denotes the overall deflection of the force element. Then, the forces acting in the spring and the damper are modeled as

$$F_S = F_S(s) \qquad \text{and} \qquad F_D \;=\; F_D(v) \;=\; F_D\left(\dot{u} - \dot{s}\right) \;, \tag{6.63}$$

where $v = \dot{u} - \dot{s}$ denotes the time derivative of the damper displacement. For this massless element, the force balance

$$F_D\,(\dot{u} - \dot{s}) \;=\; F_S(s) \tag{6.64}$$

must hold. By introducing F_D^{-1} as the inverse damper characteristic, Equation (6.64) converts into a nonlinear first-order differential equation for the force displacement s,

$$\dot{s} \;=\; -\,F_D^{-1}\,(F_S(s)) \;+\; \dot{u}\,, \tag{6.65}$$

which is driven by the time derivative $\dot{u}$ of the overall element deflection and characterizes the dynamic behavior of this force element.

6.2.2.2 Linear Characteristics

If the spring and the damper are modeled by linear characteristics, the forces in the spring and the damper are simply given by

$$F_S = c\,s \qquad \text{and} \qquad F_D \;=\; d\,(\dot{u} - \dot{s})\,, \tag{6.66}$$

where c names the spring stiffness and d denotes the damping constant. Now, the force balance $F_S = F_D$ delivers a linear first-order differential equation for the spring displacement s,

$$d\,(\dot{u} - \dot{s}) = c\,s \quad \text{or} \quad \dot{s} = -\frac{c}{d}\,s + \dot{u} \quad \text{or} \quad \frac{d}{c}\,\dot{s} = -s + \frac{d}{c}\,\dot{u}\,, \tag{6.67}$$

where the ratio between the damping coefficient d and the spring stiffness c acts as time constant $T = d/c$ hereby. In this simple case, the steady-state response to a pure harmonic excitation

$$u(t) \;=\; u_0 \sin \Omega t\,, \quad \text{and} \quad \dot{u} \;=\; u_0 \Omega \cos \Omega t\,, \quad \text{respectively,} \tag{6.68}$$

can be calculated quite easily. The steady-state response will be of the same type as the excitation. Inserting

$$s_\infty(t) \;=\; u_0\,(a\,\sin \Omega t + b\,\cos \Omega t) \tag{6.69}$$

into Equation (6.67) results in

$$\frac{d}{c}\,\underbrace{u_0\,(a\Omega \cos \Omega t - b\Omega \sin \Omega t)}_{\dot{s}_\infty} \;=\; -\,\underbrace{u_0\,(a \sin \Omega t + b \cos \Omega t)}_{s_\infty} + \frac{d}{c}\,\underbrace{u_0 \Omega \cos \Omega t}_{\dot{u}}\,. \tag{6.70}$$

Collecting all sine and cosine terms, we obtain two equations,

$$-\frac{d}{c}\,u_0\,b\Omega \;=\; -u_0\,a \quad \text{and} \quad \frac{d}{c}\,u_0\,a\,\Omega \;=\; -u_0\,b \;+\; \frac{d}{c}\,u_0 \Omega\,, \tag{6.71}$$

which can be solved for the two unknown parameters,

$$a \;=\; \frac{\Omega^2}{\Omega^2 + (c/d)^2} \qquad \text{and} \qquad b \;=\; \frac{c}{d}\,\frac{\Omega}{\Omega^2 + (c/d)^2}\,. \tag{6.72}$$

Then, the steady-state force response reads as

$$F_S \;=\; c\,s_\infty \;=\; c\,u_0\,\frac{\Omega}{\Omega^2 + (c/d)^2}\,\left(\Omega\,\sin\Omega t \;+\; \frac{c}{d}\,\cos\Omega t\right)\,, \tag{6.73}$$

which can be transformed to

$$F_S \;=\; \hat{F}_S\,\sin\left(\Omega t + \Psi\right)\,, \tag{6.74}$$

where the force magnitude $\hat{F}_S$ and the dissipation angle Ψ are given by

$$\hat{F}_S = \frac{c\,u_0\,\Omega}{\Omega^2+(c/d)^2}\,\sqrt{\Omega^2+(c/d)^2} = \frac{c\,u_0\,\Omega}{\sqrt{\Omega^2 + (c/d)^2}}\,, \tag{6.75}$$

$$\Psi = \arctan\frac{c/d}{\Omega}\,, \tag{6.76}$$

The dynamic stiffness $c_{dyn} = \hat{F}_S/u_0$ and the dissipation angle Ψ are plotted in Figure 6.14 for different damping values. With increasing frequency, the spring

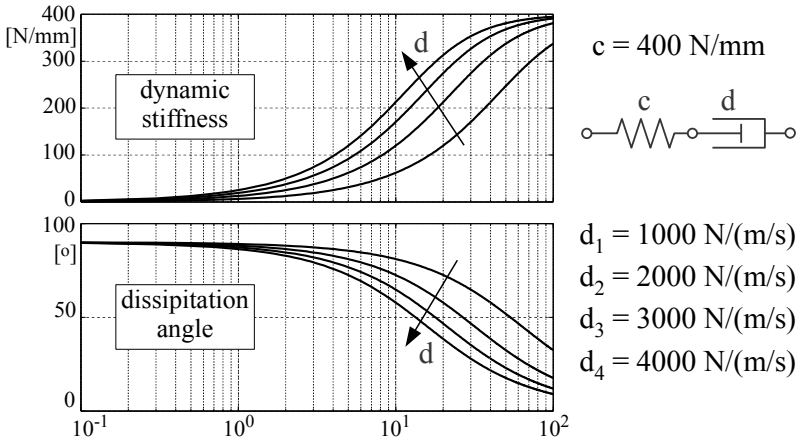

FIGURE 6.14
Frequency response of a linear spring damper combination.

damper combination changes from a pure damper performance ($c_{dyn} \to 0$ and $\Psi \approx 90°$) to a pure spring behavior ($c_{dyn} \approx c$ and $\Psi \to 0$). The frequency range, where the element provides stiffness and damping, is controlled by the value for the damping constant d.

6.2.2.3 Nonlinear Damper Topmount Combination

In Listing 6.1, a nonlinear damper characteristic $F_D = F_D(v)$ is described by a look-up table, which can easily be converted to the inverse characteristic. For the sake of simplicity, the compliance of the topmount will be described by a linear spring here. The function damper_topmount_f in Listing 6.4 provides the sweep sine excitation and computes the dynamics of the damper topmount combination.

Listing 6.4
Function `damper_topmount_f.m`: Damper Topmount Dynamics

```
function sdot = damper_topmount_f(t,s)
% damper topmount dynamics including sweep sine excitation

  global damper_inv c  p  q  amp

% sweep excitation
  ud = 2*pi*amp/(p-q*t)*cos(2*pi/q*log(p/(p-q*t)));
% spring force (linear)
  fs = c*s;
% force element dynamics
  sdot = -interp1l(damper_inv,fs) + ud ;

end
```

The corresponding MATLAB-Script damper_topmount_main provided in Listing 6.5 sets the data, runs the simulation in the frequency range from $f_0 = 0.1\,Hz$ to $f_E = 25\,Hz$, performs the least squares approximation in each cycle by solving the appropriate overdetermined system of linear equations, computes the dynamic stiffness as well as the dissipation angle, and finally plots the results. The stiff low-order solver ode23s is used for the time integration because the stiffness of the topmount is considerably large.

Listing 6.5
Function `damper_topmount_main.m`: Damper Topmount Frequency Response

```
global damper_inv c  p  q  amp

% damper characteristics F_D=F_D(v) as lookup table [ v F_D ]
ffr = 100; % define friction force and extend lookup table appropriately
damper_table = ...
[ -1.5080 -3500-ffr; ...
  -1.1310 -2800-ffr; ...
  -0.5655 -1500-ffr; ...
  -0.4524 -1250-ffr; ...
  -0.3016 -1000-ffr; ...
  -0.1508  -650-ffr; ...
  -0.0377  -200-ffr; ...
   0.0000     0-ffr; ...
   0.0000     0+ffr; ...
   0.0377   100+ffr; ...
   0.1508   150+ffr; ...
   0.3016   200+ffr; ...
```

```
18     0.4524   250+ffr; ...
19     0.5655   300+ffr; ...
20     1.1310   500+ffr; ...
21     1.5080   600+ffr ];
22
23  % inverse damper characteristic (lookup table)
24  damper_inv = [damper_table(:,2),damper_table(:,1)];
25
26  % topmount stiffness [N/m]
27  c = 400000;
28
29  % define sweep sine excitation
30  f0 =  0.1;   % lowest frequency [Hz]
31  fe =   25;   % highest frequency [Hz]
32  n  =   50;   % number of frequency interval
33  amp=  0.01;  % amplitudes [m]
34
35  % sweep sine parameter
36  q = 1/n * log ( fe/f0 ) ; p = q / ( f0 * ( 1 - (f0/fe)^(1/n) ) ) ;
37
38  % pre-allocate vars to speed up loop
39  freq=zeros(n+1,1); f0=zeros(n+1,1); fs=zeros(n+1,1); fc=zeros(n+1,1);
40
41  t0=0; s0=0; x0=s0;% initial conditions for first cycle
42  for ifreq=1:n+1
43
44  % Integrate from t0 to te results in freq = 1/(te-t0)
45    te=p/q*(1-exp(-ifreq*q));
46    freq(ifreq)=1/(te-t0); disp(['f=',num2str(freq(ifreq))])
47    [t,xout] = ode23s(@damper_topmount_f,[t0,te],x0);
48
49  % excitation
50    arg = 2*pi/q*log(p./(p-q*t)); se=sin(arg); ce=cos(arg);
51
52  % element force = force in topmount
53    s = xout(:,1);  f = c*s;
54
55  % curve fit to force (1. harmonic): f = f0 + fs*sin(arg) + fc*cos(arg)
56    A = [ones(size(arg)) se ce ] ;  coeff = A \ f ;
57    f0(ifreq) = coeff(1); % offset
58    fs(ifreq) = coeff(2); % sine part
59    fc(ifreq) = coeff(3); % cosine part
60
61  % set initial conditions for next cycle
62    t0=te; x0=xout(length(t),:)';
63
64  end
65
66  % calculate dynamic stiffness and phase angle (tan(psi)=beta/alpha)
67  cdyn = sqrt(fs.^2+fc.^2)/amp; psi = atan2(fc,fs)*180/pi;
68
69  % plot frequence response
70  subplot(3,1,1), plot(freq,cdyn,'k','Linewidth',1), grid on
71  subplot(3,1,2), plot(freq, psi,'k','Linewidth',1), grid on
72  subplot(3,1,3), plot(freq, f0,'k','Linewidth',1), grid on
```

Note that the nonlinear damper characteristic is extended to a dry friction component. This will cause the damper force F_D to jump from $-F_{Fr}$ to $-F_{Fr}$ at vanishing damper velocities $v = 0$, which results in a discontinuous damper characteristic. However, the dynamics of the damper topmount combination is computed via the inverse damper characteristic, which is still nonlinear and may have sharp bends but nevertheless is a continuous function, Figure 6.15. The frequency response of the damper topmount combination is shown in Figure 6.16. Besides the results for an excitation amplitude of $A = 1\,cm$ that will be generated by the MATLAB-Script in Listing 6.5, the results for the excitation amplitude of $A = 1\,mm$ and $A = 2\,cm$ are plotted too.

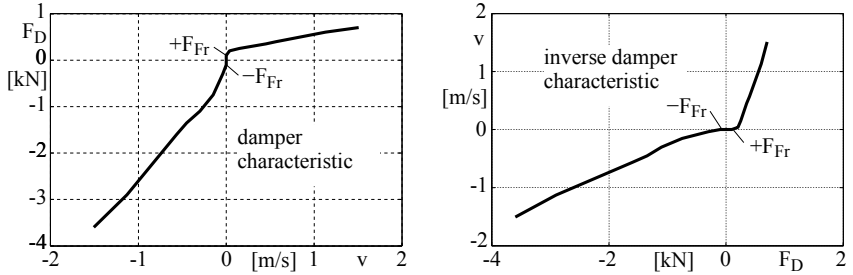

FIGURE 6.15
Nonlinear damper characteristic with dry friction and its inverse.

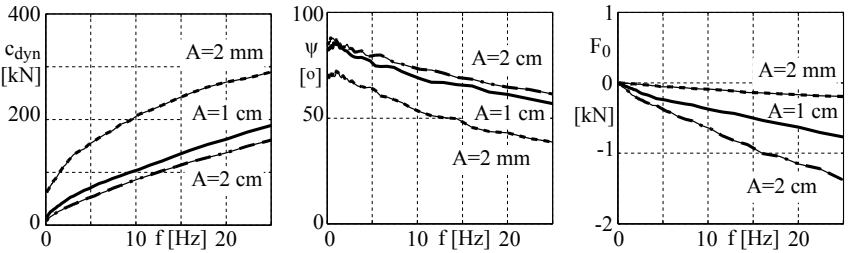

FIGURE 6.16
Frequency response of a damper topmount combination.

The overall behavior is similar to the linear spring damper element in series shown in Figure 6.14. Again, the damping properties decay with higher frequencies. This reduces the impact to the chassis when the vehicle is driven on a surface like cobble stones where higher frequencies are dominating the excitation. The frequency axis is scaled linearly because of the small frequency range. Due to the sharp bends in the inverse damper characteristic, the force element is not always perfectly in a steady-state condition, which causes small fluctuations in the frequency response, in particular visible in the phase angle ψ. In addition, the response depends on the excitation amplitude A, which

is typical for nonlinear force elements. As the damper shows more resistance during its rebound cycle than its compression cycle, the least squares approximation results in a force offset that increases with higher frequencies.

Force displacement diagrams for different amplitudes and frequencies illustrate the complex nonlinear behavior of this force element, Figure 6.17. In

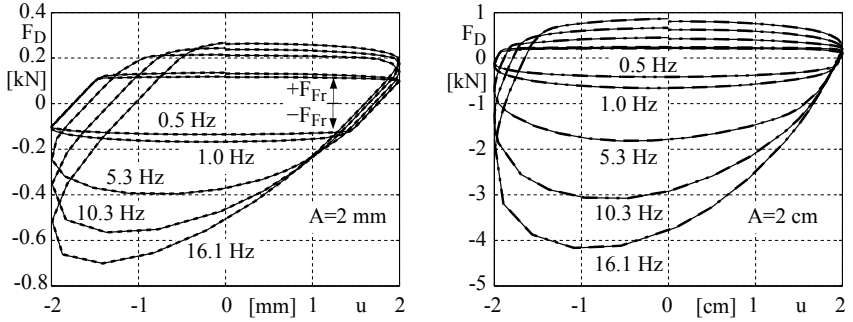

FIGURE 6.17
Force displacement diagrams of a damper topmount combination

particular, at low frequencies ($f = 0.5\,Hz$ and $f = 1\,Hz$) and small amplitudes ($A = 2\,mm$) the force displacement curves show typical stick slip cycles with an inclination at the left and right side corresponding with the stiffness $c = 400\,kN/m$ of the topmount and a a magnitude that is nearly entirely determined by the friction force $F_{Fr} = 0.1\,kN$. The results for a larger excitation amplitude ($A = 2\,cm$) are close to the pure damper response shown in Figure 6.6. However, the compliance of the topmount adds some spring effects that distort the force displacement curves accordingly.

6.2.3 General Dynamic Force Model

To approximate the complex dynamic behavior of bushings and elastic mounts, different spring damper models can be combined. Usually, several dynamic force elements consisting of a spring in series to a damper are arranged in parallel to a single spring that carries the static load and a damper, Figure 6.18. Spring damper elements in series are often referred as Maxwell models, whereas spring damper elements in parallel are known as Kelvin-Voigt or just Voigt models.

Springs and dampers may be described quite simply by their stiffness $c_0, c_1 \ldots c_N$ and their damping constants $d_0, d_1 \ldots d_N$, or by nonlinear characteristics. As done within the damper topmount model (*c.f.* Section 6.2.2.3), each dynamic force element may be supplemented by a dry friction component, F_{Fi}, $i = 1(1)N$, which will make it possible to describe hysteresis effects and to take even a stress history into account.

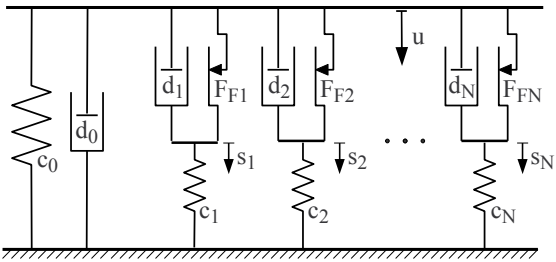

FIGURE 6.18
General dynamic force model.

6.2.4 Hydro-Mount

At first, hydro-mounts were introduced in the elastic suspension of engines to provide sufficient damping on one side and to achieve acoustic decoupling on the other side. Today, these dynamic force elements are also employed in axle suspensions. The principle and a dynamic model of a hydro-mount are shown in Figure 6.19. At small deformations, the change in the volume

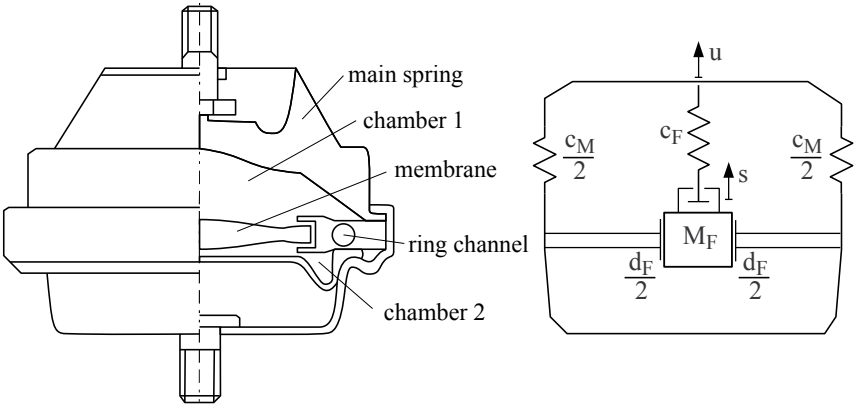

FIGURE 6.19
Hydro-mount: Layout and dynamic model.

in chamber 1 is compensated by displacements of the membrane. When the membrane reaches the stop, the liquid in chamber 1 is pressed through a ring channel into chamber 2. The ratio of the chamber cross-section to the ring channel cross-section is very large. Thus the fluid is moved through the ring channel at very high speed. This results in remarkable inertia and resistance forces (damping forces). The force effect of a hydro-mount is combined from the elasticity of the main spring and the volume change in chamber 1. The actual mass M_{FR} of the fluid in the ring channel is amplified by the ratio of

the cross-section areas A_C and A_R of the chamber and the ring channel and yields the generalized fluid mass

$$M_F \;=\; \Big(\frac{A_C}{A_R}\Big)^2 M_{FR}\,. \tag{6.77}$$

The motions of the fluid mass cause friction losses in the ring channel, which in a first approximation are modeled proportional to the velocity of the generalized fluid mass,

$$F_D \;=\; d_F\,\dot{s}\,, \tag{6.78}$$

where d_F denotes the corresponding damping constant. The force generated by the hydro-mount is given by

$$F \;=\; c_M\,u \;+\; F_F(u-s)\,, \tag{6.79}$$

where u and s denote the overall displacement and the displacement of the generalized fluid mass M_F, respectively. The force effect of the main spring $F_M = c_M\,u$ is simply modeled by a linear spring with the constant c_M and the fluid force $F_F = F_F(u-s)$ combines the compliance of the fluid and the elasticity of the membrane bearing. The fluid compliance is modeled by a linear spring with the stiffness c_F and the membrane bearing is approximated by a rounded clearance. Then, the force F_F will be provided by the function f_smooth_clear given in Listing 6.6

Listing 6.6
Function `f_smooth_clear`: Force Characteristic with Smoothed Clearance

```
1  function f = f_smooth_clear( x, c, s )
2    if abs(x) >= 2*s
3      f = sign(x) * c * ( abs(x) - s ) ;
4    else
5      f = sign(x) * c/(4*s) * x^2 ;
6    end
7  end
```

The spring is characterized by its stiffness c and the clearance, defined by the displacement s, is smoothed in the interval $-2s \le x \le +2s$ by appropriate parabolas. This is a quite realistic behavior in the case of the membrane bearing and avoids flutter problems that would occur when a sharp bend forms the transition from the clearance to the spring force. Then, the equation of motion for the fluid mass reads as

$$M_F\,\ddot{s} \;=\; -\,F_F - F_D\,. \tag{6.80}$$

The membrane clearance makes Equation (6.80) nonlinear and affects the overall force in the hydro-mount provided by Equation (6.79) too. The dynamic equations of the hydro-mount are provided in the Function hydro_mount_f, which is given in Listing 6.7.

Listing 6.7
Function `hydro_mount_f.m`: Hydro-Mount Dynamics

```
function xdot = hydro_mount_f(t,x)
% hydro mount including sweep sine excitation

  global mf  cf  sf  df   p  q  amp
% get states
  s = x(1); sdot = x(2);
% sweep sine excitation
  arg=2*pi/q*log(p/(p-q*t)); u=amp*sin(arg);
% fluid force including membran clearance
  ff = f_smooth_clear((u-s), cf, sf);
% acceleration of generalized fluid mass
  sddot = ( ff - df*sdot ) / mf ;
% state derivatives
  xdot = [ sdot; sddot ] ;

end
```

The MATLAB-Script in Listing 6.5 that computes the frequency response for a damper topmount combination can easily be adapted to the hydromount. The appropriately modified MATLAB-Script is provided in Listing 6.8.

Listing 6.8
Script `hydro_mount_main.m`: Hydro-Mount Frequency Response

```
global mf  cf  sf  df   p  q  amp

% define sweep sine excitation
f0 =  1;      % lowest frequency [Hz]
fe =  100;    % highest frequency [Hz]
n  =  50;     % number of frequency interval
amp= 0.0005; % amplitude [m]

% sweep sine parameter
q = 1/n * log ( fe/f0 ) ; p = q / ( f0 * ( 1 - (f0/fe)^(1/n) ) ) ;

% model data
mf=25;         % generalized fluid mass [kg]
cm=125000;     % stiffness of main spring [N/m]
df=750;        % fluid damping [N/(m/s)]
cf=100000;     % fluid stiffness [N/m]
sf=0.0002;     % clearance in mebrane support [m]

% pre-allocate vars to speed up loop
freq=zeros(n+1,1); f0=zeros(n+1,1); fs=zeros(n+1,1); fc=zeros(n+1,1);

t0=0; s0=0; sd0=0; x0 = [ s0 sd0 ]; % initial condition first cycle
for ifreq=1:n+1

% Integrate from t0 to te results in freq = 1/(te-t0)
  te=p/q*(1-exp(-ifreq*q));
  freq(ifreq)=1/(te-t0); disp(['f=',num2str(freq(ifreq))])
  [t,xout] = ode45(@hydro_mount_f,[t0,te],x0);
```

```
29
30 % excitation
31   arg=2*pi/q*log(p./(p-q*t)); se=sin(arg); ce=cos(arg);
32
33 % element force = force in main spring + fluid force
34   u=amp*se; f = cm*u;
35   for i=1:length(f), f(i)=f(i)+f_smooth_clear((u(i)-xout(i,1)),cf,sf); end
36
37 % curve fit to force (1. harmonic): f = f0 + fs*sin(arg) + fc*cos(arg)
38   A = [ ones(size(arg)) se ce ] ; coeff = A \ f ;
39   f0(ifreq) = coeff(1); % offset
40   fs(ifreq) = coeff(2); % sine part
41   fc(ifreq) = coeff(3); % cosine part
42
43 % set initial conditions for next cycle
44   t0=te; x0=xout(length(t),:)';
45
46 end
47
48 % calculate dynamic stiffness and phase angle (tan(psi)=beta/alpha)
49 cdyn = sqrt(fs.^2+fc.^2)/amp; psi = atan2(fc,fs)*180/pi ;
50
51 % plot frequence response
52 subplot(3,1,1), semilogx(freq,cdyn,'k','Linewidth',1), grid on
53 subplot(3,1,2), semilogx(freq, psi,'k','Linewidth',1), grid on
54 subplot(3,1,3), semilogx(freq, f0,'k','Linewidth',1), grid on
```

Note that the standard solver ode45 is used for the time integration because the dynamics of the hydro-mount are not stiff. The results, plotted in a semi logarithmic scaling, are shown in Figure 6.20. The dissipation angle ψ illustrates that the damping properties of the hydro-mount are limited to a small frequency range and reaches its maximum at $f \approx 8\,Hz$ here. In particular, at higher frequencies, damping is not noticeable at all, which represents a very good compromise between noise isolation at higher frequencies ($f > 20\,Hz$) and vibration damping in the range from 5 to 15 Hz. However, the dynamic stiffness c_{dyn} hardens significantly at higher frequencies, which will change the soft layout of an engine suspension to hard and transmit the engine shake caused by unbalanced masses to the chassis. The clearance in the membrane bearing bypasses this effect, at least at small amplitudes ($A = 0.5\,mm$) but will then provide no damping.

Exercises

6.1 According to Figure 6.4, the layout of a U-shaped anti-roll bar is defined by $a = 220\,mm$, $b = 700\,mm$ and $D = 19\,mm$. The ratio between the vertical displacements of the wheel center and the attachment points of the anti-roll bar is given by $i_{arb} = 0.7$.

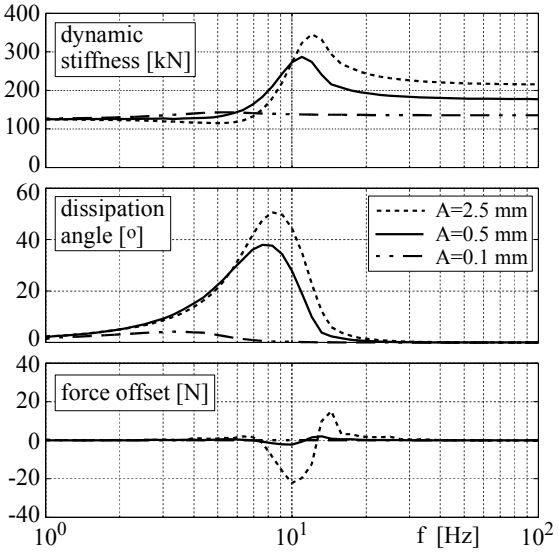

FIGURE 6.20
Frequency response of a hydro-mount.

Calculate its stiffness with respect to the vertical displacements of the attachment points and the wheel centers when the shear modulus of steel is given by $G = 85\,000\ N/mm^2$.

6.2 A damper is excited periodically with $u = u_0 \sin(2\pi f t)$ on a test rig. The tests are performed with the frequencies
$f_1 = 0.3\,Hz$, $f_2 = 0.6\,Hz$, $f_3 = 1.0\,Hz$, $f_4 = 1.5\,Hz$, $f_5 = 2.5\,Hz$, $f_6 = 4.0\,Hz$
and an amplitude of $u_0 = 0.04\,m$. The results are displayed in a force displacement diagram.

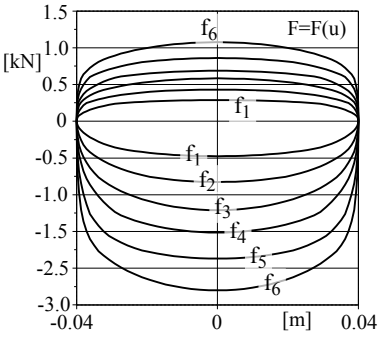

Generate the corresponding look-up table that describes the nonlinear damper characteristic $F = F(\dot{u})$.

6.3 Verify the results in Figure 6.9. Change the nonlinear damping characteristic, which according to Listing 6.1 is provided as look-up table, by multiplying the force values with appropriate factors and study its influence on the simulation results.

7

Vertical Dynamics

CONTENTS

7.1 Goals

The aim of vertical dynamics is the tuning of body suspension and damping to guarantee good ride comfort, respectively a minimal stress of the load at sufficient safety. The stress of the load can be judged fairly well by maximal or integral values of the body accelerations. The wheel load F_z is linked to the longitudinal force F_x and the lateral force F_y by the coefficient of friction. The degressive influence of F_z on F_x and F_y as well as nonstationary processes at the increase of F_x and F_y in the average lead to lower longitudinal and lateral forces at wheel load variations. Maximal driving safety can there-

fore be achieved with minimal variations in the wheel load. Small variations of the wheel load also reduce road damage. The comfort of a vehicle is subjectively judged by the driver and passengers. The vibration of a vehicle occurs in several directions, contains many frequencies, and changes over time. Via the seat it is transferred to all passengers. The driver is also exposed to the vibration of the steering wheel. Whole-body vibration may cause sensations (e.g., discomfort or annoyance), influence human performance capability, or present a health and safety risk. According to ISO-Directive 2631 [15], root-mean-square (r.m.s.) values of the body accelerations are used to judge the the effects of vibration on health and comfort. Because the human response to vibration is a function of frequency, the accelerations are filtered with frequency weighting curves. Different approaches of describing the human sense of vibrations by different metrics can be found in the literature [22].

The road excitation is transferred via the tire to the wheel, via the suspension system to the chassis and via the seat to the passengers. Soft suspension systems reduce the r.m.s. acceleration values of the chassis but will need a large suspension travel. Hence, a good ride comfort will always be a compromise between low acceleration values and limited suspension travel. The chassis acceleration and the suspension travel will thus be used as objective criteria.

7.2 From Complex to Simple Models

For detailed investigations of ride comfort and ride safety, sophisticated road and vehicle models are needed [46]. The three-dimensional vehicle model,

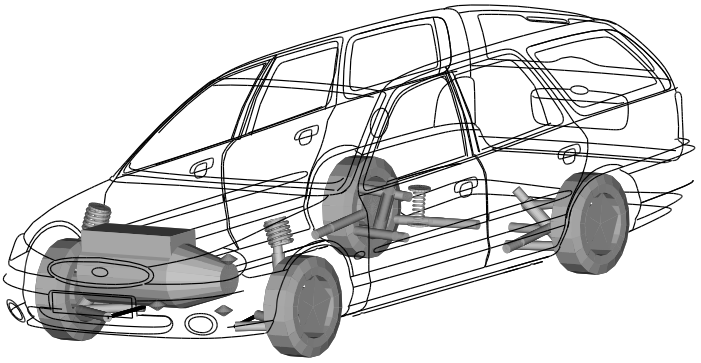

FIGURE 7.1
Full vehicle model.

shown in Figure 7.1, includes an elastically suspended engine and dynamic seat models. The elasto-kinematics of the wheel suspension was described as

fully nonlinear. In addition, dynamic force elements for the damper topmount combination and the hydro-mounts are used. Such sophisticated models not only provide simulation results that are in good conformity to measurements but also make it possible to investigate the vehicle dynamic attitude at an early design stage.

Much simpler models can be used, however, for fundamental studies of ride comfort and ride safety. If the vehicle is mainly driving straight ahead at constant speed, the hub and pitch motion of the chassis as well as the vertical motion of the axles will dominate the overall movement. Then, planar vehicle models can be used. A nonlinear planar model consisting of five rigid bodies with eight degrees of freedom is discussed in [45]. The model, shown

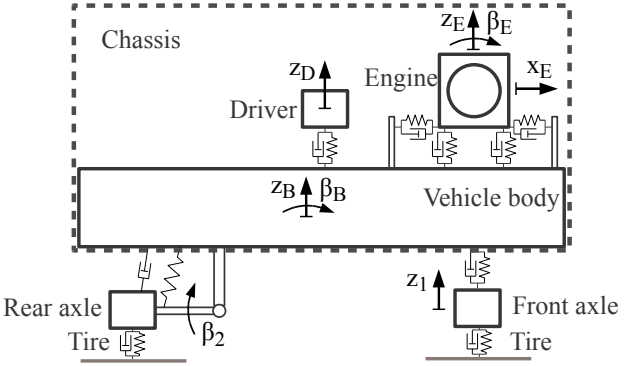

FIGURE 7.2
Sophisticated planar vehicle model.

in Figure 7.2, considers nonlinear spring characteristics of the vehicle body and the engine suspension, as well as degressive characteristics of the shock absorbers. Even the suspension of the driver's seat is taken into account here. Planar vehicle models suit perfectly with a single track road model.

In a further simplification, the chassis is considered as one rigid body. The corresponding simplified planar model has four degrees of freedom then, which at first are characterized by the hub and pitch motion of the chassis z_C, β_C, and the vertical motion of the axles z_{A1} and z_{A2}, Figure 7.3. By assuming small pitch motions ($\beta_C \ll 1$), the hub and pitch motion of the chassis can be combined to two new coordinates

$$z_{C1} = z_C - a_1\,\beta_C \quad \text{and} \quad z_{C1} = z_C + a_2\,\beta_C\,, \tag{7.1}$$

which describe the vertical motions of the chassis in the front and in the rear. In addition, mass and inertia properties of the chassis originally characterized by M and Θ are now represented by three point masses M^*, M_1, M_2, which are located in the chassis center C and on top of the front and the rear axle. The point masses must add up to the chassis mass

$$M_1 + M^* + M_2 \;=\; M\,, \tag{7.2}$$

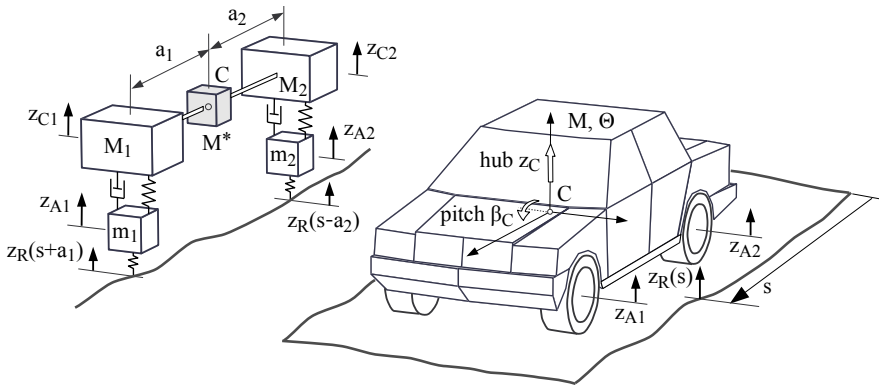

FIGURE 7.3
Vehicle model for basic comfort and safety analysis.

and they have to provide the same inertia around an axis located in the chassis center C and pointing into the lateral direction

$$a_1^2 M_1 + a_2^2 M_2 \;=\; \Theta\,. \tag{7.3}$$

The correct location of the center of gravity is assured by

$$a_1 M_1 = a_2 M_2\,. \tag{7.4}$$

Now, Equations (7.3) and (7.4) yield the main masses

$$M_1 \;=\; \frac{\Theta}{a_1(a_1+a_2)} \quad \text{and} \quad M_2 \;=\; \frac{\Theta}{a_2(a_1+a_2)}\,, \tag{7.5}$$

and the coupling mass

$$M^* \;=\; M\left(1 - \frac{\Theta}{M a_1 a_2}\right) \tag{7.6}$$

follows from Equation (7.2). If the mass and the inertia properties of a real vehicle happen to result in a vanishing or at least in a neglectible coupling mass $M^* \ll M_1, M_2$, then the planar model with four degrees of freedom can be represented by two separate models with two degrees of freedom that describe the vertical motion of the axle and the hub motion of the corresponding chassis mass on top of each axle. By using half the chassis and half the axle mass, we finally end up in quarter car models.

The data in Table 7.1 show that for a wide range of passenger cars the coupling mass is smaller than the corresponding chassis masses, $M^* < M_1$ and $M^* < M_2$. In these cases, the two mass models or the quarter car model represent quite a good approximation of the simple planar model. For commercial vehicles and trucks, however, where the coupling mass has the same

TABLE 7.1
Mass and Inertia Properties of Vehicles and Corresponding Model Data[2]

Vehicle and Model Properties		Mid-Size Car	Full-Size Car	Sports Utility Vehicle	Commercial Vehicle	Heavy Truck
Front axle mass	m_1 $[kg]$	80	100	125	120	600
Rear axle mass	m_2 $[kg]$	80	100	125	180	1100
Center of gravity	a_1 $[m]$	1.10	1.40	1.45	1.90	2.90
	a_2 $[m]$	1.40	1.40	1.38	1.40	1.90
Chassis mass	M $[kg]$	1100	1400	1950	3200	14300
Chassis inertia	Θ $[kg\,m^2]$	1500	2350	3750	5800	50000
Discrete mass model	M_1 [kg]	545	600	914	925	3592
	M^* $[kg]$	126	200	76	1020	5225
	M_2 [kg]	429	600	960	1255	5483

magnitude as the corresponding chassis masses, the quarter car model will serve for very basic studies only.

Finally, the function $z_R(s)$ provides road irregularities in the space domain, where s denotes the distance covered by the vehicle and measured at the chassis center of gravity. Then, the irregularities at the front and the rear axle are given by $z_R(s + a_1)$ and $z_R(s - a_2)$, respectively, where a_1 and a_2 locate the position of the chassis center of gravity C in the longitudinal direction. A quarter car model with a trailing arm suspension was presented in Section 1.5, further quarter car models are provided in this chapter.

For most vehicles, *c.f.* Table 7.1, the axle mass is much smaller than the corresponding chassis mass, $m_i \ll M_i$, $i = 1, 2$. Hence, for a first basic study, axle and chassis motions can be investigated independently. Now, the quarter car model is further simplified to two single mass models, Figure 7.4. The chassis model neglects the tire deflection and the inertia forces of the wheel. For the high frequent wheel motions, the chassis can be considered fixed to the inertia frame. The equations of motion for the chassis and the wheel model read as

$$M\,\ddot{z}_C \;+\; d_S\,\dot{z}_C \;+\; c_S\,z_C \;=\; d_S\,\dot{z}_R \;+\; c_S\,z_R\,, \tag{7.7}$$

$$m\,\ddot{z}_W \;+\; d_S\,\dot{z}_W \;+\; (c_S + c_T)\,z_W \;=\; c_T\,z_R\,, \tag{7.8}$$

where z_W and z_C define the vertical motions of the wheel mass and the corresponding chassis mass with respect to the steady-state position. The constants

[2]The commercial vehicle and the heavy truck is assumed to be fully laden, whereas the cars are only partly loaded by two passengers at the front seats.

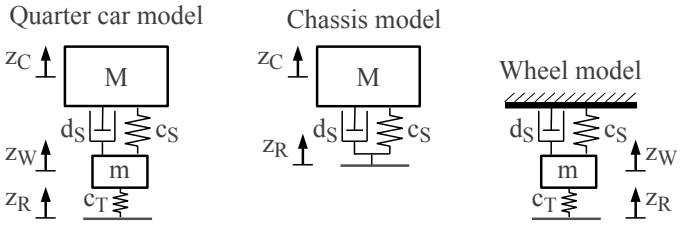

FIGURE 7.4
Simple vertical vehicle models.

c_S, d_S describe the suspension stiffness and damping. The dynamic wheel load is calculated by

$$F_T^D \;=\; c_T\,(z_R - z_W)\;, \tag{7.9}$$

where c_T is the vertical or radial stiffness of the tire and z_R denotes the road irregularities. In this simple approach the damping effects in the tire are not taken into account.

7.3 Basic Tuning

7.3.1 Natural Frequency and Damping Ratio

At an ideally even track, the right side of the equations of motion provided in Equations (7.7) and (7.8) vanishes because $z_R = 0$ and $\dot{z}_R = 0$ will hold then. The remaining homogeneous second-order differential equations can be written in a more general form as

$$\ddot{z} \;+\; 2\,\zeta\,\omega_0\,\dot{z} \;+\; \omega_0^2\,z \;=\; 0\,, \tag{7.10}$$

where ω_0 represents the undamped natural frequency and ζ is a dimensionless parameter called viscous damping ratio. For the chassis and the wheel model, the new parameter are defined by

$$\left.\begin{array}{rcl} z & \rightarrow & z_C \\ \zeta & \rightarrow & \zeta_C \\ \omega_0^2 & \rightarrow & \omega_{0C}^2 \end{array}\right\} \text{ Chassis: } \quad \zeta_C \;=\; \frac{d_S}{2\sqrt{c_S M}}\,, \qquad \omega_{0C}^2 \;=\; \frac{c_S}{M}\,,$$

$$\left.\begin{array}{rcl} z & \rightarrow & z_W \\ \zeta & \rightarrow & \zeta_W \\ \omega_0^2 & \rightarrow & \omega_{0W}^2 \end{array}\right\} \text{ Wheel: } \quad \zeta_W \;=\; \frac{d_S}{2\sqrt{(c_S+c_T)m}}\,, \quad \omega_{0W}^2 \;=\; \frac{c_S+c_T}{m}\,. \tag{7.11}$$

The solution of Equation (7.10) is of the type

$$z(t) \;=\; z_0\, e^{\lambda t}\,, \tag{7.12}$$

where t denotes the time and z_0, λ are constants yet to determine. Inserting Equation (7.12) into Equation (7.10) results in

$$(\lambda^2 + 2\,\zeta\,\omega_0\,\lambda + \omega_0^2)\, z_0\, e^{\lambda t} \;=\; 0\,. \tag{7.13}$$

Nontrivial solutions $z_0 \neq 0$ are possible if

$$\lambda^2 + 2\,\zeta\,\omega_0\,\lambda + \omega_0^2 \;=\; 0 \tag{7.14}$$

will hold. The roots of the characteristic equation (7.14) depend on the magnitude of the viscous damping ratio

$$\begin{aligned} \zeta < 1 \;:&\qquad \lambda_{1,2} = -\zeta\,\omega_0 \;\pm\; i\,\omega_0\,\sqrt{1-\zeta^2}\,, \\ \zeta \geq 1 \;:&\qquad \lambda_{1,2} = -\omega_0\,\left(\zeta \;\mp\; \sqrt{\zeta^2-1}\right)\,. \end{aligned} \tag{7.15}$$

Figure 7.5 shows the root locus of the eigenvalues for different values of the viscous damping ratio ζ. For damping ratios $\zeta \geq 1$, the eigenvalues $\lambda_{1,2}$ are

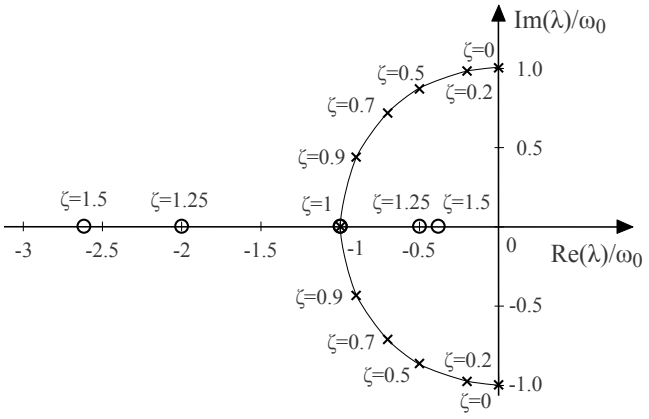

FIGURE 7.5
Eigenvalues λ_1 and λ_2 for different damping ratios ζ.

both real and negative. Hence, Eq. (7.12) will produce an exponentially decaying solution. If $\zeta < 1$ holds, the eigenvalues $\lambda_{1,2}$ will become complex, where λ_2 is the complex conjugate of λ_1. Now, the solution can be written as

$$z(t) \;=\; A\, e^{-\zeta\omega_0 t}\, \sin\left(\omega_0\,\sqrt{1-\zeta^2}\,t - \Psi\right)\,, \tag{7.16}$$

where A and Ψ are constants that must be adjusted to given initial conditions $z(0) = z_0$ and $\dot{z}(0) = \dot{z}_0$. The real part $Re\,(\lambda_{1,2}) = -\zeta\omega_0$ is always

negative and determines the decay of the solution over time. The imaginary part $Im\,(\lambda_{1,2}) = \omega_0\,\sqrt{1-\zeta^2}$ defines the actual frequency of the vibration. The actual frequency

$$\omega \;=\; \omega_0\,\sqrt{1-\zeta^2} \tag{7.17}$$

tends to zero, $\omega \to 0$, if the viscous damping ratio will approach the critical damping value $\zeta = 1$. In a more general way, the relative damping may also be judged by the ratio

$$D_\lambda = \frac{-Re(\lambda_{1,2})}{|\,\lambda_{1,2}\,|}\,. \tag{7.18}$$

For complex eigenvalues that characterize vibrations with viscous damping ratios $\zeta < 1$, the relative damping ratio equals the viscous damping ratio because the absolute value of the complex eigenvalues is given by

$$|\lambda_{1,2}| = \sqrt{Re(\lambda_{1,2})^2 + Im(\lambda_{1,2})^2} = \sqrt{(-\zeta\,\omega_0)^2 + \left(\pm\omega_0\,\sqrt{1-\zeta^2}\right)^2} = \omega_0\,. \tag{7.19}$$

Then, Equation (7.18) simply results in

$$D_\lambda^{\zeta<1} = \frac{+\zeta\,\omega_0}{\omega_0} \;=\; \zeta\,. \tag{7.20}$$

For $\zeta \geq 1$, the eigenvalues become real but are still negative. Then, its absolute value equals the negative real part and Equation (7.18) will always produce the relative damping ratio $D_\lambda^{\zeta\geq1} = 1$. In this case, the viscous damping ratio is more sensitive because, according to Equation (7.11), ζ is proportional to the damping value d.

The dimensionless ratios ζ and D_λ can be used to classify the type of the motion, Table 7.2, but they will not serve as proper judging criteria.

TABLE 7.2
Type of Motion for Single Mass Models

Damping Ratio / Type of Motion	Undamped Oscillation	Damped Oscillation	Damped Motion
Relative damping ratio	$D_\lambda = 0$	$0 < D_\lambda < 1$	$D_\lambda = 1$
Viscous damping ratio	$\zeta = 0$	$0 < \zeta < 1$	$\zeta \geq 1$

Even in this simple single mass model, the dimensionless damping ratios are a combination of several parameters. Hence, in order to evaluate the effect of the suspension damping d_S on the chassis motions and on the wheel load, the influence of the suspension stiffness c_S, the tire stiffness c_T, and the model masses M, m must also be taken into account.

7.3.2 Minimum Spring Rate

The suspension spring is loaded with the corresponding vehicle weight. For linear spring characteristics, the steady-state spring deflection is calculated from

$$u_0 \;=\; \frac{F_0}{c_S} \;=\; F_0 \frac{M\,g}{c_S}\,, \tag{7.21}$$

where M denotes the corresponding chassis mass and $F_0 = M\,g$ the preload of the the suspension spring, which is supposed to have a linear characteristic defined by its stiffness c_S. For a conventional suspension without niveau regulation, a load variation $M \rightarrow M + \Delta M$ changes the spring deflections from u_0 to $u_0 + \Delta u$. Analogous to Equation (7.21), the additional spring deflection follows from

$$\Delta u \;=\; \frac{\Delta M\,g}{c_S}\,. \tag{7.22}$$

However, the suspension travel and hence the additional spring deflection will be limited, $\Delta u \leq \Delta u_{max}$. Then, the suspension spring rate can be estimated by a lower bound

$$c_S \;\geq\; \frac{\Delta M_{max}\,g}{\Delta u_{max}}\,, \tag{7.23}$$

where ΔM_{max} denotes the maximum permissible load. In the standard design of a passenger car, the engine is located in the front and the trunk in the rear part of the vehicle. Hence, most of the load is supported by the rear axle suspension.

7.3.3 Example

As an example, we assume that 150 kg of the permissible load of 500 kg are going to the front axle. Then, each front wheel is loaded by $\Delta M_{FW} = 150\,kg/2 = 75\,kg$ and each rear wheel by $\Delta M_{RW} = (500 - 150)\,kg/2 = 175\,kg$. For standard passenger cars, the maximum wheel travel on compression is in the range of $u_{max} \approx 0.08\ m$ to $u_{max} \approx 0.10\ m$. By setting $\Delta u_{max} = u_{max}/2$, we demand that the spring deflection caused by the load should not exceed half of the maximum value. Then, according to Equation (7.23), a lower bound of the spring rate at the front axle can be estimated by

$$c_{SF}^{min} \;=\; (\,75\,kg * 9.81\,m/s^2\,)/(0.08/2)\,m \;=\; 18400\,N/m\,. \tag{7.24}$$

The maximum load over one rear wheel amounts here to $\Delta M_{RW} = 175\ kg$. Assuming that the suspension travel at the rear axle is slightly larger, $u_{max} \approx 0.10\,m$, the minimum spring rate at the rear axle can be estimated by

$$c_{SR}^{min} = (\,175\,kg * 9.81\,m/s^2\,)/(0.10/2)\,m = 34300\,N/m\,, \tag{7.25}$$

which is nearly two times the minimum value of the spring rate at the front axle. To reduce this difference, a spring rate of $c_{SF} = 20\,000\,N/m$ will be chosen at the front axle as a compromise.

7.3.4 Undamped Eigenfrequencies

In Table 7.1 the discrete mass chassis model of a full-size passenger car is described by $M_1 = M_2 = 600\,kg$ and $M^* = 200\,kg$. To separate the model into two decoupled two mass models, we have to neglect the coupling mass or, in order to achieve the same chassis mass, to distribute M^* equally to the front and the rear. Then, the corresponding chassis mass over one front wheel is obtained as

$$M_{FW} \;=\; \left(M_1 + M^*/2\right)/2 \;=\; (600\,kg + 200/2\,kg)/2 \;=\; 350\,kg\,. \qquad (7.26)$$

According to Equation (7.11), the undamped natural eigenfrequency of the simple chassis model is given by $\omega_{0C}^2 = c_S/M$. Hence, for the chosen spring rate of $c_{SF} = 20000\,N/m$, the undamped natural frequency of the unloaded car amounts to

$$f_{0C}^0 \;=\; \frac{1}{2\pi}\sqrt{\frac{20000\,N/m}{350\,kg}} \;=\; 1.2\,Hz\,, \qquad (7.27)$$

which is a typical value for most passenger cars. Due to the small amount of load, the undamped natural frequency for the loaded car does not change very much,

$$f_{0C}^L \;=\; \frac{1}{2\pi}\sqrt{\frac{20000\,N/m}{(350+75)\,kg}} \;=\; 1.1\,Hz\,. \qquad (7.28)$$

The corresponding chassis mass over the rear axle is given here by

$$M_{RW} \;=\; \left(M_2 + M^*/2\right)/2 \;=\; (600\,kg + 200/2\,kg)/2 \;=\; 350\,kg\,. \qquad (7.29)$$

The undamped natural frequencies for the quarter car chassis model at the rear axle result in

$$f_{0C}^0 \;=\; \frac{1}{2\pi}\sqrt{\frac{34\,300\,N/m}{350\,kg}} \;=\; 1.6\,Hz\,, \qquad (7.30)$$

$$f_{0C}^L \;=\; \frac{1}{2\pi}\sqrt{\frac{34\,300\,N/m}{(350+175)\,kg}} \;=\; 1.3\,Hz\,. \qquad (7.31)$$

Now, the frequencies for the loaded and unloaded car differ more and are larger than the ones at the front axle.

7.3.5 Influence of Damping

To investigate the influence of suspension damping on the chassis and wheel motion, the simple vehicle models are exposed to initial disturbances. Both time simulations start at $t = 0$ with vanishing velocities, $\dot{z}_C(t=0) = 0$, $\dot{z}_W(t=0) = 0$ and displacements, which by $z_C(t=0) = M\,g/c_S$ and

$z_W(t = 0) = (M + m)\, g/c_T$, are adjusted to the system parameters such that the suspension spring and the tire, respectively are unloaded at the very beginning. The time response of the chassis displacement $z_C(t)$ and the wheel displacement $z_W(t)$ as well as the chassis acceleration $\ddot{z}_C$ and the wheel load or the vertical tire force F_T are shown in Figure 7.6 for different damping rates ζ_C and ζ_W. The wheel load is composed of the the static wheel load

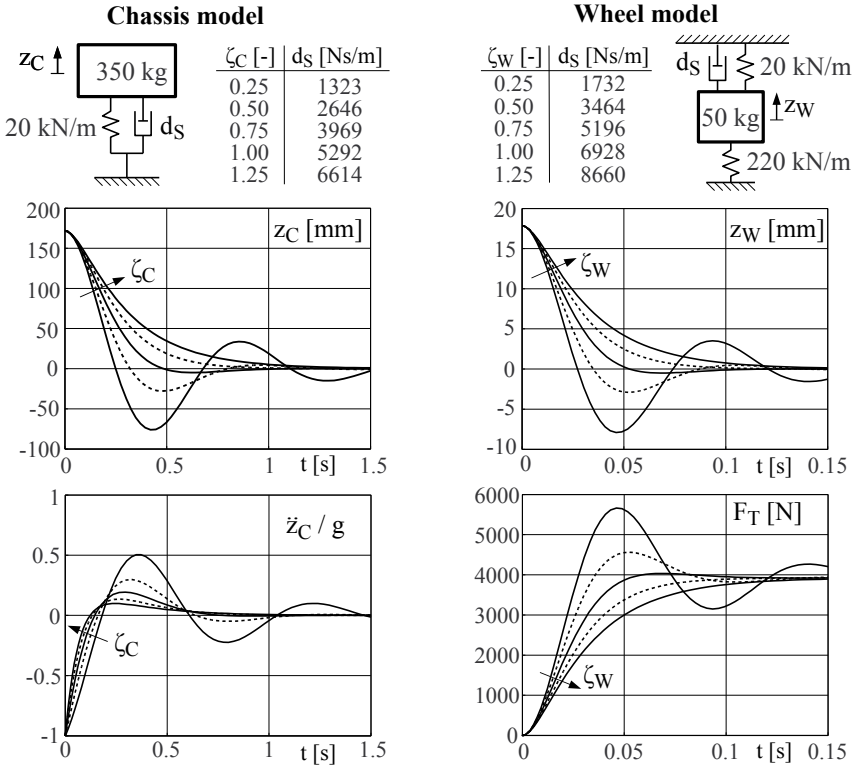

FIGURE 7.6
Time response of simple vehicle models to initial disturbances.

$F_T^0 = (M + m)\, g$ and the dynamic wheel load F_T^D, which follows from Equation (7.9). To achieve the same damping rates for the chassis and the wheel model, different values for the damping parameter d_S were needed.

With increased damping, the overshoot effect in the time history of the chassis displacement and the wheel load becomes smaller and smaller until it vanishes completely at $\zeta_C = 1$ and $\zeta_W = 1$. Note that the periods of the chassis and the wheel oscillations differ quite a lot, which justifies the decoupling of the quarter car model into two single mass oscillators. Usually, as it is here, the corresponding damping values will be different. Hence, a simple linear damper can either avoid overshoots in the chassis motions or in the wheel loads. However, the overshoot in the time history of the chassis

accelerations $\ddot{z}_C(t)$ will only vanish for $\zeta_C \to \infty$, which surely is not a desirable configuration, because then, it will take a very long time for the initial chassis displacement to fully disappear.

7.4 Optimal Damping

7.4.1 Disturbance Reaction Problem

A vehicle running over a rough road will be exposed to a series of disturbances. So, a suspension system designed such that the time history of the chassis displacement, the chassis acceleration, and the wheel load to an arbitrary disturbance will approach the corresponding steady-state values as fast as possible may be regarded as perfect or optimal. The typical time response of a damped single-mass oscillator to the initial disturbance defined by $z(t=0) = z_0$ and $\dot{z}(t=0) = 0$ is shown in Figure 7.7.

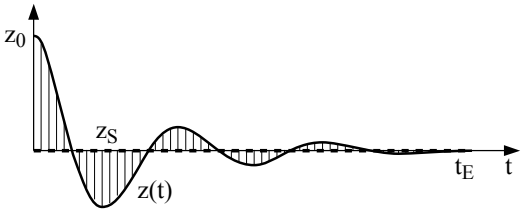

FIGURE 7.7
Evaluating a damped oscillation.

Counting the differences of the system response $z(t)$ from the steady-state value $z_S = 0$ as errors allows one to judge the attenuation. If the overall quadratic error calculated in an appropriate time interval $0 \le t \le t_E$ becomes a minimum,

$$\epsilon^2 = \int_{t=0}^{t=t_E} z(t)^2 \, dt \to Min \,, \tag{7.32}$$

then the system will surely approach the steady-state position as fast as possible. In theory, $t_E \to \infty$ will hold; for practical applications, a finite t_E must be chosen appropriately. For nonlinear systems, Equation (7.32) must be solved numerically, which may be quite time consuming. However, there exists an algebraic solution for linear systems.

In general, linear dynamic systems are described by the state equation

$$\dot{x} = A\,x + B\,u \quad \text{with} \quad x(t=0) = x_0 \,, \tag{7.33}$$

where x denotes the state vector that collects generalized coordinates and their derivatives, the state matrix A represents the dynamics of the system,

the term $B\,u$ describes the excitation, and x_0 describes the initial state. The steady-state solution $x(t \to \infty) = x_S$ to a step input at $t = 0$ with $u = u_0$ results in

$$0 \;=\; A\,x_S \;+\; B\,u_0 \quad \text{or} \quad x_S \;+\; A^{-1}\,B\,u_0\,. \tag{7.34}$$

Applying the state transformation $x = \bar{x} - x_S$ to Equation (7.33) results in

$$\frac{d}{dt}\,(\bar{x} - x_S) \;=\; A\;(\bar{x} - x_S) + B\,u \quad \text{with} \quad x(t=0) = x_0 = \bar{x}(t_0) - x_S\,, \tag{7.35}$$

which, using Equation (7.34), simplifies to

$$\dot{\bar{x}} \;=\; A\,\bar{x} \quad \text{with} \quad \bar{x}(t_0) = \bar{x}_0 = x_0 + x_S\,. \tag{7.36}$$

So, the response of a linear dynamic system to a step input $u = u_0$ at $t = 0$ is equivalent to an initial disturbance $\bar{x}_0 = x_0 + x_S$ applied to the transformed system. As an extension to Equation (7.32), the transition of the state $\bar{x}(t)$ to its steady-state value $\bar{x}(t \to \infty) = 0$ may be judged by the more general disturbance-reaction problem

$$\epsilon^2 \;=\; \int_{t=0}^{t=t_E} \bar{x}^T\,Q\,\bar{x}\,dt \;\to\; Min\,, \tag{7.37}$$

where $Q = Q^T$ is a symmetric matrix of appropriate size that allows one to weight the components of the state vector x individually [7]. For $t_E \to \infty$, the integral in Equation (7.37) is solved by

$$\int_{t=0}^{t\to\infty} \bar{x}^T\,Q\,\bar{x}\,dt \;=\; \bar{x}_0^T\,R\,\bar{x}_0\,, \tag{7.38}$$

where $\bar{x}(t \to \infty) = 0$ was taken for granted. The symmetric matrix $R = R^T$ is defined by the Ljapunov equation,

$$A^T R \;+\; R\,A \;+\; Q \;=\; 0\,. \tag{7.39}$$

In general, the Ljapunov equation will be solved numerically by appropriate algorithms. For the single-mass oscillator described by Equation (7.10), the state equation (7.36) reads as

$$\underbrace{\begin{bmatrix} \dot{z} \\ \ddot{z} \end{bmatrix}}_{\dot{\bar{x}}} = \underbrace{\begin{bmatrix} 0 & 1 \\ -\omega_0^2 & -2\zeta\omega_0 \end{bmatrix}}_{A} \underbrace{\begin{bmatrix} z \\ \dot{z} \end{bmatrix}}_{\bar{x}}\,. \tag{7.40}$$

Then, the Ljapunov equation

$$\begin{bmatrix} 0 & -\omega_0^2 \\ 1 & -2\zeta\omega_0 \end{bmatrix} \begin{bmatrix} R_{11} & R_{12} \\ R_{12} & R_{22} \end{bmatrix} + \begin{bmatrix} R_{11} & R_{12} \\ R_{12} & R_{22} \end{bmatrix} \begin{bmatrix} 0 & 1 \\ -\omega_0^2 & -2\zeta\omega_0 \end{bmatrix} + \begin{bmatrix} Q_{11} & Q_{12} \\ Q_{12} & Q_{22} \end{bmatrix} \tag{7.41}$$

delivers three linear equations,

$$\begin{aligned} -\omega_0^2\, R_{12} - \omega_0^2\, R_{12} &+ Q_{11} &= 0\,, \\ -\omega_0^2\, R_{22} + R_{11} - 2\zeta\omega_0\, R_{12} &+ Q_{12} &= 0\,, \\ R_{12} - 2\zeta\omega_0\, R_{22} + R_{12} - 2\zeta\omega_0\, R_{22} &+ Q_{22} &= 0\,, \end{aligned} \tag{7.42}$$

which can easily be solved for the elements of R. The first and third equations deliver

$$R_{12} = \frac{Q_{11}}{2\omega_0^2}\,, \quad R_{22} = \frac{1}{4\zeta\omega_0}\left(\frac{Q_{11}}{\omega_0^2} + Q_{22}\right)\,. \tag{7.43}$$

Finally, the second equation provides

$$R_{11} = \left(\zeta + \frac{1}{4\zeta}\right)\frac{Q_{11}}{\omega_0} - Q_{12} + \frac{\omega_0}{4\zeta}\, Q_{22}\,. \tag{7.44}$$

If the initial state is characterized by an initial displacement $z(t=0) = z_0$ and a vanishing initial velocity $\dot{z}(t=0) = 0$, the disturbance reaction problem defined in Equation (7.38) will simplify to

$$\begin{aligned} \int_{t=0}^{t\to\infty} x^T(t)\, Q\, x(t)\, dt \;&=\; [\, z_0 \;\, 0\,]^T \begin{bmatrix} R_{11} & R_{12} \\ R_{12} & R_{22} \end{bmatrix} \begin{bmatrix} z_0 \\ 0 \end{bmatrix} \;=\; z_0^2 R_{11} \\ &=\; z_0^2 \left[\left(\zeta + \frac{1}{4\zeta}\right)\frac{Q_{11}}{\omega_0} - Q_{12} + \frac{\omega_0}{4\zeta}\, Q_{22} \right]\,, \end{aligned} \tag{7.45}$$

where ζ and ω_0 denote the viscous damping and the natural eigenfrequency of the single-mass oscillator.

7.4.2 Optimal Safety

Ride safety may be judged by dynamic wheel load variations. In the absence of road irregularities $z_R = 0$, the dynamic wheel load computed in Equation (7.9) simplifies to $F_T^D = -c_T z_W$. Then, optimal ride safety is achieved by

$$\epsilon_S^2 \;=\; \int_{t=0}^{t\to\infty} \left(F_T^D\right)^2 dt \;=\; \int_{t=0}^{t\to\infty} \left(-c_T\, z_W\right)^2 dt \;=\; \int_{t=0}^{t\to\infty} c_T^2\, z_W^2\, dt \;\to\; Min\,. \tag{7.46}$$

This demand can easily be transformed to the corresponding general disturbance reaction problem,

$$\epsilon_S^2 = \int_{t=0}^{t\to\infty} c_T^2\, z_W^2\, dt = \int_{t=0}^{t\to\infty} \left[\, z_W \;\, \dot{z}_W \,\right] \begin{bmatrix} c_T^2 & 0 \\ 0 & 0 \end{bmatrix} \begin{bmatrix} z_W \\ \dot{z}_W \end{bmatrix} \;\to\; Min\,, \tag{7.47}$$

where $x_W^T = \left[\, z_W \;\; \dot{z}_W \,\right]$ denotes the state vector of the wheel model and the weighting matrix Q is defined by the coefficients

$$Q_{11} = c_T^2\,, \quad Q_{12} = 0\,, \quad Q_{22} = 0\,. \tag{7.48}$$

According to Equation (7.45), the integral in Equation (7.47) is solved by

$$\epsilon_S^2 = \int_{t=0}^{t\to\infty} c_T^2\, z_W^2\, dt = z_{0W}^2 \left(\zeta_W + \frac{1}{4\zeta_W}\right) \frac{c_T^2}{\omega_{0W}}\,, \tag{7.49}$$

where the specific coefficients of the weighting matrix Q provided by Equation (7.48) were already taken into account.

A soft tire ($c_T \to 0$) makes the safety criteria in Equation (7.49) small ($\epsilon_S^2 \to 0$) and thus reduces the dynamic wheel load variations. However, the tire spring stiffness cannot be reduced to arbitrary low values because this would cause too large tire deformations and finally damage the tire.

Small wheel masses ($m \to 0$) will increase the natural eigenfrequency ($\omega_{0W} = \sqrt{(c_S + c_T)/m}$) and thus reduce the safety criteria in Equation (7.49) too. So, the use of light metal rims will indeed improve the ride safety of a car because of the wheel weight reduction.

In principle, large values for the natural eigenfrequency ω_{0W} could be achieved by hardening the suspension spring $c_S \to \infty$ but this will contradict good driving comfort.

With fixed values for c_T and ω_{0W}, the merit function in Equation (7.49) will become a minimum if

$$\frac{\partial \epsilon_S^2}{\partial \zeta_W} \;=\; \frac{z_{0W}^2}{\omega_{0W}} \left(1 + \frac{-1}{4\zeta_W^2}\right) c_T^2 \;=\; 0 \tag{7.50}$$

will hold. Hence, a viscous damping rate of

$$\zeta_W^{opt}\big|_{Safety} \;=\; \frac{1}{2} \tag{7.51}$$

will guarantee optimal ride safety by minimizing the merit function in Equation (7.49). According to Equation (7.11), this corresponds to the damping parameter

$$d_S^{opt}\big|_{Safety} \;=\; \sqrt{(c_S + c_T)\, m}\,. \tag{7.52}$$

7.4.3 Optimal Comfort

To judge the ride comfort, the hub motion of the chassis z_C and its acceleration $\ddot{z}_C$ can be used as objective criteria. Hence, the demand

$$\epsilon_C^2 \;=\; \int_{t=0}^{t=t_E} \Big[\; \big(\, \alpha\, \ddot{z}_C \,\big)^2 \;+\; \big(\, \beta\, z_C \,\big)^2 \;\Big]\, dt \;\to\; Min \tag{7.53}$$

will guarantee optimal ride safety. By the factors α and β the acceleration and the hub motion can be weighted differently.

The equation of motion for the chassis model provided by Equation (7.7) can be resolved for the acceleration

$$\ddot{z}_C \;=\; -\left(\omega_{0C}^2\, z_C + 2\zeta_C\omega_{0C}\,\dot{z}_C\right)\;, \tag{7.54}$$

where the absence of road irregularities $z_R = 0$, $\dot{z}_R = 0$ was taken into account and, as done in Equation (7.11), the system parameters M, c_S, and d_S are summarized in the viscous damping ratio ζ_C and in the undamped natural eigenfrequency ω_{0C}. Then, the problem in Equation (7.53) can be written as

$$\begin{aligned}
\epsilon_C^2 \;&=\; \int_{t=0}^{t=t_E} \left[\alpha^2\,\left(\omega_{0C}^2 z_C + 2\zeta_C\omega_{0C}\dot{z}_C\right)^2 \;+\; \beta^2\, z_C^2\right] dt \\
&=\; \int_{t=0}^{t=t_E} \left[\, z_C\;\dot{z}_C \,\right] \begin{bmatrix} \alpha^2\left(\omega_{0C}^2\right)^2 + \beta^2 & \alpha^2\omega_{0C}^2 2\zeta_C\omega_{0C} \\ \alpha^2\omega_{0C}^2 2\zeta_C\omega_{0C} & \alpha^2(2\zeta_C\omega_{0C})^2 \end{bmatrix} \begin{bmatrix} z_C \\ \dot{z}_C \end{bmatrix} \;\rightarrow\; Min\,,
\end{aligned} \tag{7.55}$$

where $x_C^T = \left[\; z_C \;\; \dot{z}_C \;\right]$ is the state vector of the chassis model and the weighting matrix Q is defined by the coefficients

$$Q_{11} = \alpha^2\left(\omega_{0C}^2\right)^2 + \beta^2\,, \quad Q_{12} = 2\alpha^2\zeta_C\omega_{0C}^3\,, \quad Q_{22} = 4\alpha^2\zeta_C^2\omega_{0C}^2\,. \tag{7.56}$$

According to Equation (7.45), the integral in Equation (7.55) evaluating the ride comfort is solved by

$$\begin{aligned}
\epsilon_C^2 \;&=\; z_{C0}^2 \left[\left(\zeta_C + \frac{1}{4\zeta_C}\right)\frac{Q_{11}}{\omega_{0C}} - Q_{12} + \frac{\omega_{0C}}{4\zeta_C}\,Q_{22}\right] \\
&=\; z_{0C}^2 \left[\left(\zeta_C + \frac{1}{4\zeta_C}\right)\frac{\alpha^2\left(\omega_{0C}^2\right)^2 + \beta^2}{\omega_{0C}} - 2\alpha^2\zeta_C\omega_{0C}^3 + \frac{\omega_{0C}}{4\zeta_C}\,4\alpha^2\zeta_C^2\omega_{0C}^2\right] \\
&=\; z_{0C}^2 \left[\alpha^2\,\frac{\omega_{0C}^3}{4\zeta_C} \;+\; \beta^2\left(\zeta_C + \frac{1}{4\zeta_C}\right)\frac{1}{\omega_{0C}}\right]\,.
\end{aligned} \tag{7.57}$$

By setting $\alpha = 1$ and $\beta = 0$, the time history of the chassis acceleration $\ddot{z}_C$ is weighted only. Equation (7.57) then simplifies to

$$\epsilon_C^2\big|_{\ddot{z}_C} \;=\; z_{0C}^2\,\frac{\omega_{0C}^3}{4\zeta_C}\,, \tag{7.58}$$

which will become a minimum if either the viscous damping ratio tends to infinity or the undamped natural frequency to zero. As mentioned before, $\zeta_C \rightarrow \infty$ surely is not a desirable configuration. A low undamped natural frequency $\omega_{0C} \rightarrow 0$ is achieved by a soft suspension spring $c_S \rightarrow 0$ or a large chassis mass $M \rightarrow \infty$. However, a large chassis mass is not economical and the suspension stiffness is limited by the loading conditions. Hence, weighting the chassis accelerations only does not lead to a specific result for the system parameters here.

Practical results can be achieved if the attenuation of the chassis acceleration $\ddot{z}_C$ and the chassis displacement z_C are evaluated simultaneously. To do so, appropriate weighting factors must be chosen. In the equation of motion for the chassis mass (7.7), the terms $M\,\ddot{z}_C$ and $c_S\,z_C$ are added. Hence, $\alpha = M$ and $\beta = c_S$ or

$$\alpha \;=\; 1 \qquad \text{and} \qquad \beta \;=\; \frac{c_S}{M} \;=\; \omega_{0C}^2 \tag{7.59}$$

will provide weighting factors that are automatically adjusted to the relevant system parameters. Now, Equation (7.57) reads as

$$\epsilon_C^2 = z_{0C}^2 \left[\frac{\omega_{0C}^3}{4\zeta_C} + \left(\omega_{0C}^2\right)^2 \left(\zeta_C + \frac{1}{4\zeta_C} \right) \frac{1}{\omega_{0C}} \right] = z_{0C}^2 \omega_{0C}^2 \left[\frac{\omega_{0C}}{2\zeta_C} + \zeta_C\,\omega_{0C} \right] . \tag{7.60}$$

Again, good ride comfort will be achieved by $\omega_{0C} \to 0$. For finite undamped natural frequencies, Equation (7.60) becomes a minimum if the viscous damping rate ζ_C satisfies

$$\frac{d\,\epsilon_C^2\big|_{z_C}}{d\,\zeta_C} \;=\; z_{0C}^2\,\omega_{0C}^2 \left[\frac{-\omega_{0C}}{2\zeta_C^2} + \omega_{0C} \right] \;=\; 0\,. \tag{7.61}$$

Hence, a viscous damping rate of

$$\zeta_C^{Comfort} \;=\; \frac{1}{2}\sqrt{2} \tag{7.62}$$

or a damping parameter of

$$d_S^{opt}\Big|_{Comfort}^{\zeta_C = \frac{1}{2}\sqrt{2}} \;=\; \sqrt{2\,c_S M} \tag{7.63}$$

will provide optimal comfort by minimizing the merit function in Equation (7.60).

7.4.4 Example

For the passenger car with sprung and unsprung masses of $M = 350\,kg$ and $m = 50\,kg$ and spring rates for the suspension and the tire of $c_S = 20\,000\,N/m$ and $c_T = 220\,000\,N/m$ the damping parameter for optimal ride safety will now amount to

$$d_S^{opt}\Big|_{Safety}^{\zeta_W = \frac{1}{2}} = \sqrt{(20\,000\;N/m + 220\,000\;N/m) * 50\;kg} = 3464\;N/(m/s) \tag{7.64}$$

and the one for optimal ride comfort to

$$d_S^{opt}\Big|_{Comfort}^{\zeta_C = \frac{1}{2}\sqrt{2}} = \sqrt{2\,20\,000\;N/m\;*\;350\;kg} = 3742\;N/(m/s)\,. \tag{7.65}$$

As it is here, the values will not coincide in general. Hence, a vehicle suspension with a simple linear damper can either provide optimal ride comfort or optimal ride safety, but not both. Improvements may be achieved by nonlinear, dynamic, and active or semi-active force elements. But then, more complex vehicle models must be used.

7.5 Practical Aspects

7.5.1 General Remarks

The disturbance reaction problem in combination with two single-mass oscillators for the chassis and the wheel just provides a first approach to determine optimal values for the damping parameter. In practice, the performance of vehicles driving on real roads is of greater importance. The merit function defined in Equation (7.46) represents an objective criteria to judge the ride safety of a vehicle. In general, road irregularities are of a stochastic nature. According to Section 2.3.1, the standard deviation, which is the square root of the variance, characterizes the statistical properties of a stationary Gaussian random process. Then, optimal ride safety may be achieved by minimizing the variance of the dynamic wheel load,

$$\sigma_S^2 \;=\; \frac{1}{t_E - t_0} \int_{t_0}^{t_E} \frac{F_T^D(t)}{F_T^S}\, dt \;\rightarrow\; Min\,, \tag{7.66}$$

where the time history of the dynamic wheel load $F_T^D = F_T^D(t)$ is normalized to the static wheel load F_T^S and evaluated in an appropriate time interval from $t = t_0$ to $t = t_E$.

The demand in Equation (7.53) that provides optimal ride comfort in combination with the weighting factors defined in Equation (7.59) will hold for the simple chassis model only. In practice, the focus in evaluating the ride comfort is usually placed on the chassis accelerations at the seat mountings. During the optimization process, at least the suspension travel have to be monitored too, because it is limited by the suspension design. As a consequence, optimal driving comfort may be achieved now by minimizing an appropriate combination of the acceleration variance and the suspension travel,

$$\sigma_C^2 \;=\; \frac{1}{t_E - t_0} \int_{t_0}^{t_E} \left[\left(\frac{\ddot{z}(t)}{g} \right)^2 \;+\; \left(\frac{s(t)}{s_R} \right)^2 \right] dt \;\rightarrow\; Min\,, \tag{7.67}$$

where instead of using weighting factors, the acceleration $a = a(t)$ is normalized to the constant of gravity g and the suspension travel $s = s(t)$ to a reference value s_R.

For linear systems, the covariance analysis can be used to determine the corresponding variances. As shown in [29], an algebraic solution for a single wheel mass oscillator is possible again. It turns out, that a viscous damping ratio of $\zeta_W = 0.5$ minimizes the wheel load variance and hence will provide optimal ride safety in the case of stochastic excitation. This value exactly coincides with the value found by solving the corresponding disturbance reaction problem.

7.5.2 Quarter Car Model on Rough Road

In standard vehicle suspension systems, springs, and dampers are mounted between the wheel and the chassis. As a consequence, body and wheel/axle motions will be affected simultaneously. That is why a simple quarter car model will be used further on instead of the separate mass models for the chassis and the wheel. The equations of motion for the quarter car model, shown in Figure 7.4, are given by

$$\begin{aligned} M\,\ddot{z}_C &= F_S + F_D - M\,g\,, \\ m\,\ddot{z}_W &= F_T - F_S - F_D - m\,g\,, \end{aligned} \tag{7.68}$$

where the displacements of the chassis z_C and the wheel z_W are measured from the equilibrium position. The terms Mg and mg represent the weights of the chassis and the wheel. Assuming linear characteristics, the suspension forces and the wheel load are provided by

$$F_S = F_S^0 + c_S\,(z_W - z_C)\,, \quad F_D = d_S\,(\dot{z}_W - \dot{z}_C)\,, \quad F_T = F_T^0 + c_T\,(z_R - z_W)\,, \tag{7.69}$$

where z_W describes the irregularities of the road, the constants c_S, d_S characterize the stiffness and damping properties of the suspension, and c_T denotes the tire stiffness. The preloads of the suspension spring and the tire are simply given by

$$F_S^0 = M\,g\,, \quad F_T^0 = (M+m)\,g\,, \tag{7.70}$$

and the demand $F_T \geq 0$ will take wheel liftoff into account.

The MATLAB-Script qcm_simple_main provided in Listing 7.1 performs simulations of a simple quarter car model driving at constant speed on a rough road with different values of the suspension damping.

Listing 7.1
Script `qcm_simple_main.m`: Evaluating Ride Comfort and Safety

```
1  global grav M m  cS  dS  cT  FS0 FT0 FT
2  global v_veh Amp Om Psi
3
4  grav=9.81; sR=0.05; % gravity [m/s^2] & reference susp. travel [m]
5  M=350;   m= 50;     % chassis & wheel mass (quarter car) [kg]
6  cS=20000; cT=220000; % suspension & tire stiffness [N/m]
7  dSvar=1000:200:5000; % suspension damping [N/(m/s)]
8  tE=10; v_veh=100/3.6; % simulation time [s] & vehicle velocity [km/h->m/s]
9  Phi0=10e-6;w=2;n=1000; % spectral density, waviness & number of samples
10 Omin=2*pi/200; Omax=2*pi/0.2; % range of frequencies
11
12 % compute amplitudes and random phases
13 Om0=1; dOm=(Omax-Omin)/(n-1); Om=Omin:dOm:Omax;
14 Phi=Phi0.*(Om./Om0).^(-w); Amp=sqrt(2*Phi*dOm);
15 RandStream.setDefaultStream(RandStream('mt19937ar','seed',5489));
16 Psi=2*pi*rand(size(Om));
17
18 FS0 = M*grav; FT0 = (m+M)*grav; % spring and tire preload
19
```

```
20 % initial values (adjust to road height)
21 zr0=sum(Amp.*sin(Psi)); x0 = [ zr0; zr0; 0; 0 ] ;
22
23 % calculate merit functions for different damping values
24 eps_safety=zeros(size(dSvar)); eps_comfort=zeros(size(dSvar));
25 for k=1:length(dSvar)
26
27   dS=dSvar(k); disp(['perform simulation for dS=',num2str(dS)])
28   [tout,xout] = ode45(@qcm_simple_f,[0,tE],x0);
29
30 % normalized suspension travel
31   st = ( xout(:,1)-xout(:,2) ) / sR ;
32
33 % get normalized acceleration and normalized dynamic wheel load
34   zcdd = zeros(size(tout)); FD = zeros(size(tout));
35   for i=1:length(tout)
36     xdot = qcm_simple_f(tout(i),xout(i,:)');
37     zcdd(i) = xdot(3)/grav; FD(i)= (FT-FT0)/FT0;
38   end
39
40 % merit functions (variation of dyn. wheel load, accel. & susp travel )
41   eps_safety(k) = var(FD); eps_comfort(k) = var(zcdd) + var(st);
42
43 end
44
45 % plot criteria versus damping values
46 plot(dSvar,eps_safety,'r'), hold on, grid on
47 plot(dSvar,eps_comfort,'--k'), legend('safety','comfort')
```

As in Section 2.3.4, the random road, defined by its power spectral density, is approximated by a series of sine functions. In line 15, the seed for the random number generator is explicitly set to the MATLAB default. This will force the MATLAB-Function rand to produce exactly the same series of random numbers not only when a new MATLAB session is started, but also each time when running the script qcm_simple_main. The data correspond with the single-mass models for the wheel and the chassis. According to Equation (7.67), the ride comfort is judged by the sum of the effective values of the normalized chassis acceleration and the suspension travel. The effective value of the dynamic wheel load normalized to the static load evaluates the ride safety. The MATLAB-Function var computes the variances. The state equation of the simple quarter car model as well as the computation of pseudo-random road irregularities are provided in the function qcm_simple_f, which is given in Listing 7.2.

Listing 7.2
Function `qcm_simple_f.m`: Simple Quarter Car Model on Random Road

```
1 function xp = qcm_simple_f(t,x) % simple quarter car model
2
3 global grav M m  cS  dS  cT  FS0 FT0 FT
4 global v_veh Amp Om Psi
5
6 zc=x(1); zw=x(2); zcd=x(3); zwd=x(4); % local state variables
```

```
7   s=v_veh*t; zr=sum(Amp.*sin(Om*s+Psi)); % generate pseudo random road
8
9   FS = FS0 + cS*(zw-zc); % linear spring force
10  FD = dS*(zwd-zcd); % linear damper force
11  FT = max([0, FT0+cT*(zr-zw)]); % wheel load (including lift off)
12
13  zcdd = (    FS + FD - M*grav ) / M ; % chassis acceleration
14  zwdd = (FT - FS - FD - m*grav ) / m ; % wheel acceleration
15
16  xp = [ zcd; zwd; zcdd; zwdd ]; % state derivatives
17
18  end
```

The simulation results are plotted in Figure 7.8. A simple inspection of the plot provides the damping parameter $d_S^S = 2600\,Ns/m$ and $d_S^C = 3000\,Ns/m$, which correspond to the minimum of the variances σ_S^2 and σ_C^2 and thus will provide optimal ride safety or optimal comfort respectively. Again, either op-

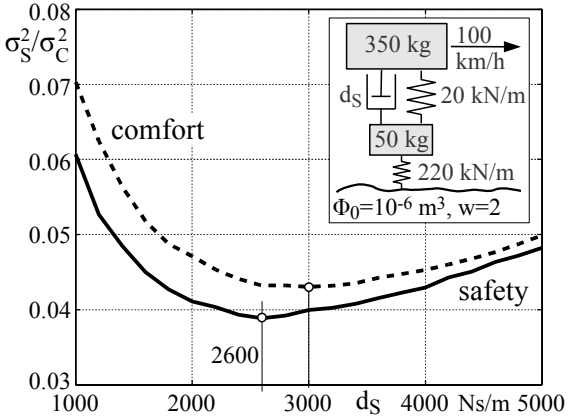

FIGURE 7.8
Variances to judge ride comfort and safety for different damping values.

timal safety or optimal comfort can be achieved here. Compared to the results of the single-mass models computed in Equations (7.64) and (7.65), the damping parameter that grants optimal safety is 25%, and the one that provides optimal comfort is 20% less than the corresponding values.

Optimization is always a delicate task. The results strongly depend on the merit function and on the complexity of the vehicle model. As shown in [46], the engine suspension for instance will have a significant influence on the chassis accelerations. Results that are in good conformity to measurements demand complex vehicle models, which include friction effects and nonlinearities. In addition, matching objective comfort criteria with the human sense of comfort is still a problem. The corresponding DIN/ISO directive [15] tries to evaluate the human exposure to whole-body vibration via frequency depen-

dent weighting functions. However, the main focus is placed here on physical fatigue and health hazards.

7.6 Nonlinear Suspension Forces

7.6.1 Progressive Spring

In order to reduce the spring rate and to avoid too large spring deflections when loaded, nonlinear spring characteristics are usually used, Figure 7.9. Adding soft bump stops, the overall spring force in the compression mode $u \geq 0$ can be modeled by the nonlinear function

$$F_S \;=\; F_S^0 \;+\; c_0\, u \left(1 + k \left(\frac{u}{\Delta u}\right)^2\right) , \tag{7.71}$$

where F_S^0 denotes the spring preload, c_0 describes the spring rate at $u = 0$, and $k \geq 0$ characterizes the intensity of the nonlinearity. The linear characteristic provides at $u = \Delta u$ the value $F_S^{lin}(\Delta u) = F_S^0 + c_S\, \Delta u$. To achieve the same value with the nonlinear spring,

$$F_S^0 + c_0\, \Delta u\, (1 + k) \;=\; F_S^0 + c_S\, \Delta u \quad \text{or} \quad c_0\, (1 + k) \;=\; c_S \tag{7.72}$$

must hold, where c_S describes the spring rate of the corresponding linear characteristics. The local spring rate is determined by the derivative

$$\frac{dF_S}{du} \;=\; c_0 \left(1 + 3\, k \left(\frac{u}{\Delta u}\right)^2\right) . \tag{7.73}$$

Then, the spring rate for the loaded car at $u = \Delta u$ is given by

$$c_L \;=\; c_0\, (1 + 3\, k) \; . \tag{7.74}$$

The intensity of the nonlinearity k can be fixed, for instance, by choosing an appropriate spring rate for the unloaded vehicle. With $c_0 = 20\,000\, N/m = 20\, kN/m$ the spring rates on the front and rear axle will here be the same for the unloaded vehicle. According to Equation (7.25), the stiffness value of a corresponding linear spring amounts to $c_S = 34\,300\, N/m = 34.3\, kN/m$. Then, Equation (7.72) delivers the intensity of the nonlinear spring by the value of

$$k \;=\; \frac{c_S}{c_0} - 1 \;=\; \frac{34.300}{20} - 1 \;=\; 0.715\, . \tag{7.75}$$

The solid line in the left plot of Figure 7.9 shows the resulting nonlinear spring characteristic that is characterized by the spring rates $c_0 = 20\, kN/m$

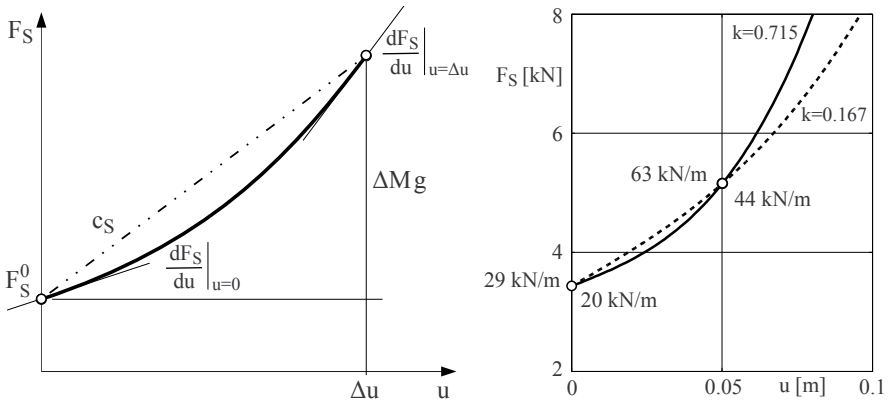

FIGURE 7.9
Principle and realizations of nonlinear spring characteristics.

and $c_L = c_0\,(1+3k) = 20 * (1+3*0.715) = 62.9\,kN/m$ for the unloaded and the loaded vehicle. Again, the undamped natural frequencies

$$f_{0C}^0 = \frac{1}{2\pi}\sqrt{\frac{20\,kN/m}{350\,kg}} = 1.20\,Hz\,, \quad f_{0C}^L = \frac{1}{2\pi}\sqrt{\frac{62.9\,kN/m}{(350{+}175)\,kg}} = 1.74\,Hz \tag{7.76}$$

for the unloaded and the loaded vehicle will differ quite a lot.

The unloaded and the loaded vehicle have the same undamped natural frequencies if

$$\frac{c_0}{M} = \frac{c_L}{M+\Delta M} \quad \text{or} \quad \frac{c_L}{c_0} = \frac{M+\Delta M}{M} \tag{7.77}$$

holds. Combining this relationship with Equation (7.74) yields

$$1+3\,k = \frac{M}{M+\Delta M} \qquad \text{or} \qquad k = \frac{1}{3}\left(\frac{M+\Delta M}{M} - 1\right) = \frac{1}{3}\,\frac{\Delta M}{M}\,. \tag{7.78}$$

Hence, for the quarter car model with $M = 350\,kg$ and $\Delta M = 175\,kg$ the intensity of the nonlinear spring reduces to $k = 1/3 * 175/350 = 0.167$. This value, combined with the corresponding linear spring stiffness $c_S = 34.3 kN/m$, will produce the dotted line in Figure 7.9. The spring rates $c_0 = c_S/(1+k) = 34.3\,N/m\,/\,(1+0.1667) = 29.4\,kN/m$ and $c_L = c_0\,(1+3k) = 29.400\,kN/m * (1+3*0.1667) = 44.1\,kN/m$, which apply for the unloaded and the loaded vehicle result from Equations (7.73) and (7.74). Now, the undamped natural frequency for the unloaded $f_{0C}^0 = \sqrt{c_0/M} = 1.46\,Hz$ and the loaded vehicle $f_{0C}^0 = \sqrt{c_L/(M+\Delta M)} = 1.46\,Hz$ are indeed the same.

7.6.2 Nonlinear Spring and Nonlinear Damper

The equations of motion for a simple quarter car model are provided in Equation (7.68). The spring travel is defined by

$$u \;=\; z_W - z_C \,, \tag{7.79}$$

where z_W and z_C describe the vertical displacements of the wheel and the chassis mass measured from the equilibrium position, Figure 7.10. Similar to

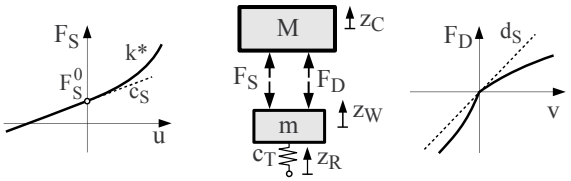

FIGURE 7.10
Quarter car model with nonlinear spring and damper elements.

Equation (7.71), the spring force is modeled by

$$F_S \;=\; F_S^0 \;+\; \begin{cases} c_S\, u & u < 0\,, \\ c_S\, u\, \left(1 + k^*\, u^2\right) & u \geq 0\,, \end{cases} \tag{7.80}$$

where c_S defines the stiffness at $u = 0$ and $F_S^0 = M\, g$ denotes the preload. The parameter $k^* \geq 0$ characterizes the nonlinearity in the compression cycle, $u > 0$, where $k^* = 0$ simply results in a linear spring with stiffness c_S. The nonlinear spring design in Section 7.6.1 provides at the rear axle the data

$$c_S = 29\,400\; N/m \quad \text{and} \quad k^* = \frac{k}{(\Delta u)^2} = \frac{0.1667}{(0.05\; m)^2} = 66.7\; m^{-2}\,. \tag{7.81}$$

The tire stiffness is given further on by $c_T = 220\,000\, N/m$ and the chassis and wheel mass are determined by $M = 350\; kg$ and $m = 50\; kg$. The function in Listing 7.2 computes linear suspension forces. Replacing the line

```
FS = FS0 + cS*(zw-zc); % linear spring force
```

by the code lines

```
u = zw - zc; % spring displacement (u>0: compression)
if u<0
  FS = FS0 + cS*u; % rebound
else
  FS = FS0 + cS*u*(1+kS*u^2); % compression
end
```

will provide a progressive spring characteristic according to Equation (7.80). In addition, the parameter kS must be added to the list of global variables not only in Listing 7.2, but also in Listing 7.1. Here, the parameter kS must be assigned a value of 66.7 and the spring constant must be changed to the value $c_S = 29\,400\, N/m$, which now holds for the rear axle.

The damper element is arranged parallel to the spring, which simply acts between the chassis and the wheel mass. Then, the time derivative of the suspension travel

$$\dot{u} \;=\; v \;=\; \dot{z}_W - \dot{z}_C \tag{7.82}$$

defines the damper velocity, where the sign convention is consistent with the spring travel. As a consequence, $u < 0$, $v < 0$ characterize tension or rebound and $u \geq 0$, $v \geq 0$ compression. As shown in Section 6.1.3, nonlinear damper characteristics are usually modeled via look-up tables. Typically, suspension dampers will have more resistance in the rebound than in the compression cycle. The piecewise linear but overall nonlinear characteristic

$$F_D(v) \;=\; \begin{cases} d_{Rb}\, v & v < 0 \\ d_{Cp}\, v & v \geq 0 \end{cases} \tag{7.83}$$

defined by the constants d_{Rb} and d_{Cp} takes this effect into account. According to Equation (7.82), $v < 0$ characterizes rebound and $v \geq 0$ the compression cycle. As a consequence, d_{Rb} describes the damping properties during rebound and d_{Cp} in the compression mode. A slight modification in Listing 7.2 will make the nonlinear damper available in the simple quarter car model. At first, the line

```
FD = dS*(zwd-zcd); % linear damper force
```

must be replaced with the code lines

```
v = zwd-zcd; % velocity (v>0: compression)
if v<0
  FD = dRb*v; % rebound
else
  FD = dCp*v; % compression
end
```

Then, the global variable dS must be replaced by dRb and dCp not only in this function, but also in Listing 7.1. Here, appropriate values must be assigned to the damping parameters also. By setting $d_{Rb} = d_{Cp}$, the linear damper characteristic is still available.

As done in Equation (7.69), the tire is modeled by a linear spring characterized by the constant c_T and the demand $F_T \geq 0$ takes wheel liftoff into account.

7.6.3 Some Results

At first, the influence of the nonlinear spring on ride comfort and safety is studied. As done in Section 7.5.2, the vehicle is driven with constant velocity on a rough road. The corresponding simulation results, computed for different values of a linear damper ($d_{Rb} = d_{Cp} = d_S$) are plotted in Figure 7.11. A comparison with the results in Figure 7.8 shows that the damping value $d_S^S = 2600\, Ns/m$, which provides optimal ride safety, is still valid. However, the damping value that grants optimal ride comfort has slightly increased

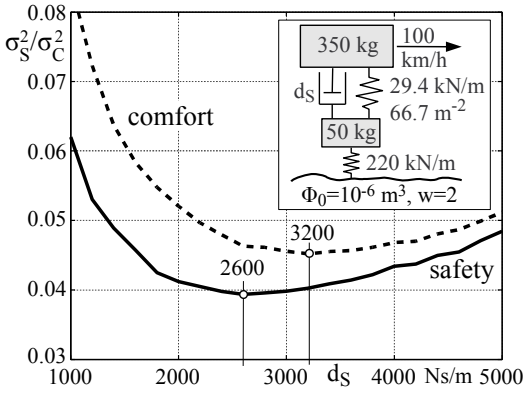

FIGURE 7.11
Comfort and safety for a nonlinear spring and a linear damper.

to $d_S^S = 3200\ Ns/m$. The single-mass approach ends up in the algebraic equations (7.52) and (7.63), which factor in the mass and stiffness properties of the quarter car model. Hence, increasing the suspension stiffness from $c_S = 20\ kN/m$ in Figure 7.8 to $c_S = 29.4\ kN/m$ in Figure 7.11 affects ride comfort and ride safety. However, the influence of the increased suspension stiffness on ride safety will hardly be noticeable because the suspension stiffness is much smaller than the tire stiffness, which was not changed here.

In general, a nonlinear damper layout with $d_{Cp} < d_{Rb}$ will generate less impact on the chassis when driving over single bumps because in the first part of the compression cycle, spring and damper force have the same sign and induce large chassis accelerations. Progressive spring characteristics, which are employed at the rear suspension in particular, will intensify this effect. Corresponding simulation results are plotted in Figure 7.12. The quarter car model, equipped with a linear and a nonlinear damper, is driven hereby with the velocity $v = 80\,km/h$ over a single obstacle. A cosine-shaped bump with a height of $H = 0.04\,m$ and a length of $L = 3.0\,m$ was used here. The damping properties in the rebound and compression cycle, are characterized by the constants $d_{Rb} = 4200\ Ns/m$ and $d_{Cp} = 1400\ Ns/m$. The average value $d_S = (d_{Rb}+d_{Cp})/2 = 2800 Ns/m$ describes the equivalent linear damper. Compared to the linear damper layout, the nonlinear damper characteristic results in significantly reduced peak values for the chassis acceleration ($6.39 m/s^2$ instead of $8.16\,m/s^2$) and for the wheel load ($7.07\,kN$ instead of $7.48\,kN$). However, the tire liftoff at $t \approx 0.16\,s$ could not be avoided here. As a quid pro quo the nonlinear damper requires a larger suspension travel ($4.0\,cm$ instead of $3.3\,cm$). Both layouts provide similar overall damping. The nonlinear spring force is described by Equation (7.80) and according to Equation (7.81), defined by the parameters $c_S = 29\,400\ N/m$ and $k^* = 66.7\,m^{-2}$.

While crossing a bump, large damper velocities occur in general. A low but constant damping rate in the compression mode will generate large damping

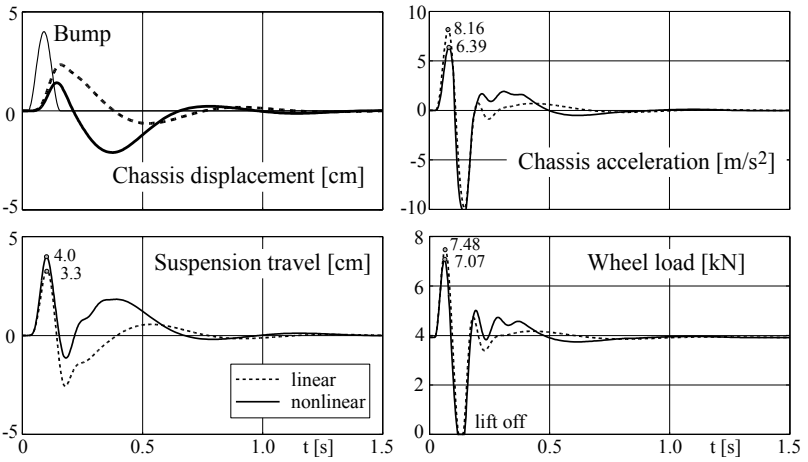

FIGURE 7.12
Quarter car model with nonlinear force characteristics driving over a bump.

forces that induce unnecessary chassis accelerations. Damper layouts that generate a degressive characteristic may reduce this impact on the chassis when crossing a bump but they in turn will increase the suspension travel.

7.7 Sky Hook Damper

7.7.1 Modeling Aspects

In a standard layout of a wheel/axle suspension system, the damper acts between the wheel or axle and the chassis, Figure 7.13a. For a linear characteristic, the damper force is given by

$$F_D \;=\; d_S\,(\dot{z}_W - \dot{z}_C)\;, \tag{7.84}$$

where d_S denotes the damping constant and $\dot{z}_C$, $\dot{z}_W$ are the time derivatives of the absolute vertical body and wheel displacements.

The sky hook damping concept starts with two independent dampers mounted between the chassis and the sky and the wheel or axle and the sky, Figure 7.13b. A practical realization in form of a controllable damper, located again in between the wheel/axle and the chassis, will then generate the damping force

$$F_D \;=\; d_{Wh}\dot{z}_W \;-\; d_{Ch}\dot{z}_C\;, \tag{7.85}$$

where instead of the single damping constant d_S two design parameter d_{Wh} and d_{Ch} are available now.

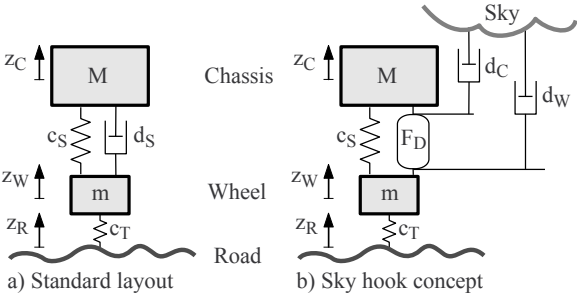

FIGURE 7.13
Quarter car model with a standard and a sky hook damper.

The equations of motion for a simple quarter car model are provided in Equation (7.68). The linear suspension spring force and the vertical tire force are defined in Equation (7.69).

7.7.2 Eigenfrequencies and Damping Ratios

Using the force definitions in Equations (7.85) and (7.69), the equations of motion provided in Equation (7.68) can be transformed to the state equation

$$\underbrace{\begin{bmatrix} \dot{z}_C \\ \dot{z}_W \\ \ddot{z}_C \\ \ddot{z}_W \end{bmatrix}}_{\dot{x}} = \underbrace{\begin{bmatrix} 0 & 0 & 1 & 0 \\ 0 & 0 & 0 & 1 \\ -\frac{c_S}{M} & \frac{c_S}{M} & -\frac{d_{Ch}}{M} & \frac{d_{Wh}}{M} \\ \frac{c_S}{m} & -\frac{c_S+c_T}{m} & \frac{d_{Ch}}{m} & -\frac{d_{Wh}}{m} \end{bmatrix}}_{A} \underbrace{\begin{bmatrix} z_C \\ z_W \\ \dot{z}_C \\ \dot{z}_W \end{bmatrix}}_{x} + \underbrace{\begin{bmatrix} 0 \\ 0 \\ 0 \\ \frac{c_T}{m} \end{bmatrix}}_{B} \underbrace{\begin{bmatrix} z_R \end{bmatrix}}_{u}, \quad (7.86)$$

where the weight forces Mg and mg were compensated by the preloads F_S^0 and F_T^0. The term $B\,u$ describes the excitation, x denotes the state vector, and A is the state matrix. In this linear approach the tire liftoff is not taken into consideration. The special case $d_{Ch} = d_{Wh} = d_S$ represents the standard layout with a linear damper.

The eigenvalues λ of the state matrix A characterize the eigendynamics[3] of the quarter car model. In case of complex eigenvalues, the damped natural eigenfrequencies are given by the imaginary parts, $\omega = Im(\lambda)$, and according to Equation (7.18), $\zeta = D_\lambda = -Re(\lambda)/\,|\lambda|$. evaluates the damping ratio. Figure 7.14 shows the eigenfrequencies $f = \omega/(2\pi)$ and the damping ratios $\zeta = D_\lambda$ for different values of the damping parameter d_S. Optimal ride comfort with a damping ratio of $\zeta_C = \frac{1}{2}\sqrt{2} \approx 0.7$ for the chassis motion can be achieved with the damping parameter $d_S = 3880\,N/(m/s)$, and the damping

[3]The MATLAB command [EV,EW]=eig(A) computes the eigenvectors (columns of EV) and eigenvalues (main diagonal elements of EW) of the matrix A.

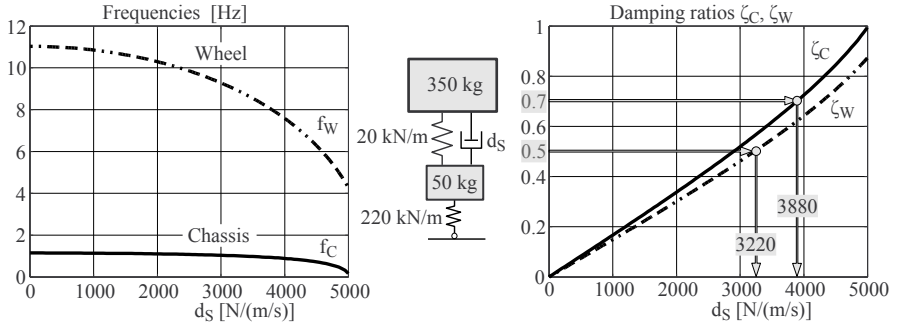

FIGURE 7.14
Quarter car model with standard damper.

parameter $d_S = 3220\ N/(m/s)$ would provide for the wheel motion a damping ratio of $\zeta_W = 0.5$, which corresponds to minimal wheel load variations. These damping parameters are very close to the values $3742\ N/(m/s)$ and $3464\ N/(m/s)$ that were calculated in Equations (7.65) and (7.64) with the single mass-models. Hence, the very simple single-mass models can be used for a first damper layout. Usually, as it is here, both optimal ride comfort and optimal ride safety cannot achieved by a standard linear damper.

The sky hook damper, modeled by Equation (7.85), provides with d_{Ch} and d_{Wh} two design parameters. Their influence on the eigenfrequencies f and the damping ratios ζ is shown in Figure 7.15. The sky hook damping parameters

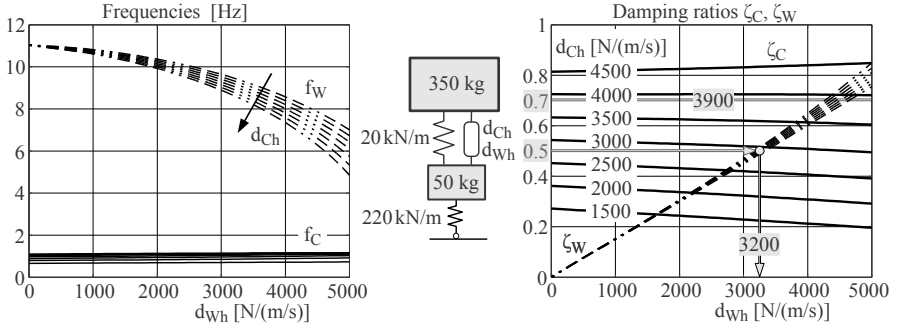

FIGURE 7.15
Quarter car model with sky hook damper.

d_{Ch} and d_{Wh} have a nearly independent influence on the damping ratios. The chassis damping ratio ζ_C mainly depends on d_{Ch}, and the wheel damping ratio ζ_W mainly depends on d_{Wh}. Hence, the damping of the chassis and the wheel motion can be adjusted to nearly each design goal. Here, a sky hook damper with $d_{Ch} = 3900\ N/(m/s)$ and $d_{Wh} = 3200\ N/(m/s)$ would generate the damping ratios $\zeta_C = 0.7$ and $\zeta_W = 0.5$ and thus combine ride comfort and ride safety within one damper layout.

7.7.3 Technical Realization

By modifying the damper law in Equation (7.85) to

$$F_D = d_{Wh}\dot{z}_W - d_{Ch}\dot{z}_C = \underbrace{\frac{d_{Wh}\dot{z}_W - d_{Ch}\dot{z}_C}{\dot{z}_W - \dot{z}_C}}_{d_{sky}} (\dot{z}_W - \dot{z}_C) \ , \tag{7.87}$$

the sky hook damper can be realized by a standard damper in the form of Equation (7.84). The new damping parameter d_{sky} now nonlinearly depends on the absolute vertical velocities of the chassis and the wheel $d_{sky} = d_{sky}(\dot{z}_C, \dot{z}_W)$. As a standard damper operates in a dissipative mode only, the damping parameter will be restricted to positive values, $d_{sky} \geq 0$. Hence, the passive realization of a sky hook damper will only match with some properties of the ideal damper law in Equation (7.85). But, compared with the standard damper, it still can provide a better ride comfort combined with sufficient ride safety.

Some continuous damping control (CDC) systems are based on the sky hook control strategy. Twin-tube dampers equipped with electromagnetically activated additional external valves make it possible to regulate the flow of the hydraulic fluid between the inner and outer damper tubes and thus vary the resistance of the damper. Vehicle sensors provide the accelerations of the chassis and the wheels, which are processed in a control unit to the desired damping parameter within milliseconds. Most commercial CDC-systems take the actual driving situation into account too. For example, a temporarily increased damping rate will reduce the pitch and roll reaction of the vehicle when cornering fast or braking hard. However, a lower damping parameter will grant a rather smooth ride on rough country roads.

7.7.4 Simulation Results

The function qcm_skyhook_f given in Listing 7.3 provides the state equation for a simple quarter car model with a nonlinear suspension spring and a sky hook damper.

Listing 7.3
Function `qcm_skyhook_f.m`: Quarter Car Model with Sky Hook Damper

```
1  function xdot = qcm_skyhook_f(t,x)
2
3  global grav  M  m  cS kS  dCh dWh TdS cT
4  global FS0  FT0  ftire z_road
5  global v_vel o_x0 o_y0 o_tp o_w o_h o_l
6
7  % get states
8  zc=x(1); zw=x(2); zcd=x(3); zwd=x(4); d=x(5);
9
10 % obstacle @ sx = o_x0, sy = o_y0
11 sx = v_vel*t; sy=0; % actual position of vehicle
```

```
12  z_road = obstacle_f(sx-o_x0,sy-o_y0,o_tp,o_w,o_h,o_l); % road height
13
14  % tire force
15  ftire = max(0,FT0+cT*(z_road-zw));
16
17  % nonlinear spring
18  u  = zw - zc; % displacement (u>0: compression)
19  if u<0,
20    fs = FS0 + cS*u; % rebound
21  else
22    fs = FS0 + cS*u*(1+kS*u^2); % compression
23  end
24
25  % damper velocity (v>0: compr.) and force via dynamic damping parameter
26  v = zwd - zcd; fd = d*v;
27
28  % compute skyhook damping parameter and its time derivative
29  if abs(v) > 0.001
30    d_sky = max(0,(dWh*zwd-dCh*zcd)/v); % nonlinear damping (d_sky>0)
31  else
32    d_sky = d; % keep old value
33  end
34  ddot = (d_sky - d)/TdS; % first order dynamics
35
36  % chassis and wheel acceleration
37  zcdd = (       (fs+fd) ) / M - grav ;
38  zwdd = ( ftire - (fs+fd) ) / m - grav ;
39
40  % state derivatives
41  xdot = [ zcd; zwd; zcdd; zwdd; ddot ];
42
43  end
```

The function obstacle_f defined in Listing 2.1 provides the actual road height. Again, the tire is modeled by a linear spring characterized by the constant cT and the code line 15 takes the wheel liftoff into account too. As done in Section 7.6.2, the parameters cS and kS model a nonlinear spring force.

In reality it will be impossible to change the resistance of a damper in an instant. That is why, the controlled damper is characterized by a dynamic damping parameter d, which is simply defined here by a first-order differential equation

$$T_{dS}\,\dot{d} \;=\; d_{sky} - d\,. \tag{7.88}$$

The time constant T_{dS} characterizes the damper dynamics and Equation (7.87) provides the sky hook damping parameter d_{sky}, which is restricted to positive values. As the computation of the sky hook damping parameter d_{sky}, will become critical at small damper velocities, a new sky hook damping parameter is calculated only if abs(v) > 0.001 holds.

The MATLAB-Script qcm_skyhook_main provided in Listing 7.4 sets the data for a simple quarter car model equipped with a nonlinear suspension spring and a sky hook damper, performs simulations where the vehicle drives with constant speed over an obstacle, does some postprocessing, and finally plots the results.

Listing 7.4
Script `qcm_skyhook_main.m`: Simulation of a Quarter Car Model with Nonlinear Spring and Sky Hook Damper Crossing an Obstacle

```
global grav  M  m  cS kS  dCh dWh TdS cT
global FS0  FT0  ftire z_road
global v_vel o_x0 o_y0 o_tp o_w o_h o_l

grav=9.81;          % constant of gravity [m/s^2]
M=350; m=50;        % chassis and wheel mass (Quarter Car) [kg]
cS=29400; kS=66.7; % spring stiffness [N/m] and nonlinerity [1/m^2]
dCh=4850; dWh=3200; % sky hook damping parameter
TdS=0.005;          % time constant [s]
cT=220000;          % Tire Stiffness [N/m]

v_vel=80/3.6;           % vehicle velocity [km/h --> m/s]
o_x0=2.0; o_y0=0; o_tp=2; % obstacle position [m] and type [-]
o_w=10; o_h=0.04; o_l=3; % obstacle width, height and length [m]

% preloads
FS0 = M*grav; FT0 = FS0 + m*grav;

% time interval
t0=0; te=1;

% initial states (steady state & average damping)
x0=[0;0;0;0; (dCh+dWh)/2];

% perform simulation
[t,x] = ode23(@qcm_skyhook_f,[t0,te],x0);

% suspension travel (st>0: compression)
st = x(:,2) - x(:,1);

% chassis acceleration, wheel load and road
ac=zeros(size(t)); FT=zeros(size(t)); zr=zeros(size(t));
for i=1:length(t)
  xdot=qcm_skyhook_f(t(i),x(i,:)');
  ac(i)=xdot(3); FT(i)=ftire; zr(i)=z_road;
end

% plot results
subplot(2,2,1)
  plot(t,x(:,5),'k','Linewidth',1), title('damping constant')
subplot(2,2,2)
  plot(t,ac,'k','Linewidth',1), title('chassis acceleration')
subplot(2,2,3)
  plot(t,st,'k','Linewidth',1), title('suspension travel & bump')
  hold on, plot(t,zr,'--b','Linewidth',1)
subplot(2,2,4)
  plot(t,FT,'k','Linewidth',1), title('wheel load')
```

As done in Section 7.7.2, the eigendynamics of the system were analyzed first. The stiffer spring ($c_S = 29.4\,kN/m$ instead of $c_S = 20\,kN/m$) results in the sky hook damping parameters $d_{Ch} = 4850N/(m/s)$ and $d_{Wh} = 3200N/(m/s)$,

which correspond with damping ratios of $\zeta_C = 0.7$ and $\zeta_W = 0.5$ and thus will provide optimal ride comfort and optimal ride safety.

The solid lines plotted in Figure 7.16 represent the simulation results. For comparison, the corresponding results of simulations with a linear and

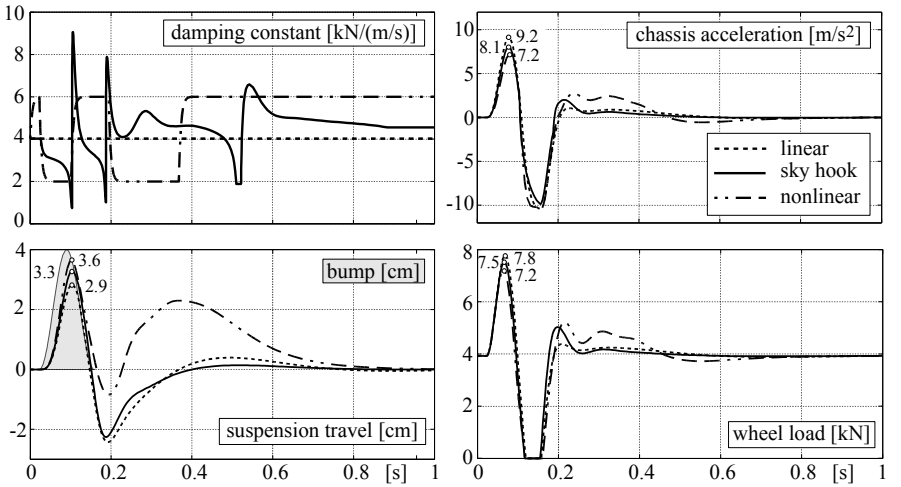

FIGURE 7.16
Quarter car model with different damper types crossing a bump.

a nonlinear damper are shown also. The linear damper is simply realized by setting both sky hook parameters to the average damping parameter, $d_{Ch} = d_{Wh} = (4850 + 3200)/2 = 4025\ N/(m/s)$. As done in Section 7.6.2, the nonlinear damper was modeled by piecewise linear functions characterized by the parameters $d_{Cp} = 2000\,N/(m/s)$ and $d_{Rb} = 6000\,N/(m/s)$, which describe the damper resistance in the compression and rebound mode. In both cases, the dynamic approach was applied. The time constant of $TdS = 0.005\,s$ makes quick changes of the damping constant possible. Whereas the damping parameter d simply jumps from $d = d_{Cp}$ to $d = d_{Rb}$ when the nonlinear damper is employed, it varies over a wide range when the sky hook damper is used instead. Compared to the linear damper, the sky hook damper generates significantly smaller peak values in the chassis acceleration ($9.2 \rightarrow 8.1\ m/s^2$) and the wheel load ($7.8 \rightarrow 7.5\,kN$) but it will require an increased suspension travel ($2.9 \rightarrow 3.3\,kN$) instead. The nonlinear damper reduces the peak values in the chassis acceleration and the wheel load further on ($8.1 \rightarrow 7.2\ m/s^2$ and $7.5 \rightarrow 7.2\,kN$) but needs still more suspension travel ($3.3 \rightarrow 3.6\,kN$) and shows a significant second overshoot at $t \approx 3.7\,s$ in the time history of the suspension travel. So, the performance of the sky hook damper regarding comfort and safety may be judged clearly superior to the linear and slightly better than the nonlinear damper layout. By applying a more sophisticated control strategy, further enhancements will be possible.

Exercises

7.1 The equations of motion for a simple planar vehicle model read as

$$\begin{aligned} M\,\ddot{z}_C &= F_1 + F_2 - M\,g\,, \\ \Theta\,\ddot{\beta}_C &= -a_1 F_1 + a_2 F_2\,, \end{aligned} \quad \text{and} \quad \begin{aligned} m_1\,\ddot{z}_{A1} &= -F_1 + F_{T1} - m_1\,g\,, \\ m_2\,\ddot{z}_{A2} &= -F_2 + F_{T2} - m_2\,g\,, \end{aligned}$$

where M, Θ denote the mass and inertia of the chassis; m_1, m_2 describe the masses of the front and rear axle; and a_1, a_2 represent the distances of the chassis center C to the front and rear axle.

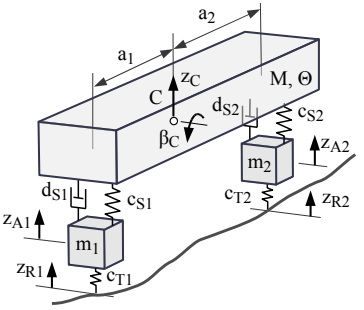

The generalized coordinates z_C and β_C as well as z_{A1} and z_{A2} characterize the hub and pitch motion of the chassis as well as the vertical movements of the front and rear axle. The coordinates are measured from the steady-state position. The road irregularities at the front and rear axle are described by z_{R1} and z_{R2} finally. Assuming linear force characteristics, the suspension forces read as

$$\begin{aligned} F_1 &= \overbrace{Mg\,\frac{a_2}{a_1+a_2}}^{F_1^0} + c_{S1}\,\overbrace{\Big[z_{A1} - (z_C - a_1\beta_C)\Big]}^{s_1} + d_{S1}\,\overbrace{\Big[\dot{z}_{A1} - \big(\dot{z}_C - a_1\dot{\beta}_C\big)\Big]}^{\dot{s}_1}\,, \\ F_2 &= \underbrace{Mg\,\frac{a_1}{a_1+a_2}}_{F_2^0} + c_{S2}\,\underbrace{\Big[z_{A2} - (z_C + a_2\beta_C)\Big]}_{s_2} + d_{S2}\,\underbrace{\Big[\dot{z}_{A2} - \big(\dot{z}_C + a_2\dot{\beta}_C\big)\Big]}_{\dot{s}_2}\,, \end{aligned}$$

where the preloads F_1^0, F_2^0 just represent the corresponding parts of the chassis weight Mg, and the displacements s_1, s_2 and their time derivatives $\dot{s}_1$, $\dot{s}_2$ are defined such that positive values represent compression. Finally, the tire forces are defined by $F_{T1} = F_1^0 + m_1 g + c_{T1}\,(z_{R1} - z_{A1})$ and $F_{T2} = F_2^0 + m_2 g + c_{T2}\,(z_{R2} - z_{A2})$, where the demands $F_{T1} > 0$ and $F_{T2} > 0$ will take tire liftoff into account.

Write a MATLAB function that provides the equations of motion in the form of $\dot{x} = f(t, x)$, where $x = [\,z_C;\, \beta_C;\, z_{A1};\, z_{A2};\, \dot{z}_C;\, \dot{\beta}_C;\, \dot{z}_{A1};\, \dot{z}_{A2}\,]$ defines the state vector and the data are supplied by global variables. Derive the linear state equation in the form of $\dot{x} = A\,x + B\,u$, where the vector $u = [\,z_{R1}; z_{R2}\,]$ contains the road irregularities. Combine the two quarter car models defined in Figure 7.8 and Figure 7.11 by neglecting the spring nonlinearity and by setting $a_1 = a_2 = 1.3\,m$. Then, calculate the eigenvalues of the state matrix A and derive the eigenfrequencies and damping ratios.

7.2 Estimate appropriate values for the suspension stiffness for the vehicles characterized by the data in Table 7.1 by assuming realistic loading scenarios. Compute suitable values for the suspension damping that will provide optimal comfort and safety. Check the results by analyzing the performance of corresponding simple quarter car and planar models on rough road and when crossing different obstacles.

8

Longitudinal Dynamics

CONTENTS

8.1 Dynamic Wheel Loads

8.1.1 Simple Vehicle Model

The vehicle is considered as one rigid body that moves along an ideally even and horizontal road. At each axle, the forces in the wheel contact points are combined into one normal and one longitudinal force. If aerodynamic forces (drag, positive and negative lift) are neglected at first, the equations of motions in the x-, z-plane will read as

$$m\,\dot{v} \;=\; F_{x1} + F_{x2}\,, \tag{8.1}$$

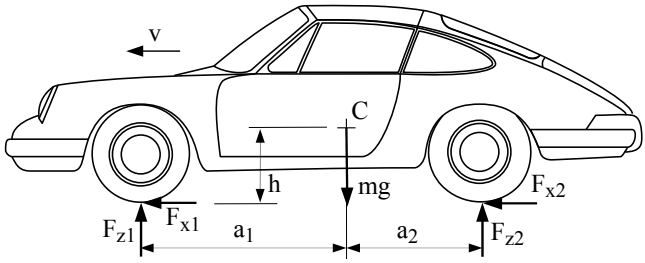

FIGURE 8.1
Simple vehicle model.

$$0 \;=\; F_{z1} + F_{z2} - m\,g\,, \tag{8.2}$$

$$0 \;=\; -F_{z1}\,a_1 + F_{z2}\,a_2 - (F_{x1} + F_{x2})\,h\,, \tag{8.3}$$

where $\dot{v} = a_x$ indicates the vehicle's acceleration, m is the mass of the vehicle, $a_1 + a_2$ is the wheel base, and h is the height of the center of gravity.

These are only three equations for the four unknown forces F_{x1}, F_{x2}, F_{z1}, F_{z2}. But, if we insert Equation (8.1) in Equation (8.3), we can eliminate two unknowns at a stroke

$$0 \;=\; -F_{z1}\,a_1 + F_{z2}\,a_2 - m\,\dot{v}\,h\,. \tag{8.4}$$

Equations (8.2) and (8.4) can be resolved for the axle loads now

$$F_{z1} \;=\; m\,g\,\frac{a_2}{a_1 + a_2} \;-\; \frac{h}{a_1 + a_2}\,m\,\dot{v}\,, \tag{8.5}$$

$$F_{z2} \;=\; m\,g\,\frac{a_1}{a_1 + a_2} \;+\; \frac{h}{a_1 + a_2}\,m\,\dot{v}\,. \tag{8.6}$$

The static parts

$$F_{z1}^{st} = m\,g\,\frac{a_2}{a_1 + a_2}\,, \qquad F_{z2}^{st} = m\,g\,\frac{a_1}{a_1 + a_2} \tag{8.7}$$

describe the weight distribution according to the horizontal position of the center of gravity. The height of the center of gravity only influences the dynamic part of the axle loads,

$$F_{z1}^{dyn} = -m\,g\,\frac{h}{a_1 + a_2}\,\frac{\dot{v}}{g}\,, \qquad F_{z2}^{dyn} = +m\,g\,\frac{h}{a_1 + a_2}\,\frac{\dot{v}}{g}\,. \tag{8.8}$$

When accelerating $\dot{v} > 0$, the front axle is relieved as the rear is when decelerating $\dot{v} < 0$.

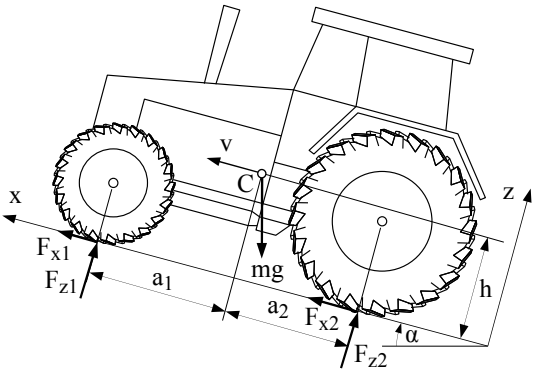

FIGURE 8.2
Vehicle on grade.

8.1.2 Influence of Grade

For a vehicle on a grade, the equations of motion, defined by Equations (8.1) to (8.3), can easily be extended to

$$\begin{aligned} m\,\dot{v} &= F_{x1} + F_{x2} - m\,g\,\sin\alpha\,, \\ 0 &= F_{z1} + F_{z2} - m\,g\,\cos\alpha\,, \\ 0 &= -F_{z1}\,a_1 + F_{z2}\,a_2 - (F_{x1} + F_{x2})\,h\,, \end{aligned} \tag{8.9}$$

where α denotes the grade angle, Figure 8.2. Now, the axle loads are given by

$$F_{z1} = \overbrace{m\,g\,\cos\alpha\,\frac{a_2 - h\tan\alpha}{a_1 + a_2}}^{F_{z1}^{st}} \overbrace{-\,\frac{h}{a_1 + a_2}\,m\,\dot{v}}^{F_{z1}^{dyn}}\,, \tag{8.10}$$

$$F_{z2} = \underbrace{m\,g\,\cos\alpha\,\frac{a_1 + h\tan\alpha}{a_1 + a_2}}_{F_{z2}^{st}} \underbrace{+\,\frac{h}{a_1 + a_2}\,m\,\dot{v}}_{F_{z2}^{dyn}}\,, \tag{8.11}$$

where the dynamic parts F_{z1}^{dyn}, F_{z2}^{dyn} remain unchanged and the static parts F_{z1}^{st}, F_{z2}^{st} also depend on the grade angle α and the height of the center of gravity h.

8.1.3 Aerodynamic Forces

The shape of most vehicles or specific wings mounted on the vehicle produce aerodynamic forces and torques. The effect of these aerodynamic forces and torques can be represented by a resistant force applied at the center of gravity and "down forces" acting at the front and rear axle, Figure 8.3. If we assume

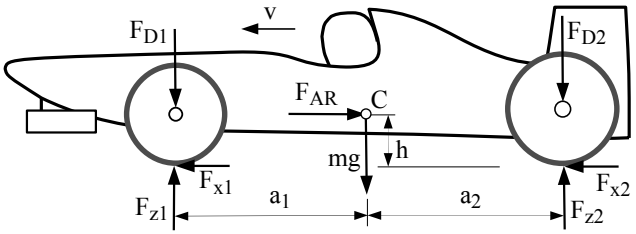

FIGURE 8.3
Vehicle with aerodynamic forces.

a positive driving speed, $v > 0$, the equations of motion will read as

$$\begin{aligned} m\,\dot{v} &= F_{x1} + F_{x2} - F_{AR}\,, \\ 0 &= F_{z1} - F_{D1} + F_{z2} - F_{D2} - m\,g\,, \\ 0 &= -\,(F_{z1} - F_{D1})\;a_1 + (F_{z2} - F_{D2})\;a_2 - (F_{x1} + F_{x2})\;h\,, \end{aligned} \tag{8.12}$$

where F_{AR} and F_{D1}, F_{D2} describe the air resistance and the down forces. For the axle loads, we get

$$F_{z1} = \overbrace{F_{D1} + m\,g\,\frac{a_2}{a_1 + a_2}}^{F_{z1}^{st}} \overbrace{-\,\frac{h}{a_1 + a_2}\,(m\,\dot{v} + F_{AR})}^{F_{z1}^{dyn}}\,, \tag{8.13}$$

$$F_{z2} = \underbrace{F_{D2} + m\,g\,\frac{a_1}{a_1 + a_2}}_{F_{z2}^{st}} \underbrace{+\,\frac{h}{a_1 + a_2}\,(m\,\dot{v} + F_{AR})}_{F_{z2}^{dyn}}\,. \tag{8.14}$$

The down forces F_{D1}, F_{D2} increase the static axle loads, and the air resistance F_{AR} generates an additional dynamic term.

8.2 Maximum Acceleration

8.2.1 Tilting Limits

Ordinary automotive vehicles can only apply pressure forces to the road. If we take the demands $F_{z1} \geq 0$ and $F_{z2} \geq 0$ into account, Equations (8.10) and (8.11) will result in

$$\frac{\dot{v}}{g} \leq \frac{a_2}{h}\cos\alpha - \sin\alpha \quad \text{and} \quad \frac{\dot{v}}{g} \geq -\frac{a_1}{h}\cos\alpha - \sin\alpha\,. \tag{8.15}$$

These two conditions can be combined into one

$$-\frac{a_1}{h}\cos\alpha \quad \leq \quad \frac{\dot{v}}{g}+\sin\alpha \quad \leq \quad \frac{a_2}{h}\cos\alpha\,. \tag{8.16}$$

Here, aerodynamic forces are not taken into account. Then, the maximum achievable accelerations ($\dot{v} > 0$) and decelerations ($\dot{v} < 0$) are limited by the grade angle α and the position a_1, a_2, h of the center of gravity. For $\dot{v} \to 0$, the tilting condition Equation (8.16) results in

$$-\frac{a_1}{h} \;\leq\; \tan\alpha \;\leq\; \frac{a_2}{h}\,, \tag{8.17}$$

which characterizes the climbing and downhill capacity of a vehicle.

The presence of aerodynamic forces complicates the tilting condition. However, aerodynamic forces become important only at high speeds. But then, the vehicle acceleration is normally limited by the engine power.

8.2.2 Friction Limits

The maximum acceleration is also restricted by the friction conditions

$$|F_{x1}| \leq \mu\, F_{z1} \quad \text{and} \quad |F_{x2}| \leq \mu\, F_{z2}\,, \tag{8.18}$$

where the same friction coefficient μ has been assumed at the front and the rear axle. In the limit case

$$F_{x1} = \pm\,\mu\, F_{z1} \quad \text{and} \quad F_{x2} = \pm\,\mu\, F_{z2}\,, \tag{8.19}$$

the linear momentum in Equation (8.9) can be written as

$$m\,\dot{v}_{max} \;=\; \pm\,\mu\;(F_{z1}+F_{z2}) - m\,g\,\sin\alpha\,. \tag{8.20}$$

Using Equations (8.10) and (8.11), one obtains

$$\left(\frac{\dot{v}}{g}\right)_{max} \;=\; \pm\,\mu\,\cos\alpha \;-\; \sin\alpha\,. \tag{8.21}$$

That means climbing ($\dot{v} > 0$, $\alpha > 0$) or downhill stopping ($\dot{v} < 0$, $\alpha < 0$) requires at least a friction coefficient $\mu \geq \tan|\alpha|$. On a horizontal road ($\alpha = 0$), the maximum longitudinal acceleration is simply determined by the coefficient of friction

$$\left(\frac{\dot{v}}{g}\right)_{max} \;=\; \pm\,\mu \qquad \text{or} \qquad a_x^{max} = \pm\,\mu\,g\,. \tag{8.22}$$

According to the vehicle dimensions a_1, a_2, h and the magnitude of the friction coefficient μ, the maximal acceleration or deceleration is restricted either by Equation (8.16) or by Equation (8.21).

If we take aerodynamic forces into account, the maximum acceleration and deceleration on a horizontal road ($\alpha = 0$) will be limited by

$$-\mu\left(1+\frac{F_{D1}}{mg}+\frac{F_{D2}}{mg}\right)-\frac{F_{AR}}{mg} \;\le\; \frac{\dot{v}}{g} \;\le\; \mu\left(1+\frac{F_{D1}}{mg}+\frac{F_{D2}}{mg}\right)-\frac{F_{AR}}{mg}\,. \quad (8.23)$$

In particular the aerodynamic forces enhance the braking performance of the vehicle.

8.3 Driving and Braking

8.3.1 Single Axle Drive

With the rear axle driven in limit situations, $F_{x1} = 0$ and $F_{x2} = \mu F_{z2}$ hold. Then, using Equation (8.6) the linear momentum Equation (8.1) results in

$$m\,\dot{v}_{RWD} \;=\; \mu\, m\, g\;\left[\;\frac{a_1}{a_1+a_2}+\frac{h}{a_1+a_2}\,\frac{\dot{v}_{RWD}}{g}\;\right], \quad (8.24)$$

where the subscript $_{RWD}$ indicates the rear wheel drive. Hence, the maximum acceleration for a rear wheel driven vehicle is given by

$$\frac{\dot{v}_{RWD}}{g} \;=\; \frac{\mu}{1-\mu\,\dfrac{h}{a_1+a_2}}\,\frac{a_1}{a_1+a_2}\,. \quad (8.25)$$

By setting $F_{x1} = \mu F_{z1}$ and $F_{x2} = 0$, the maximum acceleration for a front wheel driven vehicle can be calculated in a similar way. One gets

$$\frac{\dot{v}_{FWD}}{g} \;=\; \frac{\mu}{1+\mu\,\dfrac{h}{a_1+a_2}}\,\frac{a_2}{a_1+a_2}\,, \quad (8.26)$$

where the subscript $_{FWD}$ denotes front wheel drive. Depending on the parameter μ, a_1, a_2, and h, the accelerations may be limited by the tilting condition $\frac{\dot{v}}{g} \le \frac{a_2}{h}$. The maximum accelerations of a single-axle driven vehicle are plotted in Figure 8.4. Besides the friction limits, the hazard of tilting must be taken into account. On a horizontal road ($\alpha = 0$), Equation (8.16) yields

$$\frac{\dot{v}}{g} \;\le\; \frac{a_2}{h} \quad \text{or} \quad \frac{a_2}{a_1+a_2} \;\ge\; \frac{h}{a_1+a_2}\,\frac{\dot{v}}{g}\,, \quad (8.27)$$

where the inequality was rearranged and divided by the wheel base $a_1 + a_2$. According to Equation (8.21), the maximum acceleration is limited to the friction coefficient on a horizontal road

$$\left(\frac{\dot{v}}{g}\right)_{max} \;=\; \mu\,. \quad (8.28)$$

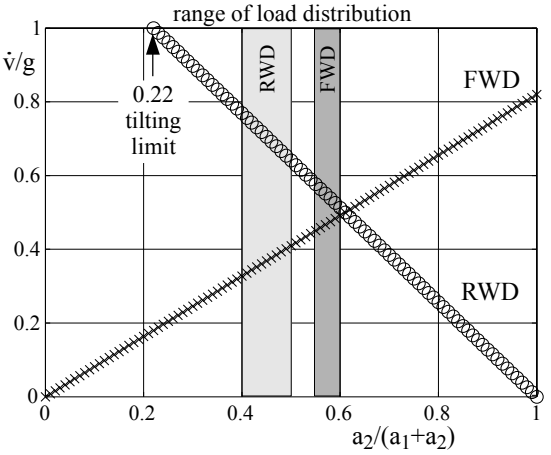

FIGURE 8.4
Single-axle driven passenger car: $\mu = 1$, $h = 0.55\,m$, $a_1 + a_2 = 2.5\,m$.

In this case, the tilting condition Equation (8.27) just delivers

$$\frac{a_2}{a_1 + a_2} \geq \frac{h}{a_1 + a_2}\,\mu \;=\; \frac{0.55}{2.5}\,1 \;=\; 0.22\,. \tag{8.29}$$

For rear wheel driven passenger cars, the parameter $a_2/(a_1{+}a_2)$ describing the static axle load distribution is usually in the range of $0.4 \leq a_2/(a_1{+}a_2) \leq 0.5$. For $\mu = 1$ and $h = 0.55$, this results in maximum accelerations in the range of $0.77 \geq \dot{v}/g \geq 0.64$. Front wheel driven passenger cars usually cover the range $0.55 \leq a_2/(a_1{+}a_2) \leq 0.60$, which produces accelerations in the range of $0.45 \leq \dot{v}/g \geq 0.49$. Hence, rear wheel driven vehicles can accelerate much faster than front wheel driven vehicles.

8.3.2 Braking at Single Axle

If only the front axle is braked, $F_{x1} = -\mu\, F_{z1}$ and $F_{x2} = 0$ will hold in the limit case. With Equation (8.5) one gets from Equation (8.1),

$$m\,\dot{v}_{FWB} \;=\; -\mu\, m\, g \left[\; \frac{a_2}{a_1 + a_2} - \frac{h}{a_1 + a_2}\,\frac{\dot{v}_{FWB}}{g} \;\right], \tag{8.30}$$

where the subscript $_{FWB}$ indicates front wheel braking. Then, the maximum deceleration is given by

$$\frac{\dot{v}_{FWB}}{g} \;=\; -\,\frac{\mu}{1 - \mu\,\dfrac{h}{a_1 + a_2}}\,\frac{a_2}{a_1 + a_2}\,. \tag{8.31}$$

If only the rear axle is braked ($F_{x1} = 0,\ F_{x2} = -\mu\, F_{z2}$), one will obtain the maximum deceleration

$$\frac{\dot{v}_{RWB}}{g} \;=\; -\,\frac{\mu}{1+\mu\,\dfrac{h}{a_1+a_2}}\;\frac{a_1}{a_1+a_2}\,, \tag{8.32}$$

where the subscript $_{RWB}$ denotes rear wheel braking. The maximum decelerations of a single-axle braked vehicle are plotted in Figure 8.5. Depending

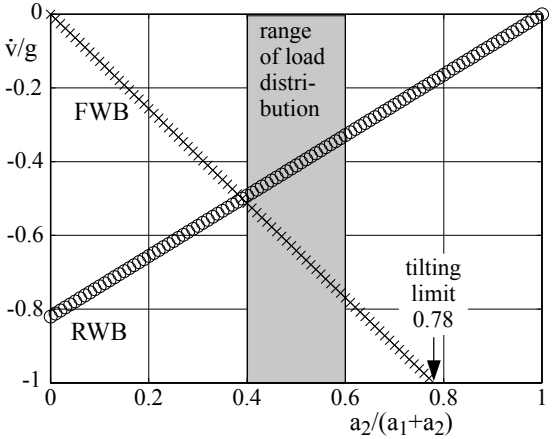

FIGURE 8.5
Single-axle braked passenger car: $\mu = 1$, $h = 0.55\,m$, $a_1 + a_2 = 2.5\,m$.

on the parameters μ, a_1, a_2, and h, the decelerations may be limited by the tilting condition $\dot{v}/g \geq -a_1/h$, which in the limit case $\dot{v}/g = -\mu$ yields

$$-\mu \;\geq\; -\frac{a_1}{h} \quad \text{or} \quad -a_1 \;\leq\; -\mu\, h \quad \text{or} \quad (a_1{+}a_2) - a_1 \;\leq\; (a_1{+}a_2) - \mu\, h \tag{8.33}$$

and finally results in

$$\frac{a_2}{a_1{+}a_2} \;\leq\; 1 - \mu\,\frac{h}{a_1{+}a_2} \;=\; 1 - 1\,\frac{0.55}{2.5} \;=\; 0.78\,. \tag{8.34}$$

For passenger cars, the load distribution parameter $a_2/(a_1{+}a_2)$ usually covers the range of 0.4 to 0.6. If only the front axle is braked, decelerations from $\dot{v}/g = -0.51$ to $\dot{v}/g = -0.77$ will be achieved. This is quite a large value compared to the deceleration range of a braked rear axle, which is in the range of $\dot{v}/g = -0.49$ to $\dot{v}/g = -0.33$. Therefore, the braking system at the front axle will have a redundant design in general.

8.3.3 Braking Stability

A small yaw disturbance of the vehicle, indicated by the side slip angle β, will cause slip angles at the wheels. Two extreme braking scenarios are shown in

in Figures 8.6 and 8.7, where the profile pattern of the tire is fully visible at locked wheels and slurred to gray at rotating ones

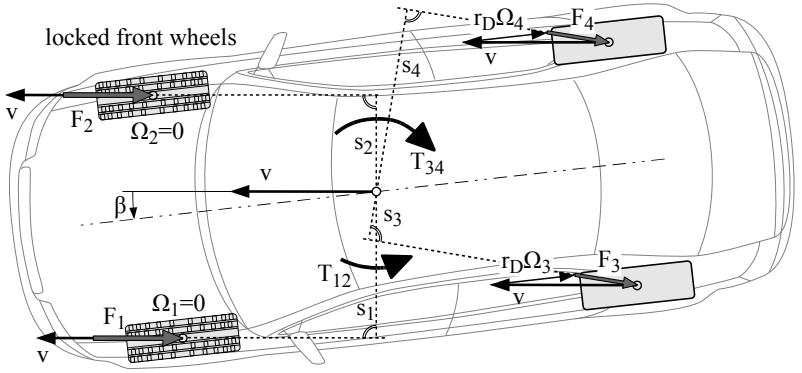

FIGURE 8.6
Locked front wheels.

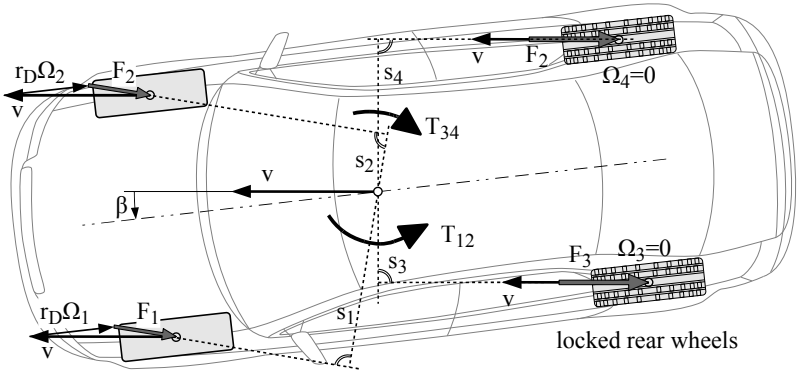

FIGURE 8.7
Locked rear wheels.

If the front wheels are locked, the tire friction forces F_1 and F_2 will point into the opposite direction of sliding velocity v, which just equals the driving velocity of the vehicle, Figure 8.6. The forces F_1 and F_2, which are approximately equal in magnitude, generate the torque T_{12} with respect to the vehicle center. As the lever arm s_1 of the force F_1 is slightly large than the lever arm s_2 of the force F_2, the torque T_{12} will increase the side slip angle β and produce a destabilizing effect to the vehicle. The rear wheels are also braked but will still rotate. Here, each sliding velocity in the contact point is the result of the the driving velocity v and the corresponding transport velocity $r_D\Omega_3$ or $r_D\Omega_4$, respectively. As a consequence, the sliding velocities and hence the

corresponding tire forces F_3 and F_4 point in a direction that is inclined to the driving direction. Now, the lever arm s_3 of the force F_3 is significantly smaller than the lever arm s_4 of the force F_4. The resulting torque $T_{34} = s_4 F_4 - s_3 F_3$ is aligned opposite to the yaw disturbance. In magnitude, it is larger than T_{12} and will thus produce an overall stabilizing effect to the vehicle.

However, if the rear wheels are locked and the front wheels are still rotating, $s_1 \gg s_2$ and $s_3 < s_4$ will hold, Figure 8.7. Then, the destabilizing torque T_{12}, is in magnitude, larger than the stabilizing torque T_{34}, which as a result will increase the yaw disturbance β, thus representing an unstable braking situation.

8.3.4 Optimal Distribution of Drive and Brake Forces

The sum of the longitudinal forces accelerates or decelerates the vehicle. In dimensionless style, Equation (8.1) reads as

$$\frac{\dot{v}}{g} = \frac{F_{x1}}{m\,g} + \frac{F_{x2}}{m\,g}\,. \tag{8.35}$$

A certain acceleration or deceleration can only be achieved by different combinations of the longitudinal forces F_{x1} and F_{x2}. According to Equation (8.19), the longitudinal forces are limited by wheel load and friction.

The optimal combination of F_{x1} and F_{x2} will be achieved when front and rear axle have the same skid resistance:

$$F_{x1} = \pm\,\nu\,\mu\,F_{z1} \quad \text{and} \quad F_{x2} = \pm\,\nu\,\mu\,F_{z2}\,. \tag{8.36}$$

Using Equations (8.5) and (8.6), one obtains

$$\frac{F_{x1}}{m\,g} = \pm\,\nu\,\mu\left(\frac{a_2}{h} - \frac{\dot{v}}{g}\right)\frac{h}{a_1 + a_2} \tag{8.37}$$

and

$$\frac{F_{x2}}{m\,g} = \pm\,\nu\,\mu\left(\frac{a_1}{h} + \frac{\dot{v}}{g}\right)\frac{h}{a_1 + a_2}\,. \tag{8.38}$$

Combining Equation (8.35) with Equations (8.37) and (8.38) results in

$$\frac{\dot{v}}{g} = \pm\,\nu\,\mu\,. \tag{8.39}$$

Here, F_{x1} and F_{x2} are assumed to have the same sign. This means that either both axles are driven or braked. Finally, inserting Equation (8.39 in Equations (8.37) and (8.38) yields

$$\frac{F_{x1}}{m\,g} = \frac{\dot{v}}{g}\left(\frac{a_2}{h} - \frac{\dot{v}}{g}\right)\frac{h}{a_1 + a_2} \tag{8.40}$$

and

$$\frac{F_{x2}}{m\,g} = \frac{\dot{v}}{g}\left(\frac{a_1}{h} + \frac{\dot{v}}{g}\right)\frac{h}{a_1 + a_2}\,. \tag{8.41}$$

Depending on the desired acceleration $\dot{v} > 0$ or deceleration $\dot{v} < 0$, the longitudinal forces that grant the same skid resistance at both axles can be calculated now.

The curve of optimal drive and brake forces for a typical passenger car is plotted in Figure 8.8. The abscissa represents the longitudinal force at the

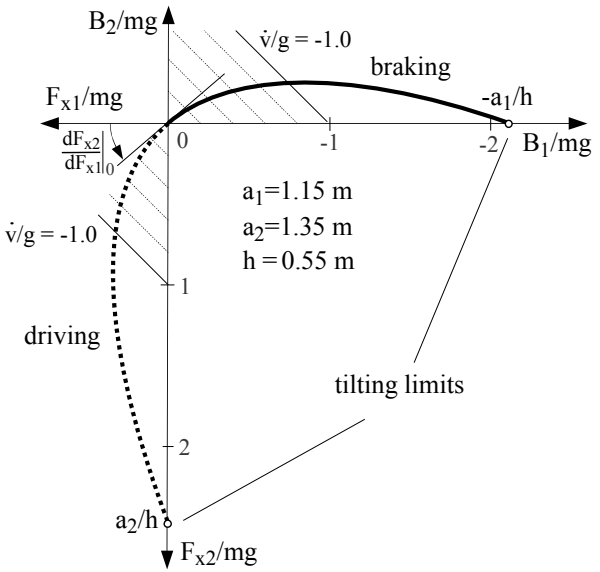

FIGURE 8.8
Optimal distribution of driving and braking forces.

front axle and the ordinate the one at the rear axle. Braking forces are indicated by negative longitudinal forces. In the diagram they are pointing to the left and upward. Rearranging Equation (8.35) generates the lines of constant acceleration and constant deceleration

$$\frac{F_{x2}}{m\,g} = \frac{\dot{v}}{g} - \frac{F_{x1}}{m\,g}\,, \tag{8.42}$$

which are also plotted in Figure 8.8 in the range of $-1.0 \le \dot{v}/g \le 1.0$.

The initial gradient of the curve of optimal drive and brake forces only depends on the steady-state distribution of the wheel loads. From Equations (8.40) and (8.41) it follows:

$$\frac{d\,\dfrac{F_{x1}}{m\,g}}{d\,\dfrac{\dot{v}}{g}} = \left(\frac{a_2}{h} - 2\,\frac{\dot{v}}{g}\right)\frac{h}{a_1 + a_2} \tag{8.43}$$

and

$$\frac{d\,\dfrac{F_{x2}}{m\,g}}{d\,\dfrac{\dot{v}}{g}} = \left(\frac{a_1}{h} + 2\,\frac{\dot{v}}{g}\right)\frac{h}{a_1 + a_2}\,. \tag{8.44}$$

For $\dot{v}/g = 0$, the initial gradient just remains as

$$\left.\frac{d\,F_{x2}}{d\,F_{x1}}\right|_0 = \frac{a_1}{a_2}\,. \tag{8.45}$$

At the tilting limits $\dot{v}/g = -a_1/h$ and $\dot{v}/g = +a_2/h$, no longitudinal forces can be applied at the lifting axle.

8.3.5 Different Distributions of Brake Forces

Practical applications aim at approximating the optimal distribution of brake forces by a linear, a limited, or a reduced distribution of brake forces as good as possible in a range of physical interest that is bounded by the maximum possible friction coefficient μ_M, Figure 8.9. When braking, the stability of a

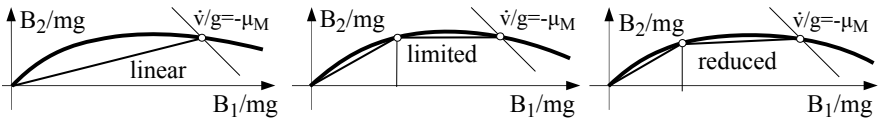

FIGURE 8.9
Different distributions of brake forces.

vehicle depends on the potential of generating a lateral force at the rear axle. Thus, a greater skid (locking) resistance is realized at the rear axle than at the front axle. Therefore, the brake force distributions are all below the optimal curve in the physically relevant area. This restricts the achievable deceleration, in particular at low friction values.

Because the optimal curve depends on the center of gravity of the vehicle, an additional safety margin must be installed when designing real brake force distributions. The distribution of brake forces is often fitted to the axle loads. There, the influence of the height of the center of gravity, which may also vary significantly on trucks, is not taken into account and must be compensated by a safety margin from the optimal curve. Only the control of brake pressure in anti-lock systems provides an optimal distribution of brake forces independently of loading conditions.

8.3.6 Braking in a Turn

The braking stability becomes apparent when a vehicle is braked while cornering. Different braking scenarios, including no braking at all, are shown in

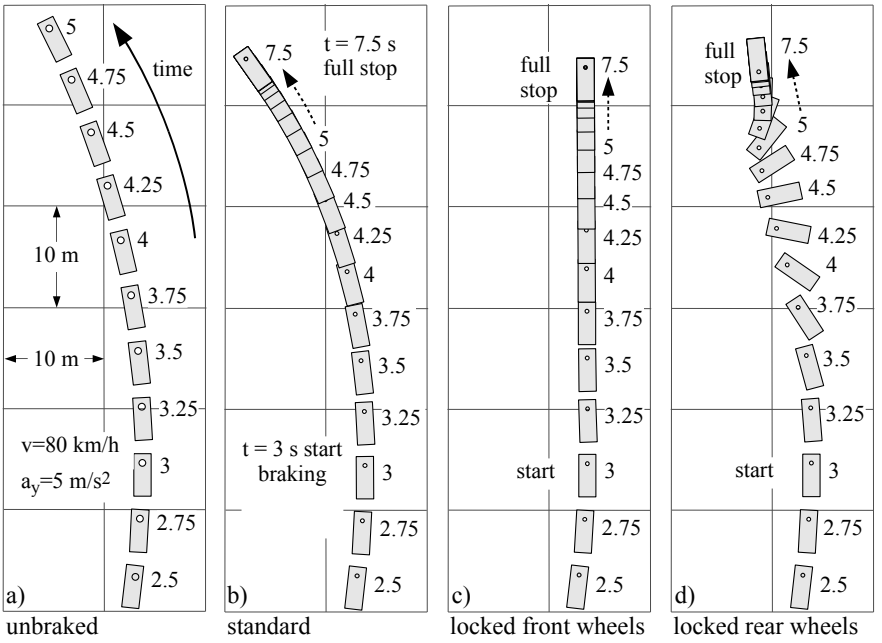

FIGURE 8.10
Braking in a turn with different scenarios.

Figure 8.10. At the beginning, the vehicle, a standard passenger car, is cornering with a driving velocity of $v = v_0 = 80\,km/h$ on a radius of $R \approx 100\,m$, which results in a lateral acceleration of $a_y \approx (80/3.6)^2/100 = 4.94\,m/s^2$. All braking scenarios start at $t = 3\,s$. In the standard case, the braking torques at the front wheels are raised within 0.1 s to 900 Nm and at the rear wheels to 270 Nm, which stops the vehicle in barely 4 seconds. The inner front wheel strongly decelerates at first, upper left plot in Figure 8.11. This brings the wheel close to a locking situation and reduces the transmittable lateral force. As a consequence, the lateral acceleration and the yaw angular velocity collapse for a short time, lower plots in Figure 8.11. The beginning deceleration of the vehicle increases the wheel load at the front axle, which enables the front tires to transmit larger lateral forces and the lateral acceleration and the yaw angular velocity again. As the vehicle has reduced its velocity in the meantime, the peak value of the lateral acceleration is below the initial value. However, the resulting peak in the yaw angular velocity exceeds the initial value and causes the vehicle to turn into the corner slightly. When the vehicle comes to a standstill at $t \approx 7\,s$, the compliance of the tire causes oscillations of the longitudinal tire forces, upper left plot in Figure 8.11.

If large braking torques of 1500 Nm are applied only at the front wheels, the vehicle will stop in nearly the same time. But, the front wheels will lock

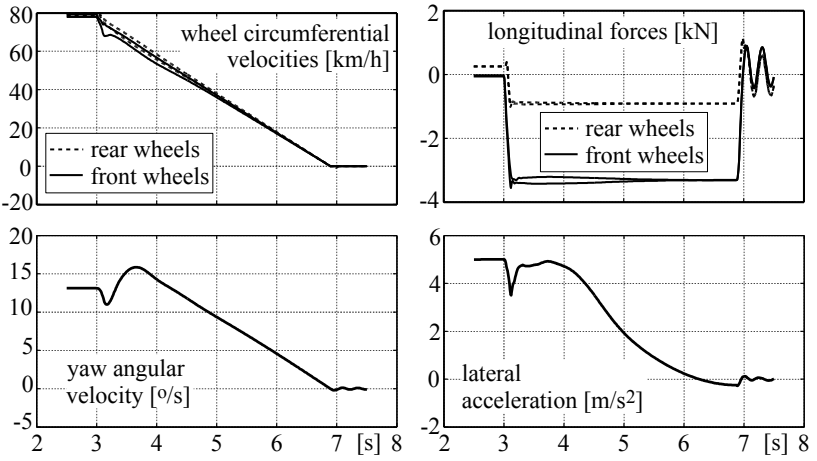

FIGURE 8.11
Baking in a turn.

now and cause the vehicle to go straight ahead instead of further cornering, third graph in Figure 8.10. If the same braking torques are put on the rear wheels only, the vehicle becomes unstable, rotates around, is then stabilized by the locked rear axle, which has come to the front, and finally comes to a stand still, rightmost graph in Figure 8.11.

8.3.7 Braking on μ-Split.

If a vehicle without an anti-lock system is braked on a μ-split surface, then the wheels running on μ_{low} will lock in an instant, thus providing small braking forces only. The wheels on the side of μ_{high}, however, generate large braking forces, $F_1 \gg F_2$ and $F_3 > F_4$, Figure 8.12. The rear wheel on μ_{low} is locked

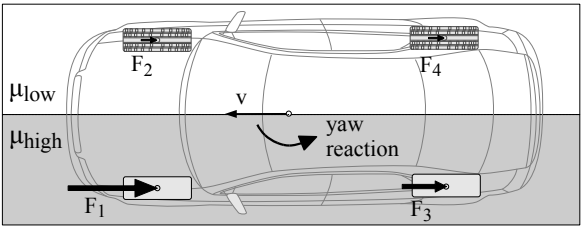

FIGURE 8.12
Yaw reaction when braking on μ-split.

and provides no lateral guidance at all. At full braking, the rear wheel on μ_{high} is close to the friction limit and therefore is not able to produce a lateral force

large enough to counteract the yaw impact. As a consequence, the vehicle starts to spin around the vertical axis.

Screen shots of a commercial trailer from the company Robert Bosch GmbH, explaining the need for the EPS system, compared with the results of a simulation with a full vehicle model are shown in Figure 8.13. Despite dif-

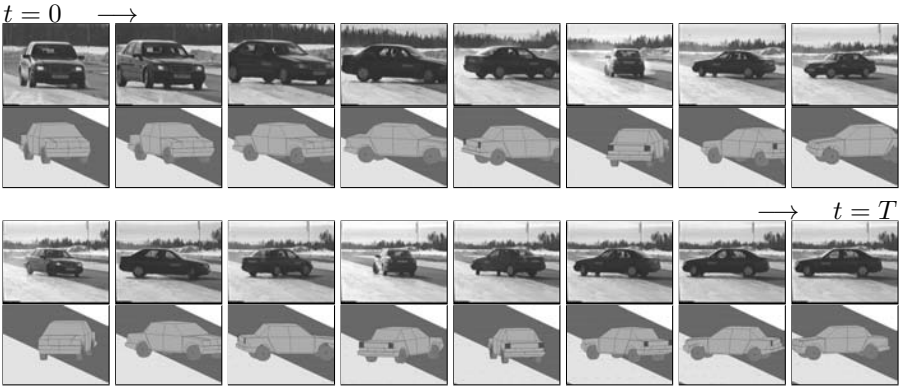

FIGURE 8.13
Braking on μ-split: Field test and simulation [40].

ferent vehicles and estimated friction coefficients for the dry ($\mu_{high} = 1$) and the icy part ($\mu_{low} = 0.05$) of the test track, the simulation results are in good conformity with field tests. Whereas the reproducibility of field tests is not always given, a computer simulation can be repeated exactly with the same environmental conditions.

8.3.8 Anti-Lock System

8.3.8.1 Basic Principle

On hard braking maneuvers, large longitudinal slip values occur. Then, the stability and/or steerability is no longer given because nearly no lateral forces can be generated. By controlling the brake torque or brake pressure, respectively, the longitudinal slip can be restricted to values that allow considerable lateral forces.

Here, the angular wheel acceleration $\dot{\Omega}$ is used as a control variable. Angular accelerations of the wheel are derived from the measured angular speeds of the wheel by differentiation. The rolling condition is fulfilled with a longitudinal slip of $s_L = 0$. Then

$$r_D \, \dot{\Omega} \; = \; \ddot{x} \tag{8.46}$$

holds, where r_D is the dynamic tire radius and $\ddot{x}$ describes the longitudinal acceleration of the vehicle. According to Equation (8.21), the maximum acceleration/deceleration of a vehicle depends on the friction coefficient, $|\ddot{x}| = \mu \, g$.

For a given friction coefficient μ, a simple control law can be realized for each wheel,

$$|\dot{\Omega}| \leq \frac{1}{r_D} |\ddot{x}| = \frac{1}{r_D} |\mu g| . \tag{8.47}$$

Because no reliable possibility to determine the local friction coefficient μ between tire and road has been found until now, useful information can only be gained from Equation (8.47) at optimal conditions on dry road. Therefore, the longitudinal slip is used as a second control variable. The control of the brake torque is done via the brake pressure, which can be "increased," "held," or "decreased" by three-way valves. To prevent vibrations, the decrement is usually made slower than the increment. In order to calculate longitudinal slips, a reference speed is estimated from all measured wheel speeds and is then used for the calculation of slip at all wheels. However, this method is too imprecise at low speeds. Therefore, no control is applied below a limit velocity. Problems also arise when all wheels lock simultaneously, which may happen on icy roads, for example.

Commercial anti-lock systems use the "select low" principle at the rear wheels. When braking on μ-split, the braking pressure at both rear wheels is controlled by the wheel running on μ_{low}. As a result, the longitudinal force of the wheel on μ_{high} is bounded to low value of the one on μ_{low}. Thus, the yaw reaction is reduced on one hand and the wheel on μ_{high} can provide a significantly larger lateral force that counteracts the remaining yaw reaction on the other hand. However, the maximum achievable deceleration is slightly reduced by this.

8.3.8.2 Simple Model

The function given in Listing 8.1 provides the state equation of a simple planar vehicle model.

Listing 8.1
Function `vehicle_2d_simple_f`: Simple Planar Vehicle Model Dynamics

```
function xp=vehicle_2d_simple_f(t,x)
% vehicle model including wheel/tire dynamics and simple ABS control

global gravity mass theta a1 a2 h csf dsf csr dsr thetaw r
global fzn  dfx0 fxm sxm fxs sxs vn cx dx
global t_tqb set_tqb dn dtqb_inc dtqb_dec
global sx fx fz tqba

% get states
posx = x( 1); posz = x( 2); pitch = x( 3); % vehicle position and orientation
velx = x( 4); velz = x( 5); pdot = x( 6); % vehicle velocities
owh = x( 7: 8); % angular velocities of front and rear wheels
xt  = x( 9:10); % longitudinal tire deflections
tqbctrl = x(11:12); % controlled braking torques

% wheel loads (linear suspension force characteristics)
fz = [ mass*gravity*a2/(a1+a2)-csf*(posz-a1*pitch)-dsf*(velz-a1*pdot); ...
```

```
18        mass*gravity*a1/(a1+a2)-csr*(posz+a2*pitch)-dsr*(velz+a2*pdot)];
19
20  % get maximum braking torque via linear interpolation
21  tqb_mx = interp1(t_tqb,set_tqb,t);
22
23  % tire and wheel dynamics (front and rear wheel)
24  xtdot=[0;0]; fx=[0;0]; tqba=[0;0]; owhdot=[0;0]; % defaults
25  for i=1:2
26    % modified transport velocities and long. slips without normalization
27    vt = abs(r*owh(i))+vn; vs=(velx-r*owh(i)); sx(i)=-vs/vt;
28    % linear wheel load influence to tire parameter
29    pt = [ dfx0, fxm, sxm, fxs, sxs] * fz(i)/fzn;
30    % generalized tire characteristics (sx only)
31    [f,fos] = tmy_fcombined( abs(sx(i)), pt(1),pt(2),pt(3),pt(4),pt(5) ) ;
32    % time derivative of long. tire deflection and long. dynamic tire force
33    xtdot(i) = -(cx*xt(i)*vt+fos*vs)/(dx*vt+fos); fx(i)=cx*xt(i)+dx*xtdot(i);
34    % limit braking torque to controlled or to maximum applied torque
35    if abs(owh(i))>vn/r, tqb_l=tqbctrl(i); else tqb_l=tqb_mx; end
36    % applied braking torque (enhanced dry friction model)
37    tqba(i)=-r*fx(i)+dn*owh(i); tqba(i)=sign(tqba(i))*min(abs(tqba(i)),tqb_l);
38    % angular momentum wheel (no driving torque)
39    owhdot(i) = ( -tqba(i) - r*fx(i) ) / thetaw;
40  end
41
42  % vehicle equations of motion (longitudinal and hub as well as pitch motion)
43  velxdot = ( fx(1) + fx(2) ) / mass;
44  velzdot = ( fz(1) + fz(2) ) / mass - gravity;
45  pdotdot = (-a1*fz(1) + a2*fz(2) - (h+posz)*(fx(1)+fx(2)) )/theta;
46
47  % ABS control (simple 2-point brake torque control)
48  tqbctrldot=[0;0]; % no change in braking torques as default
49  for i=1:2
50    if velx > vn % control braking torque only if vehicle is fast enough
51      % increase up to the limit tqb_mx (normal braking)
52      if tqbctrl(i) < tqb_mx, tqbctrldot(i) = dtqb_inc; end
53      % decrease existing torque if slip is close to maximum (90% of sxm)
54      if tqbctrl(i) > 0 && sx(i) < -0.9*sxm, tqbctrldot(i) = dtqb_dec; end
55    end
56  end
57
58  % state derivatives
59  xp = [ velx;velz;pdot; velxdot;velzdot;pdotdot; owhdot; xtdot; tqbctrldot ];
60
61  end
```

Here, the equations of motion for the simple planar vehicle model, provided in Section 8.1.1, are extended appropriately by the corresponding acceleration terms

$$m\,\ddot{x} = F_{x1} + F_{x2}\,, \tag{8.48}$$

$$m\,\ddot{z} = F_{z1} + F_{z2} - m\,g\,, \tag{8.49}$$

$$\Theta\,\ddot{\beta} = -F_{z1}\,a_1 + F_{z2}\,a_2 - (F_{x1} + F_{x2})\,(h + z)\,, \tag{8.50}$$

where the generalized coordinates x, z, and β characterize the longitudinal, the vertical, and the pitch motion of the vehicle. The inertia of the vehicle

about the y-axis is represented by Θ and $h + z$ describes the actual height of the vehicle center above a flat horizontal road. Within this simple model approach, small pitch motions, $|\beta| \ll 1$, are taken for granted. Neglecting the compliance of the tires and the dynamics of the wheel/axle masses in the vertical direction, the wheel loads will just be provided by

$$F_{z1} = m\,g\,\frac{a2}{a_1 + a_2} - c_{SF}\,(z - a_1\beta) - d_{SF}\left(\dot{z} - a_1\dot{\beta}\right), \quad (8.51)$$

$$F_{z2} = m\,g\,\frac{a1}{a_1 + a_2} - c_{SR}\,(z + a_2\beta) - d_{SR}\left(\dot{z} + a_2\dot{\beta}\right), \quad (8.52)$$

where c_{SF}, c_{SR}, d_{SF}, d_{SR} characterize the stiffness and damping properties of the front and rear suspension. Assuming that the longitudinal motion of the wheels are not affected by the pitch motion, the velocities of wheel centers of the front and rear axle are simply defined by the vehicle velocity $v = \dot{x}$. Then, the corresponding part of the simple vehicle model provided in Section 4.2.3 can be used to describe the dynamics of the longitudinal tire forces F_{x1}, F_{x2} and the wheel rotations. An enhanced dry friction model generates appropriate braking torques hereby. The function tmy_fcombined, which generates the tire force characteristic, is provided by Listing 3.3.

In reality, the functionality of an anti-lock control unit is very complex. Here, a simple two-point controller, realized in the code lines 47 to 64, is applied instead. As done in praxis, the controller operates only if the vehicle drives fast enough. The state variables tqbctrl(i), i=1,2, represent the controlled braking torques at the front and rear axle. When the brakes are applied, the controlled braking torque will be increased up to the limit tqb_mx by the ratio dtqb_inc at first. An existing controlled braking torque will be decreased by the ratio dtqb_dec if the slip exceeds 90% of the value sxm where the longitudinal tire characteristic provides the maximum force.

The MATLAB-Script in Listing 8.2 provides all data of the simple planar vehicle model, performs a simulation, and plots some results.

Listing 8.2
Script `vehicle_2d_simple_main`: Simple Planar Vehicle Model

```
1  global gravity mass theta a1 a2 h csf dsf csr dsr thetaw r
2  global fzn dfx0 fxm sxm fxs sxs vn cx dx
3  global t_tqb set_tqb dn dtqb_inc dtqb_dec
4  global sx fx fz tqba
5
6  % vehicle data
7  v0 = 80/3.6;  % [km/h -> m/s] initial vehicle velocity
8  gravity = 9.81; % [m/s^2] constant of gravity
9  mass = 700;   % [kg] corresp. vehicle mass
10 theta = 1000; % [kgm^2] corresp. vehicle inertia of wheel
11 a1 = 1.2;     % [m] distance vehicle center front axle
12 a2 = 1.3;     % [m] distance vehicle center rear axle
13 h  = 0.55;    % [m] height of vehicle center
14 csf = 20000;  % [N/m] suspension stiffness front
15 dsf = 3000;   % [N/m] suspension damping front
```

```
csr = 25000;  % [N/m] suspension stiffness rear
dsr = 3200;   % [N/m] suspension damping rear
thetaw = 1.2; % [kgm^2] wheel inertia
r = 0.3;      % [m] wheel radius

% long. tire characteristic for payload only
mu_l = 1.0;     % [-] local friction coefficient
fzn  = 3000;    % [N] payload
dfx0 = 100000;  % [N/-] initial incl. long. force char.
fxm  = 3200*mu_l; % [N] maximum long. force
sxm  = 0.1*mu_l; % [-] sx where fx=fxm
fxs  = 3000*mu_l; % [N] long. sliding force
sxs  = 0.8*mu_l; % [-] sx where fx=fxs
cx = 160000;    % [N/m] longitudinal tire stiffness
dx =  500;      % [N/(m/s)] longitudinal tire damping
vn = 0.01;      % [m/s] fictitious velocity

% adjust "damping" constant in enhanced braking torque model to wheel/tire
dn = r*sqrt(cx*thetaw);

% brake control (simple ABS)
dtqb_inc = r*fxm/0.1; % [Nm/s] amount of braking torque increase
dtqb_dec = -2*dtqb_inc; % [Nm/s] amount of braking torque decrease

% set braking torque (lookup table: time [s], torque [Nm])
t_tqb  = [ 0.0 0.05  0.10   2.50 ];
set_tqb = [ 0.0 0.00 1.00   1.00 ]*2*fxm*r;

% simple initial states
x0=[ 0; 0; 0; v0; 0; 0; v0/r; v0/r; 0; 0; 0; 0 ];

% ode23 with slightly enlarged error tolerances
options=odeset('AbsTol',1.e-5,'RelTol',5.e-3);
tic, [t,xout]=ode23(@vehicle_2d_simple_f,[0,max(t_tqb)],x0,options); toc,

% post processing
n=length(t);sxi=zeros(n,2);fxi=sxi;fzi=sxi;tqbi=sxi;xpi=zeros(size(xout));
for i=1:n
  xp = vehicle_2d_simple_f(t(i),xout(i,:)');
  sxi(i,:)=sx'; fxi(i,:)=fx'; fzi(i,:)=fz'; tqbi(i,:)=tqba'; xpi(i,:)=xp';
end

subplot(2,3,1)
 plot(t,tqbi(:,1:2)), grid on, axis([0,max(t_tqb),0,2000])
 title('applied braking torques [Nm]'), legend('front','rear')
subplot(2,3,2)
 plot(t,xpi(:,4)/gravity), grid on, axis([0,max(t_tqb),-1.2,0])
 legend('normalized vehicle acceleration [-]')
subplot(2,3,3);
 plot(t,[r*xout(:,7:8),xout(:,4)]), grid on, axis([0,max(t_tqb),0,25])
 title('Velocities [m/s]'), legend('v','r \Omega_1','r \Omega_2')
subplot(2,3,4)
 plot(t,fxi(:,1:2)/(mass*gravity)), grid on, axis([0,max(t_tqb),-1,0])
 title('normalized Longitudinal forces [N]'), legend('front','rear')
subplot(2,3,5)
 plot(t,fzi(:,1:2)/(mass*gravity)), grid on, axis([0,max(t_tqb),0,1])
 title('normalized Vertical forces [N]'), legend('front','rear')
```

```
73  subplot(2,3,6)
74   plot(t,sxi(:,1:2)), grid on, axis([0,max(t_tqb),-0.2,0])
75   title('longitudinal slips'), legend('front','rear')
```

The local friction coefficient mu_l makes it possible to adjust the tire characteristic to different tire/road friction values. The amount of braking torque increase is adjusted to the wheel tire data and amounts to dtqb_inc = 9600 Nm/s here. The amount of braking torque decrease is just set to double the value of the braking torque increase.

Within the simple two-point controller, the time derivatives of the controlled braking torques may jump from plus to minus, which will cause problems in the step size control of an ode solver. That is why ode23 with slightly reduced error tolerances is applied to this problem. Some results of simulations with mu_l = 1.0 (dry road) and mu_l = 0.4 (wet road) are plotted in Figure 8.14 and Figure 8.15. Each simulation is performed in the same time

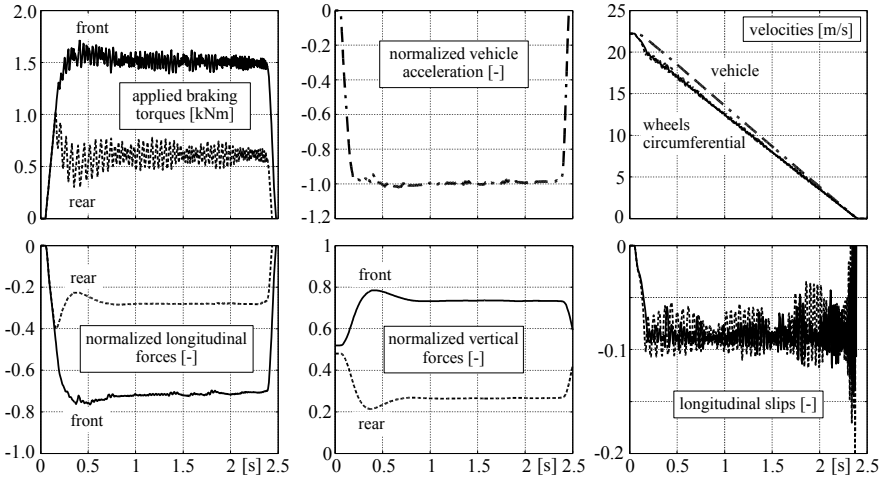

FIGURE 8.14
Controlled braking on dry road.

interval $0 \leq t \leq 2.5\ s$, with the same braking torque input and with the same initial vehicle velocity of 80 km/h or 22.22 m/s, respectively. On dry road, the vehicle decelerates with $\dot{v}/g \approx -1$ and comes to a full stop in the end, Figure 8.14. The wet surface reduces the deceleration to $\dot{v}/g \approx -0.4$, which cannot stop the vehicle in the time period under consideration, Figure 8.15. The simple two-point controller causes the longitudinal slips to oscillate rather rapidly about the desired slip values of -0.09 and -0.036, respectively. The controller of a commercial anti-lock system processes several signals and operates with more sophistication.

In steady-state, the normalized vertical wheel loads correspond with the results obtained in Section 8.1.1. Using the data provided by Listing 8.2 Equa-

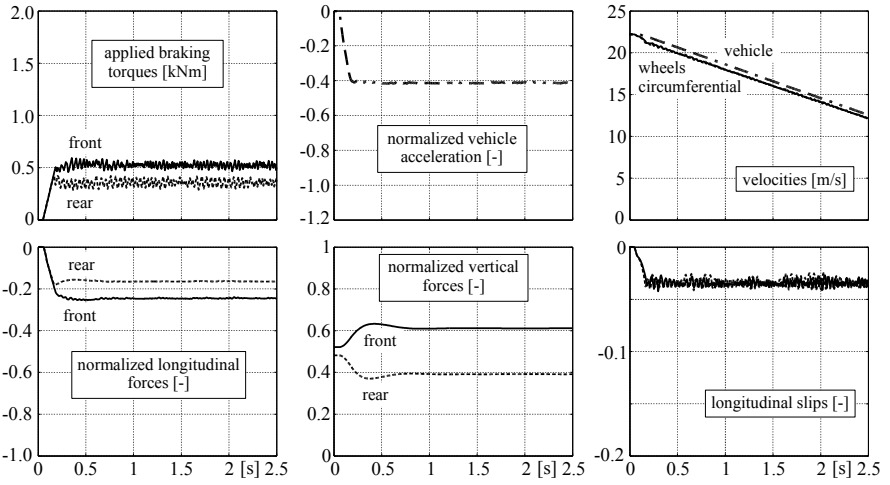

FIGURE 8.15
Controlled braking on wet road.

tions (8.5) and (8.6 deliver

$$\begin{array}{lllllllll} \dot{v}/g = -1.0 & | & F_{z1}/(m\,g) & = & 0.74 & & F_{z2}/(m\,g) & = & 0.26\,, \\ \dot{v}/g = -0.4 & | & F_{z1}/(m\,g) & = & 0.61 & & F_{z2}/(m\,g) & = & 0.39\,. \end{array} \tag{8.53}$$

In steady-state, the normalized longitudinal forces are close to the optimal ones, which are defined by Equations (8.40) and (8.41) and will produce

$$\begin{array}{lllllllll} \dot{v}/g = -1.0 & | & F_{x1}/(m\,g) & = & -0.74 & & F_{x2}/(m\,g) & = & -0.24\,, \\ \dot{v}/g = -0.4 & | & F_{x1}/(m\,g) & = & -0.26 & & F_{x2}/(m\,g) & = & -0.16\,. \end{array} \tag{8.54}$$

Regardless of the vehicle properties, an anti-lock system provides braking forces or braking torques, respectively, which are close to the optimal one. Besides avoiding completely locked wheels, this is a mayor benefit of an anti-lock system.

The slightly increased complexity of the vehicle model takes the hub and pitch motion of chassis into account too. On hard braking maneuvers, a strong pitch reaction will occur hereby, Figure 8.16. The movements of the chassis result in large suspension travel. In steady-state, the compression at the front axle amounts to 6 *cm* and the rebound at the rear axle to slightly more than 7 *cm*, *c.f.* rightmost plot in Figure 8.16. Most drivers do not like their vehicle to take a deep "bow" when braking. The straightforward solution to harden the suspension is not practicable because this will worsen the comfort significantly. A possible solution is discussed in the next section.

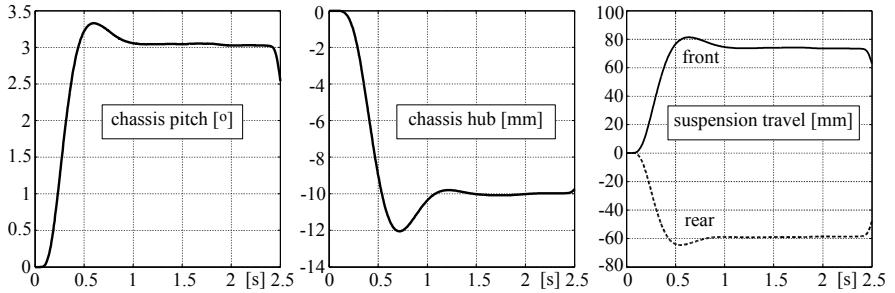

FIGURE 8.16
Brake pitch reaction of simple planar vehicle model $\dot{v}/g = -1$.

8.4 Drive and Brake Pitch

8.4.1 Enhanced Planar Vehicle Model

The planar vehicle model shown in Figure 8.17 consists of five rigid bodies: the chassis and one wheel and one knuckle at each axle. The coordinates x_C,

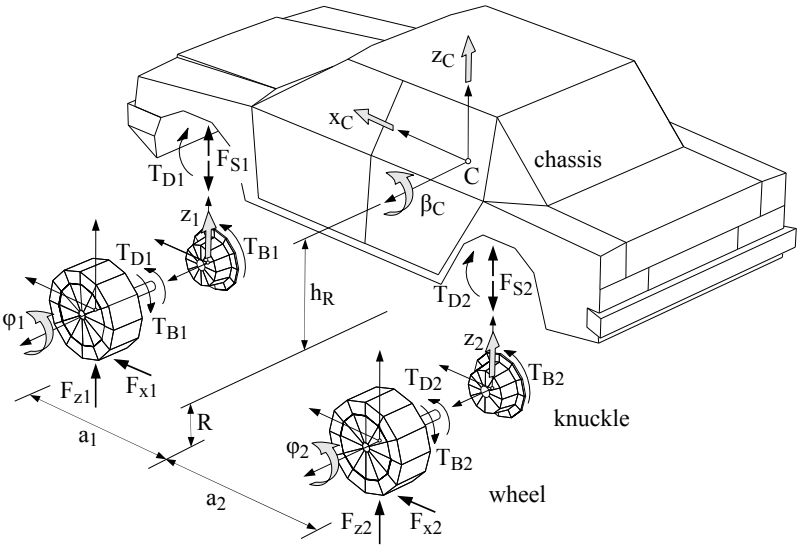

FIGURE 8.17
Planar vehicle model.

z_C, and β_C characterize the longitudinal, the vertical, and the pitch motion of the chassis. The centers of each wheel and knuckle are supposed to coincide

and z_1, z_2 represent their vertical motion relative to the chassis. Finally, the rotation angles φ_{W1} and φ_{W2} characterize the wheel rotations relative to the knuckles. The height of the chassis center is defined by $h = R + h_R$, where R denotes the wheel radius and h_r the height of the chassis center with respect to the wheel center. The distances a_1 and a_2 define the location of the chassis center with respect to the front and rear axle.

The suspension forces acting between the knuckle and the chassis are labeled F_{S1} and F_{S2}. At the wheels, drive torques T_{D1}, T_{D2}; brake torques T_{B1}, T_{B2}; longitudinal forces F_{x1}, F_{x2}; and the wheel loads F_{z1}, F_{z2} apply. In general, the brake torques are directly supported by the wheel bodies, whereas the drive torques are transmitted by the drive shafts to the chassis.

The velocity and the angular velocity of the chassis are given by

$$v_{0C,0} = \begin{bmatrix} \dot{x}_C \\ 0 \\ 0 \end{bmatrix} + \begin{bmatrix} 0 \\ 0 \\ \dot{z}_C \end{bmatrix} \quad \text{and} \quad \omega_{0C,0} = \begin{bmatrix} 0 \\ \dot{\beta}_C \\ 0 \end{bmatrix} . \tag{8.55}$$

The kinematical analysis of a double wishbone suspension system, performed in Section 5.4.6, shows that knuckle and wheel will not move simply up and down in practice. For example, the movements of the wheel center at a simple trailing arm suspension, discussed in Section 1.5, are determined by the rotation of the trailing arm about the revolute joint in B, Figure 8.18. The design

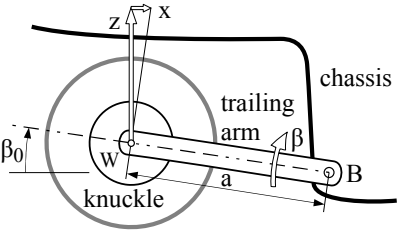

FIGURE 8.18
Trailing arm suspension.

position of the trailing arm is defined by the angle β_0. Then, the longitudinal and vertical motion of the wheel center W with respect to the chassis are just given by

$$x = a \sin(\beta_0 + \beta) \quad \text{and} \quad z = a \cos(\beta_0 + \beta) , \tag{8.56}$$

where a denotes the distance of the wheel center W to the joint in B. Within this planar model, the vertical movements of the front and rear wheel center (z_1, z_1) are used as generalized coordinates. Then, the longitudinal (x_1, x_2) and rotational motions (β_1, β_2) of each knuckle are described via functions of the corresponding vertical motions

$$x_1 = x_1(z_1) , \quad \beta_1 = \beta_1(z_1) \quad \text{and} \quad x_2 = x_2(z_2) , \quad \beta_2 = \beta_2(z_2) . \tag{8.57}$$

Under normal driving situations, small vertical displacements and a small pitch motion may be taken for granted. Then, the velocities of the knuckles and wheels are obtained by

$$v_{0K_1,0} = v_{0W_1,0} = \begin{bmatrix} \dot{x}_C \\ 0 \\ 0 \end{bmatrix} + \begin{bmatrix} 0 \\ 0 \\ \dot{z}_C \end{bmatrix} + \begin{bmatrix} -h_R\,\dot{\beta}_C \\ 0 \\ -a_1\,\dot{\beta}_C \end{bmatrix} + \begin{bmatrix} \frac{\partial x_1}{\partial z_1}\dot{z}_1 \\ 0 \\ \dot{z}_1 \end{bmatrix}, \tag{8.58}$$

$$v_{0K_2,0} = v_{0W_2,0} = \begin{bmatrix} \dot{x}_C \\ 0 \\ 0 \end{bmatrix} + \begin{bmatrix} 0 \\ 0 \\ \dot{z}_C \end{bmatrix} + \begin{bmatrix} -h_R\,\dot{\beta}_C \\ 0 \\ +a_2\,\dot{\beta}_C \end{bmatrix} + \begin{bmatrix} \frac{\partial x_2}{\partial z_2}\dot{z}_2 \\ 0 \\ \dot{z}_2 \end{bmatrix}, \tag{8.59}$$

where higher-order terms were neglected. In general, the constraint motions, here defined by Equation (8.57), may depend on more than one generalized coordinate. That is why partial derivatives are used in this approach. Finally, the angular velocities of the knuckles and wheels are defined by

$$\omega_{0K_1,0} = \begin{bmatrix} 0 \\ \dot{\beta}_C \\ 0 \end{bmatrix} + \begin{bmatrix} 0 \\ \dot{\beta}_1 \\ 0 \end{bmatrix}, \quad \omega_{0W_1,0} = \begin{bmatrix} 0 \\ \dot{\beta}_C \\ 0 \end{bmatrix} + \begin{bmatrix} 0 \\ \dot{\beta}_1 \\ 0 \end{bmatrix} + \begin{bmatrix} 0 \\ \dot{\varphi}_1 \\ 0 \end{bmatrix} \tag{8.60}$$

and

$$\omega_{0K_2,0} = \begin{bmatrix} 0 \\ \dot{\beta}_C \\ 0 \end{bmatrix} + \begin{bmatrix} 0 \\ \dot{\beta}_2 \\ 0 \end{bmatrix}, \quad \omega_{0W_2,0} = \begin{bmatrix} 0 \\ \dot{\beta}_C \\ 0 \end{bmatrix} + \begin{bmatrix} 0 \\ \dot{\beta}_2 \\ 0 \end{bmatrix} + \begin{bmatrix} 0 \\ \dot{\varphi}_2 \\ 0 \end{bmatrix}. \tag{8.61}$$

Collecting the time derivatives of the generalized coordinates in the vector of generalized velocities

$$z = \begin{bmatrix} \dot{x}_C & \dot{z}_C & \dot{\beta}_C & \dot{\beta}_1 & \dot{\varphi}_1 & \dot{\beta}_2 & \dot{\varphi}_2 \end{bmatrix}^T, \tag{8.62}$$

the velocities and angular velocities given by Equations (8.55), (8.58), (8.59), (8.60), and (8.61) can be written as

$$v_{0i} = \sum_{j=1}^{7} \frac{\partial v_{0i}}{\partial z_j}\, z_j \quad \text{and} \quad \omega_{0i} = \sum_{j=1}^{7} \frac{\partial \omega_{0i}}{\partial z_j}\, z_j\,. \tag{8.63}$$

The partial velocities $\partial v_{0i}/\partial z_j$ and partial angular velocities $\partial \omega_{0i}/\partial z_j$ for the planar vehicle model are arranged in Tables 8.1 and 8.2. The last column lists the forces and torques that apply to the corresponding model body, where g denotes the constant of gravity and m_C, m_{K1}, m_{W1}, m_{K2}, m_{W2}, Θ_C, Θ_{K1}, Θ_{W1}, Θ_{K2}, Θ_{W1} denote the mass and inertia properties.

TABLE 8.1
Partial Velocities and Applied Forces

Bodies	Partial Velocities $\partial v_{0i}/\partial z_j$							Applied Forces
	$\dot{x}_C$	$\dot{z}_C$	$\dot{\beta}_C$	$\dot{z}_1$	$\dot{\varphi}_1$	$\dot{z}_2$	$\dot{\varphi}_2$	F_i^a
Chassis	1	0	0	0	0	0	0	0
m_C	0	0	0	0	0	0	0	0
	0	1	0	0	0	0	0	$F_{S1}+F_{S2}-m_C g$
Knuckle	1	0	$-h_R$	$\frac{\partial x_1}{\partial z_1}$	0	0	0	0
front	0	0	0	0	0	0	0	0
m_{K1}	0	1	$-a_1$	1	0	0	0	$-F_{S1}-m_{K1} g$
Wheel	1	0	$-h_R$	$\frac{\partial x_1}{\partial z_1}$	0	0	0	F_{x1}
front	0	0	0	0	0	0	0	0
m_{W1}	0	1	$-a_1$	1	0	0	0	$F_{z1}-m_{W1} g$
Knuckle	1	0	$-h_R$	0	0	$\frac{\partial x_2}{\partial z_2}$	0	0
rear	0	0	0	0	0	0	0	0
m_{K2}	0	1	a_2	0	0	1	0	$-F_{S2}-m_{K2} g$
Wheel	1	0	$-h_R$	0	0	$\frac{\partial x_2}{\partial z_2}$	0	F_{x2}
rear	0	0	0	0	0	0	0	0
m_{W2}	0	1	a_2	0	0	1	0	$F_{z2}-m_{W2} g$

TABLE 8.2
Partial Angular Velocities and Applied Torques

Bodies	Partial Angular Velocities $\partial \omega_{0i}/\partial z_j$							Applied Torques
	$\dot{x}_C$	$\dot{z}_C$	$\dot{\beta}_C$	$\dot{z}_1$	$\dot{\varphi}_1$	$\dot{z}_2$	$\dot{\varphi}_2$	T_i^a
Chassis	0	0	0	0	0	0	0	0
Θ_C	0	0	1	0	0	0	0	$-T_{D1}-T_{D2}-a_1 F_{S1}+a_2 F_{S2}$
	0	0	0	0	0	0	0	0
Knuckle	0	0	0	0	0	0	0	0
front	0	0	1	$\frac{\partial \beta_1}{\partial z_1}$	0	0	0	T_{B1}
Θ_{K1}	0	0	0	0	0	0	0	0
Wheel	0	0	0	0	0	0	0	0
front	0	0	1	$\frac{\partial \beta_1}{\partial z_1}$	1	0	0	$T_{D1}-T_{B1}-R F_{x1}$
Θ_{W1}	0	0	0	0	0	0	0	0
Knuckle	0	0	0	0	0	0	0	0
rear	0	0	1	0	0	$\frac{\partial \beta_2}{\partial z_2}$	0	T_{B2}
Θ_{K2}	0	0	0	0	0	0	0	0
Wheel	0	0	0	0	0	0	0	0
rear	0	0	1	0	0	$\frac{\partial \beta_2}{\partial z_2}$	1	$T_{D2}-T_{B2}-R F_{x2}$
Θ_{W2}	0	0	0	0	0	0	0	0

8.4.2 Equations of Motion

As shown in Section 1.4.3 the accelerations and angular accelerations split into two parts. Similar to Equation (1.26), one gets

$$a_{0i} = \sum_{j=1}^{7} \left(\frac{\partial v_{0i}}{\partial z_j} \dot{z}_j + a_{0i}^R \right) \quad \text{and} \quad \alpha_{0i} = \sum_{j=1}^{7} \left(\frac{\partial \omega_{0i}}{\partial z_j} \dot{z}_j + \alpha_{0i}^R \right) . \tag{8.64}$$

The remaining terms in the accelerations,

$$a_{0i}^R = \sum_{j=1}^{7} \frac{d}{dt}\left(\frac{\partial v_{0i}}{\partial z_j}\right) \dot{z}_j \quad \text{and} \quad \alpha_{0i}^R = \sum_{j=1}^{7} \frac{d}{dt}\left(\frac{\partial \omega_{0i}}{\partial z_j}\right) \dot{z}_j \,, \tag{8.65}$$

will contain only higher-order terms here and may be neglected for basic studies. Jourdain's principle of virtual power delivers the equations of motion in the form of

$$M\,\dot{z} \;=\; Q \,, \tag{8.66}$$

where

$$M(i,j) \;=\; \sum_{k=1}^{5} \left(\frac{\partial v_{0k}}{\partial z_i}\right)^T m_k \,\frac{\partial v_{0k}}{\partial z_j} \;+\; \sum_{k=1}^{5} \left(\frac{\partial \omega_{0k}}{\partial z_i}\right)^T \Theta_k \,\frac{\partial \omega_{0k}}{\partial z_j} \tag{8.67}$$

defines the elements of the 7×7 mass matrix and the 7×1 generalized force vector

$$Q(i) \;=\; \sum_{k=1}^{5} \left(\frac{\partial v_{0k}}{\partial z_i}\right)^T F_k^e \;+\; \sum_{k=1}^{5} \left(\frac{\partial \omega_{0k}}{\partial z_i}\right)^T M_k^e \tag{8.68}$$

only processes applied forces and torques in this particular case.

8.4.3 Equilibrium

Introducing the abbreviations

$$m_1 = m_{K1} + m_{W1},\; m_2 = m_{K2} + m_{W2},\; m_V = m_C + m_1 + m_2,\; h = h_R + R \,, \tag{8.69}$$

the components of the vector of generalized forces and torques will read as

$$\begin{aligned}
Q(1) &= F_{x1} + F_{x2} \,, \\
Q(2) &= F_{z1} + F_{z2} - m_V\, g \\
Q(3) &= -a_1(F_{z1} - m_1 g) + a_2(F_{z2} - m_2 g) - h(F_{x1} + F_{x2}) \,, \\
Q(4) &= F_{z1} - m_1 g - F_{S1} + \tfrac{\partial x_1}{\partial z_1}\, F_{x1} + \tfrac{\partial \beta_1}{\partial z_1}(T_{D1} - R\, F_{x1}) \,, \\
Q(5) &= T_{D1} - T_{B1} - R\, F_{x1} \,, \\
Q(6) &= F_{z2} - m_2 g - F_{S2} + \tfrac{\partial x_2}{\partial z_2}\, F_{x2} + \tfrac{\partial \beta_2}{\partial z_2}(T_{D2} - R\, F_{x2}) \,, \\
Q(7) &= T_{D2} - T_{B2} - R\, F_{x2} \,.
\end{aligned} \tag{8.70}$$

Without any driving and braking torques,

$$T_{D1} = 0 \,, \quad T_{D2} = 0 \,, \quad T_{B1} = 0 \,, \quad T_{B2} = 0 \,, \tag{8.71}$$

one gets the steady-state longitudinal forces, the suspension preloads, and the wheel loads as

$$\begin{aligned}
F_{x1}^{st} &= 0 \,, & F_{x2}^{st} &= 0 \,, \\
F_{S1}^{st} &= \frac{a_2}{a_1 + a_2}\, m_C g \,, & F_{S2}^{st} &= \frac{a_1}{a_1 + a_2}\, m_C g \,, \\
F_{z1}^{st} &= \frac{a_2}{a_1 + a_2}\, m_C g + m_1 g \,, & F_{z2}^{st} &= \frac{a_1}{a_1 + a_2}\, m_C g + m_2 g \,.
\end{aligned} \tag{8.72}$$

As distinct from Equation (8.7), the static wheel loads are now composed of the corresponding chassis and the axle weight.

8.4.4 Driving and Braking

Assuming that on accelerating or decelerating the vehicle, the wheels neither slip nor lock, then

$$R\,\dot{\varphi}_1 \;=\; \dot{x}_C - h_R\,\dot{\beta}_C + \frac{\partial x_1}{\partial z_1}\,\dot{z}_1 \quad \text{and} \quad R\,\dot{\varphi}_2 \;=\; \dot{x}_C - h_R\,\dot{\beta}_C + \frac{\partial x_2}{\partial z_2}\,\dot{z}_2 \tag{8.73}$$

will hold. In steady-state, the pitch motion of the body and the vertical motion of the knuckles and the wheels reach constant values,

$$\beta_C = \beta_C^{st} = const.\,, \quad z_1 = z_1^{st} = const.\,, \quad z_2 = z_2^{st} = const.\,. \tag{8.74}$$

Then Equation (8.73) simplifies to

$$R\,\dot{\varphi}_1 \;=\; \dot{x}_C \quad \text{and} \quad R\,\dot{\varphi}_2 \;=\; \dot{x}_C\,. \tag{8.75}$$

In addition, the time derivative of the generalized velocities reduces to

$$\dot{z}^{st} \;=\; \left[\begin{array}{ccccccc} \ddot{x}_C & 0 & 0 & 0 & \frac{1}{R}\ddot{x}_C & 0 & \frac{1}{R}\ddot{x}_C \end{array}\right]^T \tag{8.76}$$

in this particular case. Then, the equation of motion (8.66) will result in

$$m_V\,\ddot{x}_C = F_{x1}^{dyn} + F_{x2}^{dyn}\,, \tag{8.77}$$

$$0 = F_{z1}^{dyn} + F_{z2}^{dyn}\,, \tag{8.78}$$

$$\left[-h_R(m_1+m_2)+\tfrac{\Theta_{W1}}{R}+\tfrac{\Theta_{W2}}{R}\right]\ddot{x}_C = -a_1F_{z1}^{dyn}+a_2F_{z2}^{dyn}-h(F_{x1}^{dyn}+F_{x2}^{dyn}), \tag{8.79}$$

$$\left[\tfrac{\partial x_1}{\partial z_1}m_1+\tfrac{\partial \beta_1}{\partial z_1}\tfrac{\Theta_{W1}}{R}\right]\ddot{x}_C = F_{z1}^{dyn}-F_{S1}^{dyn}+\frac{\partial x_1}{\partial z_1}\,F_{x1}^{dyn}+\frac{\partial \beta_1}{\partial z_1}(T_{D1}-RF_{x1}^{dyn})\,, \tag{8.80}$$

$$\tfrac{\Theta_{W1}}{R}\ddot{x}_C = T_{D1}-T_{B1}-RF_{x1}^{dyn}\,, \tag{8.81}$$

$$\left[\tfrac{\partial x_2}{\partial z_2}m_2+\tfrac{\partial \beta_2}{\partial z_2}\tfrac{\Theta_{W2}}{R}\right]\ddot{x}_C = F_{z2}^{dyn}-F_{S2}^{dyn}+\frac{\partial x_2}{\partial z_2}\,F_{x2}^{dyn}+\frac{\partial \beta_2}{\partial z_2}(T_{D2}-RF_{x2}^{dyn})\,, \tag{8.82}$$

$$\tfrac{\Theta_{W2}}{R}\ddot{x}_C = T_{D2}-T_{B2}-RF_{x2}^{dyn}\,, \tag{8.83}$$

where Equations (8.74), (8.75), and (8.69) were taken into account and the steady-state spring forces, longitudinal forces, and wheel loads have been separated into steady-state and dynamic terms

$$F_{xi}^{st} \;=\; F_{xi}^{st}+F_{xi}^{dyn}, \quad F_{zi}^{st} \;=\; F_{zi}^{st}+F_{zi}^{dyn}, \quad F_{Si}^{st} \;=\; F_{Si}^{st}+F_{Si}^{dyn}, \quad i=1,2. \tag{8.84}$$

Combining Equation (8.77) with Equations (8.81) and (8.83) simply results

$$\ddot{x}_C = \frac{\left(T_{D1}+T_{D2}-T_{B1}-T_{B2}\right)/R}{m_V+\Theta_{W1}/R^2+\Theta_{W2}/R^2}\,. \tag{8.85}$$

The terms in the numerator characterize the overall driving and braking forces and the denominator represents the generalized vehicle mass, which expresses the fact that besides the vehicle mass m_V, the wheels with the inertias Θ_{W1} and Θ_{W2} must be accelerated or decelerated too. Then, the tire forces are obtained as

$$F_{x1}^{dyn} = \frac{T_{D1} - T_{B1}}{R} - \frac{\Theta_{W1}}{R^2}\ddot{x}_C\,, \quad F_{x2}^{dyn} = \frac{T_{D2} - T_{B2}}{R} - \frac{\Theta_{W2}}{R^2}\ddot{x}_C\,, \tag{8.86}$$

$$F_{z1}^{dyn} = -\left(\frac{\Theta_{W1} + \Theta_{W2}}{R} + m_1 R + m_2 R + m_C h\right)\frac{\ddot{x}_C}{a_1 + a_2}\,, \tag{8.87}$$

$$F_{z2}^{dyn} = \left(\frac{\Theta_{W1} + \Theta_{W2}}{R} + m_1 R + m_2 R + m_C h\right)\frac{\ddot{x}_C}{a_1 + a_2}\,. \tag{8.88}$$

Neither the vehicle acceleration or deceleration nor the tire forces are affected by the kinematic properties of the suspension.

In general, the inertias of the wheels are small compared to the vehicle mass on normal passenger cars and may be neglected in practice. Then, the dynamic wheel loads simplify to

$$F_{z1,z2}^{dyn} \approx \mp\,(m_1 R + m_2 R + m_C h)\,\frac{\ddot{x}_C}{a_1 + a_2} = \mp m_V \frac{h_V}{a_1 + a_2}\ddot{x}_C\,, \tag{8.89}$$

where $m_V = m_1 + m_2 + m_C$ denotes the overall vehicle mass and h_V defines the height of the vehicle center of gravity. This coincides perfectly with the results obtained in Section 8.1.1.

A simple rearrangement of Equations (8.80) and (8.82) provide the suspension forces as

$$F_{S1}^{dyn} = F_{z1}^{dyn} + \left(\frac{\partial x_1}{\partial z_1} - R\frac{\partial \beta_1}{\partial z_1}\right) F_{x1}^{dyn} + \frac{\partial \beta_1}{\partial z_1} T_{D1} - \left[\frac{\partial x_1}{\partial z_1} m_1 + \frac{\partial \beta_1}{\partial z_1}\frac{\Theta_{W1}}{R}\right]\ddot{x}_C\,, \tag{8.90}$$

$$F_{S2}^{dyn} = F_{z2}^{dyn} + \left(\frac{\partial x_2}{\partial z_2} - R\frac{\partial \beta_2}{\partial z_2}\right) F_{x2}^{dyn} + \frac{\partial \beta_2}{\partial z_2} T_{D2} - \left[\frac{\partial x_2}{\partial z_2} m_2 + \frac{\partial \beta_2}{\partial z_2}\frac{\Theta_{W2}}{R}\right]\ddot{x}_C\,. \tag{8.91}$$

A complete algebraic solution is very cumbersome and will result in extremely complicated expressions. The suspension forces F_{S1}, F_{S2} and the wheel loads F_{z1}, F_{z2} support the chassis and the knuckles with the wheels. In steady-state, it holds that

$$\begin{aligned} F_{S1}^{dyn} &= \;\; c_{S1} z_1^{dyn}\,, \\ F_{S2}^{dyn} &= \;\; c_{S2} z_2^{dyn}\,, \\ F_{z1}^{dyn} &= -c_{T1}(z_C^{dyn} - a_1 \beta_C^{dyn} + z_1^{dyn})\,, \\ F_{z2}^{dyn} &= -c_{T2}(z_C^{dyn} + a_2 \beta_C^{dyn} + z_2^{dyn})\,, \end{aligned} \tag{8.92}$$

where linear spring characteristics are assumed and the tire liftoff is not taken into account.

8.4.5 Drive Pitch

The MATLAB-Script in Listing 8.3 provides the data of the enhanced planar vehicle model, sets the driving and braking torques, calculates for a fast steady-state acceleration the forces, the suspension travel, the pitch and hub motion of the chassis, and finally plots the chassis pitch angle versus different inclinations of the front knuckle/wheel motion.

Listing 8.3
MATLAB-Script `pitch_reaction_drive_dx1`: Anti-Squat

```
% vehicle data
g  = 9.81;        % Constant of Gravity
R  = 0.30;        % Tire Radius [m]
h  = 0.59;        % Height of Center of Gravity [m]
a1 = 1.20;        % Center of Gravity --> Front Axle [m]
a2 = 1.30;        % Center of Gravity --> Rear Axle [m]
mC  = 600;        % Mass of Chassis (half vehicle) [kg]
m1  = 50;         % Mass of Front Axle [kg]
m2  = 50;         % Mass of Rear Axle [kg]
ThW1 = 1.2;       % Inertia of Front Wheels [kg m^2]
ThW2 = 1.2;       % Inertia of Rear Wheels [kg m^2]
cS1 = 22000;      % Stiffness of Front Axle Suspension [N/m]
cS2 = 28600;      % Stiffness of Rear Axle Suspension [N/m]
cT1 = 220000;     % Stiffness of Front Wheels [N/m]
cT2 = 200000;     % Stiffness of Rear Wheels [N/m]

% overall and generalized vehicle mass
mV=mC+m1+m2; mg = mV+ThW1/R^2+ThW2/R^2;

% static wheel loads
Fz1_st = a2/(a1+a2)*mC*g + m1*g; Fz2_st = a1/(a1+a2)*mC*g + m2*g;

% all wheel drive no braking
TD1=643; TD2=1497; TB1=0; TB2=0;

% default axle kinematics
dx1 = 0; dx2 = 0; % inclination of front and rear wheel motion [-]
db1 = 0; db2 = 0; % y-rotation of front and rear knuckle [rad/m]

% change inclination of front knuckle/wheel motion [-]
ivar=25; dx_min=tan(-12/180*pi); dx_max=tan(12/180*pi);

for i=1:ivar

  dx1 = dx_min + (dx_max-dx_min)*(i-1)/(ivar-1);

% vehicle acceleration
  xddot = 1/R*(TD1+TD2-TB1-TB2)/mg;

% dynamic tire forces
  Fx1=(TD1-TB1)/R - ThW1/R^2*xddot;
  Fx2=(TD2-TB2)/R - ThW2/R^2*xddot;
  Fz1=-xddot*((ThW1+ThW2)/R+(m1+m2)*R+mC*h)/(a1+a2);
  Fz2= xddot*((ThW1+ThW2)/(R*h)+(m1+m2)*R/h+mC)*h/(a1+a2);

```

```
% dynamic suspension forces
  FS1=Fz1+(dx1-R*db1)*Fx1+db1*TD1-(dx1*m1+db1*ThW1/R)*xddot;
  FS2=Fz2+(dx2-R*db2)*Fx2+db2*TD2-(dx2*m2+db2*ThW2/R)*xddot;

% suspension travel
  z1 = FS1/cS1; z2=FS2/cS2;

% pitch and hub motion of chassis
  bC = (Fz1/cT1-Fz2/cT2+z1-z2)/(a1+a2); zC = a1*bC-z1-Fz1/cT1;

% plot pitch angle
  plot(dx1,bC*180/pi,'ok','MarkerSize',5), hold on, grid on

end
```

The driving torques TD1 = 643 Nm and TD2 = 1497 Nm accelerate the vehicle with $\ddot{x}_C/g = 1$. The complete results, obtained by simply omitting the semicolon at the corresponding code lines, for a plain suspension kinematics (db1=0, dx1=0, db2=0, dx2=0), where both wheels just move straight up and down are shown in Table 8.3. In this particular case, the required friction

TABLE 8.3
Vehicle with Plain Suspension Kinematics Accelerated Fast ($\ddot{x}_C/g = 1$)

Longitudinal Tire Force	Wheel Load Static+Dynamic	Suspension Forces	Suspension Travel	Chassis Motion
F_{x1}=2012N	F_{z1}=2012N	F_{S1}=−1539N	z_1=−70mm	z_C= 10.5mm
F_{x2}=4859N	F_{z2}=4855N	F_{S2}= 1539N	z_2= 54mm	β_C=−3.17°

coefficients at the front and rear wheels amount to $\mu_1 = |F_{x1}|/F_{z1} = 1$ and $\mu_2 = |F_{x2}|/F_{z2} = 1$, which will represent an all wheel drive with perfect driving torque distribution.

The suspension kinematics are characterized by the parameters db1, db2, which describe the y-rotation of the knuckles caused by their vertical motion z1, z2, and the parameters dx1, dx2, which define the inclination of the wheel motions in the xz-plane. The MATLAB-Script in Listing 8.3 varies the inclination of front knuckle/wheel movement only. A simple and straightforward code extension will produce the results plotted in Fig, 8.19. The drive shafts transmit the driving torques directly from the chassis to the wheels in a standard drive train layout. That is why the knuckle rotations caused by the jounce and rebound motion of the knuckles, here characterized by db1 and db2, will have no influence at all on the steady-state chassis pitch angle when the vehicle accelerates. "Anti-squat" suspension kinematics, which are characterized by dx1>0 and dx2<0, will reduce the pitch angle β_C when the vehicle is accelerated. However, a longitudinal motion of the knuckle caused by the suspension travel (dx1≠0, dx2≠0) forces the wheel to spin faster or slower when riding on a rough road and may excite drive train vibrations. In addition, a front axle designed with dx1>0 will cause severe problems when crossing a bump in forward drive, because knuckle and wheel will be moved

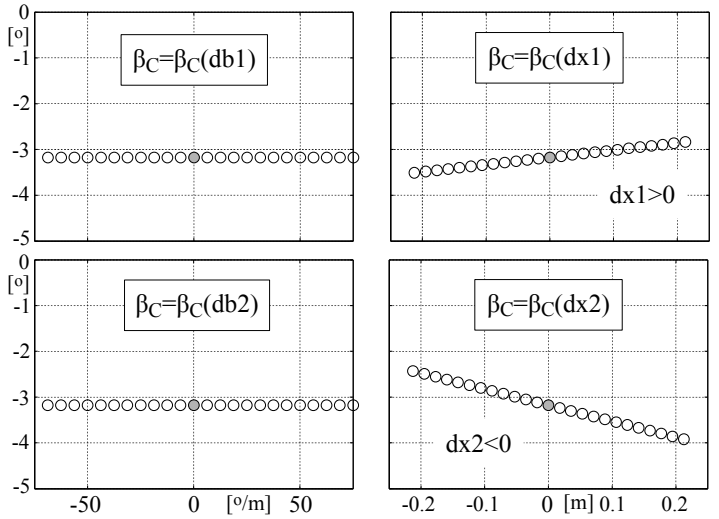

FIGURE 8.19
Influence of suspension kinematics on the chassis pitch when accelerating.

toward the bump on compression then. In practice, only sport cars are able to accelerate really fast. However, these vehicles have a rather low center of gravity, which reduces the pitch reaction anyway. In addition, a strong drive pitch reaction indicates the power of the engine and is therefore more welcome than a brake pitch.

8.4.6 Break Pitch

Vanishing driving torques TD1 = 0, TD2 = 0 and braking torques of TB1 = 1566 Nm, TB2 = 572.5 Nm will decelerate the vehicle with $\ddot{x}_C/g = -1$. The results for plain suspension kinematics (db1=0, dx1=0, db2=0, dx2=0), where both wheels just move straight up and down, are shown in Table 8.4. The required friction coefficients at the front and rear wheels amount again

TABLE 8.4
Vehicle with Plain Suspension Kinematics Braked Hard ($\ddot{x}_C/g = -1$)

Longitudinal Tire Force	Wheel Load Static+Dynamic	Suspension Forces	Suspension Travel	Chassis Motion
F_{x1}=−5089N	F_{z1}=5089N	F_{S1}= 1538N	z_1= 70mm	z_C=−10.5mm
F_{x2}=−1778N	F_{z2}=1778N	F_{S2}=−1538N	z_2=−54mm	β_C=3.17°

to $\mu_1 = |F_{x1}|/F_{z1} = 1$ and $\mu_2 = |F_{x2}|/F_{z2} = 1$, thus representing an optimal braking force distribution. The results correspond quite well with those shown in Figure 8.16 generated with the simple planar model. The simple pla-

nar model, presented in Section 8.3.8.2, neglects the compliance of the tires and the masses of the wheels. Thus, the parameters csf = 20000 N/m and csr = 25000 N/m represent an overall suspension stiffness that describes the effect of a suspension spring in series to the tire spring. The corresponding parameters, given in Listing 8.3, indeed result in

$$c_{sf} = \frac{c_{S1}\, c_{T1}}{c_{S1} + c_{T1}} = \frac{22000 * 220000}{22000 + 220000} = 20000\ N/m\ , \tag{8.93}$$

$$c_{sr} = \frac{c_{S2}\, c_{T2}}{c_{S2} + c_{T2}} = \frac{28600 * 200000}{28600 + 200000} = 25022\ N/m\ . \tag{8.94}$$

The masses of the chassis $m_C = 600\ kg$ and the wheels $m_1 = m_2 = 50\ kg$ amount to the overall vehicle mass of 700 kg, which represents half of a vehicle. Here, the height of the overall vehicle center above the road is given by

$$h_V = \frac{m_C h + m_1 R + m_2 R}{m_c + m_1 + m_2} = \frac{600 * 0.59 + 50 * 0.3 + 50 * 0.3}{600 + 50 + 50} = 0.55\ , \tag{8.95}$$

which matches the value used in the simple model approach. The suspension travel plotted in Figure 8.16 includes the tire deflection too. That is why the steady-state results $z_1^{st} \approx 73mm$ and $z_2^{st} \approx -59mm$ are slightly larger than the corresponding values given in Table 8.4. "Anti-dive" suspension kinematics, which are characterized by db1<0, dx1>0 and db2>0 and dx2<0, will reduce the pitch angle β_C significantly when the vehicle is braked, Figure 8.20. As

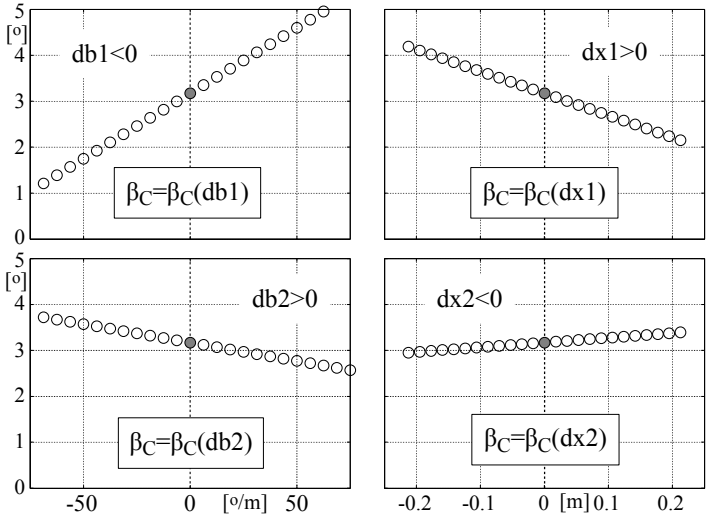

FIGURE 8.20
Influence of suspension kinematics on the chassis pitch when braking hard.

mentioned before, a longitudinal motion of the knuckle caused by the suspension travel (dx1≠0, dx2≠0) is not really desirable. That is why most axle

layouts will realize the "anti-dive" effect by just rotating the knuckles appropriately (db1<0, dx1=0 and db2>0, dx2=0).

8.4.7 Brake Pitch Pole

The pitch of the vehicle caused by braking will be felt as annoying, if too distinct. The brake pitch angle can be reduced by rotating the knuckle appropriately during suspension travel. For real suspension systems, the brake

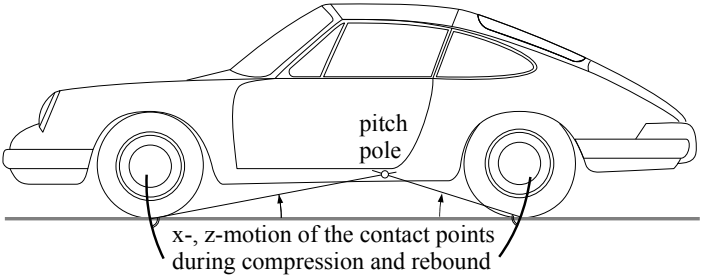

FIGURE 8.21
Brake pitch pole.

pitch pole can be calculated from the motions of the wheel contact points in the x-, z-plane, Figure 8.21. Increasing the pitch pole height above the track level means a decrease in the brake pitch angle. However, the pitch pole is not set above the height of the center of gravity in practice, because the front of the vehicle would rise at braking then.

Exercises

8.1 A minibus with a wheel base of $a = a_1 + a_2 = 4\,m$ is characterized by the following parameters:

	unladen	laden
Axle load front	$F_{Z1} = 15\,kN$	$F_{Z1} = 20\,kN$
Axle load rear	$F_{Z2} = 14\,kN$	$F_{Z2} = 23\,kN$
COG height	$h = 1.2\,m$	$h = 1.4\,m$

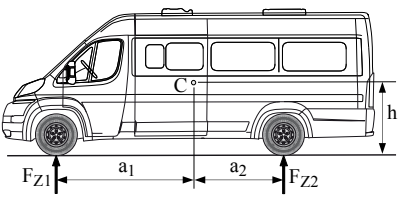

Determine the mass of the vehicle and the horizontal position of the center of gravity (COG) defined by the parameters a_1 and a_2 for the unladen and laden vehicle.

The wheels have radius $R = 0.372\,m$ and the vehicle is supposed to decelerate with $\dot{v}/g = -0.6$ now. Calculate the required braking torques at the front and rear axle when an optimal distribution is taken for granted.

8.2 The weight $G = 660\,kN$ of a heavy-duty dumper distributes to the front and rear axle with the ratio of 1:2 on a horizontal road. The height of the center of gravity is determined by $h = 2500\,mm$ hereby. Each wheel has radius of $R = 938.5\,mm$ and the wheel base amounts to $a = 3700\,mm$.

Determine the downhill and climbing capacity of the vehicle, $\alpha_D \leq \alpha \leq \alpha_C$.

The dumper moves downhill now and is supposed to decelerate with $\dot{v} = -2\,m/s^2$. The inclination of the road is given by $\alpha = -17.72°$. Determine the required coefficient of friction between the tires and the road when the dumper decelerates with an optimal braking force distribution. Specify the required braking torques too.

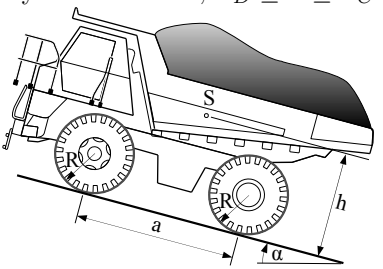

8.3 A pickup is all-wheel driven. The engine provides a maximum torque of $T_E = 480\,Nm$. The ratio of the first gear is given by $i_G = 3.5$. The center differential distributes the driving torque with a ratio of 40:60 to the front and rear axles. The differentials at the front and rear axle provide an additional gear ratio of $i_D = 3.7$ and finally distribute the torque equally to the left and right wheels. The vehicle has mass $m = 2700\,kg$. The position of the center of gravity is determined by $a_1 = 1.7\,m$, $a_2 = 1.5\,m$, $h = 0.9\,m$, and the radius of each wheel is given by $R = 0.36\,m$.

Determine the maximum acceleration of the vehicle.

Calculate the hereby required friction coefficients between tire and road at the front and rear axle.

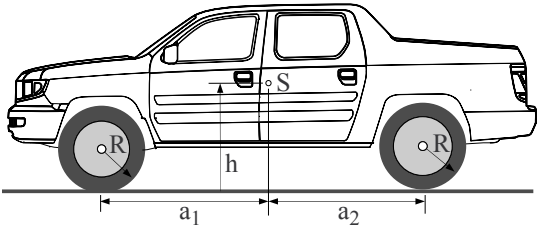

8.4 Extend the MATLAB-Script given in Listing 8.3 in order to produce the plots shown in Figs. 8.19 and 8.20.

Use part of the MATLAB-Script then to check the results of Exercise 8.1. Estimate suitable values for the axle masses, the suspension stiffness, and the tire stiffness. Try to reduce the brake pitch by an appropriate layout of the suspension kinematics.

Modify the MATLAB-Script to generate the results for vehicles with rear wheel and front wheel drive.

9

Lateral Dynamics

CONTENTS

9.1 Kinematic Approach

9.1.1 Kinematic Tire Model

When a vehicle drives through a curve at low lateral acceleration, small lateral forces will be needed for course holding. Then, lateral slip hardly occurs at the wheels. In the ideal case at vanishing lateral slip, the wheels only move in a circumferential direction. The velocity component of the contact point in the lateral direction of the tire then vanishes

$$v_y \;=\; e_y^T\, v_{0P} \;=\; 0\,. \tag{9.1}$$

This constraint equation can be used as a "kinematic tire model" for course calculation of vehicles moving in the low lateral acceleration range.

9.1.2 Ackermann Geometry

Within the validity limits of the kinematic tire model, the necessary steering angle of the front wheels can be constructed via the given momentary pivot pole M, Figure 9.1. For slowly moving vehicles, the layout of the steering

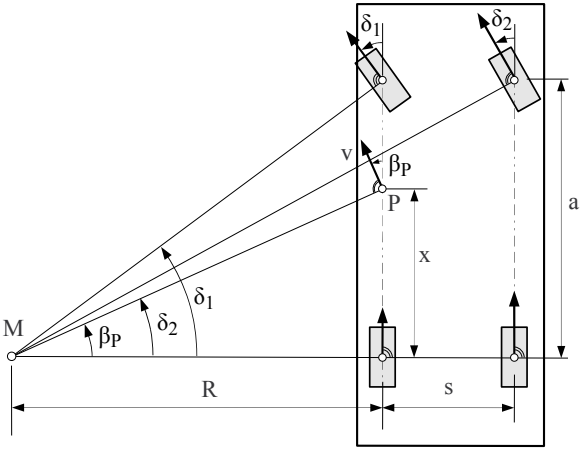

FIGURE 9.1
Ackermann steering geometry at a two-axled vehicle.

linkage is usually done according to Ackermann geometry. Then, the following relations apply,

$$\tan\delta_1 \;=\; \frac{a}{R} \qquad \text{and} \qquad \tan\delta_2 \;=\; \frac{a}{R+s}\,, \tag{9.2}$$

where s is the track width and a denotes the wheel base. Eliminating the radius of curvature R, we get

$$\tan\delta_2 \;=\; \frac{a}{\dfrac{a}{\tan\delta_1}+s} \qquad \text{or} \qquad \tan\delta_2 \;=\; \frac{a\,\tan\delta_1}{a+s\,\tan\delta_1}\,. \tag{9.3}$$

The deviations $\triangle\delta_2 = \delta_2^a - \delta_2^A$ of the actual steering angle δ_2^a from the Ackermann steering angle δ_2^A, which follows from Equation (9.3), are used, especially on commercial vehicles, to judge the quality of a steering system.

At a rotation around the momentary pivot pole M, the direction of the velocity is fixed for every point of the vehicle. The angle β between the velocity vector v and the longitudinal axis of the vehicle is called the side slip angle. The side slip angle at point P is given by

$$\tan\beta_P \;=\; \frac{x}{R} \qquad \text{or} \qquad \tan\beta_P \;=\; \frac{x}{a}\,\tan\delta_1\,, \tag{9.4}$$

where x defines the distance of P to the inner rear wheel.

9.1.3 Space Requirement

The Ackermann approach can also be used to calculate the space requirement of a vehicle during cornering, Figure 9.2. If the front wheels of a two-axled

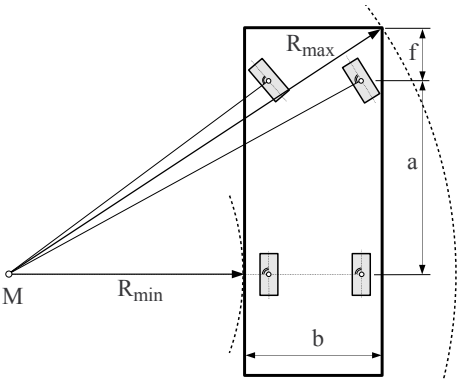

FIGURE 9.2
Space requirement.

vehicle are steered according to Ackermann geometry, the outer point of the vehicle front will run on the maximum radius R_{max}, whereas a point on the inner side of the vehicle at the location of the rear axle will run on the minimum radius R_{min}. Within this simple approach, the outer contour of a vehicle is just approximated by a box. Then it holds,

$$R_{max}^2 \;=\; (R_{min}+b)^2 + (a+f)^2\;, \tag{9.5}$$

where a, b are the wheel base and the width of the vehicle, and f specifies the distance from the front of the vehicle to the front axle. Then, the space requirement $\triangle R = R_{max} - R_{min}$ can be specified as a function of the cornering radius R_{min} for a given vehicle dimension,

$$\triangle R \;=\; R_{max} - R_{min} \;=\; \sqrt{(R_{min} + b)^2 + (a + f)^2} \;-\; R_{min}\,. \qquad (9.6)$$

The space requirement $\triangle R$ of a typical passenger car and a bus is plotted in Figure 9.3 versus the minimum cornering radius. In narrow curves, $R_{min} =$

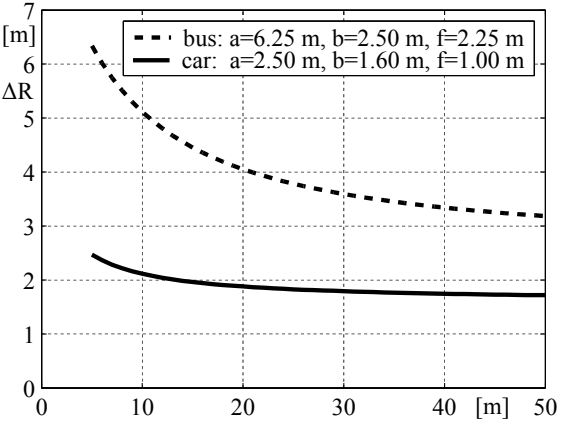

FIGURE 9.3
Space requirement of a typical passenger car and bus

5.0 m, a bus requires a space of 2.5 times the width, whereas a passenger car only needs 1.5 times the width.

9.1.4 Vehicle Model with Trailer

9.1.4.1 Kinematics

A simple model for a passenger car and a trailer is shown in Figure 9.4. Vehicle and trailer move on a horizontal track. The parameters a, b, and c describe the wheel base, the distance of the rear axle to the coupling point, and the distance from the coupling point to the axle of the trailer. The wheels at each axle are substituted by fictitious center wheels whose longitudinal direction is characterized by the axes x_1, x_2, and x_3. The rear axle of the vehicle and the trailer axle are not steered. Then, the position and the orientation of the vehicle with respect to the track-fixed axis system x_0, y_0, z_0 is defined by the position vector from the origin 0 of the earth-fixed axis system to the center of the rear axle

$$r_{02,0} \;=\; \begin{bmatrix} x \\ y \\ R \end{bmatrix} \qquad (9.7)$$

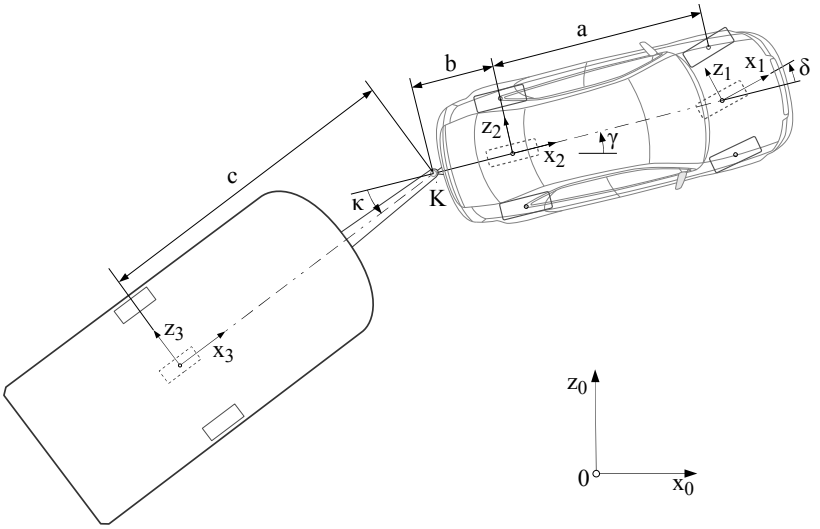

FIGURE 9.4
Vehicle and trailer with kinematic tire model.

and the rotation matrix

$$A_{02} = \begin{bmatrix} \cos\gamma & -\sin\gamma & 0 \\ \sin\gamma & \cos\gamma & 0 \\ 0 & 0 & 1 \end{bmatrix} . \tag{9.8}$$

Here, the tire radius R is considered constant, and x, y as well as the yaw angle γ are used as generalized coordinates. The position vector

$$r_{01,0} = r_{02,0} + A_{02}\, r_{21,2} \quad \text{with} \quad r_{21,2} = \begin{bmatrix} a \\ 0 \\ 0 \end{bmatrix} \tag{9.9}$$

and the rotation matrix

$$A_{01} = A_{02}\, A_{21} \quad \text{with} \quad A_{21} = \begin{bmatrix} \cos\delta & -\sin\delta & 0 \\ \sin\delta & \cos\delta & 0 \\ 0 & 0 & 1 \end{bmatrix} \tag{9.10}$$

describe the position and the orientation of the front axle, where δ denotes the steering angle. Finally, the position vector

$$r_{03,0} = r_{02,0} + A_{02} \left(r_{2K,2} + A_{23}\, r_{K3,3} \right) \tag{9.11}$$

with

$$r_{2K,2} = \begin{bmatrix} -b \\ 0 \\ 0 \end{bmatrix} \quad \text{and} \quad r_{K3,2} = \begin{bmatrix} -c \\ 0 \\ 0 \end{bmatrix} \tag{9.12}$$

and the rotation matrix

$$A_{03} \;=\; A_{02}\, A_{23} \quad \text{with} \quad A_{23} \;=\; \begin{bmatrix} \cos\kappa & -\sin\kappa & 0 \\ \sin\kappa & \cos\kappa & 0 \\ 0 & 0 & 1 \end{bmatrix} \tag{9.13}$$

define the position and the orientation of the trailer axis. Here, K denotes the coupling point and κ defines the bend angle between vehicle and trailer.

9.1.4.2 Vehicle Motion

According to the kinematic tire model, cf. Section 9.1.1, the velocity at the rear axle can only have a component in the longitudinal direction of the tire, which here corresponds with the longitudinal direction of the vehicle,

$$v_{02,2} \;=\; \begin{bmatrix} v_{x2} \\ 0 \\ 0 \end{bmatrix} . \tag{9.14}$$

The time derivative of Equation (9.7) results in

$$v_{02,0} \;=\; \dot{r}_{02,0} \;=\; \begin{bmatrix} \dot{x} \\ \dot{y} \\ 0 \end{bmatrix} . \tag{9.15}$$

The vector transformation of Equation (9.14) into the earth-fixed axis system 0 yields

$$v_{02,0} \;=\; A_{02}\, v_{02,2} \;=\; A_{02} \begin{bmatrix} v_{x2} \\ 0 \\ 0 \end{bmatrix} \;=\; \begin{bmatrix} \cos\gamma\, v_{x2} \\ \sin\gamma\, v_{x2} \\ 0 \end{bmatrix} . \tag{9.16}$$

Equating it with Equation (9.15) results in two first-order differential equations for the position coordinates x and y,

$$\dot{x} \;=\; v_{x2}\, \cos\gamma\,, \tag{9.17}$$

$$\dot{y} \;=\; v_{x2}\, \sin\gamma\,. \tag{9.18}$$

The time derivative of Equation (9.9) delivers the velocity at the front axle,

$$v_{01,0} \;=\; \dot{r}_{01,0} \;=\; \dot{r}_{02,0} \;+\; \omega_{02,0} \times A_{02}\, r_{21,2}\,. \tag{9.19}$$

The transformation into the vehicle-fixed axis system x_2, y_2, z_2 results in

$$v_{01,2} \;=\; \underbrace{\begin{bmatrix} v_{x2} \\ 0 \\ 0 \end{bmatrix}}_{v_{02,2}} + \underbrace{\begin{bmatrix} 0 \\ 0 \\ \dot{\gamma} \end{bmatrix}}_{\omega_{02,2}} \times \underbrace{\begin{bmatrix} a \\ 0 \\ 0 \end{bmatrix}}_{r_{21,2}} \;=\; \begin{bmatrix} v_{x2} \\ a\,\dot{\gamma} \\ 0 \end{bmatrix} . \tag{9.20}$$

The unit vectors

$$e_{x1,2} \;=\; \begin{bmatrix} \cos\delta \\ \sin\delta \\ 0 \end{bmatrix} \quad \text{and} \quad e_{y1,2} \;=\; \begin{bmatrix} -\sin\delta \\ \cos\delta \\ 0 \end{bmatrix} \tag{9.21}$$

define the longitudinal and lateral direction at the front center wheel. According to Equation (9.1), the velocity component lateral to the wheel must vanish,

$$e_{y1,2}^{T}\, v_{01,2} \;=\; -\sin\delta\, v_{x2} \;+\; \cos\delta\, a\, \dot{\gamma} \;=\; 0\,. \tag{9.22}$$

Whereas in longitudinal direction the velocity

$$e_{x1,2}^{T}\, v_{01,2} \;=\; \cos\delta\, v_{x2} \;+\; \sin\delta\, a\, \dot{\gamma} \;=\; v_{x1} \tag{9.23}$$

will remain. Rearranging Equation (9.22) results in a first-order differential equation for the yaw angle,

$$\dot{\gamma} \;=\; \frac{v_{x2}}{a}\, \tan\delta\,. \tag{9.24}$$

The momentary position $x = x(t)$, $y = y(t)$ and the orientation $\gamma = \gamma(t)$ of the vehicle are defined by three differential equations (9.17), (9.18), and (9.24) which are driven by the vehicle velocity v_{x2} and the steering angle δ.

9.1.4.3 Entering a Curve

In analogy with Equation (9.2), the steering angle δ can be related to the current track radius R or with $\varrho = 1/R$ to the current track curvature

$$\tan\delta \;=\; \frac{a}{R} \;=\; a\,\frac{1}{R} \;=\; a\,\varrho\,. \tag{9.25}$$

Then, the differential equation for the yaw angle reads as

$$\dot{\gamma} \;=\; v_{x2}\,\varrho\,. \tag{9.26}$$

With the curvature gradient

$$\varrho \;=\; \varrho(t) \;=\; \varrho_C\,\frac{t}{T}\,, \tag{9.27}$$

the entering of a curve is described as a continuous transition from a straight line with the curvature $\varrho = 0$ into a circle with the curvature $\varrho = \varrho_C$. Now the yaw angle of the vehicle can be calculated by simple integration,

$$\gamma(t) \;=\; \frac{v_{x2}\,\varrho_C}{T}\;\frac{t^2}{2}\,, \tag{9.28}$$

where at time $t = 0$ a vanishing yaw angle, $\gamma(t=0) = 0$, has been assumed. Then the position of the vehicle follows with Equation (9.28) from the differential equations defined by Equations (9.17) and (9.18)

$$x \;=\; v_{x2}\int_{t=0}^{t=T} \cos\left(\frac{v_{x2}\,\varrho_C}{T}\;\frac{t^2}{2}\right) dt \quad \text{and} \quad y \;=\; v_{x2}\int_{t=0}^{t=T} \sin\left(\frac{v_{x2}\,\varrho_C}{T}\;\frac{t^2}{2}\right) dt\,. \tag{9.29}$$

At constant vehicle speed, $v_{x2} = const.$, Equation (9.29) is the parameterized form of a clothoide. From Equation (9.25) the necessary steering angle can be calculated too. If only small steering angles are necessary for driving through the curve, the tangent function can be approximated by its argument. Then, the continuous steer motion

$$\delta \;=\; \delta(t) \;\approx\; a\,\varrho \;=\; a\,\varrho_C\,\frac{t}{T} \tag{9.30}$$

will drive the vehicle along a clothoide-like curve.

9.1.4.4 Trailer Motions

The time derivative of the position vector, defined in Equation (9.11), delivers the velocity of the trailer axis as

$$v_{03,0} \;=\; \dot{r}_{03,0} \;=\; \dot{r}_{02,0} \;+\; \omega_{02,0} \times A_{02}\, r_{23,2} \;+\; A_{02}\, \dot{r}_{23,2}\,. \tag{9.31}$$

The velocity $\dot{r}_{02,0} = v_{02,0}$ and the angular velocity $\omega_{02,0}$ of the vehicle are defined in Equations (9.16) and (9.20). The vector from the rear axle to the axle of the trailer is given by

$$r_{23,2} \;=\; r_{2K,2} \;+\; A_{23}\, r_{K3,3} \;=\; \begin{bmatrix} -b \,-\, c\,\cos\kappa \\ -c\,\sin\kappa \\ 0 \end{bmatrix}, \tag{9.32}$$

where $r_{2K,2}$ and $r_{K3,3}$ are defined in Equation (9.12). The time derivative of Equation (9.32) results in

$$\dot{r}_{23,2} \;=\; \underbrace{\begin{bmatrix} 0 \\ 0 \\ \dot{\kappa} \end{bmatrix}}_{\omega_{23,2}} \times \underbrace{\begin{bmatrix} -c\,\cos\kappa \\ -c\,\sin\kappa \\ 0 \end{bmatrix}}_{A_{23}\, r_{K3,3}} \;=\; \begin{bmatrix} c\,\sin\kappa\,\dot{\kappa} \\ -c\,\cos\kappa\,\dot{\kappa} \\ 0 \end{bmatrix}. \tag{9.33}$$

The velocity of the trailer axle, defined in Equation (9.31), is transformed into the vehicle-fixed axis system x_2, y_2, z_2 now

$$\begin{aligned} v_{03,2} \;&=\; \overbrace{\begin{bmatrix} v_{x2} \\ 0 \\ 0 \end{bmatrix}}^{v_{02,2}} + \overbrace{\begin{bmatrix} 0 \\ 0 \\ \dot{\gamma} \end{bmatrix}}^{\omega_{02,2}} \times \overbrace{\begin{bmatrix} -b \,-\, c\,\cos\kappa \\ -c\,\sin\kappa \\ 0 \end{bmatrix}}^{r_{23,2}} + \overbrace{\begin{bmatrix} c\,\sin\kappa\,\dot{\kappa} \\ -c\,\cos\kappa\,\dot{\kappa} \\ 0 \end{bmatrix}}^{\dot{r}_{23,2}} \\ &=\; \begin{bmatrix} v_{x2} + c\,\sin\kappa\,(\dot{\kappa}+\dot{\gamma}) \\ -b\,\dot{\gamma} - c\,\cos\kappa\,(\dot{\kappa}+\dot{\gamma}) \\ 0 \end{bmatrix}. \end{aligned} \tag{9.34}$$

The longitudinal and lateral direction at the trailer axle are defined by the unit vectors

$$e_{x3,2} \;=\; \begin{bmatrix} \cos\kappa \\ \sin\kappa \\ 0 \end{bmatrix} \quad \text{and} \quad e_{y3,2} \;=\; \begin{bmatrix} -\sin\kappa \\ \cos\kappa \\ 0 \end{bmatrix}. \tag{9.35}$$

At the trailer axle, the lateral velocity must vanish too

$$e_{y3,2}^T v_{03,2} = -\sin\kappa\left(v_{x2}+c\,\sin\kappa\,(\dot\kappa+\dot\gamma)\right)+\cos\kappa\left(-b\,\dot\gamma-c\,\cos\kappa\,(\dot\kappa+\dot\gamma)\right)=0\,, \tag{9.36}$$

whereas in longitudinal direction the velocity

$$e_{x3,2}^T v_{03,2} = \cos\kappa\left(v_{x2}+c\,\sin\kappa\,(\dot\kappa+\dot\gamma)\right)+\sin\kappa\left(-b\,\dot\gamma-c\,\cos\kappa\,(\dot\kappa+\dot\gamma)\right)=v_{x3} \tag{9.37}$$

remains. If Equation (9.24) is inserted into Equation (9.36) now, one will get a first-order differential equation for the bend angle,

$$\dot\kappa \;=\; -\frac{v_{x2}}{a}\left(\frac{a}{c}\,\sin\kappa+\left(\frac{b}{c}\,\cos\kappa+1\right)\tan\delta\right)\,. \tag{9.38}$$

The differential equations provided by Equations (9.17), (9.18), and (9.24) describe the position and the orientation of the vehicle within the x_0, y_0 plane. The differential equation (9.38), which characterizes the motion of the trailer relative to the vehicle, depends nonlinearly on the bend angle κ and becomes unstable for small bend angles when vehicle and trailer are driven backward. In steady-state, the bend angle κ^{st} is defined by

$$0 \;=\; -\frac{v_{x2}}{a}\left(\frac{a}{c}\,\sin\kappa^{st}+\left(\frac{b}{c}\,\cos\kappa^{st}+1\right)\tan\delta\right)\,, \tag{9.39}$$

which represents a trigonometric equation of type (5.54) and according to Equation (5.56) is solved by

$$\kappa^{st} \;=\; \arcsin\frac{-c\,\tan\delta}{\sqrt{(b\,\tan\delta)^2+a^2}} \;-\; \arctan\frac{b\,\tan\delta}{a}\,. \tag{9.40}$$

9.1.4.5 Course Calculations

The function given in Listing 9.1 provides the state equation of the vehicle and trailer track model.

Listing 9.1
Function `track_model_f`: Vehicle and Trailer Track Model

```
1   function xdot = track_model_f ( t, x )
2
3     global a b c v t_d d_i
4
5     x2=x(1); y2=x(2); ga=x(3); ka=x(4); % get states
6     d=interp1(t_d,d_i,t); % get steering angle (linear interpolation)
7
8   % vehicle and trailer dynamics
9     x2dot = v*cos(ga); y2dot = v*sin(ga); gadot = v/a*tan(d);
10    kadot =-v/a * ( a/c*sin(ka) + ( b/c*cos(ka) + 1 ) * tan(d) );
11
12    xdot = [ x2dot; y2dot; gadot; kadot ]; % state derivatives
13
14  end
```

The MATLAB-Function interp1 uses a look-up table to compute the actual steering angle $\delta = \delta(t)$ via a linear interpolation. The velocity of the vehicle v is kept constant here. The MATLAB-Script in Listing 9.2 provides all data of the vehicle and trailer track model, performs a simulation, and plots some results.

Listing 9.2
Script `track_model_main`: Vehicle and Trailer Track Model

```
global a b c v t_d d_i

% vehicle data
a = 2.6;   % wheel base [m]
b = 1.0;   % distance rear axle --> coupling point [m]
c = 2.0;   % coupling point --> trailer axle [m]
v = 5./3.6; % driving velocity [km/h --> m/s]

% define lookup table for steer input [time, steering angle]
t_d = [ 0  20  30 ] ;
d_i = [ 0  45  45 ]*pi/180 ; % deg --> rad

% get time interval
t0 = t_d(1); te = t_d(length(t_d)) ;

% initial conditions (vehicle position and orientation)
x0 = 0; y0 = 0; ga0 = 0/180*pi ; % yaw angle [deg --> rad]
% bending angle adjusted to steering angle (steady state solution)
d0 = interp1 ( t_d, d_i, t0 );
ka0= asin(-c*tan(d0)/sqrt((b*tan(d0))^2+a^2)) - atan2(b*tan(d0),a) ;

% time simulation
[t,xout] = ode23(@track_model_f, [t0,te], [x0; y0; ga0; ka0]);

% post processing
d = interp1(t_d,d_i,t); % time history of steering angle
kas= asin(-c*tan(d)./sqrt((b*tan(d)).^2+a^2))-atan2(b*tan(d),a); % bend angle st
x1 = xout(:,1)+a*cos(xout(:,3)); y1 = xout(:,2)+a*sin(xout(:,3)); % front axle
x2 = xout(:,1); y2 = xout(:,2); % rear axle
x3 = xout(:,1)-b*cos(xout(:,3)) - c*cos(xout(:,3)+xout(:,4)); % trailer x
y3 = xout(:,2)-b*sin(xout(:,3)) - c*sin(xout(:,3)+xout(:,4)); % trailer y

% plot some results
subplot(2,2,1)
plot(t,d*180/pi), title('\delta(t) [deg]'), grid on
subplot(2,2,2)
plot(t,v^2/a*tan(d)/9.81), title('a_y/g [-]'), grid on
subplot(2,2,3), hold on, grid on
plot(x1,y1,'k'), plot(x2,y2,'--b'),plot(x3,y3,'r'), title('path of axles')
axis equal, xlabel('[m]'), ylabel('[m]'), legend('Front','Rear','Trailer')
subplot(2,2,4)
plot(t,[xout(:,4),kas]*180/pi), title('\kappa(t) (dyn+st) [deg]'), grid on
```

The data[1] correspond with a typical passenger car and a camping trailer. The

[1]Note: Negative values for c will move the coupling point in front of the rear axle of the vehicle, which will match with the layout of a tractor semitrailer.

look-up table [t_d, d_i] will result in a slowly increasing steering angle, which is kept constant then ($t > 25\ s$). The resulting paths of the axles, which are plotted in Figure 9.5, show clothoide-like curves that end in circles when the steering angle is finally kept constant. The dynamics of the trailer motion is

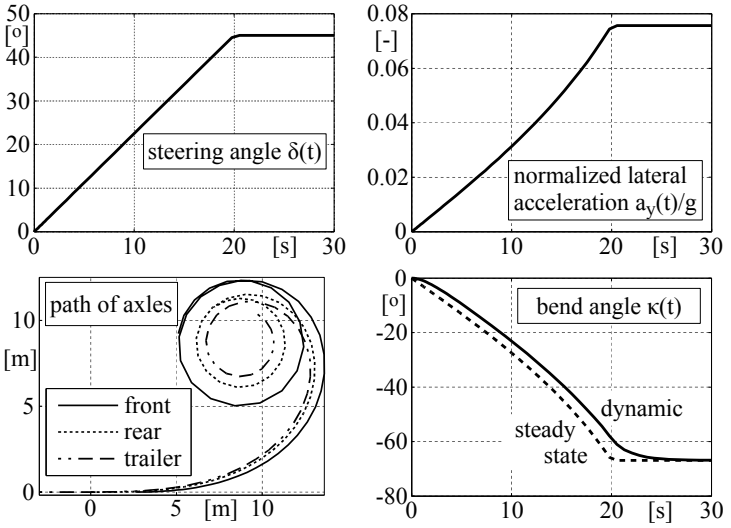

FIGURE 9.5
Entering a curve.

visible in the lower left plot. The kinematical tire model, on which this track model is based, is valid in the low range of lateral vehicle accelerations only. Here, the lateral acceleration on the rear axle is simply given by $a_{y2} = v^2/R$, where the radius of curvature is provided as $R = a/\tan(\delta)$ via the Ackermann geometry.

Setting the driving vehicle velocity to $\mathrm{v} = -2\ km/h$ or $\mathrm{v} = -0.5556\ m/s$, respectively, and replacing the code lines 10, 11 in Listing 9.2 by

```
t_d = [ 0  3   9  12  15 ] ; % [s]
d_i = [ 0 -45 45  0   0 ]*pi/180 ; % [deg --> rad]
```

will provide the steering input for backing into a parking space. Some simulation results are plotted in Figure 9.6. The paths of the front and rear axle are as expected. The rear axle just moves on an S-shaped curve and ends up with a horizontal displacement of approximately 1.8 m. The movement of the front axle is more complicated but arrives at same lateral shift. However, the path of the trailer axle is quite different. When driving backward the differential equation (9.38) becomes unstable. As a result, the bend angle increases rapidly, which would cause severe damage to the vehicle and the trailer. The path of the trailer axle shows a bifurcation point. After this point, the trailer

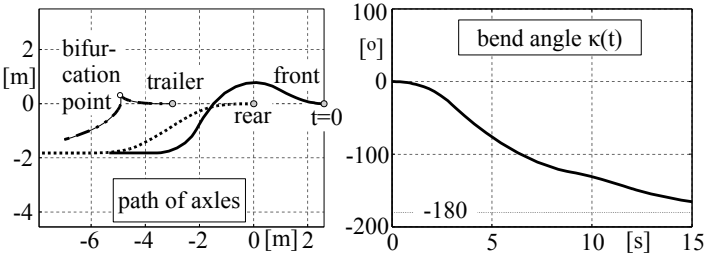

FIGURE 9.6
Backing into a parking space.

moves forward while the vehicle is still moving backward. Now, the trailer motion is stable and will tend toward $-180°$ finally.

9.2 Steady-State Cornering

9.2.1 Cornering Resistance

9.2.1.1 Two-Axled Vehicle

A two-axled vehicle is driving on a circle of the radius R with the velocity v, Figure 9.7. Then, the velocity state of the vehicle expressed in the body-fixed

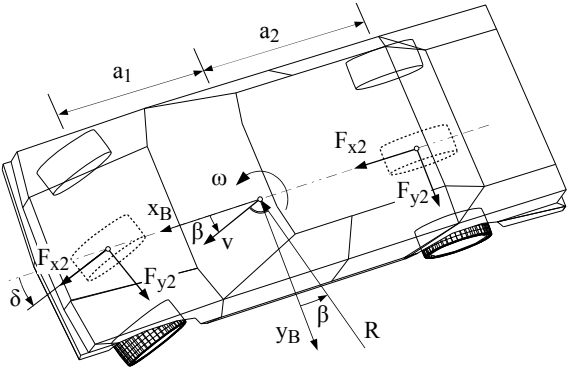

FIGURE 9.7
Two-axled vehicle in steady-state cornering.

axis system B is defined by

$$v_{0C,B} = \begin{bmatrix} v\cos\beta \\ v\sin\beta \\ 0 \end{bmatrix} \quad \text{and} \quad \omega_{0F,B} = \begin{bmatrix} 0 \\ 0 \\ \omega \end{bmatrix}, \tag{9.41}$$

where β denotes the side slip angle of the vehicle measured at the vehicle center of gravity. In steady-state cornering, the angular velocity ω is related via

$$\omega = \frac{v}{R} = \varrho\, v \tag{9.42}$$

to the vehicle velocity v and the circle radius R or the curvature ϱ, respectively.

As the vehicle is supposed to drive with constant speed ($v = const.$), the linear momentum applied in the direction of the x_B- and y_B-axis and the angular momentum about the vertical axis result in

$$m\left(-\varrho\, v^2\, \sin\beta\right) = F_{x1}\cos\delta - F_{y1}\sin\delta + F_{x2}\,, \tag{9.43}$$

$$m\left(\ \varrho\, v^2\, \cos\beta\right) = F_{x1}\sin\delta + F_{y1}\cos\delta + F_{y2}\,, \tag{9.44}$$

$$0 = a_1\ (F_{x1}\sin\delta + F_{y1}\cos\delta) - a_2\, F_{y2}\,, \tag{9.45}$$

where m denotes the mass of the vehicle; F_{x1}, F_{x2}, F_{y1}, F_{y2} are the resulting forces in the longitudinal and vertical direction applied at the front and rear axle; and δ specifies the average steering angle at the front axle.

The engine torque is distributed by the center differential to the front and rear axle in standard drive trains. Then, under steady-state conditions

$$F_{x1} = k\, F_D \quad \text{and} \quad F_{x2} = (1-k)\ F_D \tag{9.46}$$

will hold, where F_D is the driving force. The dimensionless parameter k makes it possible to model different layouts of drive trains, Table 9.1. Inserting

TABLE 9.1
Different Driving Force Distribution

$k = 0$	Rear-wheel drive	$F_{x1} = 0,\ \ F_{x2} = F_D$
$0 < k < 1$	All-wheel drive	$\dfrac{F_{x1}}{F_{x2}} = \dfrac{k}{1-k}$
$k = 1$	Front-wheel drive	$F_{x1} = F_D,\ \ F_{x2} = 0$

Equation (9.46) into Equation (9.43), one gets

$$\begin{aligned} (k\cos\delta + (1-k))\ F_D\ - \quad & \sin\delta\, F_{y1} && = -\varrho\, m\, v^2\ \sin\beta\,, \\ k\sin\delta\, F_D\ + \quad & \cos\delta\, F_{y1}\ + \quad F_{y2} = \ \ & \varrho\, m\, v^2\ \cos\beta\,, \\ a_1 k\sin\delta\, F_D\ + a_1\cos\delta\, F_{y1}\ - \ a_2\, F_{y2} &= 0\,. \end{aligned} \tag{9.47}$$

These equations can be resolved for the driving force,

$$F_D\ = \ \frac{\dfrac{a_2}{a_1+a_2}\cos\beta\,\sin\delta - \sin\beta\,\cos\delta}{k + (1-k)\,\cos\delta}\ \varrho\, m\, v^2\,. \tag{9.48}$$

The driving force will vanish if

$$\frac{a_2}{a_1 + a_2} \cos\beta \sin\delta \;=\; \sin\beta \cos\delta \quad \text{or} \quad \frac{a_2}{a_1 + a_2} \tan\delta \;=\; \tan\beta \tag{9.49}$$

holds. As a matter of fact, this fully corresponds with the Ackermann geometry. However, the Ackermann geometry applies for small lateral accelerations only. In real driving situations, the side slip angle β of a vehicle at the center of gravity will always be smaller than the Ackermann side slip angle β_A. Then, due to $\tan\beta < \tan\beta_A = a_2/(a_1 + a_2) \tan\delta$, a driving force $F_D > 0$ will be needed to overcome the "cornering resistance" of the vehicle.

9.2.1.2 Four-Axled Vehicle

Most heavy-duty trucks have more than two axles. The special-purpose truck shown in Figure 9.8 is equipped with two steerable, single-tired axles in the front and two driven axles with twin-tires at the rear. Again, the wheels on

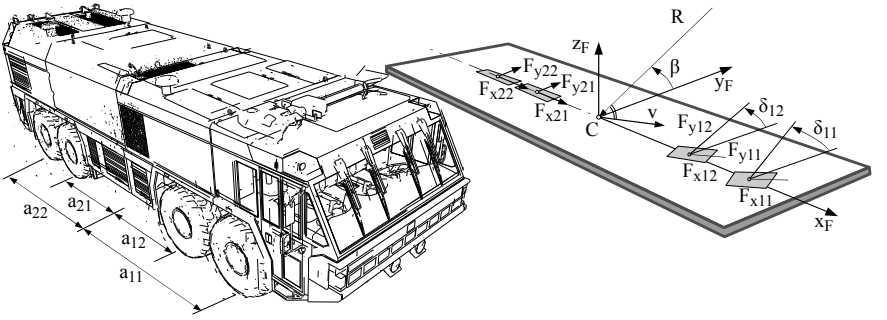

FIGURE 9.8
Four-axled vehicle.

each axle are summarized in a fictitious center wheel and the vehicle is supposed to perform a steady-state cornering. As an extension to Equation (9.43), the linear and angular momentum will now read

$$\begin{aligned} -\varrho\, m\, v^2 \sin\beta = {} & F_{x11} \cos\delta_{11} - F_{y11} \sin\delta_{11} + F_{x12} \;+ \\ & F_{x12} \cos\delta_{12} - F_{y12} \sin\delta_{12} + F_{x22}\,, \end{aligned} \tag{9.50}$$

$$\begin{aligned} \varrho\, m\, v^2 \cos\beta = {} & F_{x11} \sin\delta_{11} + F_{y11} \cos\delta_{11} + F_{y12} \;+ \\ & F_{x12} \sin\delta_{12} + F_{y12} \cos\delta_{12} + F_{y22}\,, \end{aligned} \tag{9.51}$$

$$\begin{aligned} 0 = {} & a_{11}(F_{x11} \sin\delta_{11} + F_{y11} \cos\delta_{11}) - a_{21} F_{y12} \;+ \\ & a_{12}(F_{x12} \sin\delta_{12} + F_{y12} \cos\delta_{12}) - a_{22} F_{y22}\,, \end{aligned} \tag{9.52}$$

where δ_{11} and δ_{12} denote the average steering angles at the front axles. The parameter a_{11}, a_{12}, a_{21}, and a_{22} define the location of the axles with respect to the vehicle center. All axles may be driven in general. Assuming that the

driving torque is distributed differently to the front and rear but equally to each front and rear axle, then the driving forces may be modeled by

$$F_{x11} = F_{x12} = F_{x1} = k\,F_D \quad \text{and} \quad F_{x21} = F_{x22} = F_{x2} = (1-k)\;F_D\,, \tag{9.53}$$

where F_D denotes the overall driving force and the parameter k makes it possible to describe different driving scenarios according to Table 9.1. The lateral forces are modeled as linear functions of the corresponding lateral slips in a first approximation

$$F_{y11} = c_{SF} s_{y11}\,,\; F_{y12} = c_{SF} s_{y12}\,, \quad F_{y21} = c_{SR} s_{y21}\,,\; F_{y22} = c_{SR} s_{y22}\,, \tag{9.54}$$

where c_{SF} and c_{SR} summarize the cornering stiffness of all tires at each front and rear axle. In this simple approach, it is assumed that both front and rear axles are loaded equally and are equipped with the same tires. The vehicle is neither braked nor accelerated. Then, all wheels are close to a rolling situation, which will be characterized by nearly vanishing longitudinal slips. Then, $r_D\Omega \approx v_x$ will hold, and the lateral slips defined in Equation (3.90) are given by

$$s_{y11} \;=\; -\frac{-\sin\delta_{11}\, v\cos\beta + \cos\delta_{11}\,(v\sin\beta + a_{11}\omega)}{|\,\cos\delta_{11}\, v\cos\beta + \sin\delta_{11}\,(v\sin\beta + a_{11}\omega)\,|}\,, \tag{9.55}$$

$$s_{y12} \;=\; -\frac{-\sin\delta_{12}\, v\cos\beta + \cos\delta_{12}\,(v\sin\beta + a_{12}\omega)}{|\,\cos\delta_{12}\, v\cos\beta + \sin\delta_{12}\,(v\sin\beta + a_{12}\omega)\,|}\,, \tag{9.56}$$

$$s_{y21} \;=\; -\frac{v\sin\beta - a_{21}\omega}{|\,v\cos\beta|}\,, \quad \text{and} \quad s_{y22} \;=\; -\frac{v\sin\beta - a_{22}\omega}{|\,v\cos\beta\,|}\,. \tag{9.57}$$

In steady-state cornering, the angular velocity ω is related to the vehicle velocity v and the curvature ϱ according to Equation (9.42).

For a given driving velocity v and various steering angles δ_{11}, δ_{12}, Equations (9.50) to (9.52) in combination with Equations (9.53) to (9.57) and Equation (9.42) represent a set of nonlinear equations for the side slip angle β, the curvature ϱ, and the driving force F_D or the driving resistance $f_D = F_D/(mg)$, respectively. A standard MATLAB installation provides the function fzero to solve a nonlinear equation of type $f(x) = 0$ but the algorithm is restricted to one single equation. If the MATLAB Optimization Toolbox is available, the function fsolve will be the proper choice for solving a system of nonlinear equations. Here, the system of nonlinear equations, arranged in the form of a vector equation $f(x) = 0$, will be solved by minimizing the overall quadratic error of the vector function

$$f(x) \;=\; 0 \quad\Longrightarrow\quad \epsilon^2 \;=\; f(x)^T f(x) \to \text{Minimum}\,. \tag{9.58}$$

Then, the MATLAB standard function can be used to solve the problem. The function given in Listing 9.3 provides the overall quadratic error of the set of nonlinear equations that characterize the steady-state cornering of a four-axled truck.

Listing 9.3
Function `track4a_eps2`: Four-Axled Truck in Steady-State Cornering

```
function eps2 = truck4a_eps2(x)

global grav m k a11 a12 a21 a22 csf csr v  d11 d12

rho = x(1); % curvature
be  = x(2); % side slip angle at cog
cr  = x(3); % cornering resistance

om = v*rho; % angular velocity
fd = m*grav*cr; % driving force
vx = v*cos(be); % velocity in longitudinal direction of vehicle

% longitudinal forces
fx11 = 0.5*k*fd; fx12 = fx11; fx21 = 0.5*(1-k)*fd; fx22 = fx21;

% lateral slips (sx=0 assumed)
vy11 = v*sin(be)+a11*om;
sy11 = -(-sin(d11)*vx+cos(d11)*vy11)/(cos(d11)*vx+sin(d11)*vy11);
vy12 = v*sin(be)+a12*om;
sy12 = -(-sin(d12)*vx+cos(d12)*vy12)/(cos(d12)*vx+sin(d12)*vy12);
vy21 = v*sin(be)-a21*om; sy21 = - vy21/vx ;
vy22 = v*sin(be)-a22*om; sy22 = - vy22/vx ;

% lateral forces (linearized)
fy11 = csf*sy11; fy12 = csf*sy12; fy21 = csr*sy21; fy22 = csr*sy22;

% force and torque balances
fx = fx11*cos(d11)-fy11*sin(d11) + fx21 ...
   + fx12*cos(d12)-fy12*sin(d12) + fx22 + m*v^2*rho*sin(be);
fy = fx11*sin(d11)+fy11*cos(d11) + fy21 ...
   + fx12*sin(d12)+fy12*cos(d12) + fy22 - m*v^2*rho*cos(be);
tz = a11*(fx11*sin(d11)+fy11*cos(d11)) - a21*fy21 ...
   + a12*(fx12*sin(d12)+fy12*cos(d12)) - a22*fy22;

% overall quadratic error
eps2 = fx^2 + fy^2 + tz^2;

end
```

The MATLAB-Script in Listing 9.4 provides the data, computes the cornering resistance for a variety of steering angles, and plots the results as a three-dimensional contour plot by using the MATLAB function contour3.

Listing 9.4
Script `truck4a_main`: Cornering Resistance of a Four-Axled Truck

```
global grav m k a11 a12 a21 a22 csf csr v d11 d12

% data
grav = 9.81; % [m/s^2] constant of gravity
m = 32000; % [kg] mass of vehicle
k = 0.0; % [-] drive torque distribution (rear wheel drive)
a11 = 3.3750; % [m] cog --> midth of first front axle
a12 = 1.6250; % [m] cog --> midth of second front axle
```

```
a21 = 1.2500; % [m] cog --> midth of first rear axle
a22 = 2.7500; % [m] cog --> midth of second rear axle
csf = 2*300000; % [N/-] front axle cornering stiffness
csr = 4*280000; % [N/-] rear axle cornering stiffness
v = 5/3.6; % [km/h --> m/s] vehicle velocity (low speed)
d11var=linspace(5,55,11)/180*pi; % range of steering angle 11
d12var=linspace(5,45, 9)/180*pi; % range of steering angle 12

% pre-allocate cornering resistance to speed up loops
n11=length(d11var); n12=length(d12var); crvar=zeros(n11,n12);

% solve nonlinear equations (trivial starting values)
for i=1:n11
  d11=d11var(i);
  for j=1:n12
    d12=d12var(j);
    x = fminsearch(@truck4a_eps2,[0; 0; 0]);
    rho=x(1); be=x(2); cr=x(3); crvar(i,j)=cr;
  end
end

% plot cornering resistance as a function of d11 and d12
contour3(d12var*180/pi,d11var*180/pi,crvar,100)
title('Cornering resistance'),xlabel('\delta_1_2'),ylabel('\delta_1_1')

% compute and plot cornering resistance for the Ackermann geometry
d12a=atan2(((a21+a22)/2+a12)*tan(d11var),(a21+a22)/2+a11); cr=zeros(size(d12a));
for i=1:length(d12a)
  d11=d11var(i); d12=d12a(i);
  x = fminsearch(@truck4a_eps2,[0; 0; 0]); cr(i)=x(3);
end
hold on, plot3(d12a*180/pi,d11var*180/pi,cr)
```

The MATLAB script also computes and plots the cornering resistance for steering angles that are based on Ackermann geometry, Figure 9.9. A fictitious

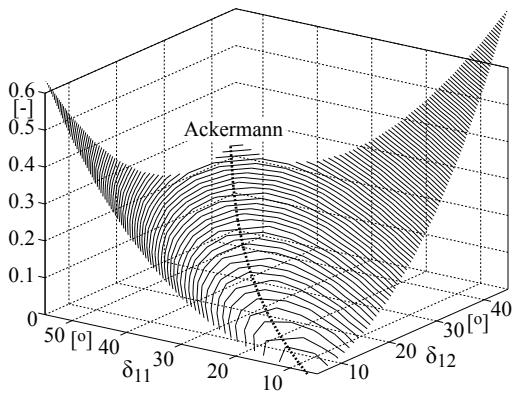

FIGURE 9.9
Cornering resistance of a four-axled truck for different steering angles.

pivot point located at a line right between the two rear axles is assumed hereby. Similar to Equation (9.2), the steering angles at the front axles will then given by

$$\tan\delta_{11} = \frac{\frac{1}{2}\,(a_{21}+a_{22}) + a_{11}}{R} \quad \text{and} \quad \tan\delta_{12} = \frac{\frac{1}{2}\,(a_{21}+a_{22}) + a_{12}}{R}\,. \tag{9.59}$$

Eliminating the curve radius R, one gets

$$\tan\delta_{12} \;=\; \frac{\frac{1}{2}\,(a_{21}+a_{22}) + a_{12}}{\frac{1}{2}\,(a_{21}+a_{22}) + a_{11}}\;\tan\delta_{11}\,. \tag{9.60}$$

The broken line in Figure 9.9 represents the cornering resistance of the four-axled truck, computed for Ackermann steering angles defined by Equation (9.60). Although the four-axled vehicle has no geometrically defined turning point, the Ackermann approach results even here in a driving performance that is characterized by a minimized or at least nearly minimized cornering resistance. That is why most commercial trucks or special-purpose vehicle are equipped with steering systems that are based on the Ackermann geometry.

9.2.2 Overturning Limit

9.2.2.1 Static Stability Factor

If a vehicle of mass m is cornering with the lateral acceleration a_y, then the centrifugal force $m\,a_y$ will be generated, Figure 9.10. Similar to the maximum

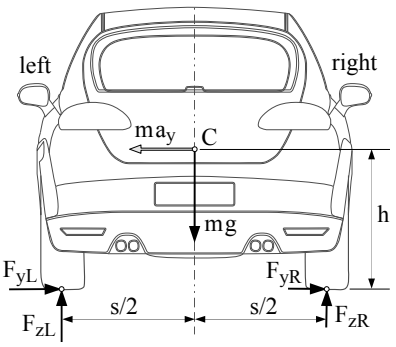

FIGURE 9.10
Vehicle in a right turn.

longitudinal acceleration a_x^{max} provided in Equation (8.22), the maximum lateral acceleration is determined by the coefficient of friction

$$a_y^{max} = \mu\, g\,. \tag{9.61}$$

However, the risk of rollover may reduce this limit further on. If the vehicle turns to the right, which is assumed in Figure 9.10, then a beginning rollover

will be indicated by the liftoff of the tires on the right. For vanishing tire forces at the right $F_{yR} = 0$ and $F_{zR} = 0$, the torque balance about a line that is defined by the left contact points simply delivers

$$m\,g\frac{s}{2} - m\,a_y^T\,h \;=\; 0 \quad \text{or} \quad a_y^T \;=\; \frac{s/2}{h}\,g\,, \tag{9.62}$$

where h is the height of the center of gravity and $s/2$ denotes half of the track width. The vehicle will overturn rather than slide if

$$a_y^T \;<\; a_y^{max} \quad \text{or} \quad \frac{s/2}{h} \;<\; \mu \tag{9.63}$$

holds. As a consequence, the risk of rollover may be judged by the "static stability factor"

$$s_F \;=\; \frac{s/2}{h}\,. \tag{9.64}$$

Values of $s_F \leq 1$ indicate a high rollover risk on paved dry roads, where $\mu = 1$ may be assumed.

9.2.2.2 Enhanced Rollover Model

However, the static stability factor serves as a rough indicator only. To determine the overturning limit, the tire deflection and the body roll have to be taken into account too, Figure 9.11. The balance of torques at the height of

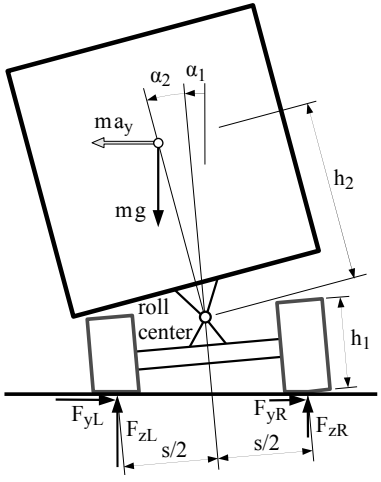

FIGURE 9.11
Overturning hazard on trucks.

the track plane applied at the already inclined vehicle results in

$$(F_{zL} - F_{zR})\,\frac{s}{2} \;=\; m\,a_y\,(h_1 + h_2) \;+\; m\,g\,[(h_1 + h_2)\alpha_1 + h_2\alpha_2]\,, \tag{9.65}$$

where a_y describes the lateral acceleration, m is the vehicle mass, and small roll angles of the axle and the body were assumed, $\alpha_1 \ll 1$, $\alpha_2 \ll 1$. For a left-hand tilt, the wheel load at the right will vanish

$$F_{zR}^T \;=\; 0\,, \tag{9.66}$$

whereas the left wheel carries the vehicle weight,

$$F_{zL}^T \;=\; m\,g\,. \tag{9.67}$$

Inserting Equations (9.66) and (9.67) into Equation (9.65) yields the lateral acceleration

$$\frac{a_y^T}{g} \;=\; \frac{\frac{s}{2}}{h_1+h_2} \;-\; \alpha_1^T \;-\; \frac{h_2}{h_1+h_2}\,\alpha_2^T\,, \tag{9.68}$$

where the vehicle will start to roll over. Taking into consideration that $h = h_1+h_2$ describes the height of the center of gravity above the road, the first term in Equation (9.68) corresponds with the static stability factor defined in Equation (9.64). However, the compliance of the tires and the suspension, which in the limit case cause the axle and body roll α_1^T and α_2^T, will increase the hazard of overturning.

If the vehicle drives straight ahead, the weight of the vehicle is equally distributed to both sides

$$F_{zR}^{stat} \;=\; F_{zL}^{stat} \;=\; \frac{1}{2}\,m\,g\,. \tag{9.69}$$

On a right turn, the wheel load at the left is increased and the one at the right is decreased by the same amount

$$F_{zL}^T = F_{zL}^{stat} + \triangle F_z \quad \text{and} \quad F_{zR}^T = F_{zR}^{stat} - \triangle F_z\,. \tag{9.70}$$

At the tilting limit,

$$\triangle F_z^T \;=\; \frac{1}{2}\,m\,g \tag{9.71}$$

will hold, which corresponds with the tire deflection

$$\triangle r^T \;=\; \frac{\triangle F_z^T}{c_R} \;=\; \frac{1}{2}\,\frac{m\,g}{c_R}\,, \tag{9.72}$$

where c_R denotes the radial tire stiffness. Because the right tire simultaneously rebounds by the same amount, the roll angle of the axle is defined by

$$2\,\triangle r^T \;=\; s\,\alpha_1^T \quad \text{or} \quad \alpha_1^T \;=\; \frac{2\,\triangle r}{s} \;=\; \frac{m\,g}{s\,c_R}\,, \tag{9.73}$$

where s denotes the track width.

In analogy with Equation (9.65), the balance of torques at the body applied at its roll center yields

$$c_W\,\alpha_2 \;=\; m\,a_y\,h_2 \;+\; m\,g\,h_2\,(\alpha_1+\alpha_2)\,, \tag{9.74}$$

where c_W describes the roll stiffness of the body suspension. In particular, at the overturning limit $a_y = a_y^T$,

$$\alpha_2^T \;=\; \frac{a_y^T}{g}\,\frac{mgh_2}{c_W - mgh_2} \;+\; \frac{mgh_2}{c_W - mgh_2}\,\alpha_1^T \tag{9.75}$$

applies. Not allowing the vehicle to overturn at $a_y^T = 0$, demands a minimum roll stiffness of $c_W > c_W^{min} = mgh_2$. With Equations (9.73) and (9.75), the overturning condition in Equation (9.68) reads as

$$(h_1+h_2)\,\frac{a_y^T}{g} \;=\; \frac{s}{2} - (h_1+h_2)\,\frac{1}{c_R^*} - h_2\,\frac{a_y^T}{g}\,\frac{1}{c_W^* - 1} - h_2\,\frac{1}{c_W^* - 1}\,\frac{1}{c_{R*}}, \tag{9.76}$$

where, for abbreviation purposes, the dimensionless quantities

$$c_R^* \;=\; \frac{s\,c_R}{m\,g} \quad \text{and} \quad c_W^* \;=\; \frac{c_W}{m\,g\,h_2} \tag{9.77}$$

have been introduced. Resolved for the normalized lateral acceleration,

$$\frac{a_y^T}{g} \;=\; \frac{\dfrac{s}{2}}{h_1 + h_2 + \dfrac{h_2}{c_W^* - 1}} \;-\; \frac{1}{c_R^*} \tag{9.78}$$

will finally remain.

For heavy trucks, a twin-tire axle may be loaded with $m = 13\,000\,kg$. The radial stiffness of one tire is given by $c_R = 800\,000\,N/m$, and the track width can be set to $s = 2\,m$. The values $h_1 = 0.8\,m$ and $h_2 = 1.0\,m$ or $h = h_1 + h_2 = 1.8\,m$ define the height of the center of gravity. The corresponding results obtained from Equations (9.78), (9.73), and (9.75) are shown in Figure 9.12. Even with a rigid body suspension $c_W^* \to \infty$, the vehicle will turn over at a

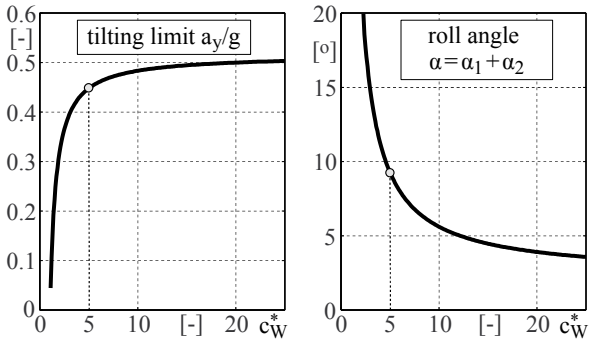

FIGURE 9.12
Tilting limit for a typical truck at steady-state cornering.

lateral acceleration of $a_y \approx 0.5\,g$. Then, the roll angle of the vehicle solely results from the tire deflection. At a normalized roll stiffness of $c_W^* = 5$, the overturning limit lies at $a_y \approx 0.45\,g$ and thus reaches 90% of the maximum. The vehicle will turn over at a roll angle of $\alpha = \alpha_1 + \alpha_2 \approx 9°$.

Depending on the shape of the tank, a liquid load may reduce the rollover threshold further on. In particular, in non-steady-state maneuvers, such as braking in a turn, dynamic sloshing forces affect vehicle behavior significantly [43].

9.2.3 Roll Support and Camber Compensation

When a vehicle drives through a curve with lateral acceleration a_y, centrifugal forces are applied to the single masses. The planar vehicle model, shown in Figure 9.13, consists of three bodies: the chassis mass m_C and two knuckles with wheels attached to each of mass m_W. The generalized coordinates y_C,

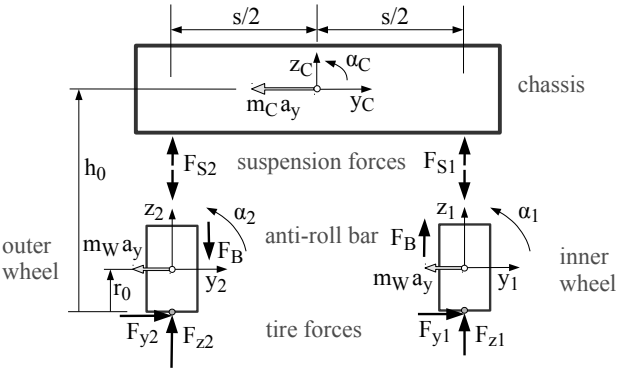

FIGURE 9.13
Simple vehicle roll model.

z_C, α_C characterize the lateral and vertical as well as the roll motion of the chassis. In addition, z_1 and z_2 describe the vertical vertical motions of the knuckles and wheels relative to the chassis.

In steady-state cornering, the vehicle forces are balanced. With the principle of virtual work

$$\delta W \;=\; 0\,, \tag{9.79}$$

the equilibrium position can be calculated. For the vehicle roll model, the suspension forces F_{S1}, F_{S2}, and the tire forces F_{y1}, F_{z1}, F_{y2}, F_{z2}, are approximated by linear spring elements with the constants c_S and c_y, c_z, respectively. As done in the kinematic approach, the lateral slip is neglected. The work W of these forces can be calculated directly or much more conveniently via the potential V, where $W = -V$ holds. For small rotations and deflections, lin-

earized kinematics can be applied and one gets as a consequence,

$$\begin{aligned} W = & -m_C\, a_y\, y_C \\ & -m_W\, a_y\, (y_C + h_R\, \alpha_C + y_1) - m_W\, a_y\, (y_C + h_R\, \alpha_C + y_2) \\ & -\tfrac{1}{2}\, c_S\, z_1^2 - \tfrac{1}{2}\, c_S\, z_2^2 \\ & -\tfrac{1}{2}\, c_B\, (z_1 - z_2)^2 \\ & -\tfrac{1}{2}\, c_y\, (y_C + h_0 \alpha_C + y_1 + r_0 \alpha_1)^2 - \tfrac{1}{2}\, c_y\, (y_C + h_0 \alpha_C + y_2 + r_0 \alpha_2)^2 \\ & -\tfrac{1}{2}\, c_z\, \left(z_A + \tfrac{s}{2} \alpha_C + z_1\right)^2 - \tfrac{1}{2}\, c_z\, \left(z_A - \tfrac{s}{2} \alpha_C + z_2\right)^2 \,, \end{aligned} \tag{9.80}$$

where the abbreviation $h_R = h_0 - r_0$ was used, and c_B denotes the stiffness of the anti-roll bar, converted to the vertical displacement of the wheel centers. The kinematics of wheel suspensions are symmetrical in general. Then, the lateral motion of the knuckles and wheels and their rotation about the longitudinal axis (chamber change), which results from the specific suspension kinematics, can be approximated by

$$y_1 = y_1(z_1) \approx \frac{\partial y}{\partial z}\, z_1 \,, \quad \alpha_1 = \alpha_1(z_1) \approx \frac{\partial \alpha}{\partial z}\, z_1 \tag{9.81}$$

and

$$y_2 = y_2(z_2) \approx -\frac{\partial y}{\partial z}\, z_2 \,, \quad \alpha_2 = \alpha_2(z_2) \approx -\frac{\partial \alpha}{\partial z}\, z_2 \,. \tag{9.82}$$

Now, the work defined by Equation (9.80) can be described as a function of the vector of generalized coordinates

$$y \;=\; [\, y_C,\, z_C,\, \alpha_C,\, z_1,\, z_2 \,]^T \;. \tag{9.83}$$

Due to $W = W(y)$, the principle of virtual work provided in Equation (9.79) leads to

$$\delta W \;=\; \frac{\partial W(y)}{\partial y}\, \delta y \;=\; 0 \,. \tag{9.84}$$

Because the virtual displacements will not vanish in general, $\delta y \neq 0$, Equation (9.84) delivers a system of linear equations in the form of

$$K\, y \;=\; b \,. \tag{9.85}$$

The matrix K and the vector b are given by

$$K = \begin{bmatrix} 2\, c_y & 0 & 2\, c_y\, h_0 & \frac{\partial \hat{y}}{\partial z} c_y & -\frac{\partial \hat{y}}{\partial z} c_y \\ 0 & 2\, c_z & 0 & c_z & c_z \\ 2\, c_y\, h_0 & 0 & c_\alpha & \frac{s}{2} c_z + h_0 \frac{\partial \hat{y}}{\partial z} c_y & -\frac{s}{2} c_z - h_0 \frac{\partial \hat{y}}{\partial z} c_y \\ \frac{\partial \hat{y}}{\partial z} c_y & c_z & \frac{s}{2} c_z + h_0 \frac{\partial \hat{y}}{\partial z} c_y & c_S^* + c_B + c_z & -c_B \\ -\frac{\partial \hat{y}}{\partial z} c_y & c_z & -\frac{s}{2} c_z - h_0 \frac{\partial \hat{y}}{\partial z} c_y & -c_B & c_S^* + c_B + c_z \end{bmatrix} \tag{9.86}$$

and

$$b = -\begin{bmatrix} m_C + 2\,m_W \\ 0 \\ (m_1 + m_2)\,h_R \\ m_W\,\partial y/\partial z \\ -m_W\,\partial y/\partial z \end{bmatrix} a_y\,, \tag{9.87}$$

where the abbreviations

$$\frac{\partial \hat{y}}{\partial z} = \frac{\partial y}{\partial z} + r_0\,\frac{\partial \alpha}{\partial z}\,, \quad c_S^* = c_S + c_y\left(\frac{\partial y}{\partial z}\right)^2, \quad c_\alpha = 2\,c_y\,h_0^2 + 2\,c_z\left(\frac{b}{2}\right)^2 \tag{9.88}$$

have been used. The MATLAB-Script in Listing 9.5 provides the data, solves the set of linear equations, computes the wheel loads, and displays the results.

Listing 9.5
Script `roll_model`: Vehicle Roll Model

```
% vehicle data
g  = 9.81 ; % [m/s^2] constant of cravity
ay = 0.75*g; % [m/s^2] set lateral acceleration
mc = 600;   % [kg]   chassis mass
mw =  50;   % [kg]   mass of each knuckle and wheel
s  = 1.5;   % [m]    track width
h0 = 0.6;   % [m]    height of center of gravity
r0 = 0.3;   % [m]    static tire radius
cs = 20000; % [N/m]  suspension stiffness
cb = 10000; % [N/m]  stiffness of anti roll bar
cy =180000; % [N/m]  tire lateral stiffness
cz =200000; % [N/m]  tire radial stiffness

% axle kinematics
dydz = 0 ;  % [-] lateral motion of wheel center caused by vertical
dadz = 0/180*pi; % [Grad/m] camber change caused by vertical motion

hr = h0-r0 ; sh = s/2; dyqdz = dydz + r0*dadz; % some abbreviations

% stiffness matrix (column by column)
K(:,1) = [      2*cy        ; ...
                 0          ; ...
               2*cy*h0      ; ...
               cy*dyqdz     ; ...
              -cy*dyqdz     ];
K(:,2) = [       0          ; ...
                2*cz        ; ...
                 0          ; ...
                 cz         ; ...
                 cz         ];
K(:,3) = [     2*cy*h0      ; ...
                  0         ; ...
          2*cz*sh^2+2*cy*h0^2 ; ...
           sh*cz+h0*dyqdz*cy ; ...
          -sh*cz-h0*dyqdz*cy ];
K(:,4) = [      cy*dyqdz    ; ...
```

```
                    cz       ; ...
              sh*cz+h0*dyqdz*cy ; ...
             cs+cb+cz+dyqdz^2*cy ; ...
                   -cb        ];
K(:,5) = [     -cy*dyqdz     ; ...
                    cz       ; ...
            -sh*cz-h0*dyqdz*cy ; ...
                    -cb      ; ...
           cs+cb+cz+dyqdz^2*cy ];

b = -[ mc+2*mw; 0; 2*mw*hr; mw*dydz; -mw*dydz ]*ay; % right hand side

x = K\b; % solve set of linear eqautions and display results
disp(['lateral displacement of chassis y_C =',num2str(x(1))])
disp(['vertical displacement of chassis z_C =',num2str(x(2))])
disp(['roll motion of chassis   alpha_C =',num2str(x(3)*180/pi)])
disp(['suspension travel inner wheel z_1 =',num2str(x(4))])
disp(['suspension travel outer wheel z_2 =',num2str(x(5))])

% compute and display wheel loads
Fz1=(mw+mc/2)*g+cz*(x(2)+s/2*x(3)+x(4)); disp(['Fz1=',num2str(Fz1)])
Fz2=(mw+mc/2)*g+cz*(x(2)-s/2*x(3)+x(5)); disp(['Fz2=',num2str(Fz2)])
```

The results for simple axle kinematics (dydz=0, dadz=0), which will be generated by a trailing arm suspension, are visualized in Figure 9.14. It can be

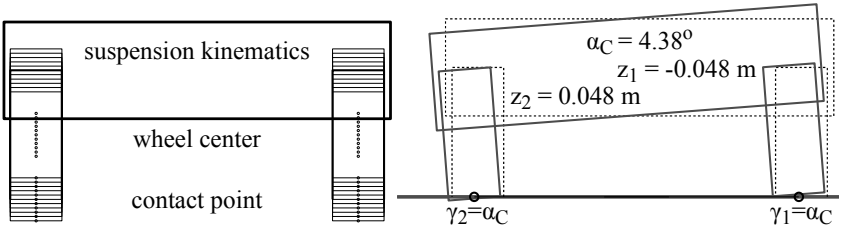

FIGURE 9.14
Vehicle roll for simple axle kinematics (dydz=0, dadz=0).

seen that due to simple kinematics, the roll angle of the chassis is transferred directly to the wheels, which will result in a tire camber angle of the same amount, $\gamma_1 = \gamma_2 = \alpha_C$.

Of course, the anti-roll bar stiffness c_B affects the roll angle strongly. For example, omitting the anti-roll bar $c_B = 0$ will increase the roll angle up to $\alpha_C = 8°$, which certainly is too much for a passenger car even when cornering hard with a lateral acceleration of $a_y = 0.75g$. On the other hand, the anti-roll bar couples the vertical motions of the left and right wheel, which affects the ride comfort in particular when crossing a bump on one side. That is why controlled anti-roll bars equipped with actuators are used in high-level cars today.

Suspension kinematics, which moves the wheels outward on jounce, will provide kinematically generated roll support, Figure 9.15. Now, the roll cen-

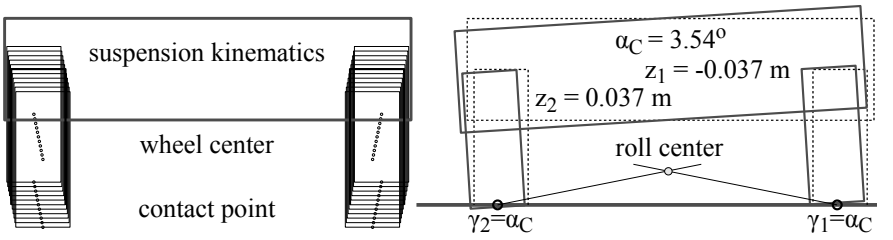

FIGURE 9.15
Roll support kinematically generated (dydz=0.2, dadz=0).

ter of the chassis is located above the road, which reduces the roll angle. But, as the wheels do not rotate on jounce and rebound, the tire camber angle is still the same as the chassis roll angle, $\gamma_1 = \gamma_2 = \alpha_C$. This kind of suspension kinematics will be generated, for instance, by a double wishbone suspension with inclined mounted wishbones of the same size. It is not really practical because the lateral movements of the contact points during jounce and rebound would cause enormous tire wear just when driving straight ahead on uneven roads.

Large tire camber angles result in unfavorable pressure distribution in the contact area, which leads to a reduction in maximally transmittable lateral forces. Thus, for more sportive vehicles, axle kinematics are employed, where the wheels are rotated around the longitudinal axis at jounce and rebound, $\alpha_1 = \alpha_1(z_1)$ and $\alpha_2 = \alpha_2(z_2)$. Even a full "camber compensation" can be achieved with $\gamma_1 \approx 0$ and $\gamma_2 \approx 0$. For simple wishbone suspension systems, the rotation of the wheels around the longitudinal move the contact points outward on jounce, which provides significant roll support in addition but will cause severe tire wear. In practice, most suspension systems generate partial camber compensation, Figure 9.16. If the rotation of the wheel around the

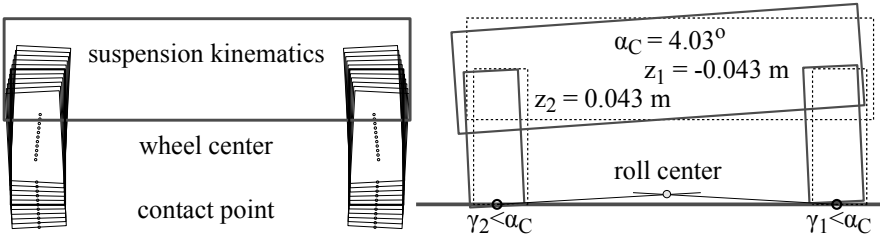

FIGURE 9.16
Partial camber compensation (dydz=-0.1, dadz=30°/m).

longitudinal axis (dadz>0) is combined with inward movement of the wheel center on jounce (dydz<0), the roll center can be placed on or slightly above

the road at least. Double wishbone suspension systems with different-sized control arms make it possible to realize camber compensation and control the amount of roll support. The kinematic analysis of a typical double wishbone suspension performed in section 5.4 shows a camber change (partial camber compensation) combined with slight outward movement of the reference point (contact point) on jounce that generates a moderate roll support, Figure 5.14.

9.2.4 Roll Center and Roll Axis

The roll center can be constructed from the lateral motion of the wheel contact points at each axle. The line through the roll center at the front and rear axle, is called the roll axis, Figure 9.17. The chassis will roll about this axis when

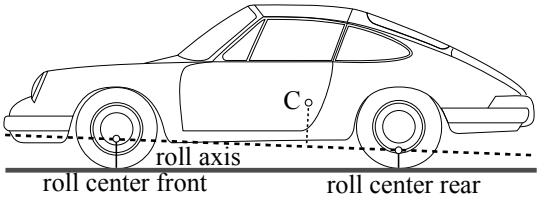

FIGURE 9.17
Roll axis.

cornering. The distance from the roll axis to the center of gravity is responsible for the amount of body roll.

9.2.5 Wheel Load Transfer

The roll angle of a vehicle during cornering depends on the roll stiffness of the axle and on the position of the roll center. Different axle layouts at the front and rear axle may result in different roll angles of the front and rear part of the chassis, Figure 9.18. A chassis with a significant torsional compliance

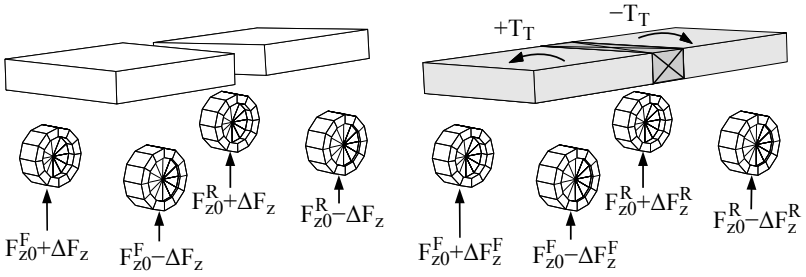

FIGURE 9.18
Wheel load transfer on a flexible and a rigid chassis.

would allow its front and rear part to roll nearly independently. Then, the load transfer $\triangle F_z$ from the inner to the outer wheels will be the same[2] at both axles, if the front and rear part have the same height of the center of gravity. On most passenger cars, the chassis is rather stiff, however. In this case, front and rear part of the chassis are forced by an internal torque T_T to an overall chassis roll angle. This torque affects the wheel loads and thus generates a different load transfer at the front and rear wheels, $\triangle F_z^F \neq \triangle F_z^F$. Due to the degressive influence of the wheel load on longitudinal and lateral tire forces, the steering tendency of a vehicle can be affected.

9.3 Simple Handling Model

9.3.1 Modeling Concept

The main vehicle motions take place in a horizontal plane defined by the earth-fixed axis system 0, Figure 9.19. The yaw angle γ describes the orientation of

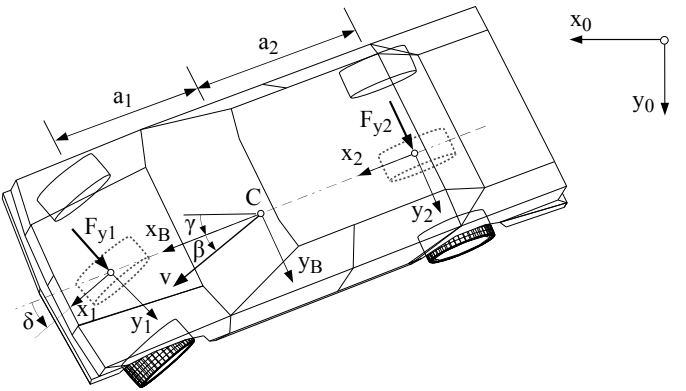

FIGURE 9.19
Simple handling model.

the body-fixed longitudinal axis x_B, whereas β indicates the direction of travel by measuring the angle between the vehicle velocity v and the longitudinal axis x_B. Again, the wheels at each axle are summarized in one fictitious wheel, where δ denotes the mean steering angle at the front axle. Only the lateral tire forces F_{y1}, F_{y2} are taken into account because the main focus is placed on the lateral dynamics here. In addition, aerodynamic forces and torques, applied at the vehicle, are not taken into consideration.

[2]This can easily be checked by running the MATLAB-Script in Listing 9.5 with different model data and observing the wheel loads.

9.3.2 Kinematics

The vehicle velocity at the center of gravity can be expressed easily in the body-fixed axis system x_B, y_B, z_B,

$$v_{C,B} = \begin{bmatrix} v\,\cos\beta \\ v\,\sin\beta \\ 0 \end{bmatrix}, \tag{9.89}$$

where β is the side slip angle and v denotes the magnitude of the vehicle velocity. The velocity vectors and the unit vectors in the longitudinal and lateral direction of the axles are needed for computation of the lateral slips. One gets

$$e_{x_1,B} = \begin{bmatrix} \cos\delta \\ \sin\delta \\ 0 \end{bmatrix}, \quad e_{y_1,B} = \begin{bmatrix} -\sin\delta \\ \cos\delta \\ 0 \end{bmatrix}, \quad v_{01,B} = \begin{bmatrix} v\,\cos\beta \\ v\,\sin\beta + a_1\,\dot{\gamma} \\ 0 \end{bmatrix} \tag{9.90}$$

as well as

$$e_{x_2,B} = \begin{bmatrix} 1 \\ 0 \\ 0 \end{bmatrix}, \quad e_{y_2,B} = \begin{bmatrix} 0 \\ 1 \\ 0 \end{bmatrix}, \quad v_{02,B} = \begin{bmatrix} v\,\cos\beta \\ v\,\sin\beta - a_2\,\dot{\gamma} \\ 0 \end{bmatrix}, \tag{9.91}$$

where a_1 and a_2 are the distances from the center of gravity C to the front and rear axle. Finally, $\dot{\gamma}$ denotes the yaw angular velocity of the vehicle.

9.3.3 Tire Forces

Unlike the kinematic tire model, now small lateral sliding motions in the contact points are permitted. For small lateral slips, the lateral force can be approximated by a linear approach

$$F_y \;=\; c_S\,s_y\,, \tag{9.92}$$

where the cornering stiffness c_S depends on the wheel load F_z, and the lateral slip s_y is defined by Equation (3.90). Because the vehicle is neither accelerated nor decelerated, the rolling condition

$$r_D\,\Omega \;=\; e_x^T\,v_{0P} \tag{9.93}$$

is fulfilled at each wheel Here, r_D is the dynamic tire radius, v_{0P} the contact point velocity, and e_x the unit vector in the longitudinal direction. With the lateral tire velocity

$$v_y \;=\; e_y^T\,v_{0P} \tag{9.94}$$

and the rolling condition defined in Equation (9.93), the lateral slip is given by

$$s_y \;=\; \frac{-e_y^T\,v_{0P}}{|\,e_x^T\,v_{0P}\,|}\,, \tag{9.95}$$

where e_y defines the unit vector in the lateral direction of the tire. So, the lateral tire forces are simply modeled as

$$F_{y1} \;=\; c_{S1}\, s_{y1} \quad \text{and} \quad F_{y2} \;=\; c_{S2}\, s_{y2}\,. \tag{9.96}$$

Even if the same tires are mounted at the front and rear axle, the cornering stiffness c_{S1} may vary from c_{S2} because of different wheel loads.

9.3.4 Lateral Slips

Using Equation (9.91), the lateral slip at the front axle defined by Equation (9.95) reads as

$$s_{y1} \;=\; \frac{+\sin\delta\,(v\,\cos\beta) - \cos\delta\,(v\,\sin\beta + a_1\,\dot\gamma)}{|\,\cos\delta\,(v\,\cos\beta) + \sin\delta\,(v\,\sin\beta + a_1\,\dot\gamma)\,|}\,. \tag{9.97}$$

The lateral slip at the rear axle,

$$s_{y2} \;=\; -\frac{v\,\sin\beta - a_2\,\dot\gamma}{|\,v\,\cos\beta\,|}\,, \tag{9.98}$$

is simpler because no steer angle is considered here. Now, the yaw velocity of the vehicle $\dot\gamma$, the side slip angle β, and the steering angle δ are assumed to be small,

$$|\,a_1\,\dot\gamma\,| \ll |v|\,, \quad |\,a_2\,\dot\gamma\,| \ll |v|\,, \tag{9.99}$$

$$|\,\beta\,| \ll 1\,, \quad \text{and} \quad |\,\delta\,| \ll 1\,. \tag{9.100}$$

Because the side slip angle β always describes the smaller angle between the velocity vector v and the vehicle longitudinal axis x_B, the straightforward linearization $v\,\sin\beta \approx v\,\beta$ is replaced by the more sophisticated one,

$$v\,\sin\beta \approx |v|\,\beta\,. \tag{9.101}$$

Comparatively small values for the yaw velocity and the side slip angle correspond quite well with normal driving situations. However, small steering angles at the front axles will exclude the simulation of parking maneuvers, for example. Now, Equations (9.97) and (9.98) result in

$$s_{y1} \;=\; -\beta \;-\; \frac{a_1}{|v|}\,\dot\gamma \;+\; \frac{v}{|v|}\,\delta\,, \tag{9.102}$$

$$s_{y2} \;=\; -\beta \;+\; \frac{a_2}{|v|}\,\dot\gamma\,, \tag{9.103}$$

where the consequences of Equations (9.99), (9.100), and (9.101) were taken into consideration.

9.3.5 Equations of Motion

The velocities, angular velocities, and accelerations are needed to derive the equations of motion. For small side slip angles $\beta \ll 1$, Equation (9.89) can be approximated by

$$v_{C,B} = \begin{bmatrix} v \\ |v|\,\beta \\ 0 \end{bmatrix} . \tag{9.104}$$

The angular velocity is given by

$$\omega_{0F,B} = \begin{bmatrix} 0 \\ 0 \\ \dot{\gamma} \end{bmatrix} . \tag{9.105}$$

The acceleration of the vehicle, expressed in the vehicle-fixed axis system x_B, y_B, z_B, is given by

$$a_{C,B} = \omega_{0F,B} \times v_{C,B} + \dot{v}_{C,B} = \begin{bmatrix} 0 \\ v\,\dot{\gamma} + |v|\,\dot{\beta} \\ 0 \end{bmatrix} , \tag{9.106}$$

where a constant vehicle velocity $v = const.$ was assumed and higher-order terms are neglected. The angular acceleration is simply defined by

$$\dot{\omega}_{0F,B} = \begin{bmatrix} 0 \\ 0 \\ \dot{\omega} \end{bmatrix} , \tag{9.107}$$

where the yaw angular velocity

$$\omega = \dot{\gamma} \tag{9.108}$$

substitutes the time derivative of the yaw angle. The linear momentum in the lateral direction of the vehicle reads as

$$m\,(v\,\omega + |v|\,\dot{\beta}) = F_{y1} + F_{y2} , \tag{9.109}$$

where, due to the small steering angle, the term $F_{y1} \cos\delta$ has been approximated by F_{y1}, and m is the vehicle mass. With Equation (9.108), the angular momentum yields

$$\Theta\,\dot{\omega} = a_1\,F_{y1} - a_2\,F_{y2} , \tag{9.110}$$

where Θ denotes the inertia of vehicle about a vertical axis located at the center of gravity. Inserting the linear description of the lateral forces Equation (9.96) combined with the lateral slips Equations (9.102), (9.103) into Equations (9.109) and (9.110) yields[3]

$$\dot{\beta} = \frac{c_{S1}}{m\,|v|}\left(-\beta - \frac{a_1}{|v|}\,\omega + \frac{v}{|v|}\,\delta\right) + \frac{c_{S2}}{m\,|v|}\left(-\beta + \frac{a_2}{|v|}\,\omega\right) - \frac{v}{|v|}\,\omega , \tag{9.111}$$

[3]This simple planar model, often called the "bicycle model," was first published by P. Riekert and T. E. Schunck: Zur Fahrmechanik des gummibereiften Kraftfahrzeugs, Ingenieur-Archiv, 11, 1940, S. 210-224. It is still used for fundamental studies or the basic layout of control systems.

$$\dot{\omega} \;=\; \frac{a_1\, c_{S1}}{\Theta}\left(-\beta - \frac{a_1}{|v|}\,\omega + \frac{v}{|v|}\,\delta\right) - \frac{a_2\, c_{S2}}{\Theta}\left(-\beta + \frac{a_2}{|v|}\,\omega\right) . \qquad (9.112)$$

This represents two coupled, but linear first-order differential equations, which can be written in the form of a linear state equation,

$$\underbrace{\begin{bmatrix}\dot{\beta}\\ \dot{\omega}\end{bmatrix}}_{\dot{x}} = \underbrace{\begin{bmatrix} -\dfrac{c_{S1}+c_{S2}}{m\,|v|} & \dfrac{a_2 c_{S2}-a_1 c_{S1}}{m\,|v||v|} - \dfrac{v}{|v|} \\ \dfrac{a_2 c_{S2}-a_1 c_{S1}}{\Theta} & -\dfrac{a_1^2 c_{S1}+a_2^2 c_{S2}}{\Theta\,|v|} \end{bmatrix}}_{A} \underbrace{\begin{bmatrix}\beta\\ \omega\end{bmatrix}}_{x} + \underbrace{\begin{bmatrix} \dfrac{v}{|v|} & \dfrac{c_{S1}}{m\,|v|} \\ \dfrac{v}{|v|} & \dfrac{a_1 c_{S1}}{\Theta} \end{bmatrix}}_{B} \underbrace{\begin{bmatrix}\delta\end{bmatrix}}_{u} . \qquad (9.113)$$

If a system can be at least approximatively described by a linear state equation, then the stability, steady-state solutions, transient response, and optimal controlling can be calculated with classic methods of system dynamics.

9.3.6 Stability

9.3.6.1 Eigenvalues

The homogeneous state equation

$$\dot{x} \;=\; A\, x \qquad (9.114)$$

describes the eigen-dynamics. If the approach

$$x_h(t) \;=\; x_0\, e^{\lambda t} \qquad (9.115)$$

is inserted into Equation (9.114), the homogeneous equation will remain,

$$(\lambda\, E \;-\; A)\; x_0 \;=\; 0\,. \qquad (9.116)$$

One gets nontrivial solutions $x_0 \neq 0$ for

$$det\,|\lambda\, E \;-\; A| \;=\; 0\,. \qquad (9.117)$$

The eigenvalues λ provide information concerning the stability of the system.

9.3.6.2 Low-Speed Approximation

The state matrix

$$A^{v\to 0} \;=\; \begin{bmatrix} -\dfrac{c_{S1}+c_{S2}}{m\,|v|} & \dfrac{a_2\, c_{S2} - a_1\, c_{S1}}{m\,|v||v|} - \dfrac{v}{|v|} \\ 0 & -\dfrac{a_1^2\, c_{S1} + a_2^2\, c_{S2}}{\Theta\,|v|} \end{bmatrix} \qquad (9.118)$$

approximates the eigen-dynamics of vehicles at low speeds, $v \to 0$. The matrix in Equation (9.118) has the eigenvalues

$$\lambda_1^{v\to 0} \;=\; -\,\frac{c_{S1}+c_{S2}}{m\,|v|} \quad \text{and} \quad \lambda_2^{v\to 0} \;=\; -\,\frac{a_1^2\,c_{S1}+a_2^2\,c_{S2}}{\Theta\,|v|}\,. \tag{9.119}$$

Both eigenvalues are real, always negative, and independent of the model data and the driving direction. Thus, all vehicles will possess an asymptotically stable driving behavior at low speed!

9.3.6.3 High-Speed Approximation

At high driving velocities, $v \to \infty$, the state matrix can be approximated by

$$A^{v\to\infty} \;=\; \begin{bmatrix} 0 & -\,\dfrac{v}{|v|} \\[2ex] \dfrac{a_2\,c_{S2}-a_1\,c_{S1}}{\Theta} & 0 \end{bmatrix}. \tag{9.120}$$

Using Equation (9.120) one obtains from Equation (9.117) the relation

$$(\lambda^{v\to\infty})^2 \;+\; \frac{v}{|v|}\,\frac{a_2\,c_{S2}-a_1\,c_{S1}}{\Theta} \;=\; 0 \tag{9.121}$$

with the solutions

$$\lambda_{1,2}^{v\to\infty} \;=\; \pm\sqrt{-\,\frac{v}{|v|}\,\frac{a_2\,c_{S2}-a_1\,c_{S1}}{\Theta}}\,. \tag{9.122}$$

When driving forward with $v > 0$, the root argument will be positive if

$$a_2\,c_{S2}-a_1\,c_{S1} \;<\; 0 \tag{9.123}$$

holds. Then, one eigenvalue will be definitely positive, and the system is unstable. Two zero-eigenvalues $\lambda_1^{v\to\infty} = 0$ and $\lambda_2^{v\to\infty} = 0$ are obtained just for

$$a_1\,c_{S1} = a_2\,c_{S2}\,. \tag{9.124}$$

The driving behavior is indifferent then. Slight parameter variations may lead to unstable behavior, however. A set of parameters, resulting in

$$a_2\,c_{S2}-a_1\,c_{S1} \;>\; 0 \quad \text{or} \quad a_1\,c_{S1} < a_2\,c_{S2} \tag{9.125}$$

will produce a negative root argument in Equation (9.122) on forward drive, $v > 0$. Then, the eigenvalues are imaginary, which characterizes undamped vibrations. To avoid instability on forward drive with high speed, vehicles have to satisfy the condition in Equation (9.125). However, the root argument in Equation (9.122) changes the sign on backward drive. As a consequence, all vehicles showing stable driving behavior at forward drive will definitely become unstable at fast backward drive!

9.3.6.4 Critical Speed

The condition for nontrivial solutions (9.117) results in a quadratic equation for the eigenvalues λ here,

$$det\,|\lambda\,E\,-\,A|\;=\;\lambda^2+k_1\lambda+k_2\;=\;0\,, \tag{9.126}$$

which is solved by

$$\lambda_{1,2}=-\frac{k_1}{2}\pm\sqrt{\left(\frac{k_1}{2}\right)^2-k_2}\;. \tag{9.127}$$

Asymptotically stable solutions ($\lambda_{1,2}$ real and $\lambda_1<0$, $\lambda_2<0$) demand at least for

$$k_1\;>\;0\quad\text{and}\quad k_2\;>\;0\,, \tag{9.128}$$

which exactly corresponds with the stability criteria of Stodola and Hurwitz [23]. According to Equation (9.113), the coefficients in Equation (9.126) can be derived from the vehicle data

$$k_1\;=\;\frac{c_{S1}+c_{S2}}{m\,|v|}+\frac{a_1^2c_{S1}+a_2^2c_{S2}}{\Theta|v|}\,, \tag{9.129}$$

$$\begin{aligned}k_2&=\frac{c_{S1}+c_{S2}}{m\,|v|}\,\frac{a_1^2c_{S1}+a_2^2c_{S2}}{\Theta|v|}-\frac{\left(a_2c_{S2}-a_1c_{S1}\right)^2}{\Theta\,m\,|v||v|}+\frac{v}{|v|}\,\frac{a_2c_{S2}-a_1c_{S1}}{\Theta}\\&=\frac{c_{S1}c_{S2}\,(a_1+a_2)^2}{m\,\Theta\,v^2}\left(1+\frac{v}{|v|}\,\frac{a_2c_{S2}-a_1c_{S1}}{c_{S1}c_{S2}\,(a_1+a_2)^2}\,m\,v^2\right)\,.\end{aligned} \tag{9.130}$$

The coefficient k_1 is always positive, whereas $k_2>0$ is fulfilled only if

$$1+\frac{v}{|v|}\,\frac{a_2c_{S2}-a_1c_{S1}}{c_{S1}c_{S2}\,(a_1+a_2)^2}\,m\,v^2\;>\;0 \tag{9.131}$$

holds. Hence, a vehicle designed stable for arbitrary velocities in the forward direction becomes unstable when it drives too fast backward. Because $k_2>0$ for $a_2c_{S2}-a_1c_{S1}>0$ and $v<0$ demands for $v>v_C^-$, where according to Equation (9.131) the critical backward velocity is given by

$$v_C^-\;=\;-\sqrt{\frac{c_{S1}c_{S2}\,(a_1+a_2)^2}{m\,(a_2c_{S2}-a_1c_{S1})}}\,. \tag{9.132}$$

On the other hand, vehicle layouts with $a_2c_{S2}-a_1c_{S1}<0$ are only stable while driving forward as long as $v<v_C^+$ holds. Here, Equation (9.131) yields the critical forward velocity of

$$v_C^+\;=\;\sqrt{\frac{c_{S1}c_{S2}\,(a_1+a_2)^2}{m\,(a_1c_{S1}-a_2c_{S2})}}\,. \tag{9.133}$$

Most vehicles are designed stable for fast forward drive. Then, the backward velocity must be limited in order to avoid stability problems. That is why, fast driving vehicles have four or more gears for forward drive but only one or two reverse gears.

9.3.6.5 Example

A passenger car is described by the data $m = 1600\,kg$, $\Theta = 2000\,kgm^2$, $a_1 = 1.1\,m$, $a_2 = 1.4\,m$, $c_{S1} = 124\,000\,N/-$, $c_{S2} = 120\,000\,N/-$. The vehicle is stable on forward drive because $a_2 * c_{S2} = 168\,000\,Nm$ is significantly larger than $a_1 * c_{S1} = 136\,400\,Nm$ here. Then, the vehicle is unstable at fast backward drive. According to Equation (9.132), the critical speed results in $v_C^- = -154.4\,km/h$ in this specific case. The eigenvalues are plotted in Figure 9.20 for different vehicle velocities, ranging from $v = -60\,km/h$ to $v = 180\,km/h$. At higher

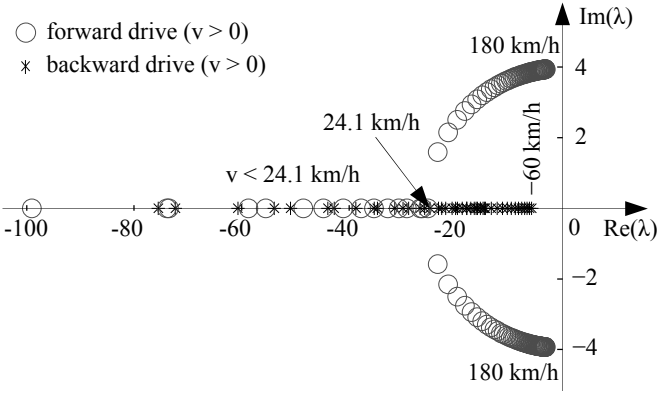

FIGURE 9.20
Stability analysis of a typical passenger car for different vehicle velocities.

velocities ($v > 24.1\,km/h$) the eigenvalues become complex conjugate, which characterizes damped vibrations. However, with increasing velocity, the real part Re(λ), which indicates the amount of damping, becomes smaller and smaller. At $v \to \infty$ it will vanish completely. On backward drive, the vehicle is stable, which is indicated by real and negative eigenvalues, as long as $v < v_C^-$ holds.

9.3.7 Steady-State Solution

9.3.7.1 Steering Tendency

At a given steering angle $\delta = \delta_0$, a stable system reaches steady-state after a certain time. Then, the vehicle will drive on a circle with the radius R_{st}, which is determined by

$$\omega_{st} \;=\; \frac{v}{R_{st}}\,, \tag{9.134}$$

where v is the velocity of the vehicle and ω_{st} denotes its steady-state angular velocity. With $x_{st} = const.$ or $\dot{x}_{st} = 0$, the state equation (9.113) simplifies to a system of linear equations,

$$A\,x_{st} \;=\; -B\,u\,. \tag{9.135}$$

Using Equation (9.134), the state vector can be described in steady-state by

$$x_{st} \;=\; \begin{bmatrix} \beta_{st} \\ v/R_{st} \end{bmatrix} , \tag{9.136}$$

where β_{st} denotes the steady-state side slip angle. With $u = [\delta_0]$, and the elements of the state matrix A and the vector B that are defined in Equation (9.113), the system of linear equations (9.135) yields

$$(c_{S1} + c_{S2})\,\beta_{st} \;+\; (m\,v\,|v| + a_1\,c_{S1} - a_2\,c_{S2})\,\frac{v}{|v|}\,\frac{1}{R_{st}} \;=\; \frac{v}{|v|}\,c_{S1}\,\delta_0 \,, \tag{9.137}$$

$$(a_1\,c_{S1} - a_2\,c_{S2})\,\beta_{st} \;+\; (a_1^2\,c_{S1} + a_2^2\,c_{S2})\,\frac{v}{|v|}\,\frac{1}{R_{st}} \;=\; \frac{v}{|v|}\,a_1\,c_{S1}\,\delta_0 \,, \tag{9.138}$$

where the first equation has been multiplied by $-m\,|v|$ and the second by $-\Theta$. Eliminating the steady-state side slip angle β_{st} results in

$$\begin{aligned} \big[mv|v|(a_1c_{S1} - a_2c_{S2}) + (a_1c_{S1} - a_2c_{S2})^2 \\ -(c_{S1}+c_{S2})(a_1^2c_{S1}+a_2^2c_{S2})\big]\,\frac{v}{|v|}\frac{1}{R_{st}} \quad = \\ [a_1c_{S1} - a_2c_{S2} - a_1(c_{S1}+c_{S2})]\,\frac{v}{|v|}c_{S1}\delta_0 \quad , \end{aligned} \tag{9.139}$$

which can be simplified to

$$\big[mv|v|(a_1c_{S1} - a_2c_{S2}) - c_{S1}c_{S2}(a_1+a_2)^2\big]\,\frac{v}{|v|}\,\frac{1}{R_{st}} = -\frac{v}{|v|}c_{S1}c_{S2}(a_1+a_2)\delta_0 \,. \tag{9.140}$$

Hence, driving the vehicle at a certain radius requires a steering angle of

$$\delta_0 \;=\; \frac{a_1 + a_2}{R_{st}} \;+\; m\,\frac{v|v|}{R_{st}}\,\frac{a_2\,c_{S2} - a_1\,c_{S1}}{c_{S1}\,c_{S2}\,(a_1 + a_2)} \,. \tag{9.141}$$

The first term is just the Ackermann steering angle, which follows from Equation (9.2) with the wheel base of $a = a_1 + a_2$ and the approximation for small steering angles $\tan\delta_0 \approx \delta_0$. In fact, the Ackermann steering angle provides a good approximation for slowly moving vehicles, because the second expression in Equation (9.141) is negligibly small at $v \to 0$. Depending on the value of $a_2\,c_{S2} - a_1\,c_{S1}$ and the driving direction, forward $v > 0$ or backward $v < 0$, the necessary steering angle differs from the Ackermann steering angle at higher speeds. The difference is proportional to the lateral acceleration

$$a_y \;=\; \frac{v|v|}{R_{st}} \;=\; \pm\,\frac{v^2}{R_{st}} \,. \tag{9.142}$$

Now, Equation (9.141) can be written as

$$\delta_0 \;=\; \delta_A \;+\; k\,a_y \,, \tag{9.143}$$

where $\delta_A = (a_1 + a_2)/R_{st}$ is the Ackermann steering angle, k summarizes the relevant vehicle parameters, and $a_y = v^2/R_{st}$ denotes the lateral acceleration of the vehicle. In a diagram where the steering angle δ_0 is plotted versus the lateral acceleration a_y, Equation (9.143) will represent a straight line, Figure 9.21. On forward drive, $v > 0$, the inclination of this line, which is also

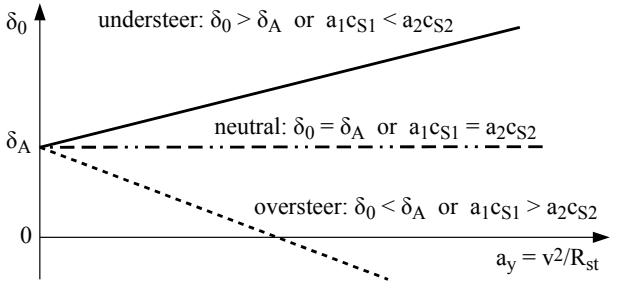

FIGURE 9.21
Different steering tendencies.

called the steering gradient, is given by

$$\frac{d\,\delta_0}{d\,a_y} \;=\; k \;=\; \frac{m\;(a_2\,c_{S2} - a_1\,c_{S1})}{c_{S1}\,c_{S2}\,(a_1 + a_2)} \quad \left[\frac{rad}{m/s^2}\right] . \tag{9.144}$$

For steady-state cornering, the amount of the steering angle $\delta_0 \lessgtr \delta_A$ and hence, the steering tendency depends at increasing velocity on the stability condition $a_2 c_{S2} - a_1 c_{S1} \lessgtr 0$. The various steering tendencies are also arranged in Table 9.2.

TABLE 9.2
Steering Tendencies of a Vehicle at Forward Driving

Understeer	$\delta_0 > \delta_0^A$	or	$a_1\,c_{S1} < a_2\,c_{S2}$	or	$a_1\,c_{S1}\,/\,a_2\,c_{S2} < 1$
Neutral	$\delta_0 = \delta_0^A$	or	$a_1\,c_{S1} = a_2\,c_{S2}$	or	$a_1\,c_{S1}\,/\,a_2\,c_{S2} = 1$
Oversteer	$\delta_0 < \delta_0^A$	or	$a_1\,c_{S1} > a_2\,c_{S2}$	or	$a_1\,c_{S1}\,/\,a_2\,c_{S2} > 1$

9.3.7.2 Side Slip Angle

Resolving Equations (9.137) and (9.138) for the steady-state side slip angle yields

$$\beta_{st} = \frac{v}{|v|}\frac{a_2}{R_{st}} - \frac{m\,v\,|v|}{R_{st}}\frac{a_1}{c_{S2}(a_1+a_2)} = \frac{v}{|v|}\left(\frac{a_2}{R_{st}} - m\,a_y\,\frac{a_1}{c_{S2}(a_1+a_2)}\right), \tag{9.145}$$

where $a_y = v^2/R_{st}$ represents the lateral acceleration. The steady-state side slip angle starts with the kinematic value

$$\beta_{st}^{v\to 0} \;=\; \frac{v}{|v|}\,\frac{a_2}{R_{st}}\,. \tag{9.146}$$

On forward drive ($v>0$), it decreases with increasing lateral acceleration. It changes sign at

$$a_y^{\beta_{st}=0} \;=\; \frac{a_2\,c_{S2}\,(a_1+a_2)}{a_1\,m\,R_{st}} \tag{9.147}$$

Note that the side slip angle defined in Equation (9.145) is not directly affected by the steering tendency. The decay of the side slip angle with increasing lateral acceleration on forward drive, and hence the sign change defined by Equation (9.147) depends on the magnitude of the cornering stiffness c_{S2} at the rear axle.

Some concepts for an additional steering of the rear axle were trying to keep the side slip angle of the vehicle, measured at the center of the vehicle, at zero by an appropriate steering or controlling. Due to numerous problems, the production stage could not yet be reached.

9.3.7.3 Curve Radius

Usually a driver estimates the required steering angle $\delta = \delta_0$ when entering a curve of a given or rated radius R. However, the actual driven radius R_{st} depends on the vehicle speed v and the steering tendency of the vehicle. Rearranging Equation (9.141) yields

$$R_{st} \;=\; \frac{a_1+a_2}{\delta_0} \;+\; m\,\frac{v|v|}{\delta_0}\,\frac{a_2\,c_{S2}-a_1\,c_{S1}}{c_{S1}\,c_{S2}\,(a_1+a_2)}\,. \tag{9.148}$$

The actual driven curve radius R_{st} is plotted in Figure 9.22 versus the driving speed v for different steering tendencies. The steering angle has been set to $\delta_0 = 1.4321°$ here, in order to let the vehicle drive a circle with the radius $R_0 = 100\,m$ at $v \to 0$. Depending on the steering tendency of the vehicle, the actual driven curve radius will increase, remain constant, or even decrease with the vehicle velocity. In order to keep the desired path, the driver must adjust the steering input appropriately in the case of a vehicle with an under- or an oversteer tendency. If a vehicle with understeer tendency is cornering fast, the driver will usually over-estimate the required steering input. As a consequence, the vehicle will drive a curve with a smaller radius, which increases the lateral acceleration and may result in a critical driving situation.

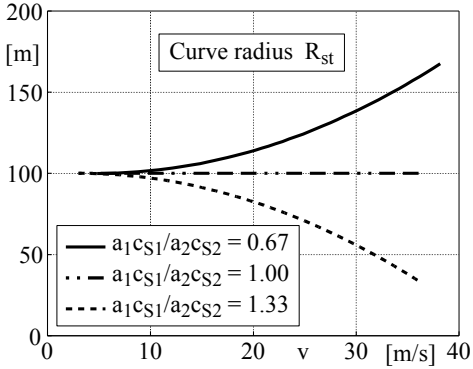

m=700 kg $\quad a_1$=1.2 m $\quad c_{S1}$=80 000 $N/-$ $\quad c_{S2} = \begin{cases} 110\,770\ N/- \\ 73\,846\ N/- \\ 55\,385\ N/- \end{cases}$

Θ=1000 $kg\,m^2$ $\quad a_2$=1.3 m

FIGURE 9.22
Curve radius at steady-state cornering with different velocities.

9.3.7.4 Lateral Slips

At steady-state, $\dot{\beta}_{st} = 0$ and $\dot{\omega}_{st} = 0$ holds. Then, the equations of motion (9.109) and (9.110) can be resolved for the lateral forces

$$\begin{aligned} F_{y1_{st}} &= \frac{a_2}{a_1 + a_2}\, m\, \frac{v^2}{R_{st}}\,, \\ F_{y2_{st}} &= \frac{a_1}{a_1 + a_2}\, m\, \frac{v^2}{R_{st}}\,, \end{aligned} \qquad \text{or} \qquad \frac{a_1}{a_2} = \frac{F_{y2_{st}}}{F_{y1_{st}}}\,, \tag{9.149}$$

where Equation (9.134) was taken into account. With the linear tire model in Equation (9.92) one gets in addition

$$F_{y1}^{st} = c_{S1}\, s_{y1}^{st} \quad \text{and} \quad F_{y2}^{st} = c_{S2}\, s_{y2}^{st}\,, \tag{9.150}$$

where $s_{y_{A1}}^{st}$ and $s_{y_{A2}}^{st}$ denote the steady-state lateral slips at the front and rear axle. Now, the Equations (9.149) and (9.150) deliver

$$\frac{a_1}{a_2} = \frac{F_{y2}^{st}}{F_{y1}^{st}} = \frac{c_{S2}\, s_{y2}^{st}}{c_{S1}\, s_{y1}^{st}} \qquad \text{or} \qquad \frac{a_1\, c_{S1}}{a_2\, c_{S2}} = \frac{s_{y2}^{st}}{s_{y1}^{st}}\,. \tag{9.151}$$

Hence, the steering tendency of a vehicle is also indicated by the lateral slip ratio. According to Equation (3.90) the lateral slip is strongly related to the slip angle. As a consequence, the slip angles at the front axle will be larger than the slip angles at the rear axle ($s_{y1}^{st} > s_{y2}^{st}$) if a vehicle shows the tendency to understeer ($a_1\, c_{S1} < a_2\, c_{S2}$) at steady-state cornering.

9.3.8 Influence of Wheel Load on Cornering Stiffness

With identical tires at the front and rear axle, given a linear influence of wheel load on the raise of the lateral force over the lateral slip,

$$c_{S1}^{lin} = c_S F_{z1} \quad \text{and} \quad c_{S2}^{lin} = c_S F_{z2} \tag{9.152}$$

holds. The weight of the vehicle $G = mg$ is distributed over the axles according to the position of the center of gravity,

$$F_{z1} = \frac{a_2}{a_1 + a_2} G \quad \text{and} \quad F_{z2} = \frac{a_1}{a_1 + a_2} G \,. \tag{9.153}$$

With Equation (9.152) and Equation (9.153) one obtains

$$a_1 c_{S1}^{lin} = a_1 c_S \frac{a_2}{a_1 + a_2} G \tag{9.154}$$

and

$$a_2 c_{S2}^{lin} = a_2 c_S \frac{a_1}{a_1 + a_2} G \,. \tag{9.155}$$

Thus, a vehicle with identical tires would be steering neutrally with a linear influence of the wheel load on the cornering stiffness, because of

$$a_1 c_{S1}^{lin} = a_2 c_{S2}^{lin} \,. \tag{9.156}$$

In practice, the lateral force is applied behind the center of the contact patch at the caster offset distance. Hence, the lever arms of the lateral forces will change to $a_1 \to a_1 - \frac{v}{|v|} n_{L_1}$ and $a_2 \to a_2 + \frac{v}{|v|} n_{L_1}$, which stabilizes the vehicle, independently from the driving direction.

For a real tire, a degressive influence of the wheel load on the tire forces is observed, Figure 9.23. According to Equation (9.110), the rotation of the

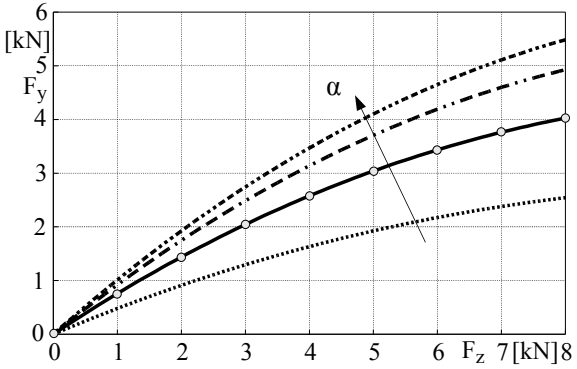

F_z [N]	F_y [N]
0	0
1000	758
2000	1438
3000	2043
4000	2576
5000	3039
6000	3434
7000	3762
8000	4025

FIGURE 9.23
Lateral force F_y versus wheel load F_z at different slip angles.

vehicle is stable if the torque from the lateral forces F_{y1} and F_{y2} is aligning, i.e.,

$$a_1 F_{y1} - a_2 F_{y2} < 0 \tag{9.157}$$

holds. For a vehicle with the wheel base $a = 2.45\,m$ the axle loads $F_{z1} = 4000N$ and $F_{z2} = 3000\,N$ yield the position of the center of gravity $a_1 = 1.05\,m$ and $a_2 = 1.40\,m$. For equal slip on front and rear axle, one gets from the table in Figure 9.23 $F_{y1} = 2576\,N$ and $F_{y2} = 2043\,N$. With this, the condition in Equation (9.157) yields $1.05 * 2576 - 1.45 * 2043 = -257.55$. The value is significantly negative and thus stabilizing.

Vehicles with $a_1 < a_2$ have a stable, i.e., understeering driving behavior. If the axle load at the rear axle is larger than at the front axle ($a_1 > a_2$), generally a stable driving behavior can only be achieved with different tires.

At increasing lateral acceleration, the vehicle is more and more supported by the outer wheels. The wheel load differences can differ at a sufficiently rigid vehicle body, because of different kinematics (roll support) or different roll stiffness. Due to the degressive influence of wheel load, the lateral force at an axle decreases with increasing wheel load difference. If the wheel load is split more strongly at the front axle than at the rear axle, the lateral force potential at the front axle will decrease more than at the rear axle and the vehicle will become more stable with an increasing lateral force, i.e., more understeering.

9.4 Mechatronic Systems

9.4.1 Electronic Stability Control (ESC)

Electronic Stability Control (ESC) is the generic term for systems designed to improve a vehicle's handling, particularly at the limits where the driver might lose control of the vehicle. Robert Bosch GmbH were the first to deploy an ESC system, called Electronic Stability Program that was used by Mercedes-Benz. ESC compares the driver's intended direction in steering and braking inputs, to the vehicle's response, via lateral acceleration, rotation (yaw), and individual wheel speeds. ESC then brakes individual front or rear wheels and/or reduces excess engine power as needed to help correct understeer or oversteer, Figure 9.24. ESC also integrates all-speed traction control, which senses drive-wheel slip under acceleration and individually brakes the slipping wheel or wheels, and/or reduces excess engine power, until control is regained. ESC combines anti-lock brakes, traction control, and yaw control.

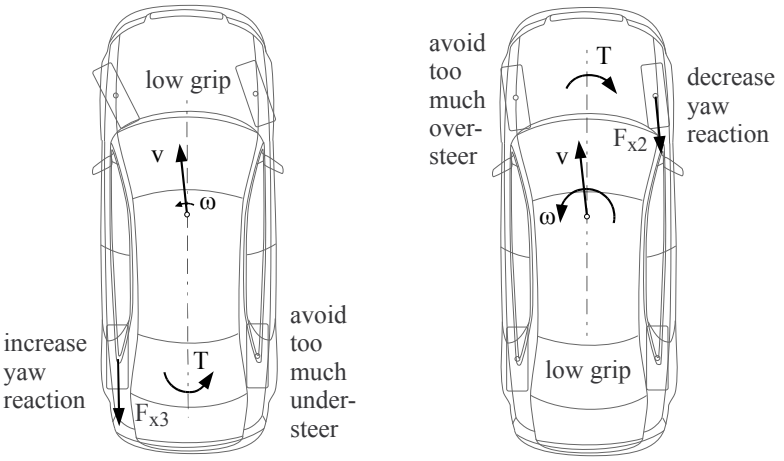

FIGURE 9.24
ESP braking concepts.

9.4.2 Steer-by-Wire

Modern steer-by-wire systems can improve the handling properties of vehicles [49]. Usually an electronically controlled actuator is used to convert the rotation of the steering wheel into steer movements of the wheels. Steer-by-wire systems are based on mechanics, micro-controllers, electro-motors, power electronics, and digital sensors. At present, fail-safe systems with a mechanical backup system are under investigation. The potential of a modern active steering system can be demonstrated by the maneuver of braking on a μ-split [41]. The layout of a modern the steering system and the different reactions of the vehicle are shown in Figure 9.25. The coefficient of friction on the left

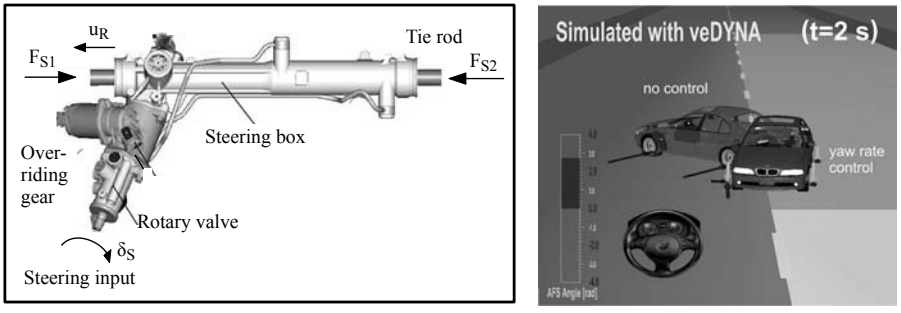

FIGURE 9.25
Steering system with over-riding gear and animated simulation screenshot of braking on μ-split with a standard and an active steering system.

side of the vehicle is supposed to be 10% of the normal friction value on the right side. The vehicle speeds to $v = 130\,km/h$ and then the driver applies full brake pressure and fixes the steering wheel like he would do first in a panic reaction. During the whole maneuver, the anti-lock brake system was disabled. The different brake forces on the left and right tires make the car spin around the vertical axis.

Only skilled drivers will be able to stabilize the car by counter steering. The success of counter steering depends on the reactions in the first few seconds. A controller, who takes appropriate actions at the steering angle, can assist the driver's task.

Exercises

9.1 A ready-mix truck with the given dimensions is equipped with two steerable front axle. The maximum steering angle of the inner wheel at the first front axle (wheel 11) amounts to $\delta_{12}^{max} = 48°$.

To improve the cornering performance, the second rear axle is designed to be steered too.

Compute the cornering radius R measured from the turning pivot point to wheel 11 and all steering angles according to the Ackermann geometry.

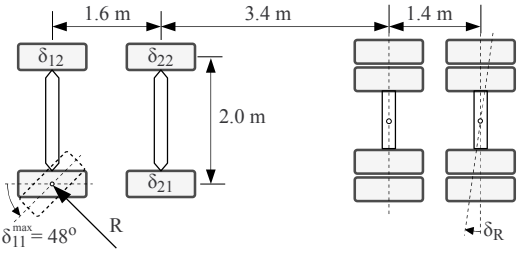

9.2 Compute the space requirement of a heavy-duty dumper with the given dimensions when cornering at a bend angle of 40°.

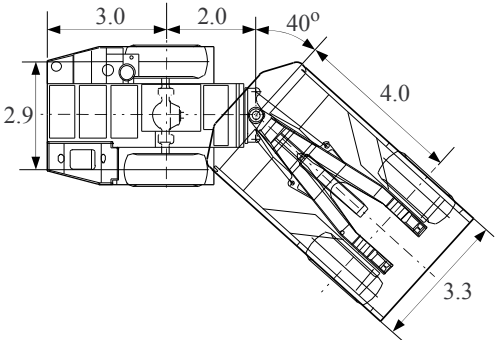

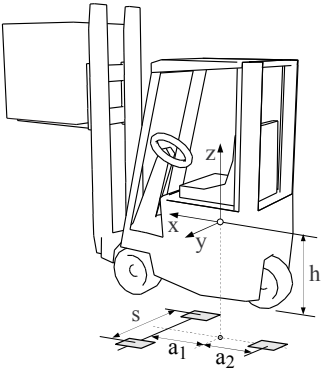

9.3 A three-wheeled forklift has a track width of $s = 1.0\,m$ at the front axle. The wheel base is defined by $a_1 = a_2 = 0.6\,m$. The coefficient of friction between the tires and the ground is given by $\mu = 0.9$.

Compute the rollover threshold for the lateral acceleration when the center of gravity is located $h = 1.1\ m$ above the ground.

Hint: Identify the potential line of rollover first. Follow the approach in Section 9.2.2.

Compute the maximum deceleration too.

9.4 Use the MATLAB-Script provided by Listing 9.2 and the MATLAB-Function in Listing 9.1 to investigate the cornering behavior of a tractor semi-trailer. Set $a = 3.5\ m$, $b = -0.25\ m$ and $c = 6.0\ m$.

Find a steering input that generates a double lane change with a lateral deviation of 5 m at a speed of 5 km/h.

9.5 A rear-wheel driven vehicle drives on a circle of radius $R = 40\ m$ with constant velocity. In the vehicle-fixed axis system, the acceleration components $a_{xB} = -0.133\ m/s^2$ and $a_{yB} = 3.998\ m/s^2$ are measured in the longitudinal and lateral direction. The average steering angle at the front axle is given by $\delta = 6.2°$. The vehicle has a mass $m = 1600\ kg$. The distances $a_1 = 1.3\ m$ and $a_2 = 1.4\ m$ define the position of the center of gravity.

Determine the side slip angle β at the vehicle center C, the velocity v of the vehicle, and its angular velocity ω. Evaluate the steering tendency of the vehicle.

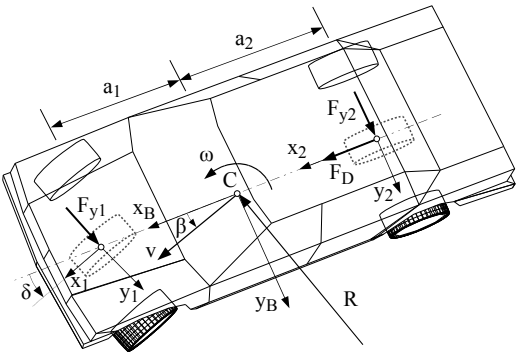

Calculate the lateral tire forces F_{y1}, F_{y2} that are required to keep the vehicle in steady-state when cornering.

Compute the required driving force F_D.

10

Driving Behavior of Single Vehicles

CONTENTS

10.1 Three-Dimensional Vehicle Model

10.1.1 Model Structure

As mentioned in Section 1.4, vehicles can be modeled by multibody systems. A full vehicle model consists of the vehicle framework supplemented by eventually separate modules for the steering system, the drive train, the tires, the load, passenger/seat models, an elastically suspended engine, and in the case of heavy trucks by an elastically suspended driver's cab. The vehicle framework represents the kernel of such a full model. It includes at least the module chassis and modules for the wheel/axle suspension systems. Typical passenger cars are characterized by a sufficiently rigid chassis and independent wheel axle suspension systems. As an extension to the enhanced planar model, described in Section 8.4.1, the three-dimensional model for the vehicle framework now consists of $n = 9$ rigid bodies: four knuckles, four wheels, and the chassis,

Figure 10.1. The vehicle-fixed axis system F is located in the middle of the

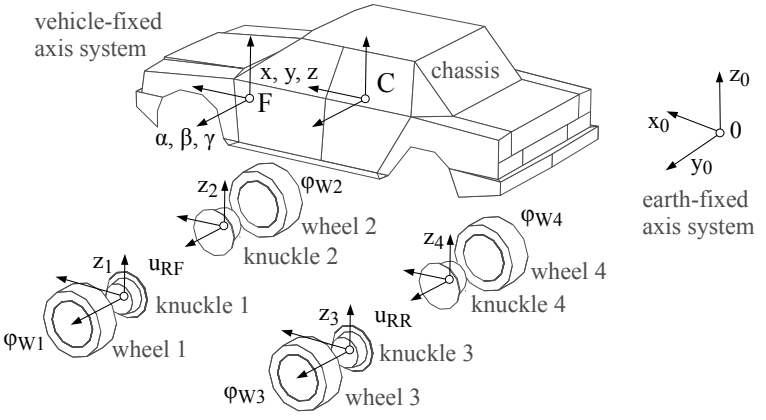

FIGURE 10.1
Bodies of the framework of a three-dimensional vehicle model.

front wheel centers; the x_F-axis points forward, the y_F-axis to the left, and the z_F-axis upward.

10.1.2 Position and Orientation

The position of the vehicle-fixed axis system with respect to the earth-fixed axis system 0 is described by the components x, y, z of the position vector

$$r_{0F,0} = \begin{bmatrix} x & y & z \end{bmatrix}^T . \tag{10.1}$$

Its orientation is defined by the rotation matrix

$$A_{0F,0} = \underbrace{\begin{bmatrix} \cos\gamma & -\sin\gamma & 0 \\ \sin\gamma & \cos\gamma & 0 \\ 0 & 0 & 1 \end{bmatrix}}_{A_\gamma} \underbrace{\begin{bmatrix} \cos\beta & 0 & \sin\beta \\ 0 & 1 & 0 \\ -\sin\beta & 0 & \cos\beta \end{bmatrix}}_{A_\beta} \underbrace{\begin{bmatrix} 1 & 0 & 0 \\ 0 & \cos\alpha & -\sin\alpha \\ 0 & \sin\alpha & \cos\alpha \end{bmatrix}}_{A_\alpha} , \tag{10.2}$$

where γ denotes the yaw angle and β, α characterize the pitch and roll motion. Now, the position and the orientation of the chassis are simply given by

$$r_{0C,0} = r_{0F,0} + A_{0F}\, r_{FC,F} \quad \text{and} \quad A_{0C} = A_{0F} , \tag{10.3}$$

where the vector $r_{FC,F}$, which describes the position of the chassis center relative to the vehicle-fixed axis system, is constant and defined by the mass distribution of the chassis. Each wheel is supposed to be fully balanced. Then, its center is located on the rotation axis. In addition, it is assumed that the center of the corresponding knuckle will be sufficiently close by or will even

coincide with the wheel center. As a consequence, the position of each knuckle, and simultaneously of each wheel, is defined by the vector

$$r_{0i,0} \;=\; r_{0F,0} + A_{0F}\, r_{Fi,F}\,, \quad i = 1(1)4\,. \tag{10.4}$$

If the rotation matrices A_{Fi}, $i = 1(1)4$ describe the orientation of each knuckle-fixed axis system relative to the vehicle-fixed axis system, then the rotation matrices

$$A_{0i} \;=\; A_{0F}\, A_{Fi}\,, \quad i = 1(1)4 \tag{10.5}$$

will define their orientation with respect to the earth-fixed axis system. A purely kinematic suspension model describes the position and orientation of each knuckle as a function of the jounce and rebound motion as well as the steering motion. The vertical motion z_i of each knuckle $i = 1(1)4$ relative to the chassis or, as done in Section 5.4, the rotation angle of the lower wishbone φ_i may be used to characterize the jounce and rebound motion. Assuming a rack and pinion steering system at both axles, the rack movements u_F and u_R at the front and rear axle will fully describe the steering motion at the corresponding axle. Then, the position and orientation of each knuckle and wheel center relative to the vehicle-fixed axis system is defined at the front ($i = 1, 2$) and at the rear axle ($i = 3, 4$) by

$$r_{Fi,F} = r_{Fi,F}\,(z_i, u_F)\,,\; A_{Fi} = A_{Fi,F}\,(z_i, u_F)\,, \quad i = 1, 2\,, \tag{10.6}$$

$$r_{Fi,F} = r_{Fi,F}\,(z_i, u_R)\,,\; A_{Fi} = A_{Fi,F}\,(z_i, u_R)\,, \quad i = 3, 4\,. \tag{10.7}$$

Finally, the angles φ_{Wi}, $i = 1(1)4$ describe the rotation of each wheel relative to the corresponding knuckle.

10.1.3 Velocities

Expressing the absolute velocity and the absolute angular velocity of the vehicle-fixed axis system in this axis system results in

$$v_{0F,F} \;=\; A_{0F}^T\, \dot{r}_{0F,0} \;=\; A_{0F}^T \begin{bmatrix} \dot{x} \\ \dot{y} \\ \dot{z} \end{bmatrix}\,, \tag{10.8}$$

$$\begin{aligned} \omega_{0F,F} &= \begin{bmatrix} \dot{\alpha} \\ 0 \\ 0 \end{bmatrix} + A_\alpha^T \left\{ \begin{bmatrix} 0 \\ \dot{\beta} \\ 0 \end{bmatrix} + A_\beta^T \begin{bmatrix} 0 \\ 0 \\ \dot{\gamma} \end{bmatrix} \right\} \\ &= \begin{bmatrix} 1 & 0 & -\sin\beta \\ 0 & \cos\alpha\, \sin\alpha\cos\beta \\ 0 & -\sin\alpha\, \cos\alpha\cos\beta \end{bmatrix} \begin{bmatrix} \dot{\alpha} \\ \dot{\beta} \\ \dot{\gamma} \end{bmatrix} = K_R \begin{bmatrix} \dot{\alpha} \\ \dot{\beta} \\ \dot{\gamma} \end{bmatrix}\,, \end{aligned} \tag{10.9}$$

where the components of $v_{0F,F}$ and $\omega_{0F,F}$ will be used as generalized velocities further on. Now, the absolute velocity and the angular velocity of the chassis are defined by

$$v_{0C,F} = v_{0F,F} + \omega_{0F,F} \times r_{FC,F} \quad \text{and} \quad \omega_{0C,F} = \omega_{0F,F}\,. \tag{10.10}$$

At first, the time derivative of Equation (10.4) results in

$$\underbrace{\dot{r}_{0i,0}}_{v_{0i,0}} = \underbrace{\dot{r}_{0F,0}}_{v_{0F,0}} + \omega_{0F,0}\, A_{0F}\, r_{Fi,F} + A_{0F}\, \dot{r}_{Fi,F}\,, \quad i = 1(1)4\,. \tag{10.11}$$

Next, the transformation into the vehicle-fixed axis system yields

$$v_{0i,F} = v_{0F,F} + \omega_{0F,F}\, r_{Fi,F} + \dot{r}_{Fi,F}\,, \quad i = 1(1)4\,, \tag{10.12}$$

where the velocity state of the vehicle-fixed axis system, characterized by $v_{0F,F}$ and $\omega_{0F,F}$, is defined in Equations (10.8) and (10.9). The time derivative of the position vectors, provided by Equations (10.6) and (10.7), results in

$$\dot{r}_{Fi,F} = \frac{\partial r_{Fi,F}}{\partial z_i}\,\dot{z}_i + \frac{\partial r_{Fi,F}}{\partial u_F}\,\dot{u}_{RF} = t_{zi,F}\,\dot{z}_i + t_{ui,F}\,\dot{u}_{RF}, \quad i = 1,2\,, \tag{10.13}$$

$$\dot{r}_{Fi,F} = \frac{\partial r_{Fi,F}}{\partial z_i}\,\dot{z}_i + \frac{\partial r_{Fi,F}}{\partial u_R}\,\dot{u}_{RR} = t_{zi,F}\,\dot{z}_i + t_{ui,F}\,\dot{u}_{RF}, \quad i = 3,4\,, \tag{10.14}$$

where $t_{zi,F}$ and $t_{ui,F}$, $i = 1(1)4$ abbreviate the corresponding partial velocities. Similary, the angular velocities of the knuckles may be written as

$$\omega_{0Ki,F} = \omega_{0F,F} + d_{zi,F}\,\dot{z}_i + d_{ui,F}\,\dot{u}_F, \quad i = 1(1)4\,, \tag{10.15}$$

where $d_{zi,F}$ and $d_{ui,F}$, $i = 1(1)4$ abbreviate the corresponding partial angular velocities. Finally, the absolute angular velocity of each wheel is given by

$$\Omega_{0Wi} = \omega_{0F,F} + d_{zi,F}\,\dot{z}_i + d_{ui,F}\,\dot{u}_R + A_{Fi}\, e_{yRi,i}\,\varphi\dot{W}i, \quad i = 1(1)4\,, \tag{10.16}$$

where the unit vectors $e_{yRi,i}$, $i = 1(1)4$, describe the orientation of the wheel rotation axis in the design position. They are defined by a wheel alignment point or via the toe and camber angles as discussed in Section 1.3.5.

The partial velocities and the partial angular velocities of the vehicle model consisting of $n = 9$ model bodies are collected in the Tables 10.1 and 10.2, where E denotes the 3×3 matrix of identity, and the cross-products in the velocity equations are substituted via $\omega \times r = -r \times \omega = -\tilde{r}\,\omega = \tilde{r}^T\omega$ by multiplication with the corresponding skew symmetric matrices. In this model approach it is assumed that the centers of each knuckle and wheel will coincide. That is why knuckle and wheel are summarized to one body in Table 10.1. The components v_x, v_y, v_z of the velocity $v_{0F,F}$ and the the components ω_x, ω_y, ω_z of the angular velocity $\omega_{0F,F}$; the time derivatives of vertical wheel center displacements $\dot{z}_1$ to $\dot{z}_2$; the time derivatives of the lateral rack movements $\dot{u}_F$ and $\dot{u}_R$; as well as the wheel angular velocities $\omega_{Wi} = \dot{\varphi}_{Wi}$, $i = 1(1)4$, are used as generalized velocities here. The three-dimensional vehicle model then has $f = 3{+}3{+}4{+}2{+}4 = 16$ degrees of freedom. All partial velocities and all inertia tensors are expressed in the vehicle-fixed reference frame. In case of double wishbone suspension systems, the partial velocities and the partial angular velocities are provided in Section 5.4. For arbitrary suspension systems, the position and orientation of each knuckle may be provided via look-up tables. A spline interpolation will then provide the partial velocities too.

TABLE 10.1
Partial Velocities: Three-Dimensional Vehicle Model

Body Name Mass	Partial Velocities $\partial v_{0i,F}/\partial z_j$											
	Vehicle		Front Susp.			Rear Susp.			Wheels			
	$v_{0F,F}$ v_x,v_y,v_z	$\omega_{0F,F}$ $\omega_x,\omega_y,\omega_z$	$\dot{z}_1$	$\dot{z}_2$	$\dot{u}_F$	$\dot{z}_3$	$\dot{z}_4$	$\dot{u}_R$	ω_1	ω_2	ω_3	ω_4
Knuckle + wheel 1 $m_{K1}+m_{W1}$	E	$\tilde{r}^T_{F1,F}$	t_{z1}	0	t_{u1}	0	0	0	0	0	0	0
Knuckle + wheel 2 $m_{K2}+m_{W2}$	E	$\tilde{r}^T_{F2,F}$	0	t_{z2}	t_{u2}	0	0	0	0	0	0	0
Knuckle + wheel 3 $m_{K3}+m_{W3}$	E	$\tilde{r}^T_{F3,F}$	0	0	0	t_{z3}	0	t_{u3}	0	0	0	0
Knuckle + wheel 4 $m_{K4}+m_{W4}$	E	$\tilde{r}^T_{F4,F}$	0	0	0	0	$t_{4\varphi}$	t_{4u}	0	0	0	0
Chassis m_C	E	$\tilde{r}^T_{FC,F}$	0	0	0	0	0	0	0	0	0	0

TABLE 10.2
Partial Angular Velocities: Three-Dimensional Vehicle Model

Body Inertia name	Partial Angular Velocities $\partial\omega_{0i,F}/\partial z_j$											
	Vehicle		Front Susp.			Rear Susp.			Wheels			
	$v_{0F,F}$ v_x,v_y,v_z	$\omega_{0F,F}$ $\omega_x,\omega_y,\omega_z$	$\dot{z}_1$	$\dot{z}_2$	$\dot{u}_F$	$\dot{z}_3$	$\dot{z}_4$	$\dot{u}_R$	ω_1	ω_2	ω_3	ω_4
Knuckle 1 Θ_{K1}	0	E	d_{z1}	0	d_{u1}	0	0	0	0	0	0	0
Wheel 1 Θ_{W1}	0	E	d_{z1}	0	d_{u1}	0	0	0	e_{yR1}	0	0	0
Knuckle 2 Θ_{K2}	0	E	0	d_{z2}	d_{u2}	0	0	0	0	0	0	0
Wheel 2 Θ_{W2}	0	E	0	d_{z2}	d_{u2}	0	0	0	0	e_{yR2}	0	0
Knuckle 3 Θ_{K3}	0	E	0	0	0	d_{z3}	0	d_{u3}	0	0	0	0
Wheel 3 Θ_{W3}	0	E	0	0	0	d_{z3}	0	d_{u3}	0	0	e_{yR3}	0
Knuckle 4 Θ_{K4}	0	E	0	0	0	0	d_{z4}	d_{u4}	0	0	0	0
Wheel 4 Θ_{W4}	0	E	0	0	0	0	d_{z4}	d_{u4}	0	0	0	e_{yR4}
Chassis Θ_C	0	E	0	0	0	0	0	0	0	0	0	0

10.1.4 Accelerations

Now, the absolute acceleration of the chassis, expressed in the vehicle-fixed axis system, is obtained as

$$a_{0C,F} = \dot{v}_{0F,F} + \dot{\omega}_{0F,F} \times r_{FC,F} + \omega_{0F,F} \times v_{0C,F} , \tag{10.17}$$

where the fact that the vector $r_{FC,F}$ is constant was already taken into account. The last term, which does not depend on the time derivatives of the generalized velocities $\dot{v}_{0F,F}$ or $\dot{\omega}_{0F,F}$ represents the remaining term $a^R_{0C,F}$ here. The absolute angular acceleration, expressed in the vehicle-fixed axis system, is given by

$$\alpha_{0C,F} = \dot{\omega}_{0C,F} + \omega_{0F,F} \times \omega_{0C,F} = \dot{\omega}_{0F,F} + \omega_{0F,F} \times \omega_{0F,F} = \dot{\omega}_{0F,F} \tag{10.18}$$

and will contain no remaining acceleration terms, $\alpha^R_{0C,F} = 0$. The absolute acceleration of the knuckles and wheel centers, $i = 1(1)4$, is obtained by

$$\begin{aligned} a_{0i,F} &= \dot{v}_{0F,F} + \dot{\omega}_{0F,F} \times r_{Fi,F} + t_{zi,F}\ddot{z}_i + t_{ui,F}\ddot{u}_j \\ &+ \omega_{0F,F} \times \dot{r}_{Fi,F} + \dot{t}_{zi,F}\dot{z}_i + \dot{t}_{ui,F}\ddot{u}_j + \omega_{0F,F} \times v_{0i,F} \,. \end{aligned} \tag{10.19}$$

The absolute angular acceleration of the knuckles, $i = 1(1)4$, is given by

$$\begin{aligned} \alpha_{0Ki,F} &= \dot{\omega}_{0F,F} + d_{zi,F}\ddot{z}_i + d_{ui,F}\ddot{u}_j \\ &+ \dot{d}_{zi,F}\dot{z}_i + \dot{d}_{ui,F}\ddot{u}_j + \omega_{0F,F} \times \omega_{0Ki,F} \,, \end{aligned} \tag{10.20}$$

and the absolute angular acceleration of the wheels, $i = 1(1)4$, reads as

$$\begin{aligned} \alpha_{0Wi,F} &= \dot{\omega}_{0F,F} + d_{zi,F}\ddot{z}_i + d_{ui,F}\ddot{u}_j + A_{Fi}e_{yRi,i}\ddot{\varphi}_{Wi} \\ &+ \dot{d}_{zi,F}\dot{z}_i + \dot{d}_{ui,F}\ddot{u}_j + \omega_{Fi,F} \times A_{Fi}e_{yRi,i}\dot{\varphi}_{Wi} + \omega_{0F,F} \times \omega_{0Wi,F} \,. \end{aligned} \tag{10.21}$$

The lateral rack movements were abbreviated by u_j, where $u_j = u_F$ holds at the front axle ($i = 1, 2$) and $u_j = u_R$ at the rear axle ($i = 3, 4$). The last line in Equations (10.19), (10.20), and (10.21) represents the remaining terms $a^R_{0Ki,F}$, $a^R_{0Wi,F}$, and $\alpha^R_{0Ki,F}$, $\alpha^R_{0Wi,F}$, respectively, which in the case of the wheel angular acceleration include the gyroscopic torques generated by the wheel rotation. The parts in the remaining accelerations, which are generated by the time derivatives of the partial velocities and partial angular velocities, are small compared to the other parts in vehicle dynamics and may thus be neglected.

10.1.5 Applied and Generalized Forces and Torques

Similar to the procedure used in Section 8.4.1, the forces and torques applied to each body may be specified in an additional column in Tables 10.1 and 10.2 and transformed via the partial velocities and the partial angular velocities to the corresponding generalized forces and torques. This method is applied here to the weight and inertia forces and to the gyroscopic torques only. According to Equation (1.31), the contribution of body i to the vector of generalized forces and torques is given by

$$\begin{aligned} q_{(i)} &= \frac{\partial v^T_{0i,F}}{\partial z}\left(m_i g_{,F} - m_i a^R_{0i,F}\right) \\ &+ \frac{\partial \omega^T_{0i,F}}{\partial z}\left(-\Theta_{i,F}\alpha^R_{0i,F} - \omega_{0i,F} \times \Theta_{i,F}\,\omega_{0i,F}\right) \,, \end{aligned} \qquad i = 1(1)n \,. \tag{10.22}$$

The three-dimensional model for the vehicle framework consists here of $n = 9$ bodies, which in the case of translational motions are reduced to five bodies by combining each knuckle and wheel into one body. All terms are expressed in the vehicle-fixed axis system now. The applied torque $T^a_{i,F}$ is omitted, and the applied force $F^a_{i,0}$ is just replaced by the body weight $G_{i,F} = m_i g_{,F}$, where $g_{,F}$ denotes the gravity vector expressed in the vehicle-fixed axis system.

All other applied forces and torques are transformed according to Equation (6.20) to generalized ones by just applying the principle of virtual power. This was already practiced for point-to-point force elements in Section 6.1.4 and for the tire forces and torques in Section 5.3.6.

The general layout of the drive train generates braking torques between knuckle and wheel and transmits driving torques via half-shafts from the chassis-mounted differentials to the wheels. In this model approach, the wheels are described relative to the knuckle and those relative to the vehicle (chassis). Then, similar to the results achieved in Equation (8.70) for the enhanced planar model, the driving and braking torques T_{Di}, T_{Bi}, $i = 1(1)4$, will act directly as generalized torques here in the components $q(13)$ to $q(16)$. Beyond that, the driving torques T_{Di}, $i = 1(1)4$, will generate the additional terms $d_{zi}^T e_{yRi} T_{Di}$, $i = 1(1)4$, in the components $q(7)$, $q(8)$, $q(10)$, $q(11)$, which are related to the jounce and rebound motions z_1 to z_4 here.

10.1.6 Equations of Motion

The equations of motion can be generated now via Jordain's principle of virtual power. According to Section 1.4.3, the equations of motion will be provided in two sets of first-order differential equations:

$$K(y)\,\dot{y} = z\,, \tag{10.23}$$

$$M(y)\,\dot{z} = q(y,z)\,. \tag{10.24}$$

Here, the vector of the generalized coordinates and generalized velocities are determined by

$$y = \left[x, y, z,\, \alpha, \beta, \gamma,\, z_1, z_2, u_F,\, z_3, z_4, u_R,\, \varphi_{W1}, \varphi_{W2}, \varphi_{W3}, \varphi_{W4}\right]^T, \tag{10.25}$$

$$z = \left[v_x, v_y, v_z,\, \omega_x, \omega_y, \omega_z,\, \dot{z}_1, \dot{z}_2, \dot{u}_F,\, \dot{z}_3, \dot{z}_4, \dot{u}_R,\, \omega_1, \omega_2, \omega_3, \omega_4\right]^T. \tag{10.26}$$

The components of the velocity v_x, v_y, v_z and angular velocity ω_x, ω_y, ω_z are related via Equations (10.8) and (10.9) to the corresponding time derivatives $\dot{x}$, $\dot{y}$, $\dot{z}$ and $\dot{\alpha}$, $\dot{\beta}$, $\dot{\gamma}$ of the generalized coordinates. In addition, the wheel angular velocities $\omega_i = \dot{\varphi}_i$, $i = 1(1)4$ just abbreviate the time derivatives of the corresponding angles. That is why the kinematical differential equation (10.23) can easily be resolved for the time derivative of the vector of generalized coordinates.

According to Equation (1.30), the elements of the 16×16-mass-matrix are defined by the masses and the inertias of each body as well as the partial velocities and the partial angular velocities, which are provided in the Tables 10.1 and 10.2 for the three-dimensional vehicle model.

The three-dimensional model for the vehicle framework must be supplemented with separate models for the tire, the drive train, and the steering system. The sophisticated handling tire model TMeasy was presented in Chapter 3. A model for a standard drive train including differentials, the gear box,

the clutch, and the engine is discussed in Section 4.4. However, the drive train with its model and vibrational complexity can be bypassed by simply applying given or controlled driving torques directly to the wheels. A quite simple model approach of a steering system will just take the torsional compliance of the steering column and the ratio of the steering box into account, *c.f.* Section 5.3.6. Then, the rotation of the steering wheel provided as simple time history or by a driver model makes it possible to simulate different driving maneuvers.

10.2 Driver Model

10.2.1 Standard Model

Many driving maneuvers require inputs by the driver at the steering wheel and the gas pedal that depend on the actual state of the vehicle. A real driver takes a lot of information provided by the vehicle and the environment into account. He acts anticipatory and adapts his reactions to the dynamics of the particular vehicle. The modeling of human actions and reactions is a challenging task. That is why driving simulators operate with real drivers instead of driver models. However, offline simulations will require a suitable driver model.

Usually, driver models are based on simple, mostly linear vehicle models where the motion of the vehicle is reduced to horizontal movements and the wheels on each axle are lumped together [48]. Standard driver models, like the one shown in Figure 10.2, usually consist of two levels: anticipatory feed-

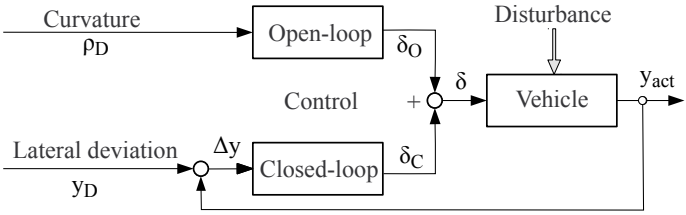

FIGURE 10.2
Two-level control driver model [22].

forward (open-loop) and compensatory (closed-loop) control. The properties of the vehicle model and the capability of the driver are used to design appropriate transfer functions for the open- and closed-loop control. The model includes a path prediction and takes the reaction time of the driver into account.

10.2.2 Enhanced Model

Different from technical controllers, a human driver normally does not simply follow a given trajectory, but sets the target course within given constraints (i.e., road width or lane width), Figure 10.3. At the anticipation level, the

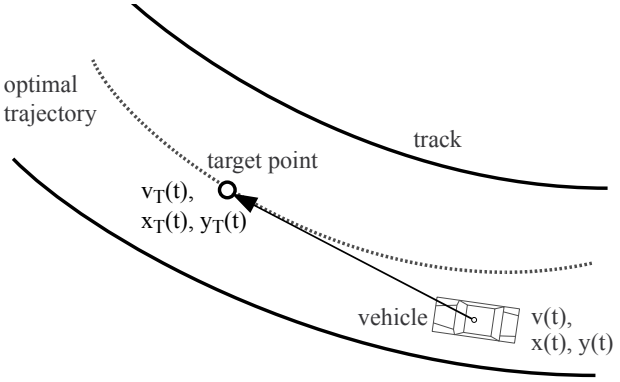

FIGURE 10.3
Enhanced driver model.

optimal trajectory for the vehicle is predicted by repeatedly solving optimal control problems for a nonlinear bicycle model whereas on the stabilization level, a position control algorithm precisely guides the vehicle along the optimal trajectory [47]. The result is a virtual driver who is able to guide the virtual vehicle on a virtual road at high speeds as well as in limit situations where skidding and sliding effects take place. A broad variety of drivers ranging from unskilled to skilled or aggressive to nonaggressive can be described by this driver model [14].

10.2.3 Simple Approach

Many driving maneuvers require a constant or a slowly varying driving velocity. The average of all circumferential wheel velocities,

$$v_W = \frac{1}{4}\sum_{i=1}^{4} r_{Di}\Omega_i \,, \tag{10.27}$$

approximates the driving velocity v_D quite well. Here, r_{Di} is the dynamic tire radius and Ω_i describes the absolute angular velocity of each wheel, $i = 1(1)4$. Then, a simple p-controller,

$$T_D \;=\; p_D\,(v_D - v_W) \;, \tag{10.28}$$

may be used to generate an appropriate driving torque, which will be distributed to the wheels according to the layout of the driving system. Of course, the control parameter p_D must be adjusted to the specific vehicle properties.

Open-loop maneuvers, like a steering step input, are operated simply by providing the steering wheel angle as a function of time. Keeping a vehicle on a straight line when driving on a rough road or performing a steady-state cornering on a circle with given radius will require an appropriate controller. Again, a p-control applied to the steering wheel angular velocity may serve as a simple driver model. In the case of steady-state cornering, the controller

$$\dot{\delta}_{SW} = p_{SW}\left(\frac{v_D}{R} - \omega_{0F,0}(3)\right) \tag{10.29}$$

generates the angular steering wheel velocity $\dot{\delta}_{SW}$ proportional to the deviation of actual yaw velocity, which is provided by the third component $\omega_{0F,0}(3)$ of the angular velocity of the vehicle-fixed axis system, from the desired yaw velocity $\omega_z = v_D/R$ when cornering with the velocity v_D on the radius R. Again, the control parameter p_{SW} must be chosen appropriately.

10.3 Standard Driving Maneuvers

10.3.1 Steady-State Cornering

The steering tendency of a real vehicle is determined by the driving maneuver called steady-state cornering. The maneuver is performed quasi-static. The driver tries to keep the vehicle on a circle with the given radius R. He slowly increases the driving speed v and, due to $a_y = v^2/R$, also the lateral acceleration until reaching the limit. Whereas in the simulation a perfectly flat road is easily realized, field test, will usually be characterized by slight disturbances induced by a nonperfect road surface, Figure 10.4. The simulation

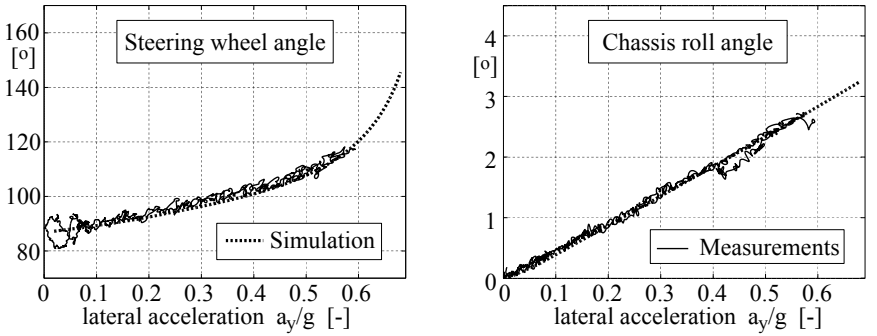

FIGURE 10.4
Steady-state cornering: Front-wheel driven passenger car.

results, obtained with a sophisticated three-dimensional vehicle model [46],

match quite well with the measurements. The passenger car has a mass of $m = 1450\,kg$ and a wheel base of $a = 2.7\,m$. The center of gravity is located closer to the front axle, $a = 1.1\,m$, which is typical for front-wheel driven cars. The maneuver was performed on a circle of radius $R = 30\,m$ here. To drive this radius with low lateral acceleration, $a_y \to 0$, a steering angle at the front wheel of $\delta_A = \arctan(2.7/30) = 0.0898 \equiv 5.143°$ will be required. Inspecting Figure 10.4 yields a steering wheel angle of $\delta_{SW}^{a_y \to 0} \approx 87°$, which results in a overall steering ratio of $i_S = 87°/5.143° = 17$. The inclination in the diagram steering angle versus lateral velocity decides about the steering tendency and stability behavior. The tendency to understeer is significant in the whole acceleration range here. When approaching the limit range, which may be estimated by $a_y^{max} \approx 0.8\,g$, the understeer tendency and, as a consequence, the stability of the vehicle too, increase more and more. The roll angle of the vehicle increases in proportion to the lateral acceleration with a ratio of approximately $4.8°/g$.

Typical results for a rear-wheel driven car are displayed in Figure 10.5. The passenger car has mass of $m = 1300\,kg$ and a wheel base $a = 2.57\,m$.

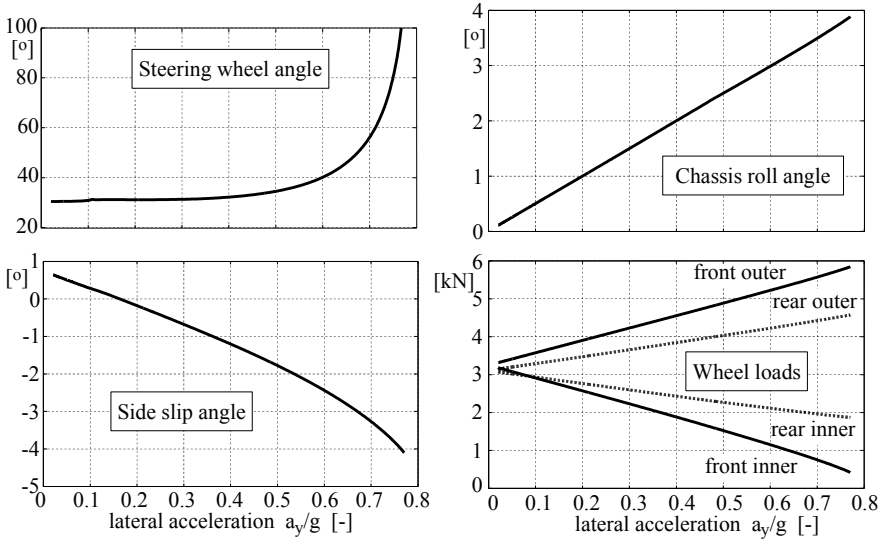

FIGURE 10.5
Steady-state cornering: Rear-wheel driven car.

The center of gravity is located nearly in the midst, at $a = 1.25\,m$, which is quite typical for rear-wheel driven cars. The vehicle is driven on a radius of $R = 100\,m$ now, which means that the potential limit range $a_y^{limit} = 0.8\,g$ is

reached at velocity

$$v^{limit} = \sqrt{a_y^{limit} R} = \sqrt{0.8 * 9.81 * 100} = 28\, m/s \quad \text{or} \quad v^{limit} = 100.8\, km/h\,. \tag{10.30}$$

This corresponds quite well with the typical travel velocity on country roads in Europe. Estimating the overall steering ratio by inspecting the upper-left plot in Figure 10.5 and computing the Ackermann angle results in $i_S = \delta_{SW}/\delta_A = 30°/1.4722° = 20.4$. In the low acceleration range, the steering tendency is nearly neutral, which is the result of nearly equal loads at the front and rear axle. The nonlinear influence of the wheel load on the tire performance is used here to design a vehicle that is weakly stable but sensitive to steer input in the lower range of lateral acceleration, and is very stable but less sensitive to steer input in the limit range. The roll angle of the vehicle increases in proportion to the lateral acceleration with a ratio of approximately $5°/g$ here.

The side slip angle, measured at the vehicle center, starts with the value $\beta^{a_y \to 0} \approx 0.75°$, which coincides with the Ackermann value $\beta^{st} = \arctan(a_2/R) = \arctan(2.57-1.25)/100 = 0.0132 \equiv 0.756°$. It changes sign at $a_y^{\beta_{st}=0} \approx 0.16\,g$. Inserting this value into Equation (9.147) delivers cornering stiffness at the rear axle of

$$c_{S2} = \frac{a_1 R\, m\, a_y^{\beta_{st}=0}}{a_2\,(a_1 + a_2)} = \frac{1.25 * 100 * 1300 * 0.16 * 9.81}{(2.57 - 1.25) * 2.57} = 75\,186\, N/m \tag{10.31}$$

which indicates rather soft tires but corresponds to the fact that the vehicle under consideration is an older one. The steering gradient, which was estimated here with $k \approx 0$, is defined in Equation (9.144). It can also be used to determine the cornering stiffness c_{S1} of the front axle.

The overturning torque is intercepted by according wheel load differences between the outer and inner wheels. With a sufficiently rigid frame, the use of an anti-roll bar at the front axle allows for increasing the wheel load difference there and for decreasing it at the rear axle accordingly. Thus, the degressive influence of the wheel load on tire properties, cornering stiffness, and maximum possible lateral forces, is stressed more strongly at the front axle, and the vehicle becomes more under-steering and stable at increasing lateral acceleration, until it drifts out of the curve over the front axle in the limit situation. Problems occur with front-wheel driven vehicles, because due to the demand for traction, the front axle cannot be relieved at will.

Having a sufficiently large test site, the steady-state cornering maneuver can also be carried out at constant speed. There, the steering wheel is slowly turned until the vehicle reaches the limit range. That way, weakly motorized vehicles can also be tested at high lateral accelerations.

10.3.2 Step Steer Input

The dynamic response of a vehicle is often tested with a step steer input. Methods for the calculation and evaluation of an ideal response, as used in

system theory or control techniques, cannot be used with a real car, as a step input at the steering wheel is not possible in practice. A real steering angle gradient is displayed in Figure 10.6. Note that the angle at the steering wheel

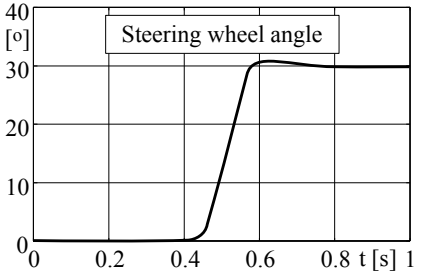

FIGURE 10.6
Time history of a typical step steer input.

is the decisive factor for the driving behavior, but the steering angle at the wheels, which can differ from the steering wheel angle because of elasticities, friction influences, and a servo-support. For very fast steering movements, the dynamics of the tire forces also play an important role.

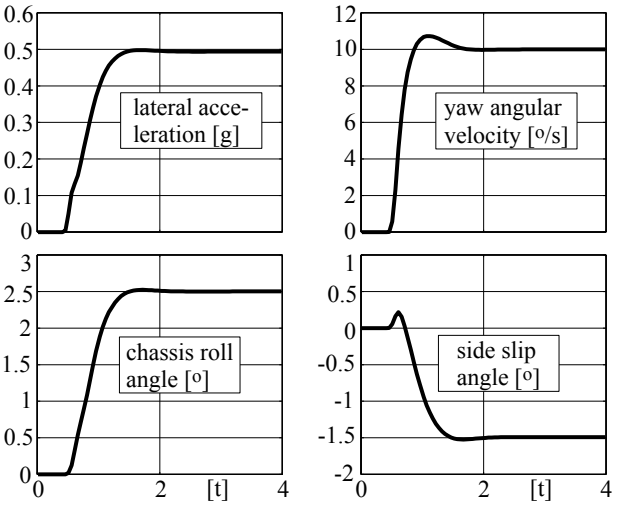

FIGURE 10.7
Step steer: Passenger car at $v = 100\,km/h$.

In practice, a step steer input is usually only used to judge vehicles subjectively, Figure 10.7. Exceedances in yaw velocity, roll angle, and especially side slip angle are felt as annoying. The vehicle under consideration behaves dynamically very well. Almost no overshoots occur in the time history of the roll

angle and the lateral acceleration. However, small overshoots can be noticed at the yaw velocity and the side slip angle.

10.3.3 Driving Straight Ahead

The irregularities of a track are of a stochastic nature in general. As discussed in Section 2.3, stochastic track irregularities may be characterized by a reference power spectral density and the waviness. A straightforward drive on an uneven track makes continuous steering corrections necessary. The histograms of the steering angle at a driving speed of $v = 90\,km/h$ are displayed in Figure 10.8. The track quality is reflected in the amount of steering actions. The steering activity is often used to judge a vehicle in practice or to compare different vehicles or vehicle concepts.

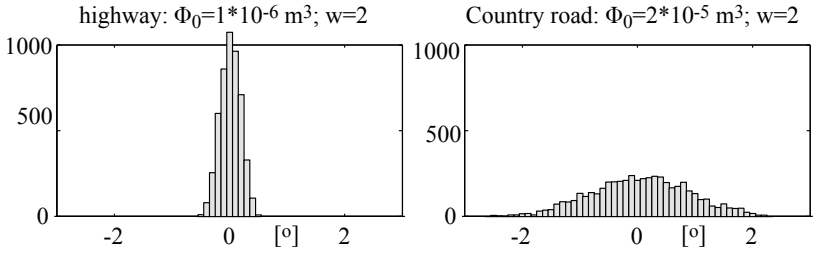

FIGURE 10.8
Steering activity on different roads.

10.4 Coach with Different Loading Conditions

10.4.1 Data

The difference between empty and laden is sometimes very large at trucks and coaches. All relevant data of a travel coach under fully laden and empty conditions are listed in Table 10.3.

The coach has a wheel base of $a = 6.25\,m$. The front axle with the track width $s_v = 2.046\,m$ has a double wishbone, single-wheel suspension. The twin-tire rear axle with track widths $s_h^o = 2.152\,m$ and $s_h^i = 1.492\,m$ is guided by two longitudinal links and an A-arm. The air springs are fitted to load variations via a niveau control.

TABLE 10.3
Data for a Laden and Empty Coach

Vehicle	Mass $[kg]$	Center of Gravity $[m]$	Inertias $[kg\,m^2]$
Empty	12 500	$-3.800 \mid 0.000 \mid 1.500$	12 500 0 0 0 155 000 0 0 0 155 000
Fully laden	18 000	$-3.860 \mid 0.000 \mid 1.600$	15 400 0 250 0 200 550 0 250 0 202 160

10.4.2 Roll Steering

While the kinematics at the front axle hardly cause steering movements at roll motions, the kinematics at the rear axle are tuned in a way to cause a notable roll steering effect, Figure 10.9. This is achieved by moving the wheel

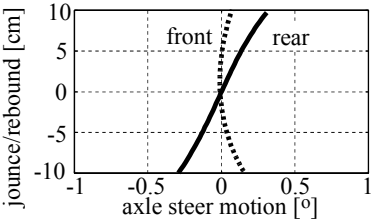

FIGURE 10.9
Roll steer motion of a solid axle.

center on jounce to the front and on rebound to the rear. As a solid axle rigidly connects both wheels, this will cause the axle to rotate about the vertical axis, thus performing a steer motion when the chassis rolls and the outer wheel is forced to a jounce and the inner to a rebound motion.

10.4.3 Steady-State Cornering

Some results of a steady-state cornering on a radius of $R = 100\,m$ are plotted in Figure 10.10. The fully laden vehicle is slightly more understeering than the empty one. The roll steer behavior affects the steering tendency differently, because the laden vehicle exhibits a larger roll motion when cornering. In general, vehicles with a twin-tired solid axle at the rear exhibit a basic understeer tendency. When cornering to the left, the forward velocities of the tire centers at the rear axle will increase from the inner left to the outer right, Figure 10.11. Taking driving or braking maneuvers not into account, each rear wheel will rotate with an average angular velocity Ω_R, which results from the

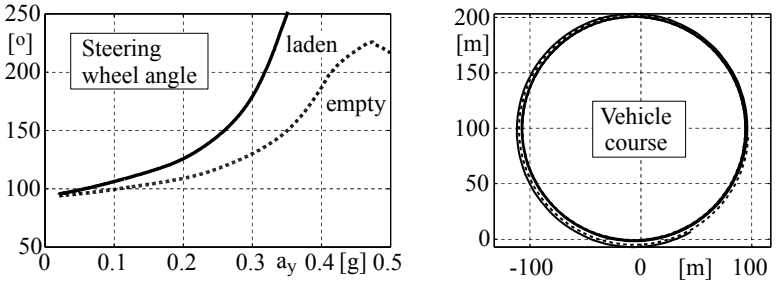

FIGURE 10.10
Coach at steady-state cornering.

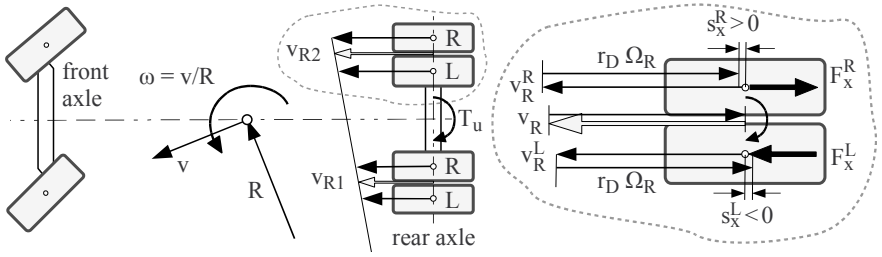

FIGURE 10.11
Vehicle with a twin-tired solid rear axle while cornering to the left.

rolling condition $v_R = r_D \Omega_R$, where r_D is the dynamic rolling radius and $v_R = \frac{1}{2}\left(v_R^R + v_R^L\right)$ represents the average forward velocity of the right and the left tire center. As both twin tires are forced to rotate with the same angular velocity, positive $s_x^R > 0$ and negative $s_x^L > 0$ longitudinal slips will result at the right and left tire as a consequence. The thereby caused couple of longitudinal forces F_x^R, F_x^L generates a torque about the vertical axes, which acts in the opposite direction of the yaw velocity ω of the vehicle. The same effect, which is similar to the tire bore torque mechanism, occurs on both wheels and adds to a significant torque T_u, thus producing the understeer tendency of those vehicles. The higher wheel loads of the laden coach will amplify this understeer effect, in addition.

The simulation was performed with p-controllers for the driving torque and the steering wheel angular velocity, which are provided in Equations (10.28) and (10.29). Despite the simple driver model, the coach is kept on a circled path quite well. When approaching the limit range, the understeer tendency of the laden coach is increasing rapidly, which results in a slight increase in the curve radius.

Due to the relatively high position of the center of gravity, the maximal lateral acceleration is limited by the overturning hazard. For the empty vehicle, the inner front wheel lifts off at a lateral acceleration of $a_y \approx 0.4\,g$, right plot

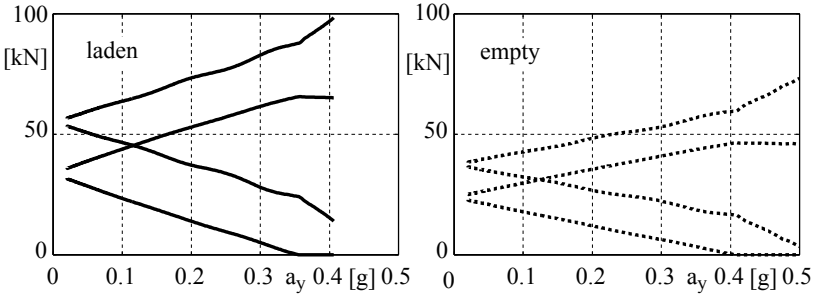

FIGURE 10.12
Wheel loads of a coach at steady-state cornering.

in Figure 10.12. If the vehicle is fully laden, this effect will occur at a lateral acceleration of $a_y \approx 0.35\,g$, left plot in Figure 10.12.

10.4.4 Step Steer Input

The results of a step steer input at the driving velocity of $v = 80\,km/h$ can be seen in Figure 10.13. To achieve comparable acceleration values in steady-

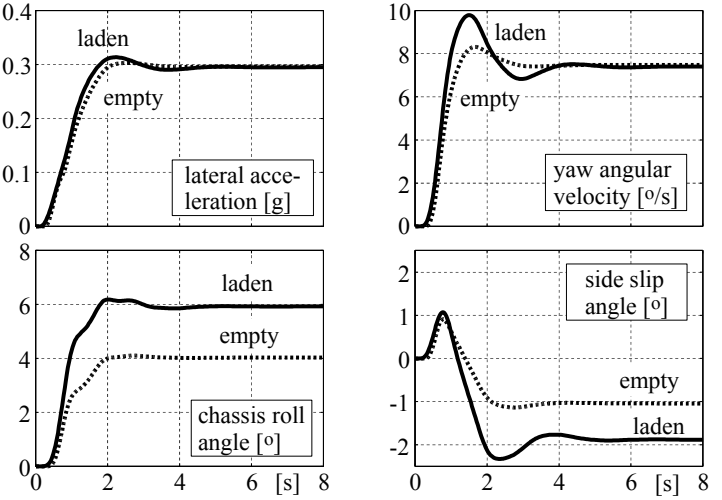

FIGURE 10.13
Step steer input to coach.

state condition, the step steer input was done for the empty vehicle with $\delta = 90°$ and for the fully laden one with $\delta = 135°$. The steady-state roll angle is 50% larger at the fully laden coach than at the empty one. By the niveau control, the air spring stiffness increases with the load. Because the damper

effect remains unchanged, the fully laden vehicle is not damped as well as the empty one. This results in larger overshoots in the time histories of the lateral acceleration, the yaw angular velocity, and the side slip angle.

10.5 Different Rear Axle Concepts for a Passenger Car

A medium-sized passenger car is equipped in standard design with a semi-trailing rear axle. By accordingly changed data, this axle can easily be transformed into a trailing arm or a single wishbone suspension. According to the roll support, the semi-trailing axle realized in serial production represents a compromise between the trailing arm and the single wishbone suspension, Figure 10.14. The influences on the driving behavior at steady-state corner-

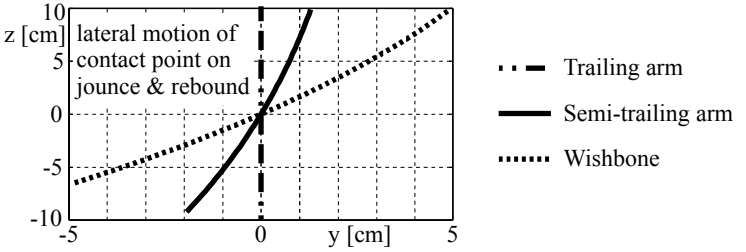

FIGURE 10.14
Kinematics of different rear axle concepts.

ing on a radius of $R = 100\,m$ are shown in Figure 10.15. Substituting the semi-trailing arm on the standard car by a single wishbone, one gets, without adaption of the other system parameters, a vehicle oversteering in the limit range. Compared to the semi-trailing arm, the single wishbone causes a notably higher roll support. This increases the wheel load difference at the rear axle, Figure 10.15. Because the wheel load difference simultaneously decreases at the front axle, the understeering tendency decreases. In the limit range, this even leads to an oversteering behavior. The vehicle with a trailing arm rear axle is, compared to the serial car, more understeering. The lack of roll support at the rear axle also causes a larger roll angle.

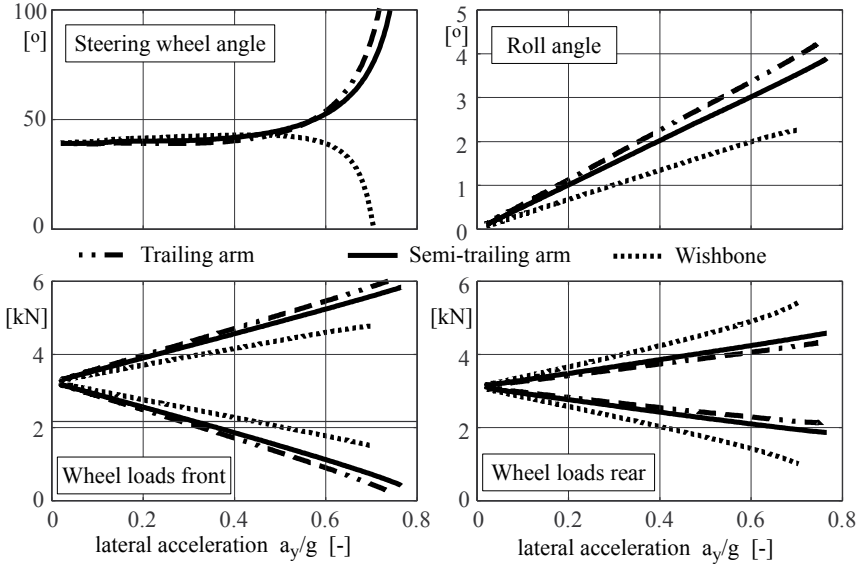

FIGURE 10.15
Steady-state cornering with different rear axle concepts.

Exercises

10.1 The solid lines represent the results of a passenger car at steady-state cornering.

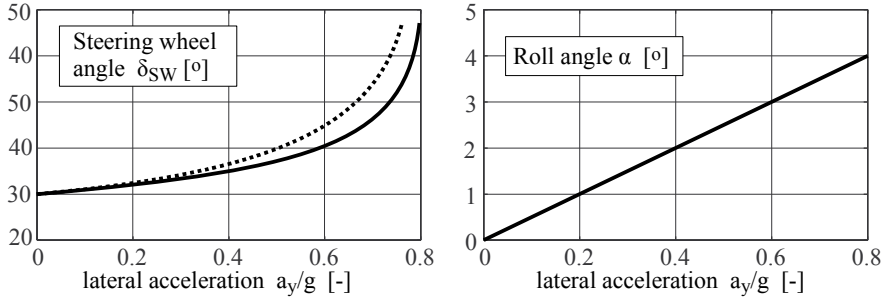

Name at least two actions that must be taken to change the steering tendency of the car to the one defined by the broken line. Will these actions affect the roll angle too?

10.2 The plot shows the results of a steady-state cornering performed with a sports car on a radius of $R = 100\,m$, where the side slip angle was measured at the vehicle's center of gravity.

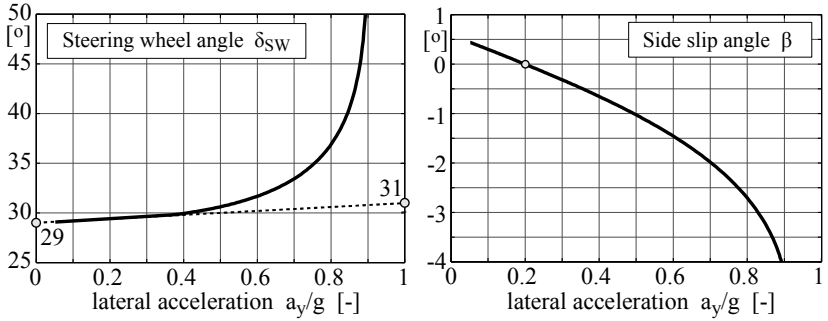

The sports car has a wheelbase of $a = 2.35\,m$ and the wheel loads at the front and rear axle are specified by 5600 N and 7000 N.

Compute the mass m and the location (a_1, a_2) of the center of gravity with respect to the front and the rear axle.

Calculate the average steering angle δ_A at the front wheels and the side slip angle β_A at the vehicle's center of gravity that hold according to Ackermann when driving with nearly vanishing lateral acceleration $a_y \to 0$ on the given radius.

Compute the overall steering ratio defined by $i_S = \delta_{SW}/\delta_A$, where δ_{SW} denotes the steering wheel angle at $a_y \to 0$ and δ_A is the Ackermann steering angle.

Calculate the cornering stiffness c_{SR} at the rear axle, the steering gradient, which according to Equation (9.144) will be defined here by

$$k = \frac{1}{i_S} \frac{d\,\delta_{SW}}{d\,a_y} ,$$

and the cornering stiffness c_{SF} at the front axle, which will all be valid in the low acceleration range.

10.3 A passenger car performs a step steer maneuver at the driving velocity of $v = 120\,km/h$.

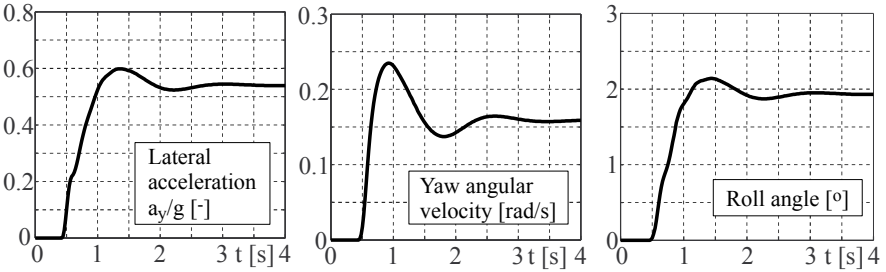

Judge the results.

At what radius is the vehicle driving at the end of the maneuver ($t = 4\,s$)?

How will the plots change if the anti-roll bar stiffness at the rear axle is doubled?

Bibliography

[1] D. Bestle and M. Beffinger. Design of progressive automotive shock absorbers. In *Proceedings of Multibody Dynamics*, Madrid, 2005.

[2] M. Blundell and D. Harty. *The Multibody System Approach to Vehicle Dynamics*. Elsevier Butterworth-Heinemann Publications, 2004.

[3] H. Braun. *Untersuchung von Fahrbahnunebenheiten und Anwendung der Ergebnisse*. PhD thesis, TU Braunschweig, 1969.

[4] T. Butz, M. Ehmann, and T.-M. Wolter. A realistic road model for real-time vehicle dynamics simulation. *Society of Automotive Engineers*, SAE Paper 2004-01-1068, 2004.

[5] Open-Source-Project CRG. *www.opencrg.org*, July 2010.

[6] C. J. Dodds and J. D. Robson. The description of road surface roughness. *Journal of Sound and Vibration*, 31(2):175–183, 1973.

[7] P. Dorato, C. Abdallah, and V. Cerone. *Linear-Quadratic Control. An Introduction*. Prentice-Hall, Englewood Cliffs, New Jersey, 1995.

[8] M. Eichler, A. Lion, U. Sonnak, and R. Schuller. Dynamik von Luftfedersystemen mit Zusatzvolumen: Modellbildung, Fahrzeugsimulationen und Potenzial. Bericht 1791, VDI, 2003.

[9] P. Fickers and B. Richter. Incorporating FEA-techniques into MSA illustrated by several rear suspension concepts. In *9th European ADAMS User Conference*, Frankfurt, 1994.

[10] M. Gipser. Ftire, a new fast tire model for ride comfort simulations. In *International ADAMS User Conference*, Berlin, 1999.

[11] Robert Bosch GmbH, editor. *Bosch Automotive Handbook*. Wiley (distributor), Hoboken, New Jersey, Chichester, 7th edition, 2007.

[12] W. Hirschberg, G. Rill, and H. Weinfurter. User-appropriate tyre-modeling for vehicle dynamics in standard and limit situations. *Vehicle System Dynamics*, 38(2):103–125, 2002.

[13] W. Hirschberg, H. Weinfurter, and Ch. Jung. Ermittlung der Potenziale zur LKW-Stabilisierung durch Fahrdynamiksimulation. In *Berechnung und Simulation im Fahrzeugbau*. VDI, 14.-15. Sept. 2000.

[14] M. Irmscher and M. Ehmann. Driver classification using ve-dyna advanced driver. *SAE International*, 01-0451, 2004.

[15] ISO 2631. Mechanical vibration and shockevaluation of human exposure to whole-body vibration. *International Standard (ISO)*, 1997.

[16] ISO 8608. Mechanical vibration - road surface profiles - reporting of measured data. *International Standard (ISO)*, 1995.

[17] P. van der Jagt. *The Road to Virtual Vehicle Prototyping; New CAE-Models for Accelerated Vehicle Dynamics Development.* ISBN 90-386-2552-9 NUGI 834, Tech. Univ. Eindhoven, 2000.

[18] R. T. Kane and D. A. Levinson. Formulation of equations of motion for complex spacecraft. *Journal of Guidance and Control*, 3(2):99–112, 1980.

[19] U. Kiencke and L. Nielsen. *Automotive Control Systems.* Springer, 2000.

[20] W. Kortüm and P. Lugner. *Systemdynamik und Regelung von Fahrzeugen.* Springer, 1993.

[21] P. Lugner and M. Plöchl. *Tire Model Performance Test (TMPT).* Taylor & Francis, 2007.

[22] M. Mitschke and H. Wallentowitz. *Dynamik der Kraftfahrzeuge, 4. Auflage.* Springer, 2004.

[23] P.C. Müller and W.O. Schiehlen. *Lineare Schwingungen.* Akad. Verlagsgesellschaft, Wiesbaden, 1976.

[24] U. Neureder. *Untersuchungen zur Übertragung von Radlastschwankungen auf die Lenkung von Pkw mit Federbeinvorderachse und Zahnstangenlenkung*, volume 12(518) of *Fortschritt-Berichte VDI.* VDI-Verlag, Düsseldorf, 2002.

[25] Parviz E. Nikravesh. *Computer-Aided Analysis of Mechanical Systems.* Prentice Hall, Englewood Cliffs, New Jersey, 1988.

[26] Ch. Oertel and A. Fandre. Ride comfort simulations and steps towards life time calculations; RMOD-K and ADAMS. In *International ADAMS User Conference*, Berlin, 1999.

[27] H.B. Pacejka and E. Bakker. The magic formula tyre model. In *1st Int. Colloquium on Tyre Models for Vehicle Dynamic Analysis*, Lisse, 1993. Swets&Zeitlinger.

[28] K. Popp and W. Schiehlen. *Fahrzeugdynamik.* Teubner, Stuttgart, 1993.

[29] K. Popp and W.O. Schiehlen. *Ground Vehicle Dynamics.* Springer, Berlin, 2010.

[30] J. Rauh. Virtual development of ride and handling characteristics for advanced passenger cars. *Vehicle System Dynamics*, 40(1–3):135–155, 2003.

[31] A. Riepl, W. Reinalter, and G. Fruhmann. Rough road simulation with tire model RMOD-K and FTire. In *Proceedings of the 18th IAVSD Symposium on the Dynamics of Vehicles on Roads and on Tracks. Kanagawa, Japan*, London, 2003. Taylor & Francis.

[32] G. Rill. The influence of correlated random road excitation processes on vehicle vibration. In K. Hedrik, editor, *The Dynamics of Vehicles on Road and on Tracks*, Lisse, 1984. Swets-Zeitlinger.

[33] G. Rill. Demands on vehicle modeling. In R.J. Anderson, editor, *The Dynamics of Vehicles on Road and on Tracks*, Lisse, 1990. Swets-Zeitlinger.

[34] G. Rill. *Simulation von Kraftfahrzeugen.* Vieweg, Braunschweig, 1994.

[35] G. Rill. Vehicle modeling for real time applications. *Journal of the Brazilian Society of Mechanical Sciences - RBCM*, XIX(2):192–206, 1997.

[36] G. Rill. First order tire dynamics. In *Proceedings of the III European Conference on Computational Mechanics Solids, Structures and Coupled Problems in Engineering*, Lisbon, Portugal, 2006.

[37] G. Rill. A modified implicit euler algorithm for solving vehicle dynamic equations. *Multibody System Dynamics*, 15(1):1–24, 2006.

[38] G. Rill. Vehicle modeling by subsystems. *Journal of the Brazilian Society of Mechanical Sciences& Engineering - ABCM*, XXVIII(4):431–443, 2006.

[39] G. Rill. Wheel dynamics. In *Proceedings of the XII International Symposium on Dynamic Problems of Mechanics (DINAME 2007)*, 2007.

[40] G. Rill and C. Chucholowski. A modeling technique for fast computer simulations of configurable vehicle systems. In *Proceedings of the 21st International Congress of Theoretical and Applied Mechanics (ICTAM)*, Warsaw, Poland, 2004.

[41] G. Rill and C. Chucholowski. Modeling concepts for modern steering systems. In *ECCOMAS Multibody Dynamics*, Madrid, Spain, 2005.

[42] G. Rill, N. Kessing, O. Lange, and J. Meier. Leaf spring modeling for real time applications. In *The Dynamics of Vehicles on Road and on Tracks - Extensive Summaries, IAVSD 03*, 2003.

[43] G. Rill and J. Rauh. Simulation von Tankfahrzeugen. In *Berechnung im Automobilbau, VDI-Bericht 1007*, Düsseldorf, 1992. VDI.

[44] G. Rill and Th. Schaeffer. *Grundlegende Methoden der Mehrkörpersimulation: mit Anwendungsbeispielen.* Vieweg+Teubner, Wiesbaden, 2010.

[45] G. Rill and W. Schiehlen. Performance assessment of time integration methods for vehicle dynamics simulations. In K. Arczewski and J. Fraczek, editors, *Multibody Dynamics 2009 (ECCOMAS Thematic Conference, Warsaw, Poland, June 29 to July 2, 2009)*, Warsaw, 2009. Faculty of Power and Aeronautical Engineering, Warsaw University of Technology, 2009.

[46] Th. Seibert and G. Rill. Fahrkomfortberechnungen unter Einbeziehung der Motorschwingungen. In *Berechnung und Simulation im Fahrzeugbau, VDI-Bericht 1411*, Düsseldorf, 1998. VDI.

[47] M. Vögel, O. von Stryk, R. Bulirsch, T.-M. Wolter, and C. Chucholowski. An optimal control approach to real-time vehicle guidance. In W. Jäger and H.-J. Krebs, editors, *Mathematics – Key Technology for the Future*, pages 84–102, Berlin, 2003. Springer.

[48] M. Weigel, P. Lugner, and M. Plöchl. A driver model for a truck-semitrailer combination. *Vehicle System Dynamics Supplement*, 41:321–331, 2004.

[49] H. Weinfurter, W. Hirschberg, and E. Hipp. Entwicklung einer Störgrößenkompensation für Nutzfahrzeuge mittels Steer-by-Wire durch Simulation. In *Berechnung und Simulation im Fahrzeugbau, VDI-Berichte 1846*, pages 923–941, Düsseldorf, 2004. VDI.

Index

Mechanical Engineering

In striving for optimal comfort and safety conditions in road vehicles, today's electronically controlled components provide a range of new options. These are developed and tested using computer simulations in software-in-the-loop or hardware-in-the-loop environments—an advancement that requires the modern automotive engineer to be able to build basic simulation models, handle higher level models, and operate simulation tools effectively.

Combining the fundamentals of vehicle dynamics with the basics of computer-simulated modeling, **Road Vehicle Dynamics: Fundamentals and Modeling** draws on lecture notes from undergraduate and graduate courses given by the author, as well as industry seminars and symposiums, to provide practical insight on the subject. Requiring only a first course in dynamics and programming language as a prerequisite, this highly accessible book offers end-of-chapter exercises to reinforce concepts as well as programming examples and results using MATLAB®.

The book uses SI-units throughout, and begins with an introduction and overview of units and quantities, terminology and definitions, multibody dynamics, and equations of motion. It then discusses the road, highlighting both deterministic and stochastic road models; tire handling including contact calculation, longitudinal and lateral forces, vertical axis torques, and measurement and modeling techniques; and drive train components and concepts such as transmission, clutch, and power source.

Later chapters discuss suspension systems, including a dynamic model of rack-and-pinion steering as well as double-wishbone suspension systems; force elements such as springs, anti-roll bars, and hydro-mounts; and vehicle dynamics in vertical, longitudinal, and lateral directions using a simple model approach to examine the effects of nonlinear, dynamic, and active force elements. Highlighting useable knowledge, the book concludes with a three-dimensional vehicle model and typical results of standard driving maneuvers

K11773

CRC Press
Taylor & Francis Group
an **informa** business
www.crcpress.com

6000 Broken Sound Parkway, NW
Suite 300, Boca Raton, FL 33487
711 Third Avenue
New York, NY 10017
2 Park Square, Milton Park
Abingdon, Oxon OX14 4RN, UK

ISBN: 978-1-4398-3898-3
90000
9 781439 838983